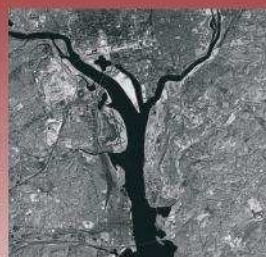


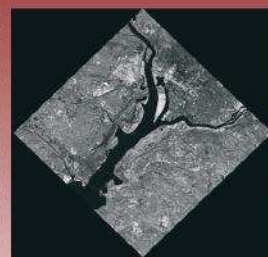
*brain*



*histogram equal*



*Washington, DC*



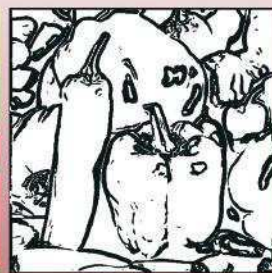
*rotated*

# Introduction to Digital Image Processing

William K. Pratt



*peppers*



*edge map*



*SMPTE girl*



*Haar wavelet*

# Introduction to Digital Image Processing



# Introduction to Digital Image Processing

William K. Pratt



CRC Press

Taylor & Francis Group

Boca Raton London New York

---

CRC Press is an imprint of the  
Taylor & Francis Group, an **informa** business

CRC Press  
Taylor & Francis Group  
6000 Broken Sound Parkway NW, Suite 300  
Boca Raton, FL 33487-2742

© 2014 by Taylor & Francis Group, LLC  
CRC Press is an imprint of Taylor & Francis Group, an Informa business

No claim to original U.S. Government works  
Version Date: 20130808

International Standard Book Number-13: 978-1-4822-1670-7 (eBook - PDF)

This book contains information obtained from authentic and highly regarded sources. Reasonable efforts have been made to publish reliable data and information, but the author and publisher cannot assume responsibility for the validity of all materials or the consequences of their use. The authors and publishers have attempted to trace the copyright holders of all material reproduced in this publication and apologize to copyright holders if permission to publish in this form has not been obtained. If any copyright material has not been acknowledged please write and let us know so we may rectify in any future reprint.

Except as permitted under U.S. Copyright Law, no part of this book may be reprinted, reproduced, transmitted, or utilized in any form by any electronic, mechanical, or other means, now known or hereafter invented, including photocopying, microfilming, and recording, or in any information storage or retrieval system, without written permission from the publishers.

For permission to photocopy or use material electronically from this work, please access [www.copyright.com](http://www.copyright.com) (<http://www.copyright.com/>) or contact the Copyright Clearance Center, Inc. (CCC), 222 Rosewood Drive, Danvers, MA 01923, 978-750-8400. CCC is a not-for-profit organization that provides licenses and registration for a variety of users. For organizations that have been granted a photocopy license by the CCC, a separate system of payment has been arranged.

**Trademark Notice:** Product or corporate names may be trademarks or registered trademarks, and are used only for identification and explanation without intent to infringe.

**Visit the Taylor & Francis Web site at**  
**<http://www.taylorandfrancis.com>**

**and the CRC Press Web site at**  
**<http://www.crcpress.com>**

*To my wife Joan who has brightened my life*



# CONTENTS

<b>Preface</b>	<b>vii</b>
<b>Acknowledgments</b>	<b>xi</b>
<b>Preamble</b>	<b>xv</b>
<b>Notation</b>	<b>xvii</b>
<b>PART 1 CONTINUOUS IMAGE CHARACTERIZATION</b>	<b>1</b>
<b>1 Continuous Image Mathematical Characterization</b>	<b>3</b>
1.1 Image Representation, 3	
1.2 Two-Dimensional Systems, 5	
1.3 Two-Dimensional Fourier Transform, 10	
1.4 Image Stochastic Characterization, 14	
1.5 Program Generation Exercises, 19	
<b>2 Psychophysical Vision Properties</b>	<b>21</b>
2.1 Light Perception, 21	
2.2 Eye Physiology, 24	
2.3 Visual Phenomena, 27	
2.4 Monochrome Vision Model, 31	



ii CONTENTS

- 2.5 Color Vision Model, 37
- 2.6 Image Manipulation Exercises, 39

**3 Photometry and Colorimetry 43**

- 3.1 Photometry, 43
- 3.2 Color Matching, 47
- 3.3 Colorimetry Concepts, 52
- 3.4 Color Spaces, 57
- 3.5 Color Space Exercises, 81

**PART 2 DIGITAL IMAGE CHARACTERIZATION 85**

**4 Image Sampling and Reconstruction 87**

- 4.1 Image Sampling and Reconstruction Concepts, 87
- 4.2 Monochrome Image Sampling Systems, 95
- 4.3 Monochrome Image Reconstruction Systems, 104
- 4.4 Color Image Sampling Systems, 110
- 4.5 Image Measurement Exercises, 115

**5 Image Quantization 119**

- 5.1 Scalar Quantization, 119
- 5.2 Processing Quantized Variables, 124
- 5.3 Monochrome and Color Image Quantization, 126
- 5.4 Image Quantization Exercises, 133

**PART 3 DISCRETE TWO-DIMENSIONAL LINEAR PROCESSING 137**

**6 Discrete Image Mathematical Characterization 139**

- 6.1 Vector-Space Image Representation, 139
- 6.2 Generalized Two-Dimensional Linear Operator, 141
- 6.3 Image Statistical Characterization, 145
- 6.4 Image Probability Density Models, 150
- 6.5 Linear Operator Statistical Representation, 153
- 6.6 Region-of-Interest Exercises, 155

**7 Superposition and Convolution 157**

- 7.1 Finite-Area Superposition and Convolution, 157
- 7.2 Sampled Image Superposition and Convolution, 166
- 7.3 Circulant Superposition and Convolution, 173



<b>12</b>	<b>Geometrical Image Modification</b>	<b>349</b>
12.1	Basic Geometrical Methods, 349	
12.2	Spatial Warping, 359	
12.3	Geometrical Image Resampling, 364	
12.4	Geometrical Image Modification Exercises, 369	
<b>PART 5</b>	<b>IMAGE ANALYSIS</b>	<b>373</b>
<b>13</b>	<b>Morphological Image Processing</b>	<b>375</b>
13.1	Binary Image Connectivity, 375	
13.2	Binary Image Hit or Miss Transformations, 378	
13.3	Binary Image Shrinking, Thinning, Skeletonizing and Thickening, 385	
13.4	Binary Image Generalized Dilation and Erosion, 396	
13.5	Binary Image Close and Open Operations, 405	
13.6	Gray Scale Image Morphological Operations, 406	
13.7	Morphological Image Processing Exercises, 412	
<b>14</b>	<b>Edge Detection</b>	<b>415</b>
14.1	Edge, Line and Spot Models, 415	
14.2	First-Order Derivative Edge Detection, 421	
14.3	Second-Order Derivative Edge Detection, 444	
14.4	Edge-Fitting Edge Detection, 451	
14.5	Luminance Edge Detector Performance, 453	
14.6	Color Edge Detection, 467	
14.7	Line and Spot Detection, 473	
14.8	Edge Detection Exercises, 475	
<b>15</b>	<b>Image Feature Extraction</b>	<b>479</b>
15.1	Image Features Evaluation, 479	
15.2	Amplitude Features, 481	
15.3	Transform Coefficient Features, 486	
15.4	Texture Characterization, 488	
15.5	Texture Features, 498	
15.6	Scale-Invariant Features, 516	
15.7	Image Feature Extraction Exercises, 516	
<b>16</b>	<b>Image Segmentation</b>	<b>521</b>
16.1	Amplitude Segmentation, 522	
16.2	Clustering Segmentation, 529	
16.3	Region Segmentation, 532	
16.4	Boundary Segmentation, 537	
16.5	Texture Segmentation, 552	

- 16.6 Segment Labeling, 555
- 16.7 Image Segmentation Exercises, 558

## **17 Shape Analysis 565**

- 17.1 Topological Attributes, 565
- 17.2 Distance, Perimeter and Area Measurements, 566
- 17.3 Spatial Moments, 573
- 17.4 Shape Orientation Descriptors, 585
- 17.5 Fourier Descriptors, 587
- 17.6 Thinning and Skeletonizing, 589
- 17.7 Shape Analysis Exercises, 590

## **18 Image Detection and Registration 595**

- 18.1 Template Matching, 595
- 18.2 Matched Filtering of Continuous Images, 599
- 18.3 Image Registration, 604
- 18.4 Image Detection and Registration Exercises, 614

## **PART 6 IMAGE AND VIDEO COMPRESSION 617**

### **19 Point Processing Image Compression 619**

- 19.1 Pulse Code Modulation Coding of Monochrome Images, 619
- 19.2 Statistical Coding of Monochrome Images, 620
- 19.3 Predictive Coding of Monochrome Images, 622
- 19.4 Point Processing Color Image Coding, 625
- 19.5 JPEG Lossless Image Coding, 626
- 19.6 Point Processing Image Compression Exercises, 628

### **20 Spatial Processing Image Compression 633**

- 20.1 Run Coding of Monochrome Images, 633
- 20.2 Interpolation Coding of Monochrome Images, 635
- 20.3 Unitary Transform Coding of Monochrome Images, 637
- 20.4 Wavelet Coding of Monochrome Images, 644
- 20.5 Spatial Processing Color Image Coding, 645
- 20.6 JPEG Baseline Image Coding Standard, 646
- 20.7 JPEG2000 Image Coding Standard, 650
- 20.8 Spatial Processing Image Compression Exercises, 652

<b>21 Video Compression</b>	<b>657</b>
21.1 Spatial Video Coding Techniques, 657	
21.2 Spatial/Temporal Video Coding Techniques, 658	
21.3 MPEG - 1 Video Coding Standard, 660	
21.4 MPEG - 2 Video Coding Standard, 668	
21-5 MPEG - 4 Video Coding Standards, 668	
<b>Appendix 1 Vector-Space Algebra Concepts</b>	<b>671</b>
<b>Appendix 2 Image Error Measures</b>	<b>681</b>
<b>Appendix 3 Image and Video Compression Standards Development</b>	<b>683</b>
<b>Appendix 4 Huffman Coding Example</b>	<b>687</b>
<b>Annex 1 PixelSoft Web Site Down Loadable Files</b>	<b>689</b>
<b>Annex 2 PIKS API Image Processing Example</b>	<b>691</b>
<b>Annex 3 PIKSTool GUI Image Processing Example</b>	<b>699</b>
<b>Annex 4 PIKSTool Chain Image Processing Example</b>	<b>709</b>
<b>Annex 5 MATLAB Image Processing Example</b>	<b>713</b>
<b>Bibliography</b>	<b>717</b>

# PREFACE

In January 1978, I began the preface to the first of four editions of the book *Digital Image Processing* with the following statement:

“The field of image processing has grown considerably during the past decade with the increased utilization of imagery in myriad applications coupled with improvements in the size, speed and cost effectiveness of digital computers and related signal processing technologies. Image processing has found a significant role in scientific, industrial, space and government applications.”

As I write this preface to this new book *Introduction to Digital Image Processing*, I find the quoted statement still to be valid. Originally many image processing techniques were of academic interest only; their execution was too slow and too costly. Today, thanks to algorithmic and implementation advances, image processing has become a vital cost-effective technology in a host of applications. Consequently, there has been an explosive growth of the field of digital image processing. This has been the motivation to write the second (1991), third (2000) and fourth (2006) editions of *Digital Image Processing*. These editions sought to correct defects in the earlier editions, delete content of marginal interest and add discussions of new, important topics.

The first four editions of *Digital Image Processing* were intended to be an “industrial strength” exposition to digital image processing to be used as a text for an electrical engineering or computer science graduate course in the subject. Also, the books were intended to be used as a reference manual for scientists who are engaged in image processing research, developers of image processing hardware

and software systems, and practicing engineers and scientists who use image processing as a tool in their applications. Mathematical derivations were provided for most algorithms. The reader was assumed to have a basic background in linear system theory, vector space algebra and random processes.

In 2010, it became evident to me that the subject of digital image processing was migrating from a graduate course to a junior or senior level course as students became proficient in mathematical background earlier in their college education. This observation became the motivation for the development of an introductory textbook on the subject of digital image processing, which, not surprisingly, is being titled *Introduction to Digital Image Processing*. This textbook is lighter in terms of mathematical derivations. It also eliminates derivations of advanced subjects. Most importantly, the textbook contains an extensive set of programming exercises for the student.

The textbook is divided into six parts. The first three parts cover the basic technologies that are needed to support image processing applications. Part 1 contains three chapters concerned with the characterization of continuous images. Topics include the mathematical representation of continuous images, the psychophysical properties of human vision, and photometry and colorimetry. In Part 2, image sampling and quantization techniques are explored along with the mathematical representation of discrete images. Part 3 discusses two-dimensional signal processing techniques, including general linear operators and unitary transforms such as the Fourier, Hadamard and Karhunen–Loeve transforms plus wavelet transforms. The final chapter in Part 3 analyzes and compares linear processing techniques implemented by direct convolution and Fourier domain filtering.

The next two parts of the book cover the two principal application areas of image processing. Part 4 presents a discussion of image enhancement and restoration techniques, including restoration models, point and spatial restoration and geometrical image modification. Part 5, entitled “Image Analysis,” concentrates on the extraction of information from an image. Specific topics include morphological image processing, edge detection, image feature extraction, image segmentation, object shape analysis and object detection.

Part 6 discusses image and video compression. Chapters 19 and 20 describe coding technique applicable to still image coding based upon point and spatial processing. Topics include run length, predictive, unitary transform and wavelet coding of monochrome and color images. This chapter also describes the widely adopted JPEG and JPEG2000 still image coding standards. Chapter 21 discusses compression techniques for temporal video sequences. The chapter describes unitary transform and wavelet methods applied to video sequences. The chapter also describes the MPEG video coding standards.

My writing style is to provide a historical background of the development of image processing techniques as well as a theoretical exposition. This is accomplished through a liberal number of historical references.

Image processing exercises are included at the end of each chapter as English language narratives of image processing operations and algorithms, which are to be

programmed by students. These exercises can be implemented using the PIKS API (a C language image processing library) or by PIKSTool (a graphical user interface, for developing image processing programs without the need for program compilation) or by MATLAB (a C language based commercially available software package) or with any other full featured image processing software package. The Preamble to this book and Annexes 1, 2 and 3 contain examples of an image processing program implemented by PIKS API, PIKSTool and MATLAB.

*Introduction to Digital Image Processing* is supported by a website, pixelsoft.com. This website provides downloading of software documentation, demonstration programs, programming exercise executables and image data bases.

The reader should be aware that this textbook only provides an introduction to the subject of digital image processing. The textbook does not attempt to describe high-end or complex algorithms and programs. The website is meant to be a repository for the description of such techniques.

Although readers should find this book reasonably comprehensive, many important topics allied to the field of digital image processing have been omitted to limit the size and cost of the book. Among the most prominent omissions are the topics of pattern recognition, image reconstruction from projections, image understanding, scientific visualization and computer graphics. References to some of these topics are provided in the bibliography.

June 2013

William K. Pratt  
Los Altos, California





# ACKNOWLEDGMENTS

The following is a cumulative acknowledgement of all who have contributed to the four editions of *Digital Image Processing* and this textbook *Introduction to Digital Image Processing*.

My research interest in the field of digital image processing began in 1960 with work on my doctoral dissertation on video compression under the guidance of Irving Reed, Professor of Electrical Engineering at the University of Southern California. His support is gratefully acknowledged.

The first edition of *Digital Image Processing* was written while I was a professor of electrical engineering at the University of Southern California (USC). Image processing research at USC began in 1962 on a very modest scale, but the program increased in size and scope with the attendant international interest in the field. In 1971, Dr. Zohrab Kaprielian, then dean of engineering and vice president of academic research and administration, announced the establishment of the USC Image Processing Institute. This environment contributed significantly to the preparation of the first edition. I am deeply grateful to Professor Kaprielian for his role in providing university support of image processing and for his personal interest in my career.

Also, I wish to thank the following past and present members of the Institute's scientific staff who rendered invaluable assistance in the preparation of the first-edition manuscript: Jean-François Abramatic, Harry Andrews, Lee Davisson, Olivier Faugeras, Werner Frei, Ali Habibi, Anil Jain, Richard Kruger, Nasser Nahi, Ramakant Nevatia, Keith Price, Guner Robinson, Alexander Sawchuk and Lloyd Welsh.

In addition, I sincerely acknowledge the technical help of my graduate students at USC during preparation of the first edition: Harry Andrews, Ikram Abdou, Behnam Ashjari, Wen-Hsiung Chen, Faramarz Davarian, Michael N. Huhns, Kenneth Laws, Sang Uk Lee, Clanton Mancill, Nelson Mascarenhas, Clifford Reader, John Roes and Robert Wallis.

The first edition was the outgrowth of notes developed for the USC course *Image Processing*. I wish to thank the many students who suffered through the early versions of the notes for their valuable comments. Also, I appreciate the reviews of the notes provided by Harry Andrews, Werner Frei, Ali Habibi and Ernest Hall, who taught the course.

With regard to the first edition, I wish to offer words of appreciation to the Information Processing Techniques Office of the Advanced Research Projects Agency, directed by Larry Roberts, which provided partial financial support of my research at USC.

During the academic year 1977 to 1978, I performed sabbatical research at the Institut de Recherche d'Informatique et Automatique in LeChesney, France and at the Université de Paris. My research was partially supported by these institutions, USC and a Guggenheim Foundation fellowship. For this support, I am indebted.

I left USC in 1979 with the intention of forming a company that would put some of my research ideas into practice. Toward that end, I joined a startup company, Compression Labs, Inc. of San Jose, California. There I worked on the development of facsimile and video coding products with Dr. Wen-Hsiung Chen and Dr. Robert Wallis. Concurrently, I directed a design team that developed a digital image processor called VICOM. The early contributors to its hardware and software design were William Bryant, Howard Halverson, Stephen Howell, Jeffrey Shaw and William Zech. In 1981, I formed Vicom Systems, Inc. of San Jose, California, to manufacture and market the VICOM image processor. Many of the photographic examples in this book were processed on a VICOM.

Work on the second edition began in 1986. In 1988, I joined Sun Microsystems, of Mountain View, California. At Sun, I collaborated with Stephen Howell and Ihtisham Kabir on the development of image processing software. During my time at Sun, I participated in the specification of the Programmers Imaging Kernel System (PIKS) application program interface, which was made an International Standards Organization standard in 1994. Much of the PIKS content is present in the third edition of the book. Some of the principal contributors to PIKS include Timothy Butler, Adrian Clark, Patrick Krolak and Gerard Paquette.

In 1993, I formed PixelSoft, Inc. of Los Altos, California, to commercialize the PIKS standard. PixelSoft developed an implementation of the PIKS Foundation version of the PIKS standard in 1994. PIKS Foundation is the base subset of the image processing technology of the standard. Contributors to its development include Timothy Butler, Larry Hubble and Gerard Paquette.

I joined Photon Dynamics, Inc. of San Jose, California, a manufacturer of machine vision equipment for the inspection of electronics displays and printed circuit boards in 1966. There, I collaborated with Larry Hubble, Sunil Sawkar and

Gerard Paquette on the development of several hardware and software products based on PIKS.

In 1988, I began writing the third edition of *Digital Image Processing*. The major purpose for that edition was to incorporate the significant amount of research advancement in digital image processing since the publication of the second edition. A secondary purpose was to entice users to adopt PIKS for educational purposes and application development. Toward that end, PixelSoft developed an implementation of the PIKS Core version of the standard. PIKS Core incorporates all of the software building blocks for application development. PIKS Core was included with each copy of the third edition. Larry Hubble and Gerard Paquette contributed to PixelSoft's PIKS Core implementation.

I began to write a fourth edition of *Digital Image Processing* in late 2004. The principal purpose for the fourth edition was to chronicle research advances since the publication of the third edition. Another motivating factor was to further promote the PIKS standard. PixelSoft has developed the PIKS Scientific version of the standard. PIKS Scientific implements most of the high-level PIKS operators. It was included with the fourth edition. Gerard Paquette was instrumental in coding PixelSoft's PIKS Scientific software. His effort is greatly appreciated.

I offer my appreciation to Ray Schmidt, who was responsible for many photographic reproductions in the first edition of the book. I thank Kris Pendelton, who created much of the line art of the first and second editions. The third, fourth and college editions were "type set" using Adobe's FrameMaker product. Tarlochan Nahal did the bulk of the initial type setting of the third edition. The company Laser Words performed the final publication rendering. FrameMaker help was provided by Luis Angulo and Paul McJones. Many thanks to Larry Hubble who developed the PIKS software CDs.

Also, thanks are given to readers of the first four editions who reported errors, both typographical and mental.

Gerard Paquette deserves special recognition for his contribution to the implementation of the PIKS API and PIKSTool. Gerry has also contributed significantly in the development of the programming exercises in the College Edition.

I wish to thank all those previously cited, and many others too numerous to mention, for their assistance in the academic and industrial phases of my career. I spent the first 14 years of my post doctoral career as a professor of electrical engineering at the University of Southern California. It was an exciting period of research investigation. I then moved on to the challenges of industry. Having participated in the design of hardware and software products has been an arduous but intellectually rewarding task. This combination of academic and industrial experience, I believe, has significantly enriched this textbook.

Finally, I wish to thank my wife Joan for her support in the writing of *Introduction to Digital Image Processing*.

W. K. P.



# PREAMBLE

*Introduction to Digital Image Processing* is meant to be a teaching aid for the subject. Accordingly, image processing programming exercises are included at the end of each chapter. These exercises can be fulfilled by development of a C language program using: (a) the PIKS API or; (b) the PIKSTool graphical user interface (GUI) or; (c) the PIKSTool Chain command string interpreter or; (d) the MATLAB software package. Alternatively, the exercises may be implemented by homemade or commercially available image processing software packages.

Annex 1 describes the PixelSoft image processing software, which can be freely down loaded from the pixelsoft.com web site. This software package includes the PIKS API executables and the PIKSTool scripts of the programming exercises. The PIKS source files of the exercises can be obtained by teaching instructors from PixelSoft upon request. The MATLAB M-files of the programming exercises can also be supplied to teaching instructors from PixelSoft upon request.

The exercises at the end of each chapter are presented as a narrative script to be followed by a reader for some software language or GUI or command string interpreter. As an example, consider the implementation of an unsharp mask operator on a source image. With this operator, a detail sharpened image is generated by subtracting an amplitude weighted version of a blurred source image from a weighted source image. Equation 10.4-2 defines the unsharp mask operation on a monochrome source image as

$$G(j, k) = \frac{c}{2c-1}F(j, k) - \frac{1-c}{2c-1}L(j, k)$$

where  $c$  is a weighting constant and  $L(j,k)$  is a low pass filtered version of the source image obtained by convolution of the source image with a low pass filter impulse response array. The narrative for this operator follows.

Develop a program that performs unsharp masking on an unsigned integer, 8-bit, monochrome image. Steps:

- (a) Import and display the source image.
- (b) Select the weighting factors.
- (c) Generate or import a  $5 \times 5$  uniform impulse response array.
- (d) Convert the source image to floating point data class.
- (e) Weight the source image.
- (f) Blur the source image by convolution with the impulse response array.
- (g) Weight the blurred source image.
- (h) Form the destination difference image.
- (i) Clipped the destination image to the range 0 to 255 for display.
- (j) Convert the destination image to 8-bit data class.
- (k) Display the 8-bit destination image.

Annex 2 contains a PIKS source program, which implements the unsharp mask operator. Annex 2 also contains a screen dump of the source image and the sharpened output image.

Annex 3 contains a series of screen dumps of a PIKSTool session, which implements the unsharp mask operator.

Annex 4 provides a PIKSTool Chain command string for the execution of the unsharp mask operator.

Annex 5 provides a MATLAB command string for the execution of the unsharp mask operator.

# NOTATION

The mathematical and digital notation utilized in this book is summarized below.

$f(x)$  denotes a one-dimensional function over the range  $-\infty < x < \infty$  printed in 10 point, italic, Times New Roman font.

$F(x, y)$  denotes a two-dimensional function over the range  $-\infty < x, y < \infty$  printed in 10 point, italic, Times New Roman font.

$f(\omega)$  denotes a one-dimensional spatial frequency function over the range  $-\infty < \omega < \infty$  printed in 10 point, italic, French Script MT font.

$\mathcal{F}(\omega_x, \omega_y)$  denotes a two-dimensional spatial frequency function over the range  $-\infty < \omega_x, \omega_y < \infty$  printed in 10 point, italic, French Script MT font

$f(n)$  denotes a one-dimensional array over the range  $1 < n < N$  printed in 10 point, italic, Times New Roman font.

$F(n_1, n_2)$  denotes a two-dimensional array over the range  $1 < n_i < N_i$  printed in 10 point, italic, Times New Roman font.

$\mathbf{f}$  denotes a  $N \times 1$  column vector printed in 10 point, bold, Times New Roman font.



**F** denotes a  $M \times N$  matrix printed in 10 point bold, Times New Roman font.

*f* denotes a  $N \times 1$  column vector of unitary transform coefficients printed in 10 point bold, italic, Times New Roman font.

*F* denotes a  $M \times N$  matrix of unitary transform coefficients printed in 10 point bold, italic Times New Roman font.

Library calls to PIKS API executables in the programming exercises at the end of each chapter are printed in 10 point courier font, e.g.:

```
example_complement_monochrome_ND.
```

In many of the text chapters, references are made to the book *Digital Image Processing, Fourth Edition* written by William K. Pratt and published by John Wiley and Sons. For simplicity, these references are made as: Pratt (4Ed.,  $n_1 - n_N$ ) where  $n_i$  is a page number.

# PART 1

---

## CONTINUOUS IMAGE CHARACTERIZATION

Although this book is concerned primarily with digital, as opposed to analog, image processing techniques. It should be remembered that most digital images represent continuous natural images. Exceptions are artificial digital images such as test patterns that are numerically created in the computer and images constructed by tomographic systems. Thus, it is important to understand the “physics” of image formation by sensors and optical systems including human visual perception. Another important consideration is the measurement of light in order quantitatively to describe images. Finally, it is useful to establish spatial and temporal characteristics of continuous image fields which, provide the basis for the interrelationship of digital image samples. These topics are covered in the following chapters.



---

# 1

---

## CONTINUOUS IMAGE MATHEMATICAL CHARACTERIZATION

In the design and analysis of image processing systems, it is convenient and often necessary mathematically to characterize the image to be processed. There are two basic mathematical characterizations of interest: deterministic and statistical. In *deterministic image representation*, a mathematical image function is defined and point properties of the image are considered. For a *statistical image representation*, the image is specified by average properties. The following sections develop the deterministic and statistical characterization of continuous images. Although the analysis is presented in the context of visual images, many of the results can be extended to general two-dimensional time-varying signals and fields.

### 1.1. IMAGE REPRESENTATION

Let  $C(x, y, t, \lambda)$  represent the spatial energy distribution of an image source of radiant energy at spatial coordinates  $(x, y)$ , at time  $t$  and wavelength  $\lambda$ . Because light intensity is a real positive quantity, that is, because intensity is proportional to the modulus squared of the electric field, the image light function is real and nonnegative. Furthermore, in all practical imaging systems, a small amount of background light is always present. The physical imaging system also imposes some restriction on the maximum intensity of an image, for example, image sensor saturation. Hence it is assumed that

$$0 < C(x, y, t, \lambda) \leq A \quad (1.1-1)$$

where  $A$  is the maximum image intensity. A physical image is necessarily limited in extent by the imaging system and image recording media. For mathematical simplicity, all images are assumed to be nonzero only over a rectangular region for which

$$-L_x \leq x \leq L_x \tag{1.1-2a}$$

$$-L_y \leq y \leq L_y \tag{1.1-2b}$$

The physical image is, of course, observable only over some finite time interval. Thus, let

$$-T \leq t \leq T \tag{1.1-2c}$$

The image light function  $C(x, y, t, \lambda)$  is, therefore, a bounded four-dimensional function with bounded independent variables. As a final restriction, it is assumed that the image function is continuous over its domain of definition.

The intensity response of a standard human observer to an image light function is commonly measured in terms of the instantaneous luminance of the light field as defined by

$$Y(x, y, t) = \int_0^\infty C(x, y, t, \lambda)V(\lambda) d\lambda \tag{1.1-3}$$

where  $V(\lambda)$  represents the *relative luminous efficiency* function, that is, the average spectral response of human vision. Similarly, the color response of a standard observer is commonly measured in terms of a set of tristimulus values that are linearly proportional to the amounts of red, green and blue light needed to match a colored light. For an arbitrary red–green–blue coordinate system, the instantaneous *tristimulus values* are

$$R(x, y, t) = \int_0^\infty C(x, y, t, \lambda)R_S(\lambda) d\lambda \tag{1.1-4a}$$

$$G(x, y, t) = \int_0^\infty C(x, y, t, \lambda)G_S(\lambda) d\lambda \tag{1.1-4b}$$

$$B(x, y, t) = \int_0^\infty C(x, y, t, \lambda)B_S(\lambda) d\lambda \tag{1.1-4c}$$

where  $R_S(\lambda)$ ,  $G_S(\lambda)$ ,  $B_S(\lambda)$  are spectral tristimulus values for the set of red, green and blue primaries. The spectral tristimulus values are, in effect, the tristimulus values required to match a unit amount of narrowband light at wavelength  $\lambda$ . In a multispectral imaging system, the image field observed is modeled as a spectrally weighted integral of the image light function. The  $i$ th spectral image field is then given as

$$F_i(x, y, t) = \int_0^{\infty} C(x, y, t, \lambda) S_i(\lambda) d\lambda \quad (1.1-5)$$

where  $S_i(\lambda)$  is the spectral response of the  $i$ th sensor.

For notational simplicity, a single image function  $F(x, y, t)$  is selected to represent an image field in a physical imaging system. For a monochrome imaging system, the image function  $F(x, y, t)$  nominally denotes the image luminance, or some converted or corrupted physical representation of the luminance, whereas in a color imaging system,  $F(x, y, t)$  signifies one of the tristimulus values, or some function of the tristimulus value. The image function  $F(x, y, t)$  is also used to denote general three-dimensional fields, such as the time-varying noise of an image scanner.

In many imaging systems, such as image projection devices, the image does not change with time, and the time variable may be dropped from the image function. For other types of systems, such as movie pictures, the image function is time sampled. It is also possible to convert the spatial variation into time variation, as in television, by an image scanning process. In the subsequent discussion, the time variable is dropped from the image field notation unless specifically required.

## 1.2. TWO-DIMENSIONAL SYSTEMS

A *two-dimensional system*, in its most general form, is simply a mapping of some input set of two-dimensional functions  $F_1(x, y), F_2(x, y), \dots, F_N(x, y)$  to a set of output two-dimensional functions  $G_1(x, y), G_2(x, y), \dots, G_M(x, y)$ , where  $(-\infty < x, y < \infty)$  denotes the independent, continuous spatial variables of the functions. This mapping may be represented by the operators  $O_m\{\cdot\}$  for  $m = 1, 2, \dots, M$ , which relate the input to output set of functions by the set of equations

$$\begin{bmatrix} G_1(x, y) = O_1\{F_1(x, y), F_2(x, y), \dots, F_N(x, y)\} \\ \vdots \\ G_m(x, y) = O_m\{F_1(x, y), F_2(x, y), \dots, F_N(x, y)\} \\ \vdots \\ G_M(x, y) = O_M\{F_1(x, y), F_2(x, y), \dots, F_N(x, y)\} \end{bmatrix} \quad (1.2-1)$$

In specific cases, the mapping may be many-to-few, few-to-many, or one-to-one. The *one-to-one mapping* is defined as

$$G(x, y) = O\{F(x, y)\}. \quad (1.2-2)$$

To proceed further with a discussion of the properties of two-dimensional systems, it is necessary to direct the discourse toward specific types of operators.

### 1.2.1. Singularity Operators

Singularity operators are widely employed in the analysis of two-dimensional systems, especially systems that involve sampling of continuous functions. The two-dimensional *Dirac delta function* is a singularity operator that possesses the following properties:

$$\int_{-\epsilon}^{\epsilon} \int_{-\epsilon}^{\epsilon} \delta(x, y) dx dy = 1 \quad \text{for } \epsilon > 0 \tag{1.2-3a}$$

$$\int_{-\infty}^{\infty} \int_{-\infty}^{\infty} F(\xi, \eta) \delta(x - \xi, y - \eta) d\xi d\eta = F(x, y) . \tag{1.2-3b}$$

In Eq. 1.2-3a,  $\epsilon$  is an infinitesimally small limit of integration; Eq. 1.2-3b is called the *sifting property* of the Dirac delta function.

The two-dimensional delta function can be decomposed into the product of two one-dimensional delta functions defined along orthonormal coordinates. Thus

$$\delta(x, y) = \delta(x)\delta(y) \tag{1.2-4}$$

where the one-dimensional delta function satisfies one-dimensional versions of Eq. 1.2-3. The delta function also can be defined as a limit on a family of functions. General examples are given in References 1 and 2.

### 1.2.2. Additive Linear Operators

A two-dimensional system is said to be an *additive linear system* if the system obeys the law of additive superposition. In the special case of one-to-one mappings, the additive superposition property requires that

$$O\{a_1 F_1(x, y) + a_2 F_2(x, y)\} = a_1 O\{F_1(x, y)\} + a_2 O\{F_2(x, y)\} \tag{1.2-5}$$

where  $a_1$  and  $a_2$  are constants that are possibly complex numbers. This additive superposition property can easily be extended to the general mapping of Eq. 1.2-1.

A system input function  $F(x, y)$  can be represented as a sum of amplitude-weighted Dirac delta functions by the sifting integral,

$$F(x, y) = \int_{-\infty}^{\infty} \int_{-\infty}^{\infty} F(\xi, \eta) \delta(x - \xi, y - \eta) d\xi d\eta \tag{1.2-6}$$

where  $F(\xi, \eta)$  is the weighting factor of the impulse located at coordinates  $(\xi, \eta)$  in the  $x$ - $y$  plane, as shown in Figure 1.2-1. If the output of a general linear one-to-one system is defined to be

$$G(x, y) = O\{F(x, y)\} . \tag{1.2-7}$$

then

$$G(x, y) = O\left\{\int_{-\infty}^{\infty}\int_{-\infty}^{\infty} F(\xi, \eta)\delta(x-\xi, y-\eta)d\xi d\eta\right\} \quad (1.2-8a)$$

or

$$G(x, y) = \int_{-\infty}^{\infty}\int_{-\infty}^{\infty} F(\xi, \eta)O\{\delta(x-\xi, y-\eta)\}d\xi d\eta. \quad (1.2-8b)$$

In moving from Eq. 1.2-8a to Eq. 1.2-8b, the application order of the general linear operator  $O\{\cdot\}$  and the integral operator have been reversed. Also, the linear operator has been applied only to the term in the integrand that is dependent on the

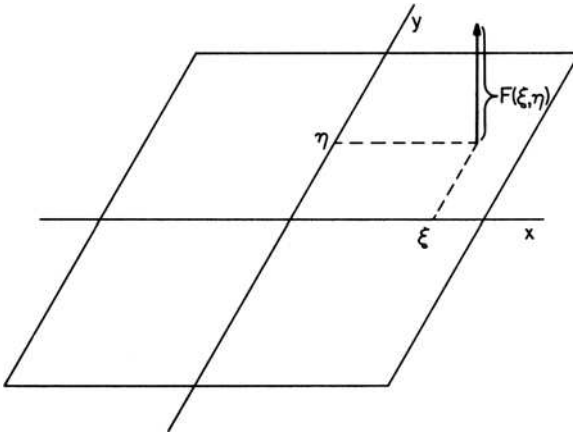


**FIGURE 1.2-1.** Decomposition of image function.

spatial variables  $(x, y)$ . The second term in the integrand of Eq. 1.2-8b, which is redefined as

$$H(x, y; \xi, \eta) \equiv O\{\delta(x-\xi, y-\eta)\} \quad (1.2-9)$$

is called the *impulse response* of the two-dimensional system. In optical systems, the impulse response is often called the *point spread function* of the system. Substitution of the impulse response function into Eq. 1.2-8b yields the additive *superposition integral*

$$G(x, y) = \int_{-\infty}^{\infty}\int_{-\infty}^{\infty} F(\xi, \eta)H(x, y; \xi, \eta)d\xi d\eta. \quad (1.2-10)$$



An additive linear two-dimensional system is called *space invariant (isoplanatic)* if its impulse response depends only on the factors  $x - \xi$  and  $y - \eta$ . In an optical system, as shown in Figure 1.2-2, this implies that the image of a point source in the focal plane will change only in location, not in functional form, as the placement of the point source moves in the object plane. For a space-invariant system

$$H(x, y; \xi, \eta) = H(x - \xi, y - \eta) \tag{1.2-11}$$

and the superposition integral reduces to the special case called the *convolution integral*, given by

$$G(x, y) = \int_{-\infty}^{\infty} \int_{-\infty}^{\infty} F(\xi, \eta) H(x - \xi, y - \eta) d\xi d\eta. \tag{1.2-12a}$$

Symbolically,

$$G(x, y) = F(x, y) \otimes H(x, y). \tag{1.2-12b}$$

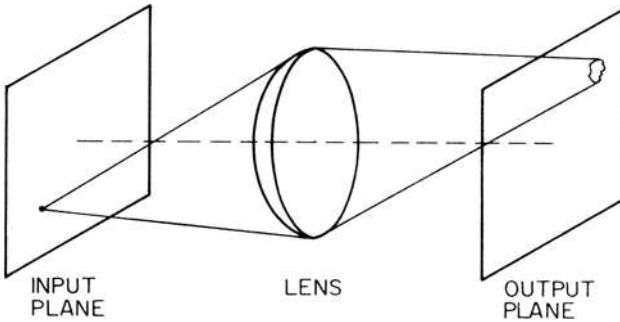


**FIGURE 1.2-2.** Point-source imaging system.

denotes the *convolution operation*. The convolution integral is symmetric in the sense that

$$G(x, y) = \int_{-\infty}^{\infty} \int_{-\infty}^{\infty} F(x - \xi, y - \eta) H(\xi, \eta) d\xi d\eta. \tag{1.2-13}$$

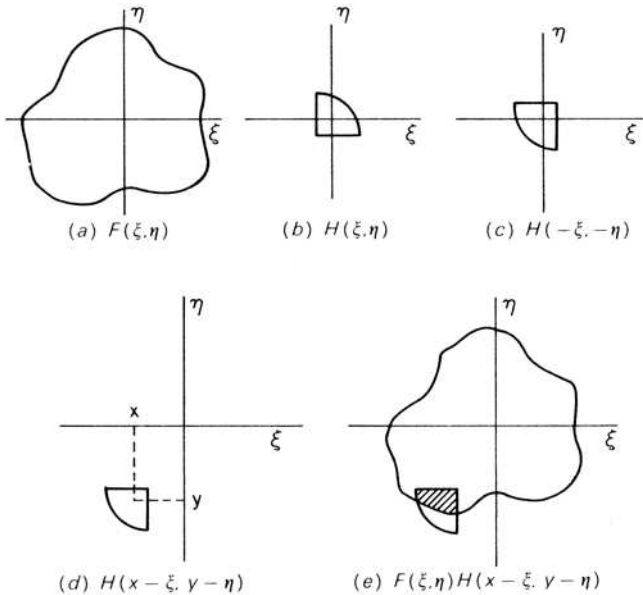


**FIGURE 1.2-3.** Graphical example of two-dimensional convolution.

Figure 1.2-3 provides a visualization of the convolution process. In Figure 1.2-3a and b, the input function  $F(x, y)$  and impulse response are plotted in the dummy coordinate system  $(\xi, \eta)$ . Next, in Figures 1.2-3c and d, the coordinates of the impulse response are reversed, and the impulse response is offset by the spatial values  $(x, y)$ . In Figure 1.2-3e, the integrand product of the convolution integral of Eq. 1.2-12 is shown as a crosshatched region. The integral over this region is the value of  $G(x, y)$  at the offset coordinate  $(x, y)$ . The complete function  $F(x, y)$  could, in effect, be computed by sequentially scanning the reversed, offset impulse response across the input function and simultaneously integrating the overlapped region.

### 1.2.3. Differential Operators

Edge detection in images is commonly accomplished by performing a spatial differentiation of the image field followed by a thresholding operation to determine points of steep amplitude change. Horizontal and vertical spatial derivatives are defined as

$$d_x = \frac{\partial F(x, y)}{\partial x} \quad (1.2-14a)$$

$$d_y = \frac{\partial F(x, y)}{\partial y}. \tag{1.2-14b}$$

The directional derivative of the image field along a vector direction  $z$  subtending an angle  $\phi$  with respect to the horizontal axis is given by (3, p. 106)

$$\nabla\{F(x, y)\} = \frac{\partial F(x, y)}{\partial z} = d_x \cos \phi + d_y \sin \phi. \tag{1.2-15}$$

The gradient magnitude is then

$$|\nabla\{F(x, y)\}| = \sqrt{d_x^2 + d_y^2}. \tag{1.2-16}$$

Spatial second derivatives in the horizontal and vertical directions are defined as

$$d_{xx} = \frac{\partial^2 F(x, y)}{\partial x^2} \tag{1.2-17a}$$

$$d_{yy} = \frac{\partial^2 F(x, y)}{\partial y^2}. \tag{1.2-17b}$$

The sum of these two spatial derivatives is called the *Laplacian operator*:

$$\nabla^2\{F(x, y)\} = \frac{\partial^2 F(x, y)}{\partial x^2} + \frac{\partial^2 F(x, y)}{\partial y^2}. \tag{1.2-18}$$

### 1.3. TWO-DIMENSIONAL FOURIER TRANSFORM

The two-dimensional *Fourier transform* of the image function  $F(x, y)$  is defined as (1,2)

$$\mathcal{F}(\omega_x, \omega_y) = \int_{-\infty}^{\infty} \int_{-\infty}^{\infty} F(x, y) \exp\{-i(\omega_x x + \omega_y y)\} dx dy \tag{1.3-1}$$

where  $\omega_x$  and  $\omega_y$  are *spatial frequencies* and  $i = \sqrt{-1}$ . Notationally, the Fourier transform is written as

$$\mathcal{F}(\omega_x, \omega_y) = O_F\{F(x, y)\}. \tag{1.3-2}$$

In general, the Fourier coefficient  $\mathcal{F}(\omega_x, \omega_y)$  is a complex number that may be represented in real and imaginary form,

$$\mathcal{F}(\omega_x, \omega_y) = \mathcal{R}(\omega_x, \omega_y) + i\mathcal{I}(\omega_x, \omega_y) \quad (1.3-3a)$$

or in magnitude and phase-angle form,

$$\mathcal{F}(\omega_x, \omega_y) = \mathcal{M}(\omega_x, \omega_y) \exp \{i\Phi(\omega_x, \omega_y)\} \quad (1.3-3b)$$

where

$$\mathcal{M}(\omega_x, \omega_y) = [\mathcal{R}^2(\omega_x, \omega_y) + \mathcal{I}^2(\omega_x, \omega_y)]^{1/2} \quad (1.3-4a)$$

$$\Phi(\omega_x, \omega_y) = \arctan \left\{ \frac{\mathcal{I}(\omega_x, \omega_y)}{\mathcal{R}(\omega_x, \omega_y)} \right\}. \quad (1.3-4b)$$

The input function  $F(x, y)$  can be recovered from its Fourier transform by the inversion formula

$$F(x, y) = \frac{1}{4\pi^2} \int_{-\infty}^{\infty} \int_{-\infty}^{\infty} \mathcal{F}(\omega_x, \omega_y) \exp \{i(\omega_x x + \omega_y y)\} d\omega_x d\omega_y \quad (1.3-5a)$$

or in operator form

$$F(x, y) = O_F^{-1} \{ \mathcal{F}(\omega_x, \omega_y) \}. \quad (1.3-5b)$$

The functions  $F(x, y)$  and  $\mathcal{F}(\omega_x, \omega_y)$  are called *Fourier transform pairs*.

The two-dimensional Fourier transform can be computed in two steps as a result of the separability of the kernel. Thus, let

$$\mathcal{F}_y(\omega_x, y) = \int_{-\infty}^{\infty} F(x, y) \exp \{-i(\omega_x x)\} dx \quad (1.3-6)$$

then

$$\mathcal{F}(\omega_x, \omega_y) = \int_{-\infty}^{\infty} \mathcal{F}_y(\omega_x, y) \exp \{-i(\omega_y y)\} dy. \quad (1.3-7)$$

Several useful properties of the two-dimensional Fourier transform are stated below. Proofs are given in References 1 and 2.

**Separability.** If the image function is spatially separable such that

$$F(x, y) = f_x(x)f_y(y) \quad (1.3-8)$$

then

$$\mathcal{F}(\omega_x, \omega_y) = f_x(\omega_x)f_y(\omega_y) \quad (1.3-9)$$

where  $f'_x(\omega_x)$  and  $f'_y(\omega_y)$  are one-dimensional Fourier transforms of  $f_x(x)$  and  $f_y(y)$ , respectively. Also, if  $F(x, y)$  and  $\mathcal{F}(\omega_x, \omega_y)$  are two-dimensional Fourier transform pairs, the Fourier transform of  $F^*(x, y)$  is  $\mathcal{F}^*(-\omega_x, -\omega_y)$ . An asterisk \* used as a superscript denotes complex conjugation of a variable (i.e. if  $F = A + iB$ , then  $F^* = A - iB$ ). Finally, if  $F(x, y)$  is symmetric such that  $F(x, y) = F(-x, -y)$ , then  $\mathcal{F}(\omega_x, \omega_y) = \mathcal{F}(-\omega_x, -\omega_y)$ .

**Linearity.** The Fourier transform is a linear operator. Thus

$$O_F\{aF_1(x, y) + bF_2(x, y)\} = a\mathcal{F}_1(\omega_x, \omega_y) + b\mathcal{F}_2(\omega_x, \omega_y) \tag{1.3-10}$$

where  $a$  and  $b$  are constants.

**Scaling.** A linear scaling of the spatial variables results in an inverse scaling of the spatial frequencies as given by

$$O_F\{F(ax, by)\} = \frac{1}{|ab|} \mathcal{F}\left(\frac{\omega_x}{a}, \frac{\omega_y}{b}\right). \tag{1.3-11}$$

Hence, stretching of an axis in one domain results in a contraction of the corresponding axis in the other domain plus an amplitude change.

**Shift.** A positional shift in the input plane results in a phase shift in the output plane:

$$O_F\{F(x - a, y - b)\} = \mathcal{F}(\omega_x, \omega_y) \exp\{-i(\omega_x a + \omega_y b)\}. \tag{1.3-12a}$$

Alternatively, a frequency shift in the Fourier plane results in the equivalence

$$O_F^{-1}\{\mathcal{F}(\omega_x - a, \omega_y - b)\} = F(x, y) \exp\{i(ax + by)\}. \tag{1.3-12b}$$

**Convolution.** The two-dimensional Fourier transform of two convolved functions is equal to the products of the transforms of the functions. Thus

$$O_F\left\{F(x, y) \otimes H(x, y)\right\} = \mathcal{F}(\omega_x, \omega_y) \mathcal{K}(\omega_x, \omega_y). \tag{1.3-13}$$

The inverse theorem states that

$$O_F\{F(x, y)H(x, y)\} = \frac{1}{4\pi^2} \mathcal{F}(\omega_x, \omega_y) \otimes \mathcal{K}(\omega_x, \omega_y). \tag{1.3-14}$$

**Parseval's Theorem.** The energy in the spatial and Fourier transform domains is related by

$$\int_{-\infty}^{\infty} \int_{-\infty}^{\infty} |F(x, y)|^2 dx dy = \frac{1}{4\pi} \int_{-\infty}^{\infty} \int_{-\infty}^{\infty} |\mathcal{F}(\omega_x, \omega_y)|^2 d\omega_x d\omega_y. \quad (1.3-15)$$

**Autocorrelation Theorem.** The Fourier transform of the spatial autocorrelation of a function is equal to the magnitude squared of its Fourier transform. Hence

$$O_F \left\{ \int_{-\infty}^{\infty} \int_{-\infty}^{\infty} F(\alpha, \beta) F^*(\alpha - x, \beta - y) d\alpha d\beta \right\} = |\mathcal{F}(\omega_x, \omega_y)|^2. \quad (1.3-16)$$

**Spatial Differentials.** The Fourier transform of the directional derivative of an image function is related to the Fourier transform by

$$O_F \left\{ \frac{\partial F(x, y)}{\partial x} \right\} = -i\omega_x \mathcal{F}(\omega_x, \omega_y) \quad (1.3-17a)$$

$$O_F \left\{ \frac{\partial F(x, y)}{\partial y} \right\} = -i\omega_y \mathcal{F}(\omega_x, \omega_y). \quad (1.3-17b)$$

Consequently, the Fourier transform of the Laplacian of an image function is equal to

$$O_F \left\{ \frac{\partial^2 F(x, y)}{\partial x^2} + \frac{\partial^2 F(x, y)}{\partial y^2} \right\} = -(\omega_x^2 + \omega_y^2) \mathcal{F}(\omega_x, \omega_y). \quad (1.3-18)$$

The Fourier transform convolution theorem stated by Eq. 1.3-13 is an extremely useful tool for the analysis of additive linear systems. Consider an image function  $F(x, y)$  that is the input to an additive linear system with an impulse response  $H(x, y)$ . The output image function is given by the convolution integral

$$G(x, y) = \int_{-\infty}^{\infty} \int_{-\infty}^{\infty} F(\alpha, \beta) H(x - \alpha, y - \beta) d\alpha d\beta. \quad (1.3-19)$$

Taking the Fourier transform of both sides of Eq. 1.3-19 and reversing the order of integration on the right-hand side results in

$$\mathcal{G}(\omega_x, \omega_y) = \int_{-\infty}^{\infty} \int_{-\infty}^{\infty} F(\alpha, \beta) \left[ \int_{-\infty}^{\infty} \int_{-\infty}^{\infty} H(x - \alpha, y - \beta) \exp\{-i(\omega_x x + \omega_y y)\} dx dy \right] d\alpha d\beta. \quad (1.3-20)$$

By the Fourier transform shift theorem of Eq. 1.3-13, the inner integral is equal to the Fourier transform of  $H(x, y)$  multiplied by an exponential phase-shift factor. Thus

$$\mathcal{G}(\omega_x, \omega_y) = \int_{-\infty}^{\infty} \int_{-\infty}^{\infty} F(\alpha, \beta) \mathcal{H}(\omega_x, \omega_y) \exp \{-i(\omega_x \alpha + \omega_y \beta)\} d\alpha d\beta. \quad (1.3-21)$$

Performing the indicated Fourier transformation gives

$$\mathcal{G}(\omega_x, \omega_y) = \mathcal{H}(\omega_x, \omega_y) \mathcal{F}(\omega_x, \omega_y). \quad (1.3-22)$$

Then an inverse transformation of Eq. 1.3-22 provides the output image function

$$G(x, y) = \frac{1}{4\pi} \int_{-\infty}^{\infty} \int_{-\infty}^{\infty} \mathcal{H}(\omega_x, \omega_y) \mathcal{F}(\omega_x, \omega_y) \exp \{i(\omega_x x + \omega_y y)\} d\omega_x d\omega_y. \quad (1.3-23)$$

Equations 1.3-19 and 1.3-23 represent two alternative means of determining the output image response of an additive, linear, space-invariant system. The analytic or operational choice between the two approaches, convolution or Fourier processing, is usually problem dependent.

### 1.4. IMAGE STOCHASTIC CHARACTERIZATION

The following presentation on the statistical characterization of images assumes general familiarity with probability theory, random variables and stochastic processes. References 2 and 4 to 7 can provide suitable background. The primary purpose of the discussion here is to introduce notation and develop stochastic image models.

It is often convenient to regard an image as a sample of a stochastic process. For continuous images, the image function  $F(x, y, t)$  is assumed to be a member of a continuous three-dimensional stochastic process with space variables  $(x, y)$  and time variable  $(t)$ .

The stochastic process  $F(x, y, t)$  can be described completely by knowledge of its *joint probability density*

$$p\{F_1, F_2, \dots, F_J; x_1, y_1, t_1, x_2, y_2, t_2, \dots, x_J, y_J, t_J\}$$

for all sample points  $J$ , where  $(x_j, y_j, t_j)$  represent space and time samples of image function  $F_j(x_j, y_j, t_j)$ . In general, high-order joint probability densities of images are usually not known, nor are they easily modeled. The first-order probability density  $p(F; x, y, t)$  can sometimes be modeled successfully on the basis of the physics of the process or histogram measurements. For example, the first-order probability density of random noise from an electronic sensor is usually well modeled by a *Gaussian density* of the form

$$p\{F; x, y, t\} = [2\pi\sigma_F^2(x, y, t)]^{-1/2} \exp \left\{ -\frac{[F(x, y, t) - \eta_F(x, y, t)]^2}{2\sigma_F^2(x, y, t)} \right\} \quad (1.4-1)$$

where the parameters  $\eta_F(x, y, t)$  and  $\sigma_F^2(x, y, t)$  denote the *mean* and *variance* of the process. The Gaussian density is also a reasonably accurate model for the probability density of the amplitude of unitary transform coefficients of an image. The probability density of the luminance function must be a one-sided density because the luminance measure is positive. Models that have found application include the *Rayleigh density*,

$$p\{F; x, y, t\} = \frac{F(x, y, t)}{\alpha^2} \exp\left\{-\frac{[F(x, y, t)]^2}{2\alpha^2}\right\} \quad (1.4-2a)$$

the *log-normal density*,

$$p\{F; x, y, t\} = [2\pi F^2(x, y, t)\sigma_F^2(x, y, t)]^{-1/2} \exp\left\{-\frac{[\log\{F(x, y, t)\} - \eta_F(x, y, t)]^2}{2\sigma_F^2(x, y, t)}\right\} \quad (1.4-2b)$$

and the *exponential density*,

$$p\{F; x, y, t\} = \alpha \exp\{-\alpha|F(x, y, t)|\} \quad (1.4-2c)$$

all defined for  $F \geq 0$  where  $\alpha$  is a constant. The *two-sided*, or *Laplacian density*,

$$p\{F; x, y, t\} = \frac{\alpha}{2} \exp\{-\alpha|F(x, y, t)|\} \quad (1.4-3)$$

where  $\alpha$  is a constant, is often selected as a model for the probability density of the difference of image samples. Finally, the *uniform density*

$$p\{F; x, y, t\} = \frac{1}{2\pi} \quad (1.4-4)$$

for  $-\pi \leq F \leq \pi$  is a common model for phase fluctuations of a random process.

Another means of describing a stochastic process is through computation of its ensemble averages. The *first moment* or *mean* of the image function is defined as

$$\eta_F(x, y, t) = E\{F(x, y, t)\} = \int_{-\infty}^{\infty} F(x, y, t)p\{F; x, y, t\} dF \quad (1.4-5)$$

where  $E\{\cdot\}$  is the *expectation operator*, as defined by the right-hand side of Eq. 1.4-5.

The *second moment* or *autocorrelation function* is given by

$$R(x_1, y_1, t_1; x_2, y_2, t_2) = E\{F(x_1, y_1, t_1)F^*(x_2, y_2, t_2)\} \quad (1.4-6a)$$

or in explicit form



$$R(x_1, y_1, t_1; x_2, y_2, t_2) = \int_{-\infty}^{\infty} \int_{-\infty}^{\infty} F(x_1, x_1, y_1) F^*(x_2, y_2, t_2) \times p\{F_1, F_2; x_1, y_1, t_1, x_2, y_2, t_2\} dF_1 dF_2 \tag{1.4-6b}$$

The autocovariance of the image process is the autocorrelation about the mean, defined as

$$K(x_1, y_1, t_1; x_2, y_2, t_2) = E\{[F(x_1, y_1, t_1) - \eta_F(x_1, y_1, t_1)][F^*(x_2, y_2, t_2) - \eta_F^*(x_2, y_2, t_2)]\} \tag{1.4-7a}$$

or

$$K(x_1, y_1, t_1; x_2, y_2, t_2) = R(x_1, y_1, t_1; x_2, y_2, t_2) - \eta_F(x_1, y_1, t_1) \eta_F^*(x_2, y_2, t_2). \tag{1.4-7b}$$

Finally, the *variance* of an image process is

$$\sigma_F^2(x, y, t) = K(x, y, t; x, y, t). \tag{1.4-8}$$

An image process is called *stationary in the strict sense* if its moments are unaffected by shifts in the space and time origins. The image process is said to be *stationary in the wide sense* if its mean is constant and its autocorrelation is dependent on the differences in the image coordinates,  $x_1 - x_2, y_1 - y_2, t_1 - t_2$ , and not on their individual values. In other words, the image autocorrelation is not a function of position or time. For stationary image processes,

$$E\{F(x, y, t)\} = \eta_F \tag{1.4-9a}$$

$$R(x_1, y_1, t_1; x_2, y_2, t_2) = R(x_1 - x_2, y_1 - y_2, t_1 - t_2). \tag{1.4-9b}$$

The autocorrelation expression may then be written as

$$R(\tau_x, \tau_y, \tau_t) = E\{F(x + \tau_x, y + \tau_y, t + \tau_t) F^*(x, y, t)\}. \tag{1.4-10}$$

Because

$$R(-\tau_x, -\tau_y, -\tau_t) = R^*(\tau_x, \tau_y, \tau_t) \tag{1.4-11}$$

then for an image function with  $F$  real, the autocorrelation is real and an even function of  $\tau_x, \tau_y, \tau_t$ . The *power spectral density*, also called the *power spectrum*, of a

stationary image process is defined as the three-dimensional Fourier transform of its autocorrelation function as given by

$$\tilde{w}(\omega_x, \omega_y, \omega_t) = \int_{-\infty}^{\infty} \int_{-\infty}^{\infty} \int_{-\infty}^{\infty} R(\tau_x, \tau_y, \tau_t) \exp\{-i(\omega_x \tau_x + \omega_y \tau_y + \omega_t \tau_t)\} d\tau_x d\tau_y d\tau_t. \tag{1.4-12}$$

In many imaging systems, the spatial and time image processes are separable so that the stationary correlation function may be written as

$$R(\tau_x, \tau_y, \tau_t) = R_{xy}(\tau_x, \tau_y)R_t(\tau_t). \tag{1.4-13}$$

Furthermore, the spatial autocorrelation function is often considered as the product of  $x$  and  $y$  axis autocorrelation functions,

$$R_{xy}(\tau_x, \tau_y) = R_x(\tau_x)R_y(\tau_y) \tag{1.4-14}$$

for computational simplicity. For scenes of manufactured objects, there is often a large amount of horizontal and vertical image structure, and the spatial separation approximation may be quite good. In natural scenes, there usually is no preferential direction of correlation; the spatial autocorrelation function tends to be rotationally symmetric and not separable. In the following, the spatial and time processes are considered to be separable.

An image field is often modeled as a sample of a first-order *Markov process* for which the correlation between points on the image field is proportional to their geometric separation. The *autocovariance* function for the two-dimensional Markov process is

$$R_{xy}(\tau_x, \tau_y) = C \exp\left\{-\sqrt{\alpha_x^2 \tau_x^2 + \alpha_y^2 \tau_y^2}\right\} \tag{1.4-15}$$

where  $C$  is an energy scaling constant and  $\alpha_x$  and  $\alpha_y$  are spatial scaling constants. The corresponding power spectrum is

$$\tilde{w}(\omega_x, \omega_y) = \frac{1}{\sqrt{\alpha_x \alpha_y}} \frac{2C}{1 + [\omega_x^2/\alpha_x^2 + \omega_y^2/\alpha_y^2]}. \tag{1.4-16}$$

As a simplifying assumption, the Markov process is often assumed to be of separable form with an autocovariance function

$$K_{xy}(\tau_x, \tau_y) = C \exp\{-\alpha_x |\tau_x| - \alpha_y |\tau_y|\}. \tag{1.4-17}$$

The power spectrum of this process is

$$\tilde{W}(\omega_x, \omega_y) = \frac{4\alpha_x \alpha_y C}{(\alpha_x^2 + \omega_x^2)(\alpha_y^2 + \omega_y^2)} \tag{1.4-18}$$

The moments of the output of a system can be obtained directly from knowledge of the output probability density, or in certain cases, indirectly in terms of the system operator. For example, if the system operator is additive linear, the mean of the system output is

$$E\{G(x, y)\} = E\{O_F\{F(x, y)\}\} = O_F\{E\{F(x, y)\}\} \tag{1.4-19}$$

Consider an additive linear space-invariant system whose output is described by the two-dimensional convolution integral

$$G(x, y) = \int_{-\infty}^{\infty} \int_{-\infty}^{\infty} F(x - \alpha, y - \beta)H(\alpha, \beta) d\alpha d\beta \tag{1.4-20}$$

where  $H(x, y)$  is the system impulse response. The mean of the output is then

$$E\{G(x, y)\} = \int_{-\infty}^{\infty} \int_{-\infty}^{\infty} E\{F(x - \alpha, y - \beta)\}H(\alpha, \beta) d\alpha d\beta \tag{1.4-21}$$

If the input image field is stationary, its mean  $\eta_F$  is a constant that may be brought outside the integral. As a result,

$$E\{G(x, y)\} = \eta_F \int_{-\infty}^{\infty} \int_{-\infty}^{\infty} H(\alpha, \beta) d\alpha d\beta = \eta_F H(0, 0) \tag{1.4-22}$$

where  $H(0, 0)$  is the transfer function of the linear system evaluated at the origin in the spatial-time frequency domain. Following the same techniques, it can easily be shown that the autocorrelation functions of the system input and output are related by

$$R_G(\tau_x, \tau_y) = R_F(\tau_x, \tau_y) \otimes H(\tau_x, \tau_y) \otimes H^*(-\tau_x, -\tau_y) \tag{1.4-23}$$

Taking Fourier transforms on both sides of Eq. 1.4-23 and invoking the Fourier transform convolution theorem, one obtains the relationship between the power spectra of the input and output image,

$$\tilde{W}_G(\omega_x, \omega_y) = \tilde{W}_F(\omega_x, \omega_y) |\mathcal{H}(\omega_x, \omega_y)|^2 \tag{1.4-24}$$

This result is found useful in analyzing the effect of noise in imaging systems.

## 1.5. PROGRAM GENERATION EXERCISES

E1.1 Develop a program that:

- (a) Opens a program session.
- (b) Reads an unsigned integer, 8-bit, monochrome source image from a file.
- (c) Displays the parameters of the source image.
- (d) Displays the source image.
- (e) Creates a destination image, which is the complement of the source image.
- (f) Displays the destination image.
- (g) Closes the program session.

The PIKS API executable `example_complement_monochrome_ND` performs this exercise.

E1.2 Develop a program that:

- (a) Creates, in application space, an unsigned integer, 8-bit, pixel array of a source ramp image whose amplitude increases from left-to-right from 0 to 255.
- (b) Imports the source image for display.
- (c) Creates a destination image by adding value 100 to each pixel
- (d) Displays the destination image

The PIKS API executable `example_import_ramp` performs this exercise.

## REFERENCES

1. J. W. Goodman, *Introduction to Fourier Optics*, Second Edition, McGraw-Hill, New York, 1996.
2. A. Papoulis, *Systems and Transforms with Applications in Optics*, McGraw-Hill, New York, 1968.
3. J. M. S. Prewitt, "Object Enhancement and Extraction," in *Picture Processing and Psychopictorics*, B. S. Lipkin and A. Rosenfeld, Eds., Academic Press, New York, 1970.
4. A. Papoulis, *Probability, Random Variables, and Stochastic Processes*, Third Edition, McGraw-Hill, New York, 1991.
5. J. B. Thomas, *An Introduction to Applied Probability Theory and Random Processes*, Wiley, New York, 1971.
6. J. W. Goodman, *Statistical Optics*, John Wiley and Sons, New York, 1985.

7. E. R. Dougherty, *Random Processes for Image and Signal Processing*, Vol. PM44, SPIE Press, Bellingham, WA., 1998.

---

# 2

---

## PSYCHOPHYSICAL VISION PROPERTIES

For efficient design of imaging systems for which the output is a photograph or display to be viewed by a human observer, it is obviously beneficial to have an understanding of the mechanism of human vision. Such knowledge can be utilized to develop conceptual models of the human visual process. These models are vital in the design of image processing systems and in the construction of measures of image fidelity and intelligibility.

### 2.1. LIGHT PERCEPTION

*Light*, according to Webster's Dictionary (1), is “radiant energy which, by its action on the organs of vision, enables them to perform their function of sight.” Much is known about the physical properties of light, but the mechanisms by which light interacts with the organs of vision is not as well understood. Light is known to be a form of electromagnetic radiation lying in a relatively narrow region of the electromagnetic spectrum over a wavelength band of about 350 to 780 nanometers (nm). A physical light source may be characterized by the rate of radiant energy (radiant intensity) that it emits at a particular spectral wavelength. Light entering the human visual system originates either from a self-luminous source or from light reflected from some object or from light transmitted through some translucent object. Let  $E(\lambda)$  represent the *spectral energy distribution* of light emitted from some primary light source, and also let  $t(\lambda)$  and  $r(\lambda)$  denote the wavelength-dependent *transmissivity* and *reflectivity*, respectively, of an object. Then, for a *transmissive object*, the

observed light spectral energy distribution is

$$C(\lambda) = t(\lambda)E(\lambda) \tag{2.1-1}$$

and for a *reflective object*

$$C(\lambda) = r(\lambda)E(\lambda). \tag{2.1-2}$$

Figure 2.1-1 shows plots of the spectral energy distribution of several common sources of light encountered in imaging systems: sunlight, a tungsten lamp, a

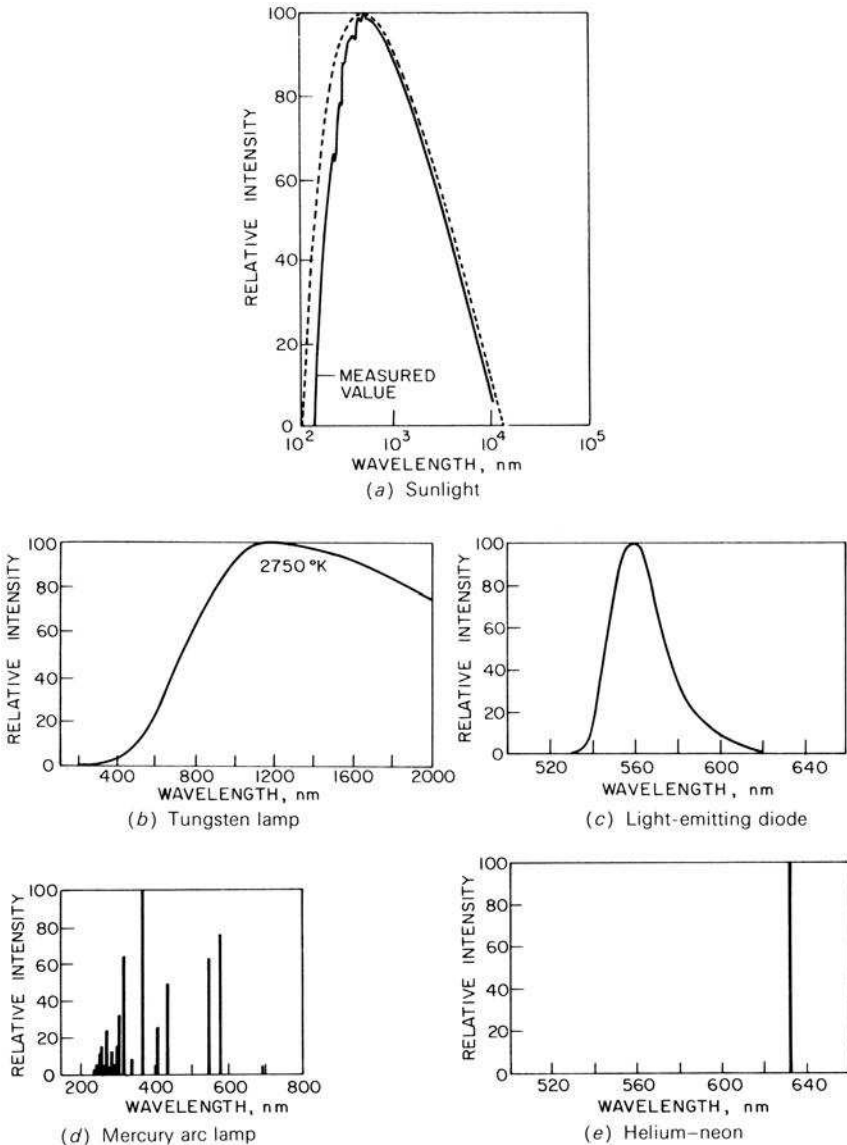


**FIGURE 2.1-1.** Spectral energy distributions of common physical light sources.

light-emitting diode, a mercury arc lamp and a helium–neon laser (2). A human being viewing each of the light sources will perceive the sources differently. Sunlight appears as an extremely bright yellowish-white light, while the tungsten light bulb appears less bright and somewhat yellowish. The light-emitting diode appears to be a dim green; the mercury arc light is a highly bright bluish-white light; and the laser produces an extremely bright and pure red beam. These observations provoke many questions. What are the attributes of the light sources that cause them to be perceived differently? Is the spectral energy distribution sufficient to explain the differences in perception? If not, what are adequate descriptors of visual perception? As will be seen, answers to these questions are only partially available.

There are three common perceptual descriptors of a light sensation: brightness, hue and saturation. The characteristics of these descriptors are considered below.

If two light sources with the same spectral shape are observed, the source of greater physical intensity will generally appear to be perceptually brighter. However, there are numerous examples in which an object of uniform intensity appears not to be of uniform *brightness*. Therefore, intensity is not an adequate quantitative measure of brightness.

The attribute of light that distinguishes a red light from a green light or a yellow light, for example, is called the *hue* of the light. A prism and slit arrangement (Figure 2.1-2) can produce narrowband wavelength light of varying color. However, it is clear that the light wavelength is not an adequate measure of color because some colored lights encountered in nature are not contained in the rainbow of light produced by a prism. For example, purple light is absent. Purple light can be produced by combining equal amounts of red and blue narrowband lights. Other counter examples exist. If two light sources with the same spectral energy distribution are observed under identical conditions, they will appear to possess the same hue. However, it is possible to have two light sources with different spectral energy distributions that are perceived identically. Such lights are called *metameric pairs*.

The third perceptual descriptor of a colored light is its *saturation*, the attribute that distinguishes a spectral light from a pastel light of the same hue. In effect, saturation describes the whiteness of a light source. Although it is possible to speak of the percentage saturation of a color referenced to a spectral color on a chromaticity diagram of the type shown in Figure 3.3-3, saturation is not usually considered to be a quantitative measure.

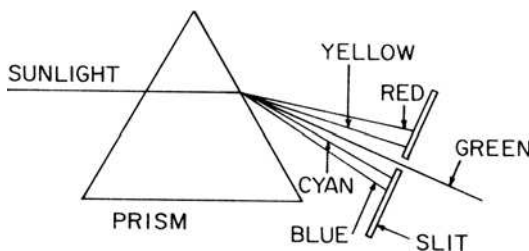


**FIGURE 2.1-2.** Refraction of light from a prism.



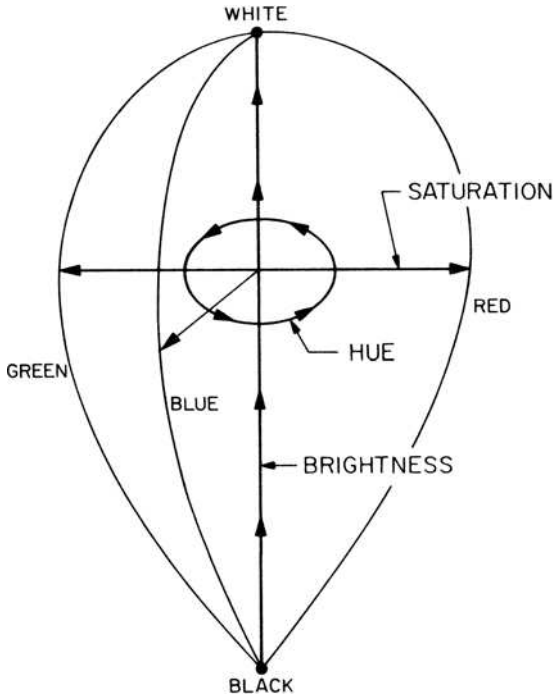


**FIGURE 2.1-3.** Perceptual representation of light.

As an aid to classifying colors, it is convenient to regard colors as being points in some color solid, as shown in Figure 2.1-3. The Munsell system of color classification actually has a form similar in shape to this figure (3). However, to be quantitatively useful, a color solid should possess metric significance. That is, a unit distance within the color solid should represent a constant perceptual color difference regardless of the particular pair of colors considered. The subject of perceptually significant color solids is considered later.

**2.2. EYE PHYSIOLOGY**

A conceptual technique for the establishment of a model of the human visual system would be to perform a physiological analysis of the eye, the nerve paths to the brain, and those parts of the brain involved in visual perception. Such a task, of course, is presently beyond human abilities because of the large number of infinitesimally small elements in the visual chain. However, much has been learned from physiological studies of the eye that is helpful in the development of visual models (4-7).

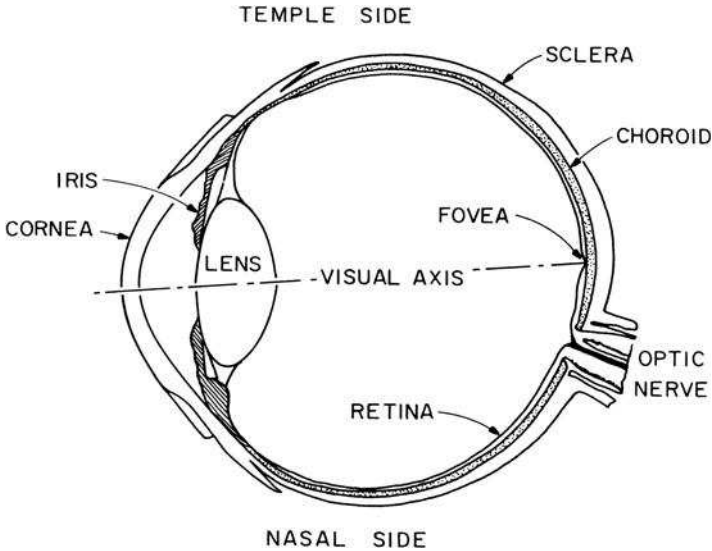


**FIGURE 2.2-1.** Eye cross section.

Figure 2.2-1 shows the horizontal cross section of a human eyeball. The front of the eye is covered by a transparent surface called the *cornea*. The remaining outer cover, called the *sclera*, is composed of a fibrous coat that surrounds the *choroid*, a layer containing blood capillaries. Inside the choroid is the *retina*, which is composed of two types of receptors: *rods* and *cones*. Nerves connecting to the retina leave the eyeball through the *optic nerve bundle*. Light entering the cornea is

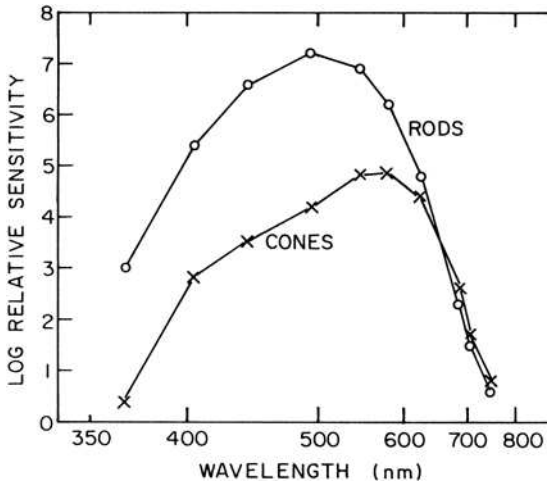


**FIGURE 2.2-2.** Sensitivity of rods and cones based on measurements by Wald.

focused on the retina surface by a *lens* that changes shape under muscular control to perform proper focusing of near and distant objects. An *iris* acts as a diaphragm to control the amount of light entering the eye.

The rods in the retina are long, slender receptors; the cones are generally shorter and thicker in structure. There are also important operational distinctions. The rods are more sensitive than the cones to light. At low levels of illumination, the rods provide a visual response called *scotopic vision*. Cones respond to higher levels of illumination; their response is called *photopic vision*. Figure 2.2-2 illustrates the relative sensitivities of rods and cones as a function of illumination wavelength (7,8). An eye contains about 6.5 million cones and 100 million rods distributed over the retina (4). Figure 2.2-3 shows the distribution of rods and cones over a horizontal line on the retina (4). At a point near the optic nerve called the *fovea*, the density of cones is greatest. This is the region of sharpest photopic vision. There are no rods or cones in the vicinity of the optic nerve, and hence the eye has a blind spot in this region.

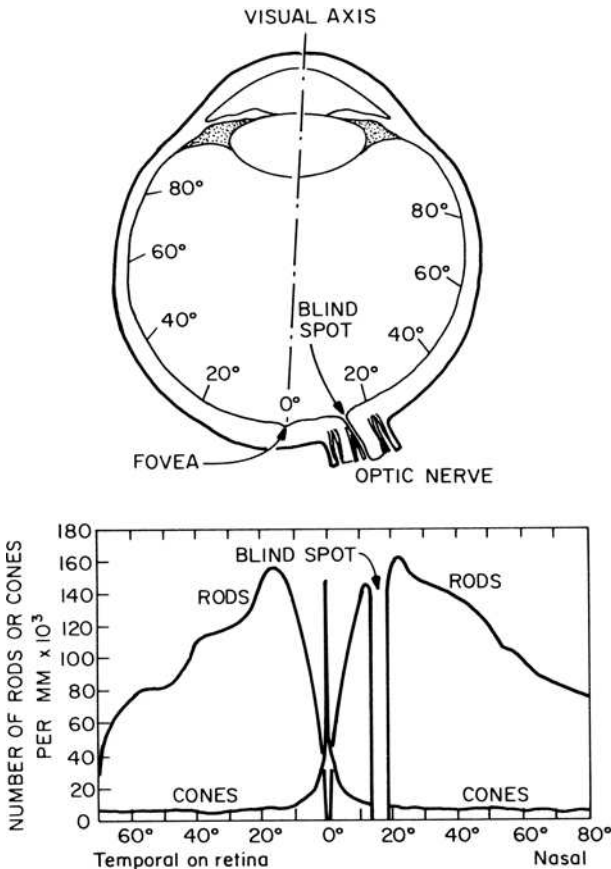


FIGURE 2.2-3. Distribution of rods and cones on the retina.

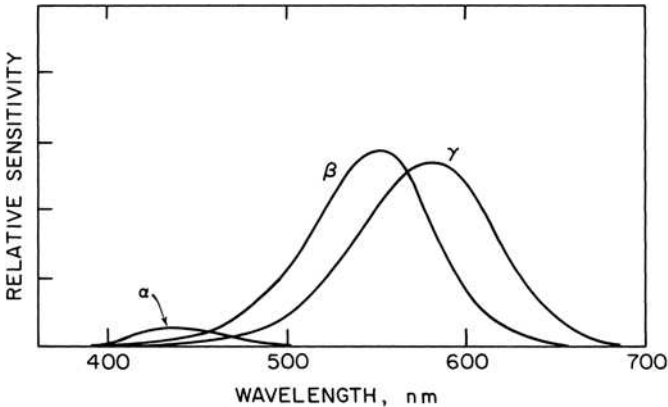


FIGURE 2.2-4. Typical spectral absorption curves of pigments of the retina.

In recent years, it has been determined experimentally that there are three basic types of cones in the retina (9, 10). These cones have different absorption characteristics as a function of wavelength with peak absorptions in the red, green and blue regions of the optical spectrum. Figure 2.2-4 shows curves of the measured spectral absorption of pigments in the retina for a particular subject (10). Two major points of note regarding the curves are that the  $\alpha$  cones, which are primarily responsible for blue light perception, have relatively low sensitivity, and the absorption curves overlap considerably. The existence of the three types of cones provides a physiological basis for the *trichromatic theory* of color vision.

When a light stimulus activates a rod or cone, a photochemical transition occurs, producing a nerve impulse. The manner in which nerve impulses propagate through the visual system is presently not well established. It is known that the optic nerve bundle contains on the order of 800,000 nerve fibers. Because there are over 100,000,000 receptors in the retina, it is obvious that in many regions of the retina, the rods and cones must be interconnected to nerve fibers on a many-to-one basis. Because neither the photochemistry of the retina nor the propagation of nerve impulses within the eye is well understood, a deterministic characterization of the visual process is unavailable. One must be satisfied with the establishment of models that characterize, and hopefully predict, human visual response. The following section describes several visual phenomena that should be considered in the modeling of the human visual process.

### 2.3. VISUAL PHENOMENA

The visual phenomena described below are interrelated, in some cases only minimally, but in others, to a very large extent. For simplification in presentation and, in some instances, lack of knowledge, the phenomena are considered disjoint.

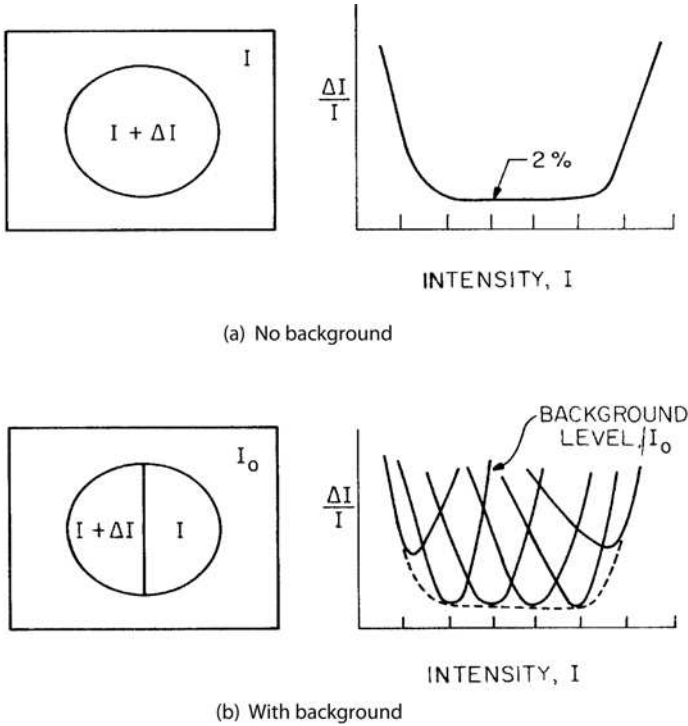
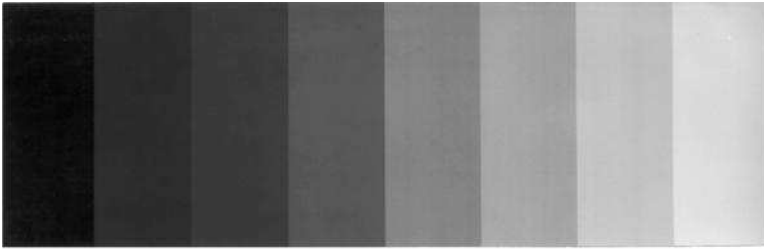
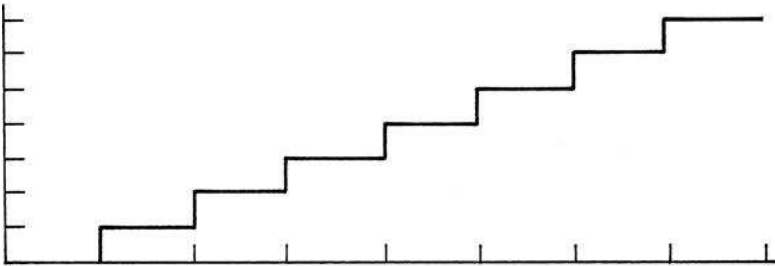


FIGURE 2.3-1. Contrast sensitivity measurements.

**Contrast Sensitivity.** The response of the eye to changes in the intensity of illumination is known to be nonlinear. Consider a patch of light of intensity  $I + \Delta I$  surrounded by a background of intensity  $I$  (Figure 2.3-1a). The just noticeable difference  $\Delta I$  is to be determined as a function of  $I$ . Over a wide range of intensities, it is found that the ratio  $\Delta I/I$ , called the *Weber fraction*, is nearly constant at a value of about 0.02 (11,12, p. 62). This result does not hold at very low or very high intensities, as illustrated by Figure 2.3-1a (13). Furthermore, contrast sensitivity is dependent on the intensity of the surround. Consider the experiment of Figure 2.3-1b, in which two patches of light, one of intensity  $I$  and the other of intensity  $I + \Delta I$ , are surrounded by light of intensity  $I_0$ . The Weber fraction  $\Delta I/I$  for this experiment is plotted in Figure 2.3-1b as a function of the intensity of the background. In this situation, it is found that the range over which the Weber fraction remains constant is reduced considerably compared to the experiment of Figure 2.3-1a. The envelope of the lower limits of the curves of Figure 2.3-1b is equivalent to the curve of Figure 2.3-1a. However, the range over which  $\Delta I/I$  is approximately constant for a fixed background intensity  $I_0$  is still comparable to the dynamic range of most electronic imaging systems.



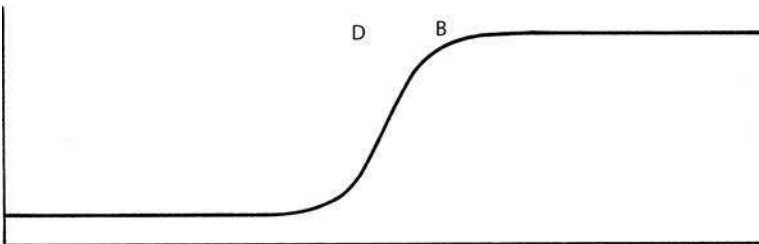
(a) Step chart photo



(b) Step chart intensity distribution



(c) Ramp chart photo



(d) Ramp chart intensity distribution

**FIGURE 2.3-2.** Mach band effect.

Because the differential of the logarithm of intensity is

$$d(\log I) = \frac{dI}{I} \tag{2.3-1}$$

equal changes in the logarithm of the intensity of a light can be related to equal just noticeable changes in its intensity over the region of intensities, for which the Weber fraction is constant. For this reason, in many image processing systems, operations are performed on the logarithm of the intensity of an image point rather than the intensity.

**Mach Band.** Consider the set of gray scale strips shown in of Figure 2.3-2a. The reflected light intensity from each strip is uniform over its width and differs from its neighbors by a constant amount; nevertheless, the visual appearance is that each strip is darker at its right side than at its left. This is called the *Mach band effect* (14). Figure 2.3-2c is a photograph of the Mach band pattern of Figure 2.3-2d. In the photograph, a bright bar appears at position *B* and a dark bar appears at *D*. Neither bar would be predicted purely on the basis of the intensity distribution. The apparent Mach band overshoot in brightness is a consequence of the spatial frequency response of the eye. As will be seen shortly, the eye possesses a lower sensitivity to high and low spatial frequencies than to midfrequencies. The implication for the designer of image processing systems is that perfect fidelity of edge contours can be sacrificed to some extent because the eye has imperfect response to high-spatial-frequency brightness transitions.

**Simultaneous Contrast.** The simultaneous contrast phenomenon (7) is illustrated in Figure 2.3-3. Each small square is actually the same intensity, but because of the different intensities of the surrounds, the small squares do not appear equally bright. The hue of a patch of light is also dependent on the wavelength composition of surrounding light. A white patch on a black background will appear to be yellowish if the surround is a blue light.

**Chromatic Adaption.** The hue of a perceived color depends on the adaption of a viewer (15). For example, the American flag will not immediately appear red, white and blue if the viewer has been subjected to high-intensity red light before viewing the flag. The colors of the flag will appear to shift in hue toward the red complement, cyan.

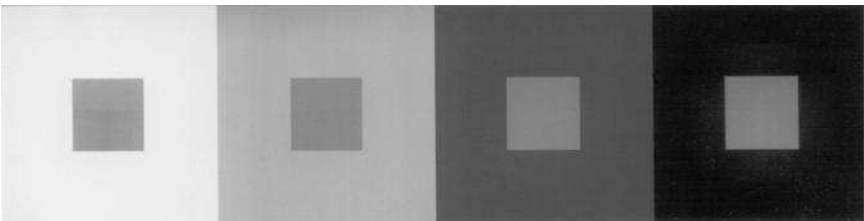


FIGURE 2.3-3. Simultaneous contrast.

**Color Blindness.** Approximately 8% of the males and 1% of the females in the world population are subject to some form of color blindness (16, p. 405). There are various degrees of color blindness. Some people, called *monochromats*, possess only rods or rods plus one type of cone, and therefore are only capable of monochromatic vision. *Dichromats* are people who possess two of the three types of cones. Both monochromats and dichromats can distinguish colors insofar as they have learned to associate particular colors with particular objects. For example, dark roses are assumed to be red, and light roses are assumed to be yellow. But if a red rose were painted yellow such that its reflectivity was maintained at the same value, a monochromat might still call the rose red. Similar examples illustrate the inability of dichromats to distinguish hue accurately.

## 2.4. MONOCHROME VISION MODEL

One of the modern techniques of optical system design entails the treatment of an optical system as a two-dimensional linear system that is linear in intensity and can be characterized by a two-dimensional transfer function (17). Consider the linear optical system of Figure 2.4-1. The system input is a spatial light distribution obtained by passing a constant-intensity light beam through a transparency with a spatial sine-wave transmittance. Because the system is linear, the spatial output intensity distribution will also exhibit sine-wave intensity variations with possible changes in the amplitude and phase of the output intensity compared to the input intensity. By varying the spatial frequency (number of intensity cycles per linear dimension) of the input transparency, and recording the output intensity level and phase, it is possible, in principle, to obtain the *optical transfer function* (OTF) of the optical system.

Let  $\mathcal{H}(\omega_x, \omega_y)$  represent the optical transfer function of a two-dimensional linear system where  $\omega_x = 2\pi/T_x$  and  $\omega_y = 2\pi/T_y$  are angular spatial frequencies with spatial periods  $T_x$  and  $T_y$  in the  $x$  and  $y$  coordinate directions, respectively. Then, with  $I_i(x, y)$  denoting the input intensity distribution of the object and  $I_o(x, y)$

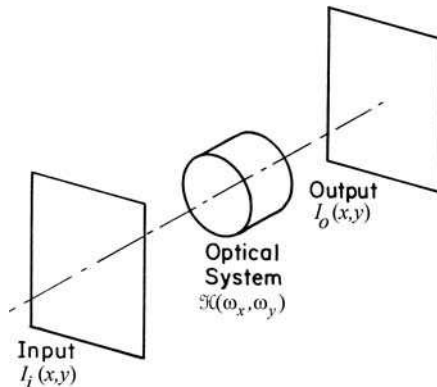


FIGURE 2.4-1. Linear systems analysis of an optical system.



representing the output intensity distribution of the image, the frequency spectra of the input and output signals are defined as

$$\mathcal{F}_I(\omega_x, \omega_y) = \int_{-\infty}^{\infty} \int_{-\infty}^{\infty} I_I(x, y) \exp\{-i(\omega_x x + \omega_y y)\} dx dy \tag{2.4-1}$$

$$\mathcal{F}_O(\omega_x, \omega_y) = \int_{-\infty}^{\infty} \int_{-\infty}^{\infty} I_O(x, y) \exp\{-i(\omega_x x + \omega_y y)\} dx dy. \tag{2.4-2}$$

The input and output intensity spectra are related by

$$\mathcal{F}_O(\omega_x, \omega_y) = \mathfrak{H}(\omega_x, \omega_y) \mathcal{F}_I(\omega_x, \omega_y). \tag{2.4-3}$$

The spatial distribution of the image intensity can be obtained by an inverse Fourier transformation of Eq. 2.4-2, yielding

$$I_O(x, y) = \frac{1}{4\pi^2} \int_{-\infty}^{\infty} \int_{-\infty}^{\infty} \mathcal{F}_O(\omega_x, \omega_y) \exp\{i(\omega_x x + \omega_y y)\} d\omega_x d\omega_y. \tag{2.4-4}$$

In many systems, the designer is interested only in the magnitude variations of the output intensity with respect to the magnitude variations of the input intensity, not the phase variations. The ratio of the magnitudes of the Fourier transforms of the input and output signals,

$$\frac{|\mathcal{F}_O(\omega_x, \omega_y)|}{|\mathcal{F}_I(\omega_x, \omega_y)|} = |\mathfrak{H}(\omega_x, \omega_y)| \tag{2.4-5}$$

is called the *modulation transfer function* (MTF) of the optical system.

Much effort has been given to application of the linear systems concept to the human visual system (18–24). A typical experiment to test the validity of the linear systems model is as follows. An observer is shown two sine-wave grating transparencies, a reference grating of constant contrast and spatial frequency and a variable-contrast test grating whose spatial frequency is set at a value different from that of the reference. *Contrast* is defined as the ratio

$$\frac{\text{max} - \text{min}}{\text{max} + \text{min}}$$

where *max* and *min* are the maximum and minimum of the grating intensity, respectively. The contrast of the test grating is varied until the brightnesses of the bright and dark regions of the two transparencies appear identical. In this manner, it is possible to develop a plot of the MTF of the human visual system. Figure 2.4-2a is a hypothetical plot of the MTF as a function of the input signal contrast. Another indication of the form of the MTF can be obtained by observation of the composite sine-wave grating of Figure 2.4-3, in which spatial frequency increases in one

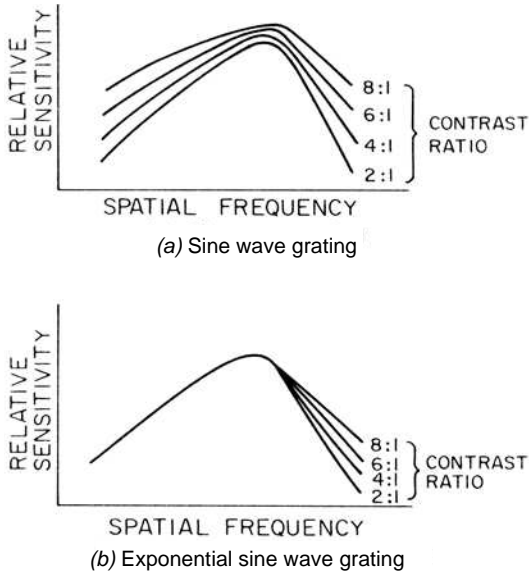


**FIGURE 2.4-2.** Hypothetical measurements of the spatial frequency response of the human visual system.

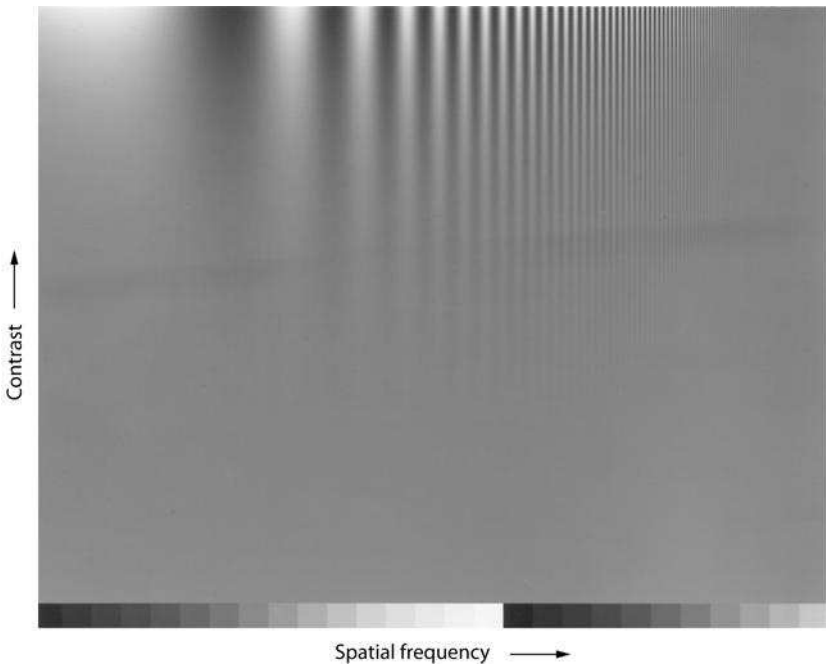


**FIGURE 2.4-3.** MTF measurements of the human visual system by modulated sine-wave grating.

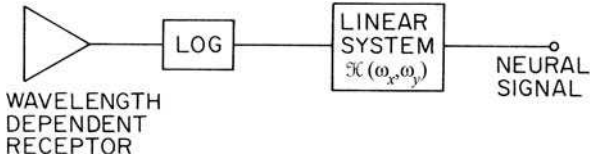


**FIGURE 2.4-4.** Logarithmic model of monochrome vision.

coordinate direction and contrast increases in the other direction. The envelope of the visible bars generally follows the MTF curves of Figure 2.4-2a (23).

Referring to Figure 2.4-2a, it is observed that the MTF measurement depends on the input contrast level. Furthermore, if the input sine-wave grating is rotated relative to the optic axis of the eye, the shape of the MTF is altered somewhat. Thus it can be concluded that the human visual system, as measured by this experiment, is nonlinear and anisotropic (rotationally variant).

It has been postulated that the nonlinear response of the eye to intensity variations is logarithmic in nature and occurs near the beginning of the visual information processing system, that is, near the rods and cones, before spatial interaction occurs between visual signals from individual rods and cones. Figure 2.4-4 shows a simple logarithmic eye model for monochromatic vision. If the eye exhibits a logarithmic response to input intensity, then if a signal grating contains a recording of an exponential sine wave, that is,  $\exp\{\sin\{I_f(x, y)\}\}$ , the human visual system can be linearized. A hypothetical MTF obtained by measuring an observer's response to an exponential sine-wave grating (Figure 2.4-2b) can be fitted reasonably well by a single curve for low- and mid-spatial frequencies. Figure 2.4-5 is a plot of the measured MTF of the human visual system obtained by Davidson (25) for an exponential sine-wave test signal. The high-spatial-frequency portion of the curve has been extrapolated for an average input contrast.

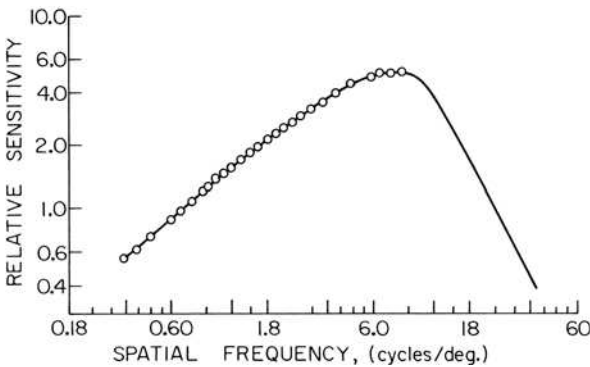


**FIGURE 2.4-5.** MTF measurements with exponential sine-wave grating.

The logarithmic/linear system eye model of Figure 2.4-4 has proved to provide a reasonable prediction of visual response over a wide range of intensities. However, at high spatial frequencies and at very low or very high intensities, observed responses depart from responses predicted by the model. To establish a more accurate model, it is necessary to consider the physical mechanisms of the human visual system.

The nonlinear response of rods and cones to intensity variations is still a subject of active research. Hypotheses have been introduced suggesting that the nonlinearity is based on chemical activity, electrical effects and neural feedback. The basic logarithmic model assumes the form

$$I_O(x, y) = K_1 \log \{ K_2 + K_3 I_I(x, y) \} \quad (2.4-6)$$

where the  $K_i$  are constants and  $I_I(x, y)$  denotes the input field to the nonlinearity and  $I_O(x, y)$  is its output. Another model that has been suggested (7, p. 253) follows the fractional response

$$I_O(x, y) = \frac{K_1 I_I(x, y)}{K_2 + I_I(x, y)} \quad (2.4-7)$$

where  $K_1$  and  $K_2$  are constants. Mannos and Sakrison (26) have studied the effect of various nonlinearities employed in an analytical visual fidelity measure. Their results, which are discussed in greater detail in Chapter 3, establish that a power law nonlinearity of the form

$$I_O(x, y) = [I_I(x, y)]^s \quad (2.4-8)$$

where  $s$  is a constant, typically  $1/3$  or  $1/2$ , provides good agreement between the visual fidelity measure and subjective assessment. The three models for the nonlinear response of rods and cones defined by Eqs. 2.4-6 to 2.4-8 can be forced to a reasonably close agreement over some mid-intensity range by an appropriate choice of scaling constants.

The physical mechanisms accounting for the spatial frequency response of the eye are partially optical and partially neural. As an optical instrument, the eye has limited resolution because of the finite size of the lens aperture, optical aberrations and the finite dimensions of the rods and cones. These effects can be modeled by a low-pass transfer function inserted between the receptor and the nonlinear response element. The most significant contributor to the frequency response of the eye is the lateral inhibition process (27). The basic mechanism of *lateral inhibition* is illustrated in

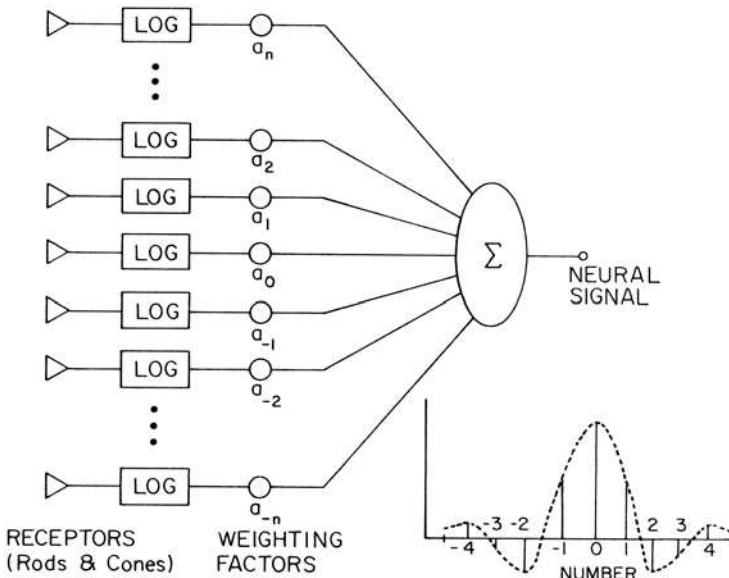


FIGURE 2.4-6. Lateral inhibition effect.

Figure 2.4-6. A neural signal is assumed to be generated by a weighted contribution of many spatially adjacent rods and cones. Some receptors actually exert an inhibitory influence on the neural response. The weighting values are, in effect, the impulse response of the human visual system beyond the retina. The two-dimensional Fourier transform of this impulse response is the post retina transfer function.

When a light pulse is presented to a human viewer, there is a measurable delay in its perception. Also, perception continues beyond the termination of the pulse for a short period of time. This delay and lag effect arising from neural temporal response limitations in the human visual system can be modeled by a linear temporal transfer function.

Figure 2.4-7 shows a model for monochromatic vision based on results of the preceding discussion. In the model, the output of the wavelength-sensitive receptor is fed to a low-pass type of linear system that represents the optics of the eye. Next follows a general monotonic nonlinearity that represents the nonlinear intensity response of rods or cones. Then the lateral inhibition process is characterized by a linear system with a bandpass response. Temporal filtering effects are modeled by the following linear system. Hall and Hall (28) have investigated this model extensively and have found transfer functions for the various elements that accurately model the total system response. The monochromatic vision model of Figure 2.4-7, with appropriately scaled parameters, seems to be sufficiently detailed for most image processing applications. In fact, the simpler logarithmic model of Figure 2.4-4 is probably adequate for the bulk of applications.

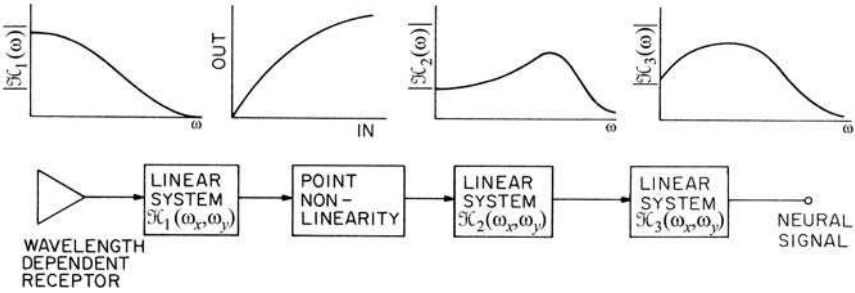


FIGURE 2.4-7. Extended model of monochrome vision.

### 2.5. COLOR VISION MODEL

There have been many theories postulated to explain human color vision, beginning with the experiments of Newton and Maxwell (29–32). The classical model of human color vision, postulated by Thomas Young in 1802 (31), is the trichromatic model in which it is assumed that the eye possesses three types of sensors, each sensitive over a different wavelength band. It is interesting to note that there was no direct physiological evidence of the existence of three distinct types of sensors until about 1960 (9,10).

Figure 2.5-1 shows a color vision model proposed by Frei (33). In this model, three receptors with spectral sensitivities  $s_1(\lambda), s_2(\lambda), s_3(\lambda)$ , which represent the absorption pigments of the retina, produce signals

$$e_1 = \int C(\lambda) s_1(\lambda) d\lambda \tag{2.5-1a}$$

$$e_2 = \int C(\lambda) s_2(\lambda) d\lambda \tag{2.5-1b}$$

$$e_3 = \int C(\lambda) s_3(\lambda) d\lambda \tag{2.5-1c}$$

where  $C(\lambda)$  is the spectral energy distribution of the incident light source. The three signals  $e_1, e_2, e_3$  are then subjected to a logarithmic transfer function and combined to produce the outputs

$$d_1 = \log e_1 \tag{2.5-2a}$$

$$d_2 = \log e_2 - \log e_1 = \log \frac{e_2}{e_1} \tag{2.5-2b}$$

$$d_3 = \log e_3 - \log e_1 = \log \frac{e_3}{e_1} \tag{2.5-2c}$$

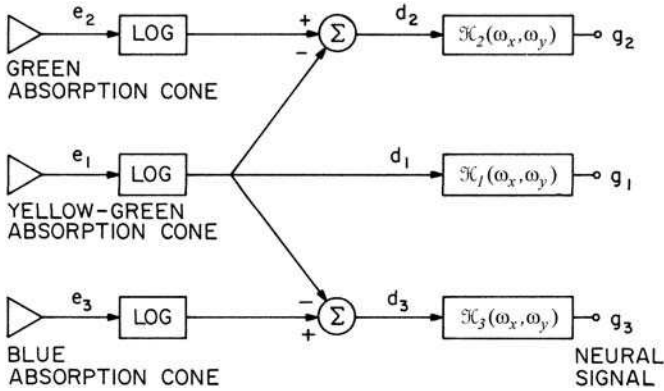


FIGURE 2.5-1 Color vision model.

Finally, the signals  $d_1, d_2, d_3$  pass through linear systems with transfer functions  $\mathcal{H}_1(\omega_x, \omega_y), \mathcal{H}_2(\omega_x, \omega_y), \mathcal{H}_3(\omega_x, \omega_y)$  to produce output signals  $g_1, g_2, g_3$  that provide the basis for perception of color by the brain.

In the model of Figure 2.5-1, the signals  $d_2$  and  $d_3$  are related to the chromaticity of a colored light while signal  $d_1$  is proportional to its luminance. This model has been found to predict many color vision phenomena quite accurately, and also to satisfy the basic laws of colorimetry. For example, it is known that if the spectral energy of a colored light changes by a constant multiplicative factor, the hue and saturation of the light, as described quantitatively by its chromaticity coordinates, remain invariant over a wide dynamic range. Examination of Eqs. 2.5-1 and 2.5-2 indicates that the chrominance signals  $d_2$  and  $d_3$  are unchanged in this case, and that the luminance signal  $d_1$  increases in a logarithmic manner. Other, more subtle evaluations of the model are described by Frei (33).

As shown in Figure 2.2-4, some indication of the spectral sensitivities  $s_i(\lambda)$  of the three types of retinal cones has been obtained by spectral absorption measurements of cone pigments. However, direct physiological measurements are difficult to perform accurately. Indirect estimates of cone spectral sensitivities have been obtained from measurements of the color response of color-blind people by Konig and Brodhun (34). Judd (35) has used these data to produce a linear transformation relating the spectral sensitivity functions  $s_i(\lambda)$  to spectral tristimulus values obtained by colorimetric testing. The resulting sensitivity curves, shown in Figure 2.5-2, are unimodal and strictly positive, as expected from physiological considerations (34).

The logarithmic color vision model of Figure 2.5-1 may easily be extended, in analogy with the monochromatic vision model of Figure 2.4-7, by inserting a linear transfer function after each cone receptor to account for the optical response of the eye. Also, a general nonlinearity may be substituted for the logarithmic transfer function. It should be noted that the order of the receptor summation and the transfer function operations can be reversed without affecting the output, because both are

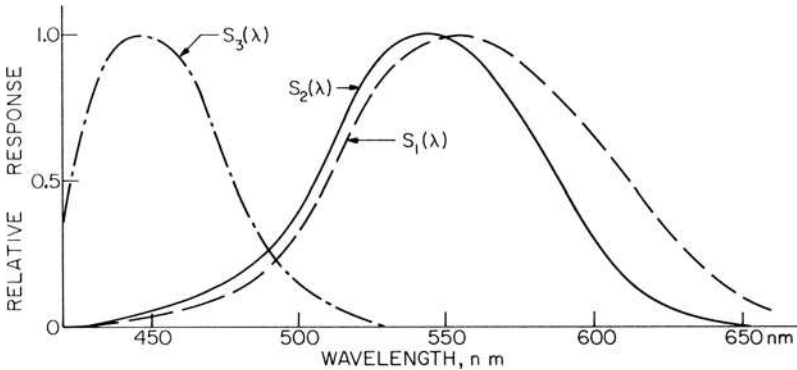


FIGURE 2.5-2. Spectral sensitivity functions of retinal cones based on Konig’s data.

linear operations. Figure 2.5-3 shows the extended model for color vision. It is expected that the spatial frequency response of the  $g_1$  neural signal through the color vision model should be similar to the luminance spatial frequency response discussed in Section 2.4.

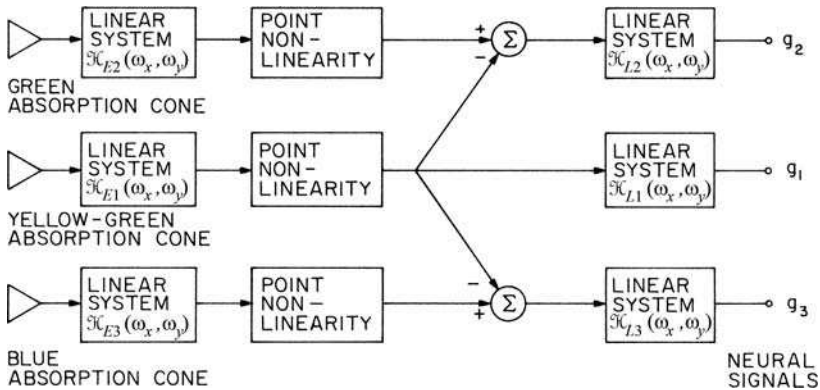


FIGURE 2.5-3. Extended model of color vision.

## 2.6. IMAGE MANIPULATION EXERCISES

E2.1 Develop a program that passes a monochrome image through the log part of the monochrome vision model of Figure 2.4-4. Steps:

- Convert an unsigned integer, 8-bit, monochrome source image to floating point datatype.
- Scale the source image over the range 1.0 to 100.0.



- (c) Compute the source image logarithmic lightness function of Eq. 5.3-4.
- (d) Scale the log source image for display.

The PIKS API executable `example_monochrome_vision` performs this exercise.

E2.2 Develop a program that passes an unsigned integer, monochrome image through a lookup table with a square root function. Steps:

- (a) Read an unsigned integer, 8-bit, monochrome source image from a file.
- (b) Display the source image.
- (c) Allocate a 256 level lookup table.
- (d) Load the lookup table with a square root function.
- (e) Pass the source image through the lookup table.
- (f) Display the destination image.

The PIKS API executable `example_lookup_monochrome_ND` performs this exercise.

E2.3 Develop a program that passes a signed integer, monochrome image through a lookup table with a square root function. Steps:

- (a) Read a signed integer, 16-bit, monochrome source image from a file.
- (b) Linearly scale the source image over its maximum range and display it.
- (c) Allocate a 32,768 level lookup table.
- (d) Load the lookup table with a square root function over the source image maximum range.
- (e) Pass the source image through the lookup table.
- (f) Linearly scale the destination image over its maximum range and display it.

The PIKS API executable `example_lookup_monochrome_SD` performs this exercise.

## REFERENCES

1. *Webster's New Collegiate Dictionary*, G. & C. Merriam Co. (The Riverside Press), Springfield, MA, 1960.
2. H. H. Malitson, "The Solar Energy Spectrum," *Sky and Telescope*, **29**, 4, March 1965, 162-165.
3. *Munsell Book of Color*, Munsell Color Co., Baltimore.
4. M. H. Pirenne, *Vision and the Eye, Second Edition*, Associated Book Publishers, London, 1967.

5. S. L. Polyak, *The Retina*, University of Chicago Press, Chicago, 1941.
6. L. H. Davson, *The Physiology of the Eye*, McGraw-Hill (Blakiston), New York, 1949.
7. T. N. Cornsweet, *Visual Perception*, Academic Press, New York, 1970.
8. G. Wald, "Human Vision and the Spectrum," *Science*, **101**, 2635, June 29, 1945, 653–658.
9. P. K. Brown and G. Wald, "Visual Pigment in Single Rods and Cones of the Human Retina," *Science*, **144**, 3614, April 3, 1964, 45–52.
10. G. Wald, "The Receptors for Human Color Vision," *Science*, **145**, 3636, September 4, 1964, 1007–1017.
11. S. Hecht, "The Visual Discrimination of Intensity and the Weber–Fechner Law," *J. General Physiology*, **7**, 1924, 241.
12. W. F. Schreiber, *Fundamentals of Electronic Imaging Systems*, Springer-Verlag, Berlin, 1986.
13. S. S. Stevens, *Handbook of Experimental Psychology*, John Wiley and Sons, New York, 1951.
14. F. Ratliff, *Mach Bands: Quantitative Studies on Neural Networks in the Retina*, Holden-Day, San Francisco, 1965.
15. G. S. Brindley, "Afterimages," *Scientific American*, **209**, 4, October 1963, 84–93.
16. G. Wyszecki and W. S. Stiles, *Color Science, Second Edition*, John Wiley and Sons, New York, 1982.
17. J. W. Goodman, *Introduction to Fourier Optics, Second Edition*, McGraw-Hill, New York, 1996.
18. F. W. Campbell, "The Human Eye as an Optical Filter," *Proc. IEEE*, **56**, 6, June 1968, 1009–1014.
19. O. Bryngdahl, "Characteristics of the Visual System: Psychophysical Measurement of the Response to Spatial Sine-Wave Stimuli in the Mesopic Region," *J. Optical Society of America*, **54**, 9, September 1964, 1152–1160.
20. E. M. Lowry and J. J. DePalma, "Sine Wave Response of the Visual System, I. The Mach Phenomenon," *J. Optical Society of America*, **51**, 7, July 1961, 740–746.
21. E. M. Lowry and J. J. DePalma, "Sine Wave Response of the Visual System, II. Sine Wave and Square Wave Contrast Sensitivity," *J. Optical Society of America*, **52**, 3, March 1962, 328–335.
22. M. B. Sachs, J. Nachmias and J. G. Robson, "Spatial Frequency Channels in Human Vision," *J. Optical Society of America*, **61**, 9, September 1971, 1176–1186.
23. T. G. Stockham, Jr., "Image Processing in the Context of a Visual Model," *Proc. IEEE*, **60**, 7, July 1972, 828–842.
24. D. E. Pearson, "A Realistic Model for Visual Communication Systems," *Proc. IEEE*, **55**, 3, March 1967, 380–389.
25. M. L. Davidson, "Perturbation Approach to Spatial Brightness Interaction in Human Vision," *J. Optical Society of America*, **58**, 9, September 1968, 1300–1308.
26. J. L. Mannon and D. J. Sakrison, "The Effects of a Visual Fidelity Criterion on the Encoding of Images," *IEEE Trans. Information Theory*, **IT-20**, 4, July 1974, 525–536.
27. F. Ratliff, H. K. Hartline and W. H. Miller, "Spatial and Temporal Aspects of Retinal Inhibitory Interaction," *J. Optical Society of America*, **53**, 1, January 1963, 110–120.

28. C. F. Hall and E. L. Hall, "A Nonlinear Model for the Spatial Characteristics of the Human Visual System," *IEEE Trans, Systems, Man and Cybernetics*, **SMC-7**, 3, March 1977, 161–170.
29. J. J. McCann, "Human Color Perception," in *Color: Theory and Imaging Systems*, R. A. Enyard, Ed., Society of Photographic Scientists and Engineers, Washington, DC, 1973, 1–23.
30. I. Newton, *Optiks, Fourth Edition*, 1730; Dover Publications, New York, 1952.
31. T. Young, *Philosophical Trans*, **92**, 1802, 12–48.
32. J. C. Maxwell, *Scientific Papers of James Clerk Maxwell*, W. D. Nevern, Ed., Dover Publications, New York, 1965.
33. W. Frei, "A New Model of Color Vision and Some Practical Limitations," USCEE Report 530, University of Southern California, Image Processing Institute, Los Angeles March 1974, 128–143.
34. A. Konig and E. Brodhun, "Experimentell Untersuchungen uber die Psycho-physische fundamental in Bezug auf den Gesichtssinn," *Zweite Mittlg. S.B. Preuss Akademik der Wissenschaften*, 1889, 641.
35. D. B. Judd, "Standard Response Functions for Protanopic and Deuteranopic Vision," *J. Optical Society of America*, **35**, 3, March 1945, 199–221.

---

# 3

---

## PHOTOMETRY AND COLORIMETRY

Chapter 2 dealt with human vision from a qualitative viewpoint in an attempt to establish models for monochrome and color vision. These models may be made quantitative by specifying measures of human light perception. Luminance measures are the subject of the science of photometry, while color measures are treated by the science of colorimetry.

### 3.1. PHOTOMETRY

A source of radiative energy may be characterized by its spectral energy distribution  $C(\lambda)$ , which specifies the time rate of energy the source emits per unit wavelength interval. The total power emitted by a radiant source, given by the integral of the spectral energy distribution,

$$P = \int_0^{\infty} C(\lambda) d\lambda \quad (3.1-1)$$

is called the *radiant flux* of the source and is normally expressed in watts (W).

A body that exists at an elevated temperature radiates electromagnetic energy proportional in amount to its temperature. A *blackbody* is an idealized type of heat radiator whose radiant flux is the maximum obtainable at any wavelength for a body

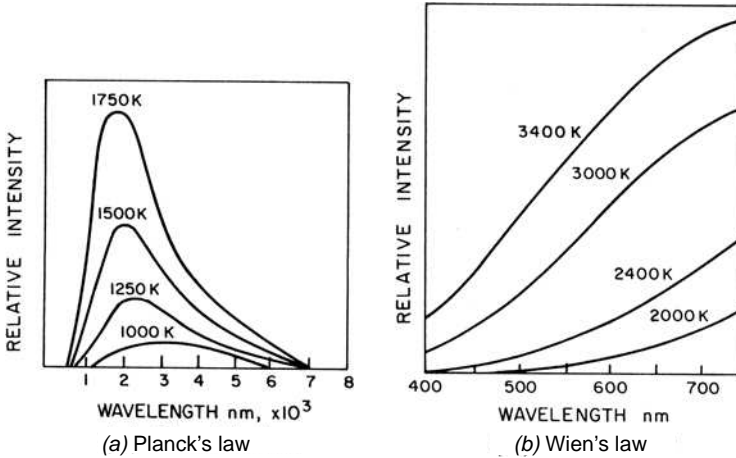


FIGURE 3.1-1. Blackbody radiation functions.

at a fixed temperature. The spectral energy distribution of a blackbody is given by *Planck's law* (1):

$$C(\lambda) = \frac{C_1}{\lambda^5 [\exp\{C_2/\lambda T\} - 1]} \tag{3.1-2}$$

where  $\lambda$  is the radiation wavelength,  $T$  is the temperature of the body and  $C_1$  and  $C_2$  are constants. Figure 3.1-1a is a plot of the spectral energy of a blackbody as a function of temperature and wavelength. In the visible region of the electromagnetic spectrum, the blackbody spectral energy distribution function of Eq. 3.1-2 can be approximated by *Wien's radiation law* (1):

$$C(\lambda) = \frac{C_1}{\lambda^5 \exp\{C_2/\lambda T\}} \tag{3.1-3}$$

Wien's radiation function is plotted in Figure 3.1-1b over the visible spectrum.

The most basic physical light source, of course, is the sun. Figure 2.1-1a shows a plot of the measured spectral energy distribution of sunlight (2). The dashed line in this figure, approximating the measured data, is a 6000 kelvin (K) blackbody curve. Incandescent lamps are often approximated as blackbody radiators of a given temperature in the range 1500 to 3500 K (3).

The Commission Internationale de l'Eclairage (CIE), which is an international body concerned with standards for light and color, has established several standard sources of light, as illustrated in Figure 3.1-2 (4). Source  $S_A$  is a tungsten filament lamp. Over the wavelength band 400 to 700 nm, source  $S_B$  approximates direct sunlight and source  $S_C$  approximates light from an overcast sky. A hypothetical source, called *Illuminant E*, is often employed in colorimetric calculations. Illuminant *E* is assumed to emit constant radiant energy at all wavelengths.

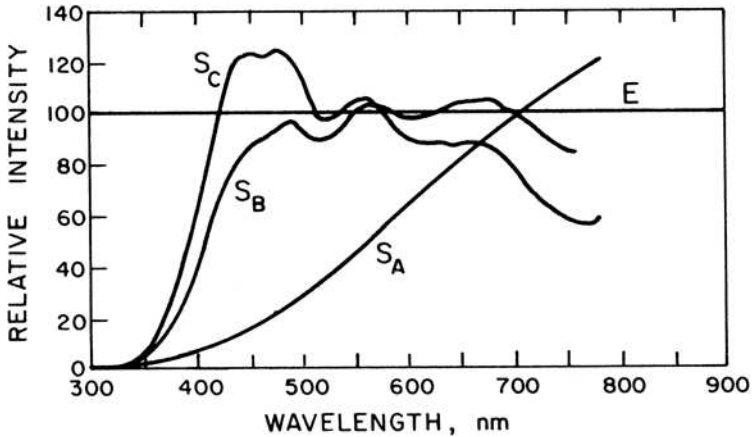


FIGURE 3.1-2. CIE standard illumination sources.

Cathode ray tube (CRT) phosphors have often been utilized as light sources in image processing systems. Figure 3.1-3 describes the spectral energy distributions of common phosphors (5). Monochrome television receivers generally use a P4 phosphor, which provides a relatively bright blue-white display. Color television displays utilize cathode ray tubes with red, green and blue emitting phosphors arranged in triad dots or strips. The P22 phosphor is typical of the spectral energy distribution of commercial phosphor mixtures. Liquid crystal displays (LCDs) typically project a white light through red, green and blue vertical strip pixels. Figure 3.1-4 is a plot of typical color filter transmissivities (6).

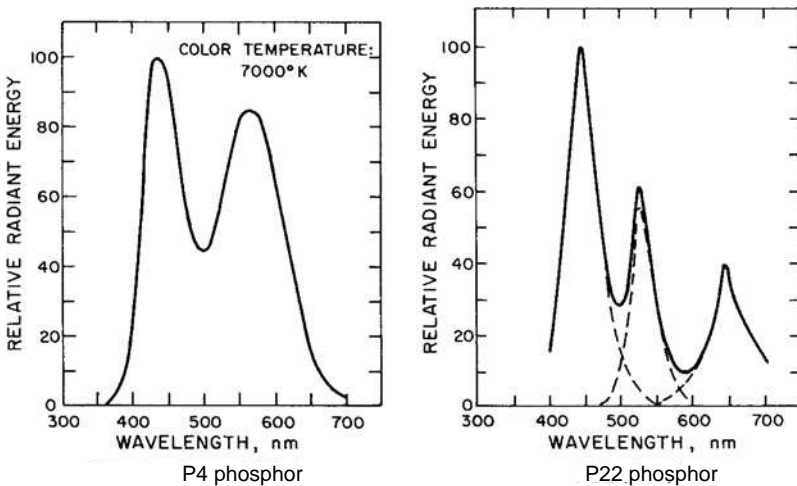


FIGURE 3.1-3. Spectral energy distribution of CRT phosphors.

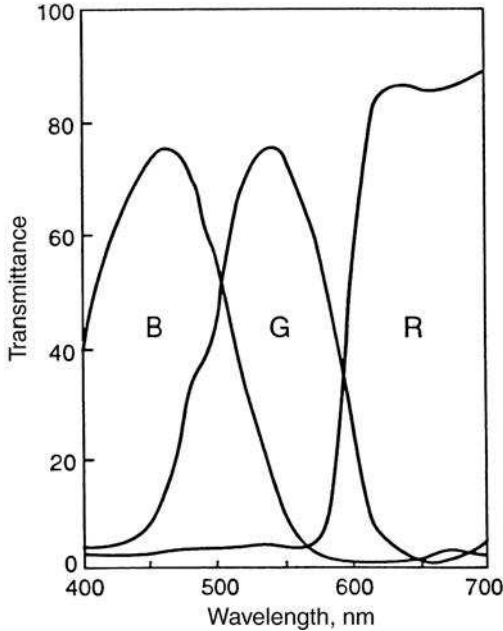


FIGURE 3.1-4. Transmissivities of LCD color filters.

Photometric measurements seek to describe quantitatively the perceptual brightness of visible electromagnetic energy (7,8). The link between photometric measurements and radiometric measurements (physical intensity measurements) is the *photopic* luminosity function, as shown in Figure 3.1-5a (9). This curve, which is a CIE standard, specifies the spectral sensitivity of the human visual system to optical radiation as a function of wavelength for a typical person referred to as the *standard observer*. In essence, the curve is a standardized version of the measurement of cone sensitivity given in Figure 2.2-2 for photopic vision at relatively high levels of illumination. The standard luminosity function for *scotopic* vision at relatively low levels of illumination is illustrated in Figure 3.1-5b. Most imaging system designs are based on the photopic luminosity function, commonly called the *relative luminous efficiency*.

The perceptual brightness sensation evoked by a light source with spectral energy distribution  $C(\lambda)$  is specified by its *luminous flux*, as defined by

$$F = K_m \int_0^\infty C(\lambda)V(\lambda) d\lambda \tag{3.1-4}$$

where  $V(\lambda)$  represents the relative luminous efficiency and  $K_m$  is a scaling constant. The modern unit of luminous flux is the lumen (lm), and the corresponding value for the scaling constant is  $K_m = 685 \text{ lm/W}$ . An infinitesimally narrowband

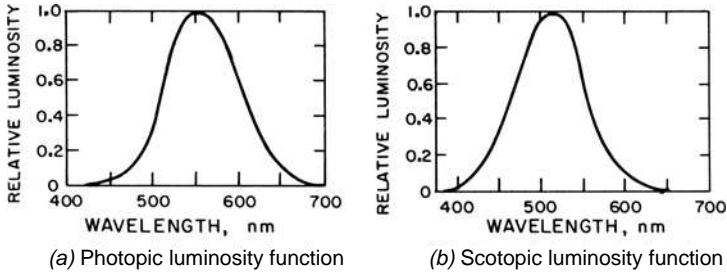


FIGURE 3.1-5. Relative luminous efficiency functions.

source of 1 W of light at the peak wavelength of 555 nm of the relative luminous efficiency curve therefore results in a luminous flux of 685 lm.

### 3.2. COLOR MATCHING

The basis of the trichromatic theory of color vision is that it is possible to match an arbitrary color by superimposing appropriate amounts of three primary colors (10–14). In an *additive color reproduction system* such as color television, the three primaries are individual red, green and blue light sources that are projected onto a common region of space to reproduce a colored light. In a *subtractive color system*, which is the basis of most color photography and color printing, a white light sequentially passes through cyan, magenta and yellow filters to reproduce a colored light.

#### 3.2.1. Additive Color Matching

An additive color-matching experiment is illustrated in Figure 3.2-1. In Figure 3.2-1a, a patch of light ( $C$ ) of arbitrary spectral energy distribution  $C(\lambda)$ , as shown in Figure 3.2-2a, is assumed to be imaged onto the surface of an ideal diffuse reflector (a surface that reflects uniformly over all directions and all wavelengths). A reference white light ( $W$ ) with an energy distribution, as in Figure 3.2-2b, is imaged onto the surface along with three primary lights ( $P_1$ ), ( $P_2$ ), ( $P_3$ ) whose spectral energy distributions are sketched in Figure 3.2-2c to e. The three primary lights are first overlapped and their intensities are adjusted until the overlapping region of the three primary lights perceptually matches the reference white in terms of brightness, hue and saturation. The amounts of the three primaries  $A_1(W)$ ,  $A_2(W)$ ,  $A_3(W)$  are then recorded in some physical units, such as watts. These are the matching values of the reference white. Next, the intensities of the primaries are adjusted until a match is achieved with the colored light ( $C$ ), if a match is possible. The procedure to be followed if a match cannot be achieved is considered later. The intensities of the primaries  $A_1(C)$ ,  $A_2(C)$ ,  $A_3(C)$  when a match is



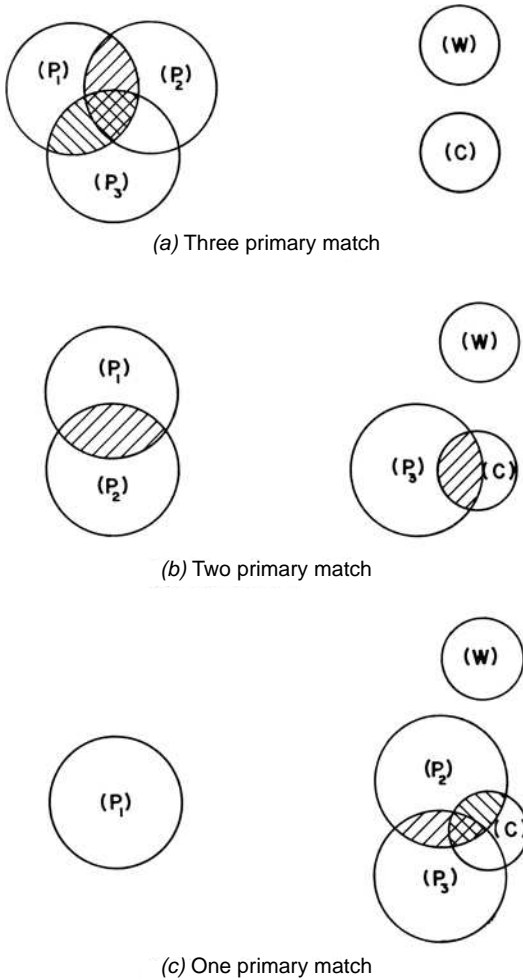


**FIGURE 3.2-1.** Color matching.

obtained are recorded, and normalized matching values  $T_1(C)$ ,  $T_2(C)$ ,  $T_3(C)$ , called *tristimulus values*, are computed as

$$T_1(C) = \frac{A_1(C)}{A_1(W)}, \quad T_2(C) = \frac{A_2(C)}{A_2(W)}, \quad T_3(C) = \frac{A_3(C)}{A_3(W)}. \quad (3.2-1)$$

If a match cannot be achieved by the procedure illustrated in Figure 3.2-1a, it is often possible to perform the color matching outlined in Figure 3.2-1b. One of the

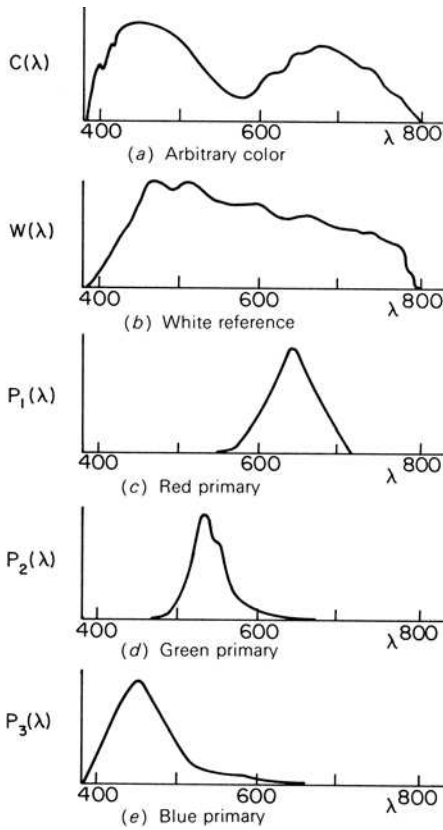


**FIGURE 3.2-2.** Spectral energy distributions.

primaries, say ( $P_3$ ), is superimposed with the light ( $C$ ), and the intensities of all three primaries are adjusted until a match is achieved between the overlapping region of primaries ( $P_1$ ) and ( $P_2$ ) with the overlapping region of ( $P_3$ ) and ( $C$ ). If such a match is obtained, the tristimulus values are

$$T_1(C) = \frac{A_1(C)}{A_1(W)}, \quad T_2(C) = \frac{A_2(C)}{A_2(W)}, \quad T_3(C) = \frac{-A_3(C)}{A_3(W)}. \quad (3.2-2)$$

In this case, the tristimulus value  $T_3(C)$  is negative. If a match cannot be achieved with this geometry, a match is attempted between ( $P_1$ ) plus ( $P_3$ ) and ( $P_2$ ) plus ( $C$ ). If a match is achieved by this configuration, tristimulus value  $T_2(C)$  will be negative. If this configuration fails, a match is attempted between ( $P_2$ ) plus ( $P_3$ ) and ( $P_1$ ) plus ( $C$ ). A correct match is denoted with a negative value for  $T_1(C)$ .

Finally, in the rare instance in which a match cannot be achieved by either of the configurations of Figure 3.2-1a or b, two of the primaries are superimposed with (C) and an attempt is made to match the overlapped region with the remaining primary. In the case illustrated in Figure 3.2-1c, if a match is achieved, the tristimulus values become

$$T_1(C) = \frac{A_1(C)}{A_1(W)}, \quad T_2(C) = \frac{-A_2(C)}{A_2(W)}, \quad T_3(C) = \frac{-A_3(C)}{A_3(W)}. \quad (3.2-3)$$

If a match is not obtained by this configuration, one of the other two possibilities will yield a match.

The process described above is a direct method for specifying a color quantitatively. It has two drawbacks: The method is cumbersome and it depends on the perceptual variations of a single observer. In Section 3.3, standardized quantitative color measurement is considered in detail.

### 3.2.2. Subtractive Color Matching

A subtractive color-matching experiment is shown in Figure 3.2-3. An illumination source with spectral energy distribution  $E(\lambda)$  passes sequentially through three dye filters that are nominally cyan, magenta and yellow. The spectral absorption of the dye filters is a function of the dye concentration. It should be noted that the spectral transmissivities of practical dyes change shape in a nonlinear manner with dye concentration.

In the first step of the subtractive color-matching process, the dye concentrations of the three spectral filters are varied until a perceptual match is obtained with a reference white (W). The dye concentrations are the matching values of the color match  $A_1(W)$ ,  $A_2(W)$ ,  $A_3(W)$ . Next, the three dye concentrations are varied until a match is obtained with a desired color (C). These matching values  $A_1(C)$ ,  $A_2(C)$ ,  $A_3(C)$ , are then used to compute the tristimulus values  $T_1(C)$ ,  $T_2(C)$ ,  $T_3(C)$ , as in Eq. 3.2-1.

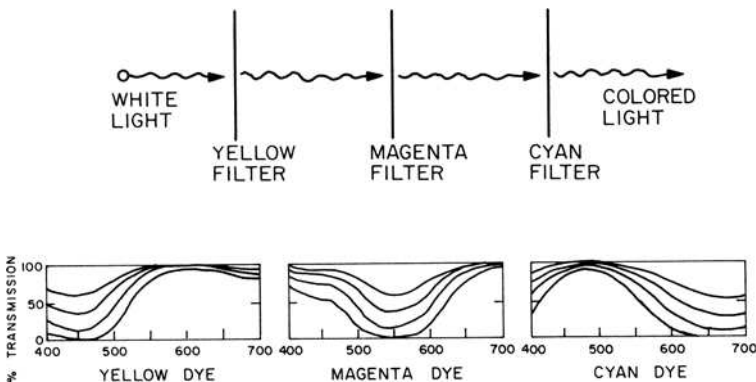


FIGURE 3.2-3. Subtractive color matching.

It should be apparent that there is no fundamental theoretical difference between color matching by an additive or a subtractive system. In a subtractive system, the yellow dye acts as a variable absorber of blue light, and with ideal dyes, the yellow dye effectively forms a blue primary light. In a similar manner, the magenta filter ideally forms the green primary, and the cyan filter ideally forms the red primary. Subtractive color systems ordinarily utilize cyan, magenta and yellow dye spectral filters rather than red, green and blue dye filters because the cyan, magenta and yellow filters are notch filters, which permit a greater transmission of light energy than do narrowband red, green and blue bandpass filters. In color printing, a fourth filter layer of variable gray level density is often introduced to achieve a higher contrast in reproduction because common dyes do not possess a wide density range.

### 3.2.3. Axioms of Color Matching

The color-matching experiments described for additive and subtractive color matching have been performed quite accurately by a number of researchers. It has been found that perfect color matches sometimes cannot be obtained at either very high or very low levels of illumination. Also, the color matching results do depend to some extent on the spectral composition of the surrounding light. Nevertheless, the simple color matching experiments have been found to hold over a wide range of conditions.

Grassman (15) has developed a set of eight axioms that define trichromatic color matching and that serve as a basis for quantitative color measurements. In the following presentation of these axioms, the symbol  $\cap$  indicates the set intersection; the symbol  $\diamond$  indicates a color match; the symbol  $\oplus$  indicates an additive color mixture; the symbol  $\bullet$  indicates units of a color. These axioms are:

1. Any color can be matched by a mixture of no more than three colored lights.
2. A color match at one radiance level holds over a wide range of levels.
3. Components of a mixture of colored lights cannot be resolved by the human eye.
4. The luminance of a color mixture is equal to the sum of the luminance of its components.
5. *Law of addition.* If color ( $M$ ) matches color ( $N$ ) and color ( $P$ ) matches color ( $Q$ ), then color ( $M$ ) mixed with color ( $P$ ) matches color ( $N$ ) mixed with color ( $Q$ ):

$$(M) \diamond (N) \cap (P) \diamond (Q) \Rightarrow [(M) \oplus (P)] \diamond [(N) \oplus (Q)]. \tag{3.2-4}$$

6. *Law of subtraction.* If the mixture of ( $M$ ) plus ( $P$ ) matches the mixture of ( $N$ ) plus ( $Q$ ) and if ( $P$ ) matches ( $Q$ ), then ( $M$ ) matches ( $N$ ):

$$[(M) \oplus (P)] \diamond [(N) \oplus (Q)] \cap [(P) \diamond (Q)] \Rightarrow (M) \diamond (N). \tag{3.2-5}$$

7. *Transitive law.* If ( $M$ ) matches ( $N$ ) and if ( $N$ ) matches ( $P$ ), then ( $M$ ) matches ( $P$ ):

$$[(M) \diamond (N)] \cap [(N) \diamond (P)] \Rightarrow (M) \diamond (P). \tag{3.2-6}$$

8. *Color matching.* (a)  $c$  units of ( $C$ ) matches the mixture of  $m$  units of ( $M$ ) plus  $n$  units of ( $N$ ) plus  $p$  units of ( $P$ ):

$$c \bullet C \diamond [m \bullet (M)] \oplus [n \bullet (N)] \oplus [p \bullet (P)]. \tag{3.2-7}$$

or (b) a mixture of  $c$  units of  $C$  plus  $m$  units of  $M$  matches the mixture of  $n$  units of  $N$  plus  $p$  units of  $P$ :

$$[c \bullet (C)] \oplus [m \bullet (M)] \diamond [n \bullet (N)] \oplus [p \bullet (P)]. \tag{3.2-8}$$

or (c) a mixture of  $c$  units of ( $C$ ) plus  $m$  units of ( $M$ ) plus  $n$  units of ( $N$ ) matches  $p$  units of  $P$ :

$$[c \bullet (C)] \oplus [m \bullet (M)] \oplus [n \bullet (N)] \diamond [p \bullet (P)]. \tag{3.2-9}$$

With Grassman's laws now specified, consideration is given to the development of a quantitative theory for color matching.

### 3.3. COLORIMETRY CONCEPTS

*Colorimetry* is the science of quantitatively measuring color. In the trichromatic color system, color measurements are in terms of the tristimulus values of a color or a mathematical function of the tristimulus values.

Referring to Section 3.2.3, the axioms of color matching state that a color  $C$  can be matched by three primary colors  $P_1, P_2, P_3$ . The qualitative match is expressed as

$$(C) \diamond [A_1(C) \bullet (P_1)] \oplus [A_2(C) \bullet (P_2)] \oplus [A_3(C) \bullet (P_3)]. \tag{3.3-1}$$

where  $A_1(C), A_2(C), A_3(C)$  are the matching values of the color ( $C$ ). Because the intensities of incoherent light sources add linearly, the spectral energy distribution of a color mixture is equal to the sum of the spectral energy distributions of its components. As a consequence of this fact and Eq. 3.3-1, the spectral energy distribution  $C(\lambda)$  can be replaced by its color-matching equivalent according to the relation

$$C(\lambda) \diamond A_1(C)P_1(\lambda) + A_2(C)P_2(\lambda) + A_3(C)P_3(\lambda) = \sum_{j=1}^3 A_j(C)P_j(\lambda). \tag{3.3-2}$$

Equation 3.3-2 simply means that the spectral energy distributions on both sides of the equivalence operator  $\diamond$  evoke the same color sensation. Color matching is usually specified in terms of tristimulus values, which are normalized matching values, as defined by

$$T_j(C) = \frac{A_j(C)}{A_j(W)} \tag{3.3-3}$$

where  $A_j(W)$  represents the matching value of the reference white. By this substitution, Eq. 3.3-2 assumes the form

$$C(\lambda) \diamond \sum_{j=1}^3 T_j(C)A_j(W)P_j(\lambda) . \tag{3.3-4}$$

From Grassman’s fourth law, the luminance of a color mixture  $Y(C)$  is equal to the luminance of its primary components. Hence

$$Y(C) = \int C(\lambda)V(\lambda)d\lambda = \sum_{j=1}^3 \int A_j(C)P_j(\lambda)V(\lambda)d\lambda \tag{3.3-5a}$$

or

$$Y(C) = \sum_{j=1}^3 \int T_j(C)A_j(W)P_j(\lambda)V(\lambda) d\lambda \tag{3.3-5b}$$

where  $V(\lambda)$  is the relative luminous efficiency and  $P_j(\lambda)$  represents the spectral energy distribution of a primary. Equations 3.3-4 and 3.3-5 represent the quantitative foundation for colorimetry.<sup>1</sup>

### 3.3.1. Tristimulus Value Calculation

It is possible indirectly to compute the tristimulus values of an arbitrary color for a particular set of primaries if the tristimulus values of the spectral colors (narrowband light) are known for that set of primaries. Figure 3.3-1 is a typical sketch of the tristimulus values required to match a unit energy spectral color with three arbitrary primaries. These tristimulus values, which are fundamental to the definition of a primary system, are denoted as  $T_{s_1}(\lambda)$ ,  $T_{s_2}(\lambda)$ ,  $T_{s_3}(\lambda)$ , where  $\lambda$  is a particular wavelength in the visible region. A unit energy spectral light ( $C_\psi$ ) at wavelength  $\psi$  with energy distribution  $\delta(\lambda - \psi)$  is matched according to the equation

$$e_i(C_\psi) = \int \delta(\lambda - \psi)s_i(\lambda) d\lambda = \sum_{j=1}^3 \int A_j(W)P_j(\lambda)T_{s_j}(\psi)s_i(\lambda) d\lambda . \tag{3.3-6}$$

---

1. In *Digital Image Processing, Fourth Edition*, Pratt shows that the color vision model presented in Section 2.5 satisfies the axioms of color matching.

Now, consider an arbitrary color ( $C$ ) with spectral energy distribution  $C(\lambda)$ . At wavelength  $\psi$ ,  $C(\psi)$  units of the color are matched by  $C(\psi)T_{s_1}(\psi)$ ,  $C(\psi)T_{s_2}(\psi)$ ,  $C(\psi)T_{s_3}(\psi)$  tristimulus units of the primaries as governed by

$$\int C(\psi)\delta(\lambda - \psi)s_i(\lambda) d\lambda = \sum_{j=1}^3 \int A_j(W)P_j(\lambda)C(\psi)T_{s_j}(\psi)s_i(\lambda) d\lambda. \quad (3.3-7)$$

Integrating each side of Eq. 3.3-7 over  $\psi$  and invoking the sifting integral gives the cone signal for the color ( $C$ ). Thus

$$\iint C(\psi)\delta(\lambda - \psi)s_i(\lambda) d\lambda d\psi = e_i(C) = \sum_{j=1}^3 \iint A_j(W)P_j(\lambda)C(\psi)T_{s_j}(\psi)s_i(\lambda) d\psi d\lambda. \quad (3.3-8)$$

The tristimulus values of ( $C$ ) must be equivalent to the second integral on the right of Eq. 3.3-8. Hence

$$T_j(C) = \int C(\psi)T_{s_j}(\psi) d\psi. \quad (3.3-9)$$

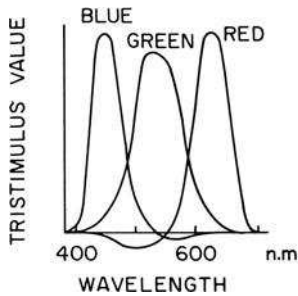


**FIGURE 3.3-1.** Tristimulus values of typical red, green and blue primaries required to match unit energy throughout the spectrum.

From Figure 3.3-1 it is seen that the tristimulus values may be negative at some wavelengths. Because the tristimulus values represent units of energy, the physical interpretation of this mathematical result is that a color match can be obtained by adding the primary with negative tristimulus value to the original color and then matching this resultant color with the remaining primary. In this sense, any color can be matched by any set of primaries. However, from a practical viewpoint, negative tristimulus values are not physically realizable, and hence there are certain colors that cannot be matched in a practical color display (e.g., a color television receiver) with fixed primaries. Fortunately, it is possible to choose primaries so that most commonly occurring natural colors can be matched.

The three tristimulus values  $T_1, T_2, T_3$  can be considered to form the three axes of a color space as illustrated in Figure 3.3-2. A particular color may be described as a vector in the color space, but it must be remembered that it is the coordinates of the vectors (tristimulus values), rather than the vector length, that specify the color. In Figure 3.3-2, a triangle, called a *Maxwell triangle*, has been drawn between the three primaries. The intersection point of a color vector with the triangle gives an indication of the hue and saturation of the color in terms of the distances of the point from the vertices of the triangle.

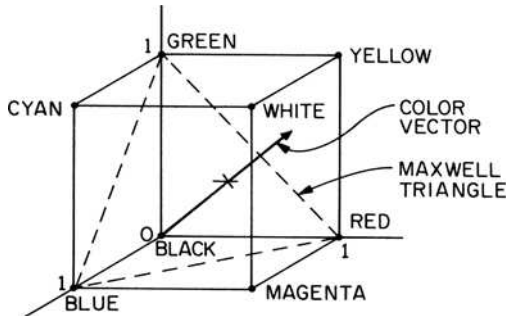


FIGURE 3.3-2. Color space for typical red, green and blue primaries.

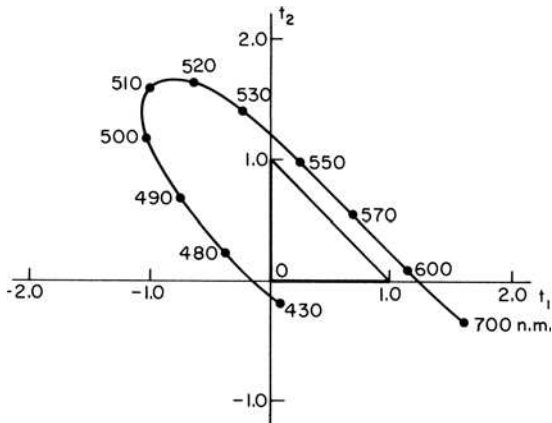


FIGURE 3.3-3. Chromaticity diagram for typical red, green and blue primaries.

Often the luminance of a color is not of interest in a color match. In such situations, the hue and saturation of color ( $C$ ) can be described in terms of *chromaticity coordinates*, which are normalized tristimulus values, as defined by



$$t_1 \equiv \frac{T_1}{T_1 + T_2 + T_3}, \tag{3.3-10a}$$

$$t_2 \equiv \frac{T_2}{T_1 + T_2 + T_3}, \tag{3.3-10b}$$

$$t_3 \equiv \frac{T_3}{T_1 + T_2 + T_3}. \tag{3.3-10c}$$

Clearly,  $t_3 = 1 - t_1 - t_2$ , and hence only two chromaticity coordinates are necessary to describe a color match. Figure 3.3-3 is a plot of the chromaticity coordinates of the spectral colors for typical primaries. Only those colors within the triangle defined by the three primaries are realizable by physical primary light sources.

**3.3.2. Luminance Calculation**

The tristimulus values of a color specify the amounts of the three primaries required to match a color where the units are measured relative to a match of a reference white. Often, it is necessary to determine the absolute rather than the relative amount of light from each primary needed to reproduce a color match. This information is found from luminance measurements of calculations of a color match.

From Eq. 3.3-5 it is noted that the *luminance* of a matched color  $Y(C)$  is equal to the sum of the luminances of its primary components according to the relation

$$Y(C) = \sum_{j=1}^3 T_j(C) \int A_j(C) P_j(\lambda) V(\lambda) d\lambda. \tag{3.3-11}$$

The integrals of Eq. 3.3-11,

$$Y(P_j) = \int A_j(C) P_j(\lambda) V(\lambda) d\lambda \tag{3.3-12}$$

are called *luminosity coefficients* of the primaries. These coefficients represent the luminances of unit amounts of the three primaries for a match to a specific reference white. Hence, the luminance of a matched color can be written as

$$Y(C) = T_1(C)Y(P_1) + T_2(C)Y(P_2) + T_3(C)Y(P_3). \tag{3.3-13}$$

Multiplying the right and left sides of Eq. 3.3-13 by the right and left sides, respectively, of the definition of the chromaticity coordinate

$$t_1(C) = \frac{T_1(C)}{T_1(C) + T_2(C) + T_3(C)} \tag{3.3-14}$$

and rearranging gives

$$T_1(C) = \frac{t_1(C)Y(C)}{t_1(C)Y(P_1) + t_2(C)Y(P_2) + t_3(C)Y(P_3)}. \quad (3.3-15a)$$

Similarly,

$$T_2(C) = \frac{t_2(C)Y(C)}{t_1(C)Y(P_1) + t_2(C)Y(P_2) + t_3(C)Y(P_3)} \quad (3.3-15b)$$

$$T_3(C) = \frac{t_3(C)Y(C)}{t_1(C)Y(P_1) + t_2(C)Y(P_2) + t_3(C)Y(P_3)}. \quad (3.3-15c)$$

Thus, if the tristimulus values are known for a given set of primaries, conversion to another set of primaries merely entails a simple linear transformation of coordinates (16).

### 3.4. COLOR SPACES

It has been shown that a color ( $C$ ) can be matched by its tristimulus values  $T_1(C)$ ,  $T_2(C)$ ,  $T_3(C)$  for a given set of primaries. Alternatively, the color may be specified by its chromaticity values  $t_1(C)$ ,  $t_2(C)$  and its luminance  $Y(C)$ . Appendix 2 presents formulas for color coordinate conversion between tristimulus values and chromaticity coordinates for various representational combinations. A third approach in specifying a color is to represent the color by a linear or nonlinear invertible function of its tristimulus or chromaticity values.

In this section, several standard and nonstandard color spaces for the representation of color images are described. They are categorized as colorimetric, subtractive, video or nonstandard. Figure 3.4-1 illustrates the relationship between these color spaces. The figure also lists several example color spaces.

Natural color images, as opposed to computer-generated images, usually originate from a color scanner or a color video camera. These devices incorporate three sensors that are spectrally sensitive to the red, green and blue portions of the light spectrum. The color sensors typically generate red, green and blue color signals that are linearly proportional to the amount of red, green and blue light detected by each sensor. These signals are linearly proportional to the tristimulus values of a color at each pixel. As indicated in Figure 3.4-1, linear *RGB* images are the basis for the generation of the various color space image representations.

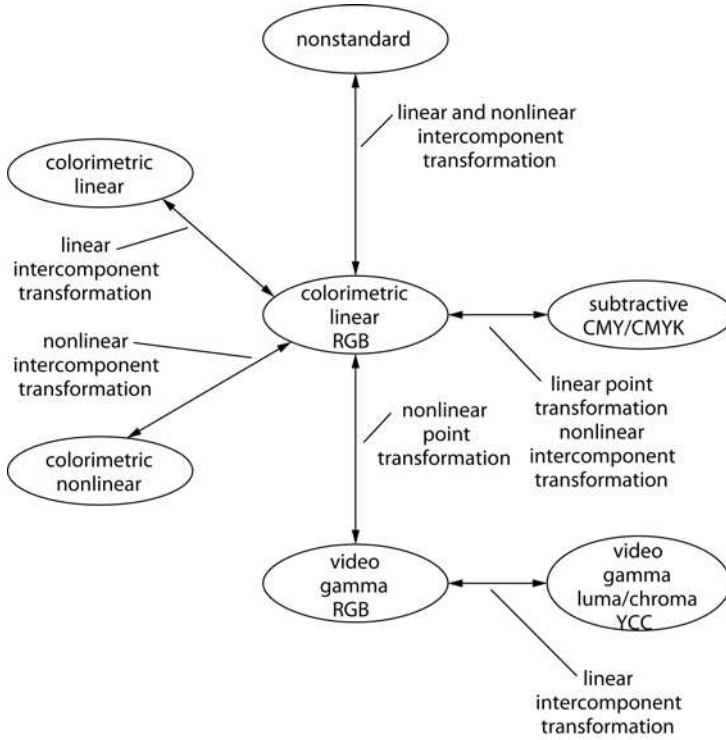


FIGURE 3.4-1. Relationship of color spaces.

### 3.4.1. Colorimetric Color Spaces

The class of colorimetric color spaces includes all linear *RGB* images and the standard colorimetric images derived from them by linear and nonlinear intercomponent transformations.

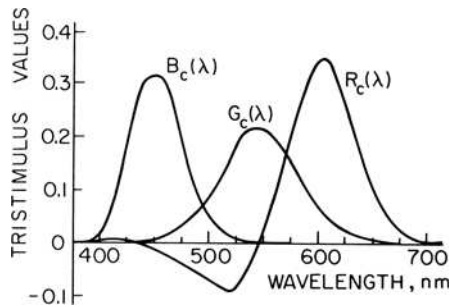
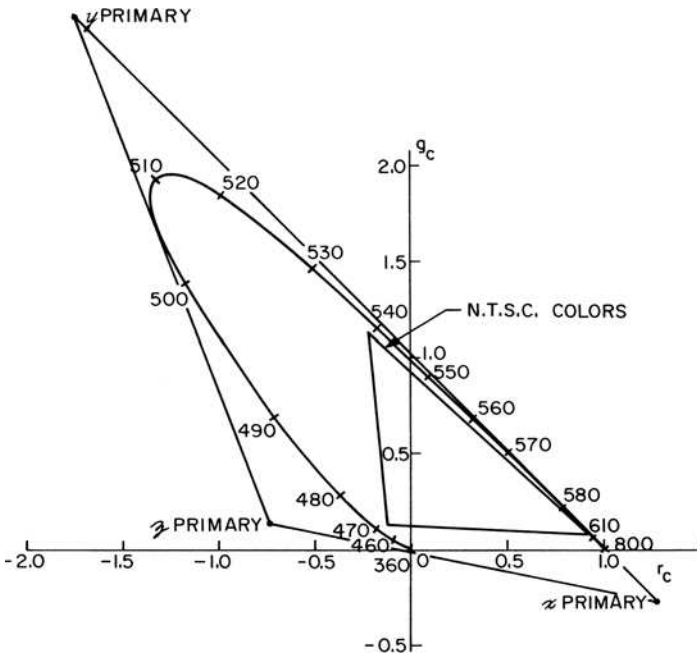


FIGURE 3.4-2. Tristimulus values of CIE spectral primaries required to match unit energy throughout the spectrum. Red = 700 nm, green = 546.1 nm and blue = 435.8 nm.

**$R_C G_C B_C$  Spectral Primary Color Coordinate System.** In 1931, the CIE developed a standard primary reference system with three monochromatic primaries at wavelengths: red = 700 nm; green = 546.1 nm; blue = 435.8 nm (11). The units of the tristimulus values are such that the tristimulus values  $R_C$ ,  $G_C$ ,  $B_C$  are equal when matching an equal-energy white, called *Illuminant E*, throughout the visible spectrum. The primary system is defined by tristimulus curves of the spectral colors, as shown in Figure 3.4-2. These curves have been obtained indirectly by experimental color-matching experiments performed by a number of observers. The collective color-matching response of these observers has been called the *CIE Standard Observer*. Figure 3.4-3 is a chromaticity diagram for the CIE spectral coordinate system.



**FIGURE 3.4-3.** Chromaticity diagram for CIE spectral primary system.

**$R_N G_N B_N$  NTSC Receiver Primary Color Coordinate System.** When the United States color television system was standardized in 1953 (14), commercial television receivers employed a cathode ray tube with three phosphors that glow in the red, green and blue regions of the visible spectrum. Although the phosphors of commercial television receivers differ from manufacturer to manufacturer, it is common practice to reference them to the National Television Systems Committee (NTSC) receiver phosphor standard (14). The standard observer data for the CIE spectral primary system is related to the NTSC primary system by a pair of linear coordinate conversions.

Figure 3.4-4 is a chromaticity diagram for the NTSC primary system. In this system, the units of the tristimulus values are normalized so that the tristimulus

values are equal when matching the *Illuminant C* white reference. The NTSC phosphors are not pure monochromatic sources of radiation, and hence the gamut of colors producible by the NTSC phosphors is smaller than that available from the spectral primaries. This fact is clearly illustrated by Figure 3.4-3, in which the gamut of NTSC reproducible colors is plotted in the spectral primary chromaticity diagram (11). In modern practice, the NTSC chromaticities are combined with *Illuminant D65*.

**$R_E G_E B_E$  EBU Receiver Primary Color Coordinate System.** The European Broadcast Union (EBU) has established a receiver primary system whose chromaticities are close in value to the CIE chromaticity coordinates, and the reference white is Illuminant C (17). The EBU chromaticities are also combined with the D65 illuminant.

**$R_R G_R B_R$  CCIR Receiver Primary Color Coordinate Systems.** In 1990, the International Telecommunications Union (ITU) issued its Recommendation 601, which

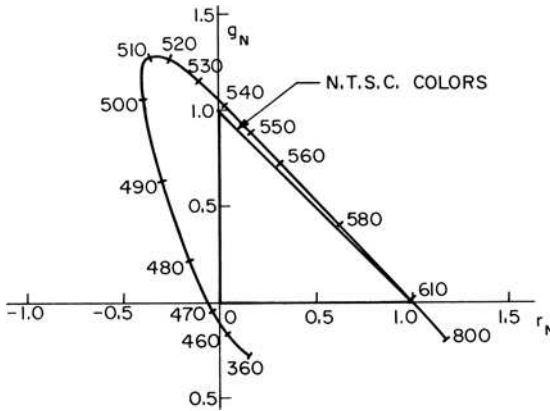


FIGURE 3.4-4. Chromaticity diagram for NTSC receiver phosphor primary system.

specified the receiver primaries for standard resolution digital television (18). Also, in 1990, the ITU published its Recommendation 709 for digital high-definition television systems (19). Both standards are popularly referenced as CCIR Rec. 601 and CCIR Rec. 709, abbreviations of the former name of the standards committee, Comité Consultatif International des Radiocommunications.

**$R_S G_S B_S$  SMPTE Receiver Primary Color Coordinate System.** The Society of Motion Picture and Television Engineers (SMPTE) has established a standard receiver primary color coordinate system with primaries that match modern receiver

phosphors better than did the older NTSC primary system (20). In this coordinate system, the reference white is Illuminant D65.

**XYZ Color Coordinate System.** In the CIE spectral primary system, the tristimulus values required to achieve a color match are sometimes negative. The CIE has developed a standard artificial primary coordinate system in which all tristimulus values required to match colors are positive (4). These artificial primaries are shown in the CIE primary chromaticity diagram of Figure 3.4-3 (11). The XYZ system primaries have been chosen so that the *Y* tristimulus value is equivalent to the luminance of the color to be matched. Figure 3.4-5 is the chromaticity diagram for the CIE XYZ primary system referenced to equal-energy white (4).

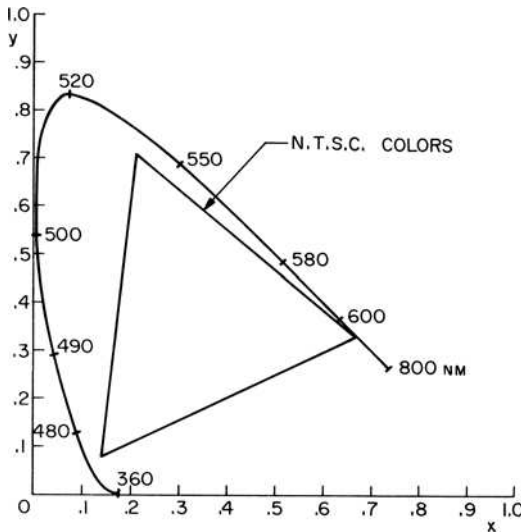


FIGURE 3.4-5. Chromaticity diagram for CIE XYZ primary system.

The linear transformations between  $R_C G_C B_C$  and XYZ are given by

$$\begin{bmatrix} X \\ Y \\ Z \end{bmatrix} = \begin{bmatrix} 0.49018626 & 0.30987954 & 0.19993420 \\ 0.17701522 & 0.81232418 & 0.01066060 \\ 0.00000000 & 0.01007720 & 0.98992280 \end{bmatrix} \begin{bmatrix} R_C \\ G_C \\ B_C \end{bmatrix} \quad (3.4-1a)$$

$$\begin{bmatrix} R_C \\ G_C \\ B_C \end{bmatrix} = \begin{bmatrix} 2.36353918 & -0.89582361 & -0.46771557 \\ -0.51511248 & 1.42643694 & 0.08867553 \\ 0.00524373 & -0.01452082 & 1.00927709 \end{bmatrix} \begin{bmatrix} X \\ Y \\ Z \end{bmatrix}. \quad (3.4-1b)$$

The color conversion matrices of Eq. 3.4-1 and those color conversion matrices defined later are quoted to eight decimal places (21,22). In many instances, this quotation is to a greater number of places than the original specification. The number of places has been increased to reduce computational errors when concatenating transformations between color representations.

The color conversion matrix between XYZ and any other linear RGB color space can be computed by the following algorithm.

1. Compute the colorimetric weighting coefficients  $a(1)$ ,  $a(2)$ ,  $a(3)$  from

$$\begin{bmatrix} a(1) \\ a(2) \\ a(3) \end{bmatrix} = \begin{bmatrix} x_R & x_G & x_B \\ y_R & y_G & y_B \\ z_R & z_G & z_B \end{bmatrix}^{-1} \begin{bmatrix} x_W/y_W \\ 1 \\ z_W/y_W \end{bmatrix} \quad (3.4-2a)$$

where  $x_k, y_k, z_k$  are the chromaticity coordinates of the RGB primary set.

2. Compute the RGB-to-XYZ conversion matrix.

$$\begin{bmatrix} M(1, 1) & M(1, 2) & M(1, 3) \\ M(2, 1) & M(2, 2) & M(2, 3) \\ M(3, 1) & M(3, 2) & M(3, 3) \end{bmatrix} = \begin{bmatrix} x_R & x_G & x_B \\ y_R & y_G & y_B \\ z_R & z_G & z_B \end{bmatrix} \begin{bmatrix} a(1) & 0 & 0 \\ 0 & a(2) & 0 \\ 0 & 0 & a(3) \end{bmatrix}. \quad (3.4-2b)$$

The XYZ-to-RGB conversion matrix is, of course, the matrix inverse of **M**. Table 3.4-1 lists the XYZ tristimulus values of several standard illuminates. The XYZ chromaticity coordinates of the standard linear RGB color systems are presented in Table 3.4-2.

From Eqs. 3.4-1 and 3.4-2 it is possible to derive a matrix transformation between  $R_C G_C B_C$  and any linear colorimetric RGB color space. Reference (22) lists the transformation matrices between the standard RGB color coordinate systems and XYZ and UVW, defined below.

**TABLE 3.4-1. XYZ Tristimulus Values of Standard Illuminates**

Illuminant	$X_0$	$Y_0$	$Z_0$
A	1.098700	1.000000	0.355900
C	0.980708	1.000000	1.182163
D50	0.964296	1.000000	0.825105
D65	0.950456	1.000000	1.089058
E	1.000000	1.000000	1.000000

**TABLE 3.4-2. XYZ Chromaticity Coordinates of Standard Primaries**

Standard	$x$	$y$	$z$
CIE $R_C$	0.640000	0.330000	0.030000
$G_C$	0.300000	0.600000	0.100000
$B_C$	0.150000	0.060000	0.790000
NTSC $R_N$	0.670000	0.330000	0.000000
$G_N$	0.210000	0.710000	0.080000
$B_N$	0.140000	0.080000	0.780000
SMPTE $R_S$	0.630000	0.340000	0.030000
$G_S$	0.310000	0.595000	0.095000
$B_S$	0.155000	0.070000	0.775000
EBU $R_E$	0.640000	0.330000	0.030000
$G_E$	0.290000	0.600000	0.110000
$B_E$	0.150000	0.060000	0.790000
CCIR $R_R$	0.640000	0.330000	0.030000
$G_R$	0.300000	0.600000	0.100000
$B_R$	0.150000	0.060000	0.790000

**UVW Uniform Chromaticity Scale Color Coordinate System.** In 1960, the CIE adopted a coordinate system, called the *Uniform Chromaticity Scale* (UCS), in which, to a good approximation, equal changes in the chromaticity coordinates result in equal, just noticeable changes in the perceived hue and saturation of a color. The  $V$  component of the UCS coordinate system represents luminance. The  $u, v$  chromaticity coordinates are related to the  $x, y$  chromaticity coordinates by the relations (23):



$$u = \frac{4x}{-2x + 12y + 3} \tag{3.4-3a}$$

$$v = \frac{6y}{-2x + 12y + 3} \tag{3.4-3b}$$

$$x = \frac{3u}{2u - 8v - 4} \tag{3.4-3c}$$

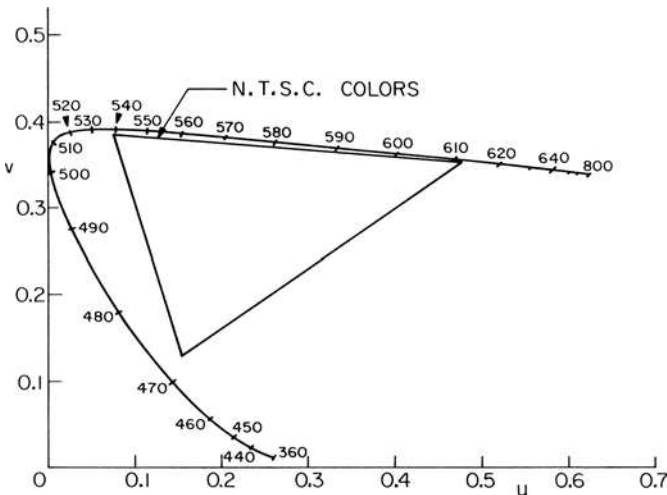
$$y = \frac{2v}{2u - 8v - 4} \tag{3.4-3d}$$

Figure 3.4-6 is a UCS chromaticity diagram.

The tristimulus values of the uniform chromaticity scale coordinate system  $UVW$  are related to the tristimulus values of the spectral coordinate primary system by

$$\begin{bmatrix} U \\ V \\ W \end{bmatrix} = \begin{bmatrix} 0.32679084 & 0.20658636 & 0.13328947 \\ 0.17701522 & 0.81232418 & 0.01066060 \\ 0.02042971 & 1.06858510 & 0.41098519 \end{bmatrix} \begin{bmatrix} R_C \\ G_C \\ B_C \end{bmatrix} \tag{3.4-4a}$$

$$\begin{bmatrix} R_C \\ G_C \\ B_C \end{bmatrix} = \begin{bmatrix} 2.84373542 & 0.50732308 & -0.93543113 \\ -0.63965541 & 1.16041034 & 0.17735107 \\ 1.52178123 & -3.04235208 & 2.01855417 \end{bmatrix} \begin{bmatrix} U \\ V \\ W \end{bmatrix} \tag{3.4-4b}$$



**FIGURE 3.4-6.** Chromaticity diagram for CIE uniform chromaticity scale primary system.

***U\*V\*W\* Color Coordinate System.*** The  $U^*V^*W^*$  color coordinate system, adopted by the CIE in 1964, is an extension of the  $UVW$  coordinate system in an attempt to obtain a color solid for which unit shifts in luminance and chrominance are uniformly perceptible. The  $U^*V^*W^*$  coordinates are defined as (24)

$$U^* = 13W^*(u - u_o) \tag{3.4-5a}$$

$$V^* = 13W^*(v - v_o) \tag{3.4-5b}$$

$$W^* = 25(100Y)^{1/3} - 17 \tag{3.4-5c}$$

where the luminance  $Y$  is measured over a scale of 0.0 to 1.0 and  $u_o$  and  $v_o$  are the chromaticity coordinates of the reference illuminant.

The  $UVW$  and  $U^*V^*W^*$  coordinate systems were rendered obsolete in 1976 by the introduction by the CIE of the more accurate  $L^*a^*b^*$  and  $L^*u^*v^*$  color coordinate systems. Although depreciated by the CIE, much valuable data has been collected in the  $UVW$  and  $U^*V^*W^*$  color systems.

***L\*a\*b\* Color Coordinate System.*** The  $L^*a^*b^*$  cube root color coordinate system was developed to provide a computationally simple measure of color in agreement with the Munsell color system (25). The color coordinates are:

$$L^* = 116\left(\frac{Y}{Y_o}\right)^{1/3} - 16 \quad \text{for } \frac{Y}{Y_o} > 0.008856 \tag{3.4-6a}$$

$$L^* = 903.3\frac{Y}{Y_o} \quad \text{for } 0.0 \leq \frac{Y}{Y_o} \leq 0.008856 \tag{3.4-6b}$$

$$a^* = 500\left[f\left\{\frac{X}{X_o}\right\} - f\left\{\frac{Y}{Y_o}\right\}\right] \tag{3.4-6c}$$

$$b^* = 200\left[f\left\{\frac{X}{X_o}\right\} - f\left\{\frac{Z}{Z_o}\right\}\right] \tag{3.4-6d}$$

where

$$f(w) = w^{1/3} \quad \text{for } w > 0.008856 \tag{3.4-6e}$$

$$f(w) = 7.787(w) + 0.1379 \quad \text{for } 0.0 \leq w \leq 0.008856 \tag{3.4-6f}$$

The terms  $X_o, Y_o, Z_o$  are the tristimulus values for the reference white. Basically,  $L^*$  is correlated with brightness,  $a^*$  with redness-greenness and  $b^*$  with yellowness-blueness. The inverse relationship between  $L^*a^*b^*$  and  $XYZ$  is

$$X = X_o \left[ g \left\{ \frac{L^* + 16}{25} \right\} \right] \tag{3.4-7a}$$

$$Y = Y_o \left[ g \left\{ f \left\{ \frac{Y}{Y_o} \right\} + \frac{a^*}{500} \right\} \right] \tag{3.4-7b}$$

$$Z = Z_o \left[ g \left\{ f \left\{ \frac{Y}{Y_o} \right\} - \frac{b^*}{200} \right\} \right] \tag{3.4-7c}$$

where

$$g(w) = w^3 \quad \text{for } w > 0.20681 \tag{3.4-7d}$$

$$g(w) = 0.1284(w - 0.1379) \quad \text{for } 0.0 \leq w \leq 0.20681 \tag{3.4-7e}$$

***L\*u\*v\* Color Coordinate System.*** The *L\*u\*v\** coordinate system (26), which has evolved from the *L\*a\*b\** and the *U\*V\*W\** coordinate systems, became a CIE standard in 1976. It is defined as

$$L^* = 25 \left( 100 \frac{Y}{Y_o} \right)^{1/3} - 16 \quad \text{for } \frac{Y}{Y_o} \geq 0.008856 \tag{3.4-8a}$$

$$L^* = 903.3 \frac{Y}{Y_o} \quad \text{for } \frac{Y}{Y_o} < 0.008856 \tag{3.4-8b}$$

$$u^* = 13L^*(u' - u'_o) \tag{3.4-8c}$$

$$v^* = 13L^*(v' - v'_o) \tag{3.4-8d}$$

where

$$u' = \frac{4X}{X + 15Y + 3Z} \tag{3.4-8e}$$

$$v' = \frac{9Y}{X + 15Y + 3Z} \tag{3.4-8f}$$

and *u'\_o* and *v'\_o* are obtained by substitution of the tristimulus values *X\_o*, *Y\_o*, *Z\_o* for the reference white. The inverse relationship is given by:

$$X = \frac{9u'}{4v'} Y \tag{3.4-9a}$$

$$Y = Y_o \left( \frac{L^* + 16}{25} \right)^3 \tag{3.4-9b}$$

$$Z = Y \frac{12 - 3u' - 20v'}{4v'} \tag{3.4-9c}$$

where

$$u' = \frac{u^*}{13L^*} + u'_o \tag{3.4-9d}$$

$$v' = \frac{v^*}{13L^*} + u'_o . \tag{3.4-9e}$$

Figure 3.4-7 shows the linear *RGB* components of an NTSC receiver primary color image. If printed properly, the color image and its monochromatic component images will appear to be of “normal” brightness. When displayed electronically, the linear images will appear too dark. Section 3.4.3 discusses the proper display of electronic images. Figures 3.4-8 to 3.4-10 show the *XYZ*, *Yxy* and *L\*a\*b\** components of Figure 3.4-7. Section 10.1.1 describes amplitude-scaling methods for the display of image components outside the unit amplitude range. The amplitude range of each component is printed below each photograph.

### 3.4.2. Subtractive Color Spaces

The color printing and color photographic processes are based on a subtractive color representation. In color printing, the linear *RGB* color components are transformed to cyan (*C*), magenta (*M*) and yellow (*Y*) inks, which are overlaid at each pixel on a, usually, white paper. The simplest transformation relationship is:

$$C = 1.0 - R \tag{3.4-10a}$$

$$M = 1.0 - G \tag{3.4-10b}$$

$$Y = 1.0 - B \tag{3.4-10c}$$

where the linear *RGB* components are tristimulus values over [0.0, 1.0]. The inverse relations are:

$$R = 1.0 - C \tag{3.4-11a}$$

$$G = 1.0 - M \tag{3.4-11b}$$

$$B = 1.0 - Y . \tag{3.4-11c}$$



(a) Linear color



(b) Linear R, 0.000 to 0.965



(c) Linear G, 0.000 to 1.000



(d) Linear B, 0.000 to 0.965

**FIGURE 3.4-7.** Linear *RGB* components of the `dolls_linear` color image. For monochrome printers and displays, see the web site for a color representation of this figure.

In high-quality printing systems, the *RGB*-to-*CMY* transformations, which are usually proprietary, involve color component cross-coupling and point nonlinearities.

To achieve dark black printing without using excessive amounts of *CMY* inks, it is common to add a fourth component, a black ink, called the *key* (*K*) or *black component*. The black component is set proportional to the smallest of the *CMY* components as computed by Eq. 3.4-10. The common *RGB*-to-*CMYK* transformation, which is based on the *undercolor removal algorithm* (27), is:



(a) X, 0.000 to 0.952



(b) Y, 0.000 to 0.985



(c) Z, 0.000 to 1,143

**FIGURE 3.4-8.** XYZ components of the dolls\_linear color image.

$$C = 1.0 - R - uK_b \tag{3.4-12a}$$

$$M = 1.0 - G - uK_b \tag{3.4-12b}$$

$$Y = 1.0 - B - uK_b \tag{3.4-12c}$$

$$K = bK_b \tag{3.4-12d}$$

where

$$K_b = \text{MIN}\{1.0 - R, 1.0 - G, 1.0 - B\}. \tag{3.4-12e}$$



(a)  $Y$ , 0.000 to 0.965



(b)  $x$ , 0.140 to 0.670



(c)  $y$ , 0.080 to 0.710

**FIGURE 3.4-9.**  $Yxy$  components of the dolls\_linear color image.

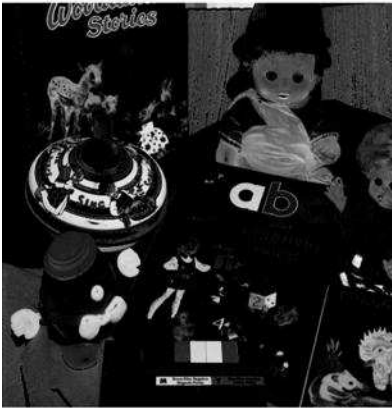
and  $0.0 \leq u \leq 1.0$  is the undercolor removal factor and  $0.0 \leq b \leq 1.0$  is the blackness factor. Figure 3.4-11 presents the  $CMY$  components of the color image of Figure 3.4-7.

### 3.4.3. Video Color Spaces

The red, green and blue signals from video camera sensors typically are linearly proportional to the light striking each sensor. However, the light generated by cathode tube displays is approximately proportional to the display amplitude drive signals



(a)  $L^*$ , -16.000 to 99.434



(b)  $a^*$ , -55.928 to 69.291



(c)  $b^*$ , -65.224 to 90.171

**FIGURE 3.4-10.**  $L^*a^*b^*$  components of the dolls\_linear color image.

raised to a power in the range 2.0 to 3.0 (28). To obtain a good-quality display, it is necessary to compensate for this point nonlinearity. The compensation process, called *gamma correction*, involves passing the camera sensor signals through a point nonlinearity with a power, typically, of about 0.45. In television systems, to reduce receiver cost, gamma correction is performed at the television camera rather than at the receiver. A linear *RGB* image that has been gamma corrected is called a *gamma RGB image*. Liquid crystal displays are reasonably linear in the sense that the light generated is approximately proportional to the display amplitude drive signal. But because LCDs are used in lieu of CRTs in many applications, they usually employ circuitry to compensate for the gamma correction at the sensor.





FIGURE 3.4-11. CMY components of the dolls\_linear color image.

In high-precision applications, gamma correction follows a linear law for low-amplitude components and a power law for high-amplitude components according to the relations (22)

$$\tilde{K} = c_1 K^{c_2} + c_3 \quad \text{for } K \geq b \quad (3.4-13a)$$

$$\tilde{K} = c_4 K \quad \text{for } 0.0 \leq K < b \quad (3.4-13b)$$

where  $K$  denotes a linear  $RGB$  component and  $\tilde{K}$  is the gamma-corrected component. The constants  $c_k$  and the breakpoint  $b$  are specified in Table 3.4-3 for the

general case and for conversion to the SMPTE, CCIR and CIE lightness components. Figure 3.4-12 is a plot of the gamma correction curve for the CCIR Rec. 709 primaries.

**TABLE 3.4-3. Gamma Correction Constants**

	General	SMPTE	CCIR	CIE L*
$c_1$	1.00	1.1115	1.099	116.0
$c_2$	0.45	0.45	0.45	0.3333
$c_3$	0.00	-0.1115	-0.099	-16.0
$c_4$	0.00	4.0	4.5	903.3
$b$	0.00	0.0228	0.018	0.008856

The inverse gamma correction relation is:

$$k = \left( \frac{\tilde{K} - c_3}{c_1} \right)^{1/c_2} \quad \text{for } \tilde{K} \geq c_4 b \quad (3.4-14a)$$

$$k = \frac{\tilde{K}}{c_4} \quad \text{for } 0.0 \leq \tilde{K} < c_4 b \quad (3.4-14b)$$

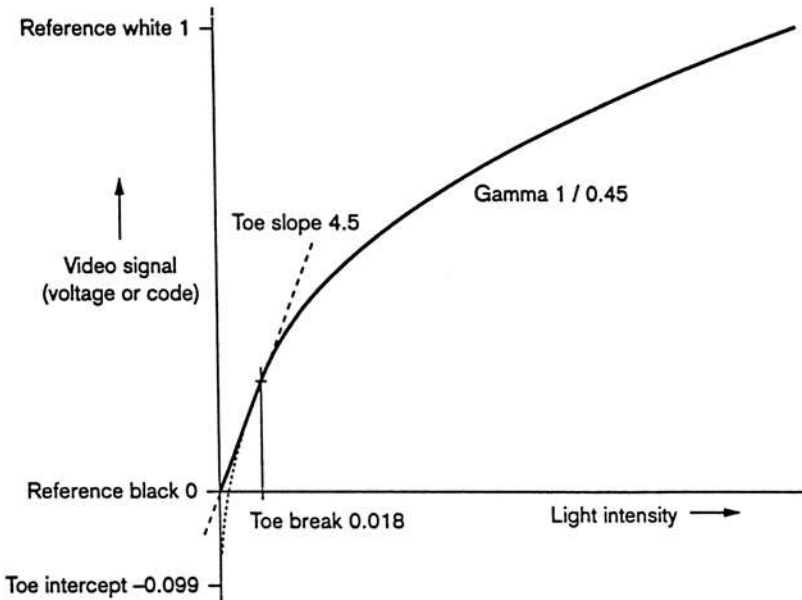


**FIGURE 3.4-12.** Gamma correction curve for the CCIR Rec. 709 primaries.



(a) Gamma color



(b) Gamma R, 0.000 to 0.984



(c) Gamma G, 0.000 to 1.000



(d) Gamma B, 0.000 to 0.984

**FIGURE 3.4-13.** Gamma *RGB* components of the dolls\_gamma color image. For monochrome printers and displays, see the web site for a color representation of this figure.

Figure 3.4-13 shows the gamma *RGB* components of the color image of Figure 3.4-7. The gamma color image is printed in the color insert. The gamma components have been printed as if they were linear components to illustrate the effects of the point transformation. When viewed on an electronic display, the gamma *RGB* color image will appear to be of “normal” brightness.

**YIQ NTSC Transmission Color Coordinate System.** In the development of the color television system in the United States, the NTSC formulated a color coordinate system for transmission composed of three values, *Y, I, Q* (14). The *Y* value, called *luma*, is proportional to the gamma-corrected luminance of a color. The other two components, *I* and *Q*, called *chroma*, jointly describe the hue and saturation

attributes of an image. The reasons for transmitting the  $YIQ$  components rather than the gamma-corrected  $\tilde{R}_N\tilde{G}_N\tilde{B}_N$  components directly from a color camera were two fold: The  $Y$  signal alone could be used with existing monochrome receivers to display monochrome images; and it was found possible to limit the spatial bandwidth of the  $I$  and  $Q$  signals without noticeable image degradation. As a result of the latter property, a clever analog modulation scheme was developed such that the bandwidth of a color television carrier could be restricted to the same bandwidth as a monochrome carrier.

The  $YIQ$  transformations for an Illuminant C reference white are given by:

$$\begin{bmatrix} Y \\ I \\ Q \end{bmatrix} = \begin{bmatrix} 0.29889531 & 0.58662247 & 0.11448223 \\ 0.59597799 & -0.27417610 & -0.32180189 \\ 0.21147017 & -0.52261711 & 0.31114694 \end{bmatrix} \begin{bmatrix} \tilde{R}_N \\ \tilde{G}_N \\ \tilde{B}_N \end{bmatrix} \tag{3.4-15a}$$

$$\begin{bmatrix} \tilde{R}_N \\ \tilde{G}_N \\ \tilde{B}_N \end{bmatrix} = \begin{bmatrix} 1.00000000 & 0.95608445 & 0.62088850 \\ 1.00000000 & -0.27137664 & -0.64860590 \\ 1.00000000 & -1.10561724 & 1.70250126 \end{bmatrix} \begin{bmatrix} Y \\ I \\ Q \end{bmatrix} \tag{3.4-15b}$$

where the tilde denotes that the component has been gamma corrected.

Figure 3.4-14 presents the  $YIQ$  components of the gamma color image of Figure 3.4-13.

***YUV EBU Transmission Color Coordinate System.*** In the PAL and SECAM color television systems (29) used in many countries, the luma  $Y$  and two color differences,

$$U = \frac{\tilde{B}_E - Y}{2.03} \tag{3.4-16a}$$

$$V = \frac{\tilde{R}_E - Y}{1.14} \tag{3.4-16b}$$

are used as transmission coordinates, where  $\tilde{R}_E$  and  $\tilde{B}_E$  are the gamma-corrected EBU red and blue components, respectively. The  $YUV$  coordinate system was initially proposed as the NTSC transmission standard but was later replaced by the  $YIQ$  system because it was found (4) that the  $I$  and  $Q$  signals could be reduced in bandwidth to a greater degree than the  $U$  and  $V$  signals for an equal level of visual quality. The  $I$  and  $Q$  signals are related to the  $U$  and  $V$  signals by a simple rotation of coordinates in color space:



(a) Y, 0.000 to 0.994



(b) I, -0.276 to 0.347



(c) Q, -0.147 to 0.169

FIGURE 3.4-14. *YIQ* components of the gamma corrected dolls\_gamma color image.

$$I = -U \sin 33^\circ + V \cos 33^\circ \tag{3.4-17a}$$

$$Q = U \cos 33^\circ + V \sin 33^\circ . \tag{3.4-17b}$$

It should be noted that the *U* and *V* components of the *YUV* video color space are not equivalent to the *U* and *V* components of the *UVW* uniform chromaticity system.

***YCbCr CCIR Rec. 601 Transmission Color Coordinate System.*** The CCIR Rec. 601 color coordinate system *YCbCr* is defined for the transmission of luma and chroma components coded in the integer range 0 to 255. The *YCbCr* transformations for unit range components are defined as (28)

$$\begin{bmatrix} Y \\ Cb \\ Cr \end{bmatrix} = \begin{bmatrix} 0.29900000 & 0.58700000 & 0.11400000 \\ -0.16873600 & -0.33126400 & 0.50000000 \\ 0.50000000 & -0.4186680 & -0.08131200 \end{bmatrix} \begin{bmatrix} \tilde{R}_S \\ \tilde{G}_S \\ \tilde{B}_S \end{bmatrix} \quad (3.4-18a)$$

$$\begin{bmatrix} \tilde{R}_S \\ \tilde{G}_S \\ \tilde{B}_S \end{bmatrix} = \begin{bmatrix} 1.00000000 & -0.0009264 & 1.40168676 \\ 1.00000000 & -0.34369538 & -0.71416904 \\ 1.00000000 & 1.77216042 & 0.00099022 \end{bmatrix} \begin{bmatrix} Y \\ Cb \\ Cr \end{bmatrix} \quad (3.4-18b)$$

where the tilde denotes that the component has been gamma corrected.

**Photo YCC Color Coordinate System.** The Eastman Kodak company has developed an image storage system, called *PhotoCD*, in which a photographic negative is scanned, converted to a luma/chroma format similar to Rec. 601 *YCbCr*; and recorded in a proprietary compressed form on a compact disk. The PhotoYCC format and its associated *RGB* display format have become defacto standards. PhotoYCC employs the CCIR Rec. 709 primaries for scanning. The conversion to YCC is defined as (27,28,30):

$$\begin{bmatrix} Y \\ C_1 \\ C_2 \end{bmatrix} = \begin{bmatrix} 0.299 & 0.587 & 0.114 \\ -0.299 & -0.587 & 0.500 \\ 0.500 & -0.587 & 0.114 \end{bmatrix} \begin{bmatrix} \tilde{R}_{709} \\ \tilde{G}_{709} \\ \tilde{B}_{709} \end{bmatrix} \quad (3.4-19a)$$

Transformation from PhotoCD components for display is not an exact inverse of Eq. 3.4-19a, in order to preserve the extended dynamic range of film images. The  $YC_1C_2$ -to- $R_DG_DB_D$  display components is given by:

$$\begin{bmatrix} R_D \\ G_D \\ B_D \end{bmatrix} = \begin{bmatrix} 0.969 & 0.000 & 1.000 \\ 0.969 & -0.194 & -0.509 \\ 0.969 & 1.000 & 0.000 \end{bmatrix} \begin{bmatrix} Y \\ C_1 \\ C_2 \end{bmatrix} \quad (3.4-19b)$$

### 3.4.4. Nonstandard Color Spaces

Several nonstandard color spaces used for image processing applications are described in this section.

**IHS Color Coordinate System.** The IHS coordinate system (31) has been used within the image processing community as a quantitative means of specifying the intensity, hue and saturation of a color. It is defined by the relations

$$\begin{bmatrix} I \\ V_1 \\ V_2 \end{bmatrix} = \begin{bmatrix} \frac{1}{3} & \frac{1}{3} & \frac{1}{3} \\ \frac{-1}{\sqrt{6}} & \frac{-1}{\sqrt{6}} & \frac{2}{\sqrt{6}} \\ \frac{1}{\sqrt{6}} & \frac{-1}{\sqrt{6}} & 0 \end{bmatrix} \begin{bmatrix} R \\ G \\ B \end{bmatrix} \tag{3.4-20a}$$

$$H = \arctan \left\{ \frac{V_2}{V_1} \right\} \tag{3.4-20b}$$

$$S = (V_1^2 + V_2^2)^{1/2} . \tag{3.4-20c}$$

By this definition, the color blue is the zero reference for hue. The inverse relationship is:

$$V_1 = S \cos \{H\} \tag{3.4-21a}$$

$$V_2 = S \sin \{H\} \tag{3.4-21b}$$

$$\begin{bmatrix} R \\ G \\ B \end{bmatrix} = \begin{bmatrix} 1 & \frac{-\sqrt{6}}{6} & \frac{\sqrt{6}}{2} \\ 1 & \frac{\sqrt{6}}{6} & \frac{-\sqrt{6}}{2} \\ 1 & \frac{\sqrt{6}}{3} & 0 \end{bmatrix} \begin{bmatrix} I \\ V_1 \\ V_2 \end{bmatrix} . \tag{3.4-21c}$$

Figure 3.4-15 shows the *IHS* components of the gamma *RGB* image of Figure 3.4-13.

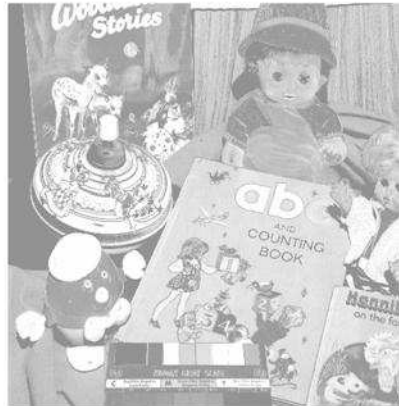
**Karhunen–Loeve Color Coordinate System.** Typically, the *R*, *G* and *B* tristimulus values of a color image are highly correlated with one another (32). In the development of efficient quantization, coding and processing techniques for color images, it is often desirable to work with components that are uncorrelated. If the second-order moments of the *RGB* tristimulus values are known, or at least estimable, it is possible to derive an orthogonal coordinate system, in which the components are uncorrelated, by a Karhunen–Loeve (K-L) transformation of the *RGB* tristimulus values. The K-L color transform is defined as:



(a) I, 0.000 to 0.989



(b) H, -3.136 to 3.142



(c) S, 0.000 to 0.476

FIGURE 3.4-15. *IHS* components of the `dolls_gamma` color image.

$$\begin{bmatrix} K_1 \\ K_2 \\ K_3 \end{bmatrix} = \begin{bmatrix} m_{11} & m_{12} & m_{13} \\ m_{21} & m_{22} & m_{23} \\ m_{31} & m_{32} & m_{33} \end{bmatrix} \begin{bmatrix} R \\ G \\ B \end{bmatrix} \tag{3.4-22a}$$

$$\begin{bmatrix} R \\ G \\ B \end{bmatrix} = \begin{bmatrix} m_{11} & m_{21} & m_{31} \\ m_{12} & m_{22} & m_{32} \\ m_{13} & m_{23} & m_{33} \end{bmatrix} \begin{bmatrix} K_1 \\ K_2 \\ K_3 \end{bmatrix} \tag{3.4-22b}$$



where the transformation matrix with general term  $m_{ij}$  composed of the eigenvectors of the  $RGB$  covariance matrix with general term  $u_{ij}$ . The transformation matrix satisfies the relation:

$$\begin{bmatrix} m_{11} & m_{12} & m_{13} \\ m_{21} & m_{22} & m_{23} \\ m_{31} & m_{32} & m_{33} \end{bmatrix} \begin{bmatrix} u_{11} & u_{12} & u_{13} \\ u_{12} & u_{22} & u_{23} \\ u_{13} & u_{23} & u_{33} \end{bmatrix} \begin{bmatrix} m_{11} & m_{21} & m_{31} \\ m_{12} & m_{22} & m_{32} \\ m_{13} & m_{23} & m_{33} \end{bmatrix} = \begin{bmatrix} \lambda_1 & 0 & 0 \\ 0 & \lambda_2 & 0 \\ 0 & 0 & \lambda_3 \end{bmatrix} \tag{3.4-23}$$

where  $\lambda_1, \lambda_2, \lambda_3$  are the eigenvalues of the covariance matrix and

$$u_{11} = E\{(R - \bar{R})^2\} \tag{3.4-24a}$$

$$u_{22} = E\{(G - \bar{G})^2\} \tag{3.4-24b}$$

$$u_{33} = E\{(B - \bar{B})^2\} \tag{3.4-24c}$$

$$u_{12} = E\{(R - \bar{R})(G - \bar{G})\} \tag{3.4-24d}$$

$$u_{13} = E\{(R - \bar{R})(B - \bar{B})\} \tag{3.4-24e}$$

$$u_{23} = E\{(G - \bar{G})(B - \bar{B})\}. \tag{3.4-24f}$$

In Eq. 3.4-23,  $E\{\cdot\}$  is the expectation operator and the overbar denotes the mean value of a random variable.

**Retinal Cone Color Coordinate System.** As indicated in Chapter 2, in the discussion of models of the human visual system for color vision, indirect measurements of the spectral sensitivities  $s_1(\lambda), s_2(\lambda), s_3(\lambda)$  have been made for the three types of retinal cones. It has been found that these spectral sensitivity functions can be linearly related to spectral tristimulus values established by colorimetric experimentation. Hence, a set of cone signals  $T_1, T_2, T_3$  may be regarded as tristimulus values in a retinal cone color coordinate system. The tristimulus values of the retinal cone color coordinate system are related to the  $XYZ$  system by the coordinate conversion matrix (33):

$$\begin{bmatrix} T_1 \\ T_2 \\ T_3 \end{bmatrix} = \begin{bmatrix} 0.000000 & 1.000000 & 0.000000 \\ -0.460000 & 1.359000 & 0.101000 \\ 0.000000 & 0.000000 & 1.000000 \end{bmatrix} \begin{bmatrix} X \\ Y \\ Z \end{bmatrix} \tag{3.4-25}$$

### 3.5. COLOR SPACE EXERCISES

E3.1 Develop a program that converts a linear *RGB* unsigned integer, 8-bit, color image to the *XYZ* color space and converts the *XYZ* color image back to the *RGB* color space. Steps:

- (a) Display the *RGB* source linear color image.
- (b) Display the *R*, *G* and *B* components as monochrome images.
- (c) Convert the source image to unit range.
- (d) Convert the *RGB* source image to *XYZ* color space.
- (e) Display the *X*, *Y* and *Z* components as monochrome images.
- (f) Convert the *XYZ* destination image to *RGB* color space.
- (g) Display the *RGB* destination image.

The executable PIKS API `example_colour_conversion_RGB_XYZ` performs this exercise.<sup>1</sup>

E3.2 Develop a program that converts a linear *RGB* color image to the  $L^*a^*b^*$  color space and converts the  $L^*a^*b^*$  color image back to the *RGB* color space. Steps:

- (a) Display the *RGB* source linear color image.
- (b) Display the *R*, *G* and *B* components as monochrome images.
- (c) Convert the source image to unit range.
- (d) Convert the *RGB* source image to  $L^*a^*b^*$  color space.
- (e) Display the  $L^*$ ,  $a^*$  and  $b^*$  components as monochrome images.
- (f) Convert the  $L^*a^*b^*$  destination image to *RGB* color space.
- (g) Display the *RGB* destination image.

The PIKS API executable `example_colour_conversion_RGB_Lab` performs this exercise.

E3.3 Develop a program that converts a linear *RGB* color image to a gamma corrected *RGB* color image and converts the gamma color image back to the linear *RGB* color space. Steps:

- (a) Display the *RGB* source linear color image.
- (b) Display the *R*, *G* and *B* components as monochrome images.
- (c) Convert the source image to unit range.
- (d) Perform gamma correction on the linear *RGB* source image.

---

1. The PIKS API standard utilizes the British version of English language spelling, e.g. colour instead of color.

- (e) Display the gamma corrected *RGB* destination image.
- (f) Display the *R*, *G* and *B* gamma corrected components as monochrome images.
- (g) Convert the gamma corrected destination image to linear *RGB* color space.
- (h) Display the linear *RGB* destination image.

The PIKS API executable `example_colour_gamma_correction` performs this exercise.

E3.4 Develop a program that converts a gamma *RGB* color image to the *YCbCr* color space and converts the *YCbCr* color image back to the gamma *RGB* color space. Steps:

- (a) Display the *RGB* source gamma color image.
- (b) Display the *R*, *G* and *B* components as monochrome images.
- (c) Convert the source image to unit range.
- (d) Convert the *RGB* source image to *YCbCr* color space.
- (e) Display the *Y*, *Cb* and *Cr* components as monochrome images.
- (f) Convert the *YCbCr* destination image to gamma *RGB* color space.
- (g) Display the gamma *RGB* destination image.

The PIKS API executable `example_colour_conversion_RGB_YCbCr` performs this exercise.

E3.5 Develop a program that converts a gamma *RGB* color image to the *IHS* color space and converts the *IHS* color image back to the gamma *RGB* color space. Steps:

- (a) Display the *RGB* source gamma color image.
- (b) Display the *R*, *G* and *B* components as monochrome images.
- (c) Convert the source image to unit range.
- (d) Convert the *RGB* source image to *IHS* color space.
- (e) Display the *I*, *H* and *S* components as monochrome images.
- (f) Convert the *IHS* destination image to gamma *RGB* color space.
- (g) Display the gamma *RGB* destination image.

The PIK API executable `example_colour_conversion_RGB_IHS` performs this exercise.

## REFERENCES

1. T. P. Merrit and F. F. Hall, Jr., "Blackbody Radiation," *Proc. IRE*, **47**, 9, September 1959, 1435–1442.
2. H. H. Malitson, "The Solar Energy Spectrum," *Sky and Telescope*, **29**, 4, March 1965, 162–165.
3. R. D. Larabee, "Spectral Emissivity of Tungsten," *J. Optical of Society America*, **49**, 6, June 1959, 619–625.
4. *The Science of Color*, Crowell, New York, 1973.
5. D. G. Fink, Ed., *Television Engineering Handbook*, McGraw-Hill, New York, 1957.
6. Toray Industries, Inc. *LCD Color Filter Specification*.
7. J. W. T. Walsh, *Photometry*, Constable, London, 1953.
8. M. Born and E. Wolf, *Principles of Optics, Sixth Edition*, Pergamon Press, New York, 1981.
9. K. S. Weaver, "The Visibility of Radiation at Low Intensities," *J. Optical Society of America*, **27**, 1, January 1937, 39–43.
10. G. Wyszecki and W. S. Stiles, *Color Science, Second Edition*, John Wiley and Sons, New York, 1982.
11. R. W. G. Hunt, *The Reproduction of Color, Fifth Edition*, John Wiley and Sons, New York, 1957.
12. W. D. Wright, *The Measurement of Color*, Adam Hilger, London, 1944, 204–205.
13. R. A. Enyord, Ed., *Color: Theory and Imaging Systems*, Society of Photographic Scientists and Engineers, Washington, DC, 1973.
14. F. J. Bingley, "Color Vision and Colorimetry," in *Television Engineering Handbook*, D. G. Fink, Ed., McGraw-Hill, New York, 1957.
15. H. Grassman, "On the Theory of Compound Colors," *Philosophical Magazine*, Ser. 4, **7**, April 1854, 254–264.
16. W. T. Wintringham, "Color Television and Colorimetry," *Proc. IRE*, **39**, 10, October 1951, 1135–1172.
17. "EBU Standard for Chromaticity Tolerances for Studio Monitors," Technical Report 3213-E, European Broadcast Union, Brussels, 1975.
18. "Encoding Parameters of Digital Television for Studios," Recommendation ITU-R BT.601-4, (International Telecommunications Union, Geneva; 1990).
19. "Basic Parameter Values for the HDTV Standard for the Studio and for International Programme Exchange," Recommendation ITU-R BT 709, International Telecommunications Unions, Geneva; 1990.
20. L. E. DeMarsh, "Colorimetric Standards in U.S. Color Television. A Report to the Subcommittee on Systems Colorimetry of the SMPTE Television Committee," *J. Society of Motion Picture and Television Engineers*, **83**, 1974.
21. "Information Technology, Computer Graphics and Image Processing, Image Processing and Interchange, Part 1: Common Architecture for Imaging," ISO/IEC 12087-1:1995(E).
22. "Information Technology, Computer Graphics and Image Processing, Image Processing and Interchange, Part 2: Programmer's Imaging Kernel System Application Program Interface," ISO/IEC 12087-2:1995(E).

23. D. L. MacAdam, "Projective Transformations of ICI Color Specifications," *J. Optical Society of America*, **27**, 8, August 1937, 294–299.
24. G. Wyszecki, "Proposal for a New Color-Difference Formula," *J. Optical Society of America*, **53**, 11, November 1963, 1318–1319.
25. "CIE Colorimetry Committee Proposal for Study of Color Spaces," Technical, Note, *J. Optical Society of America*, **64**, 6, June 1974, 896–897.
26. *Colorimetry, Second Edition*, Publication 15.2, Central Bureau, Commission Internationale de l'Eclairage, Vienna, 1986.
27. W. K. Pratt, *Developing Visual Applications, XIL: An Imaging Foundation Library*, Sun Microsystems Press, Mountain View, CA, 1997.
28. C. A. Poynton, *A Technical Introduction to Digital Video*, John Wiley and Sons, New York, 1996.
29. P. S. Carnot and G. B. Townsend, *Color Television Vol. 2; PAL, SECAM and Other Systems*, Iliffe, London, 1969.
30. I. Kabir, *High Performance Computer Imaging*, Manning Publications, Greenwich, CT, 1996.
31. W. Niblack, *An Introduction to Digital Image Processing*, Prentice Hall, Englewood Cliffs, NJ, 1985.
32. W. K. Pratt, "Spatial Transform Coding of Color Images," *IEEE Trans. Communication Technology*, **COM-19**, 12, December 1971, 980–992.
33. D. B. Judd, "Standard Response Functions for Protanopic and Deuteranopic Vision," *J. Optical Society of America*, **35**, 3, March 1945, 199–221.

## **PART 2**

---

### **DIGITAL IMAGE CHARACTERIZATION**

Digital image processing is based on the conversion of a continuous image field to equivalent digital form. This part of the book considers the image sampling and quantization processes that perform the analog image to digital image conversion. The inverse operation of producing continuous image displays from digital image arrays is also analyzed.



---

# 4

---

## IMAGE SAMPLING AND RECONSTRUCTION

In digital image processing systems, one usually deals with arrays of numbers obtained by spatially sampling points of a physical image. After processing, another array of numbers is produced, and these numbers are then used to reconstruct a continuous image for viewing. Image samples nominally represent some physical measurements of a continuous image field, for example, measurements of the image intensity or photographic density. Measurement uncertainties exist in any physical measurement apparatus. It is important to be able to model these measurement errors in order to specify the validity of the measurements and to design processes for compensation of the measurement errors. Also, it is often not possible to measure an image field directly. Instead, measurements are made of some function related to the desired image field, and this function is then inverted to obtain the desired image field. Inversion operations of this nature are discussed in the chapter on image restoration. In this chapter, the image sampling and reconstruction process is considered for both theoretically exact and practical systems.

### 4.1. IMAGE SAMPLING AND RECONSTRUCTION CONCEPTS

In the design and analysis of image sampling and reconstruction systems, input images are usually regarded as deterministic fields (1–5). However, in some situations it is advantageous to consider the input to an image processing system, especially a noise input, as a sample of a two-dimensional random process (5–7). Both viewpoints are developed here for the analysis of image sampling and reconstruction methods.



**4.1.1. Sampling Deterministic Fields**

Let  $F_I(x, y)$  denote a continuous, infinite-extent, ideal image field representing the luminance, photographic density or some desired parameter of a physical image. In a perfect image sampling system, spatial samples of the ideal image would, in effect, be obtained by multiplying the ideal image by a spatial sampling function

$$S(x, y) = \sum_{j=-\infty}^{\infty} \sum_{k=-\infty}^{\infty} \delta(x-j \Delta x, y-k \Delta y) \tag{4.1-1}$$

composed of an infinite array of Dirac delta functions arranged in a grid of spacing  $(\Delta x, \Delta y)$  as shown in Figure 4.1-1. The sampled image is then represented as

$$F_p(x, y) = F_I(x, y)S(x, y) = \sum_{j=-\infty}^{\infty} \sum_{k=-\infty}^{\infty} F_I(j \Delta x, k \Delta y)\delta(x-j \Delta x, y-k \Delta y) \tag{4.1-2}$$

where it is observed that  $F_I(x, y)$  may be brought inside the summation and evaluated only at the sample points  $(j \Delta x, k \Delta y)$ . It is convenient, for purposes of analysis, to consider the spatial frequency domain representation  $\mathcal{F}_p(\omega_x, \omega_y)$  of the sampled image obtained by taking the continuous two-dimensional Fourier transform of the sampled image. Thus

$$\mathcal{F}_p(\omega_x, \omega_y) = \int_{-\infty}^{\infty} \int_{-\infty}^{\infty} F_p(x, y) \exp\{-i(\omega_x x + \omega_y y)\} dx dy. \tag{4.1-3}$$

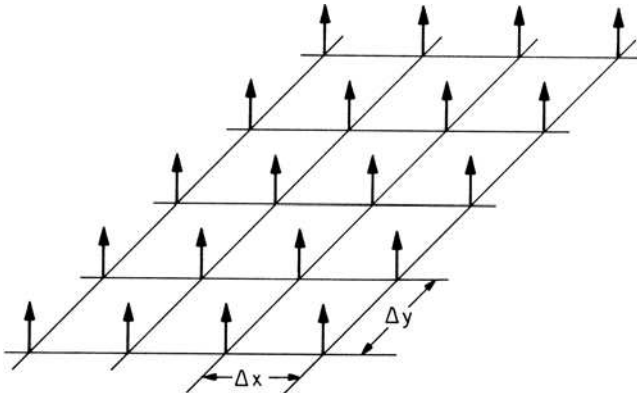


**FIGURE 4.1-1.** Dirac delta function sampling array.

By the Fourier transform convolution theorem, the Fourier transform of the sampled image can be expressed as the convolution of the Fourier transforms of the ideal image  $\mathcal{F}_I(\omega_x, \omega_y)$  and the sampling function  $\mathcal{S}(\omega_x, \omega_y)$  as expressed by

$$\mathcal{F}_P(\omega_x, \omega_y) = \frac{1}{4\pi^2} \left( \mathcal{F}_I(\omega_x, \omega_y) \otimes \mathcal{S}(\omega_x, \omega_y) \right). \tag{4.1-4}$$

The two-dimensional Fourier transform of the spatial sampling function is an infinite array of Dirac delta functions in the spatial frequency domain as given by (4, p. 22)

$$\mathcal{S}(\omega_x, \omega_y) = \frac{4\pi^2}{\Delta x \Delta y} \sum_{j=-\infty}^{\infty} \sum_{k=-\infty}^{\infty} \delta(\omega_x - j \omega_{xs}, \omega_y - k \omega_{ys}) \tag{4.1-5}$$

where  $\omega_{xs} = 2\pi/\Delta x$  and  $\omega_{ys} = 2\pi/\Delta y$  represent the Fourier domain sampling frequencies. It will be assumed that the spectrum of the ideal image is bandlimited to some bounds such that  $\mathcal{F}_I(\omega_x, \omega_y) = 0$  for  $|\omega_x| > \omega_{xc}$  and  $|\omega_y| > \omega_{yc}$ . Performing the convolution of Eq. 4.1-4 yields

$$\begin{aligned} \mathcal{F}_P(\omega_x, \omega_y) &= \frac{1}{\Delta x \Delta y} \int_{-\infty}^{\infty} \int_{-\infty}^{\infty} \mathcal{F}_I(\omega_x - \alpha, \omega_y - \beta) \\ &\quad \times \sum_{j=-\infty}^{\infty} \sum_{k=-\infty}^{\infty} \delta(\omega_x - j \omega_{xs}, \omega_y - k \omega_{ys}) d\alpha d\beta. \end{aligned} \tag{4.1-6}$$

Upon changing the order of summation and integration and invoking the sifting property of the delta function, the sampled image spectrum becomes

$$\mathcal{F}_P(\omega_x, \omega_y) = \frac{1}{\Delta x \Delta y} \sum_{j=-\infty}^{\infty} \sum_{k=-\infty}^{\infty} \mathcal{F}_I(\omega_x - j \omega_{xs}, \omega_y - k \omega_{ys}). \tag{4.1-7}$$

As can be seen from Figure 4.1-2, the spectrum of the sampled image consists of the spectrum of the ideal image infinitely repeated over the frequency plane in a grid of resolution  $(2\pi/\Delta x, 2\pi/\Delta y)$ . It should be noted that if  $\Delta x$  and  $\Delta y$  are chosen too large with respect to the spatial frequency limits of  $\mathcal{F}_I(\omega_x, \omega_y)$ , the individual spectra will overlap.

A continuous image field may be obtained from the image samples of  $\mathcal{F}_P(x, y)$  by linear spatial interpolation or by linear spatial filtering of the sampled image. Let  $R(x, y)$  denote the continuous domain impulse response of an interpolation filter and  $\mathcal{R}(\omega_x, \omega_y)$  represent its transfer function.

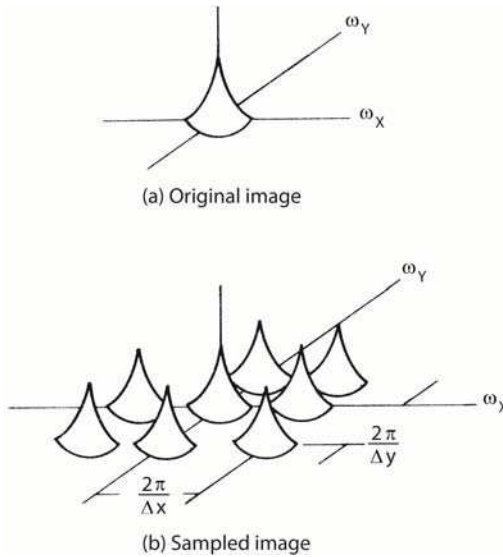


FIGURE 4.1-2. Typical sampled image spectra.

Then, the reconstructed image is obtained by a convolution of the samples with the reconstruction filter impulse response. The reconstructed image then becomes

$$F_R(x, y) = F_P(x, y) \otimes R(x, y). \tag{4.1-8}$$

Upon substituting for  $F_P(x, y)$  from Eq. 4.1-2 and performing the convolution, one obtains

$$F_R(x, y) = \sum_{j=-\infty}^{\infty} \sum_{k=-\infty}^{\infty} F_I(j \Delta x, k \Delta y) R(x - j \Delta x, y - k \Delta y). \tag{4.1-9}$$

Thus, it is seen that the impulse response function  $R(x, y)$  acts as a two-dimensional interpolation waveform for the image samples. The spatial frequency spectrum of the reconstructed image obtained from Eq. 4.1-8 is equal to the product of the reconstruction filter transform and the spectrum of the sampled image,

$$\mathcal{F}_R(\omega_x, \omega_y) = \mathcal{F}_P(\omega_x, \omega_y) \mathcal{R}(\omega_x, \omega_y) \tag{4.1-10}$$

or, from Eq. 4.1-7,

$$\mathcal{F}_R(\omega_x, \omega_y) = \frac{1}{\Delta x \Delta y} \mathcal{R}(\omega_x, \omega_y) \sum_{j=-\infty}^{\infty} \sum_{k=-\infty}^{\infty} \mathcal{F}_I(\omega_x - j \omega_{xs}, \omega_y - k \omega_{ys}). \tag{4.1-11}$$

It is clear from Eq. 4.1-11 that if there is no spectrum overlap and if  $\mathcal{R}(\omega_x, \omega_y)$  filters out all spectra for  $j, k \neq 0$ , the spectrum of the reconstructed image can be made equal to the spectrum of the ideal image, and, therefore, the images themselves can be made identical. The first condition is met for a bandlimited image if the sampling period is chosen such that the rectangular region bounded by the image cutoff frequencies  $(\omega_{xc}, \omega_{yc})$  lies within a rectangular region defined by one-half the sampling frequency. Hence

$$\omega_{xc} \leq \frac{\omega_{xs}}{2} \qquad \omega_{yc} \leq \frac{\omega_{ys}}{2} \qquad (4.1-12a)$$

or, equivalently,

$$\Delta x \leq \frac{\pi}{\omega_{xc}} \qquad \Delta y \leq \frac{\pi}{\omega_{yc}} \qquad (4.1-12b)$$

In physical terms, the sampling period must be equal to or smaller than one-half the period of the finest detail within the image. This sampling condition is equivalent to the one-dimensional sampling theorem constraint for time-varying signals that requires a time-varying signal to be sampled at a rate of at least twice its highest-frequency component. If equality holds in Eq. 4.1-12, the image is said to be sampled at its *Nyquist rate*; if  $\Delta x$  and  $\Delta y$  are smaller than required by the *Nyquist criterion*, the image is called *oversampled*; and if the opposite case holds, the image is *undersampled*.

If the original image is sampled at a spatial rate sufficient to prevent spectral overlap in the sampled image, exact reconstruction of the ideal image can be achieved by spatial filtering the samples with an appropriate filter. For example, as shown in Figure 4.1-3, a filter with a transfer function of the form

$$\mathcal{R}(\omega_x, \omega_y) = K \qquad \text{for } |\omega_x| \leq \omega_{xL} \text{ and } |\omega_y| \leq \omega_{yL} \qquad (4.1-13a)$$

$$\mathcal{R}(\omega_x, \omega_y) = 0 \qquad \text{otherwise} \qquad (4.1-13b)$$

where  $K$  is a scaling constant, satisfies the condition of exact reconstruction if  $\omega_{xL} > \omega_{xc}$  and  $\omega_{yL} > \omega_{yc}$ . The point-spread function or impulse response of this reconstruction filter is

$$R(x, y) = \frac{K\omega_{xL}\omega_{yL}}{\pi^2} \frac{\sin\{\omega_{xL}x\}}{\omega_{xL}x} \frac{\sin\{\omega_{yL}y\}}{\omega_{yL}y} \qquad (4.1-14)$$

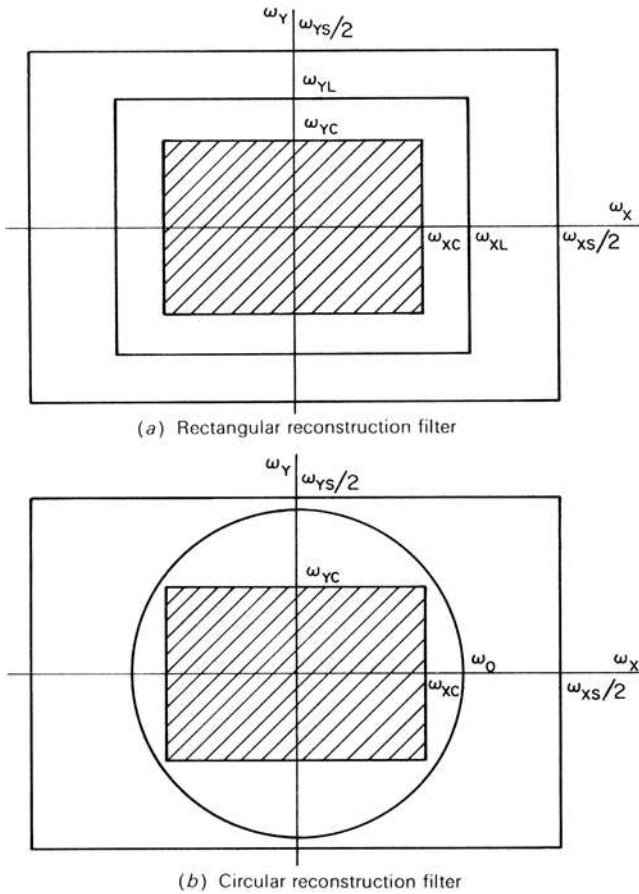


FIGURE 4.1-3. Sampled image reconstruction filters.

With this filter, an image is reconstructed with an infinite sum of  $(\sin\theta)/\theta$  functions, called *sinc functions*. Another type of reconstruction filter that could be employed is the cylindrical filter with a transfer function

$$\mathcal{R}(\omega_x, \omega_y) = K \quad \text{for } \sqrt{\omega_x^2 + \omega_y^2} \leq \omega_0 \quad (4.1-15a)$$

$$\mathcal{R}(\omega_x, \omega_y) = 0 \quad \text{otherwise} \quad (4.1-15b)$$

provided that  $\omega_0^2 > \omega_{xc}^2 + \omega_{yc}^2$ . The impulse response for this filter is

$$R(x, y) = 2\pi\omega_0 K \frac{J_1\left\{\omega_0\sqrt{x^2 + y^2}\right\}}{\sqrt{x^2 + y^2}} \tag{4.1-16}$$

where  $J_1\{.\}$  is a first-order *Bessel function*. There are a number of reconstruction filters or, equivalently, interpolation waveforms, that could be employed to provide perfect image reconstruction. In practice, however, it is often difficult to implement optimum reconstruction filters for imaging systems.

### 4.1.2. Sampling Random Image Fields

In the previous discussion of image sampling and reconstruction, the ideal input image field has been considered to be a deterministic function. It has been shown that if the Fourier transform of the ideal image is bandlimited, then discrete image samples taken at the Nyquist rate are sufficient to reconstruct an exact replica of the ideal image with proper sample interpolation. It will now be shown that similar results hold for sampling two-dimensional random fields.

Let  $F_I(x, y)$  denote a continuous two-dimensional stationary random process with known mean  $\eta_{F_I}$  and autocorrelation function

$$R_{F_I}(\tau_x, \tau_y) = E\{F_I(x_1, y_1)F_I^*(x_2, y_2)\} \tag{4.1-17}$$

where  $\tau_x = x_1 - x_2$  and  $\tau_y = y_1 - y_2$ . This process is spatially sampled by a Dirac sampling array yielding

$$F_P(x, y) = F_I(x, y)S(x, y) = F_I(x, y) \sum_{j=-\infty}^{\infty} \sum_{k=-\infty}^{\infty} \delta(x - j \Delta x, y - k \Delta y). \tag{4.1-18}$$

The autocorrelation of the sampled process is then

$$\begin{aligned} R_{F_P}(\tau_x, \tau_y) &= E\{F_P(x_1, y_1)F_P^*(x_2, y_2)\} \tag{4.1-19} \\ &= E\{F_I(x_1, y_1)F_I^*(x_2, y_2)\}S(x_1, y_1)S(x_2, y_2). \end{aligned}$$

The first term on the right-hand side of Eq. 4.1-19 is the autocorrelation of the stationary ideal image field. It should be observed that the product of the two Dirac sampling functions on the right-hand side of Eq. 4.1-19 is itself a Dirac sampling function of the form

$$S(x_1, y_1)S(x_2, y_2) = S(x_1 - x_2, y_1 - y_2) = S(\tau_x, \tau_y). \tag{4.1-20}$$

Hence, the sampled random field is also stationary with an autocorrelation function

$$R_{F_p}(\tau_x, \tau_y) = R_{F_I}(\tau_x, \tau_y)S(\tau_x, \tau_y). \tag{4.1-21}$$

Taking the two-dimensional Fourier transform of Eq. 4.1-21 yields the power spectrum of the sampled random field. By the Fourier transform convolution theorem

$$\mathcal{W}_{F_p}(\omega_x, \omega_y) = \frac{1}{4\pi^2} \left( \mathcal{W}_{F_I}(\omega_x, \omega_y) \otimes \mathcal{S}(\omega_x, \omega_y) \right) \tag{4.1-22}$$

where  $\mathcal{W}_{F_I}(\omega_x, \omega_y)$  and  $\mathcal{W}_{F_p}(\omega_x, \omega_y)$  represent the power spectral densities of the ideal image and sampled ideal image, respectively, and  $\mathcal{S}(\omega_x, \omega_y)$  is the Fourier transform of the Dirac sampling array. Then, by the derivation leading to Eq. 4.1-7, it is found that the spectrum of the sampled field can be written as

$$\mathcal{W}_{F_p}(\omega_x, \omega_y) = \frac{1}{\Delta x \Delta y} \sum_{j=-\infty}^{\infty} \sum_{k=-\infty}^{\infty} \mathcal{W}_{F_I}(\omega_x - j \omega_{xs}, \omega_y - k \omega_{ys}). \tag{4.1-23}$$

Thus, the sampled image power spectrum is composed of the power spectrum of the continuous ideal image field replicated over the spatial frequency domain at integer multiples of the sampling spatial frequency  $(2\pi/\Delta x, 2\pi/\Delta y)$ . If the power spectrum of the continuous ideal image field is bandlimited such that  $\mathcal{W}_{F_I}(\omega_x, \omega_y) = 0$  for  $|\omega_x| > \omega_{xc}$  and  $|\omega_y| > \omega_{yc}$ , where  $\omega_{xc}$  and  $\omega_{yc}$  are cutoff frequencies, the individual spectra of Eq. 4.1-23 will not overlap if the spatial sampling periods are chosen such that  $\Delta x < \pi/\omega_{xc}$  and  $\Delta y < \pi/\omega_{yc}$ . A continuous random field  $F_R(x, y)$  may be reconstructed from samples of the random ideal image field by the interpolation formula

$$F_R(x, y) = \sum_{j=-\infty}^{\infty} \sum_{k=-\infty}^{\infty} F_I(j \Delta x, k \Delta y)R(x - j \Delta x, y - k \Delta y) \tag{4.1-24}$$

where  $R(x, y)$  is the deterministic interpolation function. The reconstructed field and the ideal image field can be made equivalent in the mean-square sense (5, p. 284), that is,

$$E\{|F_I(x, y) - F_R(x, y)|^2\} = 0 \tag{4.1-25}$$

if the Nyquist sampling criteria are met and if suitable interpolation functions, such as the sinc function or Bessel function of Eqs. 4.1-14 and 4.1-16, are utilized.

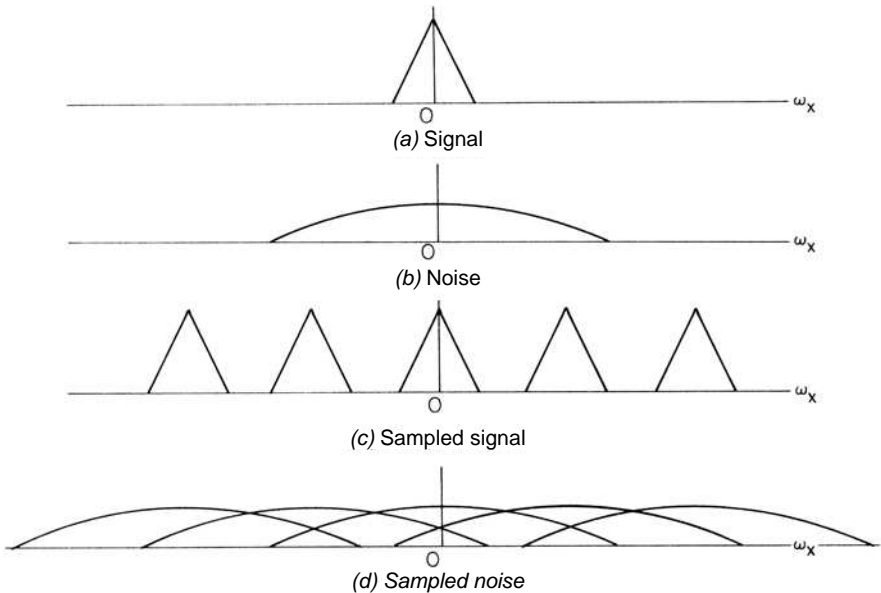


**FIGURE 4.1-4.** Spectra of a sampled noisy image.

The preceding results are directly applicable to the practical problem of sampling a deterministic image field plus additive noise, which is modeled as a random field. Figure 4.1-4 shows the spectrum of a sampled noisy image. This sketch indicates a significant potential problem. The spectrum of the noise may be wider than the ideal image spectrum, and if the noise process is undersampled, its tails will overlap into the passband of the image reconstruction filter, leading to additional noise artifacts. A solution to this problem is to prefilter the noisy image before sampling to reduce the noise bandwidth.

## 4.2. MONOCHROME IMAGE SAMPLING SYSTEMS

In a physical monochrome image sampling system, the sampling array will be of finite extent, the sampling pulses will be of finite width, and the image may be undersampled. The consequences of nonideal sampling are explored next.

As a basis for the discussion, Figure 4.2-1 illustrates a generic optical image scanning system. In operation, a narrow light beam is scanned directly across a positive monochrome photographic transparency of an ideal image. The light passing through the transparency is collected by a condenser lens and is directed toward the surface of a photo detector. The electrical output of the photo detector is integrated over the time period during which the light beam strikes a resolution cell.



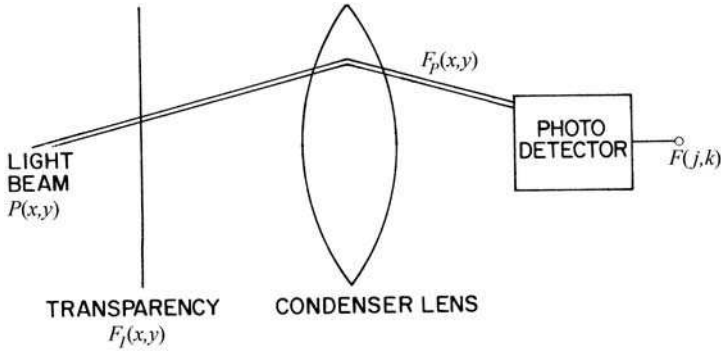


FIGURE 4.2-1. Optical image scanning system.

In the analysis, it will be assumed that the sampling is noise-free. The results developed in Section 4.1 for sampling noisy images can be combined with the results developed in this section quite readily.

### 4.2.1. Sampling Pulse Effects

Under the assumptions stated above, the sampled image function is given by

$$F_p(x, y) = F_f(x, y)S(x, y) \tag{4.2-1}$$

where the sampling array

$$S(x, y) = \sum_{i=-J}^J \sum_{k=-K}^K P(x-j \Delta x, y-k \Delta y) \tag{4.2-2}$$

is composed of  $(2J + 1)(2K + 1)$  identical pulses  $P(x, y)$  arranged in a grid of spacing  $\Delta x, \Delta y$ . The symmetrical limits on the summation are chosen for notational simplicity. The sampling pulses are assumed scaled such that

$$\int_{-\infty}^{\infty} \int_{-\infty}^{\infty} P(x, y) dx dy = 1. \tag{4.2-3}$$

For purposes of analysis, the sampling function may be assumed to be generated by a finite array of Dirac delta functions  $D_T(x, y)$  passing through a linear filter with impulse response  $P(x, y)$ . Thus

$$S(x, y) = D_T(x, y) \otimes P(x, y) \tag{4.2-4}$$

where

$$D_T(x, y) = \sum_{j=-J}^J \sum_{k=-K}^K \delta(x-j \Delta x, y-k \Delta y) \tag{4.2-5}$$

Combining Eqs. 4.2-1 and 4.2-2 results in an expression for the sampled image function,

$$F_P(x, y) = \sum_{j=-J}^J \sum_{k=-K}^K F_f(j \Delta x, k \Delta y)P(x-j \Delta x, y-k \Delta y) \tag{4.2-6}$$

The spectrum of the sampled image function is given by

$$\mathcal{F}_P(\omega_x, \omega_y) = \frac{1}{4\pi^2} \left( \mathcal{F}_f(\omega_x, \omega_y) \otimes [\mathcal{D}_T(\omega_x, \omega_y) \mathcal{A}(\omega_x, \omega_y)] \right) \tag{4.2-7}$$

where  $\mathcal{A}(\omega_x, \omega_y)$  is the Fourier transform of  $P(x, y)$ . The Fourier transform of the truncated sampling array is found to be (5, p. 105)

$$\mathcal{D}_T(\omega_x, \omega_y) = \frac{\sin \left\{ \omega_x \left( J + \frac{1}{2} \right) \Delta x \right\} \sin \left\{ \omega_y \left( K + \frac{1}{2} \right) \Delta y \right\}}{\sin \{ \omega_x \Delta x / 2 \} \sin \{ \omega_y \Delta y / 2 \}} \tag{4.2-8}$$

Figure 4.2-2 depicts  $\mathcal{D}_T(\omega_x, \omega_y)$ . In the limit as  $J$  and  $K$  become large, the right-hand side of Eq. 4.2-7 becomes an array of Dirac delta functions.

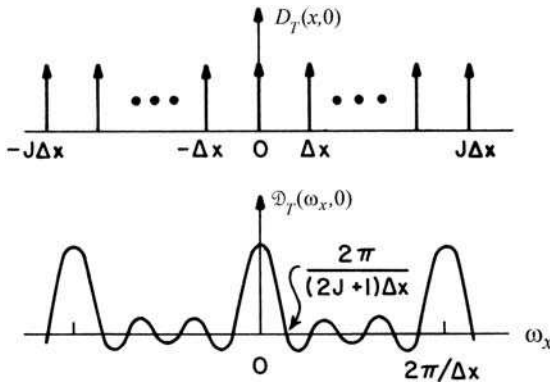


FIGURE 4.2-2. Truncated sampling train and its Fourier spectrum.

In an image reconstruction system, an image is reconstructed by interpolation of its samples. Ideal interpolation waveforms such as the sinc function of Eq. 4.1-14 or the Bessel function of Eq. 4.1-16 generally extend over the entire image field. If the sampling array is truncated, the reconstructed image will be in error near its boundary because the tails of the interpolation waveforms will be truncated in the vicinity of the boundary (8,9). However, the error is usually negligibly small at distances of about 8 to 10 Nyquist samples or greater from the boundary.

The actual numerical samples of an image are obtained by a spatial integration of  $F_S(x, y)$  over some finite resolution cell. In the scanning system of Figure 4.2-1, the integration is inherently performed on the photo detector surface. The image sample value of the resolution cell  $(j, k)$  may then be expressed as

$$F_S(j \Delta x, k \Delta y) = \int_{j \Delta x - A_x}^{j \Delta x + A_x} \int_{k \Delta y - A_y}^{k \Delta y + A_y} F_I(x, y) P(x - j \Delta x, y - k \Delta y) dx dy \quad (4.2-9)$$

where  $A_x$  and  $A_y$  denote the maximum dimensions of the resolution cell. It is assumed that only one sample pulse exists during the integration time of the detector. If this assumption is not valid, consideration must be given to the difficult problem of sample crosstalk. In the sampling system under discussion, the width of the resolution cell may be larger than the sample spacing. Thus, the model provides for sequentially overlapped samples in time.

By a simple change of variables, Eq. 4.2-9 may be rewritten as

$$F_S(j \Delta x, k \Delta y) = \int_{-A_x}^{A_x} \int_{-A_y}^{A_y} F_I(j \Delta x - \alpha, k \Delta y - \beta) P(-\alpha, -\beta) dx dy. \quad (4.2-10)$$

Because only a single sampling pulse is assumed to occur during the integration period, the limits of Eq. 4.2-10 can be extended infinitely. In this formulation, Eq. 4.2-10 is recognized to be equivalent to a convolution of the ideal continuous image  $F_I(x, y)$  with an impulse response function  $P(-x, -y)$  with reversed coordinates, followed by sampling over a finite area with Dirac delta functions. Thus, neglecting the effects of the finite size of the sampling array, the model for finite extent pulse sampling becomes

$$F_S(j \Delta x, k \Delta y) = \left[ F_I(x, y) \otimes P(-x, -y) \right] \delta(x - j \Delta x, y - k \Delta y). \quad (4.2-11)$$

In most sampling systems, the sampling pulse is symmetric, so that  $P(-x, -y) = P(x, y)$ .

Equation 4.2-11 provides a simple relation that is useful in assessing the effect of finite extent pulse sampling. If the ideal image is bandlimited and  $A_x$  and  $A_y$  satisfy the Nyquist criterion, the finite extent of the sample pulse represents an equivalent linear spatial degradation (an image blur) that occurs before ideal sampling. Part 4 considers methods of compensating for this degradation. A finite-extent sampling pulse is not always a detriment, however. Consider the situation in which the ideal image is insufficiently bandlimited so that it is undersampled. The finite-extent

pulse, in effect, provides a low-pass filtering of the ideal image, which, in turn, serves to limit its spatial frequency content, and hence to minimize aliasing error.

**4.2.2. Aliasing Effects**

To achieve perfect image reconstruction in a sampled imaging system, it is necessary to bandlimit the image to be sampled, spatially sample the image at the Nyquist or higher rate, and properly interpolate the image samples. Sample interpolation is considered in the next section; an analysis is presented here of the effect of undersampling an image.

If there is spectral overlap resulting from undersampling, as indicated by the shaded regions in Figure 4.2-3, spurious spatial frequency components will be introduced into the reconstruction. The effect is called an *aliasing error* (10,11). Aliasing effects in an actual image are shown in Figure 4.2-4. Spatial undersampling of the image creates artificial low-spatial-frequency components in the reconstruction. In the field of optics, aliasing errors are called *moiré patterns*.

From Eq. 4.1-7 the spectrum of a sampled image can be written in the form

$$\mathcal{F}_p(\omega_x, \omega_y) = \frac{1}{\Delta x \Delta y} [\mathcal{F}_f(\omega_x, \omega_y) + \mathcal{F}_Q(\omega_x, \omega_y)] \tag{4.2-12}$$

where  $\mathcal{F}_f(\omega_x, \omega_y)$  represents the spectrum of the original image sampled at period  $(\Delta x, \Delta y)$ .

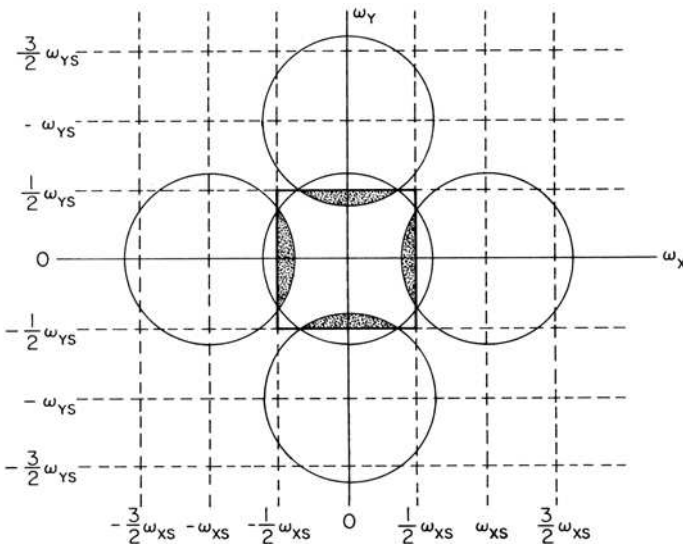
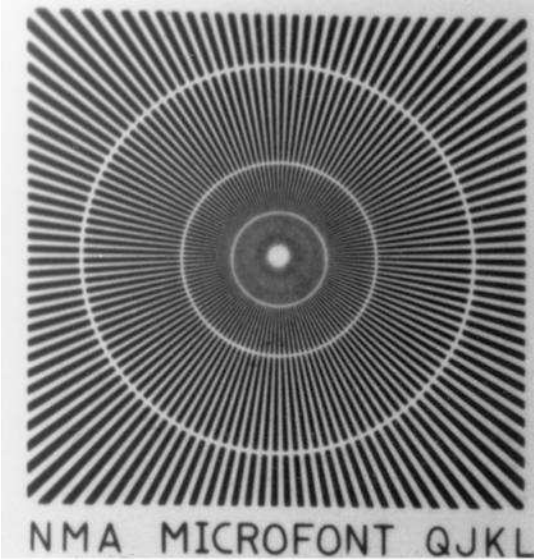
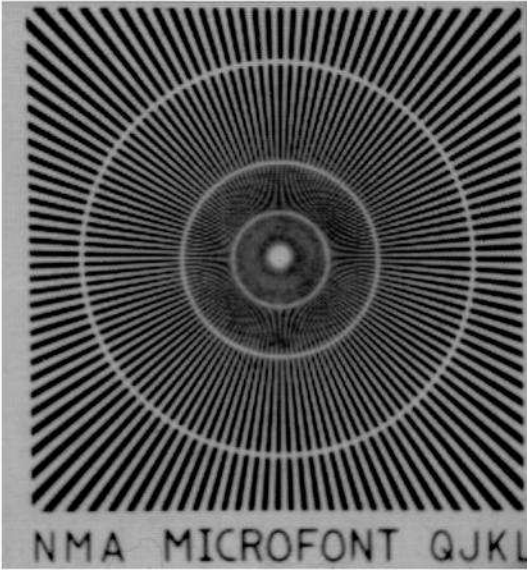


**FIGURE 4.2-3.** Spectra of undersampled two-dimensional function.



(a) Original image



(b) Sampled image

**FIGURE 4.2-4.** Example of aliasing error in a sampled image.

The term

$$\mathcal{F}_Q(\omega_x, \omega_y) = \frac{1}{\Delta x \Delta y} \sum_{j=-\infty}^{\infty} \sum_{k=-\infty}^{\infty} \mathcal{F}_I(\omega_x - j \omega_{xs}, \omega_y - k \omega_{ys}) \quad (4.2-13)$$

for  $j \neq 0$  and  $k \neq 0$  describes the spectrum of the higher-order components of the sampled image repeated over spatial frequencies  $\omega_{xs} = 2\pi/\Delta x$  and  $\omega_{ys} = 2\pi/\Delta y$ . If there were no spectral fold over, optimal interpolation of the sampled image components could be obtained by passing the sampled image through a zonal low-pass filter defined by

$$\mathcal{R}(\omega_x, \omega_y) = K \quad \text{for } |\omega_x| \leq \omega_{xs}/2 \text{ and } |\omega_y| \leq \omega_{ys}/2 \quad (4.2-14a)$$

$$\mathcal{R}(\omega_x, \omega_y) = 0 \quad \text{otherwise} \quad (4.2-14b)$$

where  $K$  is a scaling constant.

Applying this interpolation strategy to an undersampled image yields a reconstructed image field

$$F_R(x, y) = F_I(x, y) + A(x, y) \quad (4.2-15)$$

where

$$A(x, y) = \frac{1}{4\pi^2} \int_{-\omega_{xs}/2}^{\omega_{xs}/2} \int_{-\omega_{ys}/2}^{\omega_{ys}/2} \mathcal{F}_Q(\omega_x, \omega_y) \exp\{i(\omega_x x + \omega_y y)\} d\omega_x d\omega_y \quad (4.2-16)$$

represents the aliasing error artifact in the reconstructed image. The factor  $K$  has absorbed the amplitude scaling factors. Figure 4.2-5 shows the reconstructed image spectrum that illustrates the spectral fold over in the zonal low-pass filter passband. The aliasing error component of Eq. 4.2-16 can be reduced substantially by low-pass filtering before sampling to attenuate the spectral fold over.

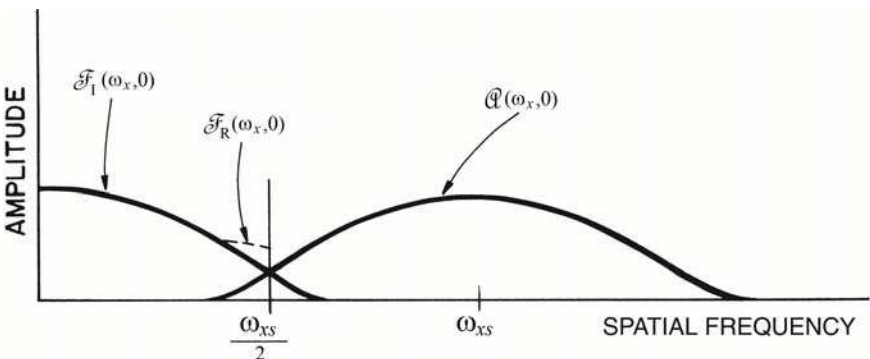


FIGURE 4.2-5. Reconstructed image spectrum.

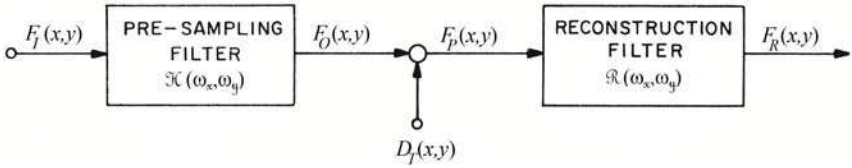


FIGURE 4.2-6. Model for analysis of aliasing effect.

Figure 4.2-6 shows a model for the quantitative analysis of aliasing effects. In this model, the ideal image  $F_I(x, y)$  is assumed to be a sample of a two-dimensional random process with known power-spectral density  $\tilde{W}_{F_I}(\omega_x, \omega_y)$ . The ideal image is linearly filtered by a presampling spatial filter with a transfer function  $\mathcal{K}(\omega_x, \omega_y)$ . This filter is assumed to be a low-pass type of filter with a smooth attenuation of high spatial frequencies (i.e., not a zonal low-pass filter with a sharp cutoff). The filtered image is then spatially sampled by an ideal Dirac delta function sampler at a resolution  $\Delta x, \Delta y$ . Next, a reconstruction filter interpolates the image samples to produce a replica of the ideal image. From Eq. 1.4-27, the power spectral density at the presampling filter output is found to be

$$\tilde{W}_{F_O}(\omega_x, \omega_y) = |\mathcal{K}(\omega_x, \omega_y)|^2 \tilde{W}_{F_I}(\omega_x, \omega_y) \tag{4.2-17}$$

and the Fourier spectrum of the sampled image field is

$$\tilde{W}_{F_P}(\omega_x, \omega_y) = \frac{1}{\Delta x \Delta y} \sum_{j=-\infty}^{\infty} \sum_{k=-\infty}^{\infty} \tilde{W}_{F_O}(\omega_x - j \omega_{xs}, \omega_y - k \omega_{ys}). \tag{4.2-18}$$

Figure 4.2-7 shows the sampled image power spectral density and the fold over aliasing spectral density from the first sideband with and without presampling low-pass filtering.

It is desirable to isolate the undersampling effect from the effect of improper reconstruction. Therefore, assume for this analysis that the reconstruction filter  $\mathcal{R}(\omega_x, \omega_y)$  is an optimal filter of the form given in Eq. 4.2-14. The energy passing through the reconstruction filter for  $j = k = 0$  is then

$$E_R = \int_{-\omega_{xs}/2}^{\omega_{xs}/2} \int_{-\omega_{ys}/2}^{\omega_{ys}/2} \tilde{W}_{F_I}(\omega_x, \omega_y) |\mathcal{K}(\omega_x, \omega_y)|^2 d\omega_x d\omega_y. \tag{4.2-19}$$

Ideally, the presampling filter should be a low-pass zonal filter with a transfer function identical to that of the reconstruction filter as given by Eq. 4.2-14. In this case, the sampled image energy would assume the maximum value

$$E_{RM} = \int_{-\omega_{xs}/2}^{\omega_{xs}/2} \int_{-\omega_{ys}/2}^{\omega_{ys}/2} \tilde{W}_{F_I}(\omega_x, \omega_y) d\omega_x d\omega_y \tag{4.2-20}$$

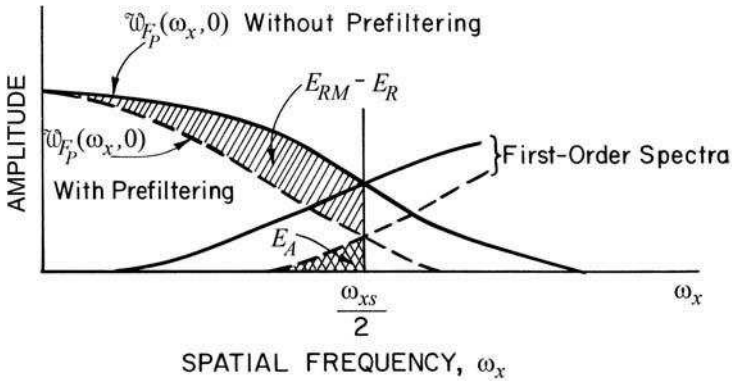


FIGURE 4.2-7. Effect of presampling filtering on a sampled image.

Image resolution degradation resulting from the presampling filter may then be measured by the ratio

$$E_R = \frac{E_{RM} - E_R}{E_{RM}} \tag{4.2-21}$$

The aliasing error in a sampled image system is generally measured in terms of the energy, from higher-order sidebands, that folds over into the passband of the reconstruction filter. Assume, for simplicity, that the sampling rate is sufficient so that the spectral foldover from spectra centered at  $(\pm j \omega_{xs}/2, \pm k \omega_{ys}/2)$  is negligible for  $j \geq 2$  and  $k \geq 2$ . The total aliasing error energy, as indicated by the doubly cross-hatched region of Figure 4.2-7, is then

$$E_A = E_O - E_R \tag{4.2-22}$$

where

$$E_O = \int_{-\infty}^{\infty} \int_{-\infty}^{\infty} \tilde{w}_{F_I}(\omega_x, \omega_y) |\mathcal{K}(\omega_x, \omega_y)|^2 d\omega_x d\omega_y \tag{4.2-23}$$

denotes the energy of the output of the presampling filter. The aliasing error is defined as (10)

$$E_A = \frac{E_A}{E_O} \tag{4.2-24}$$

Aliasing error can be reduced by attenuating high spatial frequencies of  $F_I(x, y)$  with the presampling filter. However, any attenuation within the passband of the



reconstruction filter represents a loss of resolution of the sampled image. As a result, there is a trade-off between sampled image resolution and aliasing error.

The analysis of sampling pulse and aliasing effects presented in this section has been derived for the optical image scanning system of Figure 4.2-1. This analysis is easily extended to the physical image sampling systems of Table 4.2-1. In this table, the flying spot scanner, microdensitometer scanner and the vidicon camera have been included in the table for historical consistency. These technologies have been obsoleted by the solid state sensing technologies: *Charge Coupled Device (CCD)*; *Complementary Metal-Oxide Semiconductor (CMOS)*; *Contact Image Sensor (CIS)*. Reference (13) provides a survey of the operating principles of the CCD, CMOS and CIS scanners and cameras.

Pratt (4Ed., 108-110) has analyzed the aliasing error versus resolution performance of several practical types of presampling filters implemented as finite size scanning spots.

**TABLE 4.2-1. Spot Shape of Image Scanners and Systems**

System	Spot Shape
Flying Spot Scanner	Gaussian
Microdensitometer Scanner	Square
CCD Line Scanner	Square
CIS Scanner	Square
Orthicon Camera	Gaussian
Vidicon Camera	Gaussian
CCD Camera	Square
CMOS Camera	Square
CIS Camera	Square

**4.3. MONOCHROME IMAGE RECONSTRUCTION SYSTEMS**

In Section 4.1, the conditions for exact image reconstruction were stated: The original image must be spatially sampled at a rate of at least twice its highest spatial frequency, and the reconstruction filter, or equivalent interpolator, must be designed to pass the spectral component at  $j = 0, k = 0$  without distortion and reject all spectra for which  $j, k \neq 0$ . With physical image reconstruction systems, these conditions are impossible to achieve exactly. Consideration is now given to the effects of using imperfect reconstruction functions.

### 4.3.1. Image Reconstruction Implementation Techniques

In most digital image processing systems, electrical image samples are sequentially output from the processor in a normal raster scan fashion. A continuous image is generated from these electrical samples by driving an optical display such as a cathode ray tube (CRT) or liquid crystal display (LCD) with the intensity of each point set proportional to the image sample amplitude. The light array can then be viewed directly or imaged onto photographic film for recording. Images can be recorded directly using laser printer or inkjet recording technologies. These systems are only capable of recording bi-level images. In order to achieve gray level recording, it is necessary to employ halftoning (14), as is done in newspaper printing of photographs. Reference (13) describes the operating principles of LCD displays, laser printers and inkjet printers.

A common means of image reconstruction is by use of electro-optical techniques. For example, image reconstruction can be performed quite simply by electrically defocusing the writing spot of a CRT display. The drawback of this technique is the difficulty of accurately controlling the spot shape over the image field. For recording purposes, a CRT or LCD display can be projected onto photographic film with a slightly out of focus lens. The resulting image reconstruction is simple to perform, but far from optimal.

If a small display spot can be achieved with an image display, it is possible approximately to synthesize any desired interpolation by subscanning a resolution cell, as shown in Figure 4.3-1.

The following subsections introduce several one- and two-dimensional interpolation functions and discuss their theoretical performance. Chapter 12 presents methods of digitally implementing image reconstruction systems.

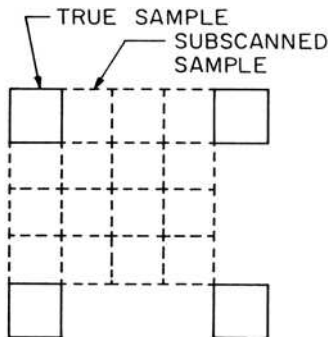


FIGURE 4.3-1. Image reconstruction by subscanning.

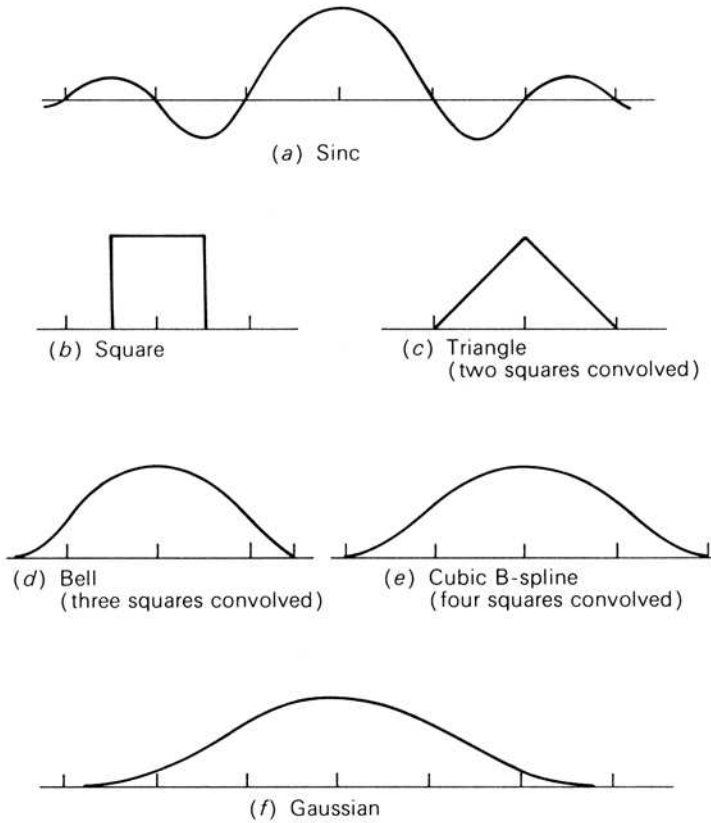


FIGURE 4.3-2. One-dimensional interpolation waveforms.

**4.3.2. Interpolation Functions**

Figure 4.3-2 illustrates several one-dimensional interpolation functions. As stated previously, the sinc function provides an exact reconstruction, but it cannot be physically generated by an incoherent optical filtering system. It is possible to approximate the sinc function by truncating it and then performing subsampling (Figure 4.3-1). The simplest interpolation waveform is the square pulse function, which results in a zero-order interpolation of the samples. It is defined mathematically as

$$R_0(x) = 1 \quad \text{for } -\frac{1}{2} \leq x \leq \frac{1}{2} \quad (4.3-1)$$

and zero otherwise, where, for notational simplicity, the sample spacing is assumed to be of unit dimension. A triangle function, defined as

$$R_1(x) = x + 1 \quad \text{for } -1 \leq x \leq 0 \quad (4.3-2a)$$

$$R_1(x) = 1 - x \quad \text{for } 0 < x \leq 1 \quad (4.3-2b)$$

provides the first-order linear sample interpolation with triangular interpolation waveforms. Figure 4.3-3 illustrates one-dimensional interpolation using sinc, square and triangle functions.

The triangle function may be considered to be the result of convolving a square function with itself. Convolution of the triangle function with the square function yields a bell-shaped interpolation waveform (in Figure 4.3-2d). It is defined as

$$R_2(x) = \begin{cases} \frac{1}{2}(x + \frac{3}{2})^2 & \text{for } -\frac{3}{2} \leq x \leq -\frac{1}{2} \end{cases} \quad (4.3-3a)$$

$$R_2(x) = \begin{cases} \frac{3}{4} - (x)^2 & \text{for } -\frac{1}{2} < x \leq \frac{1}{2} \end{cases} \quad (4.3-3b)$$

$$R_2(x) = \begin{cases} \frac{1}{2}(x - \frac{3}{2})^2 & \text{for } \frac{1}{2} < x \leq \frac{3}{2} \end{cases} \quad (4.3-3c)$$

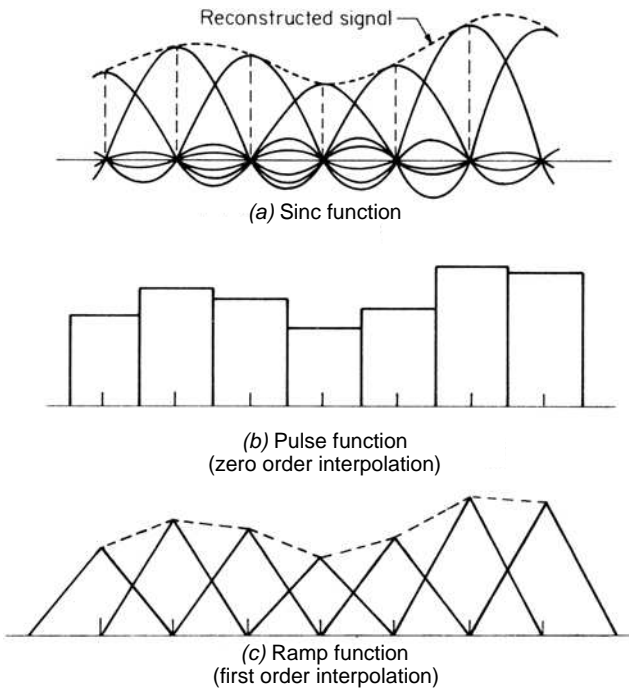


FIGURE 4.3-3. One-dimensional interpolation.

This process quickly converges to the Gaussian-shaped waveform of Figure 4.3-2f. Convolution of the bell-shaped waveform with the square function results in a third-order polynomial function called a *cubic B-spline* (15-17). It is defined mathematically as

$$R_3(x) = \begin{cases} \frac{2}{3} + \frac{1}{2}|x|^3 - (x)^2 & \text{for } 0 \leq |x| \leq 1 & (4.3-4a) \\ \frac{1}{6}(2 - |x|)^3 & \text{for } 1 < |x| \leq 2. & (4.3-4b) \end{cases}$$

The cubic B-spline is a particularly attractive candidate for image interpolation because of its properties of continuity and smoothness at the sample points. It can be shown by direct differentiation of Eq. 4.3-4 that  $R_3(x)$  is continuous in its first and second derivatives at the sample points.

As mentioned earlier, the sinc function can be approximated by truncating its tails. Typically, this is done over a four-sample interval. The problem with this approach is that the slope discontinuity at the ends of the waveform leads to amplitude ripples in a reconstructed function. This problem can be eliminated by generating a cubic convolution function (18,19), which forces the slope of the ends of the interpolation to be zero. The *cubic convolution* interpolation function can be expressed in the following general form:

$$R_c(x) = \begin{cases} A_1|x|^3 + B_1|x|^2 + C_1|x| + D_1 & \text{for } 0 \leq |x| \leq 1 & (4.3-5a) \\ A_2|x|^3 + B_2|x|^2 + C_2|x| + D_2 & \text{for } 1 < |x| \leq 2 & (4.3-5b) \end{cases}$$

where  $A_i, B_i, C_i, D_i$  are weighting factors. The weighting factors are determined by satisfying two sets of extraneous conditions:

1.  $R_c(x) = 1$  at  $x = 0$ , and  $R_c(x) = 0$  at  $x = 1, 2$ .
2. The first-order derivative  $R'_c(x) = 0$  at  $x = 0, 1, 2$ .

These conditions result in seven equations for the eight unknowns and lead to the parametric expression

$$R_c(x) = \begin{cases} (a + 2)|x|^3 - (a + 3)|x|^2 + 1 & \text{for } 0 \leq |x| \leq 1 & (4.3-6a) \\ a|x|^3 - 5a|x|^2 + 8a|x| - 4a & \text{for } 1 < |x| \leq 2 & (4.3-6b) \end{cases}$$

where  $a \equiv A_2$  of Eq. 4.3-5 is the remaining unknown weighting factor. Rifman (18) and Bernstein (19) have set  $a = -1$ , which causes  $R_c(x)$  to have the same slope,

minus 1, at  $x = 1$  as the sinc function. Keys (19) has proposed setting  $a = -1/2$ , which provides an interpolation function that approximates the original unsampled image to as high a degree as possible in the sense of a power series expansion. The factor  $a$  in Eq. 4.3-6 can be used as a tuning parameter to obtain a best visual interpolation (21, 22). Reichenbach and Geng (23) have developed a method of non-separable, two-dimensional cubic convolution. They report a slight improvement in interpolation accuracy in comparison to separable cubic convolution.

Table 4.3-1 defines several orthogonally separable two-dimensional interpolation functions for which  $R(x, y) = R(x)R(y)$ . The separable square function has a square

**TABLE 4.3-1. Two-Dimensional Interpolation Functions**

Function	Definition
Separable sinc	$R(x, y) = \frac{4}{T_x T_y} \frac{\sin\{2\pi x/T_x\}}{2\pi x/T_x} \frac{\sin\{2\pi y/T_y\}}{2\pi y/T_y}$ $T_x = \frac{2\pi}{\omega_{xs}}$ $T_y = \frac{2\pi}{\omega_{ys}}$ $\mathcal{R}(\omega_x, \omega_y) = \begin{cases} 1 &  \omega_x  \leq \omega_{xs}, \quad  \omega_y  \leq \omega_{ys} \\ 0 & \text{otherwise} \end{cases}$
Separable square	$R_0(x, y) = \begin{cases} \frac{1}{T_x T_y} &  x  \leq \frac{T_x}{2}, \quad  y  \leq \frac{T_y}{2} \\ 0 & \text{otherwise} \end{cases}$ $\mathcal{R}_0(\omega_x, \omega_y) = \frac{\sin\{\omega_x T_x/2\} \sin\{\omega_y T_y/2\}}{(\omega_x T_x/2)(\omega_y T_y/2)}$
Separable triangle	$R_1(x, y) = R_0(x, y) \otimes R_0(x, y)$ $\mathcal{R}_1(\omega_x, \omega_y) = R_0^2(\omega_x, \omega_y)$
Separable bell	$R_2(x, y) = R_0(x, y) \otimes R_1(x, y)$ $\mathcal{R}_2(\omega_x, \omega_y) = R_0^3(\omega_x, \omega_y)$
Separable cubic B-spline	$R_3(x, y) = R_0((x, y) \otimes R_2(x, y))$ $\mathcal{R}_3(\omega_x, \omega_y) = R_0^4(\omega_x, \omega_y)$
Gaussian	$R(x, y) = [2\pi\sigma_w^2]^{-1} \exp\left\{-\frac{x^2 + y^2}{2\sigma_w^2}\right\}$ $\mathcal{R}(\omega_x, \omega_y) = \exp\left\{-\frac{\sigma_w^2(\omega_x^2 + \omega_y^2)}{2}\right\}$

peg shape. The separable triangle function has the shape of a pyramid. Using a triangle interpolation function for one-dimensional interpolation is equivalent to linearly connecting adjacent sample peaks as shown in Figure 4.3-3c. The extension to two dimensions does not hold because, in general, it is not possible to fit a plane to four adjacent samples. One approach, illustrated in Figure 4.3-4a, is to perform a planar fit in a piecewise fashion. In region I of Figure 4.3-4a, points are linearly interpolated in the plane defined by pixels A, B, C, while in region II, interpolation is performed in the plane defined by pixels B, C, D. A computationally simpler method, called *bilinear interpolation*, is described in Figure 4.3-4b. Bilinear interpolation is performed by linearly interpolating points along separable orthogonal coordinates of the continuous image field. The resultant interpolated surface of Figure 4.3-4b, connecting pixels A, B, C, D, is generally nonplanar. Chapter 11 shows that bilinear interpolation is equivalent to interpolation with a pyramid function.

The performance of practical image reconstruction systems has been analyzed by Pratt (4Ed., 117-120).

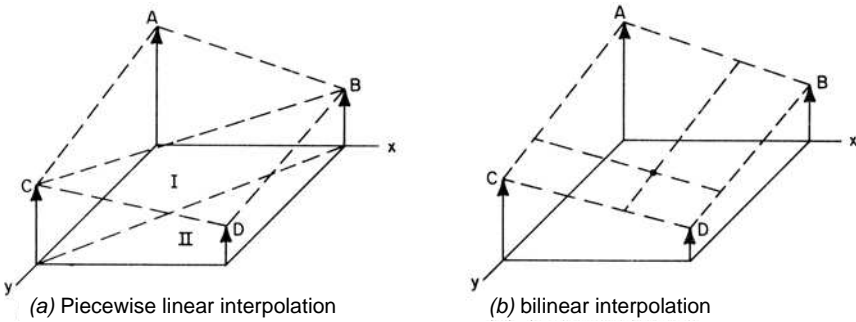


FIGURE 4.3-4. Two-dimensional linear interpolation.

#### 4.4. COLOR IMAGE SAMPLING SYSTEMS

There are two generic methods of sampling a color image: the tri-filter method; and the Bayer color filter array method.

##### 4.4.1. Tri-Filter Method

Figure 4.4-1 shows a conceptual tri-filter color image sampling system. In operation, a lens images a scene to an upper beam splitter, which splits the light beam through a blue filter onto a CCD or CMOS array sensor. The light beam also strikes the lower beam splitter, which splits the light beam through a red filter and a green filter to red and green sensor arrays. The three sensor arrays must be aligned

spatially to prevent color artifacts. Most high-end digital color cameras are based upon this method. Its disadvantage, with respect to the other methods, is the cost of three sensors.

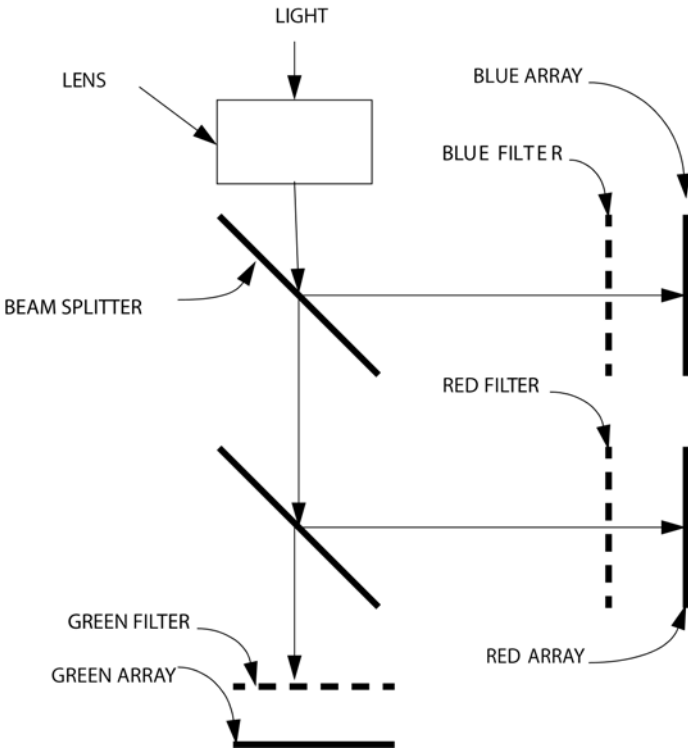


FIGURE 4.4-1. Tri-filter color image sampling method.

**4.4.2. Bayer Color Filter Array Method**

The Bayer color filter array sensor, named after its inventor (24), is a CCD or CMOS sensor chip containing  $M$  columns and  $N$  rows (25-31). A color filter is affixed to the sensor as shown below

*G R G R G . . .*  
*B G B G B . . .*  
*G R G R G . . .*  
 . . . . .



where the letters  $R$ ,  $G$  and  $B$  denote red, green and blue color filters placed over the sensor pixels.<sup>1</sup> Electrically, the sensor chip produces an  $M \times N$  array  $P(x, y)$ , whose values are linearly proportional to the luminance of light incident upon each sensor pixel. Each

$$\begin{matrix} G & R \\ B & G \end{matrix}$$

quad corresponds to a one half-resolution white pixel.

Some form of spatial interpolation is necessary to generate  $M \times N$  full resolution  $RGB$  arrays  $R(x, y)$ ,  $G(x, y)$  and  $B(x, y)$ . This interpolation process is often called *demosaicking* in the literature. Consider a  $4 \times 4$  pixel array surrounding a  $2 \times 2$  pixel quad, as shown below.

$$\begin{matrix} P(x-1, y-1) & P(x, y-1) & P(x+1, y-1) & P(x+2, y-1) \\ P(x-1, y) & P(x, y) & P(x+1, y) & P(x+2, y) \\ P(x-1, y+1) & P(x, y+1) & P(x+1, y+1) & P(x+2, y+1) \\ P(x-1, y+2) & P(x, y+2) & P(x+1, y+2) & P(x+2, y+2) \end{matrix}$$

It is assumed that, as shown above,  $P(x, y)$  corresponds to a green filter color pixel  $G(x, y)$ ,  $P(x+1, y)$  corresponds to the red filter pixel  $R(x+1, y)$ ,  $P(x, y+1)$  corresponds to the blue filter pixel  $B(x, y+1)$  and  $P(x+1, y+1)$  corresponds to the green color pixel  $G(x+1, y+1)$ .

The simplest form of interpolation is nearest neighbor interpolation, for which the center  $RGB$  pixel quad is generated from the center quad of the  $P$  array according to the following relations.

$$R(x, y) = P(x+1, y) \tag{4.4-1a}$$

$$R(x+1, y) = P(x+1, y) \tag{4.4-1b}$$

$$R(x, y+1) = P(x+1, y) \tag{4.4-1c}$$

$$R(x+1, y+1) = P(x+1, y) \tag{4.4-1d}$$

$$G(x, y) = P(x, y) \tag{4.4-2a}$$

$$G(x+1, y) = P(x, y) \tag{4.4-2b}$$

$$G(x, y+1) = P(x+1, y+1) \tag{4.4-2c}$$

$$G(x+1, y+1) = P(x+1, y+1) \tag{4.4-2d}$$

---

1. In the literature, the Bayer color filter array is also represented with  $R$  and  $B$  along the positive diagonal.

$$B(x, y) = P(x, y + 1) \quad (4.4-3a)$$

$$B(x + 1, y) = P(x, y + 1) \quad (4.4-3b)$$

$$B(x, y + 1) = P(x, y + 1) \quad (4.4-3c)$$

$$B(x + 1, y + 1) = P(x, y + 1) \quad (4.4-3d)$$

Better results can be obtained by averaging neighboring pixels of the same color according to the following relations.

$$R(x, y) = \frac{P(x - 1, y) + P(x + 1, y)}{2} \quad (4.4-4a)$$

$$R(x + 1, y) = P(x + 1, y) \quad (4.4-4b)$$

$$R(x, y + 1) = \frac{P(x - 1, y) + P(x + 1, y) + P(x - 1, y + 2) + P(x + 1, y + 2)}{4} \quad (4.4-4c)$$

$$R(x + 1, y + 1) = \frac{P(x + 1, y) + P(x + 1, y + 2)}{2} \quad (4.4-4d)$$

$$G(x, y) = P(x, y) \quad (4.4-5a)$$

$$G(x + 1, y) = \frac{P(x + 1, y - 1) + P(x, y) + P(x + 1, y + 1) + P(x + 2, y)}{4} \quad (4.4-5b)$$

$$G(x, y + 1) = \frac{P(x, y) + P(x - 1, y + 1) + P(x + 1, y + 1) + P(x, y + 2)}{4} \quad (4.4-5c)$$

$$G(x + 1, y + 1) = P(x + 1, y + 1) \quad (4.4-5d)$$

$$B(x, y) = \frac{P(x, y - 1) + P(x, y + 1)}{2} \quad (4.4-6a)$$

$$B(x + 1, y) = \frac{P(x, y - 1) + P(x + 2, y - 1) + P(x, y + 1) + P(x + 2, y + 1)}{4} \quad (4.4-6b)$$

$$B(x, y + 1) = P(x, y + 1) \quad (4.4-6c)$$

$$B(x + 1, y + 1) = \frac{P(x, y + 1) + P(x + 2, y + 1)}{2} \quad (4.4-6d)$$

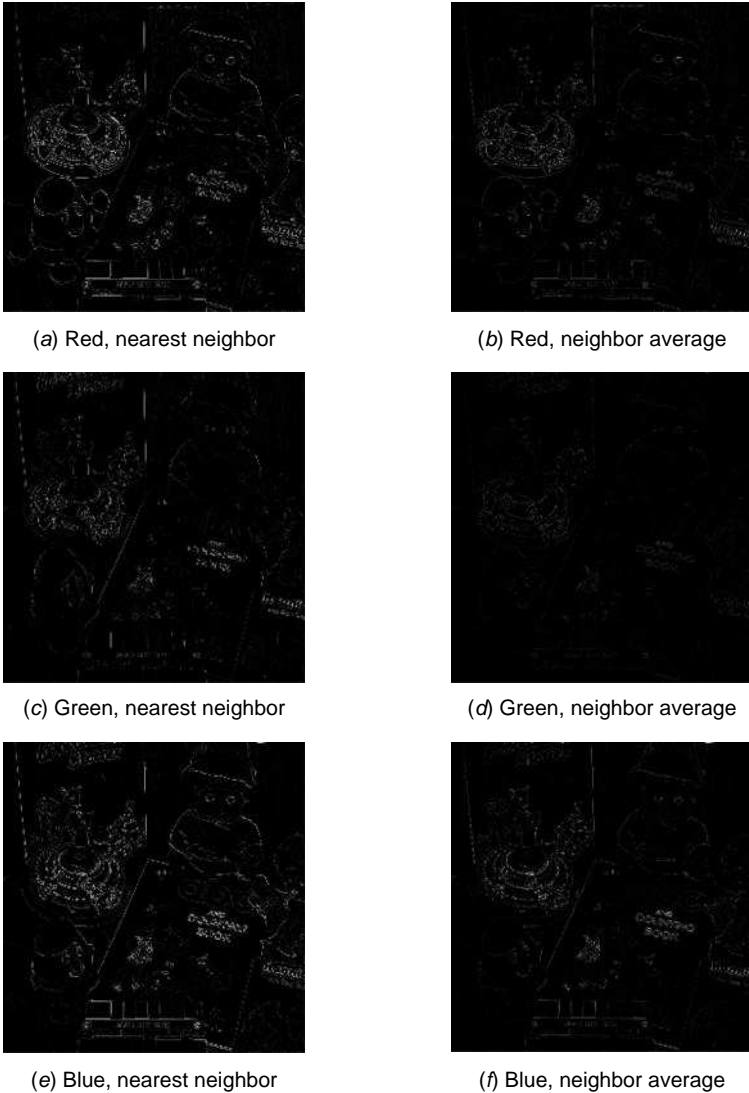


**FIGURE 4.4-3.** Bayer interpolation differences with nearest neighbor and neighbor average interpolation for the `doll's_gamma` image; clipped squared image display.

Special cases exist when the *RGB* pixel quad is at the edge of the *P* array. It should be noted that neighbor average interpolation can be computed with a set of four  $3 \times 3$  impulse response arrays. Figure 4.4-3 shows the interpolation differences of the `doll's_gamma` *RGB* image for nearest neighbor and neighbor average interpolation. References (32-39) discuss more complex image-dependent interpolation schemes to reduce interpolation error.

## 4.5. IMAGE MEASUREMENT EXERCISES

E4.1 Develop a program that computes the extrema of the *RGB* components of an unsigned integer, 8-bit, color image. Steps:

- (a) Display the source color image.
- (b) Compute extrema of the color image and print results for all bands.

The PIKS API executable `example_extrema_colour` performs this exercise.

E4.2 Develop a program that computes the mean and standard deviation of an unsigned integer, 8-bit, monochrome image. Steps:

- (a) Display the source monochrome image.
- (b) Compute moments of the monochrome image and print results.

The PIKS API executable `example_moments_monochrome` performs this exercise.

E4.3 Develop a program that computes the first-order histogram of an unsigned integer, 8-bit, monochrome image with 16 amplitude bins. Steps:

- (a) Display the source monochrome image.
- (b) Compute the histogram of the source image.
- (c) Display or printout the histogram.

The PIKS API executable `example_histogram_monochrome` performs this exercise.

## REFERENCES

1. F. T. Whittaker, "On the Functions Which Are Represented by the Expansions of the Interpolation Theory," *Proc. Royal Society of Edinburgh*, **A35**, 1915, 181–194.
2. C. E. Shannon, "Communication in the Presence of Noise," *Proc. IRE*, **37**, 1, January 1949, 10–21.
3. H. J. Landa, "Sampling, Data Transmission and the Nyquist Rate," *Proc. IEEE*, **55**, 10, October 1967, 1701–1706.
4. J. W. Goodman, *Introduction to Fourier Optics, Second Edition*, McGraw-Hill, New York, 1996.
5. A. Papoulis, *Systems and Transforms with Applications in Optics*, McGraw-Hill, New York, 1966.
6. S. P. Lloyd, "A Sampling Theorem for Stationary (Wide Sense) Stochastic Processes," *Trans. American Mathematical Society*, **92**, 1, July 1959, 1–12.
7. H. S. Shapiro and R. A. Silverman, "Alias-Free Sampling of Random Noise," *J. SIAM*, **8**, 2, June 1960, 225–248.
8. J. L. Brown, Jr., "Bounds for Truncation Error in Sampling Expansions of Band-Limited Signals," *IEEE Trans. Information Theory*, **IT-15**, 4, July 1969, 440–444.

9. H. D. Helms and J. B. Thomas, "Truncation Error of Sampling Theory Expansions," *Proc. IRE*, **50**, 2, February 1962, 179–184.
10. J. J. Downing, "Data Sampling and Pulse Amplitude Modulation," in *Aerospace Telemetry*, H. L. Stiltz, Ed., Prentice Hall, Englewood Cliffs, NJ, 1961.
11. D. G. Childers, "Study and Experimental Investigation on Sampling Rate and Aliasing in Time Division Telemetry Systems," *IRE Trans. Space Electronics and Telemetry*, **SET-8**, December 1962, 267–283.
12. E. L. O'Neill, *Introduction to Statistical Optics*, Addison-Wesley, Reading, MA, 1963.
13. M. Vrhel, E. Saber and H. J. Trussell, Color Image Generation and Display Technologies, *IEEE Signal Processing Magazine*, **22**, 1, January 2005, 23–33.
14. J. P. Allebach, *Digital Halftoning*, **MS154**, SPIE Press, Bellingham, WA, 1999.
15. H. S. Hou and H. C. Andrews, "Cubic Splines for Image Interpolation and Digital Filtering," *IEEE Trans. Acoustics, Speech and Signal Processing*, **ASSP-26**, 6, December 1978, 508–517.
16. T. N. E. Greville, "Introduction to Spline Functions," in *Theory and Applications of Spline Functions*, T. N. E. Greville, Ed., Academic Press, New York, 1969.
17. M. Unser, "Splines — A Perfect Fit for Signal and Image Processing," *IEEE Signal and Image Processing*, **16**, 6, November 1999, 22–38.
18. S. S. Rifman, "Digital Rectification of ERTS Multispectral Imagery," *Proc. Symposium on Significant Results Obtained from ERTS-1 (NASA SP-327)*, **I**, Sec. B, 1973, 1131–1142.
19. R. Bernstein, "Digital Image Processing of Earth Observation Sensor Data," *IBM J. Research and Development*, **20**, 1976, 40–57.
20. R. G. Keys, "Cubic Convolution Interpolation for Digital Image Processing," *IEEE Trans. Acoustics, Speech and Signal Processing*, **AASP-29**, 6, December 1981, 1153–1160.
21. K. W. Simon, "Digital Image Reconstruction and Resampling of Landsat Imagery," *Proc. Symposium on Machine Processing of Remotely Sensed Data*, Purdue University, Lafayette, IN, IEEE 75, CH 1009-0-C, June 1975, 3A-1–3A-11.
22. S. K. Park and R. A. Schowengerdt, "Image Reconstruction by Parametric Cubic Convolution," *Computer Vision, Graphics and Image Processing*, **23**, 3, September 1983, 258–272.
23. S. E. Reichenbach, "Two-Dimensional Cubic Convolution," *IEEE Transactions on Image Processing*, **12**, 8, August 2003, 857–865.
24. B. E. Bayer, "Color Imaging Array," U.S. Patent 3,971,065, July 20, 1976.
25. P. L. P. Dillon and B. E. Bayer, "Signal Processing for Discrete-Sample-Type-Color-Video Signal," U.S. Patent 4,176,373, November 27, 1979.
26. D. R. Cok, "Signal Processing Method and Apparatus for Sampled Image Signals," U.S. Patent 4,630,307, December 16, 1986.
27. D. R. Cok, "Signal Processing Method and Apparatus for Producing Interpolated Chrominance Values in a Sampled Color Image Signal," U.S. Patent 4,642,678, February 10, 1987.
28. C. A. Laroche and M. A. Prescott, "Apparatus and Method for Adaptively Interpolating a Full Color Image Utilizing Chrominance Gradients," U.S. Patent 5,373,322, December 13, 1994.

29. R. H. Hibbard, "Apparatus and Method for Adaptively Interpolating a Full Color Image Utilizing Luminance Gradients," U.S. Patent 5,382,976, January 17, 1995.
30. J. E. Adams, Jr. and J. F. Hamilton, Jr., "Adaptive Color Plan Interpolation in Single Sensor Color Electronic Camera," U.S. Patent 5,506,619, April 9, 1996.
31. J. F. Hamilton, Jr. and J. E. Adams, Jr., "Adaptive Color Plane Interpolation in Single Sensor Color Electronic Camera," U.S. Patent 5,629,734, May 13, 1997.
32. R. Kimmel, "Demosaiicing: Image Reconstruction from CCD Samples," *IEEE Transactions on Image Processing*, **8**, 8, August 1999, 1221–1228.
33. H. J. Trussell and R. E. Hartwig, "Mathematics for Demosaicing," *IEEE Transactions on Image Processing*, **11**, 4, April 2002, 485–592.
34. B. K. Gunturk, Y. Altunbasak and R. M. Mersereau, "Color Plane Interpolation Using Alternating Projections," *IEEE Transactions on Image Processing*, **11**, September 2002, 997–1013.
35. B. Bahadir et al., "Demosaiicing: Color Filter Array Interpolation," *IEEE Signal Processing Magazine*, **44**, 1, January 2005, 44–54.
36. D. D. Muresan and T. W. Parks, "Demosaiicing Using Optimal Recovery," *IEEE Transactions on Image Processing*, **14**, 2, February 2005, 267–278.
37. K. Hirakawa and T. W. Parks, "Adaptive Homogeneity-Directed Demosaicing Algorithm," *IEEE Transactions on Image Processing*, **14**, 3, March 2005, 360–369.
38. D. Allysson, S. Susstrunk and J. Herault, "Linear Demosaicing Inspired by the Human Visual System," *IEEE Transactions on Image Processing*, **14**, 4, April 2005, 439–449.
39. L. Zhang and X. Wu, "Color Demosaicking Via Directional Linear Mean Square-Error Estimation," *IEEE Transactions on Image Processing*, **14**, 12, December 2005, 2167–2178.



---

# 5

---

## IMAGE QUANTIZATION

Any analog quantity that is to be processed by a digital computer or digital system must be converted to an integer number proportional to its amplitude. The conversion process between analog samples and discrete-valued samples is called *quantization*. The following section includes an analytic treatment of the quantization process, which is applicable not only for images but for a wide class of signals encountered in image processing systems. Section 5.2 considers the processing of quantized variables. The last section discusses the subjective effects of quantizing monochrome and color images.

### 5.1. SCALAR QUANTIZATION

Figure 5.1-1 illustrates a typical example of the quantization of a scalar signal. In the quantization process, the amplitude of an analog signal sample is compared to a set of decision levels. If the sample amplitude falls between two decision levels, it is quantized to a fixed reconstruction level lying in the quantization band. In a digital system, each quantized sample is assigned a binary code. An equal-length binary code is indicated in the example.

For the development of quantitative scalar signal quantization techniques, let  $f$  and  $\hat{f}$  represent the amplitude of a real, scalar signal sample and its quantized value, respectively. It is assumed that  $f$  is a sample of a random process with known prob-



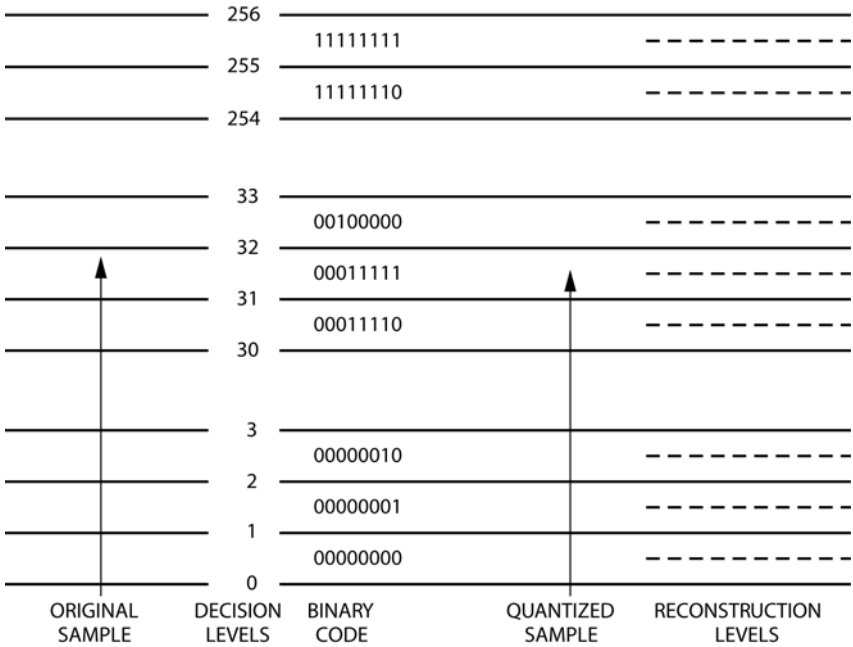


FIGURE 5.1-1. Sample quantization.

ability density  $p(f)$ . Furthermore, it is assumed that  $f$  is constrained to lie in the range

$$a_L \leq f \leq a_U \tag{5.1-1}$$

where  $a_U$  and  $a_L$  represent upper and lower limits.

Quantization entails specification of a set of *decision levels*  $d_j$  and a set of *reconstruction levels*  $r_j$  such that if

$$d_j \leq f < d_{j+1} \tag{5.1-2}$$

the sample is quantized to a reconstruction value  $r_j$ . Figure 5.1-2a illustrates the placement of decision and reconstruction levels along an image row for  $J$  quantization levels. The staircase representation of Figure 5.1-2b is another common form of description.

Decision and reconstruction levels are chosen to minimize some desired quantization error measure between  $f$  and  $\hat{f}$ . The quantization error measure usually employed is the mean-square error because this measure is tractable, and it usually

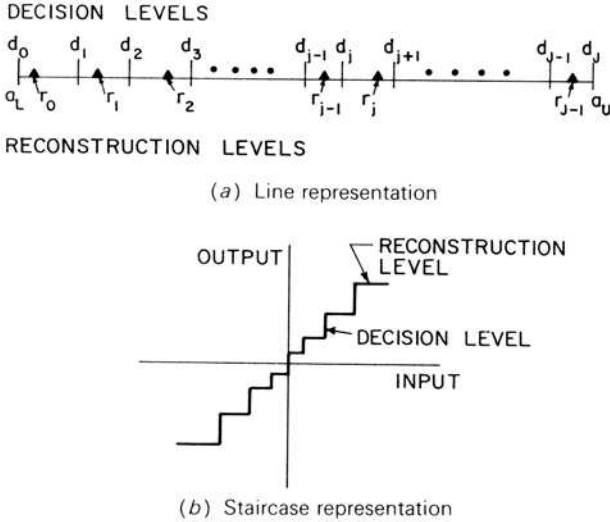


FIGURE 5.1-2. Quantization decision and reconstruction levels.

correlates reasonably well with subjective criteria. For  $J$  quantization levels, the mean-square quantization error is

$$\mathcal{E} = E\{(f - \hat{f})^2\} = \int_{a_L}^{a_U} (f - \hat{f})^2 p(f) df = \sum_{i=0}^{J-1} (f - r_j)^2 p(f) df \quad (5.1-3)$$

For a large number of quantization levels  $J$ , the probability density may be represented as a constant value  $p(r_j)$  over each quantization band. Hence,

$$\mathcal{E} = \sum_{i=0}^{J-1} p(r_j) \int_{d_j}^{d_{j+1}} (f - r_j)^2 df \quad (5.1-4)$$

which evaluates to

$$\mathcal{E} = \frac{1}{3} \sum_{i=0}^{J-1} p(r_j) [(d_{j+1} - r_j)^3 - (d_j - r_j)^3] \quad (5.1-5)$$

The optimum placing of the reconstruction level  $r_j$  within the range  $d_{j-1}$  to  $d_j$  can be determined by minimization of  $\mathcal{E}$  with respect to  $r_j$ . Setting

$$\frac{d\mathcal{E}}{dr_j} = 0 \quad (5.1-6)$$

yields

$$r_j = \frac{d_{j+1} + d_j}{2} . \tag{5.1-7}$$

Therefore, the optimum placement of reconstruction levels is at the midpoint between each pair of decision levels. Substitution for this choice of reconstruction levels into the expression for the quantization error yields

$$\mathcal{E} = \frac{1}{12} \sum_{i=0}^{J-1} p(r_j)(d_{j+1} - d_j)^3 . \tag{5.1-8}$$

The optimum choice for decision levels may be found by minimization of  $\mathcal{E}$  in Eq. 5.1-8 by the method of *Lagrange multipliers*. Following this procedure, Panter and Dite (1) found that the decision levels may be computed to a good approximation from the integral equation

$$d_j = \frac{(a_U - a_L) \int_{a_L}^{a_j} [p(f)]^{-1/3} df}{\int_{a_L}^{a_U} [p(f)]^{-1/3} df} \tag{5.1-9a}$$

where

$$a_j = \frac{j(a_U - a_L)}{J} + a_L \tag{5.1-9b}$$

for  $j = 0, 1, \dots, J$ . If the probability density of the sample is uniform, the decision levels will be uniformly spaced. For nonuniform probability densities, the spacing of decision levels is narrow in large-amplitude regions of the probability density function and widens in low-amplitude portions of the density. Equation 5.1-9 does not reduce to closed form for most probability density functions commonly encountered in image processing systems models, and hence, the decision levels must be obtained by numerical integration.

If the number of quantization levels is not large, the approximation of Eq. 5.1-4 becomes inaccurate, and exact solutions must be explored. From Eq. 5.1-3, setting the partial derivatives of the error expression with respect to the decision and reconstruction levels equal to zero yields

$$\frac{\partial \mathcal{E}}{\partial d_j} = (d_j - r_j)^2 p(d_j) - (d_j - r_{j-1})^2 p(d_j) = 0 \tag{5.1-10a}$$

$$\frac{\partial \mathcal{E}}{\partial r_j} = 2 \int_{d_j}^{d_{j+1}} (f - r_j) p(f) df = 0 . \tag{5.1-10b}$$

Upon simplification, the set of equations

$$r_j = 2d_j - r_{j-1} \tag{5.1-11a}$$

$$r_j = \frac{\int_{d_j}^{d_{j+1}} fp(f) df}{\int_{d_j}^{d_{j+1}} p(f) df} \tag{5.1-11b}$$

is obtained. Recursive solution of these equations for a given probability distribution  $p(f)$  provides optimum values for the decision and reconstruction levels. Max (2) has developed a solution for optimum decision and reconstruction levels for a Gaussian density and has computed tables of optimum levels as a function of the number of quantization steps.

If the decision and reconstruction levels are selected to satisfy Eq. 5.1-11, it can easily be shown that the mean-square quantization error becomes

$$\epsilon_{\min} = \sum_{j=0}^{J-1} \left[ \int_{d_j}^{d_{j+1}} f^2 p(f) df - r_j^2 \int_{d_j}^{d_{j+1}} p(f) df \right]. \tag{5.1-12}$$

In the special case of a uniform probability density, the minimum mean-square quantization error becomes

$$\epsilon_{\min} = \frac{1}{12J^2}. \tag{5.1-13}$$

Quantization errors for most other densities must be determined by computation.

It is possible to perform nonlinear quantization by a companding operation, as shown in Figure 5.1-3, in which the sample is transformed nonlinearly, linear quantization is performed, and the inverse nonlinear transformation is taken (3). In the companding system of quantization, the probability density of the transformed samples is forced to be uniform. Thus, from Figure 5.1-3, the transformed sample value is

$$g = T\{f\} \tag{5.1-14}$$



FIGURE 5.1-3. Companding quantizer.

where the nonlinear transformation  $T\{ \cdot \}$  is chosen such that the probability density of  $g$  is uniform. Thus

$$p(g) = 1 \tag{5.1-15}$$

for  $-\frac{1}{2} \leq g \leq \frac{1}{2}$ . If  $f$  is a zero mean random variable, the proper transformation function is (4)

$$T\{f\} = \int_{-\infty}^f p(z) dz - \frac{1}{2}. \tag{5.1-16}$$

That is, the nonlinear transformation function is equivalent to the cumulative probability distribution of  $f$ . It should be noted that nonlinear quantization by the companding technique is an approximation to optimum quantization, as specified by the Max solution. The accuracy of the approximation improves as the number of quantization levels increases.

### 5.2. PROCESSING QUANTIZED VARIABLES

Numbers within a digital computer that represent image variables, such as luminance or tristimulus values, normally are input as the integer codes corresponding to the quantization reconstruction levels of the variables, as illustrated in Figure 5.1-1. If the quantization is linear, the  $j$ th integer value is given by

$$j = \left[ (J-1) \frac{f - a_L}{a_U - a_L} \right]_N \tag{5.2-1}$$

where  $J$  is the maximum integer value,  $f$  is the unquantized pixel value over a lower-to-upper range of  $a_L$  to  $a_U$ , and  $[ \cdot ]_N$  denotes the nearest integer value of the argument. The corresponding reconstruction value is

$$r_j = \frac{a_U - a_L}{J} j + \frac{a_U - a_L}{2J} + a_L. \tag{5.2-2}$$

Hence,  $r_j$  is linearly proportional to  $j$ . If the computer processing operation is itself linear, the integer code  $j$  can be numerically processed rather than the real number  $r_j$ . However, if nonlinear processing is to be performed, for example, taking the logarithm of a pixel, it is necessary to process  $r_j$  as a real variable rather than the integer  $j$  because the operation is scale dependent. If the quantization is nonlinear, all processing must be performed in the real variable domain.

In a digital computer, there are two major forms of numeric representation: real and integer. Real numbers are stored in floating-point form, and typically have a large dynamic range with fine precision. Integer numbers can be strictly positive or bipolar (negative or positive). The two's complement number system is

commonly used in computers and digital processing hardware for representing bipolar integers. The general format is as follows:

$$S.M_1,M_2,\dots,M_{B-1}$$

where  $S$  is a sign bit (0 for positive, 1 for negative), followed, conceptually, by a binary point,  $M_b$  denotes a magnitude bit, and  $B$  is the number of bits in the computer word. Table 5.2-1 lists the two's complement correspondence between integer, fractional and decimal numbers for a 4-bit word. In this representation, all pixels

**TABLE 5.2-1. Two's Complement Code for 4-Bit Code Word**

Code	Fractional Value	Decimal Value
0.111	$+\frac{7}{8}$	+0.875
0.110	$+\frac{6}{8}$	+0.750
0.101	$+\frac{5}{8}$	+0.625
0.100	$+\frac{4}{8}$	+0.500
0.011	$+\frac{3}{8}$	+0.375
0.010	$+\frac{2}{8}$	+0.250
0.001	$+\frac{1}{8}$	+0.125
0.000	0	0.000
1.111	$-\frac{1}{8}$	-0.125
1.110	$-\frac{2}{8}$	-0.250
1.101	$-\frac{3}{8}$	-0.375
1.100	$-\frac{4}{8}$	-0.500
1.011	$-\frac{5}{8}$	-0.625
1.010	$-\frac{6}{8}$	-0.750
1.001	$-\frac{7}{8}$	-0.875
1.000	$-\frac{8}{8}$	-1.000

are scaled in amplitude between  $-1.0$  and  $1.0 - 2^{-(B-1)}$ . One of the advantages of this representation is that pixel scaling is independent of precision in the sense that a pixel  $F(j, k)$  is bounded over the range

$$-1.0 \leq F(j, k) < 1.0$$

regardless of the number of bits in a word.

### 5.3. MONOCHROME AND COLOR IMAGE QUANTIZATION

This section considers the subjective and quantitative effects of the quantization of monochrome and color images.

#### 5.3.1. Monochrome Image Quantization

Monochrome images are typically input to a digital image processor as a sequence of uniform-length binary code words. In the literature, the binary code is often called a *pulse code modulation* (PCM) code. Because uniform-length code words are used for each image sample, the number of amplitude quantization levels is determined by the relationship

$$L = 2^B \quad (5.3-1)$$

where  $B$  represents the number of code bits allocated to each sample.

A bit rate compression can be achieved for PCM coding by the simple expedient of restricting the number of bits assigned to each sample. If image quality is to be judged by an analytic measure,  $B$  is simply taken as the smallest value that satisfies the minimal acceptable image quality measure. For a subjective assessment,  $B$  is lowered until quantization effects become unacceptable. The eye is only capable of judging the absolute brightness of about 10 to 15 shades of gray, but it is much more sensitive to the difference in the brightness of adjacent gray shades. For a reduced number of quantization levels, the first noticeable artifact is a *gray scale contouring* caused by a jump in the reconstructed image brightness between quantization levels in a region where the original image is slowly changing in brightness. The minimal number of quantization bits required for basic PCM coding to prevent gray scale contouring is dependent on a variety of factors, including the linearity of the image display and noise effects before and after the image digitizer.

Assuming that an image sensor produces an output pixel sample proportional to the image intensity, a question of concern then is: Should the image intensity itself, or some function of the image intensity, be quantized? Furthermore, should the quantization scale be linear or nonlinear? Linearity or nonlinearity of the quantization scale can be viewed as a matter of implementation. A given nonlinear quantization scale can be realized by the companding operation of Figure 5.1-3, in which a nonlinear amplification weighting of the continuous signal to be quantized is performed,

followed by linear quantization, followed by an inverse weighting of the quantized amplitude. Consideration is limited here to linear quantization of companded pixel samples.

There have been many experimental studies to determine the number and placement of quantization levels required to minimize the effect of gray scale contouring (5–8). Goodall (5) performed some of the earliest experiments on digital television and concluded that 6 bits of intensity quantization (64 levels) were required for good quality and that 5 bits (32 levels) would suffice for a moderate amount of contouring. Other investigators have reached similar conclusions. In most studies, however, there has been some question as to the linearity and calibration of the imaging system. As noted in Section 3.5.3, most television cameras and monitors exhibit a nonlinear response to light intensity. Also, the photographic film that is often used to record the experimental results is highly nonlinear. Finally, any camera or monitor noise tends to diminish the effects of contouring.

Figure 5.3-1 contains photographs of an image linearly quantized with a variable number of quantization levels. The source image is a split image in which the left side is a luminance image and the right side is a computer-generated linear ramp. In Figure 5.3-1, the luminance signal of the image has been uniformly quantized with from 8 to 256 levels (3 to 8 bits). Gray scale contouring in these pictures is apparent in the ramp part of the split image for 6 or fewer bits. The contouring of the luminance image part of the split image becomes noticeable for 5 bits.

As discussed in Section 2.4, it has been postulated that the eye responds logarithmically or to a power law of incident light amplitude. There have been several efforts to quantitatively model this nonlinear response by a *lightness function*  $\Lambda$ , which is related to incident luminance. Priest et al. (9) have proposed a square-root nonlinearity

$$\Lambda = (100.0Y)^{1/2} \quad (5.3-2)$$

where  $0.0 \leq Y \leq 1.0$  and  $0.0 \leq \Lambda \leq 10.0$ . Ladd and Pinney (10) have suggested a cube-root scale

$$\Lambda = 2.468(100.0Y)^{1/3} - 1.636 \quad (5.3-3)$$

A logarithm scale

$$\Lambda = 5.0[\log_{10}\{100.0Y\}] \quad (5.3-4)$$

where  $0.01 \leq Y \leq 1.0$  has also been proposed by Foss et al. (11). Figure 5.3-2 compares these three scaling functions.



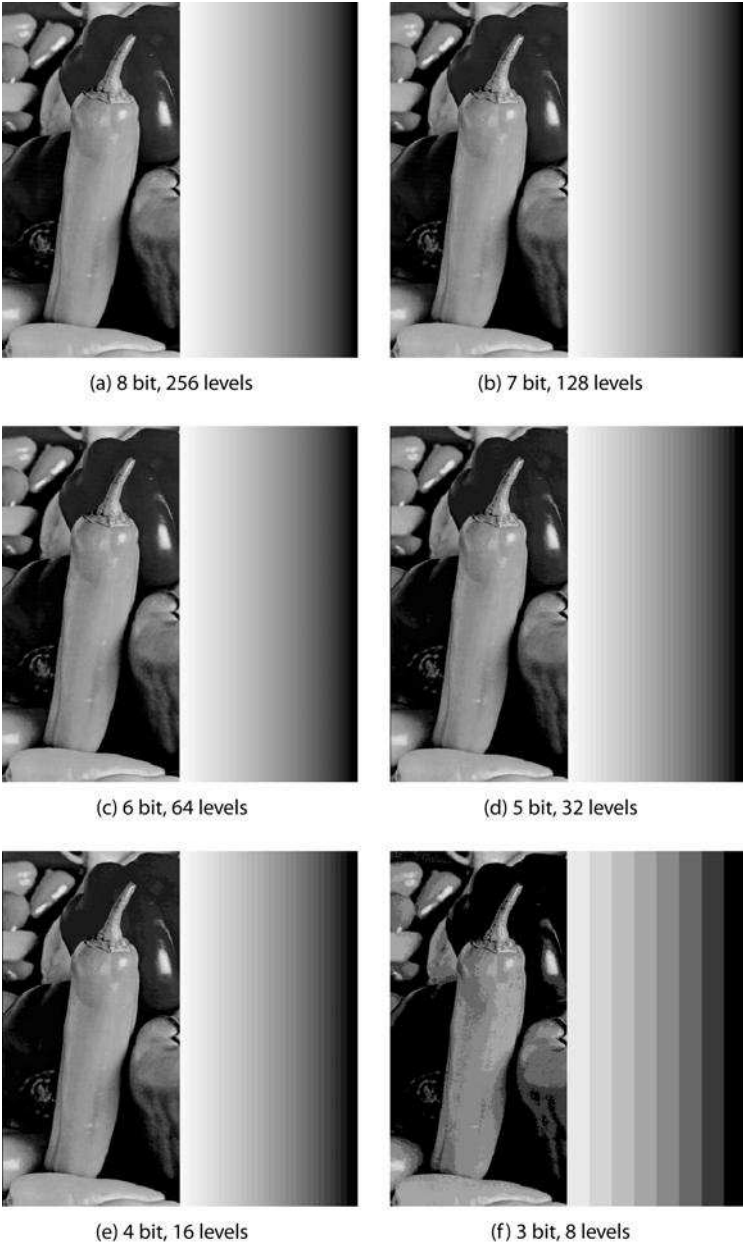


**FIGURE 5.3-1.** Uniform quantization of the peppers\_ramp\_luminance monochrome image.

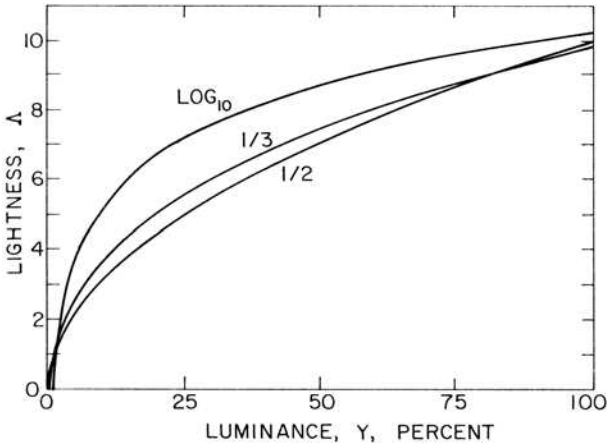


FIGURE 5.3-2. Lightness scales.

In an effort to reduce the gray scale contouring of linear quantization, it is reasonable to apply a lightness scaling function prior to quantization, and then to apply its inverse to the reconstructed value in correspondence to the companding quantizer of Figure 5.1-3. Figure 5.3-3 presents a comparison of linear, square-root, cube-root and logarithmic quantization for a 4-bit quantizer. Among the lightness scale quantizers, the gray scale contouring appears least for the square-root scaling. The lightness quantizers exhibit less contouring than the linear quantizer in dark areas but worse contouring for bright regions.

### 5.3.2. Color Image Quantization

A color image may be represented by its red, green and blue source tristimulus values or any linear or nonlinear invertible function of the source tristimulus values. If the red, green and blue tristimulus values are to be quantized individually, the selection of the number and placement of quantization levels follows the same general considerations as for a monochrome image. The eye exhibits a nonlinear response to spectral lights as well as white light, and, therefore, it is subjectively preferable to compand the tristimulus values before quantization. It is known, however, that the eye is most sensitive to brightness changes in the blue region of the spectrum, moderately sensitive to brightness changes in the green spectral region and least sensitive to red changes. Thus, it is possible to assign quantization levels on this basis more efficiently than simply using an equal number for each tristimulus value.



**FIGURE 5.3-3.** Comparison of lightness scale quantization of the peppers\_ramp\_luminance image for 4 bit quantization.

Figure 5.3-4 is a general block diagram for a color image quantization system. A source image described by source tristimulus values  $R, G, B$  is converted to three components  $x(1), x(2), x(3)$ , which are then quantized. Next, the quantized components  $\hat{x}(1), \hat{x}(2), \hat{x}(3)$  are converted back to the original color coordinate system, producing the quantized tristimulus values  $\hat{R}, \hat{G}, \hat{B}$ . The quantizer in Figure 5.3-4 effectively partitions the color space of the color coordinates  $x(1), x(2), x(3)$  into quantization cells and assigns a single color value to all colors within a cell. To be most efficient, the three color components  $x(1), x(2), x(3)$  should be quantized jointly. However, implementation considerations often dictate separate quantization of the color components. In such a system,  $x(1), x(2), x(3)$  are individually quantized over

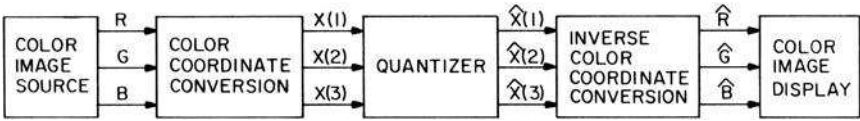


FIGURE 5.3-4 Color image quantization model.

their maximum ranges. In effect, the physical color solid is enclosed in a rectangular solid, which is then divided into rectangular quantization cells.

If the source tristimulus values are converted to some other coordinate system for quantization, some immediate problems arise. As an example, consider the quantization of the  $UVW$  tristimulus values. Figure 5.3-5 shows the locus of reproducible colors for the  $RGB$  source tristimulus values plotted as a cube and the transformation of this color cube into the  $UVW$  coordinate system. It is seen that the  $RGB$  cube becomes a parallelepiped. If the  $UVW$  tristimulus values are to be quantized individually over their maximum and minimum limits, many of the quantization cells represent non reproducible colors and hence are wasted. It is only worthwhile to quantize colors within the parallelepiped, but this generally is a difficult operation to implement efficiently.

In the present analysis, it is assumed that each color component is linearly quantized over its maximum range into  $2^{B(i)}$  levels, where  $B(i)$  represents the number of bits assigned to the component  $x(i)$ . The total number of bits allotted to the coding is fixed at

$$B_T = B(1) + B(2) + B(3) . \tag{5.3-5}$$

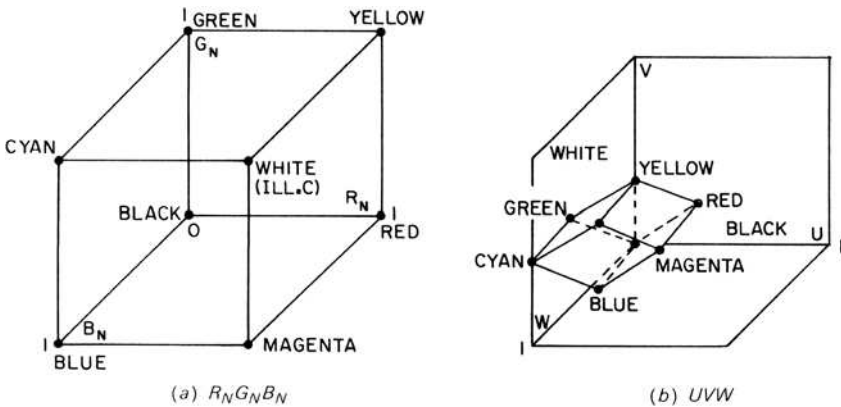


FIGURE 5.3-5. Loci of reproducible colors for  $R_N G_N B_N$  and  $UVW$  coordinate systems.

Let  $a_U(i)$  represent the upper bound of  $x(i)$  and  $a_L(i)$  the lower bound. Then each quantization cell has dimension

$$q(i) = \frac{a_U(i) - a_L(i)}{2^{B(i)}} \tag{5.3-6}$$

Any color with color component  $x(i)$  within the quantization cell will be quantized to the color component value  $\hat{x}(i)$ . The maximum quantization error along each color coordinate axis is then

$$\varepsilon(i) = |x(i) - \hat{x}(i)| = \frac{a_U(i) - a_L(i)}{2^{B(i)+1}} \tag{5.3-7}$$

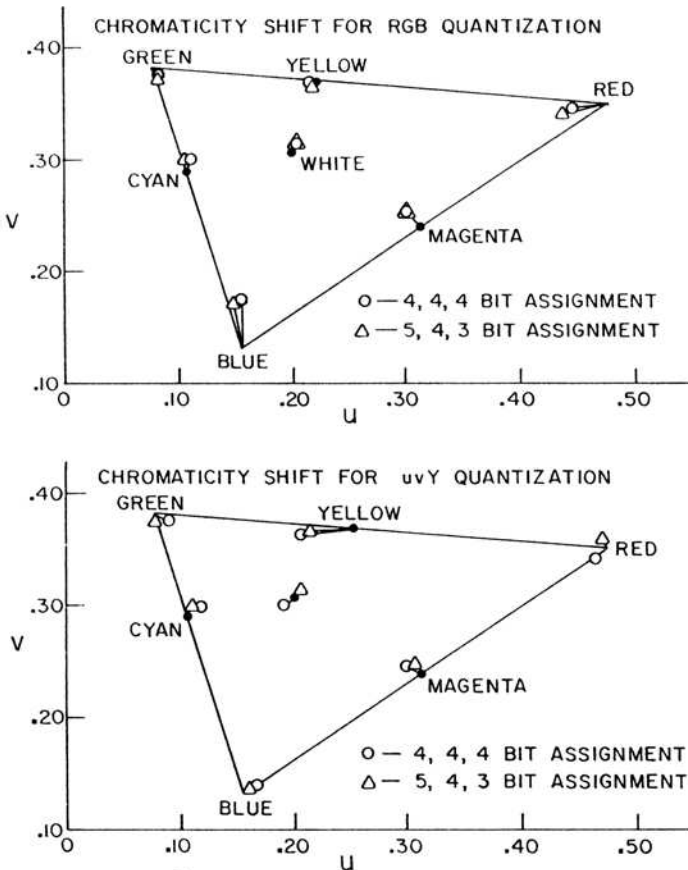


FIGURE 5.3-6. Chromaticity shifts resulting from uniform quantization of the `smpte_girl_linear` color image.

Thus, the coordinates of the quantized color become

$$\hat{x}(i) = x(i) \pm \varepsilon(i) \quad (5.3-8)$$

subject to the conditions  $a_L(i) \leq \hat{x}(i) \leq a_U(i)$ . It should be observed that the values of  $\hat{x}(i)$  will always lie within the smallest cube enclosing the color solid for the given color coordinate system. Figure 5.3-6 illustrates chromaticity shifts of various colors for quantization in the  $R_N G_N B_N$  and  $Yuv$  coordinate systems (12).

Jain and Pratt (12) have investigated the optimal assignment of quantization decision levels for color images in order to minimize the geodesic color distance between an original color and its reconstructed representation. Interestingly enough, it was found that quantization of the  $R_N G_N B_N$  color coordinates provided better results than for other common color coordinate systems. The primary reason was that all quantization levels were occupied in the  $R_N G_N B_N$  system, but many levels were unoccupied with the other systems. This consideration seemed to override the metric non uniformity of the  $R_N G_N B_N$  color space. Sharma and Trussell (13) have surveyed color image quantization for reduced memory image displays.

## 5.4. IMAGE QUANTIZATION EXERCISES

E5.1 Develop a program that re-quantizes an unsigned integer, 8-bit, monochrome image linearly to three bits per pixel and reconstructs it to eight bits per pixel. Steps:

- (a) Display the source image.
- (b) Perform a right overflow shift by five bits on the source image<sup>1</sup>.
- (c) Perform a left overflow shift by five bits on the right bit-shifted source image.
- (d) Scale the reconstruction levels to 3-bit values.
- (e) Display the destination image.

The PIKS API executable `example_linear_quantizer` performs this exercise.

E5.2 Develop a program that quantizes an unsigned integer, 8-bit, monochrome image according to the cube root lightness function of Eq. 6.3-4 and reconstructs it to eight bits per pixel. Steps:

- (a) Display the source image.
- (b) Scale the source image to unit range.
- (c) Perform the cube root lightness transformation.

---

1. The *right* bit of an unsigned integer is its least significant bit. The *left* bit of an unsigned integer is its most significant bit.

- (d) Scale the lightness function image to 0 to 255.
- (e) Perform a right overflow shift by five bits on the source image.
- (f) Perform a left overflow shift by five bits on the right bit-shifted source image.
- (g) Scale the reconstruction levels to 3-bit values.
- (h) Scale the reconstruction image to the lightness function range.
- (i) Perform the inverse lightness function.
- (j) Scale the inverse lightness function to the display range.
- (k) Display the destination image.

The PIKS API executable `example_lightness_quantizer` performs this exercise.

**E5.3** Develop a program that re-quantizes an unsigned integer, 8-bit, color image linearly to three bits per pixel per component and reconstructs it to eight bits per pixel per component. Steps:

- (a) Display the source image.
- (b) Perform a right overflow shift by five bits of all components of the source image.
- (c) Perform a left overflow shift by five bits on the right bit-shifted source image.
- (d) Display the destination image.

The PIKS API executable `example_linear_quantizer_colour` performs this exercise.

## REFERENCES

1. P. F. Panter and W. Dite, "Quantization Distortion in Pulse Code Modulation with Non-uniform Spacing of Levels," *Proc. IRE*, **39**, 1, January 1951, 44–48.
2. J. Max, "Quantizing for Minimum Distortion," *IRE Trans. Information Theory*, **IT-6**, 1, March 1960, 7–12.
3. V. R. Algazi, "Useful Approximations to Optimum Quantization," *IEEE Trans. Communication Technology*, **COM-14**, 3, June 1966, 297–301.
4. R. M. Gray, "Vector Quantization," *IEEE ASSP Magazine*, April 1984, 4–29.
5. W. M. Goodall, "Television by Pulse Code Modulation," *Bell System Technical J.*, January 1951.
6. R. L. Cabrey, "Video Transmission over Telephone Cable Pairs by Pulse Code Modulation," *Proc. IRE*, **48**, 9, September 1960, 1546–1551.
7. L. H. Harper, "PCM Picture Transmission," *IEEE Spectrum*, **3**, 6, June 1966, 146.

8. F. W. Scoville and T. S. Huang, "The Subjective Effect of Spatial and Brightness Quantization in PCM Picture Transmission," *NEREM Record*, 1965, 234–235.
9. I. G. Priest, K. S. Gibson, and H. J. McNicholas, "An Examination of the Munsell Color System, I. Spectral and Total Reflection and the Munsell Scale of Value," Technical Paper 167, National Bureau of Standards, Washington, DC, 1920.
10. J. H. Ladd and J. E. Pinney, "Empirical Relationships with the Munsell Value Scale," *Proc. IRE (Correspondence)*, **43**, 9, 1955, 1137.
11. C. E. Foss, D. Nickerson and W. C. Granville, "Analysis of the Oswald Color System," *J. Optical Society of America*, **34**, 1, July 1944, 361–381.
12. A. K. Jain and W. K. Pratt, "Color Image Quantization," IEEE Publication 72 CH0 601-5-NTC, *National Telecommunications Conference 1972 Record*, Houston, TX, December 1972.
13. G. Sharma and H. J. Trussell, "Digital Color Imaging," *IEEE Trans. Image Processing*, **6**, 7, July 1997, 901–932.





## **PART 3**

---

# **DISCRETE TWO-DIMENSIONAL PROCESSING**

Part 3 of the book is concerned with a unified analysis of discrete two-dimensional processing operations. Vector-space methods of image representation are developed for deterministic and stochastic image arrays. Several forms of discrete two-dimensional superposition and convolution operators are developed and related to one another. Two-dimensional unitary transforms, such as the Fourier, Hartley, cosine and Karhunen–Loeve transforms, are introduced along with wavelet transforms. Consideration is given to the utilization of two-dimensional transforms as an alternative means of achieving convolutional processing more efficiently.



---

# 6

---

## DISCRETE IMAGE MATHEMATICAL CHARACTERIZATION

Chapter 1 presented a mathematical characterization of continuous image fields. This chapter develops a vector-space algebra formalism for representing discrete image fields from a deterministic and statistical viewpoint. Appendix 1 presents a summary of vector-space algebra concepts.

### 6.1. VECTOR-SPACE IMAGE REPRESENTATION

In Chapter 1, a generalized continuous image function  $F(x, y, t)$  was selected to represent the luminance, tristimulus value, or some other appropriate measure of a physical imaging system. Image sampling techniques, discussed in Chapter 4, indicated means by which a discrete array  $F(j, k)$  could be extracted from the continuous image field at some time instant over some rectangular area  $-J \leq j \leq J$ ,  $-K \leq k \leq K$ . It is often helpful to regard this sampled image array as a  $N_1 \times N_2$  element matrix

$$\mathbf{F} = [F(n_1, n_2)] \quad (6.1-1)$$

for  $1 \leq n_i \leq N_i$  where the indices of the sampled array are reindexed for consistency with standard vector-space notation. Figure 6.1-1 illustrates the geometric relationship between the Cartesian coordinate system of a continuous image and its matrix array of samples. Each image sample is called a *pixel*.

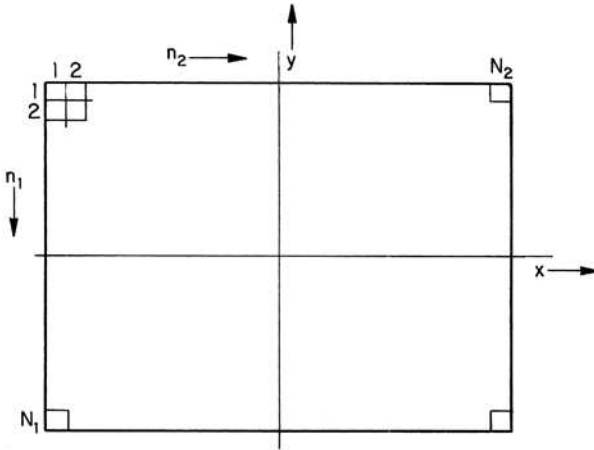


**FIGURE 6.1-1.** Geometric relationship between a continuous image and its matrix array of samples.

For purposes of analysis, it is often convenient to convert the image matrix to vector form by column (or row) scanning  $\mathbf{F}$ , and then stringing the elements together in a long vector ( $\mathbf{f}$ ). An equivalent scanning operation can be expressed in quantitative form by the use of a  $N_2 \times 1$  operational vector  $\mathbf{v}_n$  and a  $N_1 \cdot N_2 \times N_2$  matrix  $\mathbf{N}_n$  defined as

$$\mathbf{v}_n = \begin{bmatrix} 0 \\ \vdots \\ 0 \\ 1 \\ 0 \\ \vdots \\ 0 \end{bmatrix} \begin{matrix} 1 \\ \vdots \\ n-1 \\ n \\ n+1 \\ \vdots \\ N_2 \end{matrix} \quad \mathbf{N}_n = \begin{bmatrix} \mathbf{0} \\ \vdots \\ \mathbf{0} \\ \mathbf{1} \\ \mathbf{0} \\ \vdots \\ \mathbf{0} \end{bmatrix} \begin{matrix} 1 \\ \vdots \\ n-1 \\ n \\ n+1 \\ \vdots \\ N_2 \end{matrix} \quad (6.1-2)$$

Then, the vector representation of the image matrix  $\mathbf{F}$  is given by the *stacking operation*

$$\mathbf{f} = \sum_{n=1}^{N_2} \mathbf{N}_n \mathbf{F} \mathbf{v}_n \quad (6.1-3)$$

In essence, the vector  $\mathbf{v}_n$  extracts the  $n$ th column from  $\mathbf{F}$  and the matrix  $\mathbf{N}_n$  places this column into the  $n$ th segment of the vector  $\mathbf{f}$ . Thus,  $\mathbf{f}$  contains the column-scanned elements of  $\mathbf{F}$ . The inverse relation of casting the vector  $\mathbf{f}$  into matrix form is obtained from

$$\mathbf{F} = \sum_{n=1}^{N_2} \mathbf{N}_n^T \mathbf{f} \mathbf{v}_n^T \tag{6.1-4}$$

With the matrix-to-vector operator of Eq. 6.1-3 and the vector-to-matrix operator of Eq. 6.1-4, it is now possible easily to convert between vector and matrix representations of a two-dimensional array. The advantages of dealing with images in vector form are a more compact notation and the ability to apply results derived previously for one-dimensional signal processing applications. It should be recognized that Eqs 6.1-3 and 6.1-4 represent more than a lexicographic ordering between an array and a vector; these equations define mathematical operators that may be manipulated analytically. Numerous examples of the applications of the *stacking operators* are given in subsequent sections.

### 6.2. GENERALIZED TWO-DIMENSIONAL LINEAR OPERATOR

A large class of image processing operations are linear in nature; an output image field is formed from linear combinations of pixels of an input image field. Such operations include superposition, convolution, unitary transformation, wavelet transformation and discrete linear filtering.

Consider the  $N_1 \times N_2$  element input image array  $F(n_1, n_2)$ . A generalized linear operation on this image field results in a  $M_1 \times M_2$  output image array  $P(m_1, m_2)$  as defined by

$$P(m_1, m_2) = \sum_{n_1=1}^{N_1} \sum_{n_2=1}^{N_2} F(n_1, n_2) O(n_1, n_2; m_1, m_2) \tag{6.2-1}$$

where the operator kernel  $O(n_1, n_2; m_1, m_2)$  represents a weighting constant, which, in general, is a function of both input and output image coordinates (1).

For the analysis of linear image processing operations, it is convenient to adopt the vector-space formulation developed in Section 6.1. Thus, let the input image array  $F(n_1, n_2)$  be represented as matrix  $\mathbf{F}$  or alternatively, as a vector  $\mathbf{f}$  obtained by column scanning  $\mathbf{F}$ . Similarly, let the output image array  $P(m_1, m_2)$  be represented by the matrix  $\mathbf{P}$  or the column-scanned vector  $\mathbf{p}$ . For notational simplicity, in the subsequent discussions, the input and output image arrays are assumed to be square and of dimensions  $N_1 = N_2 = N$  and  $M_1 = M_2 = M$ , respectively. Now, let  $\mathbf{T}$  denote the  $M^2 \times N^2$  matrix performing a linear transformation on the  $N^2 \times 1$  input image vector  $\mathbf{f}$  yielding the  $M^2 \times 1$  output image vector

$$\mathbf{p} = \mathbf{Tf} \tag{6.2-2}$$

The matrix  $\mathbf{T}$  may be partitioned into  $M \times N$  submatrices  $\mathbf{T}_{mn}$  and written as

$$\mathbf{T} = \begin{bmatrix} \mathbf{T}_{11} & \mathbf{T}_{12} & \cdots & \mathbf{T}_{1N} \\ \mathbf{T}_{21} & \mathbf{T}_{22} & \cdots & \mathbf{T}_{2N} \\ \vdots & \vdots & & \vdots \\ \mathbf{T}_{M1} & \mathbf{T}_{M2} & \cdots & \mathbf{T}_{MN} \end{bmatrix}. \tag{6.2-3}$$

From Eq. 6.1-3, it is possible to relate the output image vector  $\mathbf{p}$  to the input image matrix  $\mathbf{F}$  by the equation

$$\mathbf{p} = \sum_{n=1}^N \mathbf{T}\mathbf{N}_n\mathbf{F}\mathbf{v}_n. \tag{6.2-4}$$

Furthermore, from Eq. 6.1-4, the output image matrix  $\mathbf{P}$  is related to the input image vector  $\mathbf{p}$  by

$$\mathbf{P} = \sum_{m=1}^M \mathbf{M}_m^T \mathbf{p} \mathbf{u}_m^T. \tag{6.2-5}$$

Combining the above yields the relation between the input and output image matrices,

$$\mathbf{P} = \sum_{m=1}^M \sum_{n=1}^N (\mathbf{M}_m^T \mathbf{T}\mathbf{N}_n) \mathbf{F} (\mathbf{v}_n \mathbf{u}_m^T) \tag{6.2-6}$$

where it is observed that the operators  $\mathbf{M}_m$  and  $\mathbf{N}_n$  simply extract the partition  $\mathbf{T}_{mn}$  from  $\mathbf{T}$ . Hence,

$$\mathbf{P} = \sum_{m=1}^M \sum_{n=1}^N \mathbf{T}_{mn} \mathbf{F} (\mathbf{v}_n \mathbf{u}_m^T). \tag{6.2-7}$$

If the linear transformation is separable such that  $\mathbf{T}$  may be expressed in the direct product form (See Appendix A1.1-15.)

$$\mathbf{T} = \mathbf{T}_C \otimes \mathbf{T}_R \tag{6.2-8}$$

where  $\mathbf{T}_R$  and  $\mathbf{T}_C$  are row and column operators on  $\mathbf{F}$ , then

$$\mathbf{T}_{mn} = T_R(m, n) \mathbf{T}_C \tag{6.2-9}$$

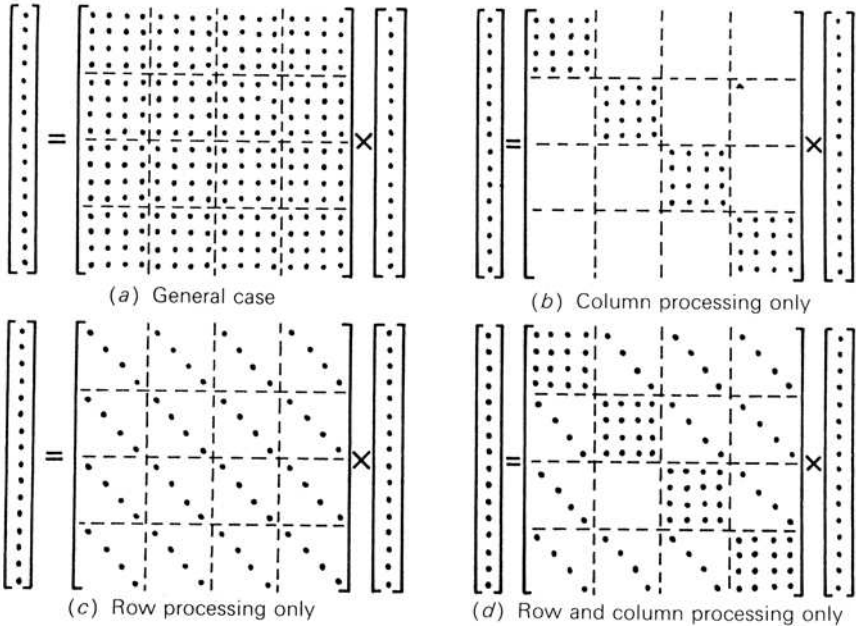


FIGURE 6.2-1. Structure of linear operator matrices.

As a consequence,

$$\mathbf{P} = \mathbf{T}_C \mathbf{F} \sum_{m=1}^M \sum_{n=1}^N T_R(m, n) \mathbf{v}_n \mathbf{u}_m^T = \mathbf{T}_C \mathbf{F} \mathbf{T}_R^T \tag{6.2-10}$$

Hence, the output image matrix  $\mathbf{P}$  can be produced by sequential row and column operations.

In many image processing applications, the linear transformations operator  $\mathbf{T}$  is highly structured, and computational simplifications are possible. Special cases of interest are listed below and illustrated in Figure 6.2-1 for the case in which the input and output images are of the same dimension,  $M = N$ .

1. *Column processing of  $\mathbf{F}$ :*

$$\mathbf{T} = \text{diag}[\mathbf{T}_{C1}, \mathbf{T}_{C2}, \dots, \mathbf{T}_{CN}] \tag{6.2-11}$$

where  $\mathbf{T}_{Cj}$  is the transformation matrix for the  $j$ th column.

2. *Identical column processing of  $\mathbf{F}$ :*

$$\mathbf{T} = \text{diag}[\mathbf{T}_C, \mathbf{T}_C, \dots, \mathbf{T}_C] = \mathbf{T}_C \otimes \mathbf{I}_N \tag{6.2-12}$$



where  $\mathbf{I}_N$  is a  $N \times N$  identity matrix. (See Appendix A1.1-6.)

3. Row processing of  $\mathbf{F}$ :

$$\mathbf{T}_{mn} = \text{diag}[T_{R1}(m, n), T_{R2}(m, n), \dots, T_{RN}(m, n)] \tag{6.2-13}$$

where  $\mathbf{T}_{Rj}$  is the transformation matrix for the  $j$ th row.

4. Identical row processing of  $\mathbf{F}$ :

$$\mathbf{T}_{mn} = \text{diag}[T_R(m, n), T_R(m, n), \dots, T_R(m, n)] \tag{6.2-14a}$$

and

$$\mathbf{T} = \mathbf{I}_N \otimes \mathbf{T}_R. \tag{6.2-14b}$$

5. Identical row and identical column processing of  $\mathbf{F}$ :

$$\mathbf{T} = \mathbf{T}_C \otimes \mathbf{I}_N + \mathbf{I}_N \otimes \mathbf{T}_R. \tag{6.2-15}$$

The number of computational operations for each of these cases is tabulated in Table 6.2-1.

Equation 6.2-10 indicates that separable two-dimensional linear transforms can be computed by sequential one-dimensional row and column operations on a data array. As indicated by Table 6.2-1, a considerable savings in computation is possible for such transforms: computation by Eq 6.2-2 in the general case requires  $M^2N^2$  operations; computation by Eq. 6.2-10, when it applies, requires only  $MN^2 + M^2N$  operations. Furthermore,  $\mathbf{F}$  may be stored in a serial memory and fetched line by line. With this technique, however, it is necessary to transpose the result of the column transforms in order to perform the row transforms. References 2 and 3 describe algorithms for line storage matrix transposition.

**TABLE 6.2-1. Computational Requirements for Linear Transform Operator.**

Case	Operations (Multiply and Add)
General	$N_4$
Column processing	$N_3$
Row processing	$N^3$
Row and column processing	$2N^3 - N^2$
Separable row and column processing matrix form	$2N^3$

### 6.3. IMAGE STATISTICAL CHARACTERIZATION

The statistical descriptors of continuous images presented in Chapter 1 can be applied directly to characterize discrete images. In this section, expressions are developed for the statistical moments of discrete image arrays. Joint probability density models for discrete image fields are described in the following section. Reference 4 provides background information for this subject.

The moments of a discrete image process may be expressed conveniently in vector-space form. The mean value of the discrete image function is a matrix of the form

$$E\{\mathbf{F}\} = [E\{F(n_1, n_2)\}] \tag{6.3-1}$$

If the image array is written as a column-scanned vector, the mean of the image vector is

$$\eta_{\mathbf{f}} = E\{\mathbf{f}\} = \sum_{n=1}^{N_2} \mathbf{N}_n E\{\mathbf{F}\} \mathbf{v}_n \tag{6.3-2}$$

The correlation function of the image array is given by

$$R(n_1, n_2; n_3, n_4) = E\{F(n_1, n_2)F^*(n_3, n_4)\} \tag{6.3-3}$$

where the  $n_i$  represent points of the image array. Similarly, the covariance function of the image array is

$$K(n_1, n_2; n_3, n_4) = E\{[F(n_1, n_2) - E\{F(n_1, n_2)\}][F^*(n_3, n_4) - E\{F^*(n_3, n_4)\}]\} \tag{6.3-4}$$

Finally, the *variance function* of the image array is obtained directly from the covariance function as

$$\sigma^2(n_1, n_2) = K(n_1, n_2; n_1, n_2) \tag{6.3-5}$$

If the image array is represented in vector form, the correlation matrix of  $\mathbf{f}$  can be written in terms of the correlation of elements of  $\mathbf{F}$  as

$$\mathbf{R}_{\mathbf{f}} = E\{\mathbf{f}\mathbf{f}^{*T}\} = E\left\{ \left( \sum_{m=1}^{N_2} \mathbf{N}_m \mathbf{F} \mathbf{v}_m \right) \left( \sum_{n=1}^{N_2} \mathbf{v}_n^T \mathbf{F}^{*T} \mathbf{N}_n^T \right) \right\} \tag{6.3-6a}$$

or

$$\mathbf{R}_{\mathbf{f}} = \sum_{m=1}^{N_2} \sum_{n=1}^{N_2} \mathbf{N}_m E\left\{ \mathbf{F} \mathbf{v}_m \mathbf{v}_n^T \mathbf{F}^{*T} \right\} \mathbf{N}_n^T \tag{6.3-6b}$$

The term

$$E\left\{\mathbf{F}\mathbf{v}_m\mathbf{v}_n^T\mathbf{F}^{*T}\right\} = \mathbf{R}_{mn} \tag{6.3-7}$$

is the  $N_1 \times N_1$  correlation matrix of the  $m$ th and  $n$ th columns of  $\mathbf{F}$ . Hence, it is possible to express  $\mathbf{R}_f$  in partitioned form as

$$\mathbf{R}_f = \begin{bmatrix} \mathbf{R}_{11} & \mathbf{R}_{12} & \cdots & \mathbf{R}_{1N_2} \\ \mathbf{R}_{21} & \mathbf{R}_{22} & \cdots & \mathbf{R}_{2N_2} \\ \vdots & \vdots & \ddots & \vdots \\ \mathbf{R}_{N_21} & \mathbf{R}_{N_22} & \cdots & \mathbf{R}_{N_2N_2} \end{bmatrix} \tag{6.3-8}$$

The covariance matrix of  $\mathbf{f}$  can be found from its correlation matrix and mean vector by the relation

$$\mathbf{K}_f = \mathbf{R}_f - \eta_f\eta_f^{*T} \tag{6.3-9}$$

A variance matrix  $\mathbf{V}_F$  of the array  $F(n_1, n_2)$  is defined as a matrix whose elements represent the variances of the corresponding elements of the array. The elements of this matrix may be extracted directly from the covariance matrix partitions of  $\mathbf{K}_f$ . That is,

$$\mathbf{V}_F(n_1, n_2) = \mathbf{K}_{n_2, n_2}(n_1, n_1) \tag{6.3-10}$$

If the image matrix  $\mathbf{F}$  is wide-sense stationary, the correlation function can be expressed as

$$R(n_1, n_2; n_3, n_4) = R(n_1 - n_3, n_2 - n_4) = R(j, k) \tag{6.3-11}$$

where  $j = n_1 - n_3$  and  $k = n_2 - n_4$ . Correspondingly, the covariance matrix partitions of Eq. 6.3-9 are related by

$$\mathbf{K}_{mn} = \mathbf{K}_k \quad m \geq n \tag{6.3-12a}$$

$$\mathbf{K}_{mn}^* = \mathbf{K}_k^* \quad m < n \tag{6.3-12b}$$

where  $k = |m - n| + 1$ . Hence, for a wide-sense-stationary image array

$$\mathbf{K}_f = \begin{bmatrix} \mathbf{K}_1 & \mathbf{K}_2 & \cdots & \mathbf{K}_{N_2} \\ \mathbf{K}_2^* & \mathbf{K}_1 & \cdots & \mathbf{K}_{N_2-1} \\ \vdots & \vdots & \ddots & \vdots \\ \mathbf{K}_{N_2}^* & \mathbf{K}_{N_2-1}^* & \cdots & \mathbf{K}_1 \end{bmatrix} \tag{6.3-13}$$

The matrix of Eq. 6.3-13 is of *block Toeplitz* form (5). Finally, if the covariance between elements is separable into the product of row and column covariance functions, then the covariance matrix of the image vector can be expressed as the direct product of row and column covariance matrices. Under this condition

$$\mathbf{K}_f = \mathbf{K}_C \otimes \mathbf{K}_R = \begin{bmatrix} \mathbf{K}_R(1, 1)\mathbf{K}_C & \mathbf{K}_R(1, 2)\mathbf{K}_C & \dots & \mathbf{K}_R(1, N_2)\mathbf{K}_C \\ \mathbf{K}_R(2, 1)\mathbf{K}_C & \mathbf{K}_R(2, 2)\mathbf{K}_C & \dots & \mathbf{K}_R(2, N_2)\mathbf{K}_C \\ \vdots & \vdots & \dots & \vdots \\ \mathbf{K}_R(N_2, 1)\mathbf{K}_C & \mathbf{K}_R(N_2, 2)\mathbf{K}_C & \dots & \mathbf{K}_R(N_2, N_2)\mathbf{K}_C \end{bmatrix} \tag{6.3-14}$$

where  $\mathbf{K}_C$  is a  $N_1 \times N_1$  covariance matrix of each column of  $\mathbf{F}$  and  $\mathbf{K}_R$  is a  $N_2 \times N_2$  covariance matrix of the rows of  $\mathbf{F}$ .

As a special case, consider the situation in which adjacent pixels along an image row have a correlation of  $(0.0 \leq \rho_R \leq 1.0)$  and a self-correlation of unity. Then the covariance matrix reduces to

$$\mathbf{K}_R = \sigma_R^2 \begin{bmatrix} 1 & \rho_R & \dots & \rho_R^{N_2-1} \\ \rho_R & 1 & \dots & \rho_R^{N_2-2} \\ \vdots & \vdots & \dots & \vdots \\ \rho_R^{N_2-1} & \rho_R^{N_2-2} & \dots & 1 \end{bmatrix} \tag{6.3-15}$$

where  $\sigma_R^2$  denotes the variance of pixels along a row. This is an example of the covariance matrix of a *Markov process*, analogous to the continuous autocovariance function  $\exp(-\alpha|x|)$ .

Figure 6.3-1 contains a plot by Davisson (6) of the measured covariance of pixels along an image row of the monochrome image of Figure 6.3-2. The data points can be fit quite well with a Markov covariance function with  $\rho = 0.953$ . Similarly, the covariance between lines can be modeled well with a Markov covariance function with  $\rho = 0.965$ . If the horizontal and vertical covariances were exactly separable, the covariance function for pixels along the image diagonal would be equal to the product of the horizontal and vertical axis covariance functions. In this example, the approximation was found to be reasonably accurate for up to five pixel separations.

The discrete power-spectral density of a discrete image random process may be defined, in analogy with the continuous power spectrum of Eq. 1.4-13, as the two-dimensional discrete Fourier transform of its stationary autocorrelation function. Thus, from Eq. 6.3-11

$$\mathcal{W}(u, v) = \sum_{j=0}^{N_1-1} \sum_{k=0}^{N_2-1} R(j, k) \exp\left\{-2\pi i \left(\frac{ju}{N_1} + \frac{kv}{N_2}\right)\right\}. \tag{6.3-16}$$

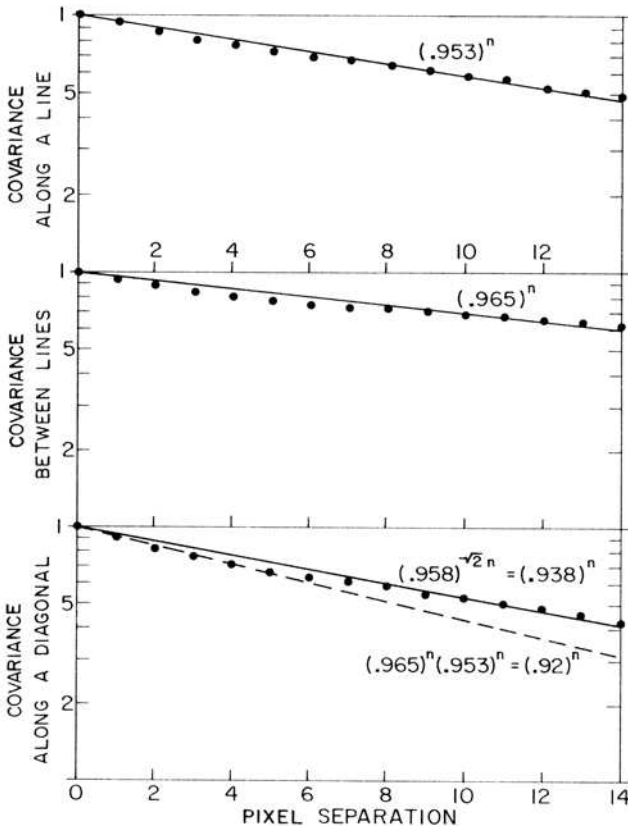
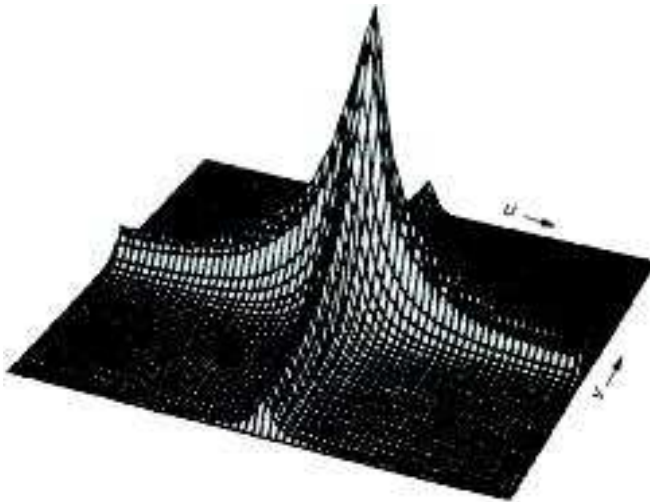


**FIGURE 6.3-1.** Covariance measurements of the `smpte_girl_luminance` monochrome image.

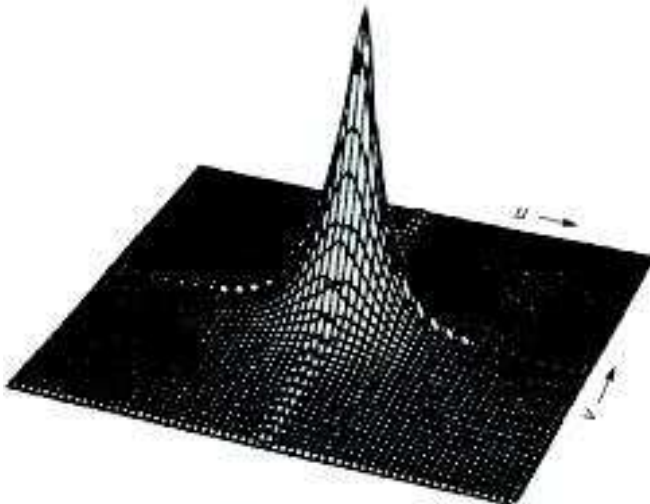


**FIGURE 6.3-2.** Photograph of `smpte_girl_luminance` image.

Figure 6.3-3 shows perspective plots of the power-spectral densities for separable and circularly symmetric Markov processes.



(a) Seperable



(b) Circularly symmetric

**FIGURE 6.3-3.** Power spectral densities of Markov process sources;  $N = 256$ , log magnitude displays.

### 6.4. IMAGE PROBABILITY DENSITY MODELS

A discrete image array  $F(n_1, n_2)$  can be completely characterized statistically by its joint probability density, written in matrix form as

$$p(\mathbf{F}) \equiv p\{F(1, 1), F(2, 1), \dots, F(N_1, N_2)\} \tag{6.4-1a}$$

or in corresponding vector form as

$$p(\mathbf{f}) \equiv p\{f(1), f(2), \dots, f(Q)\} \tag{6.4-1b}$$

where  $Q = N_1 \cdot N_2$  is the order of the joint density. If all pixel values are statistically independent, the joint density factors into the product

$$p(\mathbf{f}) \equiv p\{f(1)\}p\{f(2)\} \dots p\{f(Q)\} \tag{6.4-2}$$

of its first-order marginal densities.

The most common joint probability density is the joint Gaussian, which may be expressed as

$$p(\mathbf{f}) = (2\pi)^{-Q/2} |\mathbf{K}_f|^{-1/2} \exp\left\{-\frac{1}{2}(\mathbf{f} - \eta_f)^T \mathbf{K}_f^{-1} (\mathbf{f} - \eta_f)\right\} \tag{6.4-3}$$

where  $\mathbf{K}_f$  is the covariance matrix of  $\mathbf{f}$ ,  $\eta_f$  is the mean of  $\mathbf{f}$  and  $|\mathbf{K}_f|$  denotes the determinant of  $\mathbf{K}_f$ . The joint Gaussian density is useful as a model for the density of unitary transform coefficients of an image. However, the Gaussian density is not an adequate model for the luminance values of an image because luminance is a positive quantity and the Gaussian variables are bipolar.

Expressions for joint densities, other than the Gaussian density, are rarely found in the literature. Huhns (7) has developed a technique of generating high-order densities in terms of specified first-order marginal densities and a specified covariance matrix between the ensemble elements.

In Chapter 5, techniques were developed for quantizing variables to some discrete set of values called *reconstruction levels*. Let  $r_{j_q}(q)$  denote the reconstruction level of the pixel at vector coordinate ( $q$ ). Then the probability of occurrence of the possible states of the image vector can be written in terms of the joint probability distribution as

$$P(\mathbf{f}) = p\{f(1) = r_{j_1}(1)\}p\{f(2) = r_{j_2}(2)\} \dots p\{f(Q) = r_{j_Q}(Q)\} \tag{6.4-4}$$

where  $0 \leq j_q \leq j_Q = J - 1$ . Normally, the reconstruction levels are set identically for each vector component and the joint probability distribution reduces to

$$P(\mathbf{f}) = p\{f(1) = r_{j_1}\}p\{f(2) = r_{j_2}\} \dots p\{f(Q) = r_{j_Q}\}. \tag{6.4-5}$$

Probability distributions of image values can be estimated by *histogram measurements*. For example, the first-order probability distribution

$$P[f(q)] = P_R[f(q) = r_j] \tag{6.4-6}$$

of the amplitude value at vector coordinate  $q$  can be estimated by examining a large collection of images representative of a given image class (e.g., chest x-rays, aerial scenes of crops). The *first-order histogram* estimate of the probability distribution is the frequency ratio

$$H_E(j; q) = \frac{N_p(j)}{N_p} \tag{6.4-7}$$

where  $N_p$  represents the total number of images examined and  $N_p(j)$  denotes the number of occurrences for which  $f(q) = r_j$  for  $j = 0, 1, \dots, J - 1$ . If the image source is statistically stationary, the first-order probability distribution of Eq. 6.4-6 will be the same for all vector components  $q$ . Furthermore, if the image source is *ergodic*, ensemble averages (measurements over a collection of pictures) can be replaced by spatial averages. Under the ergodic assumption, the first-order probability distribution can be estimated by measurement of the spatial histogram

$$H_S(j) = \frac{N_S(j)}{Q} \tag{6.4-8}$$

where  $N_S(j)$  denotes the number of pixels in an image for which  $f(q) = r_j$  for  $1 \leq q \leq Q$  and  $0 \leq j \leq J - 1$ . For example, for an image with 256 gray levels,  $H_S(j)$  denotes the number of pixels possessing gray level  $j$  for  $0 \leq j \leq 255$ .

Figure 6.4-1 shows first-order histograms of the red, green and blue components of a color image. Most natural images possess many more dark pixels than bright pixels, and their histograms tend to fall off exponentially at higher luminance levels.

Estimates of the second-order probability distribution for ergodic image sources can be obtained by measurement of the *second-order spatial histogram*, which is a measure of the joint occurrence of pairs of pixels separated by a specified distance. With reference to Figure 6.4-2, let  $F(n_1, n_2)$  and  $F(n_3, n_4)$  denote a pair of pixels separated by  $r$  radial units at an angle  $\theta$  with respect to the horizontal axis. As a consequence of the rectilinear grid, the separation parameters may only assume certain discrete values. The second-order spatial histogram is then the frequency ratio

$$H_S(j_1, j_2; r, \theta) = \frac{N_S(j_1, j_2)}{Q_T} \tag{6.4-9}$$

where  $N_S(j_1, j_2)$  denotes the number of pixel pairs for which  $F(n_1, n_2) = r_{j_1}$  and  $F(n_3, n_4) = r_{j_2}$ . The factor  $Q_T$  in the denominator of Eq. 6.4-9 represents the total number of pixels lying in an image region for which the separation is  $(r, \theta)$ . Because of boundary effects,  $Q_T < Q$ .



Second-order spatial histograms of a monochrome image are presented in Figure 6.4-3 as a function of pixel separation distance and angle. As the separation increases, the pairs of pixels become less correlated and the histogram energy tends to spread more uniformly about the plane.

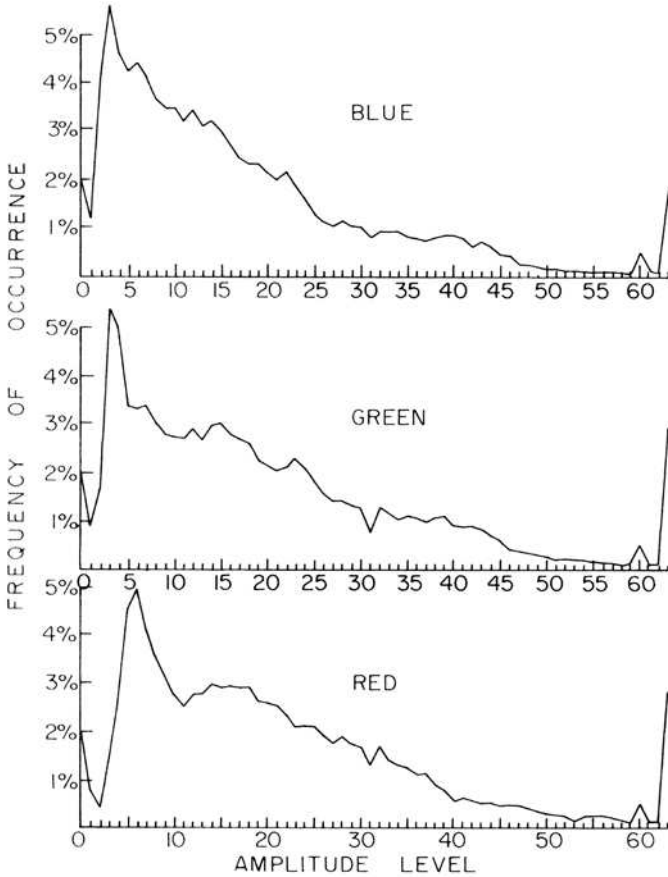


**FIGURE 6.4-1.** Histograms of the red, green and blue components of the `smpte_girl_linear` color image.

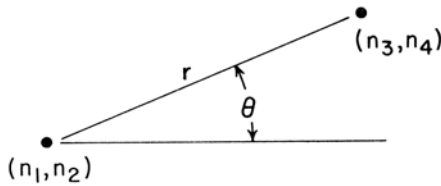


FIGURE 6.4-2. Geometric relationships of pixel pairs.

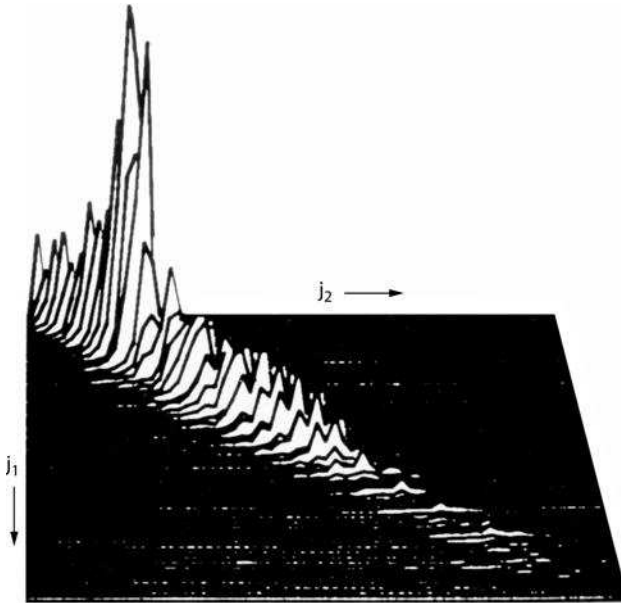


FIGURE 6.4-3. Second-order histogram of the `smpte_girl_luminance` monochrome image;  $r = 1$  and  $\theta = 0$ .

### 6.5. LINEAR OPERATOR STATISTICAL REPRESENTATION

If an input image array is considered to be a sample of a random process with known first and second-order moments, the first- and second-order moments of the output image array can be determined for a given linear transformation. First, the mean of the output image array is

$$E\{P(m_1, m_2)\} = E\left\{ \sum_{n_1=1}^{N_1} \sum_{n_2=1}^{N_2} F(n_1, n_2) O(n_1, n_2; m_1, m_2) \right\}. \quad (6.5-1a)$$

Because the expectation operator is linear,

$$E\{P(m_1, m_2)\} = \sum_{n_1=1}^{N_1} \sum_{n_2=1}^{N_2} E\{F(n_1, n_2)\}O(n_1, n_2; m_1, m_2). \quad (6.5-1b)$$

The correlation function of the output image array is

$$R_P(m_1, m_2; m_3, m_4) = E\{P(m_1, m_2)P^*(m_3, m_4)\} \quad (6.5-2a)$$

or in expanded form

$$R_P(m_1, m_2; m_3, m_4) = E\left\{ \left[ \sum_{n_1=1}^{N_1} \sum_{n_2=1}^{N_2} F(n_1, n_2)O(n_1, n_2; m_1, m_2) \right] \times \left[ \sum_{n_3=1}^{N_1} \sum_{n_4=1}^{N_2} F^*(n_3, n_4)O^*(n_3, n_4; m_3, m_4) \right] \right\}. \quad (6.5-2b)$$

After multiplication of the series, and performance of the expectation operation, one obtains

$$R_P(m_1, m_2; m_3, m_4) = \sum_{n_1=1}^{N_1} \sum_{n_2=1}^{N_2} \sum_{n_3=1}^{N_1} \sum_{n_4=1}^{N_2} R_F(n_1, n_2, n_3, n_4)O(n_1, n_2; m_1, m_2) \times O^*(n_3, n_4; m_3, m_4) \quad (6.5-3)$$

where  $R_F(n_1, n_2; n_3, n_4)$  represents the correlation function of the input image array. In a similar manner, the covariance function of the output image is found to be

$$K_P(m_1, m_2; m_3, m_4) = \sum_{n_1=1}^{N_1} \sum_{n_2=1}^{N_2} \sum_{n_3=1}^{N_1} \sum_{n_4=1}^{N_2} K_F(n_1, n_2, n_3, n_4)O(n_1, n_2; m_1, m_2) \times O^*(n_3, n_4; m_3, m_4). \quad (6.5-4)$$

If the input and output image arrays are expressed in vector form, the formulation of the moments of the transformed image becomes much more compact. The mean of the output vector  $\mathbf{p}$  is

$$\eta_{\mathbf{p}} = E\{\mathbf{p}\} = E\{\mathbf{T}\mathbf{f}\} = \mathbf{T}E\{\mathbf{f}\} = \mathbf{T}\eta_{\mathbf{f}} \quad (6.5-5)$$

and the correlation matrix of  $\mathbf{p}$  is

$$\mathbf{R}_p = E\{\mathbf{p}\mathbf{p}^{*T}\} = E\{\mathbf{T}\mathbf{f}\mathbf{f}^{*T}\mathbf{T}^{*T}\} = \mathbf{T}\mathbf{R}_f\mathbf{T}^{*T}. \quad (6.5-6)$$

Finally, the covariance matrix of  $\mathbf{p}$  is

$$\mathbf{K}_p = \mathbf{T}\mathbf{K}_f\mathbf{T}^{*T}. \quad (6.5-7)$$

Applications of this theory to superposition and unitary transform operators are given in following chapters.

A special case of the general linear transformation  $\mathbf{p} = \mathbf{T}\mathbf{f}$ , of fundamental importance, occurs when the covariance matrix of Eq. 6.5-7 assumes the form

$$\mathbf{K}_p = \mathbf{T}\mathbf{K}_f\mathbf{T}^{*T} = \Lambda \quad (6.5-8)$$

where  $\Lambda$  is a diagonal matrix. In this case, the elements of  $\mathbf{p}$  are uncorrelated. From Appendix A1.2, it is found that the transformation  $\mathbf{T}$ , which produces the diagonal matrix  $\Lambda$ , has rows that are eigenvectors of  $\mathbf{K}_f$ . The diagonal elements of  $\Lambda$  are the corresponding eigenvalues of  $\mathbf{K}_f$ . This operation is called both a *matrix diagonalization* and a *principal components transformation*.

## 6.6. REGION-OF-INTEREST EXERCISES

E6.1 Develop a program that forms the complement of an unsigned integer, 8-bit, 512 x 512, monochrome, image under region-of-interest control (8,9).

Case 1: Full source and destination ROIs.

Case 2: Rectangular source ROI, upper left corner at (50, 100), lower right corner at (300, 350) and full destination ROI.

Case 3: Full source ROI and rectangular destination ROI, upper left corner at (150, 200), lower right corner at (400, 450).

Case 4: Rectangular source ROI, upper left corner at (50, 100), lower right corner at (300, 350) and rectangular destination ROI, upper left corner at (150, 200), lower right corner at (400, 450).

Steps:

- (a) Display the source monochrome image.
- (b) Create source and destination ROIs.
- (c) Complement the source image into the destination image.
- (d) Display the destination image.
- (e) Create a constant destination image of value 150.
- (f) Bind the source ROI to the source image.

- (g) Complement the source image into the destination image.
- (h) Display the destination image.
- (i) Create a constant destination image of value 150.
- (j) Bind the destination ROI to the destination image.
- (k) Complement the source image into the destination image.
- (l) Display the destination image.
- (m) Create a constant destination image of value 150.
- (n) Bind the source ROI to the source image and bind the destination ROI to the destination image.
- (o) Complement the source image into the destination image.
- (p) Display the destination image.

The PIKS API executable `example_complement_monochrome_roi` performs this exercise.

## REFERENCES

1. W. K. Pratt, "Vector Formulation of Two Dimensional Signal Processing Operations," *Computer Graphics and Image Processing*, **4**, 1, March 1975, 1–24.
2. J. O. Eklundh, "A Fast Computer Method for Matrix Transposing," *IEEE Trans. Computers*, **C-21**, 7, July 1972, 801–803.
3. R. E. Twogood and M. P. Ekstrom, "An Extension of Eklundh's Matrix Transposition Algorithm and Its Applications in Digital Image Processing," *IEEE Trans. Computers*, **C-25**, 9, September 1976, 950–952.
4. A. Papoulis, *Probability, Random Variables, and Stochastic Processes, Third Edition*, McGraw-Hill, New York, 1991.
5. U. Grenander and G. Szego, *Toeplitz Forms and Their Applications*, University of California Press, Berkeley, CA, 1958.
6. L. D. Davisson, private communication.
7. M. N. Huhns, "Optimum Restoration of Quantized Correlated Signals," USCPI Report 600, University of Southern California, Image Processing Institute, Los Angeles, August 1975.
8. W. K. Pratt, *Digital Image Processing, Fourth Edition*, Chapter 20, Wiley-Interscience, Hoboken, NJ, 2007.
9. See website at [pixelsoft.com](http://pixelsoft.com) for soft copy of Reference 8.

---

# 7

---

## SUPERPOSITION AND CONVOLUTION

In Chapter 1, superposition and convolution operations were derived for continuous two-dimensional image fields. This chapter provides a derivation of these operations for discrete two-dimensional images. Three types of superposition and convolution operators are defined: finite area, sampled image and circulant area. The finite-area operator is a linear filtering process performed on a discrete image data array. The sampled image operator is a discrete model of a continuous two-dimensional image filtering process. The circulant area operator provides a basis for a computationally efficient means of performing either finite-area or sampled image superposition and convolution.

### 7.1. FINITE-AREA SUPERPOSITION AND CONVOLUTION

Mathematical expressions for finite-area superposition and convolution are developed below for both series and vector-space formulations.

#### 7.1.1. Finite-Area Superposition and Convolution: Series Formulation

Let  $F(n_1, n_2)$  denote an image array for  $n_1, n_2 = 1, 2, \dots, N$ . For notational simplicity, all arrays in this chapter are assumed square. In correspondence with Eq. 1.2-6, the image array can be represented at some point  $(m_1, m_2)$  as a sum of amplitude weighted Dirac delta functions by the discrete sifting summation

$$F(m_1, m_2) = \sum_{n_1} \sum_{n_2} F(n_1, n_2) \delta(m_1 - n_1 + 1, m_2 - n_2 + 1). \tag{7.1-1}$$

The term

$$\delta(m_1 - n_1 + 1, m_2 - n_2 + 1) = \begin{cases} 1 & \text{if } m_1 = n_1 \text{ and } m_2 = n_2 & (7.1-2a) \\ 0 & \text{otherwise} & (7.1-2b) \end{cases}$$

is a discrete delta function. Now consider a spatial linear operator  $O\{\cdot\}$  that produces an output image array

$$Q(m_1, m_2) = O\{F(m_1, m_2)\} \tag{7.1-3}$$

by a linear spatial combination of pixels within a neighborhood of  $(m_1, m_2)$ . From the sifting summation of Eq. 7.1-1,

$$Q(m_1, m_2) = O\left\{ \sum_{n_1} \sum_{n_2} F(n_1, n_2) \delta(m_1 - n_1 + 1, m_2 - n_2 + 1) \right\} \tag{7.1-4a}$$

or

$$Q(m_1, m_2) = \sum_{n_1} \sum_{n_2} F(n_1, n_2) O\{\delta(m_1 - n_1 + 1, m_2 - n_2 + 1)\} \tag{7.1-4b}$$

recognizing that  $O\{\cdot\}$  is a linear operator and that  $F(n_1, n_2)$  in the summation of Eq. 7.1-4a is a constant in the sense that it does not depend on  $(m_1, m_2)$ . The term  $O\{\delta(t_1, t_2)\}$  for  $t_i = m_i - n_i + 1$  is the response at output coordinate  $(m_1, m_2)$  to a unit amplitude input at coordinate  $(n_1, n_2)$ . It is called the *impulse response function array* of the linear operator and is written as

$$\delta(m_1 - n_1 + 1, m_2 - n_2 + 1; m_1, m_2) = O\{\delta(t_1, t_2)\} \quad \text{for } 1 \leq t_1, t_2 \leq L \tag{7.1-5}$$

and is zero otherwise.

In Eq. 7.1-5, it is assumed that the impulse response array is of limited spatial extent. This means that an output image pixel is influenced by input image pixels only within some finite area  $L \times L$  neighborhood of the corresponding output image pixel. The output coordinates  $(m_1, m_2)$  in Eq. 7.1-5 following the semicolon indicate that in the general case, called *finite area superposition*, the impulse response array can change form for each point  $(m_1, m_2)$  in the processed array  $Q(m_1, m_2)$ .

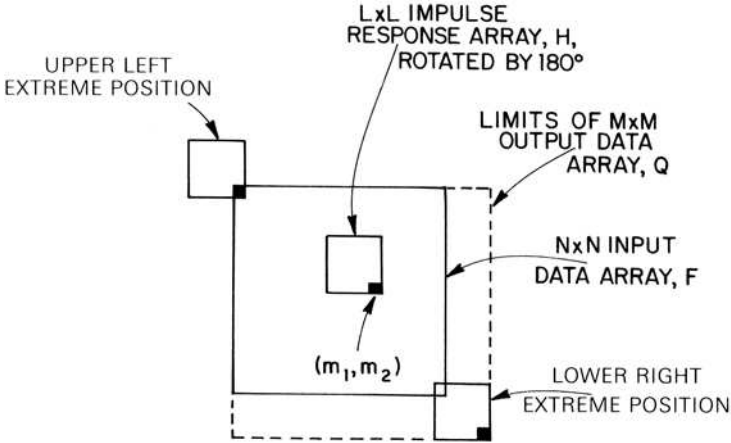


**FIGURE 7.1-1.** Relationships between input data, output data and impulse response arrays for finite-area superposition; upper left corner justified array definition.

Following this nomenclature, the finite area superposition operation is defined as

$$Q(m_1, m_2) = \sum_{n_1} \sum_{n_2} F(n_1, n_2)H(m_1 - n_1 + 1, m_2 - n_2 + 1; m_1, m_2). \quad (7.1-6)$$

The limits of the summation are

$$\text{MAX}\{1, m_i - L + 1\} \leq n_i \leq \text{MIN}\{N, m_i\} \quad (7.1-7)$$

where  $\text{MAX}\{a, b\}$  and  $\text{MIN}\{a, b\}$  denote the maximum and minimum of the arguments, respectively. Examination of the indices of the impulse response array at its extreme positions indicates that  $M = N + L - 1$ , and hence, the processed output array  $Q$  is of larger dimension than the input array  $F$ . Figure 7.1-1 illustrates the geometry of finite-area superposition. If the impulse response array  $H$  is spatially invariant, the superposition operation reduces to the convolution operation.

$$Q(m_1, m_2) = \sum_{n_1} \sum_{n_2} F(n_1, n_2)H(m_1 - n_1 + 1, m_2 - n_2 + 1). \quad (7.1-8)$$

Figure 7.1-2 presents a graphical example of convolution with a  $3 \times 3$  impulse response array.

Equation 7.1-6 expresses the finite-area superposition operation in *left-justified form* in which the input and output arrays are aligned at their upper left corners. It is often notationally convenient to utilize a definition in which the output array is



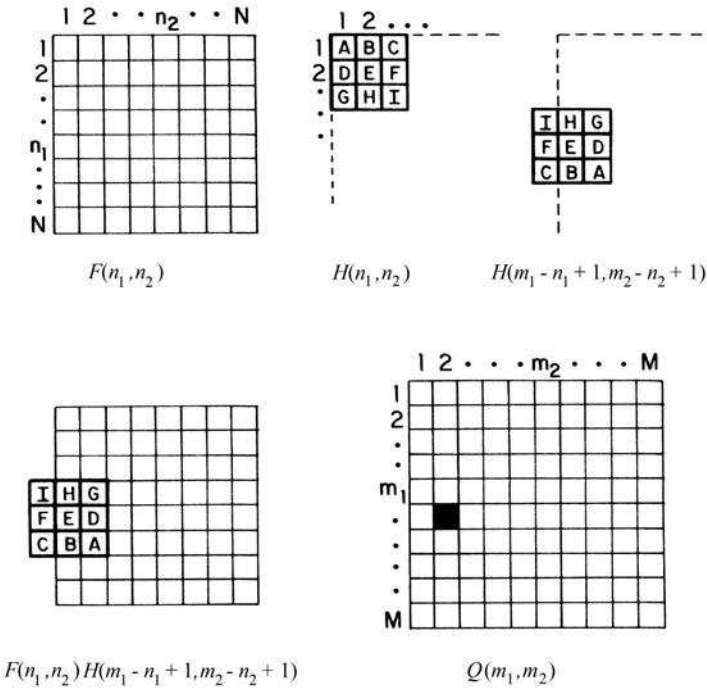


**FIGURE 7.1-2.** Graphical example of finite-area convolution with a 3 × 3 impulse response array; upper left corner justified array definition.

centered with respect to the input array. This definition of *centered superposition* is given by

$$Q_c(j_1, j_2) = \sum_{n_1} \sum_{n_2} F(n_1, n_2)H(j_1 - n_1 + L_c, j_2 - n_2 + L_c; j_1, j_2) \quad (7.1-9)$$

where  $-(L-3)/2 \leq j_i \leq N + (L-1)/2$  and  $L_c = (L+1)/2$ . The limits of the summation are

$$\text{MAX}\{1, j_i - (L-1)/2\} \leq n_i \leq \text{MIN}\{N, j_i + (L-1)/2\}. \quad (7.1-10)$$

Figure 7.1-3 shows the spatial relationships between the arrays  $F$ ,  $H$  and  $Q_c$  for centered superposition with a 5 × 5 impulse response array.

In digital computers and digital image processors, it is often convenient to restrict the input and output arrays to be of the same dimension. For such systems, Eq. 7.1-9 needs only to be evaluated over the range  $1 \leq j_i \leq N$ . When the impulse response

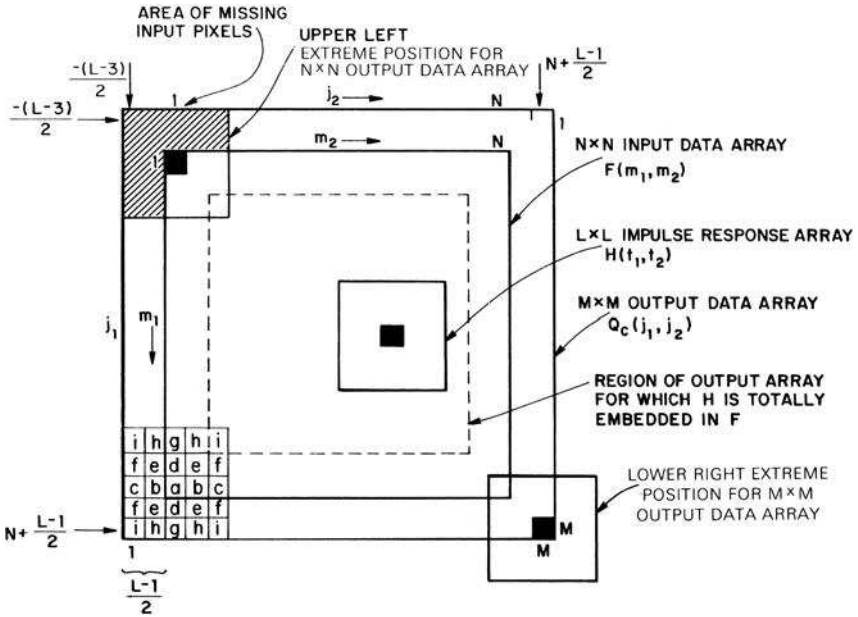


**FIGURE 7.1-3.** Relationships between input data, output data and impulse response arrays for finite-area superposition; centered array definition.

array is located on the border of the input array, the product computation of Eq. 7.1-9 does not involve all of the elements of the impulse response array. This situation is illustrated in Figure 7.1-3, where the impulse response array is in the upper left corner of the input array. The input array pixels “missing” from the computation are shown crosshatched in Figure 7.1-3. Several methods have been proposed to deal with this border effect. One method is to perform the computation of all of the impulse response elements as if the missing pixels are of some constant value. If the constant value is zero, the result is called *centered, zero padded superposition*. A variant of this method is to regard the missing pixels to be mirror images of the input array pixels, as indicated in the lower left corner of Figure 7.1-3. In this case, the *centered, reflected boundary superposition* definition becomes

$$Q_c(j_1, j_2) = \sum_{n_1} \sum_{n_2} F(n'_1, n'_2) H(j_1 - n_1 + L_c, j_2 - n_2 + L_c; j_1, j_2) \quad (7.1-11)$$

where the summation limits are

$$j_i - (L - 1)/2 \leq n_i \leq j_i + (L - 1)/2 \quad (7.1-12)$$

and

$$n'_i = \begin{cases} 2 - n_i & \text{for } n_i \leq 0 & (7.1-13a) \\ n_i & \text{for } 1 \leq n_i \leq N & (7.1-13b) \\ 2N - n_i & \text{for } n_i > N. & (7.1-13c) \end{cases}$$

In many implementations, the superposition computation is limited to the range  $(L + 1)/2 \leq j_i \leq N - (L - 1)/2$ , and the border elements of the  $N \times N$  array  $Q_c$  are set to zero. In effect, the superposition operation is computed only when the impulse response array is fully embedded within the confines of the input array. This region is described by the dashed lines in Figure 7.1-3. This form of superposition is called *centered, zero boundary superposition*.

If the impulse response array  $H$  is spatially invariant, the centered definition for convolution becomes

$$Q_c(j_1, j_2) = \sum_{n_1} \sum_{n_2} F(n_1, n_2) H(j_1 - n_1 + L_c, j_2 - n_2 + L_c). \quad (7.1-14)$$

The  $3 \times 3$  impulse response array, which is called a *small generating kernel* (SGK), is fundamental to many image processing algorithms (1). When the SGK is totally embedded within the input data array, the general term of the centered convolution operation can be expressed explicitly as

$$\begin{aligned} Q_c(j_1, j_2) = & H(3, 3)F(j_1 - 1, j_2 - 1) + H(3, 2)F(j_1 - 1, j_2) + H(3, 1)F(j_1 - 1, j_2 + 1) \\ & + H(2, 3)F(j_1, j_2 - 1) + H(2, 2)F(j_1, j_2) + H(2, 1)F(j_1, j_2 + 1) \\ & + H(1, 3)F(j_1 + 1, j_2 - 1) + H(1, 2)F(j_1 + 1, j_2) + H(1, 1)F(j_1 + 1, j_2 + 1) \end{aligned} \quad (7.1-15)$$

for  $2 \leq j_i \leq N - 1$ . Pratt(4Ed., 241-243) shows that convolution with arbitrary-size impulse response arrays can be achieved by sequential convolutions with SGKs.

The four different forms of superposition and convolution are each useful in various image processing applications. The upper left corner-justified definition is appropriate for computing the correlation function between two images. The centered, zero padded and centered, reflected boundary definitions are generally employed for image enhancement filtering. Finally, the centered, zero boundary definition is used for the computation of spatial derivatives in edge detection. In this application, the derivatives are not meaningful in the border region.

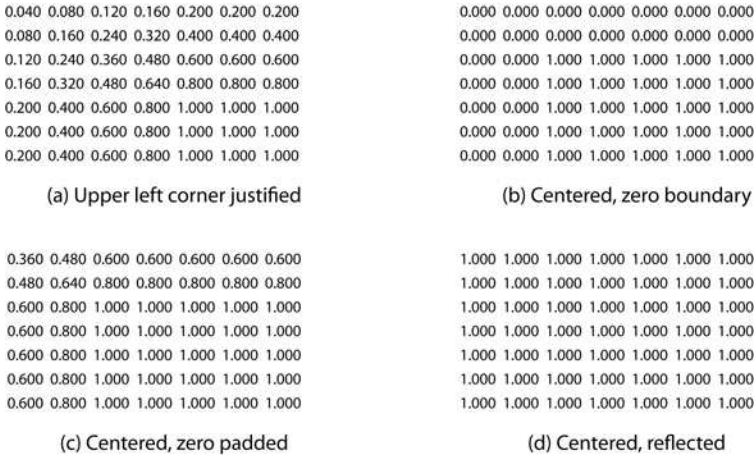


**FIGURE 7.1-4** Finite-area convolution boundary conditions, upper left corner of convolved image.

Figure 7.1-4 shows computer printouts of pixels in the upper left corner of a convolved image for the four types of convolution boundary conditions. In this example, the source image is constant of maximum value 1.0. The convolution impulse response array is a  $5 \times 5$  uniform array.

**7.1.2. Finite-Area Superposition and Convolution: Vector-Space Formulation**

If the arrays  $F$  and  $Q$  of Eq. 7.1-6 are represented in vector form by the  $N^2 \times 1$  vector  $\mathbf{f}$  and the  $M^2 \times 1$  vector  $\mathbf{q}$ , respectively, the finite-area superposition operation can be written as (2)

$$\mathbf{q} = \mathbf{D}\mathbf{f} \tag{7.1-16}$$

where  $\mathbf{D}$  is a  $M^2 \times N^2$  matrix containing the elements of the impulse response. It is convenient to partition the superposition operator matrix  $\mathbf{D}$  into submatrices of dimension  $M \times N$ . Observing the summation limits of Eq. 7.1-7, it is seen that

$$\mathbf{D} = \begin{bmatrix} \mathbf{D}_{1,1} & \mathbf{0} & \dots & \mathbf{0} \\ \mathbf{D}_{2,1} & \mathbf{D}_{2,2} & & \vdots \\ \vdots & \vdots & & \mathbf{0} \\ \mathbf{D}_{L,1} & \mathbf{D}_{L,2} & & \mathbf{D}_{M-L+1,N} \\ \mathbf{0} & \mathbf{D}_{L+1,1} & & \vdots \\ \vdots & \vdots & & \vdots \\ \mathbf{0} & \dots & \mathbf{0} & \mathbf{D}_{M,N} \end{bmatrix} \tag{7.1-17}$$

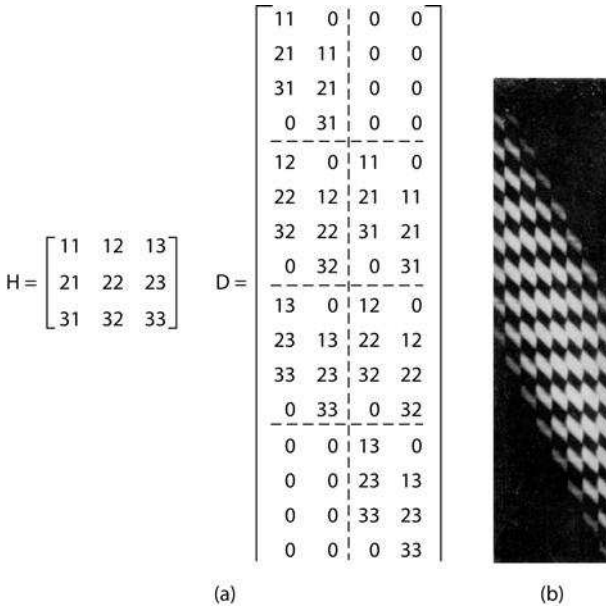


**FIGURE 7.1-5** Finite-area convolution operators: (a) general impulse array,  $M = 4, N = 2, L = 3$ ; (b) Gaussian-shaped impulse array,  $M = 16, N = 8, L = 9$ .

The general nonzero term of  $\mathbf{D}$  is then given by

$$D_{m_2, n_2}(m_1, n_1) = H(m_1 - n_1 + 1, m_2 - n_2 + 1; m_1, m_2) \tag{7.1-18}$$

Thus, it is observed that  $\mathbf{D}$  is highly structured and quite sparse, with the center band of submatrices containing stripes of zero-valued elements.

If the impulse response is position invariant, the structure of  $\mathbf{D}$  does not depend explicitly on the output array coordinate  $(m_1, m_2)$ . Also,

$$\mathbf{D}_{m_2, n_2} = \mathbf{D}_{m_2 + 1, n_2 + 1} \tag{7.1-19}$$

As a result, the columns of  $\mathbf{D}$  are shifted versions of the first column. Under these conditions, the finite-area superposition operator is known as the *finite-area convolution operator*. Figure 7.1-5a contains a notational example of the finite-area convolution operator for a  $2 \times 2$  ( $N = 2$ ) input data array, a  $4 \times 4$  ( $M = 4$ ) output data array and a  $3 \times 3$  ( $L = 3$ ) impulse response array. The integer pairs  $(i, j)$  at each element of  $\mathbf{D}$  represent the element  $(i, j)$  of  $H(i, j)$ . The basic structure of  $\mathbf{D}$  can be seen more clearly in the larger matrix depicted in Figure 7.1-5b. In this example,  $M = 16, N = 8, L = 9$ , and the impulse response has a symmetrical Gaussian shape. Note that  $\mathbf{D}$  is a  $256 \times 64$  matrix in this example.

Following the same technique as that leading to Eq. 6.2-7, the matrix form of the superposition operator may be written as

$$\mathbf{Q} = \sum_{m=1}^M \sum_{n=1}^N \mathbf{D}_{m,n} \mathbf{F} \mathbf{v}_n \mathbf{u}_m^T \tag{7.1-20}$$

If the impulse response is spatially invariant and is of separable form such that

$$\mathbf{H} = \mathbf{h}_C \mathbf{h}_R^T \tag{7.1-21}$$

where  $\mathbf{h}_R$  and  $\mathbf{h}_C$  are column vectors representing row and column impulse responses, respectively, then

$$\mathbf{D} = \mathbf{D}_C \otimes \mathbf{D}_R \tag{7.1-22}$$

The matrices  $\mathbf{D}_R$  and  $\mathbf{D}_C$  are  $M \times N$  matrices of the form

$$\mathbf{D}_R = \begin{bmatrix} h_R(1) & 0 & \dots & 0 \\ h_R(2) & h_R(1) & & \vdots \\ h_R(3) & h_R(2) & \dots & 0 \\ \vdots & & & h_R(1) \\ h_R(L) & & & \vdots \\ 0 & & & \vdots \\ \vdots & & & \vdots \\ 0 & \dots & 0 & h_R(L) \end{bmatrix} \tag{7.1-23}$$

The two-dimensional convolution operation may then be computed by sequential row and column one-dimensional convolutions. Thus,

$$\mathbf{Q} = \mathbf{D}_C \mathbf{F} \mathbf{D}_R^T \tag{7.1-24}$$

In vector form, the general finite-area superposition or convolution operator requires  $N^2 L^2$  operations if the zero-valued multiplications of  $\mathbf{D}$  are avoided. The separable operator of Eq. 7.1-24 can be computed with only  $NL(M + N)$  operations.

7.2. SAMPLED IMAGE SUPERPOSITION AND CONVOLUTION

Many applications in image processing require a discretization of the superposition integral relating the input and output continuous fields of a linear system. For example, image blurring by an optical system, sampling with a finite-area aperture or imaging through atmospheric turbulence, may be modeled by the superposition integral equation

$$\tilde{G}(x, y) = \int_{-\infty}^{\infty} \int_{-\infty}^{\infty} \tilde{F}(\alpha, \beta) \tilde{J}(x, y; \alpha, \beta) d\alpha d\beta \tag{7.2-1a}$$

where  $\tilde{F}(x, y)$  and  $\tilde{G}(x, y)$  denote the input and output fields of a linear system, respectively, and the kernel  $\tilde{J}(x, y; \alpha, \beta)$  represents the impulse response of the linear system model. In this chapter, a tilde over a variable indicates that the spatial indices of the variable are bipolar; that is, they range from negative to positive spatial limits. In this formulation, the impulse response may change form as a function of its four indices: the input and output coordinates. If the linear system is space invariant, the output image field may be described by the convolution integral

$$\tilde{G}(x, y) = \int_{-\infty}^{\infty} \int_{-\infty}^{\infty} \tilde{F}(\alpha, \beta) \tilde{J}(x - \alpha, y - \beta) d\alpha d\beta. \tag{7.2-1b}$$

For discrete processing, physical image sampling will be performed on the output image field. Numerical representation of the integral must also be performed in order to relate the physical samples of the output field to points on the input field.

Numerical representation of a superposition or convolution integral is an important topic because improper representations may lead to gross modeling errors or numerical instability in an image processing application. Also, selection of a numerical representation algorithm usually has a significant impact on digital processing computational requirements.

As a first step in the discretization of the superposition integral, the output image field is physically sampled by a  $(2J + 1) \times (2J + 1)$  array of Dirac pulses at a resolution  $\Delta S$  to obtain an array

$$\tilde{G}(j_1 \Delta S, j_2 \Delta S) = \int_{-\infty}^{\infty} \int_{-\infty}^{\infty} \tilde{F}(\alpha, \beta) \tilde{J}(j_1 \Delta S, j_2 \Delta S; \alpha, \beta) d\alpha d\beta \tag{7.2-2}$$

where  $-J \leq j_i \leq J$ . Equal horizontal and vertical spacing of sample pulses is assumed for notational simplicity. It should be noted that the physical sampling is performed on the observed image spatial variables  $(x, y)$ ; physical sampling does not affect the dummy variables of integration  $(\alpha, \beta)$ .

Next, the impulse response must be truncated to some spatial bounds. Thus, let

$$\tilde{J}(x, y; \alpha, \beta) = 0 \tag{7.2-3}$$

for  $|x| > T$  and  $|y| > T$ . Then,

$$\tilde{G}(j_1 \Delta S, j_1 \Delta S) = \int_{j_1 \Delta S - T}^{j_1 \Delta S + T} \int_{j_2 \Delta S - T}^{j_2 \Delta S + T} \tilde{F}(\alpha, \beta) \tilde{J}(j_1 \Delta S, j_2 \Delta S; \alpha, \beta) d\alpha d\beta. \quad (7.2-4)$$

Truncation of the impulse response is equivalent to multiplying the impulse response by a window function  $V(x, y)$ , which is unity for  $|x| < T$  and  $|y| < T$  and zero elsewhere. By the Fourier convolution theorem, the Fourier spectrum of  $G(x, y)$  is equivalently convolved with the Fourier transform of  $V(x, y)$ , which is a two-dimensional sinc function. This distortion of the Fourier spectrum of  $G(x, y)$  results in the introduction of high-spatial-frequency artifacts (a Gibbs phenomenon) at spatial frequency multiples of  $2\pi/T$ . Truncation distortion can be reduced by using a shaped window, such as the Bartlett, Blackman, Hamming or Hanning window (3), as specified in Section 9.4.2, which smooth the sharp cutoff effects of a rectangular window. This step is especially important for image restoration modeling because ill-conditioning of the superposition operator may lead to severe amplification of the truncation artifacts.

In the next step of the discrete representation, the continuous ideal image array  $\tilde{F}(\alpha, \beta)$  is represented by mesh points on a rectangular grid of resolution  $\Delta I$  and dimension  $(2K + 1) \times (2K + 1)$ . This is not a physical sampling process, but merely an abstract numerical representation whose general term is described by

$$\tilde{F}(k_1 \Delta I, k_2 \Delta I) = \tilde{F}(\alpha, \beta) \delta(\alpha - k_1 \Delta I, \alpha - k_2 \Delta I) \quad (7.2-5)$$

where  $K_L \leq k_i \leq K_U$ , with  $K_U$  and  $K_L$  denoting the upper and lower index limits.

If the ultimate objective is to estimate the continuous ideal image field by processing the physical observation samples, the mesh spacing  $\Delta I$  should be fine enough to satisfy the Nyquist criterion for the ideal image. That is, if the spectrum of the ideal image is band limited and the limits are known, the mesh spacing should be set at the corresponding Nyquist spacing. Ideally, this will permit perfect interpolation of the estimated points  $\tilde{F}(k_1 \Delta I, k_2 \Delta I)$  to reconstruct  $\tilde{F}(x, y)$ .

The continuous integration of Eq. 7.2-4 can now be approximated by a discrete summation by employing a quadrature integration formula (4). The physical image samples may then be expressed as

$$\tilde{G}(j_1 \Delta S, j_2 \Delta S) = \sum_{k_1 = K_L}^{K_U} \sum_{k_2 = K_L}^{K_U} \tilde{F}(k_1 \Delta I, k_2 \Delta I) \tilde{W}(k_1, k_2) \tilde{J}(j_1 \Delta S, j_2 \Delta S; k_1 \Delta I, k_2 \Delta I) \quad (7.2-6)$$

where  $\tilde{W}(k_1, k_2)$  is a weighting coefficient for the particular quadrature formula employed. Usually, a rectangular quadrature formula is used, and the weighting coefficients are unity. In any case, it is notationally convenient to lump the weighting coefficient and the impulse response function together so that

$$\tilde{H}(j_1 \Delta S, j_2 \Delta S; k_1 \Delta I, k_2 \Delta I) = \tilde{W}(k_1, k_2) \tilde{J}(j_1 \Delta S, j_2 \Delta S; k_1 \Delta I, k_2 \Delta I). \quad (7.2-7)$$



Then,

$$\tilde{G}(j_1 \Delta S, j_2 \Delta S) = \sum_{k_1 = K_L}^{K_U} \sum_{k_2 = K_L}^{K_U} \tilde{F}(k_1 \Delta I, k_2 \Delta I) \tilde{H}(j_1 \Delta S, j_2 \Delta S; k_1 \Delta I, k_2 \Delta I) \dots \tag{7.2-8}$$

Again, it should be noted that  $\tilde{H}$  is not spatially discretized; the function is simply evaluated at its appropriate spatial argument. The limits of summation of Eq. 7.2-8 are

$$K_L = \left[ j_i \frac{\Delta S}{\Delta I} - \frac{T}{\Delta I} \right]_N \quad K_U = \left[ j_i \frac{\Delta S}{\Delta I} + \frac{T}{\Delta I} \right]_N \tag{7.2-9}$$

where  $[\cdot]_N$  denotes the nearest integer value of the argument.

Figure 7.2-1 provides an example relating actual physical sample values  $\tilde{G}(j_1 \Delta S, j_2 \Delta S)$  to mesh points  $\tilde{F}(k_1 \Delta I, k_2 \Delta I)$  on the ideal image field. In this example, the mesh spacing is twice as large as the physical sample spacing. In the figure, the values of the impulse response function that are utilized in the summation of Eq. 7.2-8 are represented as dots.

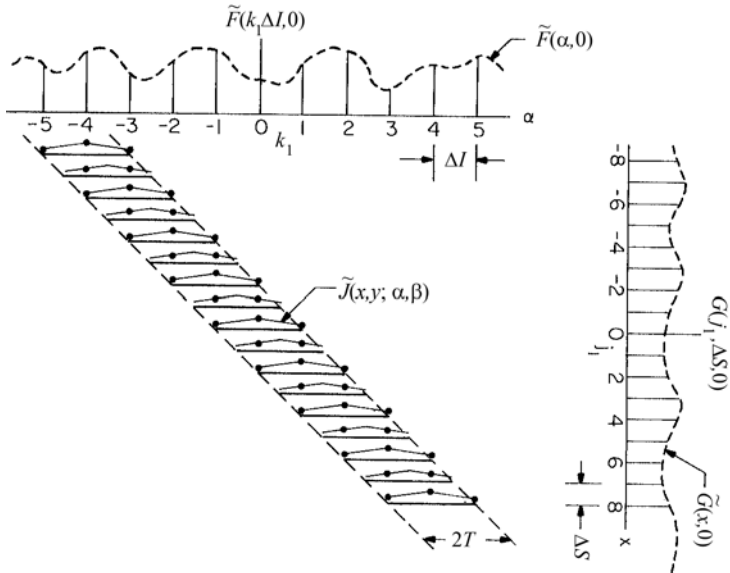


**FIGURE 7.2-1.** Relationship of physical image samples to mesh points on an ideal image field for numerical representation of a superposition integral.

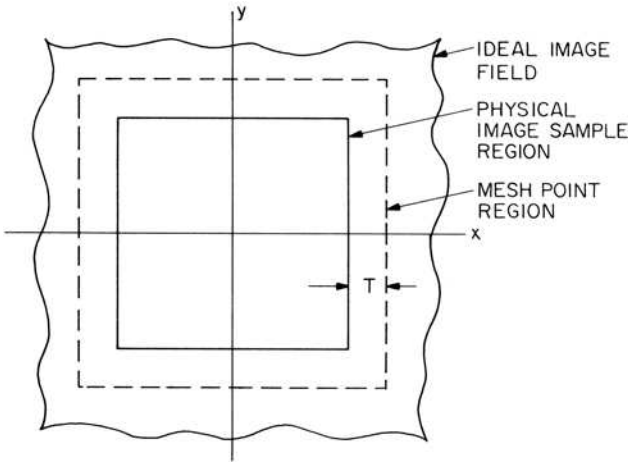


**FIGURE 7.2-2.** Relationship between regions of physical samples and mesh points for numerical representation of a superposition integral.

An important observation should be made about the discrete model of Eq. 7.2-8 for a sampled superposition integral; the physical area of the ideal image field  $\tilde{F}(x, y)$  containing mesh points contributing to physical image samples is larger than the sample image  $\tilde{G}(j_1 \Delta S, j_2 \Delta S)$  regardless of the relative number of physical samples and mesh points. The dimensions of the two image fields, as shown in Figure 7.2-2, are related by

$$J \Delta S + T = K \Delta I \tag{7.2-10}$$

to within an accuracy of one sample spacing.

At this point in the discussion, a discrete and finite model for the sampled superposition integral has been obtained in which the physical samples  $\tilde{G}(j_1 \Delta S, j_2 \Delta S)$  are related to points on an ideal image field  $\tilde{F}(k_1 \Delta I, k_2 \Delta I)$  by a discrete mathematical superposition operation. This discrete superposition is an approximation to continuous superposition because of the truncation of the impulse response function  $\tilde{J}(x, y; \alpha, \beta)$  and quadrature integration. The truncation approximation can, of course, be made arbitrarily small by extending the bounds of definition of the impulse response, but at the expense of large dimensionality. Also, the quadrature integration approximation can be improved by use of complicated formulas of quadrature, but again the price paid is computational complexity. It should be noted, however, that discrete superposition is a perfect approximation to continuous superposition if the spatial functions of Eq. 7.2-1 are all bandlimited and the physical sampling and numerical representation periods are selected to be the corresponding Nyquist period (5).

It is often convenient to reformulate Eq. 7.2-8 into vector-space form. Toward this end, the arrays  $\tilde{G}$  and  $\tilde{F}$  are reindexed to  $M \times M$  and  $N \times N$  arrays, respectively, such that all indices are positive. Let

$$F(n_1 \Delta I, n_2 \Delta I) = \tilde{F}(k_1 \Delta I, k_2 \Delta I) \tag{7.2-11a}$$

where  $n_i = k_i + K + 1$  and let

$$G(m_1 \Delta S, m_2 \Delta S) = G(j_1 \Delta S, j_2 \Delta S) \tag{7.2-11b}$$

where  $m_i = j_i + J + 1$ . Also, let the impulse response be redefined such that

$$H(m_1 \Delta S, m_2 \Delta S; n_1 \Delta I, n_2 \Delta I) = \tilde{H}(j_1 \Delta S, j_2 \Delta S; k_1 \Delta I, k_2 \Delta I). \tag{7.2-11c}$$

Figure 7.2-3 illustrates the geometrical relationship between these functions.

The discrete superposition relationship of Eq. 7.2-8 for the shifted arrays becomes

$$G(m_1 \Delta S, m_2 \Delta S) = \sum_{n_1 = N_{1L}}^{N_{1U}} \sum_{n_2 = N_{2L}}^{N_{2U}} F(n_1 \Delta I, n_2 \Delta I) H(m_1 \Delta S, m_2 \Delta S; n_1 \Delta I, n_2 \Delta I) \tag{7.2-12}$$

for  $(1 \leq m_i \leq M)$  where

$$N_{iL} = \left\lceil m_i \frac{\Delta S}{\Delta I} \right\rceil_N \qquad N_{iU} = \left\lfloor m_i \frac{\Delta S}{\Delta I} + \frac{2T}{\Delta I} \right\rfloor_N$$

Following the techniques outlined in Chapter 6, the vectors  $\mathbf{g}$  and  $\mathbf{f}$  may be formed by column scanning the matrices  $\mathbf{G}$  and  $\mathbf{F}$  to obtain

$$\mathbf{g} = \mathbf{B}\mathbf{f} \tag{7.2-13}$$

where  $\mathbf{B}$  is a  $M^2 \times N^2$  matrix of the form

$$\mathbf{B} = \begin{bmatrix} \mathbf{B}_{1,1} & \mathbf{B}_{1,2} & \cdots & \mathbf{B}_{(1,L)} & \mathbf{0} & \cdots & \mathbf{0} \\ \mathbf{0} & \mathbf{B}_{2,2} & & \vdots & & & \vdots \\ \vdots & & & \vdots & & & \mathbf{0} \\ \mathbf{0} & \cdots & \mathbf{0} & \mathbf{B}_{M,N-L+1} & \cdots & \mathbf{B}_{M,N} \end{bmatrix} \tag{7.2-14}$$

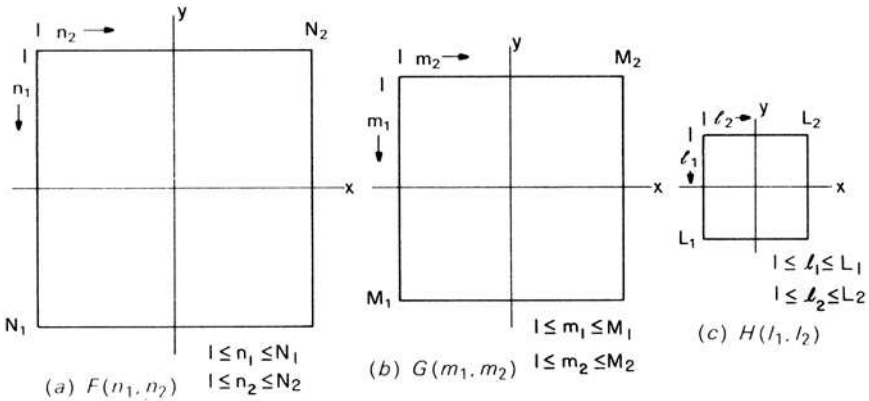


FIGURE 7.2-3. Sampled image arrays.

The general term of **B** is defined as

$$B_{m_2, n_2}(m_1, n_1) = H(m_1 \Delta S, m_2 \Delta S; n_1 \Delta I, n_2 \Delta I) \tag{7.2-15}$$

for  $1 \leq m_i \leq M$  and  $m_i \leq n_i \leq m_i + L - 1$  where  $L = [2T/\Delta I]_N$  represents the nearest odd integer dimension of the impulse response in resolution units  $\Delta I$ . For descriptive simplicity, **B** is called the *blur matrix* of the superposition integral.

If the impulse response function is translation invariant such that

$$H(m_1 \Delta S, m_2 \Delta S; n_1 \Delta I, n_2 \Delta I) = H(m_1 \Delta S - n_1 \Delta I, m_2 \Delta S - n_2 \Delta I) \tag{7.2-16}$$

then the discrete superposition operation of Eq. 7.2-12 becomes a discrete convolution operation of the form

$$G(m_1 \Delta S, m_2 \Delta S) = \sum_{n_1 = N_{1L}}^{N_{1U}} \sum_{n_2 = N_{2L}}^{N_{2U}} F(n_1 \Delta I, n_2 \Delta I) H(m_1 \Delta S - n_1 \Delta I, m_2 \Delta S - n_2 \Delta I). \tag{7.2-17}$$

If the physical sample and quadrature mesh spacings are equal, the general term of the blur matrix assumes the form

$$B_{m_2, n_2}(m_1, n_1) = H(m_1 - n_1 + L, m_2 - n_2 + L). \tag{7.2-18}$$

In Eq. 7.2-18, the mesh spacing variable  $\Delta I$  is understood. In addition,

$$\mathbf{B}_{m_2, n_2} = \mathbf{B}_{m_2 + 1, n_2 + 1}. \tag{7.2-19}$$

$$\mathbf{H} = \begin{bmatrix} 11 & 12 & 13 \\ 21 & 22 & 23 \\ 31 & 32 & 33 \end{bmatrix}$$

$$\mathbf{B} = \begin{bmatrix} 33 & 23 & 13 & 0 & 32 & 22 & 12 & 0 & 31 & 21 & 11 & 0 & 0 & 0 & 0 & 0 \\ 0 & 33 & 23 & 13 & 0 & 32 & 22 & 12 & 0 & 31 & 21 & 11 & 0 & 0 & 0 & 0 \\ 0 & 0 & 0 & 0 & 33 & 23 & 13 & 0 & 32 & 22 & 12 & 0 & 31 & 21 & 11 & 0 \\ 0 & 0 & 0 & 0 & 0 & 33 & 23 & 13 & 0 & 32 & 22 & 12 & 0 & 31 & 21 & 11 \end{bmatrix}$$

(a)

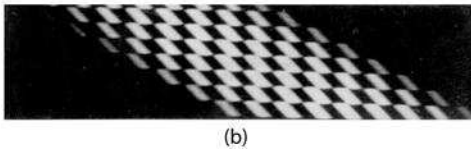


**FIGURE 7.2-4.** Sampled infinite area convolution operators: (a) General impulse array,  $M = 2, N = 4, L = 3$ ; (b) Gaussian-shaped impulse array,  $M = 8, N = 16, L = 9$ .

Consequently, the rows of  $\mathbf{B}$  are shifted versions of the first row. The operator  $\mathbf{B}$  then becomes a sampled infinite area convolution operator, and the series form representation of Eq. 7.2-17 reduces to

$$G(m_1 \Delta S, m_2 \Delta S) = \sum_{n_1 = m_1}^{m_1 + L - 1} \sum_{n_2 = m_2}^{m_2 + L - 1} F(n_1, n_2) H(m_1 - n_1 + L, m_2 - n_2 + L) \quad (7.2-20)$$

where the sampling spacing is understood.

Figure 7.2-4a is a notational example of the sampled image convolution operator for a  $4 \times 4$  ( $N = 4$ ) data array, a  $2 \times 2$  ( $M = 2$ ) filtered data array, and a  $3 \times 3$  ( $L = 3$ ) impulse response array. An extension to larger dimension is shown in Figure 7.2-4b for  $M = 8, N = 16, L = 9$  and a Gaussian-shaped impulse response.

When the impulse response is spatially invariant and orthogonally separable,

$$\mathbf{B} = \mathbf{B}_C \otimes \mathbf{B}_R \quad (7.2-21)$$

where  $\mathbf{B}_R$  and  $\mathbf{B}_C$  are  $M \times N$  matrices of the form

$$\mathbf{B}_R = \begin{bmatrix} h_R(L) & h_R(L-1) & \cdots & h_R(1) & 0 & \cdots & 0 \\ 0 & h_R(L) & & & & & \vdots \\ \vdots & & & & & & 0 \\ 0 & \cdots & 0 & h_R(L) & \cdots & h_R(1) \end{bmatrix} \quad (7.2-22)$$

The two-dimensional convolution operation then reduces to sequential row and column convolutions of the matrix form of the image array. Thus

$$\mathbf{G} = \mathbf{B}_c \mathbf{F} \mathbf{B}_R^T \tag{7.2-23}$$

The superposition or convolution operator expressed in vector form requires  $M^2 L^2$  operations if the zero multiplications of  $\mathbf{B}$  are avoided. A separable convolution operator can be computed in matrix form with only  $ML(M + N)$  operations.

### 7.3. CIRCULANT SUPERPOSITION AND CONVOLUTION

In circulant superposition (2), the input data, the processed output and the impulse response arrays are all assumed spatially periodic over a common period. To unify the presentation, these arrays will be defined in terms of the spatially limited arrays considered previously. First, let the  $N \times N$  data array  $F(n_1, n_2)$  be embedded in the upper left corner of a  $J \times J$  array ( $J > N$ ) of zeros, giving

$$F_E(n_1, n_2) = \begin{cases} F(n_1, n_2) & \text{for } 1 \leq n_i \leq N \\ 0 & \text{for } N + 1 \leq n_i \leq J. \end{cases} \tag{7.3-1a}$$

$$\tag{7.3-1b}$$

In a similar manner, an extended impulse response array is created by embedding the spatially limited impulse array in a  $J \times J$  matrix of zeros. Thus, let

$$H_E(l_1, l_2; m_1, m_2) = \begin{cases} H(l_1, l_2; m_1, m_2) & \text{for } 1 \leq l_i \leq L \\ 0 & \text{for } L + 1 \leq l_i \leq J. \end{cases} \tag{7.3-2a}$$

$$\tag{7.3-2b}$$

Periodic arrays  $F_E(n_1, n_2)$  and  $H_E(l_1, l_2; m_1, m_2)$  are now formed by replicating the extended arrays over the spatial period  $J$ . Then, the circulant superposition of these functions is defined as

$$K_E(m_1, m_2) = \sum_{n_1=1}^J \sum_{n_2=1}^J F_E(n_1, n_2) H_E(m_1 - n_1 + 1, m_2 - n_2 + 1; m_1, m_2). \tag{7.3-3}$$

Similarity of this equation with Eq. 7.1-6 describing finite-area superposition is evident. In fact, if  $J$  is chosen such that  $J = N + L - 1$ , the terms  $F_E(n_1, n_2) = F(n_1, n_2)$  for  $1 \leq n_i \leq N$ . The similarity of the circulant superposition operation and the sam-

pled image superposition operation should also be noted. These relations become clearer in the vector-space representation of the circulant superposition operation.

Let the arrays  $F_E$  and  $K_E$  be expressed in vector form as the  $J^2 \times 1$  vectors  $\mathbf{f}_E$  and  $\mathbf{k}_E$ , respectively. Then, the circulant superposition operator can be written as

$$\mathbf{k}_E = \mathbf{C}\mathbf{f}_E \tag{7.3-4}$$

where  $\mathbf{C}$  is a  $J^2 \times J^2$  matrix containing elements of the array  $H_E$ . The circulant superposition operator can then be conveniently expressed in terms of  $J \times J$  submatrices  $\mathbf{C}_{mn}$  as given by

$$\mathbf{C} = \begin{bmatrix} \mathbf{C}_{1,1} & \mathbf{0} & \mathbf{0} \cdots & \mathbf{0} & \mathbf{C}_{1,J-L+2} \cdots & \mathbf{C}_{1,J} \\ \mathbf{C}_{2,1} & \mathbf{C}_{2,2} & \mathbf{0} \cdots & \mathbf{0} & \mathbf{0} & \vdots & \vdots \\ \vdots & \cdot & & & & \mathbf{0} & \mathbf{C}_{L-1,J} \\ \mathbf{C}_{2,1} & \mathbf{C}_{L,2} & \mathbf{0} & & \cdots & & \mathbf{0} \\ \mathbf{0} & \mathbf{C}_{L+1,2} & & & & & \vdots \\ \mathbf{0} & & & & & & \vdots \\ \vdots & & & & & & \vdots \\ \mathbf{0} & & \cdots & \mathbf{0} & \mathbf{C}_{J,J-L+1} & \mathbf{C}_{J,J-L+2} \cdots & \mathbf{C}_{J,J} \end{bmatrix} \tag{7.3-5}$$

where

$$\mathbf{C}_{m_2, n_2}(m_1, n_1) = H_E(k_1, k_2; m_1, m_2) \tag{7.3-6}$$

for  $1 \leq n_i \leq J$  and  $1 \leq m_i \leq J$  with  $k_i = (m_i - n_i + 1)$  modulo  $J$  and  $H_E(0, 0) = 0$ . It should be noted that each row and column of  $\mathbf{C}$  contains  $L$  nonzero submatrices. If the impulse response array is spatially invariant, then

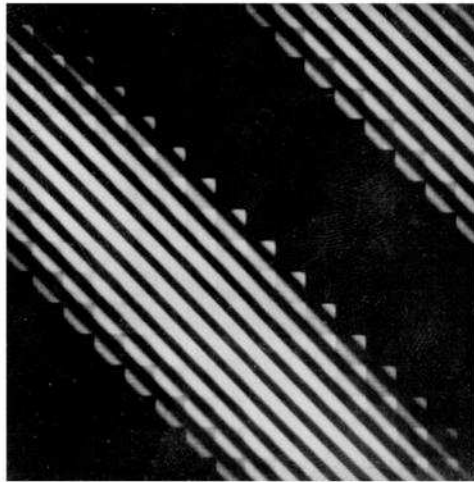
$$\mathbf{C}_{m_2, n_2} = \mathbf{C}_{m_2+1, n_2+1} \tag{7.3-7}$$

and the submatrices of the rows (columns) can be obtained by a circular shift of the first row (column). Figure 7.3-1a illustrates the circulant convolution operator for  $16 \times 16$  ( $J = 4$ ) data and filtered data arrays and for a  $3 \times 3$  ( $L = 3$ ) impulse response array. In Figure 7.3-1b, the operator is shown for  $J = 16$  and  $L = 9$  with a Gaussian-shaped impulse response.

$$H = \begin{bmatrix} 11 & 12 & 13 \\ 21 & 22 & 23 \\ 31 & 32 & 33 \end{bmatrix}$$

$$C = \begin{bmatrix} 11 & 0 & 31 & 21 & 0 & 0 & 0 & 0 & 13 & 0 & 33 & 23 & 12 & 0 & 32 & 22 \\ 21 & 11 & 0 & 31 & 0 & 0 & 0 & 0 & 23 & 13 & 0 & 33 & 22 & 12 & 0 & 32 \\ 31 & 21 & 11 & 0 & 0 & 0 & 0 & 0 & 33 & 23 & 13 & 0 & 32 & 22 & 12 & 0 \\ 0 & 31 & 21 & 11 & 0 & 0 & 0 & 0 & 0 & 33 & 23 & 13 & 0 & 32 & 22 & 12 \\ \hline 12 & 0 & 32 & 22 & 11 & 0 & 31 & 21 & 0 & 0 & 0 & 0 & 13 & 0 & 33 & 23 \\ 22 & 12 & 0 & 32 & 21 & 11 & 0 & 31 & 0 & 0 & 0 & 0 & 23 & 13 & 0 & 33 \\ 32 & 22 & 12 & 0 & 31 & 21 & 11 & 0 & 0 & 0 & 0 & 0 & 33 & 23 & 13 & 0 \\ 0 & 32 & 22 & 12 & 0 & 31 & 21 & 11 & 0 & 0 & 0 & 0 & 0 & 33 & 23 & 13 \\ \hline 13 & 0 & 33 & 23 & 12 & 0 & 32 & 22 & 11 & 0 & 31 & 21 & 0 & 0 & 0 & 0 \\ 23 & 13 & 0 & 33 & 22 & 12 & 0 & 32 & 21 & 11 & 0 & 31 & 0 & 0 & 0 & 0 \\ \hline 33 & 23 & 13 & 0 & 32 & 22 & 12 & 0 & 31 & 21 & 11 & 0 & 0 & 0 & 0 & 0 \\ 0 & 33 & 23 & 13 & 0 & 32 & 22 & 12 & 0 & 31 & 21 & 11 & 0 & 0 & 0 & 0 \\ \hline 0 & 0 & 0 & 0 & 13 & 0 & 33 & 23 & 12 & 0 & 32 & 22 & 11 & 0 & 31 & 21 \\ 0 & 0 & 0 & 0 & 23 & 13 & 0 & 33 & 22 & 12 & 0 & 32 & 21 & 11 & 0 & 31 \\ \hline 0 & 0 & 0 & 0 & 33 & 23 & 13 & 0 & 32 & 22 & 12 & 0 & 31 & 21 & 11 & 0 \\ 0 & 0 & 0 & 0 & 0 & 33 & 23 & 13 & 0 & 32 & 22 & 12 & 0 & 31 & 21 & 11 \end{bmatrix}$$

(a)



(b)

**FIGURE 7.3-1.** Circulant convolution operators: (a) General impulse array,  $J = 4, L = 3$ ; (b) Gaussian-shaped impulse array,  $J = 16, L = 9$ .



Finally, when the impulse response is spatially invariant and orthogonally separable,

$$\mathbf{C} = \mathbf{C}_C \otimes \mathbf{C}_R \tag{7.3-8}$$

where  $\mathbf{C}_R$  and  $\mathbf{C}_C$  are  $J \times J$  matrices of the form

$$\mathbf{C}_R = \begin{bmatrix} h_R(1) & 0 & \dots & 0 & h_R(L) & \dots & h_R(3) & h_R(2) \\ h_R(2) & h_R(1) & \dots & 0 & 0 & & \vdots & h_R(3) \\ \vdots & \vdots & & & & & & \vdots \\ h_R(L-1) & & & & \dots & 0 & & h_R(L) \\ h_R(L) & h_R(L-1) & & & & & & 0 \\ 0 & h_R(L) & & & & & & \vdots \\ \vdots & & & & & & & 0 \\ 0 & \dots & 0 & h_R(L) & \dots & \dots & h_R(2) & h_R(1) \end{bmatrix} \tag{7.3-9}$$

Two-dimensional circulant convolution may then be computed as

$$\mathbf{K}_E = \mathbf{C}_C \mathbf{F}_E \mathbf{C}_R^T \tag{7.3-10}$$

### 7.4. SUPERPOSITION AND CONVOLUTION OPERATOR RELATIONSHIPS

The elements of the finite-area superposition operator  $\mathbf{D}$  and the elements of the sampled image superposition operator  $\mathbf{B}$  can be extracted from circulant superposition operator  $\mathbf{C}$  by use of selection matrices defined as (2)

$$\mathbf{S1}_J^{(K)} = \begin{bmatrix} \mathbf{I}_K | \mathbf{0} \end{bmatrix} \tag{7.4-1a}$$

$$\mathbf{S2}_J^{(K)} = \begin{bmatrix} \mathbf{0}_A | \mathbf{I}_K | \mathbf{0} \end{bmatrix} \tag{7.4-1b}$$

where  $\mathbf{S1}_J^{(K)}$  and  $\mathbf{S2}_J^{(K)}$  are  $K \times J$  matrices,  $\mathbf{I}_K$  is a  $K \times K$  identity matrix and  $\mathbf{0}_A$  is a  $K \times L - 1$  matrix.

Examination of the structure of the various superposition operators indicates that

$$\mathbf{D} = [\mathbf{S1}_J^{(M)} \otimes \mathbf{S1}_J^{(M)}] \mathbf{C} [\mathbf{S1}_J^{(N)} \otimes \mathbf{S1}_J^{(N)}]^T \tag{7.4-2a}$$

$$\mathbf{B} = [\mathbf{S2}_J^{(M)} \otimes \mathbf{S2}_J^{(M)}] \mathbf{C} [\mathbf{S1}_J^{(N)} \otimes \mathbf{S1}_J^{(N)}]^T \tag{7.4-2b}$$

That is, the matrix **D** is obtained by extracting the first  $M$  rows and  $N$  columns of submatrices  $C_{mn}$  of **C**. The first  $M$  rows and  $N$  columns of each submatrix are also extracted. A similar explanation holds for the extraction of **B** from **C**. In Figure 7.3-1, the elements of **C** to be extracted to form **D** and **B** are indicated by boxes.

Pratt (4Ed., 184-186) has shown that

$$\mathbf{Q} = [\mathbf{S1}_J^{(M)}] \mathbf{K}_E [\mathbf{S1}_J^{(M)}]^T \tag{7.4-3}$$

and

$$\mathbf{G} = [\mathbf{S2}_J^{(M)}] \mathbf{K}_E [\mathbf{S2}_J^{(M)}]^T \tag{7.4-9}$$

Figure 7.4-1 illustrates the locations of the elements of **G** and **Q** extracted from  $\mathbf{K}_E$  for finite-area and sampled infinite-area superposition.

In summary, it has been shown that the output data vectors for either finite-area or sampled image superposition can be obtained by a simple selection operation on the output data vector of circulant superposition. Computational advantages that can be realized from this result are considered in Chapter 9.

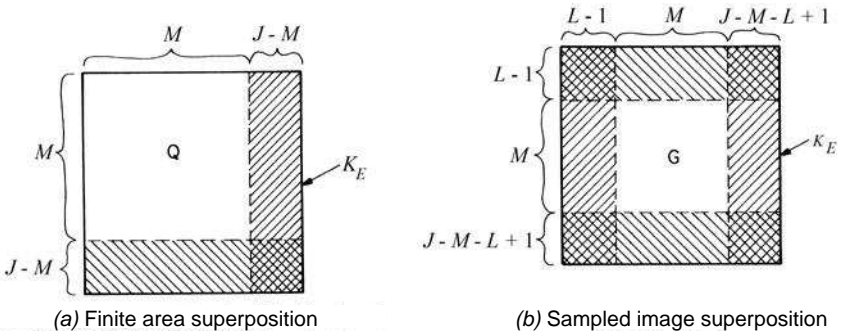


**FIGURE 7.4-1.** Location of elements of processed data  $Q$  and  $G$  from  $K_E$ .

### 7.5. CONVOLUTION EXERCISES

E7.1 Develop a program that convolves a test image with a  $3 \times 3$  uniform impulse response array for three convolution boundary conditions. Steps:

- (a) Create a  $101 \times 101$  pixel, real datatype test image consisting of a  $2 \times 2$  cluster of amplitude 1.0 pixels in the upper left corner and a single pixel of amplitude 1.0 in the image center. Set all other pixels to 0.0.
- (b) Create a  $3 \times 3$  uniform impulse response array.

- (c) Convolve the source image with the impulse response array for the following three boundary conditions: enclosed array, zero exterior, reflected exterior.
- (d) Print a  $5 \times 5$  pixel image array about the upper left corner and image center for each boundary condition and explain the results.

The PIKS API executable `example_convolve_boundary` performs this exercise.

E7.2 Develop a program that convolves an unsigned integer, 8-bit, color image with a  $5 \times 5$  uniform impulse response array. Steps:

- (a) Display the source color image.
- (b) Fetch the impulse response array from a data object repository.
- (c) Convolve the source image with the impulse response array.
- (d) Display the destination image.

The PIKS API executable `example_repository_convolve_colour` performs this exercise.

## REFERENCES

1. J. F. Abramatic and O. D. Faugeras, "Design of Two-Dimensional FIR Filters from Small Generating Kernels," *Proc. IEEE Conference on Pattern Recognition and Image Processing*, Chicago, May 1978.
2. W. K. Pratt, "Vector Formulation of Two Dimensional Signal Processing Operations," *Computer Graphics and Image Processing*, **4**, 1, March 1975, 1–24.
3. A. V. Oppenheim and R. W. Schaefer (Contributor), *Digital Signal Processing*, Prentice Hall, Englewood Cliffs, NJ, 1975.
4. T. R. McCalla, *Introduction to Numerical Methods and FORTRAN Programming*, Wiley, New York, 1967.
5. A. Papoulis, *Systems and Transforms with Applications in Optics, Second Edition*, McGraw-Hill, New York, 1981.

---

# 8

---

## UNITARY AND WAVELET TRANSFORMS

Two-dimensional unitary and wavelet transforms have found two major applications in image processing. Transforms have been utilized to extract features from images. For example, with the Fourier transform, the average value or *DC term* is proportional to the average image amplitude, and the high-frequency terms (*AC term*) give an indication of the amplitude and orientation of edges within an image. Dimensionality reduction in computation is a second image processing application. Stated simply, those transform coefficients that are small may be excluded from processing operations, such as filtering, without much loss in processing accuracy. Another application in the field of image coding is transform image coding, in which a bandwidth reduction is achieved by discarding or grossly quantizing low-magnitude transform coefficients. In this chapter, consideration is given to the properties of unitary and wavelet transforms commonly used in image processing.

### 8.1. GENERAL UNITARY TRANSFORMS

A *unitary transform* is a specific type of linear transformation in which the basic linear operation of Eq. 6.2-1 is exactly invertible and the operator kernel satisfies certain orthogonality conditions (1,2). The forward unitary transform of the  $N_1 \times N_2$  image array  $F(n_1, n_2)$  results in a  $N_1 \times N_2$  transformed image array as defined by

$$\mathcal{F}(m_1, m_2) = \sum_{n_1=1}^{N_1} \sum_{n_2=1}^{N_2} F(n_1, n_2)A(n_1, n_2; m_1, m_2) \tag{8.1-1}$$

where  $A(n_1, n_2; m_1, m_2)$  represents the forward transform kernel. A reverse or inverse transformation provides a mapping from the transform domain to the image space as given by

$$F(n_1, n_2) = \sum_{m_1=1}^{N_1} \sum_{m_2=1}^{N_2} \mathcal{F}(m_1, m_2)B(n_1, n_2; m_1, m_2) \tag{8.1-2}$$

where  $B(n_1, n_2; m_1, m_2)$  denotes the inverse transform kernel. The transformation is unitary if the following *orthonormality conditions* are met:

$$\sum_{m_1} \sum_{m_2} A(n_1, n_2; m_1, m_2)A^*(j_1, j_2; m_1, m_2) = \delta(n_1 - j_1, n_2 - j_2) \tag{8.1-3a}$$

$$\sum_{m_1} \sum_{m_2} B(n_1, n_2; m_1, m_2)B^*(j_1, j_2; m_1, m_2) = \delta(n_1 - j_1, n_2 - j_2) \tag{8.1-3b}$$

$$\sum_{n_1} \sum_{n_2} A(n_1, n_2; m_1, m_2)A^*(n_1, n_2; k_1, k_2) = \delta(m_1 - k_1, m_2 - k_2) \tag{8.1-3c}$$

$$\sum_{n_1} \sum_{n_2} B(n_1, n_2; m_1, m_2)B^*(n_1, n_2; k_1, k_2) = \delta(m_1 - k_1, m_2 - k_2). \tag{8.1-3d}$$

The transformation is said to be separable if its kernels can be written in the form

$$A(n_1, n_2; m_1, m_2) = A_C(n_1, m_1)A_R(n_2, m_2) \tag{8.1-4a}$$

$$B(n_1, n_2; m_1, m_2) = B_C(n_1, m_1)B_R(n_2, m_2) \tag{8.1-4b}$$

where the kernel subscripts indicate row and column one-dimensional transform operations. A separable two-dimensional unitary transform can be computed in two steps. First, a one-dimensional transform is taken along each column of the image, yielding

$$P(m_1, n_2) = \sum_{n_1=1}^{N_1} F(n_1, n_2)A_C(n_1, m_1). \tag{8.1-5}$$

Next, a second one-dimensional unitary transform is taken along each row of  $P(m_1, n_2)$ , giving

$$\mathcal{F}(m_1, m_2) = \sum_{n_2=1}^{N_2} P(m_1, n_2)A_R(n_2, m_2). \tag{8.1-6}$$

Unitary transforms can conveniently be expressed in vector-space form (3). Let  $\mathbf{F}$  and  $\mathbf{f}$  denote the matrix and vector representations of an image array, and let  $F$  and  $f$  be the matrix and vector forms of the transformed image. Then, the two-dimensional unitary transform written in vector form is given by

$$f = \mathbf{A}\mathbf{f} \tag{8.1-7}$$

where  $\mathbf{A}$  is the forward transformation matrix. The reverse transform is

$$\mathbf{f} = \mathbf{B}f \tag{8.1-8}$$

where  $\mathbf{B}$  represents the inverse transformation matrix. It is obvious then that

$$\mathbf{B} = \mathbf{A}^{-1}. \tag{8.1-9}$$

For a unitary transformation, the matrix inverse is given by

$$\mathbf{A}^{-1} = \mathbf{A}^{*T} \tag{8.1-10}$$

and  $\mathbf{A}$  is said to be a *unitary matrix*. A real unitary matrix is called an *orthogonal matrix*. For such a matrix,

$$\mathbf{A}^{-1} = \mathbf{A}^T. \tag{8.1-11}$$

If the transform kernels are separable such that

$$\mathbf{A} = \mathbf{A}_C \otimes \mathbf{A}_R \tag{8.1-12}$$

where  $\mathbf{A}_R$  and  $\mathbf{A}_C$  are row and column unitary transform matrices, then the transformed image matrix can be obtained from the image matrix by

$$F = \mathbf{A}_C \mathbf{F} \mathbf{A}_R^T. \tag{8.1-13a}$$

The inverse transformation is given by

$$\mathbf{F} = \mathbf{B}_C \mathbf{F} \mathbf{B}_R^T \tag{8.1-13b}$$

where  $\mathbf{B}_C = \mathbf{A}_C^{-1}$  and  $\mathbf{B}_R = \mathbf{A}_R^{-1}$ .

Separable unitary transforms can also be expressed in a hybrid series–vector space form as a sum of vector outer products. Let  $\mathbf{a}_C(n_1)$  and  $\mathbf{a}_R(n_2)$  represent rows

$n_1$  and  $n_2$  of the unitary matrices  $\mathbf{A}_R$  and  $\mathbf{A}_R$ , respectively. Then, it is easily verified that

$$\mathbf{F} = \sum_{n_1=1}^{N_1} \sum_{n_2=1}^{N_2} F(n_1, n_2) \mathbf{a}_C(n_1) \mathbf{a}_R^T(n_2). \tag{8.1-14a}$$

Similarly,

$$\mathbf{F} = \sum_{m_1=1}^{N_1} \sum_{m_2=1}^{N_2} F(m_1, m_2) \mathbf{b}_C(m_1) \mathbf{b}_R^T(m_2). \tag{8.1-14b}$$

where  $\mathbf{b}_C(m_1)$  and  $\mathbf{b}_R(m_2)$  denote rows  $m_1$  and  $m_2$  of the unitary matrices  $\mathbf{B}_C$  and  $\mathbf{B}_R$ , respectively. The vector outer products of Eq. 8.1-14 form a series of matrices, called *basis matrices*, that provide matrix decompositions of the image matrix  $\mathbf{F}$  or its unitary transformation  $\mathbf{F}$ .

There are several ways in which a unitary transformation may be viewed. An image transformation can be interpreted as a decomposition of the image data into a generalized two-dimensional spectrum (4). Each spectral component in the transform domain corresponds to the amount of energy of the spectral function within the original image. In this context, the concept of frequency may now be generalized to include transformations by functions other than sine and cosine waveforms. This type of generalized spectral analysis is useful in the investigation of specific decompositions that are best suited for particular classes of images. Another way to visualize an image transformation is to consider the transformation as a multidimensional rotation of coordinates. One of the major properties of a unitary transformation is that measure is preserved. For example, the mean-square difference between two images is equal to the mean-square difference between the unitary transforms of the images. A third approach to the visualization of image transformation is to consider Eq. 8.1-2 as a means of synthesizing an image with a set of two-dimensional mathematical functions  $B(n_1, n_2; m_1, m_2)$  for a fixed transform domain coordinate  $(m_1, m_2)$ . In this interpretation, the kernel  $B(n_1, n_2; m_1, m_2)$  is called a *two-dimensional basis function* and the transform coefficient  $\mathcal{F}(m_1, m_2)$  is the amplitude of the basis function required in the synthesis of the image.

In the remainder of this chapter, to simplify the analysis of two-dimensional unitary transforms, all image arrays are considered square of dimension  $N$ . Furthermore, when expressing transformation operations in series form, as in Eqs. 8.1-1 and 8.1-2, the indices are renumbered and renamed. Thus, the input image array is denoted by  $F(j, k)$  for  $j, k = 0, 1, 2, \dots, N - 1$ , and the transformed image array is represented by  $\mathcal{F}(u, v)$  for  $u, v = 0, 1, 2, \dots, N - 1$ . With these definitions, the forward unitary transform becomes

$$\mathcal{F}(u, v) = \sum_{j=0}^{N-1} \sum_{k=0}^{N-1} F(j, k) A(j, k; u, v) \tag{8.1-15a}$$

and the inverse transform is

$$F(j, k) = \sum_{u=0}^{N-1} \sum_{v=0}^{N-1} \mathcal{F}(u, v) B(j, k; u, v). \quad (8.1-15b)$$

## 8.2. FOURIER TRANSFORM

The discrete two-dimensional *Fourier transform* of an image array is defined in series form as (5-10)

$$\mathcal{F}(u, v) = \frac{1}{N} \sum_{j=0}^{N-1} \sum_{k=0}^{N-1} F(j, k) \exp\left\{\frac{-2\pi i}{N}(uj + vk)\right\} \quad (8.2-1a)$$

where  $i = \sqrt{-1}$ , and the discrete inverse transform is given by

$$F(j, k) = \frac{1}{N} \sum_{u=0}^{N-1} \sum_{v=0}^{N-1} \mathcal{F}(u, v) \exp\left\{\frac{2\pi i}{N}(uj + vk)\right\}. \quad (8.2-1b)$$

The indices  $(u, v)$  are called the *spatial frequencies* of the transformation in analogy with the continuous Fourier transform. It should be noted that Eq. 8.2-1 is not universally accepted by all authors; some prefer to place all scaling constants in the inverse transform equation, while still others employ a reversal in the sign of the kernels.

Because the transform kernels are separable and symmetric, the two dimensional transforms can be computed as sequential row and column one-dimensional transforms. The basis functions of the transform are complex exponentials that may be decomposed into sine and cosine components. The resulting Fourier transform pairs then become

$$A(j, k; u, v) = \exp\left\{\frac{-2\pi i}{N}(uj + vk)\right\} = \cos\left\{\frac{2\pi}{N}(uj + vk)\right\} - i \sin\left\{\frac{2\pi}{N}(uj + vk)\right\} \quad (8.2-2a)$$

$$B(j, k; u, v) = \exp\left\{\frac{2\pi i}{N}(uj + vk)\right\} = \cos\left\{\frac{2\pi}{N}(uj + vk)\right\} + i \sin\left\{\frac{2\pi}{N}(uj + vk)\right\}. \quad (8.2-2b)$$

Figure 8.2-1 shows plots of the sine and cosine components of the one-dimensional Fourier basis functions for  $N = 16$ . It should be observed that the basis functions are a rough approximation to continuous sinusoids only for low frequencies; in fact, the highest-frequency basis function is a square wave. Also, there are obvious redundancies between the sine and cosine components.



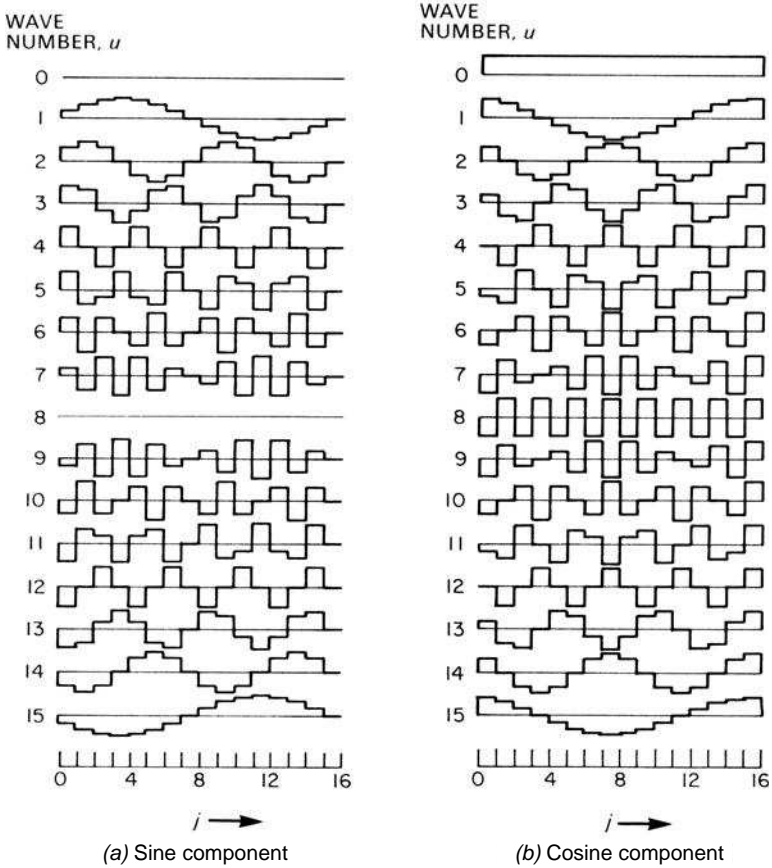


**FIGURE 8.2-1** Fourier transform basis functions,  $N = 16$ .

The Fourier transform plane possesses many interesting structural properties. The spectral component at the origin of the Fourier domain

$$\mathcal{F}(0, 0) = \frac{1}{N} \sum_{j=0}^{N-1} \sum_{k=0}^{N-1} F(j, k) \tag{8.2-3}$$

is equal to  $N$  times the spatial average of the image plane. Making the substitutions  $u = u + mN$ ,  $v = v + nN$  in Eq. 8.2-1, where  $m$  and  $n$  are constants, results in

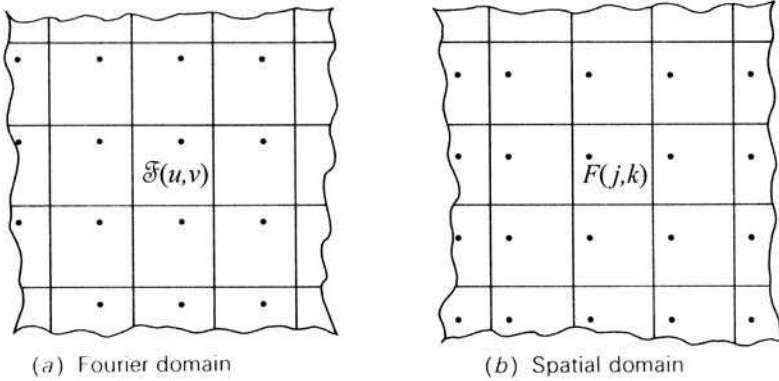


**FIGURE 8.2-2.** Periodic image and Fourier transform arrays.

$$\mathcal{F}(u + mN, v + nN) = \frac{1}{N} \sum_{j=0}^{N-1} \sum_{k=0}^{N-1} F(j, k) \exp\left\{\frac{-2\pi i}{N}(uj + vk)\right\} \exp\{-2\pi i(mj + nk)\}. \tag{8.2-4}$$

For all integer values of  $m$  and  $n$ , the second exponential term of Eq. 8.2-5 assumes a value of unity, and the transform domain is found to be periodic. Thus, as shown in Figure 8.2-2a,

$$\mathcal{F}(u + mN, v + nN) = \mathcal{F}(u, v) \tag{8.2-5}$$

for  $m, n = 0, \pm 1, \pm 2, \dots$

The two-dimensional Fourier transform of an image is essentially a Fourier series representation of a two-dimensional field. For the Fourier series representation to be valid, the field must be periodic. Thus, as shown in Figure 8.2-2b, the original image must be considered to be periodic horizontally and vertically. The right side of the image therefore abuts the left side, and the top and bottom of the image are adjacent. Spatial frequencies along the coordinate axes of the transform plane arise from these transitions.

If the image array represents a luminance field,  $F(j, k)$  will be a real positive function. However, its Fourier transform will, in general, be complex. Because the transform domain contains  $2N^2$  components, the real and imaginary, or phase and magnitude components, of each coefficient, it might be thought that the Fourier transformation causes an increase in dimensionality. This, however, is not the case because  $\mathcal{F}(u, v)$  exhibits a property of conjugate symmetry. From Eq. 8.2-4, with  $m$  and  $n$  set to integer values, conjugation yields

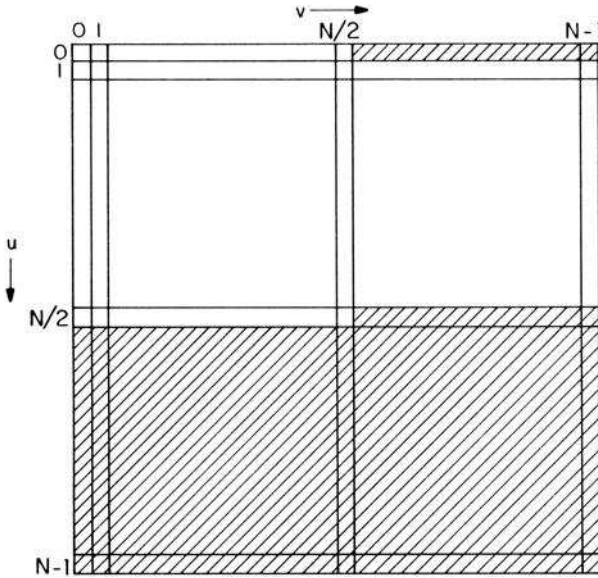


FIGURE 8.2-3. Fourier transform frequency domain.

$$\mathcal{F}^*(u + mN, v + nN) = \frac{1}{N} \sum_{j=0}^{N-1} \sum_{k=0}^{N-1} F(j, k) \exp\left\{\frac{-2\pi i}{N}(uj + vk)\right\}. \quad (8.2-6)$$

By the substitution  $u = -u$  and  $v = -v$  it can be shown that

$$\mathcal{F}(u, v) = F^*(-u + mN, -v + nN) \quad (8.2-7)$$

for  $n = 0, \pm 1, \pm 2, \dots$ . As a result of the conjugate symmetry property, almost one-half of the transform domain samples are redundant; that is, they can be generated from other transform samples. Figure 8.2-3 shows the transform plane with a set of redundant components crosshatched. It is possible, of course, to choose the left half-plane samples rather than the upper plane samples as the non redundant set.

Figure 8.2-4 shows a monochrome test image and various versions of its Fourier transform, as computed by Eq. 8.2-1a, where the test image has been scaled over unit range  $0.0 \leq F(j, k) \leq 1.0$ . Because the dynamic range of transform components is much larger than the exposure range of photographic film, it is necessary to compress the coefficient values to produce a useful display. Amplitude compression to a unit range display array  $\mathcal{D}(u, v)$  can be obtained by clipping large-magnitude values according to the relation

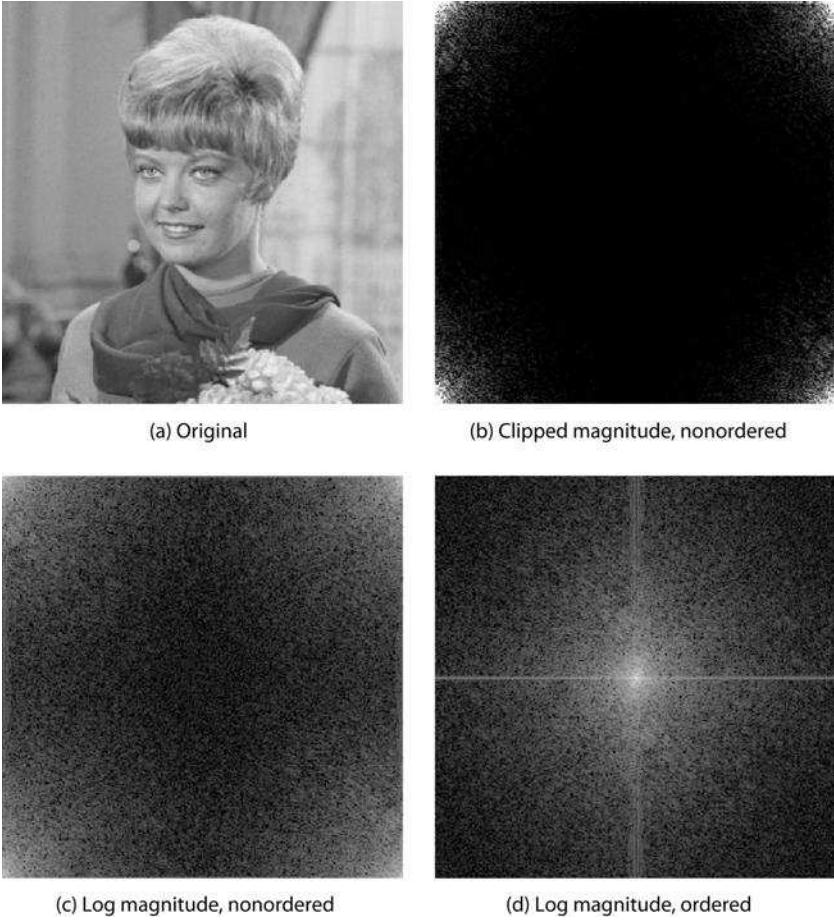


**FIGURE 8.2-4.** Fourier transform of the `smpte_girl_luma` image.

$$\mathcal{D}(u, v) = 1.0 \quad \text{if } |\mathcal{F}(u, v)| \geq c|\mathcal{F}_{max}| \quad (8.2-8a)$$

$$\mathcal{D}(u, v) = \frac{|\mathcal{F}(u, v)|}{c|\mathcal{F}_{max}|} \quad \text{if } |\mathcal{F}(u, v)| < c|\mathcal{F}_{max}| \quad (8.2-8b)$$

where  $0.0 < c \leq 1.0$  is the clipping factor and  $|\mathcal{F}_{max}|$  is the maximum coefficient magnitude. Another form of amplitude compression is to take the logarithm of each component as given by

$$\mathcal{D}(u, v) = \frac{\log\{a + b|\mathcal{F}(u, v)|\}}{\log\{a + b|\mathcal{F}_{max}|\}} \quad (8.2-9)$$

where  $a$  and  $b$  are scaling constants. Figure 8.2-4b is a clipped magnitude display of the magnitude of the Fourier transform coefficients. Figure 8.2-4c is a logarithmic display for  $a = 1.0$  and  $b = 100.0$ .

In mathematical operations with continuous signals, the origin of the transform domain is usually at its geometric center. Similarly, the Fraunhofer diffraction pattern of a photographic transparency of transmittance  $F(x, y)$  produced by a coherent optical system has its zero-frequency term at the center of its display. A computer-generated two-dimensional discrete Fourier transform with its origin at its center can be produced by a simple reordering of its transform coefficients. Alternatively, the quadrants of the Fourier transform, as computed by Eq. 8.2-1a, can be reordered automatically by multiplying the image function by the factor  $(-1)^{j+k}$  prior to the Fourier transformation. The proof of this assertion follows from Eq. 8.2-4 with the substitution  $m = n = \frac{1}{2}$ . Then, by the identity

$$\exp\{i\pi(j+k)\} = (-1)^{j+k} \tag{8.2-10}$$

Eq. 8.2-5 can be expressed as

$$\mathcal{F}(u + N/2, v + N/2) = \frac{1}{N} \sum_{j=0}^{N-1} \sum_{k=0}^{N-1} F(j, k)(-1)^{j+k} \exp\left\{\frac{-2\pi i}{N}(uj + vk)\right\} \tag{8.2-11}$$

Figure 8.2-4d contains a log magnitude display of the reordered Fourier components. The conjugate symmetry in the Fourier domain is readily apparent from the photograph.

The Fourier transform written in series form in Eq. 8.2-1 may be redefined in vector-space form as

$$\mathbf{f} = \mathbf{A}\mathbf{f} \tag{8.2-12a}$$

$$\mathbf{f} = \mathbf{A}^*{}^T \mathbf{f} \tag{8.2-12b}$$

where  $\mathbf{f}$  and  $f$  are vectors obtained by column scanning the matrices  $\mathbf{F}$  and  $F$ , respectively. The transformation matrix  $\mathbf{A}$  can be written in direct product form as

$$\mathbf{A} = \mathbf{A}_C \otimes \mathbf{A}_R \tag{8.2-13}$$

where

$$\mathbf{A}_R = \mathbf{A}_C = \begin{bmatrix} W^0 & W^0 & W^0 & \dots & W^0 \\ W^0 & W^1 & W^2 & \dots & W^{N-1} \\ W^0 & W^2 & W^4 & \dots & W^{2(N-1)} \\ \vdots & & & & \vdots \\ W^0 & \cdot & \cdot & \dots & W^{(N-1)^2} \end{bmatrix} \tag{8.2-14}$$

with  $W = \exp\{-2\pi i/N\}$ . As a result of the direct product decomposition of  $\mathbf{A}$ , the image matrix and transformed image matrix are related by

$$\mathbf{F} = \mathbf{A}_C \mathbf{F} \mathbf{A}_R \tag{8.2-15a}$$

$$\mathbf{F} = \mathbf{A}_C^* \mathbf{F} \mathbf{A}_R^* \tag{8.2-15b}$$

The properties of the Fourier transform previously proved in series form obviously hold in the matrix formulation.

One of the major contributions to the field of image processing was the discovery (5) of an efficient computational algorithm for the discrete Fourier transform (DFT). Brute-force computation of the discrete Fourier transform of a one-dimensional sequence of  $N$  values requires on the order of  $N^2$  complex multiply and add operations. A fast Fourier transform (FFT) requires on the order of  $N \log N$  operations. For large images the computational savings are substantial. The original FFT algorithms were limited to images whose dimensions are a power of 2 (e.g.,  $N = 2^9 = 512$ ). Modern algorithms exist for less restrictive image dimensions.

Although the Fourier transform possesses many desirable analytic properties, it has a major drawback: Complex, rather than real number computations are necessary. Also, for image coding it does not provide as efficient image energy compaction as other transforms.

### 8.3. COSINE, SINE AND HARTLEY TRANSFORMS

The cosine, sine and Hartley transforms are unitary transforms that utilize sinusoidal basis functions, as does the Fourier transform. The cosine and sine transforms are not simply the cosine and sine parts of the Fourier transform. In fact, the cosine and sine parts of the Fourier transform, individually, are not orthogonal functions. The Hartley transform jointly utilizes sine and cosine basis functions, but its coefficients are real numbers, as contrasted with the Fourier transform whose coefficients are, in general, complex numbers.

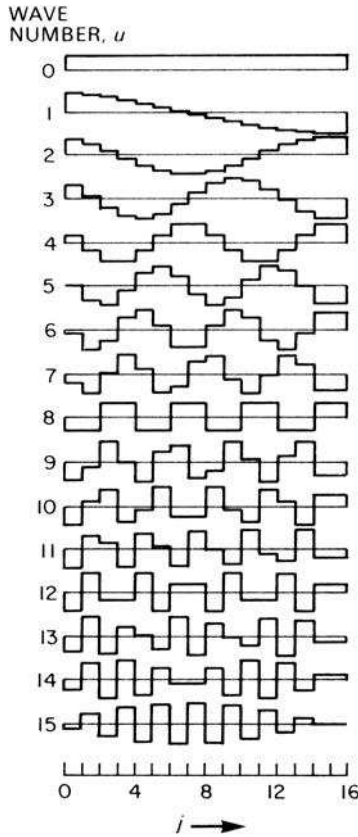


FIGURE 8.3-1. Cosine transform basis functions,  $N = 16$ .

### 8.3.1. Cosine Transform

The *cosine transform*, discovered by Ahmed et al. (12), has found wide application in transform image coding. In fact, it is the foundation of the JPEG standard (13) for still image coding and the MPEG standard for the coding of moving images (14). The cosine transform pair is defined as (12)

$$\mathcal{F}(u, v) = \frac{2}{N} \mathcal{A}(u) \mathcal{A}(v) \sum_{j=0}^{N-1} \sum_{k=0}^{N-1} F(j, k) \cos \left\{ \frac{\pi}{N} \left[ u \left( j + \frac{1}{2} \right) \right] \right\} \cos \left\{ \frac{\pi}{N} \left[ v \left( k + \frac{1}{2} \right) \right] \right\} \tag{8.3-1a}$$

$$F(j, k) = \frac{2}{N} \sum_{u=0}^{N-1} \sum_{v=0}^{N-1} \mathcal{A}(u) \mathcal{A}(v) \mathcal{F}(u, v) \cos \left\{ \frac{\pi}{N} \left[ u \left( j + \frac{1}{2} \right) \right] \right\} \cos \left\{ \frac{\pi}{N} \left[ v \left( k + \frac{1}{2} \right) \right] \right\}. \tag{8.3-1b}$$

where  $\mathcal{C}(0) = (2)^{-1/2}$  and  $\mathcal{C}(w) = 1$  for  $w = 1, 2, \dots, N - 1$ . It has been observed that the basis functions of the cosine transform are actually a class of discrete Chebyshev polynomials (12).

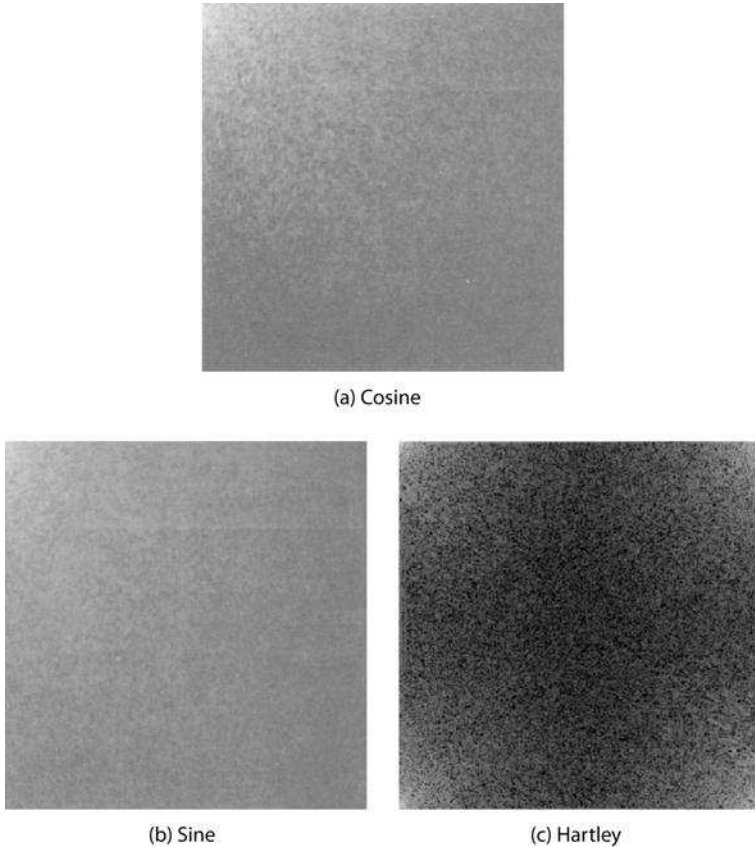


**FIGURE 8.3-2.** Cosine, sine and Hartley transforms of the `smpte_girl_luma` image, log magnitude displays.

Figure 8.3-1 is a plot of the cosine transform basis functions for  $N = 16$ . A photograph of the cosine transform of the test image of Figure 8.2-4a is shown in Figure 8.3-2a. The origin is placed in the upper left corner of the picture, consistent with matrix notation. It should be observed that, as with the Fourier transform, the image energy tends to concentrate toward the lower spatial frequencies.

The cosine transform of a  $N \times N$  image can be computed by reflecting the image about its edges to obtain a  $2N \times 2N$  array, taking the FFT of the array and then extracting the real parts of the Fourier transform (15). Algorithms also exist for the



direct computation of each row or column of Eq. 8.3-1 with on the order of  $N \log N$  real arithmetic operations (12,16).

### 8.3.2. Sine Transform

The *sine transform*, introduced by Jain (17), as a fast algorithmic substitute for the Karhunen–Loeve transform of a Markov process, is defined in two-dimensional form as

$$\mathcal{F}(u, v) = \frac{2}{N+1} \sum_{j=0}^{N-1} \sum_{k=0}^{N-1} F(j, k) \sin\left\{\frac{(j+1)(u+1)\pi}{N+1}\right\} \sin\left\{\frac{(k+1)(v+1)\pi}{N+1}\right\} \tag{8.3-2}$$

for  $u, j = 0, 1, 2, \dots, N - 1$ . Its inverse is of identical form.

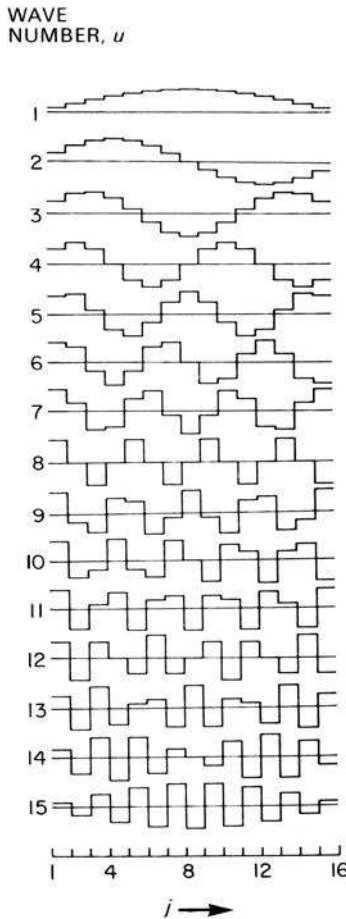


FIGURE 8.3-3. Sine transform basis functions,  $N = 15$ .

Sine transform basis functions are plotted in Figure 8.3-3 for  $N = 15$ . Figure 8.3-2b is a photograph of the sine transform of the test image. The sine transform can also be computed directly from Eq. 8.3-2, or efficiently with a Fourier transform algorithm (17).

### 8.3.3. Hartley Transform

Bracewell (19,20) has proposed a discrete real-valued unitary transform, called the *Hartley transform*, as a substitute for the Fourier transform in many filtering applications. The name derives from the continuous integral version introduced by Hartley in 1942 (21). The discrete two-dimensional Hartley transform is defined by the transform pair

$$\mathcal{F}(u, v) = \frac{1}{N} \sum_{j=0}^{N-1} \sum_{k=0}^{N-1} F(j, k) \operatorname{cas} \left\{ \frac{2\pi}{N}(uj + vk) \right\} \tag{8.3-3a}$$

$$F(j, k) = \frac{1}{N} \sum_{u=0}^{N-1} \sum_{v=0}^{N-1} \mathcal{F}(u, v) \operatorname{cas} \left\{ \frac{2\pi}{N}(uj + vk) \right\}. \tag{8.3-3b}$$

where  $\operatorname{cas}\theta \equiv \cos\theta + \sin\theta$ . The structural similarity between the Fourier and Hartley transforms becomes evident when comparing Eq. 8.3-3 and Eq. 8.2-2.

It can be readily shown (17) that the  $\operatorname{cas}\theta$  function is an orthogonal function. Also, the Hartley transform possesses equivalent but not mathematically identical structural properties of the discrete Fourier transform (20). Figure 8.3-2c is a photograph of the Hartley transform of the test image.

The Hartley transform can be computed efficiently by a FFT-like algorithm (20). The choice between the Fourier and Hartley transforms for a given application is usually based on computational efficiency. In some computing structures, the Hartley transform may be more efficiently computed, while in other computing environments, the Fourier transform may be computationally superior.

## 8.4. HADAMARD, HAAR AND DAUBECHIES TRANSFORMS

The Hadamard, Haar and Daubechies transforms are related members of a family of non sinusoidal transforms.

### 8.4.1. Hadamard Transform

The *Hadamard transform* (22,23) is based on the *Hadamard matrix* (24), which is a square array of plus and minus ones whose rows and columns are orthogonal. A normalized  $N \times N$  Hadamard matrix satisfies the relation

$$\mathbf{H}\mathbf{H}^T = \mathbf{I}. \tag{8.4-1}$$

The smallest orthonormal Hadamard matrix is the  $2 \times 2$  Hadamard matrix given by

$$\mathbf{H}_2 = \frac{1}{\sqrt{2}} \begin{bmatrix} 1 & 1 \\ 1 & -1 \end{bmatrix}. \tag{8.4-2}$$

		Sign Changes
$\mathbf{H}_4 = \frac{1}{2}$	$\begin{bmatrix} 1 & 1 & 1 & 1 \\ 1 & -1 & 1 & -1 \\ 1 & 1 & -1 & -1 \\ 1 & -1 & -1 & 1 \end{bmatrix}$	0 3 1 2

		Sign Changes
$\mathbf{H}_8 = \frac{1}{2\sqrt{2}}$	$\begin{bmatrix} 1 & 1 & 1 & 1 & 1 & 1 & 1 & 1 \\ 1 & -1 & 1 & -1 & 1 & -1 & 1 & -1 \\ 1 & 1 & -1 & -1 & 1 & 1 & -1 & -1 \\ 1 & -1 & -1 & 1 & 1 & -1 & -1 & 1 \\ \hline 1 & 1 & 1 & 1 & -1 & -1 & -1 & -1 \\ 1 & -1 & 1 & -1 & -1 & 1 & -1 & 1 \\ 1 & 1 & -1 & -1 & -1 & -1 & 1 & 1 \\ 1 & -1 & -1 & 1 & -1 & 1 & 1 & -1 \end{bmatrix}$	0 7 3 4 1 6 2 5

**FIGURE 8.4-1.** Nonordered Hadamard matrices of size 4 and 8.

It is known that if a Hadamard matrix of size  $N$  exists ( $N > 2$ ), then  $N = 0$  modulo 4 (22). The existence of a Hadamard matrix for every value of  $N$  satisfying this requirement has not been shown, but constructions are available for nearly all permissible values of  $N$  up to 200. The simplest construction is for a Hadamard matrix of size  $N = 2n$ , where  $n$  is an integer. In this case, if  $\mathbf{H}_N$  is a Hadamard matrix of size  $N$ , the matrix

$$\mathbf{H}_{2N} = \frac{1}{\sqrt{2}} \begin{bmatrix} \mathbf{H}_N & \mathbf{H}_N \\ \mathbf{H}_N & -\mathbf{H}_N \end{bmatrix} \tag{8.4-3}$$

is a Hadamard matrix of size  $2N$ . Figure 8.4-1 shows Hadamard matrices of size 4 and 8 obtained by the construction of Eq. 8.4-3.

Harmuth (25) has suggested a frequency interpretation for the Hadamard matrix generated from the core matrix of Eq. 8.4-3; the number of sign changes along each row of the Hadamard matrix divided by 2 is called the *sequency* of the row. It is pos-

sible to construct a Hadamard matrix of order  $N = 2^n$  whose number of sign changes per row increases from 0 to  $N - 1$ . This attribute is called the *sequency property* of the unitary matrix.

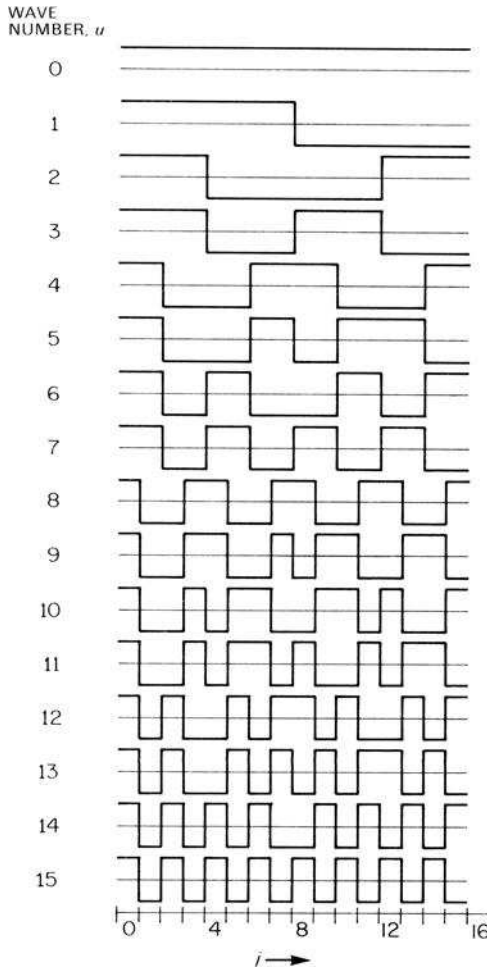
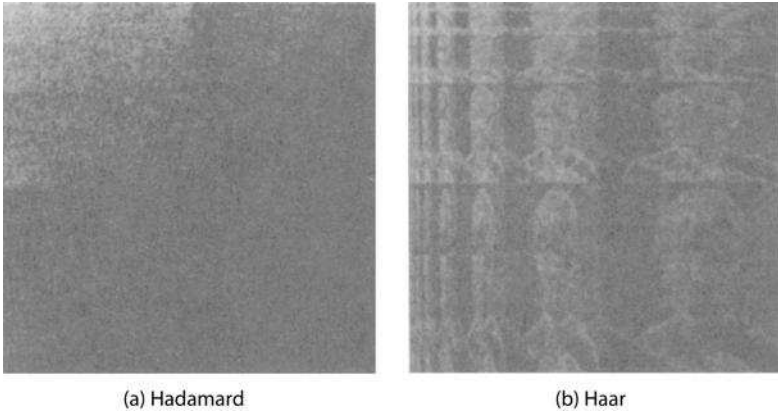


FIGURE 8.4-2. Hadamard transform basis functions,  $N = 16$ .

The rows of the Hadamard matrix of Eq. 8.4-3 can be considered to be samples of rectangular waves with a subperiod of  $1/N$  units. These continuous functions are called *Walsh functions* (26). In this context, the Hadamard matrix merely performs the decomposition of a function by a set of rectangular waveforms rather than the sine-cosine waveforms with the Fourier transform. A series formulation exists for the Hadamard transform (23).

Hadamard transform basis functions for the ordered transform with  $N = 16$  are shown in Figure 8.4-2. The ordered Hadamard transform of the test image is shown in Figure 8.4-3a.



**FIGURE 8.4-3.** Hadamard and Haar transforms of the `smpte_girl_luma` image, log magnitude displays.

### 8.4.2. Haar Transform

The *Haar transform* (1,26,27) is derived from the *Haar matrix*. The following are  $4 \times 4$  and  $8 \times 8$  orthonormal Haar matrices:

$$\mathbf{H}_4 = \frac{1}{2} \begin{bmatrix} 1 & 1 & 1 & 1 \\ 1 & 1 & -1 & -1 \\ \sqrt{2} & -\sqrt{2} & 0 & 0 \\ 0 & 0 & \sqrt{2} & -\sqrt{2} \end{bmatrix} \tag{8.4-4}$$

$$\mathbf{H}_8 = \frac{1}{\sqrt{8}} \begin{bmatrix} 1 & 1 & 1 & 1 & 1 & 1 & 1 & 1 \\ 1 & 1 & 1 & 1 & -1 & -1 & -1 & -1 \\ \sqrt{2} & \sqrt{2} & -\sqrt{2} & -\sqrt{2} & 0 & 0 & 0 & 0 \\ 0 & 0 & 0 & 0 & \sqrt{2} & \sqrt{2} & -\sqrt{2} & -\sqrt{2} \\ 2 & -2 & 0 & 0 & 0 & 0 & 0 & 0 \\ 0 & 0 & 2 & -2 & 0 & 0 & 0 & 0 \\ 0 & 0 & 0 & 0 & 2 & -2 & 0 & 0 \\ 0 & 0 & 0 & 0 & 0 & 0 & 2 & -2 \end{bmatrix}. \tag{8.4-5}$$

Extensions to higher-order Haar matrices follow the structure indicated by Eqs. 8.4-4 and 8.4-5. Figure 8.4-4 is a plot of the Haar basis functions for  $N = 16$ .

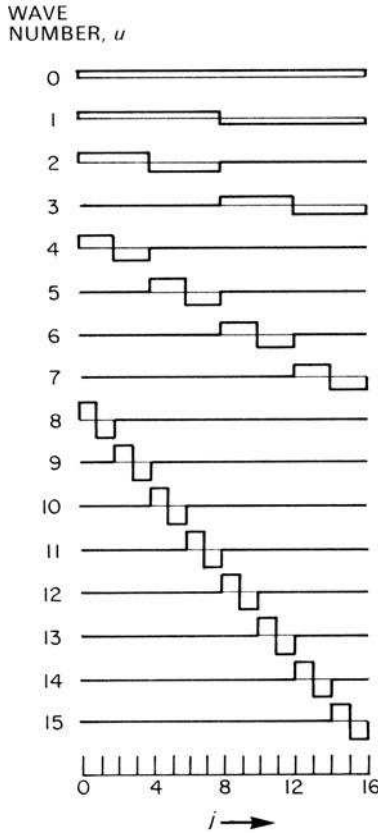


FIGURE 8.4-4. Haar transform basis functions,  $N = 16$ .

The Haar transform can be computed recursively (29) using the following  $N \times N$  recursion matrix

$$\mathbf{R}_N = \begin{bmatrix} \mathbf{V}_N \\ \mathbf{W}_N \end{bmatrix} \tag{8.4-6}$$

where  $\mathbf{V}_N$  is a  $N/2 \times N$  scaling matrix and  $\mathbf{W}_N$  is a  $N/2 \times N$  wavelet matrix defined as

$$\mathbf{V}_N = \frac{1}{\sqrt{2}} \begin{bmatrix} 1 & 1 & 0 & 0 & 0 & 0 & \cdots & 0 & 0 & 0 & 0 \\ 0 & 0 & 1 & 1 & 0 & 0 & \cdots & 0 & 0 & 0 & 0 \\ 0 & 0 & 0 & 0 & 0 & 0 & \cdots & 1 & 1 & 0 & 0 \\ 0 & 0 & 0 & 0 & 0 & 0 & \cdots & 0 & 0 & 1 & 1 \end{bmatrix} \tag{8.4-7a}$$

$$\mathbf{W}_N = \frac{1}{\sqrt{2}} \begin{bmatrix} 1 & -1 & 0 & 0 & 0 & 0 & \dots & 0 & 0 & 0 & 0 \\ 0 & 0 & 1 & -1 & 0 & 0 & \dots & 0 & 0 & 0 & 0 \\ & & \vdots & & & & & & \vdots & & \\ 0 & 0 & 0 & 0 & 0 & 0 & \dots & 1 & -1 & 0 & 0 \\ 0 & 0 & 0 & 0 & 0 & 0 & \dots & 0 & 0 & 1 & -1 \end{bmatrix}. \quad (8.4-7b)$$

The elements of the rows of  $\mathbf{V}_N$  are called *first-level scaling signals*, and the elements of the rows of  $\mathbf{W}_N$  are called *first-level Haar wavelets* (29).

The first-level Haar transform of a  $N \times 1$  vector  $\mathbf{f}$  is

$$\mathbf{f}_1 = \mathbf{R}_N \mathbf{f} = [\mathbf{a}_1 | \mathbf{d}_1]^T \quad (8.4-8)$$

where

$$\mathbf{a}_1 = \mathbf{V}_N \mathbf{f} \quad (8.4-9a)$$

$$\mathbf{d}_1 = \mathbf{W}_N \mathbf{f}. \quad (8.4-9b)$$

The vector  $\mathbf{a}_1$  represents the running average or *trend* of the elements of  $\mathbf{f}$ , and the vector  $\mathbf{d}_1$  represents the running fluctuation of the elements of  $\mathbf{f}$ . The next step in the recursion process is to compute the second-level Haar transform from the trend part of the first-level transform and concatenate it with the first-level fluctuation vector. This results in

$$\mathbf{f}_2 = [\mathbf{a}_2 | \mathbf{d}_2 | \mathbf{d}_1]^T \quad (8.4-10)$$

where

$$\mathbf{a}_2 = \mathbf{V}_{N/2} \mathbf{a}_1 \quad (8.4-11a)$$

$$\mathbf{d}_2 = \mathbf{W}_{N/2} \mathbf{a}_1 \quad (8.4-11b)$$

are  $N/4 \times 1$  vectors. The process continues until the full transform

$$\mathbf{f} \equiv \mathbf{f}_n = [\mathbf{a}_n | \mathbf{d}_n | \mathbf{d}_{n-1} | \dots | \mathbf{d}_1]^T \quad (8.4-12)$$

is obtained where  $N = 2^n$ . It should be noted that the intermediate levels are unitary transforms.

The Haar transform can be likened to a sampling process in which rows of the transform matrix sample an input data sequence with finer and finer resolution increasing in powers of 2. In image processing applications, the Haar transform provides a transform domain in which a type of differential energy is concentrated in localized regions.

### 8.4.3. Daubechies Transforms

Daubechies (30) has discovered a class of transforms that utilize running averages and running differences of the elements of a vector, as with the Haar transform. The difference between the Haar and Daubechies transforms is that the averages and differences are grouped in four or more elements.

The *Daubechies transform* of support four, called *Daub4*, can be defined in a manner similar to the Haar recursive generation process. The first-level scaling and wavelet matrices are defined as

$$\mathbf{V}_N = \begin{bmatrix} \alpha_1 & \alpha_2 & \alpha_3 & \alpha_4 & 0 & 0 & \dots & 0 & 0 & 0 & 0 \\ 0 & 0 & \alpha_1 & \alpha_2 & \alpha_3 & \alpha_4 & \dots & 0 & 0 & 0 & 0 \\ \vdots & \vdots & \vdots & \vdots & \vdots & \vdots & & \vdots & \vdots & \vdots & \vdots \\ 0 & 0 & 0 & 0 & 0 & 0 & \dots & \alpha_1 & \alpha_2 & \alpha_3 & \alpha_4 \\ \alpha_3 & \alpha_4 & 0 & 0 & 0 & 0 & \dots & 0 & 0 & \alpha_1 & \alpha_2 \end{bmatrix} \tag{8.4-13a}$$

$$\mathbf{W}_N = \begin{bmatrix} \beta_1 & \beta_2 & \beta_3 & \beta_4 & 0 & 0 & \dots & 0 & 0 & 0 & 0 \\ 0 & 0 & \beta_1 & \beta_2 & \beta_3 & \beta_4 & \dots & 0 & 0 & 0 & 0 \\ \vdots & \vdots & \vdots & \vdots & \vdots & \vdots & & \vdots & \vdots & \vdots & \vdots \\ 0 & 0 & 0 & 0 & 0 & 0 & \dots & \beta_1 & \beta_2 & \beta_3 & \beta_4 \\ \beta_3 & \beta_4 & 0 & 0 & 0 & 0 & \dots & 0 & 0 & \beta_1 & \beta_2 \end{bmatrix} \tag{8.4-13b}$$

where

$$\alpha_1 = -\beta_4 = \frac{1 + \sqrt{3}}{4\sqrt{2}} \tag{8.4-14a}$$

$$\alpha_2 = \beta_3 = \frac{3 + \sqrt{3}}{4\sqrt{2}} \tag{8.4-14b}$$

$$\alpha_3 = -\beta_2 = \frac{3 - \sqrt{3}}{4\sqrt{2}} \tag{8.4-14c}$$

$$\alpha_4 = \beta_1 = \frac{1 - \sqrt{3}}{4\sqrt{2}} \tag{8.4-14d}$$

In Eqs. 8.4-13a and 8.4-13b, the row-to-row shift is by two elements, and the last two scale factors wrap around on the last rows. Following the recursion process of the Haar transform results in the Daub4 transform final stage:

$$\mathbf{f} \equiv \mathbf{f}_n = [\mathbf{a}_n | \mathbf{d}_n | \mathbf{d}_{n-1} | \dots | \mathbf{d}_1]^T \tag{8.4-15}$$



Daubechies has extended the concept to higher degrees of support, 6, 8, 10, ..., by straightforward extension of Eq. 8.4-13 (29). Daubechies also has also constructed another family of wavelets, called *coiflets*, after a suggestion of Coifman (29). Section 8.6 generalizes the development of Daubechies transforms to a class of wavelet transforms, which are based upon sub-band coding.

### 8.5. KARHUNEN–LOEVE TRANSFORM

Techniques for transforming continuous signals into a set of uncorrelated representational coefficients were originally developed by Karhunen (31) and Loeve (32). Hotelling (33) has been credited (34) with the conversion procedure that transforms discrete signals into a sequence of uncorrelated coefficients. However, most of the literature in the field refers to both discrete and continuous transformations as either a *Karhunen–Loeve transform* or an *eigenvector transform*.

The Karhunen–Loeve transformation is a transformation of the general form

$$\mathcal{F}(u, v) = \sum_{j=0}^{N-1} \sum_{k=0}^{N-1} F(j, k)A(j, k; u, v) \tag{8.5-1}$$

for which the kernel  $A(j, k; u, v)$  satisfies the equation

$$\lambda(u, v)A(j, k; u, v) = \sum_{j'=0}^{N-1} \sum_{k'=0}^{N-1} K_F(j, k; j', k')A(j', k'; u, v) \tag{8.5-2}$$

where  $K_F(j, k; j', k')$  denotes the covariance function of the image array and  $\lambda(u, v)$  is a constant for fixed  $(u, v)$ . The set of functions defined by the kernel are the eigenfunctions of the covariance function, and  $\lambda(u, v)$  represents the eigenvalues of the covariance function. It is usually not possible to express the kernel in explicit form.

If the covariance function is separable such that

$$K_F(j, k; j', k') = K_C(j, j')K_R(k, k') \tag{8.5-3}$$

then the Karhunen–Loeve kernel is also separable and

$$A(j, k; u, v) = A_C(u, j)A_R(v, k). \tag{8.5-4}$$

The row and column kernels satisfy the equations

$$\lambda_R(u)A_R(v, k) = \sum_{k'=0}^{N-1} K_R(k, k')A_R(v, k') \tag{8.5-5a}$$

$$\lambda_C(v)A_C(u, j) = \sum_{j'=0}^{N-1} K_C(j, j')A_C(u, j'). \tag{8.5-5b}$$

In the special case in which the covariance matrix is of separable first-order Markov process form, the eigenfunctions can be written in explicit form (35,36).

If the image array and transformed image array are expressed in vector form, the Karhunen-Loeve transform pairs are

$$\mathbf{f} = \mathbf{A}\mathbf{f} \tag{8.5-6}$$

$$\mathbf{f} = \mathbf{A}^T\mathbf{f}. \tag{8.5-7}$$

The transformation matrix  $\mathbf{A}$  satisfies the relation

$$\mathbf{A}\mathbf{K}_f = \mathbf{\Lambda}\mathbf{A} \tag{8.5-8}$$

where  $\mathbf{K}_f$  is the covariance matrix of  $\mathbf{f}$ ,  $\mathbf{A}$  is a matrix whose rows are eigenvectors of  $\mathbf{K}_f$ , and  $\mathbf{\Lambda}$  is a diagonal matrix of the form

$$\mathbf{\Lambda} = \begin{bmatrix} \lambda(1) & 0 & \dots & 0 \\ 0 & \lambda(2) & & \vdots \\ \vdots & & \dots & 0 \\ 0 & \dots & 0 & \lambda(N^2) \end{bmatrix}. \tag{8.5-9}$$

If  $\mathbf{K}_f$  is of separable form, then

$$\mathbf{A} = \mathbf{A}_C \otimes \mathbf{A}_R \tag{8.5-10}$$

where  $\mathbf{A}_R$  and  $\mathbf{A}_C$  satisfy the relations

$$\mathbf{A}_R\mathbf{K}_R = \mathbf{\Lambda}_R\mathbf{A}_R \tag{8.5-11a}$$

$$\mathbf{A}_C\mathbf{K}_C = \mathbf{\Lambda}_C\mathbf{A}_C \tag{8.5-11b}$$

and  $\lambda(w) = \lambda_R(v)\lambda_C(u)$  for  $u, v = 1, 2, \dots, N$ .

Figure 8.5-1 is a plot of the Karhunen-Loeve basis functions for a one-dimensional Markov process with adjacent element correlation  $\rho = 0.9$ .

The Karhunen-Loeve transform previously developed in this section applies to a transform of spatial data. The concept applies also to a transform across spectral bands of images or a transform of a temporal sequence of correlated images. Equation 3.4-22a defines the K-L transform of a *RGB* color image. If the number of spectral bands or the number of temporal images is large, brute force computation of the K-L transform may become very time consuming. Levy and Lindenbaum (37) have developed a fast sequential K-L transform algorithm based upon the *Singular Value*

*Decomposition* (SVD) of the transform matrix. See Appendix A1.2 for a definition of the SVD.

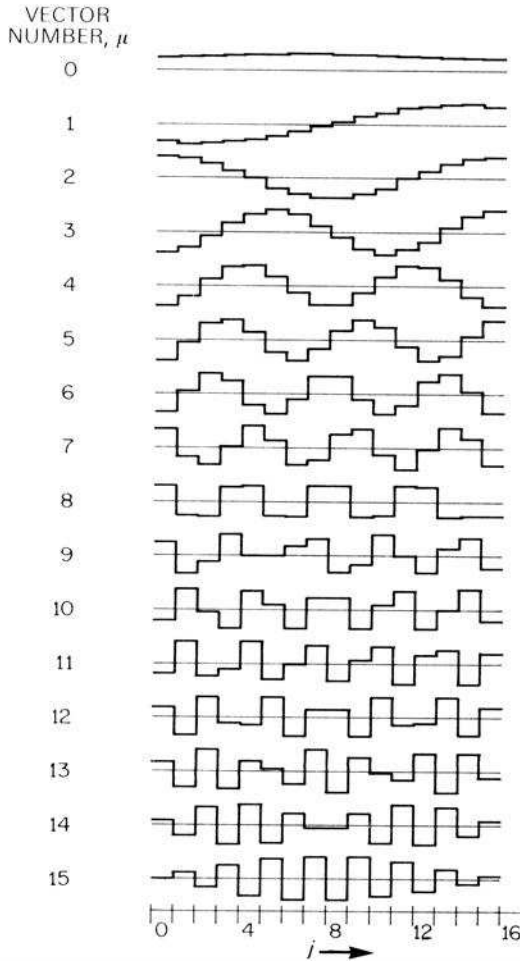


**FIGURE 8.5-1.** Karhunen–Loeve transform basis functions,  $N = 16$ .

### 8.6. WAVELET TRANSFORMS

A discrete Wavelet Transform (DWT) is a member of a class of transforms based upon a family of transformation kernels, which employ expansions of small duration waves called *wavelets* (29,38). Figure 8.6-1 shows a comparison between a one-dimensional continuous wave and a wavelet  $\psi(t)$ , which is a basis function called a *mother wavelet*.

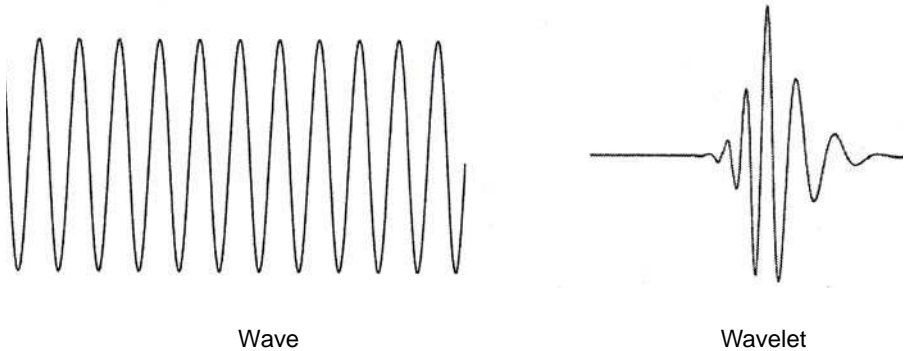


**FIGURE 8.6-1.** Continuous one-dimensional wave and wavelet.

The Continuous Wavelet Transform (CWT) of a continuous, one-dimensional signal  $x(t)$  is defined as (29,38)

$$y(\tau, s) = \frac{1}{\sqrt{s}} \int x(t) \psi\left(\frac{t-\tau}{s}\right) dt. \tag{8.6-1}$$

In this equation,  $\tau$  represents a translation (time shifting) of the mother wavelet and  $s$  is scaling parameter (dilation or compression) of the mother wavelet. The scale parameter  $s$  is inversely related to the frequency of  $x(t)$ . Large scale values (low frequencies) dilate the signal, while small scale values (high frequencies) compress the signal, and provide global information about it. The wavelet transform of Eq. 8.6-1 is a convolution of a signal and its basis function.

As noted in Eq. 8.6-1, the CWT is dependent upon the structure of the mother wavelet chosen for analysis as well as the translation and scaling factors. As a consequence, it is not possible to formulate the CWT by a pair of forward and inverse transforms, as is possible for unitary transforms.

A wavelet series can be obtained by straight forward sampling of the CWT. However, this approach is not computationally efficient. Mallat (39) has developed an efficient Discrete Wavelet Transform (DWT), which is based upon sub-band coding. It can be computed by successive low pass and high pass filtering of a discrete time domain signal as shown in Figure 8.6-2 for three transformation stages or levels. In

the literature, this decomposition is called a Mallat tree decomposition. In the figure, the signal is denoted by the sequence  $x(n)$  where  $n$  is an integer. The low-pass filter impulse response array is  $h_L$  and the high pass filter impulse response array is  $h_H$ . At each level of the decomposition, a high-pass filter produces detail data  $d(n)$  while the low-pass filter, associated with scaling, produces coarse approximation data  $a(n)$ . At each level, each half band filter produces a signal spanning half its frequency band. This permits subsampling by a factor of two (all even numbered samples are deleted, as indicated by the down arrow) without any loss of information. The filtering and decimation process is continued until a desired result is achieved. For a 512 point signal, the maximum number of levels is nine.

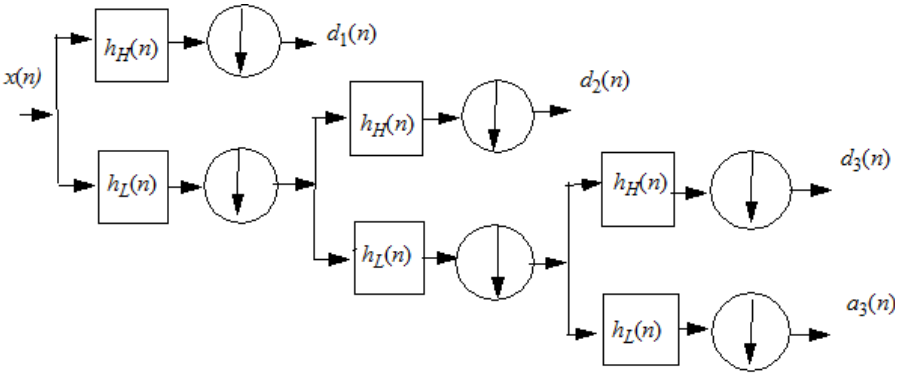


Figure 8.6-2. Three-level wavelet decomposition of a one-dimensional signal.

Figure 8.6-3 describes the reconstruction process of the three-level wavelet decomposition. The approximation and detail coefficients at each level are upsampled by a factor of two (zeros are interspersed between adjacent samples.) At each

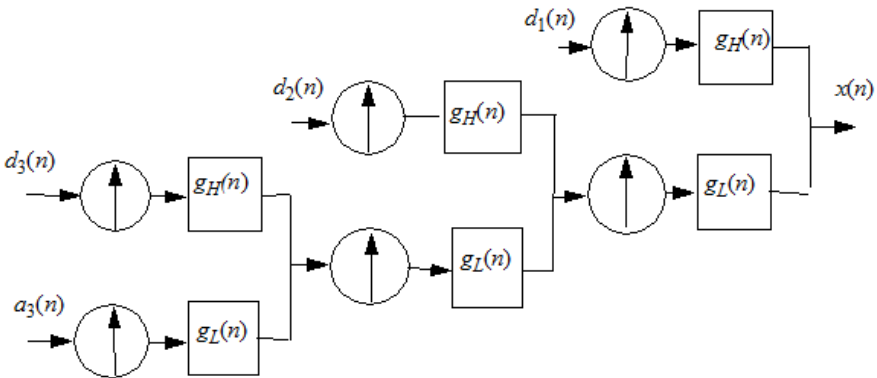


Figure 8.6-3. Three-level wavelet reconstruction of a one-dimensional signal.

level, the upsampled signals are convolved with high-pass and low-pass filters with impulse response arrays  $g_H(n)$  and  $g_L(n)$ , respectively, and added together. The process is continued until the original signal is obtained. It should be noted that the number of levels processed can be terminated before the decomposition limit is reached.

The decomposition (analysis) and reconstruction (synthesis) high-pass and low-pass filters of Figures 8.6-2 and 8.6-3 are not necessarily the same in some DWT applications. To achieve perfect reconstruction, the analysis and synthesis filters have to satisfy certain orthogonality conditions (38).

A two-dimensional DWT can be achieved by wavelet transforming an image array along its rows, and then transforming along the columns of the previous result (40, p 246). This is possible because the wavelet function is orthogonally separable in the same sense as the transformation kernel of a Fourier transform. Figure 8.6-4 contains a block diagram of the first level, two-dimensional decomposition. In this figure, the array coordinates  $(m, n)$  follow the matrix notation of an image array.  $W^A(j+1, m, n)$  represents the approximation image array from the previous level,  $W^A(j, m, n)$  represents the present approximation array and  $W^H$ ,  $W^V$ ,  $W^D$  are the horizontal, vertical and diagonal detail coefficients. In order to avoid border distortions between adjacent image quadrants, it is necessary to pad each quadrant array by a mirror reflection of length and width of one-half the convolution array size.

Figure 8.6-5 shows the first level decomposition of a  $256 \times 256$  image using  $2 \times 1$  and  $1 \times 2$  Haar wavelet impulse response arrays  $[0.707 \ 0.707]$  and  $[-0.707 \ 0.707]$ . The upper left corner approximation array is the source for the next decomposition level.

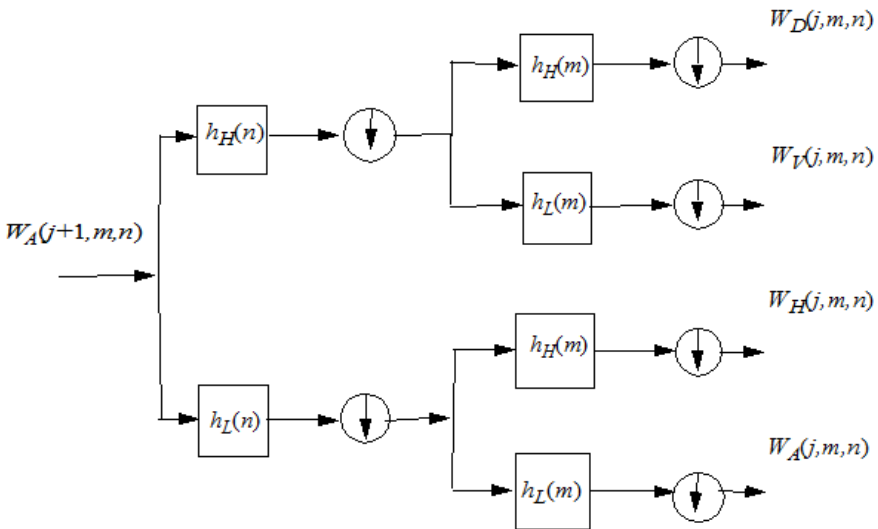


Figure 8.6-4. First-level wavelet decomposition of a two-dimensional signal.

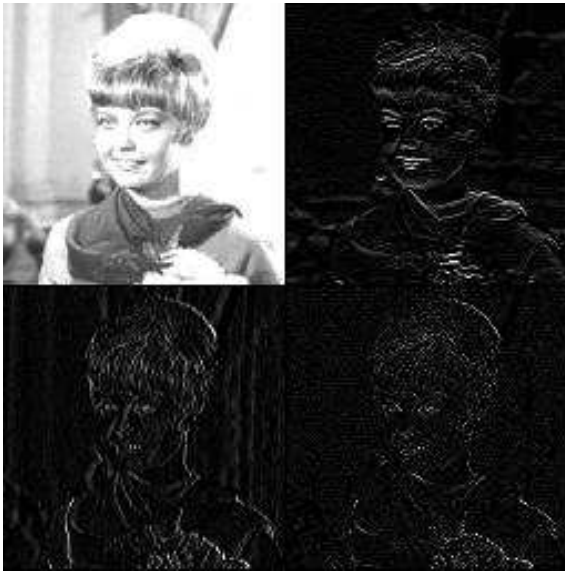


Figure 8.6-5. First level decomposition of the `smpte_girl_luma` image.

### 8.7. UNITARY AND WAVELET TRANSFORM EXERCISES

E8.1 Develop a program that generates the Fourier transform log magnitude ordered display of Figure 8.2-4d for the `smpte_girl_luma` image. Steps:

- (a) Display the source monochrome image.
- (b) Scale the source image to unit amplitude.
- (c) Perform a two-dimensional Fourier transform on the unit amplitude source image with the ordered display option.
- (d) Scale the log magnitude according to Eq. 8.2-9 where  $a = 1.0$  and  $b = 100.0$ .
- (e) Display the Fourier transformed image.

The PIKS API executable `example_transform_fourier` performs this exercise.

E8.2 Develop a program that generates the Hartley transform log magnitude ordered display of Figure 8.3-2c for the `smpte_girl_luma` image by manipulation of the Fourier transform coefficients of the image. Steps:

- (a) Display the source monochrome image.
- (b) Scale the source image to unit amplitude.

- (c) Perform a two-dimensional Fourier transform on the unit amplitude source image with the dc term at the origin option.
- (d) Extract the Hartley components from the Fourier components.
- (e) Scale the log magnitude according to Eq. 8.2-9 where  $a = 1.0$  and  $b = 100.0$ .
- (f) Display the Hartley transformed image.

The PIKS API executable `example_transform_hartley` performs this exercise.

E8.3 Develop a program that generates the Hadamard transform in  $8 \times 8$  pixel blocks for the `smpte_girl_luma` image. Steps:

- (a) Display the source monochrome image.
- (b) Scale the source image to unit amplitude.
- (c) Perform a two-dimensional Hadamard transform in  $8 \times 8$  pixel blocks on the unit amplitude source image.
- (d) Display the Hadamard transformed image.

The PIKS API executable `example_transform_hadamard` performs this exercise.

E8.4 Develop a program that generates the Haar wavelet transform for the `smpte_girl_luma` image following Figure 8.6-4. Steps:

- (a) Display the source monochrome image.
- (b) Create the Haar low-pass filter impulse array as  $[0.707 \ 0.707]$
- (c) Create the Haar high-pass filter impulse array as  $[-0.707 \ 0.707]$
- (d) Convolve the rows of the source image with the high-pass filter and subsample each row by 2.
- (e) Convolve the rows of the source image with the low-pass filter and subsample each row by 2.
- (f) Convolve the columns of the upper path array with the high-pass filter and subsample each column by 2 to produce the array  $W^D(j, m, n)$ .
- (g) Convolve the columns of the upper path array with the low-pass filter and subsample each column by 2 to produce the array  $W^V(j, m, n)$ .
- (h) Convolve the columns of the lower path array with the high-pass filter and subsample each column by 2 to produce the array  $W^H(j, m, n)$ .
- (i) Convolve the columns of the lower path array with the low-pass filter and subsample each column by 2 to produce the array  $W^A(j, m, n)$ .
- (j) Compose the four output arrays into a destination image.
- (k) Display the scaled magnitude of the destination image.



The PIKS API executable `example_haar_wavelet` performs this exercise.

## REFERENCES

1. H. C. Andrews, *Computer Techniques in Image Processing*, Academic Press, New York, 1970.
2. H. C. Andrews, "Two Dimensional Transforms," in *Topics in Applied Physics: Picture Processing and Digital Filtering*, Vol. 6, T. S. Huang, Ed., Springer-Verlag, New York, 1975.
3. R. Bellman, *Introduction to Matrix Analysis, Second Edition*, Society for Industrial and Applied Mathematics, Philadelphia, 1997.
4. H. C. Andrews and K. Caspari, "A Generalized Technique for Spectral Analysis," *IEEE Trans. Computers*, **C-19**, 1, January 1970, 16–25.
5. J. W. Cooley and J. W. Tukey, "An Algorithm for the Machine Calculation of Complex Fourier Series," *Mathematics of Computation* **19**, 90, April 1965, 297–301.
6. *IEEE Trans. Audio and Electroacoustics*, Special Issue on Fast Fourier Transforms, **AU-15**, 2, June 1967.
7. W. T. Cochran et al., "What Is the Fast Fourier Transform?" *Proc. IEEE*, **55**, 10, 1967, 1664–1674.
8. *IEEE Trans. Audio and Electroacoustics*, Special Issue on Fast Fourier Transforms, **AU-17**, 2, June 1969.
9. J. W. Cooley, P. A. Lewis and P. D. Welch, "Historical Notes on the Fast Fourier Transform," *Proc. IEEE*, **55**, 10, October 1967, 1675–1677.
10. B. O. Brigham and R. B. Morrow, "The Fast Fourier Transform," *IEEE Spectrum*, **4**, 12, December 1967, 63–70.
11. C. S. Burrus and T. W. Parks, *DFT/FFT and Convolution Algorithms*, Wiley-Interscience, New York, 1985.
12. N. Ahmed, T. Natarajan and K. R. Rao, "On Image Processing and a Discrete Cosine Transform," *IEEE Trans. Computers*, **C-23**, 1, January 1974, 90–93.
13. W. B. Pennebaker and J. L. Mitchell, *JPEG Still Image Data Compression Standard*, Van Nostrand Reinhold, New York, 1993.
14. K. R. Rao and J. J. Hwang, *Techniques and Standards for Image, Video and Audio Coding*, Prentice Hall, Upper Saddle River, NJ, 1996.
15. R. W. Means, H. J. Whitehouse and J. M. Speiser, "Television Encoding Using a Hybrid Discrete Cosine Transform and a Differential Pulse Code Modulator in Real Time," *Proc. National Telecommunications Conference*, San Diego, CA, December 1974, 61–66.
16. W. H. Chen, C. Smith and S. C. Fralick, "Fast Computational Algorithm for the Discrete Cosine Transform," *IEEE Trans. Communications.*, **COM-25**, 9, September 1977, 1004–1009.
17. A. K. Jain, "A Fast Karhunen–Loeve Transform for Finite Discrete Images," *Proc. National Electronics Conference*, Chicago, October 1974, 323–328.
18. A. K. Jain and E. Angel, "Image Restoration, Modeling and Reduction of Dimensionality," *IEEE Trans. Computers*, **C-23**, 5, May 1974, 470–476.
19. R. M. Bracewell, "The Discrete Hartley Transform," *J. Optical Society of America*, **73**, 12, December 1983, 1832–1835.

20. R. M. Bracewell, *The Hartley Transform*, Oxford University Press, Oxford, 1986.
21. R. V. L. Hartley, "A More Symmetrical Fourier Analysis Applied to Transmission Problems," *Proc. IRE*, **30**, 1942, 144–150.
22. J. E. Whelchel, Jr. and D. F. Guinn, "The Fast Fourier–Hadamard Transform and Its Use in Signal Representation and Classification," *EASCON 1968 Convention Record*, 1968, 561–573.
23. W. K. Pratt, H. C. Andrews and J. Kane, "Hadamard Transform Image Coding," *Proc. IEEE*, **57**, 1, January 1969, 58–68.
24. J. Hadamard, "Resolution d'une question relative aux determinants," *Bull. Sciences Mathematiques*, Ser. 2, 17, Part I, 1893, 240–246.
25. H. F. Harmuth, *Transmission of Information by Orthogonal Functions*, Springer-Verlag, New York, 1969.
26. J. L. Walsh, "A Closed Set of Orthogonal Functions," *American J. Mathematics*, **45**, 1923, 5–24.
27. A. Haar, "Zur Theorie der Orthogonalen-Funktionen," *Mathematische Annalen*, **5**, 1955, 17–31.
28. K. R. Rao, M. A. Narasimhan and K. Revuluri, "Image Data Processing by Hadamard–Haar Transforms," *IEEE Trans. Computers*, **C-23**, 9, September 1975, 888–896.
29. J. S. Walker, *A Primer on Wavelets and Their Scientific Applications*, Chapman & Hall/CRC Press, Boca Raton, FL, 1999.
30. I. Daubechies, *Ten Lectures on Wavelets*, SIAM, Philadelphia, 1992.
31. H. Karhunen, 1947, English translation by I. Selin, "On Linear Methods in Probability Theory," Doc. T-131, Rand Corporation, Santa Monica, CA, August 11, 1960.
32. M. Loeve, *Fonctions Aldatories de Seconde Ordre*, Hermann, Paris, 1948.
33. H. Hotelling, "Analysis of a Complex of Statistical Variables into Principal Components," *J. Educational Psychology*, **24**, 1933, 417–441, 498–520.
34. P. A. Wintz, "Transform Picture Coding," *Proc. IEEE*, **60**, 7, July 1972, 809–820.
35. W. D. Ray and R. M. Driver, "Further Decomposition of the Karhunen–Loeve Series Representation of a Stationary Random Process," *IEEE Trans. Information Theory*, **IT-16**, 6, November 1970, 663–668.
36. W. K. Pratt, "Generalized Wiener Filtering Computation Techniques," *IEEE Trans. Computers*, **C-21**, 7, July 1972, 636–641.
37. A. Levy and M. Lindenbaum, "Sequential Karhunen–Loeve Basis Extraction and Its Application to Images," *IEEE Trans. Image Processing*, **9**, 8, August 2000, 1371–1374.
38. T. Acharya and A. K. Ray, *Image Processing Principles and Applications*, Wiley-Interscience, New York, 2005.
39. S. Mallat, "A Theory for Multiresolution Signal Decomposition: The Wavelet Representation," *IEEE Trans. Pattern Analysis and Machine Intelligence*, **11**, 7, July 1989, 674–693.
40. R. C. Gonzalez, R. E. Woods and S. L. Eddins, *Digital Image Processing Using MATLAB*, Pearson Prentice Hall, Upper Saddle River, NJ, 2004.



---

# 9

---

## LINEAR PROCESSING TECHNIQUES

Most discrete image processing computational algorithms are linear in nature; an output image array is produced by a weighted linear combination of elements of an input array. The popularity of linear operations stems from the relative simplicity of spatial linear processing as opposed to spatial nonlinear processing. However, for image processing operations on large image arrays, conventional linear processing is often computationally infeasible without efficient computational algorithms. This chapter considers indirect computational techniques that permit more efficient linear processing than by conventional methods.

### 9.1. TRANSFORM DOMAIN PROCESSING

Two-dimensional linear transformations have been defined in Section 5.2 in series form as

$$P(m_1, m_2) = \sum_{n_1=1}^{N_1} \sum_{n_2=1}^{N_2} F(n_1, n_2) T(n_1, n_2; m_1, m_2) \quad (9.1-1)$$

and defined in vector form as

$$\mathbf{p} = \mathbf{Tf}. \quad (9.1-2)$$

It will now be demonstrated that such linear transformations can often be computed more efficiently by an indirect computational procedure utilizing two-dimensional unitary transforms than by the direct computation indicated by Eq. 9.1-1 or 9.1-2.

Figure 9.1-1 is a block diagram of the indirect computation technique called *generalized linear filtering* (1). In the process, the input array  $F(n_1, n_2)$  undergoes a two-dimensional unitary transformation, resulting in an array of transform coefficients  $\mathcal{F}(u_1, u_2)$ . Next, a linear combination of these coefficients is taken according to the general relation

$$\tilde{\mathcal{F}}(w_1, w_2) = \sum_{u_1=1}^{M_1} \sum_{u_2=1}^{M_2} \mathcal{F}(u_1, u_2) \mathcal{F}(u_1, u_2; w_1, w_2) \tag{9.1-3}$$

where  $\mathcal{F}(u_1, u_2; w_1, w_2)$  represents the linear filtering transformation function. Finally, an inverse unitary transformation is performed to reconstruct the processed array  $P(m_1, m_2)$ . If this computational procedure is to be more efficient than direct computation by Eq. 9.1-1, it is necessary that fast computational algorithms exist for the unitary transformation, and also the kernel  $\mathcal{F}(u_1, u_2; w_1, w_2)$  must be reasonably sparse; that is, it must contain many zero elements, which can be passed over in the computation.

The generalized linear filtering process can also be defined in terms of vector-space computations as shown in Figure 9.1-2. For notational simplicity, let  $N_1 = N_2 = N$  and  $M_1 = M_2 = M$ . Then, the generalized linear filtering process can be described by the equations

$$f = [A_{N^2}]f \tag{9.1-4a}$$

$$\tilde{f} = Tf \tag{9.1-4b}$$

$$p = [A_{M^2}]^{-1}\tilde{f}. \tag{9.1-4c}$$

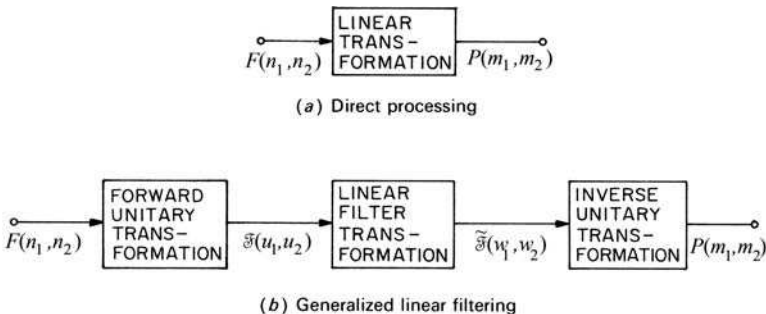
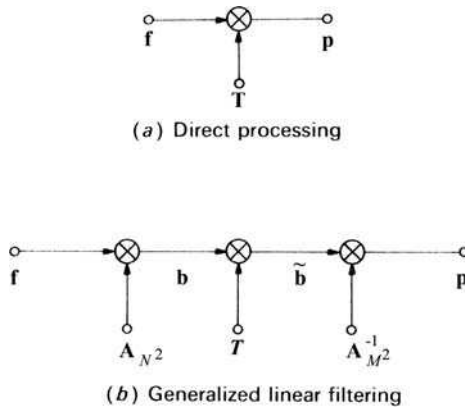


FIGURE 9.1-1. Direct processing and generalized linear filtering; series formulation.



**FIGURE 9.1-2.** Direct processing and generalized linear filtering; vector formulation.

where  $\mathbf{A}_{N^2}$  is a  $N^2 \times N^2$  unitary transform matrix,  $T$  is a  $M^2 \times N^2$  linear filtering transform operation and  $\mathbf{A}_{M^2}$  is a  $M^2 \times M^2$  unitary transform matrix. From Eq. 9.1-4, the input and output vectors are related by

$$\mathbf{p} = [\mathbf{A}_{M^2}]^{-1} T [\mathbf{A}_{N^2}] \mathbf{f}. \tag{9.1-5}$$

Therefore, equating Eqs. 9.1-2 and 9.1-5 yields the relations between  $T$  and  $\mathbf{T}$  given by

$$\mathbf{T} = [\mathbf{A}_{M^2}]^{-1} T [\mathbf{A}_{N^2}] \tag{9.1-6a}$$

$$T = [\mathbf{A}_{M^2}] \mathbf{T} [\mathbf{A}_{N^2}]^{-1}. \tag{9.1-6b}$$

If direct processing is employed, computation by Eq. 9.1-2 requires  $k_p(M^2N^2)$  operations, where  $0 \leq k_p \leq 1$  is a measure of the sparseness of  $T$ . With the generalized linear filtering technique, the number of operations required for a given operator are:

- Forward transform:*  $N^4$  by direct transformation  
 $2N^2 \log_2 N$  by fast transformation
- Filter multiplication:*  $k_T M^2 N^2$
- Inverse transform:*  $M^4$  by direct transformation  
 $2M^2 \log_2 M$  by fast transformation

where  $0 \leq k_T \leq 1$  is a measure of the sparseness of  $T$ . If  $k_T = 1$  and direct unitary transform computation is performed, it is obvious that the generalized linear filtering concept is not as efficient as direct computation. However, if fast transform algorithms, similar in structure to the fast Fourier transform, are employed, generalized linear filtering will be more efficient than direct processing if the sparseness index satisfies the inequality

$$k_T < k_P - \frac{2}{M^2} \log_2 N - \frac{2}{N^2} \log_2 M. \tag{9.1-7}$$

In many applications,  $T$  will be sufficiently sparse such that the inequality will be satisfied. In fact, unitary transformation tends to decorrelate the elements of  $T$  causing  $T$  to be sparse. Also, it is often possible to render the filter matrix sparse by setting small-magnitude elements to zero without seriously affecting computational accuracy (1).

In subsequent sections, the structure of superposition and convolution operators is analyzed to determine the feasibility of generalized linear filtering in these applications.

## 9.2. TRANSFORM DOMAIN SUPERPOSITION

The superposition operations discussed in Chapter 7 can often be performed more efficiently by transform domain processing rather than by direct processing. Figure 9.2-1a and b illustrate block diagrams of the computational steps involved in direct finite area or sampled image superposition. In Figure 9.2-1d and e, an alternative form of processing is illustrated in which a unitary transformation operation is performed on the data vector  $\mathbf{f}$  before multiplication by a finite area filter matrix  $\mathbf{D}$  or sampled image filter matrix  $\mathbf{B}$ . An inverse transform reconstructs the output vector. From Figure 9.2-1, for finite-area superposition, because

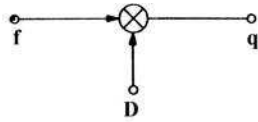
$$\mathbf{q} = \mathbf{D}\mathbf{f} \tag{9.2-1a}$$

and

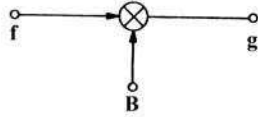
$$\mathbf{q} = [\mathbf{A}_{M^2}]^{-1} \mathbf{D} [\mathbf{A}_{N^2}] \mathbf{f} \tag{9.2-1b}$$

then clearly the finite-area filter matrix may be expressed as

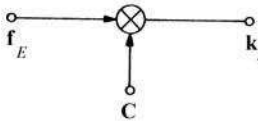
$$\mathbf{D} = [\mathbf{A}_{M^2}] \mathbf{D} [\mathbf{A}_{N^2}]^{-1}. \tag{9.2-2a}$$



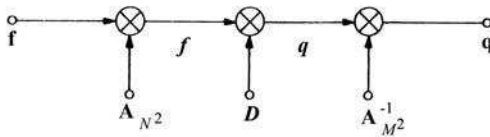
(a) Finite area superposition



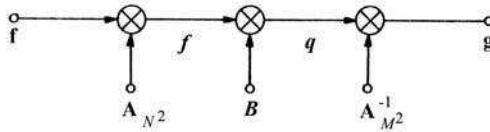
(b) Sampled image superposition



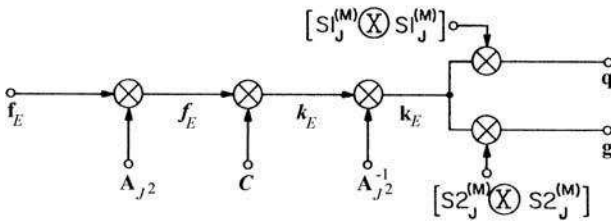
(c) Circulant superposition



(d) Transform domain finite area superposition



(e) Transform domain sampled image superposition



(f) Transform domain circulant superposition

FIGURE 9.2-1. Data and transform domain superposition.



Similarly,

$$\mathbf{B} = [\mathbf{A}_{M^2}] \mathbf{B} [\mathbf{A}_{N^2}]^{-1}. \tag{9.2-2b}$$

If direct finite-area superposition is performed, the required number of computational operations is approximately  $N^2 L^2$ , where  $L$  is the dimension of the impulse response matrix. In this case, the sparseness index of  $\mathbf{D}$  is

$$k_D = \left(\frac{L}{N}\right)^2. \tag{9.2-3a}$$

Direct sampled image superposition requires on the order of  $M^2 L^2$  operations, and the corresponding sparseness index of  $\mathbf{B}$  is

$$k_B = \left(\frac{L}{M}\right)^2. \tag{9.2-3b}$$

Figure 9.2-1f is a block diagram of a system for performing circulant superposition by transform domain processing. In this case, the input vector  $\mathbf{k}_E$  is the *extended data vector*, obtained by embedding the input image array  $F(n_1, n_2)$  in the left corner of a  $J \times J$  array of zeros and then column scanning the resultant matrix. Following the same reasoning as above, it is seen that

$$\mathbf{k}_E = \mathbf{C} \mathbf{f}_E = [\mathbf{A}_{J^2}]^{-1} \mathbf{C} [\mathbf{A}_{J^2}] \mathbf{f} \tag{9.2-4a}$$

and hence,

$$\mathbf{C} = [\mathbf{A}_{J^2}] \mathbf{C} [\mathbf{A}_{J^2}]^{-1}. \tag{9.2-4b}$$

As noted in Chapter 7, the equivalent output vector for either finite-area or sampled image superposition can be obtained by an element selection operation on  $\mathbf{k}_E$ . For finite-area superposition,

$$\mathbf{q} = [\mathbf{S1}_J^{(M)} \otimes \mathbf{S1}_J^{(M)}] \mathbf{k}_E \tag{9.2-5a}$$

and for sampled image superposition

$$\mathbf{g} = [\mathbf{S2}_J^{(M)} \otimes \mathbf{S2}_J^{(M)}] \mathbf{k}_E. \tag{9.2-5b}$$

Also, the matrix form of the output for finite-area superposition is related to the extended image matrix  $\mathbf{K}_E$  by

$$\mathbf{Q} = [\mathbf{S1}_J^{(M)}] \mathbf{K}_E [\mathbf{S1}_J^{(M)}]^T. \tag{9.2-6a}$$

For sampled image superposition,

$$\mathbf{G} = [\mathbf{S}\mathbf{2}_J^{(M)}] \mathbf{K}_E [\mathbf{S}\mathbf{2}_J^{(M)}]^T \tag{9.2-6b}$$

The number of computational operations required to obtain  $\mathbf{k}_E$  by transform domain processing is given by the previous analysis for  $M = N = J$ :

$$\begin{aligned} \text{Direct transformation} & \quad 3J^4 \\ \text{Fast transformation:} & \quad J^2 + 4J^2 \log_2 J \end{aligned}$$

If  $C$  is sparse, many of the  $J^2$  filter multiplication operations can be avoided.

From the discussion above, it can be seen that the secret to computationally efficient superposition is to select a transformation that possesses a fast computational algorithm that results in a relatively sparse transform domain superposition filter matrix. As an example, consider finite-area convolution performed by Fourier domain processing (2,3). Referring to Figure 9.2-1, let

$$\mathbf{A}_{K^2} = \mathbf{A}_K \otimes \mathbf{A}_K \tag{9.2-7}$$

where

$$\mathbf{A}_K = \left[ \frac{1}{\sqrt{K}} W^{(x-1)(y-1)} \right] \quad \text{with } W \equiv \exp \left\{ \frac{-2\pi i}{K} \right\}$$

for  $x, y = 1, 2, \dots, K$ . Also, let  $\mathbf{h}_E^{(K)}$  denote the  $K^2 \times 1$  vector representation of the extended spatially invariant impulse response array of Eq. 7.3-2 for  $J = K$ . The Fourier transform of  $\mathbf{h}_E^{(K)}$  is denoted as

$$\mathbf{h}_E^{(K)} = [\mathbf{A}_{K^2}] \mathbf{h}_E^{(K)} \tag{9.2-8}$$

These transform components are then inserted as the diagonal elements of a  $K^2 \times K^2$  matrix

$$\mathbf{H}^{(K)} = \text{diag}[\mathbf{h}_E^{(K)}(1), \dots, \mathbf{h}_E^{(K)}(K^2)] \tag{9.2-9}$$

Then, it can be shown, after considerable manipulation, that the Fourier transform domain superposition matrices for finite area and sampled image convolution can be written as (4)

$$\mathbf{D} = \mathbf{H}^{(M)} [\mathbf{P}_D \otimes \mathbf{P}_D] \tag{9.2-10}$$

for  $N = M - L + 1$  and

$$\mathbf{B} = [\mathbf{P}_B \otimes \mathbf{P}_B] \mathbf{H}^{(N)} \tag{9.2-11}$$

where  $N = M + L + 1$  and

$$P_D(u, v) = \frac{1}{\sqrt{M}} \frac{1 - W_M^{-(u-1)(L-1)}}{1 - W_M^{-(u-1)} - W_N^{-(v-1)}} \tag{9.2-12a}$$

$$P_B(u, v) = \frac{1}{\sqrt{N}} \frac{1 - W_N^{-(v-1)(L-1)}}{1 - W_M^{-(u-1)} - W_N^{-(v-1)}}. \tag{9.2-12b}$$

Thus, the transform domain convolution operators each consist of a scalar weighting matrix  $H^{(K)}$  and an interpolation matrix ( $\mathbf{P} \otimes \mathbf{P}$ ) that performs the dimensionality conversion between the  $N^2$ -element input vector and the  $M^2$ -element output vector. Generally, the interpolation matrix is relatively sparse, and therefore, transform domain superposition is quite efficient.

Now, consider circulant area convolution in the transform domain. Following the previous analysis it is found (4) that the circulant area convolution filter matrix reduces to a scalar operator

$$\mathbf{C} = \mathbf{JH}^{(J)}. \tag{9.2-13}$$

Thus, as indicated in Eqs. 9.2-10 to 9.2-13, the Fourier domain convolution filter matrices can be expressed in a compact closed form for analysis or operational storage. No closed-form expressions have been found for other unitary transforms.

Fourier domain convolution is computationally efficient because the convolution operator  $\mathbf{C}$  is a circulant matrix, and the corresponding filter matrix  $\mathbf{C}$  is of diagonal form. Actually, as can be seen from Eq. 9.1-6, the Fourier transform basis vectors are eigenvectors of  $\mathbf{C}$  (5). This result does not hold true for superposition in general, nor for convolution using other unitary transforms. However, in many instances, the filter matrices  $\mathbf{D}$ ,  $\mathbf{B}$  and  $\mathbf{C}$  are relatively sparse, and computational savings can often be achieved by transform domain processing.

Figure 9.2-2 shows the Fourier and Hadamard domain filter matrices for the three forms of convolution for a one-dimensional input vector and a Gaussian-shaped impulse response (6). As expected, the transform domain representations are much more sparse than the data domain representations. Also, the Fourier domain circulant convolution filter is seen to be of diagonal form. Figure 9.2-3 illustrates the structure of the three convolution matrices for two-dimensional convolution (4).

### 9.3. FAST FOURIER TRANSFORM CONVOLUTION

As noted previously, the equivalent output vector for either finite-area or sampled image convolution can be obtained by an element selection operation on the extended output vector  $\mathbf{k}_E$  for circulant convolution or its matrix counterpart  $\mathbf{K}_E$ .

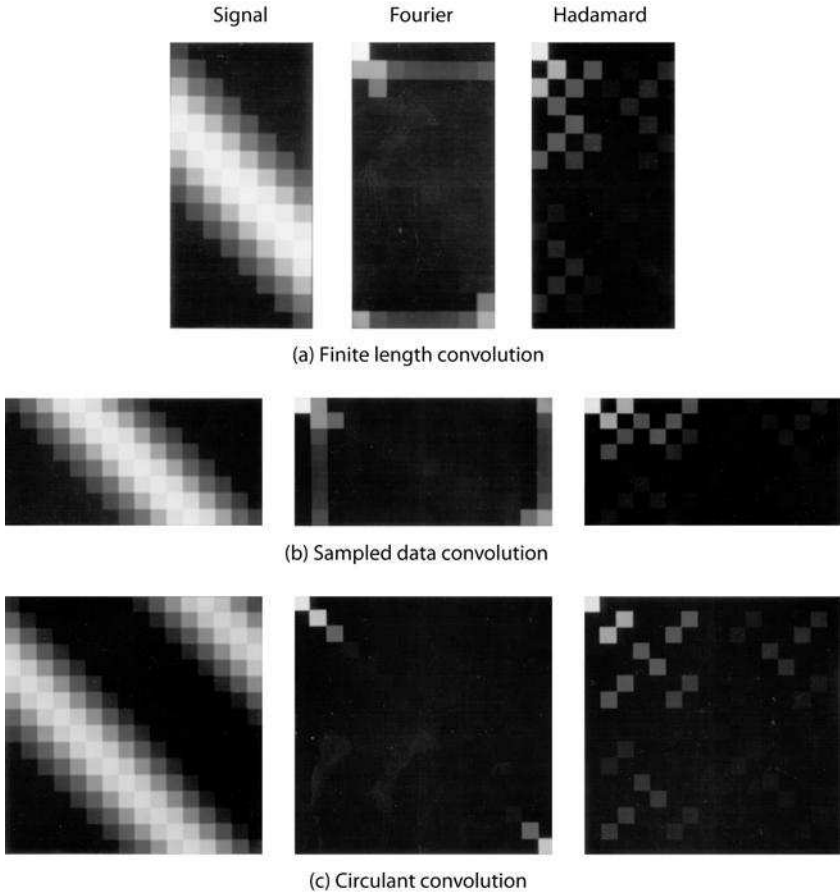


**FIGURE 9.2-2.** One-dimensional Fourier and Hadamard domain convolution matrices.

This result, combined with Eq. 9.2-13, leads to a particularly efficient means of convolution computation indicated by the following steps:

1. Embed the impulse response matrix in the upper left corner of an all-zero  $J \times J$  matrix,  $J \geq M$  for finite-area convolution or  $J \geq N$  for sampled infinite-area convolution, and take the two-dimensional Fourier transform of the extended impulse response matrix, giving

$$\mathbf{H}_E = \mathbf{A}_J \mathbf{H}_E \mathbf{A}_J^* \tag{9.3-1}$$

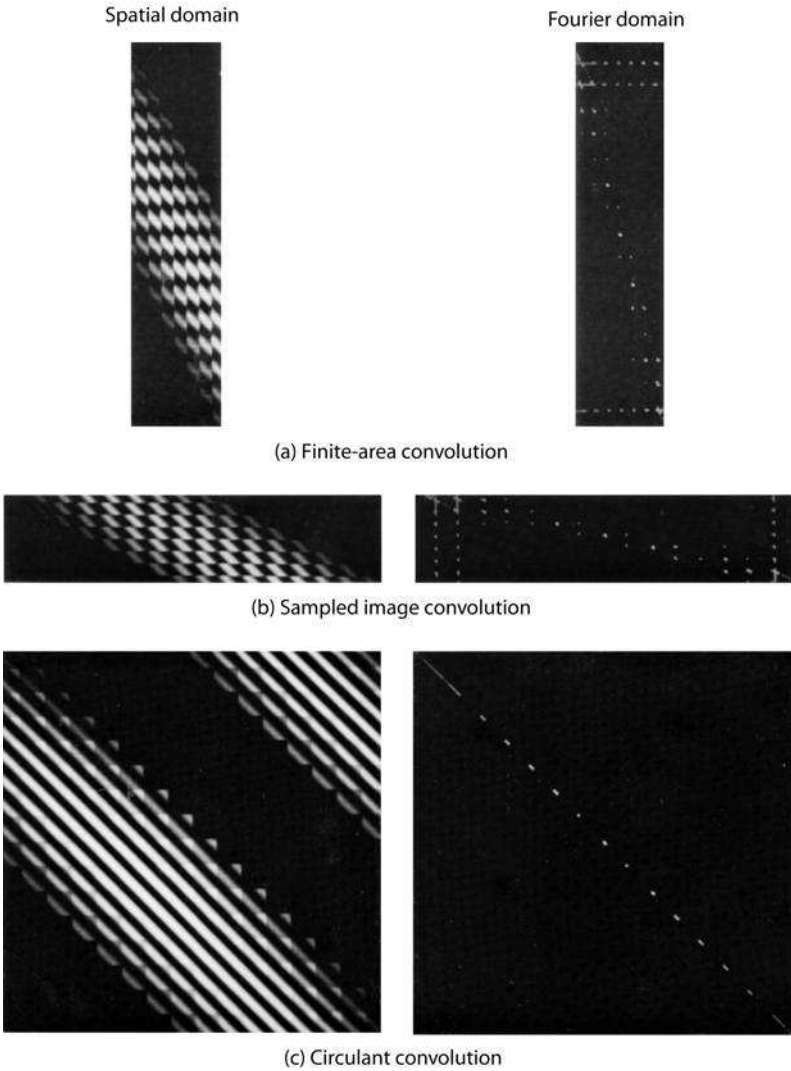


FIGURE 9.2-3. Two-dimensional Fourier domain convolution matrices.

2. Embed the input data array in the upper left corner of an all-zero  $J \times J$  matrix, and take the two-dimensional Fourier transform of the extended input data matrix to obtain

$$F_E = \mathbf{A}_J \mathbf{F}_E \mathbf{A}_J. \tag{9.3-2}$$

3. Perform the scalar multiplication

$$K_E(m, n) = JH_E(m, n)F_E(m, n) \tag{9.3-3}$$

where  $1 \leq m, n \leq J$ .

4. Take the inverse Fourier transform

$$\mathbf{K}_E = [\mathbf{A}_{J^2}]^{-1} \mathbf{H}_E [\mathbf{A}_{J^2}]^{-1}. \tag{9.3-4}$$

5. Extract the desired output matrix

$$\mathbf{Q} = [\mathbf{S1}_J^{(M)}] \mathbf{K}_E [\mathbf{S1}_J^{(M)}]^T \tag{9.3-5a}$$

or

$$\mathbf{G} = [\mathbf{S2}_J^{(M)}] \mathbf{K}_E [\mathbf{S2}_J^{(M)}]^T. \tag{9.3-5b}$$

It is important that the size of the extended arrays in steps 1 and 2 be chosen large enough to satisfy the inequalities indicated. If the computational steps are performed with  $J = N$ , the resulting output array, shown in Figure 9.3-1, will contain erroneous terms in a boundary region of width  $L - 1$  elements, on the top and left-hand side of the output field. This is the *wraparound error* associated with incorrect use of the Fourier domain convolution method. In addition, for finite area ( $D$ -type) convolution, the bottom and right-hand-side strip of output elements will be missing. If the computation is performed with  $J = M$ , the output array will be completely filled with the correct terms for  $D$ -type convolution. To force  $J = M$  for  $B$ -type convolution, it is necessary to truncate the bottom and right-hand side of the input array. As a consequence, the top and left-hand-side elements of the output array are erroneous.

Figure 9.3-2 illustrates the Fourier transform convolution process with proper zero padding. The example in Figure 9.3-3 shows the effect of no zero padding. In both examples, the image has been filtered using a  $11 \times 11$  uniform impulse response array. The source image of Figure 9.3-3 is  $512 \times 512$  pixels. The source image of Figure 9.3-2 is  $502 \times 502$  pixels. It has been obtained by truncating the bottom 10 rows and right 10 columns of the source image of Figure 9.3-3. Figure 9.3-4 shows computer printouts of the upper left corner of the processed images. Figure 9.3-4a is the result of finite-area convolution. The same output is realized in Figure 9.3-4b for proper zero padding. Figure 9.3-4c shows the wraparound error effect for no zero padding.

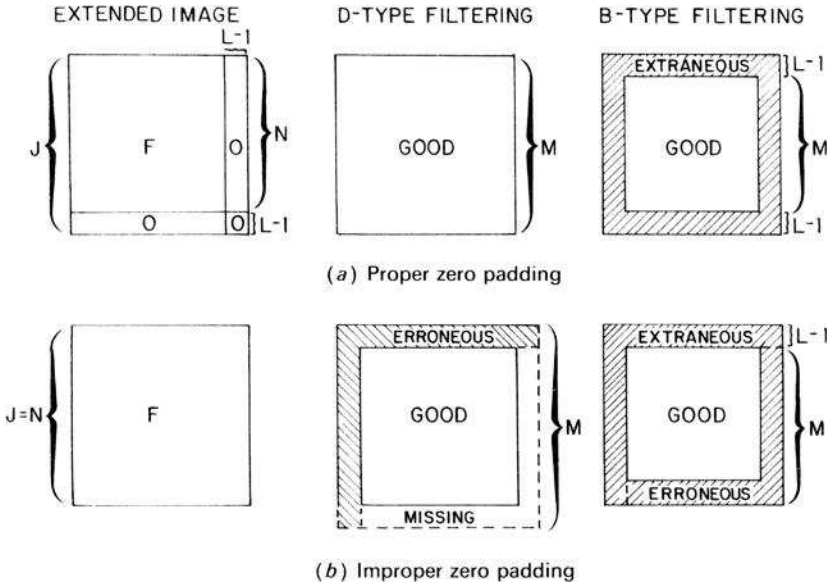
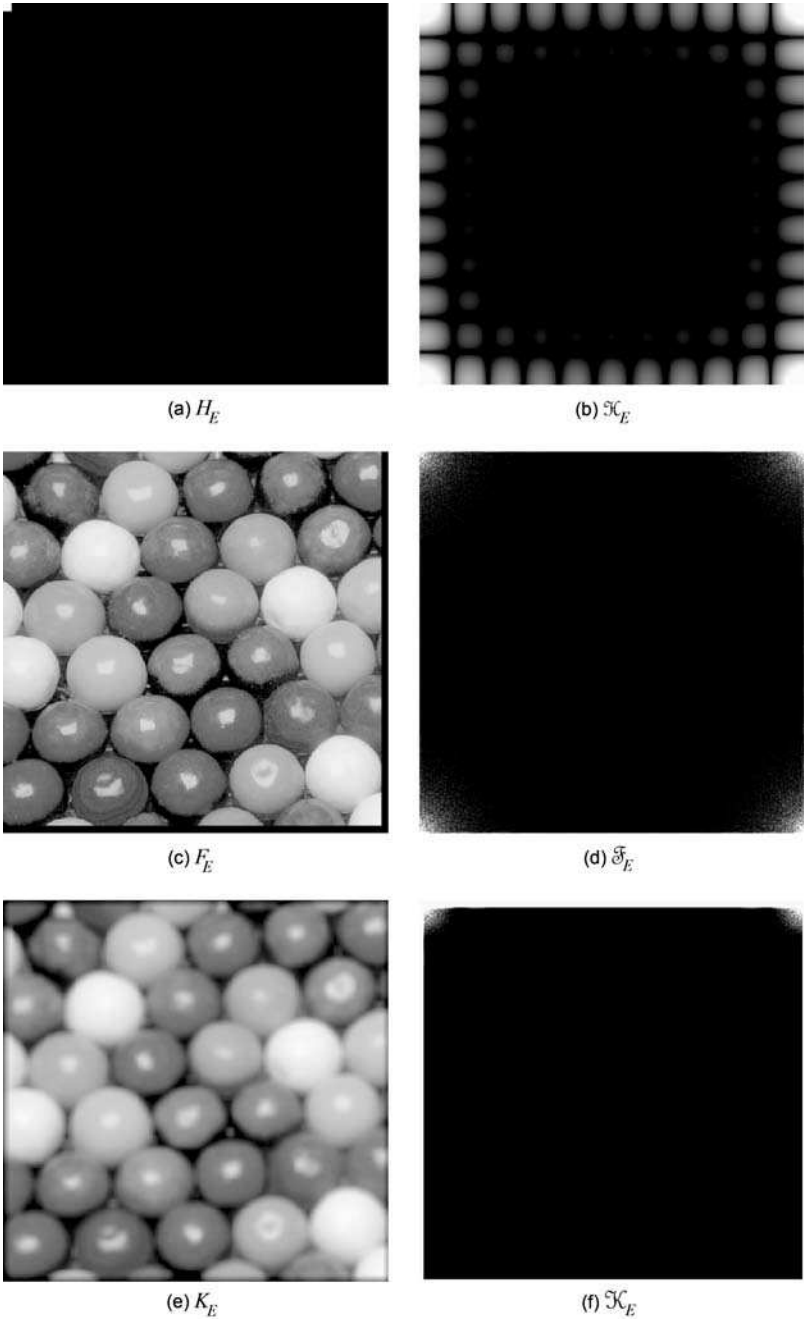


FIGURE 9.3-1. Wraparound error effects.

In many signal processing applications, the same impulse response operator is used on different data, and hence step 1 of the computational algorithm need not be repeated. The filter matrix  $H_E$  may be either stored functionally or indirectly as a computational algorithm. Using a fast Fourier transform algorithm, the forward and inverse transforms require on the order of  $2J^2 \log_2 J$  operations each. The scalar multiplication requires  $J^2$  operations, in general, for a total of  $J^2(1 + 4 \log_2 J)$  operations. For an  $N \times N$  input array, an  $M \times M$  output array and an  $L \times L$  impulse response array, finite-area convolution requires  $N^2 L^2$  operations, and sampled image convolution requires  $M^2 L^2$  operations. If the dimension of the impulse response  $L$  is sufficiently large with respect to the dimension of the input array  $N$ , Fourier domain convolution will be more efficient than direct convolution, perhaps by an order of magnitude or more. Figure 9.3-5 is a plot of  $L$  versus  $N$  for equality between direct and Fourier domain finite area convolution. The jaggedness of the plot, in this example, arises from discrete changes in  $J$  (64, 128, 256,...) as  $N$  increases.



**FIGURE 9.3-2.** Fourier transform convolution of the candy\_502\_1uma image with proper zero padding, clipped magnitude displays of Fourier images.



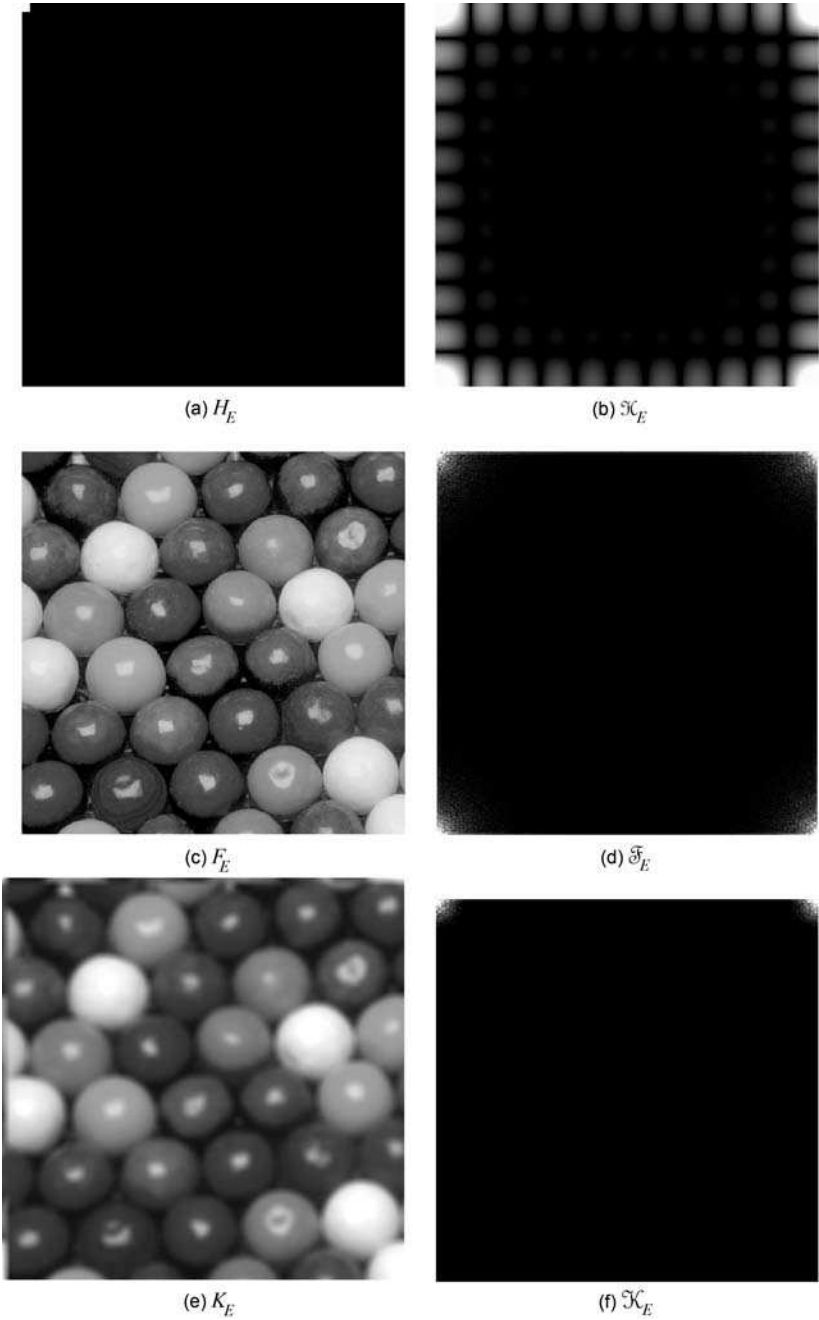


**FIGURE 9.3-3.** Fourier transform convolution of the candy\_512\_luma image with improper zero padding, clipped magnitude displays of Fourier images.

0.001	0.002	0.003	0.005	0.006	0.007	0.008	0.009	0.010	0.011	0.013	0.013	0.013	0.013	0.013
0.002	0.005	0.007	0.009	0.011	0.014	0.016	0.018	0.021	0.023	0.025	0.025	0.026	0.026	0.026
0.003	0.007	0.010	0.014	0.017	0.020	0.024	0.027	0.031	0.034	0.038	0.038	0.038	0.039	0.039
0.005	0.009	0.014	0.018	0.023	0.027	0.032	0.036	0.041	0.046	0.050	0.051	0.051	0.051	0.051
0.006	0.011	0.017	0.023	0.028	0.034	0.040	0.045	0.051	0.057	0.063	0.063	0.063	0.064	0.064
0.007	0.014	0.020	0.027	0.034	0.041	0.048	0.054	0.061	0.068	0.075	0.076	0.076	0.076	0.076
0.008	0.016	0.024	0.032	0.040	0.048	0.056	0.064	0.072	0.080	0.088	0.088	0.088	0.088	0.088
0.009	0.018	0.027	0.036	0.045	0.054	0.064	0.073	0.082	0.091	0.100	0.100	0.100	0.100	0.101
0.010	0.020	0.031	0.041	0.051	0.061	0.071	0.081	0.092	0.102	0.112	0.112	0.112	0.113	0.113
0.011	0.023	0.034	0.045	0.056	0.068	0.079	0.090	0.102	0.113	0.124	0.124	0.125	0.125	0.125
0.012	0.025	0.037	0.050	0.062	0.074	0.087	0.099	0.112	0.124	0.136	0.137	0.137	0.137	0.137
0.012	0.025	0.037	0.049	0.062	0.074	0.086	0.099	0.111	0.124	0.136	0.136	0.136	0.136	0.136
0.012	0.025	0.037	0.049	0.062	0.074	0.086	0.099	0.111	0.123	0.135	0.135	0.135	0.135	0.135
0.012	0.025	0.037	0.049	0.061	0.074	0.086	0.098	0.110	0.123	0.135	0.135	0.135	0.135	0.134
0.012	0.025	0.037	0.049	0.061	0.074	0.086	0.098	0.110	0.122	0.134	0.134	0.134	0.134	0.134

(a) Finite-area convolution

0.001	0.002	0.003	0.005	0.006	0.007	0.008	0.009	0.010	0.011	0.013	0.013	0.013	0.013	0.013
0.002	0.005	0.007	0.009	0.011	0.014	0.016	0.018	0.021	0.023	0.025	0.025	0.026	0.026	0.026
0.003	0.007	0.010	0.014	0.017	0.020	0.024	0.027	0.031	0.034	0.038	0.038	0.038	0.039	0.039
0.005	0.009	0.014	0.018	0.023	0.027	0.032	0.036	0.041	0.046	0.050	0.051	0.051	0.051	0.051
0.006	0.011	0.017	0.023	0.028	0.034	0.040	0.045	0.051	0.057	0.063	0.063	0.063	0.064	0.064
0.007	0.014	0.020	0.027	0.034	0.041	0.048	0.054	0.061	0.068	0.075	0.076	0.076	0.076	0.076
0.008	0.016	0.024	0.032	0.040	0.048	0.056	0.064	0.072	0.080	0.088	0.088	0.088	0.088	0.088
0.009	0.018	0.027	0.036	0.045	0.054	0.064	0.073	0.082	0.091	0.100	0.100	0.100	0.100	0.101
0.010	0.020	0.031	0.041	0.051	0.061	0.071	0.081	0.092	0.102	0.112	0.112	0.112	0.113	0.113
0.011	0.023	0.034	0.045	0.056	0.068	0.079	0.090	0.102	0.113	0.124	0.124	0.125	0.125	0.125
0.012	0.025	0.037	0.050	0.062	0.074	0.087	0.099	0.112	0.124	0.136	0.137	0.137	0.137	0.137
0.012	0.025	0.037	0.049	0.062	0.074	0.086	0.099	0.111	0.124	0.136	0.136	0.136	0.136	0.136
0.012	0.025	0.037	0.049	0.062	0.074	0.086	0.099	0.111	0.123	0.135	0.135	0.135	0.135	0.135
0.012	0.025	0.037	0.049	0.061	0.074	0.086	0.098	0.110	0.123	0.135	0.135	0.135	0.135	0.134
0.012	0.025	0.037	0.049	0.061	0.074	0.086	0.098	0.110	0.122	0.134	0.134	0.134	0.134	0.134

(b) Fourier transform convolution with proper zero padding

0.771	0.700	0.626	0.552	0.479	0.407	0.334	0.260	0.187	0.113	0.040	0.036	0.034	0.033	0.034
0.721	0.655	0.587	0.519	0.452	0.385	0.319	0.252	0.185	0.118	0.050	0.047	0.044	0.044	0.045
0.673	0.612	0.550	0.488	4.426	0.365	0.304	0.243	0.182	0.122	0.061	0.057	0.055	0.055	0.055
0.624	0.569	0.513	0.456	0.399	0.344	0.288	0.234	0.180	0.125	0.071	0.067	0.065	0.065	0.065
0.578	0.528	0.477	0.426	0.374	0.324	0.274	0.225	0.177	0.129	0.081	0.078	0.076	0.075	0.075
0.532	0.488	0.442	0.396	0.350	0.305	0.260	0.217	0.174	0.133	0.091	0.088	0.086	0.085	0.086
0.486	0.448	0.407	0.367	0.326	0.286	0.246	0.208	0.172	0.136	0.101	0.098	0.096	0.096	0.096
0.438	0.405	0.371	0.336	0.301	0.266	0.232	0.200	0.169	0.139	0.110	0.108	0.107	0.106	0.106
0.387	0.361	0.333	0.304	0.275	0.246	0.218	0.191	0.166	0.142	0.119	0.118	0.117	0.116	0.116
0.334	0.313	0.292	0.270	0.247	0.225	0.203	0.182	0.163	0.145	0.128	0.127	0.127	0.127	0.127
0.278	0.264	0.249	0.233	0.218	0.202	0.186	0.172	0.159	0.148	0.136	0.137	0.137	0.137	0.137
0.273	0.260	0.246	0.231	0.216	0.200	0.185	0.171	0.158	0.147	0.136	0.136	0.136	0.136	0.136
0.266	0.254	0.241	0.228	0.213	0.198	0.183	0.169	0.157	0.146	0.135	0.135	0.135	0.135	0.135
0.257	0.246	0.234	0.222	0.209	0.195	0.181	0.168	0.156	0.145	0.135	0.135	0.135	0.135	0.134
0.247	0.237	0.227	0.215	0.204	0.192	0.179	0.166	0.155	0.144	0.134	0.134	0.134	0.134	0.134

(c) Fourier transform convolution without zero padding

**FIGURE 9.3-4.** Wraparound error for Fourier transform convolution, upper left corner of processed image.

Fourier domain processing is more computationally efficient than direct processing for image convolution if the impulse response is sufficiently large. However, if the image to be processed is large, the relative computational advantage of Fourier domain processing diminishes. Also, there are attendant problems of computational accuracy with large Fourier transforms. Both difficulties can be alleviated by a

block-mode filtering technique in which a large image is separately processed in adjacent overlapped blocks (2, 7-9).

### 9.4 FOURIER TRANSFORM FILTERING

The discrete Fourier transform convolution processing algorithm of Section 9.3 is often utilized for computer simulation of continuous Fourier domain filtering. In this section, discrete Fourier transform filter design techniques are considered.

#### 9.4.1. Transfer Function Generation

The first step in the discrete Fourier transform filtering process is generation of the discrete domain transfer function. For simplicity, the following discussion is limited to one-dimensional signals. The extension to two dimensions is straightforward.

Consider a one-dimensional continuous signal  $f_C(x)$  of wide extent, which is band limited such that its Fourier transform  $f_C(\omega)$  is zero for  $|\omega|$  greater than a cutoff frequency  $\omega_0$ . This signal is to be convolved with a continuous impulse function  $h_C(x)$  whose transfer function  $h_C(\omega)$  is also band limited to  $\omega_0$ . From Chapter 1 it is known that the convolution can be performed either in the spatial domain by the operation

$$g_C(x) = \int_{-\infty}^{\infty} f_C(\alpha)h_C(x - \alpha) d\alpha \tag{9.4-1a}$$

or in the continuous Fourier domain by

$$g_C(x) = \frac{1}{2\pi} \int_{-\infty}^{\infty} f_C(\omega)h_C(\omega) \exp\{i\omega x\} d\omega \tag{9.4-1b}$$

Chapter 7 has presented techniques for the discretization of the convolution integral of Eq. 9.4-1. In this process, the continuous impulse response function  $h_C(x)$  must be truncated by spatial multiplication of a window function  $y(x)$  to produce the windowed impulse response

$$b_C(x) = h_C(x)y(x) \tag{9.4-2}$$

where  $y(x) = 0$  for  $|x| > T$ . The window function is designed to smooth the truncation effect. The resulting convolution integral is then approximated as

$$g_C(x) = \int_{x-T}^{x+T} f_C(\alpha)b_C(x - \alpha) d\alpha . \tag{9.4-3}$$

Next, the output signal  $g_C(x)$  is sampled over  $2J + 1$  points at a resolution  $\Delta = \pi/\omega_0$ , and the continuous integration is replaced by a quadrature summation at the same resolution  $\Delta$ , yielding the discrete representation

$$g_C(j\Delta) = \sum_{k=i-K}^{j+K} f_C(k\Delta)b_C[(j-k)\Delta] \tag{9.4-4}$$

where  $K$  is the nearest integer value of the ratio  $T/\Delta$ .

Computation of Eq. 9.4-4 by discrete Fourier transform processing requires formation of the discrete domain transfer function  $b_D(u)$ . If the continuous domain impulse response function  $h_C(x)$  is known analytically, the samples of the windowed impulse response function are inserted as the first  $L = 2K + 1$  elements of a  $J$ -element sequence and the remaining  $J - L$  elements are set to zero. Thus, let

$$b_D(p) = \underbrace{b_C(-K), \dots, b_C(0), \dots, b_C(K)}_{L \text{ terms}}, 0, \dots, 0 \tag{9.4-5}$$

where  $0 \leq p \leq P - 1$ . The terms of  $b_D(p)$  can be extracted from the continuous impulse response function  $h_C(x)$  and the window function by the sampling operation

$$b_D(p) = y(x)h_C(x)\delta(x - p\Delta). \tag{9.4-6}$$

The next step in the discrete Fourier transform convolution algorithm is to perform a discrete Fourier transform of  $b_D(p)$  over  $P$  points to obtain

$$\ell_D(u) = \frac{1}{\sqrt{P}} \sum_{p=1}^{P-1} b_D(p) \exp\left\{\frac{-2\pi i p u}{P}\right\} \tag{9.4-7}$$

where  $0 \leq u \leq P - 1$ .

If the continuous domain transfer function  $h_C(\omega)$  is known analytically, then  $\ell_D(u)$  can be obtained directly. It can be shown that

$$\ell_D(u) = \frac{1}{4\sqrt{P}\pi^2} \exp\left\{\frac{-i\pi(L-1)u}{P}\right\} \ell_C\left(\frac{2\pi u}{P\Delta}\right) \tag{9.4-8a}$$

$$\ell_D(P-u) = \ell_D^*(u) \tag{9.4-8b}$$

for  $u = 0, 1, \dots, P/2$ , where

$$\ell_C(\omega) = \ell_C(\omega) \otimes y(\omega) \tag{9.4-8c}$$

and  $y(\omega)$  is the continuous domain Fourier transform of the window function  $y(x)$ . If  $h_C(\omega)$  and  $y(\omega)$  are known analytically, then, in principle,  $h_C(\omega)$  can be obtained by analytically performing the convolution operation of Eq. 9.4-8c and evaluating the resulting continuous function at points  $2\pi u/P\Delta$ . In practice, the analytic convolution is often difficult to perform, especially in two dimensions. An alternative is to perform an analytic inverse Fourier transformation of the transfer function  $h_C(\omega)$  to obtain its continuous domain impulse response  $h_C(x)$  and then form  $h_D(u)$  from the steps of Eqs. 9.4-5 to 9.4-7. Still another alternative is to form  $h_D(u)$  from  $h_C(\omega)$  according to Eqs. 9.4-8a and 9.4-8b, take its discrete inverse Fourier transform, window the resulting sequence, and then form  $h_D(u)$  from Eq. 9.4-7.

### 9.4.2. Windowing Functions

The windowing operation performed explicitly in the spatial domain according to Eq. 9.4-6 or implicitly in the Fourier domain by Eq. 9.4-8 is absolutely imperative if the wraparound error effect described in Section 9.3 is to be avoided. A common mistake in image filtering is to set the values of the discrete impulse response function arbitrarily equal to samples of the continuous impulse response function. The corresponding extended discrete impulse response function will generally possess nonzero elements in each of its  $J$  elements. That is, the length  $L$  of the discrete impulse response embedded in the extended vector of Eq. 9.4-5 will implicitly be set equal to  $J$ . Therefore, all elements of the output filtering operation will be subject to wraparound error.

A variety of window functions have been proposed for discrete linear filtering (10–12). Several of the most common are listed in Table 9.4-1 and sketched in Figure 9.4-1. Figure 9.4-1 shows plots of the transfer functions of these window functions. The window transfer functions consist of a main lobe and side lobes whose peaks decrease in magnitude with increasing frequency. Examination of the structure of Figure 9.4-8 indicates that the main lobe causes a loss in frequency response over the signal passband from 0 to  $\omega_0$ , while the side lobes are responsible for an aliasing error because the windowed impulse response function  $h_C(\omega)$  is not band limited. A tapered window function reduces the magnitude of the side lobes and consequently attenuates the aliasing error, but the main lobe becomes wider, causing the signal frequency response within the passband to be reduced. A design trade-off must be made between these complementary sources of error. Both sources of degradation can be reduced by increasing the truncation length of the windowed impulse response, but this strategy will either result in a shorter length output sequence or an increased number of computational operations.

The window functions in Table 9.4-1 tend to over attenuate an image. It is common practice to stretch a window function such that the left and right sides extend  $L$  pixels and the window center is unity in value.

**TABLE 9.4-1. Window Functions<sup>a</sup>**

Function	Definition
Rectangular	$w(n) = 1 \quad 0 \leq n \leq L - 1$
Barlett (triangular)	$w(n) = \begin{cases} \frac{2n}{L-1} & 0 \leq n < \frac{L-1}{2} \\ 2 - \frac{2}{L-1} & \frac{L-1}{2} \leq n \leq L-1 \end{cases}$
Hanning	$w(n) = \frac{1}{2} \left( 1 - \cos \left\{ \frac{2\pi n}{L-1} \right\} \right) \quad 0 \leq n \leq L-1$
Hamming	$w(n) = 0.54 - 0.46 \cos \left\{ \frac{2\pi n}{L-1} \right\} \quad 0 \leq n \leq L-1$
Blackman	$w(n) = 0.42 - 0.5 \cos \left\{ \frac{2\pi n}{L-1} \right\} + 0.08 \cos \left\{ \frac{4\pi n}{L-1} \right\} \quad 0 \leq n \leq L-1$
Kaiser	$\frac{I_0 \left\{ \omega_a [((L-1)/2)^2 - [n - ((L-1)/2)]^2]^{1/2} \right\}}{I_0 \{ \omega_a [(L-1)/2] \}} \quad 0 \leq n \leq L-1$

<sup>a</sup> $I_0 \{ \cdot \}$  is the modified zeroth-order Bessel function of the first kind and  $\omega_a$  is a design parameter.

**9.4.3. Discrete Domain Transfer Functions**

In practice, it is common to define the discrete domain transform directly in the discrete Fourier transform frequency space. The following are definitions of several widely used transfer functions for a  $N \times N$  pixel image. Applications of these filters are presented in Chapter 10.

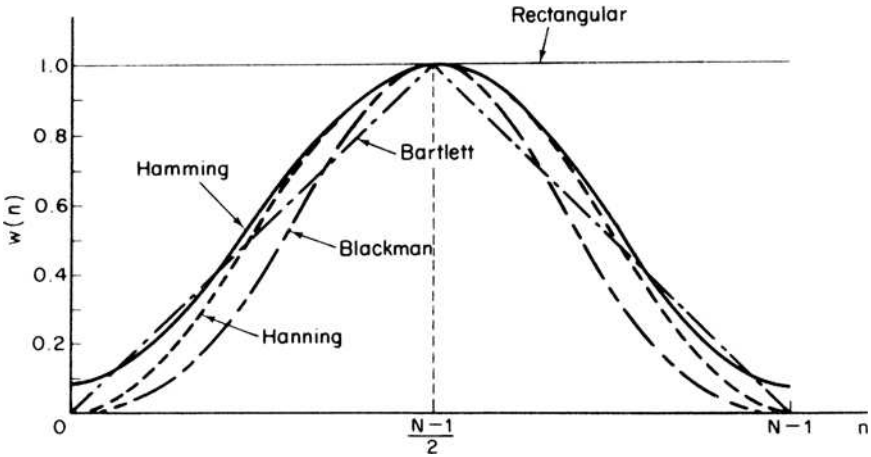


FIGURE 9.4-1. One-dimensional window functions.

**1. Zonal low-pass filter:**

$$\begin{aligned}
 \mathcal{H}(u, v) = 1 \quad & 0 \leq u \leq C-1 \quad \text{and } 0 \leq v \leq C-1 \\
 & 0 \leq u \leq C-1 \quad \text{and } N+1-C \leq v \leq N-1 \\
 & N+1-C \leq u \leq N-1 \quad \text{and } 0 \leq v \leq C-1 \\
 & N+1-C \leq u \leq N-1 \quad \text{and } N+1-C \leq v \leq N-1 \quad (9.4-9a)
 \end{aligned}$$

$$\mathcal{H}(u, v) = 0 \quad \text{otherwise} \quad (9.4-9b)$$

where  $C$  is the filter cutoff frequency for  $0 < C \leq 1 + N/2$ . Figure 9.4-3 illustrates the low-pass filter zones.

**2. Zonal high-pass filter:**

$$\mathcal{H}(0, 0) = 0 \quad (9.4-10a)$$

$$\begin{aligned}
 \mathcal{H}(u, v) = 0 \quad & 0 \leq u \leq C-1 \quad \text{and } 0 \leq v \leq C-1 \\
 & 0 \leq u \leq C-1 \quad \text{and } N+1-C \leq v \leq N-1 \\
 & N+1-C \leq u \leq N-1 \quad \text{and } 0 \leq v \leq C-1 \\
 & N+1-C \leq u \leq N-1 \quad \text{and } N+1-C \leq v \leq N-1 \quad (9.4-10b)
 \end{aligned}$$

$$\mathcal{H}(u, v) = 1 \quad \text{otherwise} \quad (9.4-10c)$$

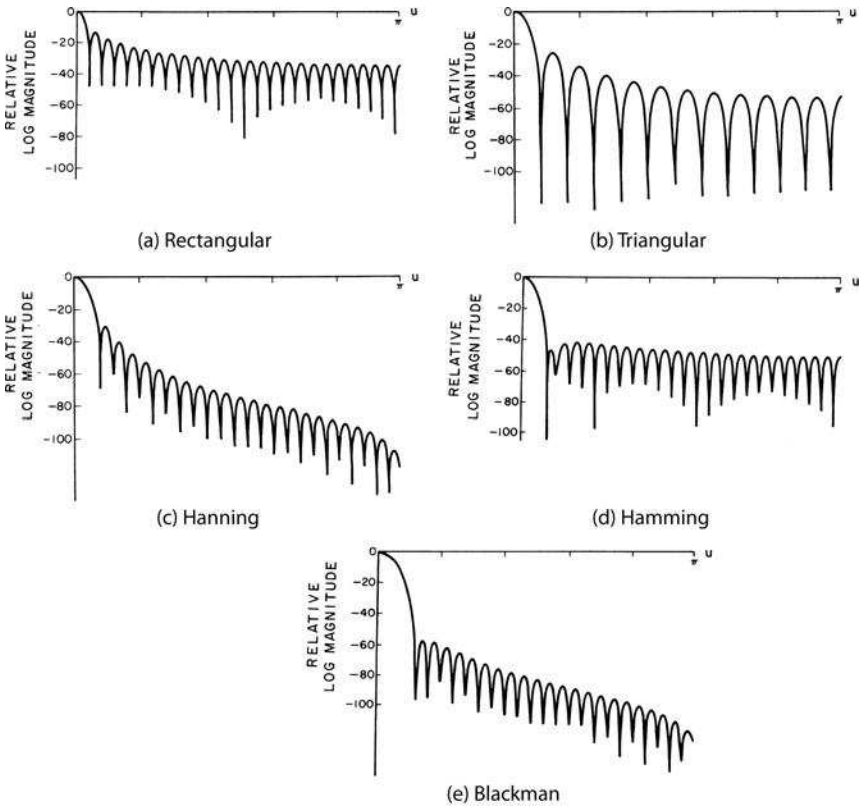


FIGURE 9.4-2. Transfer functions of one-dimensional window functions.

3. Gaussian filter:

$$\begin{aligned}
 \mathcal{H}(u, v) = \mathcal{G}(u, v) \quad & 0 \leq u \leq N/2 & \text{and } 0 \leq v \leq N/2 \\
 & 0 \leq u \leq N/2 & \text{and } 1 + N/2 \leq v \leq N - 1 \\
 & 1 + N/2 \leq u \leq N - 1 & \text{and } 0 \leq v \leq N/2 \\
 & 1 + N/2 \leq u \leq N - 1 & \text{and } 1 + N/2 \leq v \leq N - 1
 \end{aligned} \tag{9.4-11a}$$

where

$$\mathcal{G}(u, v) = \exp\left\{-\frac{1}{2}[(s_u u)^2 + (s_v v)^2]\right\} \tag{9.4-11b}$$

and  $s_u$  and  $s_v$  are the Gaussian filter spread factors.



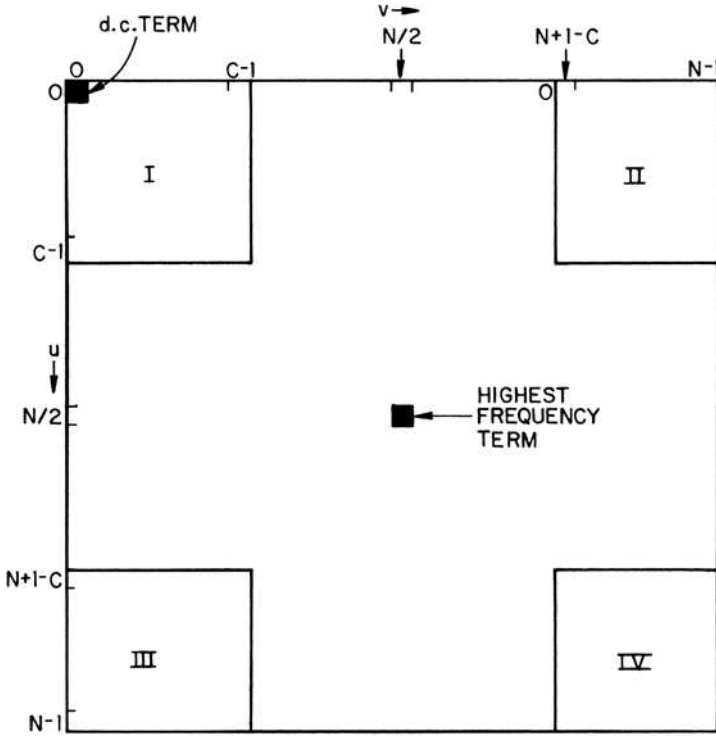


FIGURE 9.4-3. Zonal filter transfer function definition.

4. *Butterworth low-pass filter:*

$$\begin{aligned}
 \mathcal{H}(u, v) = \mathcal{B}(u, v) \quad & 0 \leq u \leq N/2 \quad \text{and} \quad 0 \leq v \leq N/2 \\
 & 0 \leq u \leq N/2 \quad \text{and} \quad 1 + N/2 \leq v \leq N-1 \\
 & 1 + N/2 \leq u \leq N-1 \quad \text{and} \quad 0 \leq v \leq N/2 \\
 & 1 + N/2 \leq u \leq N-1 \quad \text{and} \quad 1 + N/2 \leq v \leq N-1 \quad (9.4-12a)
 \end{aligned}$$

where

$$\mathcal{B}(u, v) = \frac{1}{1 + \left[ \frac{(u^2 + v^2)^{1/2}}{C} \right]^{2n}} \quad (9.4-12b)$$

where the integer variable  $n$  is the order of the filter. The Butterworth low-pass filter provides an attenuation of 50% at the cutoff frequency  $C = (u^2 + v^2)^{1/2}$ .

**5. Butterworth high-pass filter:**

$$\begin{aligned}
 \mathcal{H}(u, v) = \mathcal{B}(u, v) \quad & 0 \leq u \leq N/2 \quad \text{and} \quad 0 \leq v \leq N/2 \\
 & 0 \leq u \leq N/2 \quad \text{and} \quad 1 + N/2 \leq v \leq N - 1 \\
 & 1 + N/2 \leq u \leq N - 1 \quad \text{and} \quad 0 \leq v \leq N/2 \\
 & 1 + N/2 \leq u \leq N - 1 \quad \text{and} \quad 1 + N/2 \leq v \leq N - 1 \quad (9.4-13a)
 \end{aligned}$$

where

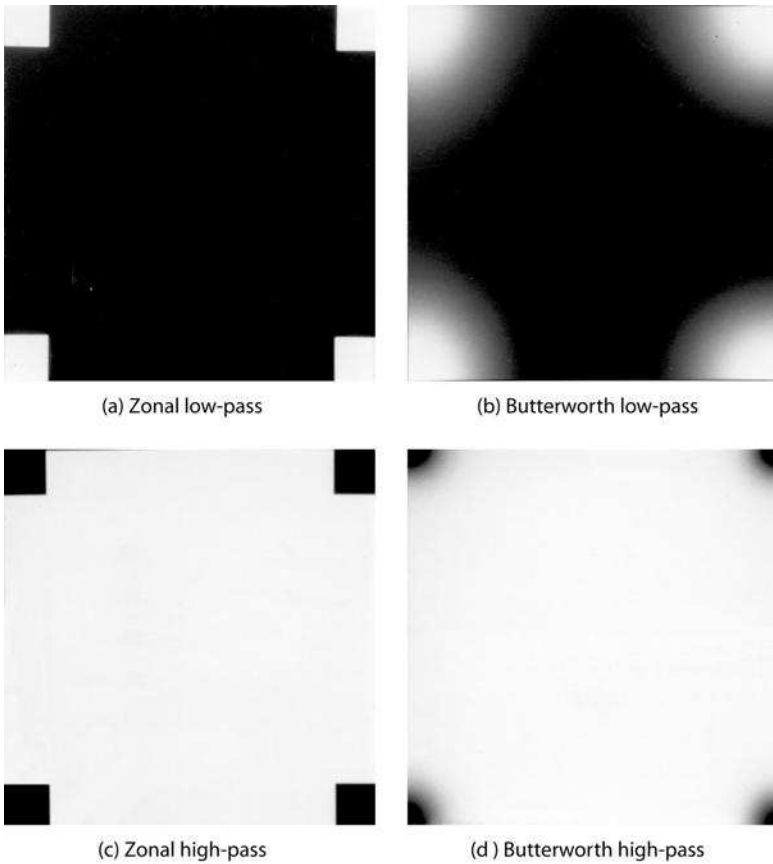
$$\mathcal{B}(u, v) = \frac{1}{1 + \left[ \frac{C}{(u^2 + v^2)^{1/2}} \right]^{2n}} \quad (9.4-13b)$$

Figure 9.4-4 shows the transfer functions of zonal and Butterworth low-pass and high-pass filters for a  $512 \times 512$  pixel image.

**9.5. LINEAR PROCESSING EXERCISES**

E9.1 Develop a program that performs fast Fourier transform convolution following the steps of Section 9.3. Execute this program using an  $11 \times 11$  uniform impulse response array on an unsigned integer, 8-bit,  $512 \times 512$  monochrome image without zero padding. Steps:

- (a) Display the source monochrome image.
- (b) Scale the source image to unit range.
- (c) Perform a two-dimensional Fourier transform of the source image.
- (d) Display the clipped magnitude of the source Fourier transform.
- (e) Create an  $11 \times 11$  uniform impulse response array.
- (f) Convert the impulse response array to an image and embed it in a  $512 \times 512$  zero background image.
- (g) Perform a two-dimensional Fourier transform of the embedded impulse image.
- (h) Display the clipped magnitude of the embedded impulse Fourier transform.
- (i) Multiply the source and embedded impulse Fourier transforms.
- (j) Perform a two-dimensional inverse Fourier transform of the product image.



**FIGURE 9.4-4.** Zonal and Butterworth low- and high-pass transfer functions;  $512 \times 512$  images; cutoff frequency = 64.

- (k) Display the destination image.
- (l) Printout the erroneous pixels along a mid image row.

The PIKS API executable `example_fourier_filtering` performs this exercise.

E9.2 Develop a program that performs Fourier transform filtering of an unsigned integer, 8-bit,  $512 \times 512$  monochrome image with a Gaussian low-pass filter. Steps:

- (a) Display the source monochrome image.

- (b) Create a Gaussian low-pass filter transfer function or fetch it from a repository.
- (c) Perform Fourier transform linear filtering on the source image.
- (f) Display the filtered destination image.

The PIKS API executable `example_gaussian_low_pass_filtering` performs this exercise.

## REFERENCES

1. W. K. Pratt, "Generalized Wiener Filtering Computation Techniques," *IEEE Trans. Computers*, **C-21**, 7, July 1972, 636–641.
2. T. G. Stockham, Jr., "High Speed Convolution and Correlation," *Proc. Spring Joint Computer Conference*, 1966, 229–233.
3. W. M. Gentleman and G. Sande, "Fast Fourier Transforms for Fun and Profit," *Proc. Fall Joint Computer Conference*, 1966, 563–578.
4. W. K. Pratt, "Vector Formulation of Two-Dimensional Signal Processing Operations," *Computer Graphics and Image Processing*, **4**, 1, March 1975, 1–24.
5. B. R. Hunt, "A Matrix Theory Proof of the Discrete Convolution Theorem," *IEEE Trans. Audio and Electroacoustics*, **AU-19**, 4, December 1973, 285–288.
6. W. K. Pratt, "Transform Domain Signal Processing Techniques," *Proc. National Electronics Conference*, Chicago, 1974.
7. H. D. Helms, "Fast Fourier Transform Method of Computing Difference Equations and Simulating Filters," *IEEE Trans. Audio and Electroacoustics*, **AU-15**, 2, June 1967, 85–90.
8. M. P. Ekstrom and V. R. Algazi, "Optimum Design of Two-Dimensional Nonrecursive Digital Filters," *Proc. 4th Asilomar Conference on Circuits and Systems*, Pacific Grove, CA, November 1970.
9. B. R. Hunt, "Computational Considerations in Digital Image Enhancement," *Proc. Conference on Two-Dimensional Signal Processing*, University of Missouri, Columbia, MO, October 1971.
10. A. V. Oppenheim and R. W. Schaffer, *Digital Signal Processing*, Prentice Hall, Englewood Cliffs, NJ, 1975.
11. R. B. Blackman and J. W. Tukey, *The Measurement of Power Spectra*, Dover Publications, New York, 1958.
12. J. F. Kaiser, "Digital Filters," Chapter 7 in *Systems Analysis by Digital Computer*, F. F. Kuo and J. F. Kaiser, Eds., Wiley, New York, 1966.



## **PART 4**

---

### **IMAGE IMPROVEMENT**

The use of digital processing techniques for image improvement has received much interest with the publicity given to applications in space imagery and medical research. Other applications include image improvement for photographic surveys and industrial radiographic analysis.

Image improvement is a term coined to denote three types of image manipulation processes: image enhancement, image restoration and geometrical image modification. Image enhancement entails operations that improve the appearance to a human viewer, or operations to convert an image to a format better suited to machine processing. Image restoration has commonly been defined as the modification of an observed image in order to compensate for defects in the imaging system that produced the observed image. Geometrical image modification includes image magnification, minification, rotation and nonlinear spatial warping.

Chapter 10 describes several techniques of monochrome and color image enhancement. The chapter that follows develops models for image formation and image restoration. The final chapter of this part considers geometrical image modification.



---

# 10

---

## IMAGE ENHANCEMENT

Image enhancement processes consist of a collection of techniques that seek to improve the visual appearance of an image or to convert the image to a form better suited for analysis by a human or a machine. In an image enhancement system, there is no conscious effort to improve the fidelity of a reproduced image with regard to some ideal form of the image, as is done in image restoration. Actually, there is some evidence to indicate that often a distorted image, for example, an image with amplitude overshoot and undershoot about its object edges, is more subjectively pleasing than a perfectly reproduced original.

For image analysis purposes, the definition of image enhancement stops short of information extraction. As an example, an image enhancement system might emphasize the edge outline of objects in an image by high-frequency filtering. This edge-enhanced image would then serve as an input to a machine that would trace the outline of the edges, and perhaps make measurements of the shape and size of the outline. In this application, the image enhancement processor would emphasize salient features of the original image and simplify the processing task of a data-extraction machine.

There is no general unifying theory of image enhancement at present because there is no general standard of image quality that can serve as a design criterion for an image enhancement processor. Consideration is given here to a variety of techniques that have proved useful for human observation improvement and image analysis.



### 10.1. CONTRAST MANIPULATION

One of the most common defects of photographic or electronic images is poor contrast resulting from a reduced, and perhaps nonlinear, image amplitude range. Image contrast can often be improved by amplitude rescaling of each pixel (1,2). Figure 10.1-1*a* illustrates a transfer function for contrast enhancement of a typical continuous amplitude low-contrast image. For continuous amplitude images, the transfer function operator can be implemented by photographic techniques, but it is often difficult to realize an arbitrary transfer function accurately. For quantized amplitude images, implementation of the transfer function is a relatively simple task. However, in the design of the transfer function operator, consideration must be given to the effects of amplitude quantization. With reference to Figure 10.1-1*b*, suppose that an original image is quantized to  $J$  levels, but it occupies a smaller range. The output image is also assumed to be restricted to  $J$  levels, and the mapping is linear. In the mapping strategy indicated in Figure 10.1-1*b*, the output level chosen is that level closest to the exact mapping of an input level. It is obvious from the diagram that the output image will have unoccupied levels within its range, and some of the gray scale transitions will be larger than in the original image. The latter effect may result in noticeable gray scale contouring. If the output image is quantized to more levels than the input image, it is possible to approach a linear placement of output levels, and hence, decrease the gray scale contouring effect.

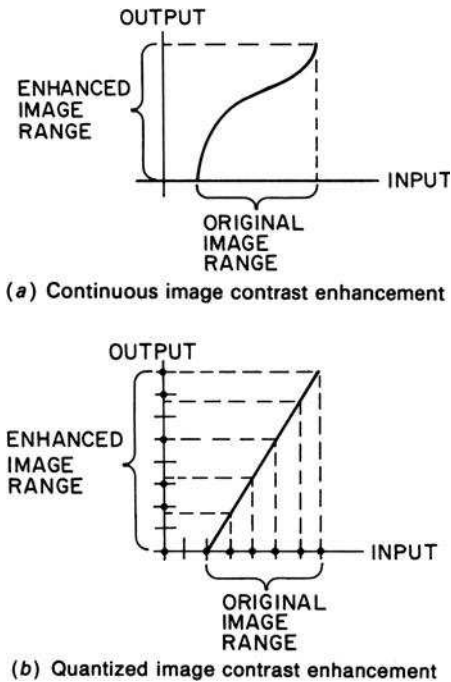
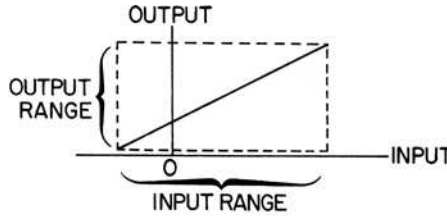


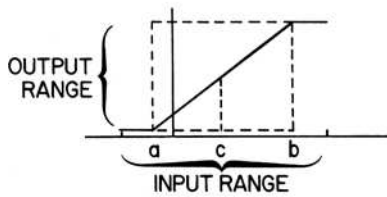
FIGURE 10.1-1. Continuous and quantized image contrast enhancement.

### 10.1.1. Amplitude Scaling

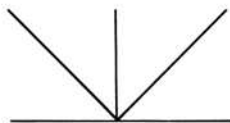
A digitally processed image may occupy a range different from the range of the original image. In fact, the numerical range of the processed image may encompass negative values, which cannot be mapped directly into a light intensity range. Figure 10.1-2 illustrates several possibilities of scaling an output image back into the domain of values occupied by the original image. By the first technique, the processed image is linearly mapped over its entire range, while by the second technique, the extreme amplitude values of the processed image are clipped to maximum and minimum limits. The second technique is often subjectively preferable, especially for images in which a relatively small number of pixels exceed the limits. Contrast enhancement algorithms often possess an option to clip a fixed percentage of the amplitude values on each end of the amplitude scale. In medical image enhancement applications, the contrast modification operation shown in Figure 10.1-2b, for  $a \geq 0$ , is called a *window-level transformation*. The window value is the width of the linear slope,  $b - a$ ; the level is located at the midpoint  $c$  of the slope line. The third technique of amplitude scaling, shown in Figure 10.1-2c, utilizes an absolute value transformation for visualizing an image with negatively valued pixels. This is a useful transformation for systems that utilize the two's complement numbering



(a) Linear image scaling



(b) Linear image scaling with clipping



(c) Absolute value scaling

**FIGURE 10.1-2.** Image scaling methods.



(a) Linear, full range, - 0.147 to 0.169



(b) Clipping, 0.000 to 0.169



(c) Absolute value, 0.000 to 0.169

**FIGURE 10.1-3.** Image scaling of the  $Q$  component of the  $YIQ$  representation of the dolls\_gamma color image.

convention for amplitude representation. In such systems, if the amplitude of a pixel overshoots +1.0 (maximum luminance white) by a small amount, it wraps around by the same amount to -1.0, which is also maximum luminance white. Similarly, pixel undershoots remain near black.

Figure 10.1-3 illustrates the amplitude scaling of the  $Q$  component of the  $YIQ$  transformation, shown in Figure 3.5-14, of a monochrome image containing negative pixels. Figure 10.1-3a presents the result of amplitude scaling with the linear function of Figure 10.1-2a over the amplitude range of the image. In this example, the most negative pixels are mapped to black (0.0), and the most positive pixels are mapped to white (1.0). Amplitude scaling in which negative value pixels are clipped to zero is shown in Figure 10.1-3b. The black regions of the image correspond to negative pixel values of the  $Q$  component. Absolute value scaling is presented in Figure 10.1-3c.

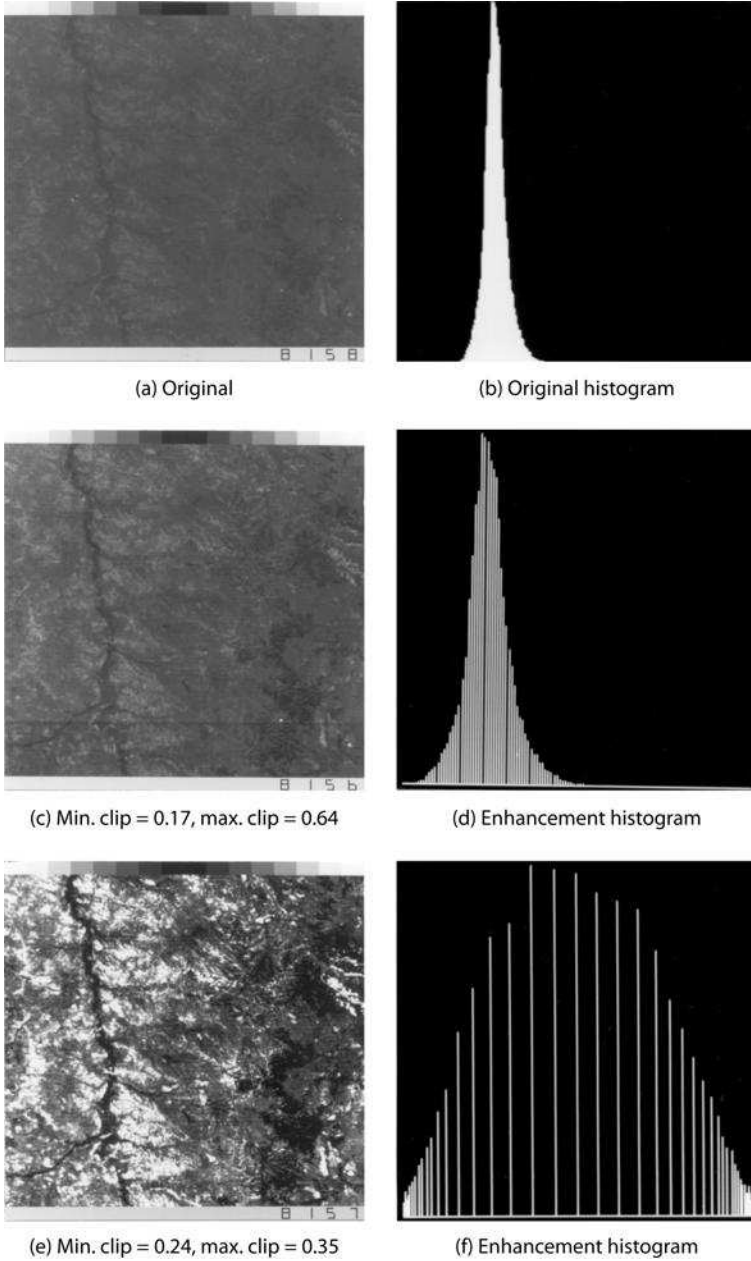


**FIGURE 10.1-4.** Window-level contrast stretching of an earth satellite image.

Figure 10.1-4 shows examples of contrast stretching of a poorly digitized original satellite image along with gray scale histograms of the original and enhanced pictures.

In Figure 10.1-4c, the clip levels are set at the histogram limits of the original while in Figure 10.1-4e, the clip levels truncate 5% of the original image upper and lower level amplitudes. It is readily apparent from the histogram of Figure 10.1-4f that the contrast-stretched image of Figure 10.1-4e has many unoccupied amplitude levels. Gray scale contouring is at the threshold of visibility.

### 10.1.2. Contrast Modification

Section 10.1.1 dealt with amplitude scaling of images that do not properly utilize the dynamic range of a display; they may lie partly outside the dynamic range or occupy only a portion of the dynamic range. In this section, attention is directed to point transformations that modify the contrast of an image within a display's dynamic range.

Figure 10.1-5a contains an original image of a jet aircraft that has been digitized to 256 gray levels and numerically scaled over the range of 0.0 (Black) to 1.0 (White). The histogram of the image is shown in Figure 10.1-5b. Examination

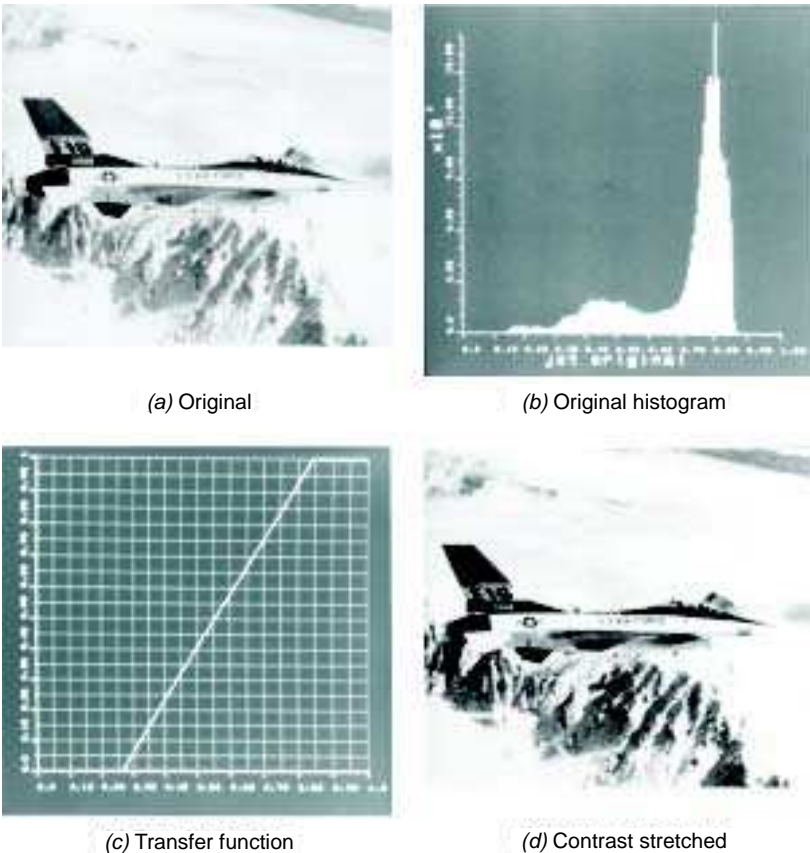
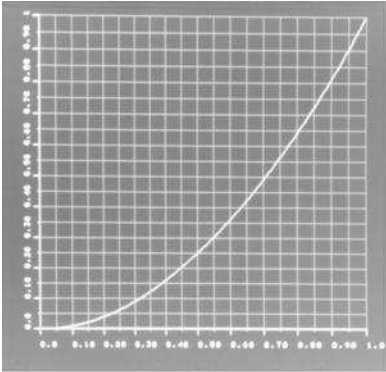


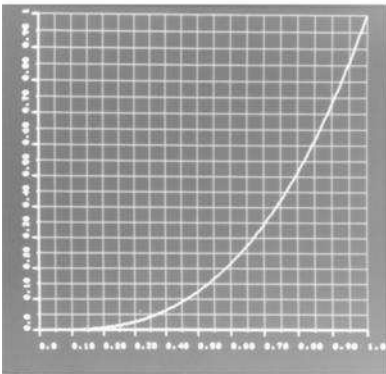
FIGURE 10.1-5. Window-level contrast stretching of the jet\_mon image.



(a) Square function



(b) Square output



(c) Cube function



(d) Cube output

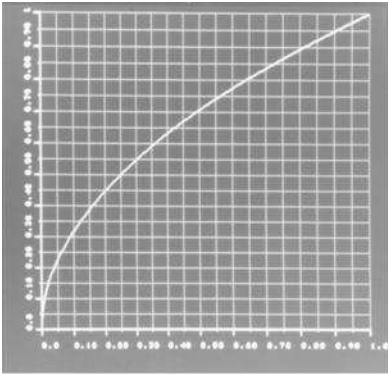
**FIGURE 10.1-6.** Square and cube contrast modification of the jet\_mon image.

of the histogram of the image reveals that the image contains relatively few low- or high-amplitude pixels. Consequently, applying the window-level contrast stretching function of Figure 10.1-5c results in the image of Figure 10.1-5d, which possesses better visual contrast but does not exhibit noticeable visual clipping.

Consideration will now be given to several nonlinear point transformations, some of which will be seen to improve visual contrast, while others clearly impair visual contrast. Figures 10.1-6 and 10.1-7 provide examples of power law point transformations in which the processed image is defined by

$$G(j, k) = [F(j, k)]^p \tag{10.1-1}$$

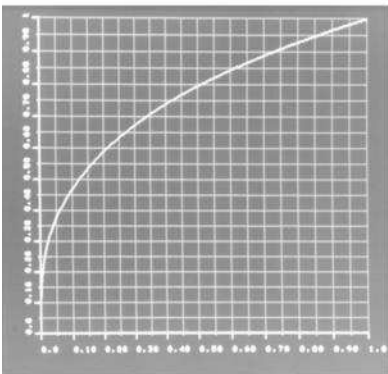
where  $0.0 \leq F(j, k) \leq 1.0$  represents the original image and  $p$  is the power law variable. It is important that the amplitude limits of Eq. 10.1-1 be observed; processing of the integer code (e.g., 0 to 255) by Eq. 10.1-1 will give erroneous results. The



(a) Square root function



(b) Square root output



(c) Cube root function



(d) Cube root output

**FIGURE 10.1-7.** Square root and cube root contrast modification of the jet\_mon image.

square function provides the best visual result. The rubber band transfer function shown in Figure 10.1-8a provides a simple piecewise linear approximation to the power law curves. It is often useful in interactive enhancement machines in which the inflection point is interactively placed.

The Gaussian error function behaves like a square function for low-amplitude pixels and like a square root function for high-amplitude pixels. It is defined as

$$G(j, k) = \frac{\operatorname{erf}\left\{\frac{F(j, k) - 0.5}{a\sqrt{2}}\right\} + \frac{0.5}{a\sqrt{2}}}{2 \operatorname{erf}\left\{\frac{0.5}{a\sqrt{2}}\right\}} \quad (10.1-2a)$$

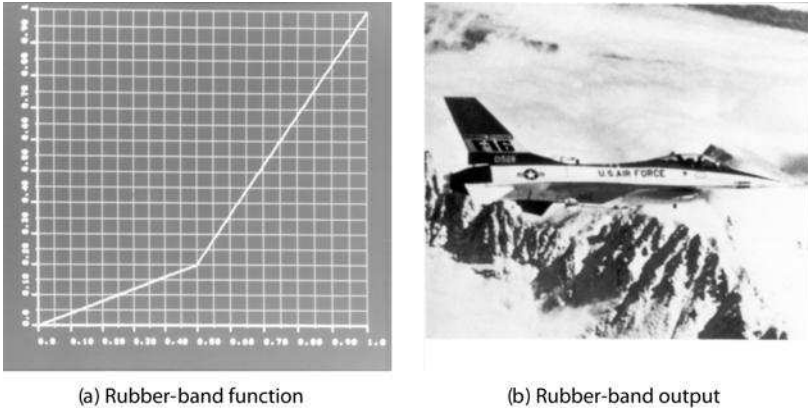


**FIGURE 10.1-8.** Rubber-band contrast modification of the `jet_mon` image.

where

$$\text{erf}\{x\} = \frac{2}{\sqrt{\pi}} \int_0^x \exp\{-y^2\} dy \tag{10.1-2b}$$

and  $a$  is the standard deviation of the Gaussian distribution.

The logarithm function is useful for scaling image arrays with a very wide dynamic range. The logarithmic point transformation is given by

$$G(j, k) = \frac{\log_e\{1.0 + aF(j, k)\}}{\log_e\{2.0\}} \tag{10.1-3}$$

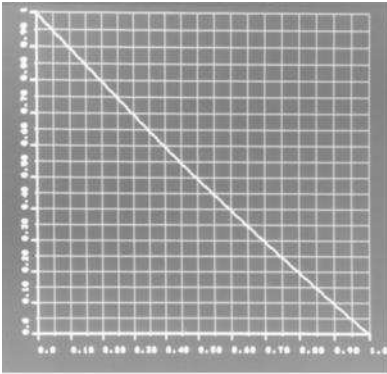
under the assumption that  $0.0 \leq F(j, k) \leq 1.0$  where  $a$  is a positive scaling factor. Figure 8.2-4 illustrates the logarithmic transformation applied to an array of Fourier transform coefficients.

There are applications in image processing in which monotonically decreasing and nonmonotonic amplitude scaling is useful. For example, contrast reverse and contrast inverse transfer functions, as illustrated in Figure 10.1-9, are often helpful in visualizing detail in dark areas of an image. The reverse function is defined as

$$G(j, k) = 1.0 - F(j, k) \tag{10.1-4}$$

where  $0.0 \leq F(j, k) \leq 1.0$ .

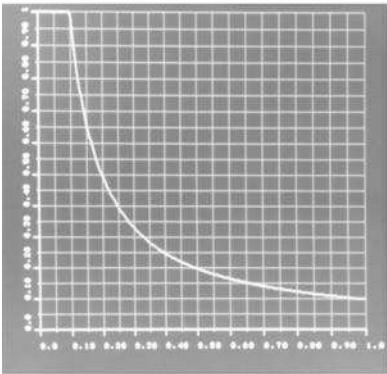




(a) Reverse function



(b) Reverse function output



(c) Inverse function



(d) Inverse function output

**FIGURE 10.1-9.** Reverse and inverse function contrast modification of the `jet_mon` image.

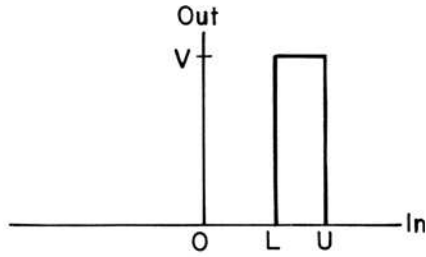
The inverse function

$$G(j, k) = 1.0 \quad \text{for } 0.0 \leq F(j, k) < 0.1 \quad (10.1-5a)$$

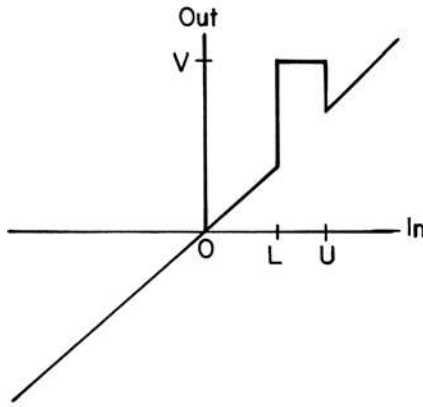
$$G(j, k) = \frac{0.1}{F(j, k)} \quad \text{for } 0.1 \leq F(j, k) \leq 1.0 \quad (10.1-5b)$$

is clipped at the 10% input amplitude level to maintain the output amplitude within the range of unity.

Amplitude-level slicing, as illustrated in Figure 10.1-10, is a useful interactive tool for visually analyzing the spatial distribution of pixels of certain amplitude within an image. With the function of Figure 10.1-10a, all pixels within the amplitude passband are rendered maximum white in the output, and pixels outside the passband are rendered black. Pixels outside the amplitude passband are displayed in their original state with the function of Figure 10.1-10b.



(a) Zero background scaling transformation



(b) Image background scaling transformation

**FIGURE 10.1-10.** Level slicing contrast modification functions.

In many imaging applications, a source image sensor may have a much greater dynamic range than an associated display device. In such instances, application of the contrast modification procedures presented previously fail to adequately display both low-amplitude and high-amplitude image detail simultaneously. Pardo and Sapiro (3) have proposed a different approach for the visualization of wide dynamic source images in which the source image is sequentially divided into  $N$  amplitude ranges by an amplitude segmentation process, and window-level scaling is performed to produce  $N$  output images. For  $N = 3$ , their procedure produces a low-amplitude, a mid-amplitude and a high-amplitude image. Pratt (4Ed., 257,258) contains an example of this procedure.

### 10.2. HISTOGRAM MODIFICATION

The luminance histogram of a typical natural scene that has been linearly quantized is usually highly skewed toward the darker levels; a majority of the pixels possess a luminance less than the average. In such images, detail in the darker regions is often not perceptible. One means of enhancing these types of images is a technique called *histogram modification*, in which the original image is rescaled so that the histogram of the enhanced image follows some desired form. Andrews, Hall and others (4-6) have produced enhanced imagery by a *histogram equalization* process for which the histogram of the enhanced image is forced to be uniform. Frei (7) has explored the use of histogram modification procedures that produce enhanced images possessing exponential or hyperbolic-shaped histograms. Ketcham (8) and Hummel (9) have demonstrated improved results by an adaptive histogram modification procedure.

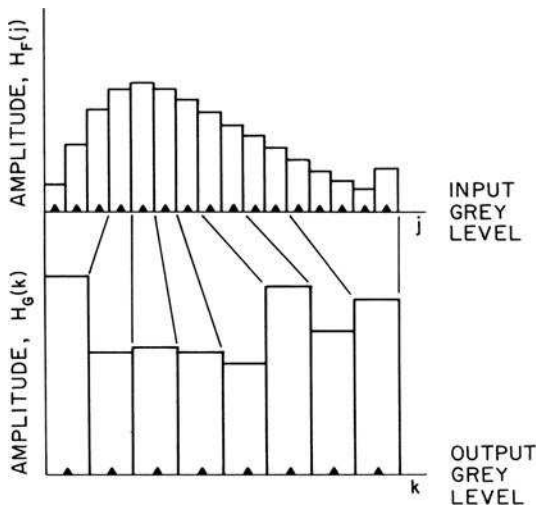


**FIGURE 10.2-1.** Approximate gray level histogram equalization with unequal number of quantization levels.

#### 10.2.1. Nonadaptive Histogram Modification

Figure 10.2-1 gives an example of histogram equalization. In the figure,  $H_F(c)$  for  $c = 1, 2, \dots, C$ , represents the fractional number of pixels in an input image whose amplitude is quantized to the  $c$ th reconstruction level. Histogram equalization seeks to produce an output image field  $G$  by point rescaling such that the normalized gray-level histogram  $H_G(d) = 1/D$  for  $d = 1, 2, \dots, D$ . In the example of Figure 10.2-1, the number of output levels is set at one-half of the number of

input levels. The scaling algorithm is developed as follows. The average value of the histogram is computed. Then, starting at the lowest gray level of the original, the pixels in the quantization bins are combined until the sum is closest to the average. All of these pixels are then rescaled to the new first reconstruction level at the mid-point of the enhanced image first quantization bin. The process is repeated for higher-value gray levels. If the number of reconstruction levels of the original image is large, it is possible to rescale the gray levels so that the enhanced image histogram is almost constant. It should be noted that the number of reconstruction levels of the enhanced image must be less than the number of levels of the original image to provide proper gray scale redistribution if all pixels in each quantization level are to be treated similarly. This process results in a somewhat larger quantization error. It is possible to perform the gray scale histogram equalization process with the same number of gray levels for the original and enhanced images, and still achieve a constant histogram of the enhanced image, by randomly redistributing pixels from input to output quantization bins

The histogram modification process can be considered to be a monotonic point transformation  $g_d = T\{f_c\}$  for which the input amplitude variable  $f_1 \leq f_c \leq f_C$  is mapped into an output variable  $g_1 \leq g_d \leq g_D$  such that the output probability distribution  $P_R\{g_d = b_d\}$  follows some desired form for a given input probability distribution  $P_R\{f_c = a_c\}$  where  $a_c$  and  $b_d$  are reconstruction values of the  $c$ th and  $d$ th levels. Clearly, the input and output probability distributions must each sum to unity. Thus,

$$\sum_{c=1}^C P_R\{f_c = a_c\} = 1 \tag{10.2-1a}$$

$$\sum_{d=1}^D P_R\{g_d = b_d\} = 1 \tag{10.2-1b}$$

Furthermore, the cumulative distributions must equate for any input index  $c$ . That is, the probability that pixels in the input image have an amplitude less than or equal to  $a_c$  must be equal to the probability that pixels in the output image have amplitude less than or equal to  $b_d$ , where  $b_d = T\{a_c\}$  because the transformation is monotonic. Hence,

$$\sum_{n=1}^a P_R\{g_n = b_n\} = \sum_{m=1}^c P_R\{f_m = a_m\} \tag{10.2-2}$$

The summation on the right is the cumulative probability distribution of the input image. For a given image, the cumulative distribution is replaced by the cumulative histogram to yield the relationship

$$\sum_{n=1}^a P_R\{g_n = b_n\} = \sum_{m=1}^c H_F(m). \tag{10.2-3}$$

Equation 10.2-3 now must be inverted to obtain a solution for  $g_d$  in terms of  $f_c$ . In general, this is a difficult or impossible task to perform analytically, but certainly possible by numerical methods. The resulting solution is simply a table that indicates the output image level for each input image level.

The histogram transformation can be obtained in approximate form by replacing the discrete probability distributions of Eq. 10.2-2 by continuous probability densities. The resulting approximation is

$$\int_{g_{\min}}^g p_g(g)dg = \int_{f_{\min}}^f pf(f)df \tag{10.2-4}$$

where  $p_f(f)$  and  $p_g(g)$  are the probability densities of  $f$  and  $g$ , respectively. The integral on the right is the cumulative distribution function  $P_f(f)$  of the input variable  $f$ . Hence

$$\int_{g_{\min}}^g p_g(g) dg = P_f(f). \tag{10.2-5}$$

In the special case, for which the output density is forced to be the uniform density,

$$p_g(g) = \frac{1}{g_{\max} - g_{\min}} \tag{10.2-6}$$

for  $g_{\min} \leq g \leq g_{\max}$ , the histogram equalization transfer function becomes

$$g = (g_{\max} - g_{\min})P_f(f) + g_{\min}. \tag{10.2-7}$$

Table 10.2-1 lists several output image histograms and their corresponding transfer functions.

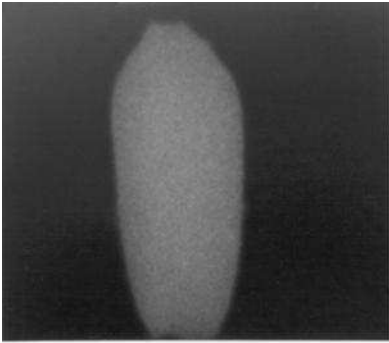
Figure 10.2-2 provides an example of histogram equalization for an x-ray of a projectile. The original image and its histogram are shown in Figure 10.2-2a and b, respectively. The transfer function of Figure 10.2-2c is equivalent to the cumulative histogram of the original image. In the histogram equalized result of Figure 10.2-2, ablating material from the projectile, not seen in the original, is clearly visible. The histogram of the enhanced image appears peaked, but close examination reveals that many gray level output values are unoccupied. If the high occupancy gray levels were to be averaged with their unoccupied neighbors, the resulting histogram would be much more uniform.

TABLE 10.2-1. Histogram Modification Transfer Functions

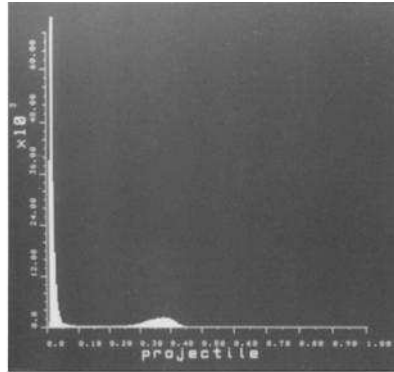
Output Probability Density Model	Transfer Function <sup>a</sup>
Uniform	$p_g(g) = \frac{1}{g_{\max} - g_{\min}} \quad g_{\min} \leq g \leq g_{\max}$ $g = (g_{\max} - g_{\min})P_f(f) + g_{\min}$
Exponential	$p_g(g) = \alpha \exp\{-\alpha(g - g_{\min})\} \quad g \leq g_{\min}$ $g = g_{\min} - \frac{1}{\alpha} \ln\{1 - P_f(f)\}$
Rayleigh	$p_g(g) = \frac{g - g_{\min}}{\alpha^2} \exp\left\{-\frac{(g - g_{\min})^2}{2\alpha^2}\right\} \quad g \geq g_{\min}$ $g = g_{\min} + \left[2\alpha^2 \ln\left\{\frac{1}{1 - P_f(f)}\right\}\right]^{1/2}$
Hyperbolic (Cube root)	$p_g(g) = \frac{1}{3} \frac{g^{-2/3}}{g_{\max}^{1/3} - g_{\min}^{1/3}}$ $g = \left[g_{\max}^{1/3} - g_{\min}^{1/3} [P_f(f)] + g_{\max}^{1/3}\right]^3$
Hyperbolic (Logarithmic)	$p_g(g) = \frac{1}{g[\ln\{g_{\max}\} - \ln\{g_{\min}\}]}$ $g = g_{\min} \left(\frac{g_{\max}}{g_{\min}}\right)^{P_f(f)}$

<sup>a</sup>The cumulative probability distribution  $P_f(f)$  of the input image is approximated by its cumulative histogram:

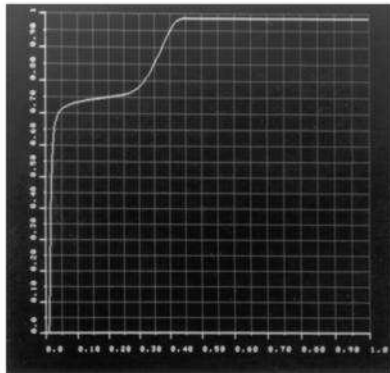
$$P_f(f) \approx \sum_{m=0}^J H_F(m)$$



(a) Original



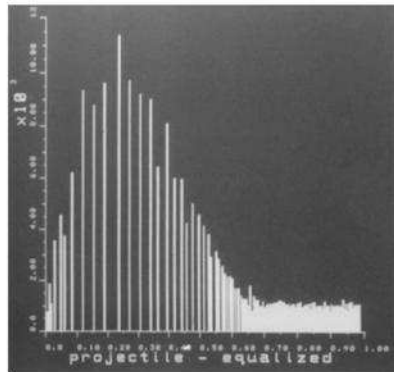
(b) Original histogram



(c) Transfer function



(d) Enhanced



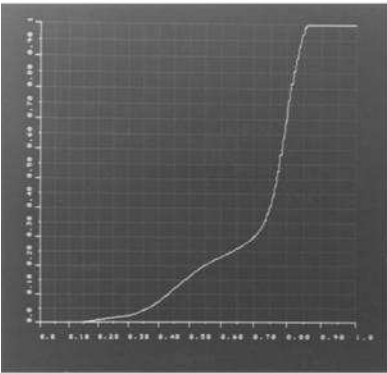
(e) Enhanced histogram

**FIGURE 10.2-2.** Histogram equalization of the projectile image.

Histogram equalization usually performs best on images with detail hidden in dark regions. Good-quality originals are often degraded by histogram equalization. As an example, Figure 10.2-3 shows the result of histogram equalization on the jet image



(a) Original



(b) Transfer function



(c) Histogram equalized

**FIGURE 10.2-3.** Histogram equalization of the jet\_mon image.

Frei (7) has suggested the *histogram hyperbolization* procedure listed in Table 10.2-1 and described in Figure 10.2-4. With this method, the input image histogram is modified by a transfer function such that the output image probability density is of hyperbolic form. Then the resulting gray scale probability density following the assumed logarithmic or cube root response of the photoreceptors of the eye model will be uniform. In essence, histogram equalization is conceptually performed after the cones of the retina.



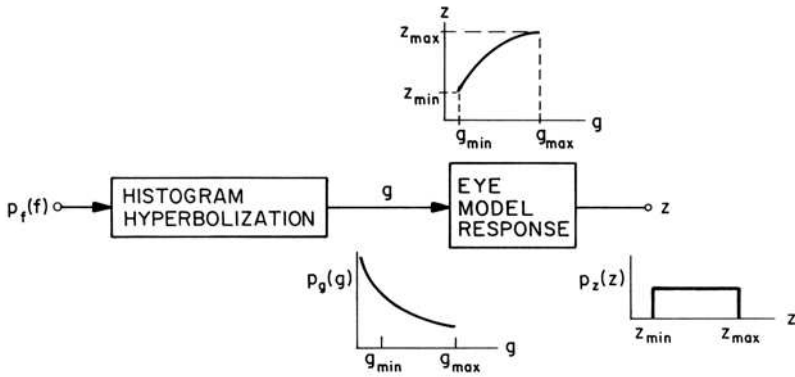


FIGURE 10.2-4. Histogram hyperbolization

**10.2.2. Adaptive Histogram Modification**

The histogram modification methods discussed in Section 10.2.1 involve application of the same transformation or mapping function to each pixel in an image. The mapping function is based on the histogram of the entire image. This process can be made spatially adaptive by applying histogram modification to each pixel based on the histogram of pixels within a moving window neighborhood. This technique is obviously computationally intensive, as it requires histogram generation, mapping function computation and mapping function application at each pixel.

Pizer et al. (10) have proposed an adaptive histogram equalization technique in which histograms are generated only at a rectangular grid of points and the mappings at each pixel are generated by interpolating mappings of the four nearest grid points. Figure 10.2-5 illustrates the geometry. A histogram is computed at each grid point in a window about the grid point. The window dimension can be smaller or larger than the grid spacing. Let  $M_{00}, M_{10}, M_{01}, M_{11}$  denote the histogram modification mappings generated at four neighboring grid points. The mapping to be applied at pixel  $F(j, k)$  is determined by a bilinear interpolation of the mappings of the four nearest grid points as given by

$$M = (1 - a)(1 - b)M_{00} + a(1 - b)M_{10} + (1 - a)bM_{01} + abM_{11} \quad (10.2-8a)$$

where

$$a = \frac{j - j_0}{j_1 - j_0} \tag{10.2-8b}$$

$$b = \frac{k - k_0}{k_1 - k_0} \tag{10.2-8c}$$

Pixels in the border region of the grid points are handled as special cases of Eq. 10.2-8. Equation 10.2-8 is best suited for general-purpose computer calculation. For parallel processors, it is often more efficient to use the histogram generated in the histogram window of Figure 10.2-5 and apply the resultant mapping function to all pixels in the mapping window of the figure. This process is then repeated at all grid points. At each pixel coordinate  $(j, k)$ , the four histogram modified pixels obtained from the four overlapped mappings are combined by bilinear interpolation. Figure 10.2-6 presents a comparison between nonadaptive and adaptive histogram equalization of a monochrome image. In the adaptive histogram equalization example, the histogram window is  $64 \times 64$ .

Images generated by the adaptive histogram equalization process sometimes can be harsh in visual appearance. Stark (11) has proposed adaptive blurring of the window histogram prior to forming the cumulative histogram as a means of improving image quality.

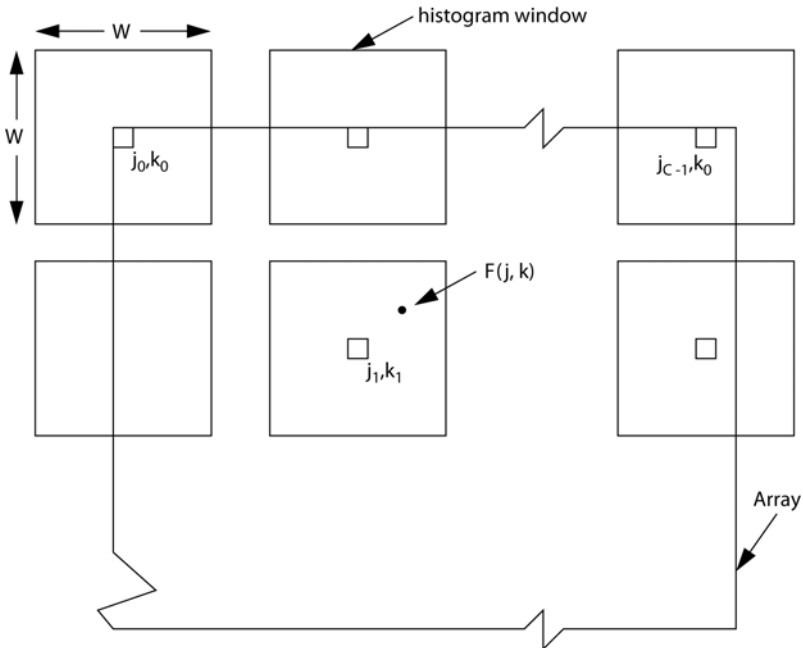
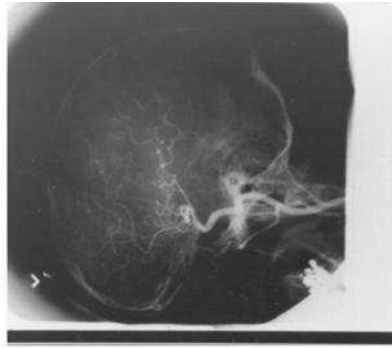
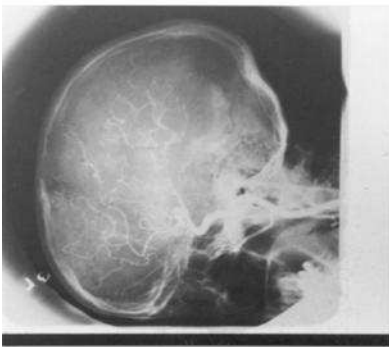


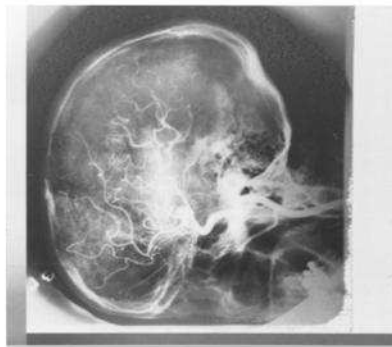
**FIGURE 10.2-5.** Array geometry for interpolative adaptive histogram modification.  
 □ Grid point; • pixel to be computed.



(a) Original



(b) Nonadaptive



(c) Adaptive

**FIGURE 10.2-6.** Nonadaptive and adaptive histogram equalization of the brainscan image.

### 10.3. NOISE CLEANING

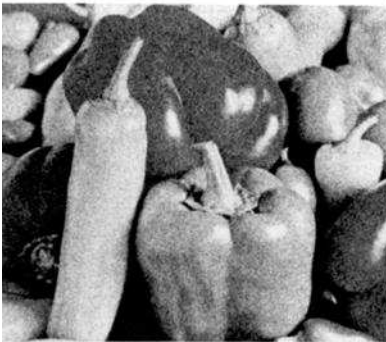
An image may be subject to noise and interference from several sources, including electrical sensor noise, photographic grain noise and channel errors. These noise effects can be reduced by classical statistical filtering techniques to be discussed in Chapter 12. Another approach, discussed in this section, is the application of ad hoc *noise cleaning* techniques.

Image noise arising from a noisy sensor or channel transmission errors usually appears as discrete isolated pixel variations that are not spatially correlated. Pixels that are in error often appear visually to be markedly different from their neighbors. This observation is the basis of many noise cleaning algorithms (12–15). In this section, several linear and nonlinear techniques that have proved useful for noise reduction are described.

Figure 10.3-1 shows two test images, which will be used to evaluate noise cleaning techniques. Figure 10.3-1*b* has been obtained by adding uniformly distributed noise to the original image of Figure 10.3-1*a*. In the impulse noise example of Figure 10.3-1*c*, maximum-amplitude pixels replace original image pixels in a spatially random manner.



(a) Original



(b) Original with uniform noise



(c) Original with impulse noise

**FIGURE 10.3-1.** Noisy test images derived from the `peppers_mon` image.

### 10.3.1. Linear Noise Cleaning

Noise added to an image generally has a higher-spatial-frequency spectrum than the normal image components because of its spatial decorrelatedness. Hence, simple low-pass filtering can be effective for noise cleaning. Consideration will now be given to convolution and Fourier domain methods of noise cleaning.

**Spatial Domain Processing.** Following the techniques outlined in Chapter 7, a spatially filtered output image  $G(j, k)$  can be formed by discrete convolution of an input image  $F(j, k)$  with a  $L \times L$  impulse response array  $H(j, k)$  according to the relation

$$G(j, k) = \sum \sum F(m, n)H(m + j + C, n + k + C) \quad (10.3-1)$$

where  $C = (L + 1)/2$ . Equation 10.3-1 utilizes the centered convolution notation developed by Eq. 7.1-14, whereby the input and output arrays are centered with respect to one another, with the outer boundary of  $G(j, k)$  of width  $(L - 1)/2$  pixels set to zero.

For noise cleaning,  $H$  should be of low-pass form, with all positive elements. Several common  $3 \times 3$  pixel impulse response arrays of low-pass form are listed below.

**Mask 1:** 
$$\mathbf{H} = \frac{1}{9} \begin{bmatrix} 1 & 1 & 1 \\ 1 & 1 & 1 \\ 1 & 1 & 1 \end{bmatrix} \quad (10.3-2a)$$

**Mask 2:** 
$$\mathbf{H} = \frac{1}{10} \begin{bmatrix} 1 & 1 & 1 \\ 1 & 2 & 1 \\ 1 & 1 & 1 \end{bmatrix} \quad (10.3-2b)$$

**Mask 3:** 
$$\mathbf{H} = \frac{1}{16} \begin{bmatrix} 1 & 2 & 1 \\ 2 & 4 & 2 \\ 1 & 2 & 1 \end{bmatrix} \quad (10.3-2c)$$

These arrays, called *noise cleaning masks*, are normalized to unit weighting so that the noise-cleaning process does not introduce an amplitude bias in the processed image. The effect of noise cleaning with the arrays on the uniform noise and impulse noise test images is shown in Figure 10.3-2. Mask 1 and 3 of Eq. 10.3-2 are special cases of a  $3 \times 3$  *parametric low-pass filter* whose impulse response is defined as

$$\mathbf{H} = \left( \frac{1}{b+2} \right)^2 \begin{bmatrix} 1 & b & 1 \\ b & b^2 & b \\ 1 & b & 1 \end{bmatrix}. \quad (10.3-3)$$



(a) Uniform noise, mask 1



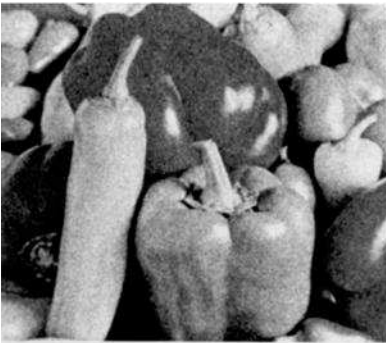
(b) Impulse noise, mask 1



(c) Uniform noise, mask 2



(d) Impulse noise, mask 2



(e) Uniform noise, mask 3



(f) Impulse noise, mask 3

**FIGURE 10.3-2.** Noise cleaning with  $3 \times 3$  low-pass impulse response arrays on the noisy test images.



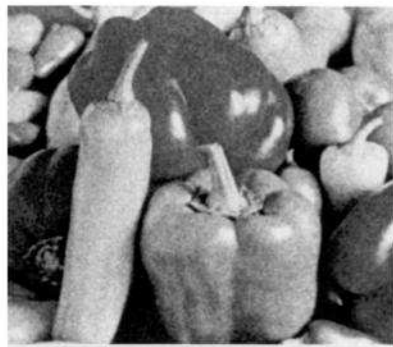
(a) Uniform rectangle



(b) Uniform circular



(c) Pyramid



(d) Gaussian, s = 1.0

**FIGURE 10.3-3.** Noise cleaning with  $7 \times 7$  impulse response arrays on the noisy test image with uniform noise.

The concept of low-pass filtering noise cleaning can be extended to larger impulse response arrays. Figures 10.3-3 and 10.3-4 present noise cleaning results for several  $7 \times 7$  impulse response arrays for uniform and impulse noise. As expected, use of a larger impulse response array provides more noise smoothing, but at the expense of the loss of fine image detail.

**Fourier Domain Processing.** It is possible to perform linear noise cleaning in the Fourier domain (15) using the techniques outlined in Section 9.3. Properly executed, there is no difference in results between convolution and Fourier filtering; the choice is a matter of implementation considerations.

High-frequency noise effects can be reduced by Fourier domain filtering with a zonal low-pass filter with a transfer function defined by Eq. 9.4-9. The sharp cutoff characteristic of the zonal low-pass filter leads to *ringing* artifacts in a filtered image. This deleterious effect can be eliminated by the use of a smooth cutoff filter,



(a) Uniform rectangle



(b) Uniform circular



(c) Pyramid

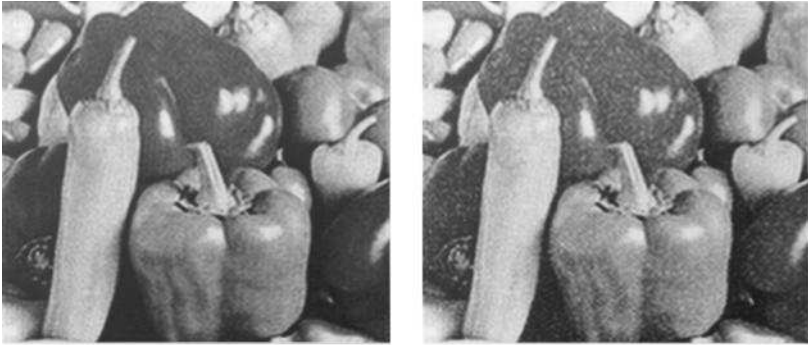
(d) Gaussian,  $s = 1.0$ 

**FIGURE 10.3-4.** Noise cleaning with  $7 \times 7$  impulse response arrays on the noisy test image with impulse noise.

such as the Butterworth low-pass filter whose transfer function is specified by Eq. 9.4-12. Figure 10.3-5 shows the results of zonal and Butterworth low-pass filtering of noisy images.

Unlike convolution, Fourier domain processing, often provides quantitative and intuitive insight into the nature of the noise process, which is useful in designing noise cleaning spatial filters. As an example, Figure 10.3-6a shows an original image subject to periodic interference. Its two-dimensional Fourier transform, shown in Figure 10.3-6b, exhibits a strong response at the two points in the Fourier plane corresponding to the frequency response of the interference. When multiplied point by point with the Fourier transform of the original image, the bandstop filter of Figure 10.3-6c attenuates the interference energy in the Fourier domain. Figure 10.3-6d shows the noise-cleaned result obtained by taking an inverse Fourier transform of the product.





(a) Uniform noise, zonal

(b) Impulse noise, zonal



(c) Uniform noise, Butterworth



(d) Impulse noise, Butterworth

**FIGURE 10.3-5.** Noise cleaning with zonal and Butterworth low-pass filtering on the noisy test images; cutoff frequency = 64.

**Homomorphic Filtering.** Homomorphic filtering (16) is a useful technique for image enhancement when an image is subject to multiplicative noise or interference. Figure 10.3-7 describes the process. The input image  $F(j, k)$  is assumed to be modeled as the product of a noise-free image  $S(j, k)$  and an illumination interference array  $I(j, k)$ . Thus,

$$F(j, k) = I(j, k)S(j, k). \tag{10.3-4}$$

Ideally,  $I(j, k)$  would be a constant for all  $(j, k)$ . Taking the logarithm of Eq. 10.3-4 yields the additive linear result

$$\log \{F(j, k)\} = \log \{I(j, k)\} + \log \{S(j, k)\}. \tag{10.3-5}$$

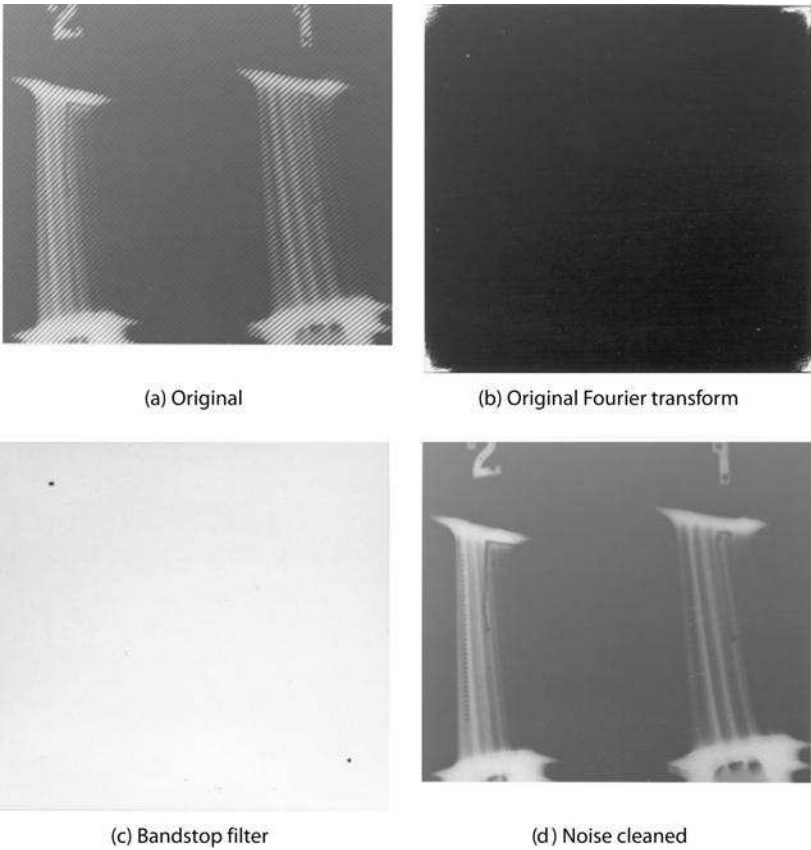


**FIGURE 10.3-6.** Noise cleaning with Fourier domain band stop filtering on the parts image with periodic interference.

Conventional linear filtering techniques can now be applied to reduce the log interference component. Exponentiation after filtering completes the enhancement process. Figure 10.3-8 provides an example of homomorphic filtering. In this example, the illumination field  $I(j, k)$  increases from left to right from a value of 0.1 to 1.0.

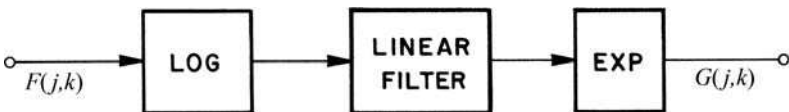
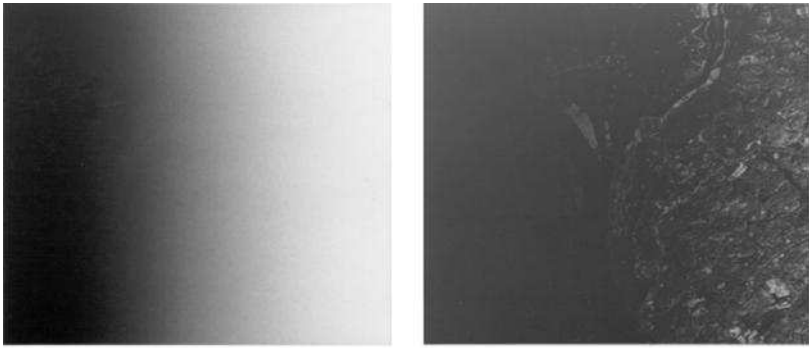
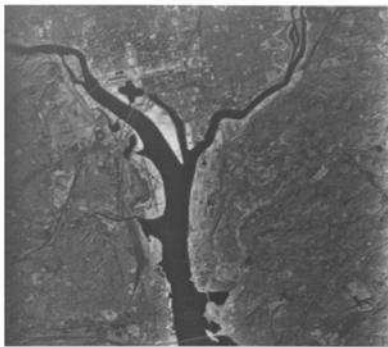


**FIGURE 10.3-7.** Homomorphic filtering.



(a) Illumination field

(b) Original



(c) Homomorphic filtering

**FIGURE 10.3-8.** Homomorphic filtering on the `washington_ir` image with a Butterworth high-pass filter; cutoff frequency = 4.

Therefore, the observed image appears quite dim on its left side. Homomorphic filtering (Figure 10.3-8c) compensates for the nonuniform illumination.

### 10.3.2. Nonlinear Noise Cleaning

The linear processing techniques described previously perform reasonably well on images with continuous noise, such as additive uniform or Gaussian distributed noise. However, they tend to provide too much smoothing for impulse like noise. Nonlinear techniques often provide a better trade-off between noise smoothing and the retention of fine image detail. Several nonlinear techniques are presented below. Mastin (17) has performed subjective testing of several of these operators.

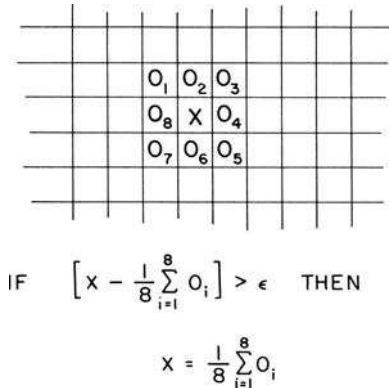


FIGURE 10.3-9. Outlier noise cleaning algorithm.

**Outlier.** Figure 10.3-9 describes a simple outlier noise cleaning technique in which each pixel is compared to the average of its eight neighbors. If the magnitude of the difference is greater than some threshold level, the pixel is judged to be noisy, and it is replaced by its neighborhood average. The eight-neighbor average can be computed by convolution of the observed image with the impulse response array

$$\mathbf{H} = \frac{1}{8} \begin{bmatrix} 1 & 1 & 1 \\ 1 & 0 & 1 \\ 1 & 1 & 1 \end{bmatrix}. \tag{10.3-6}$$

Figure 10.3-10 presents the results of outlier noise cleaning for a threshold level of 10%.



(a) Uniform noise (b) Impulse noise

FIGURE 10.3-10. Noise cleaning with the outlier algorithm on the noisy test images.

The outlier operator can be extended straight forwardly to larger windows. Davis and Rosenfeld (18) have suggested a variant of the outlier technique in which the center pixel in a window is replaced by the average of its  $k$  neighbors whose amplitudes are closest to the center pixel. Lee has proposed another variant of the outlier algorithm, called the *sigma filter* (19). With the sigma filter, the neighborhood sum includes only those pixels in an amplitude range of  $2\sigma$  where  $\sigma$  is the standard deviation of the corrupting Gaussian noise. Kenny et al. (20) have proposed the use of the Fisher discriminant to determine a “peer group” of neighboring pixels to be used in the neighbor average.

**Median Filter.** *Median filtering* is a nonlinear signal processing technique developed by Tukey (21) that is useful for noise suppression in images. In one-dimensional form, the median filter consists of a sliding window encompassing an odd number of pixels. The center pixel in the window is replaced by the median of the pixels in the window. The median of a discrete sequence  $a_1, a_2, \dots, a_N$  for  $N$  odd is that member of the sequence for which  $(N - 1)/2$  elements are smaller or equal in value and  $(N - 1)/2$  elements are larger or equal in value. For example, if the values of the pixels within a window are 0.1, 0.2, 0.9, 0.4, 0.5, the center pixel would be replaced by the value 0.4, which is the median value of the sorted sequence 0.1, 0.2, 0.4, 0.5, 0.9. In this example, if the value 0.9 were a noise spike in a monotonically increasing sequence, the median filter would result in a considerable improvement. On the other hand, the value 0.9 might represent a valid signal pulse for a wide-bandwidth sensor, and the resultant image would suffer some loss of resolution. Thus, in some cases the median filter will provide noise suppression, while in other cases it will cause signal suppression.

Figure 10.3-11 illustrates some examples of the operation of a median filter and a mean (smoothing) filter for a discrete step function, ramp function, pulse function and a triangle function with a window of five pixels. It is seen from these examples that the median filter has the usually desirable property of not affecting step functions or ramp functions. Pulse functions, whose periods are less than one-half the window width, are suppressed. But the peak of the triangle is flattened.

Operation of the median filter can be analyzed to a limited extent. It can be shown that the median of the product of a constant  $K$  and a sequence  $f(j)$  is

$$\text{MED}\{K[f(j)]\} = K[\text{MED}\{f(j)\}]. \tag{10.3-7}$$

However, for two arbitrary sequences  $f(j)$  and  $g(j)$ , it does not follow that the median of the sum of the sequences is equal to the sum of their medians. That is, in general,

$$\text{MED}\{f(j) + g(j)\} \neq \text{MED}\{f(j)\} + \text{MED}\{g(j)\}. \tag{10.3-8}$$

The sequences 0.1, 0.2, 0.3, 0.4, 0.5 and 0.1, 0.2, 0.3, 0.2, 0.1 are examples for which the additive linearity property does not hold.

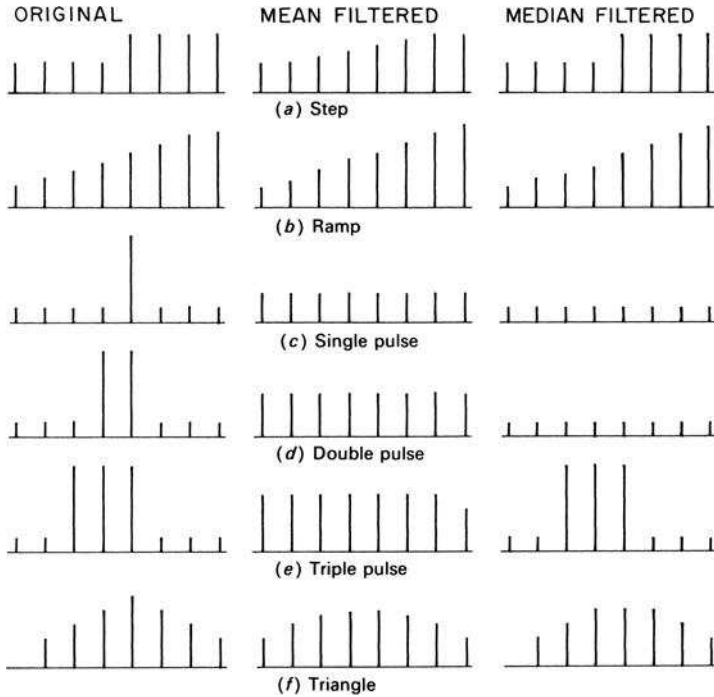


**FIGURE 10.3-11.** Median filtering on one-dimensional test signals.

There are various strategies for application of the median filter for noise suppression. One method would be to try a median filter with a window of length 3. If there is no significant signal loss, the window length could be increased to 5 for median filtering of the original. The process would be terminated when the median filter begins to do more harm than good. It is also possible to perform cascaded median filtering on a signal using a fixed-or-variable-length window. In general, regions that are unchanged by a single pass of the filter will remain unchanged in subsequent passes. Regions in which the signal period is lower than one-half the window width will be continually altered by each successive pass. Usually, the process will continue until the resultant period is greater than one-half the window width, but it can be shown that some sequences will never converge (22).

The concept of the median filter can be extended easily to two dimensions by utilizing a two-dimensional window of some desired shape such as a rectangle or discrete approximation to a circle. It is obvious that a two-dimensional  $L \times L$  median filter will provide a greater degree of noise suppression than sequential processing with  $L \times 1$  median filters, but two-dimensional processing also results in greater signal suppression. Figure 10.3-12 illustrates the effect of two-dimensional median

filtering of a spatial peg function with a  $3 \times 3$  square filter and a  $5 \times 5$  plus sign-shaped filter. In this example, the square median has deleted the corners of the peg, but the plus median has not affected the corners.

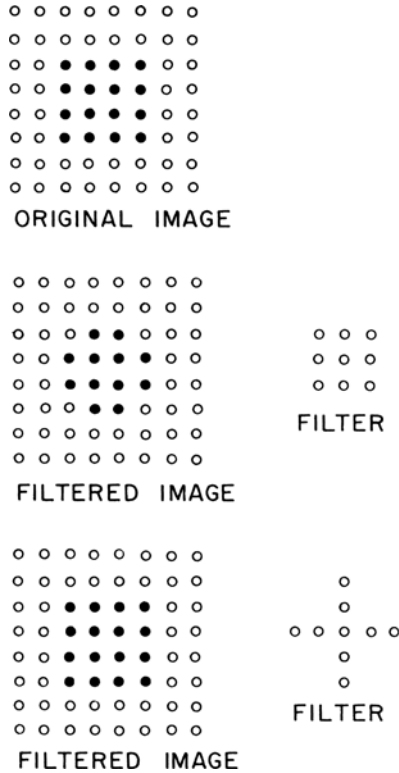


**FIGURE 10.3-12.** Median filtering on two-dimensional test signals.

Figures 10.3-13 and 10.3-14 show results of plus sign-shaped median filtering on the noisy test images of Figure 10.3-1 for impulse and uniform noise, respectively. In the impulse noise example, application of the  $3 \times 3$  median significantly reduces the noise effect, but some residual noise remains. Applying two  $3 \times 3$  median filters in cascade provides further improvement. The  $5 \times 5$  median filter removes almost all of the impulse noise. There is no visible impulse noise in the  $7 \times 7$  median filter result, but the image has become somewhat blurred. In the case of uniform noise, median filtering provides little visual improvement.

Huang et al. (23) and Astola and Campbell (24) have developed fast median filtering algorithms. The latter can be generalized to implement any rank ordering.



(a) 3 x 3 median filter



(b) 3 x 3 cascaded median filter



(c) 5 x 5 median filter



(d) 7 x 7 median filter

**FIGURE 10.3-13.** Median filtering on the noisy test image with uniform noise.

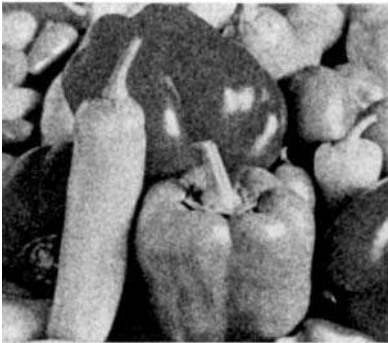
Median filtering is computationally intensive; the number of operations grows exponentially with window size. Pratt et al. (25) have proposed a computationally simpler operator, called the *pseudomedian filter*, which possesses many of the properties of the median filter. See Pratt(4Ed., 280-283) for a derivation of the pseudomedian filter.

**Wavelet Denoising.** Section 8.4-3 introduced wavelet transforms. The usefulness of wavelet transforms for image coding derives from the property that most of the energy of a transformed image is concentrated in the trend transform coefficients rather than the fluctuation coefficients (26). The fluctuation coefficients may be grossly quantized without serious image degradation. This energy compaction property can also be exploited for noise removal. The basic concept, called *wavelet denoising* (26,27), is quite simple. The wavelet transform coefficients are thresholded such that the presumably noisy, low-amplitude coefficients are set to zero.





(a) 3 x 3 median filter



(b) 5 x 5 median filter



(c) 7 x 7 median filter

**FIGURE 10.3-14.** Median filtering on the noisy test image with uniform noise.

Zhong and Ning (28) have developed a method of classifying wavelet coefficients as being edge-related, regular coefficients or irregular coefficients based upon a measurement of the local statistical self-similarity at different resolution scales. The irregular coefficients are denoised using a minimum mean-squared error estimation method; the edge-related, regular coefficients are processed by a fuzzy weighted mean filter. Balster et al. (29) have proposed a two-threshold wavelet coefficient selection method. The first threshold is used to distinguish coefficients of large magnitude, and the second threshold is used to distinguish coefficients of spatial regularity, which are then selected for reconstruction. Both algorithms have been reported to provide good denoising results (28,29).

**Adaptive Processing.** Several methods of adaptive denoising have been developed. Eng and Ma (30) employ a first stage noise detection process to identify pixels that are to undergo no filtering, standard median filtering or fuzzy weighted median filtering in the second stage. Chan et al. (31) have proposed a two-stage scheme in which an adaptive median filter is used to identify pixels that are likely to have been contaminated by noise. In the second stage, the noise candidates are smoothed using a regularization algorithm.

## 10.4. EDGE CRISPENING

Psychophysical experiments indicate that a photograph or visual signal with accentuated or *crispended* edges is often more subjectively pleasing than an exact photometric reproduction. *Edge crispening* can be accomplished in a variety of ways.

### 10.4.1. Linear Edge Crispening

Edge crispening can be performed by discrete convolution, as defined by Eq. 10.3-1, in which the impulse response array  $H$  is of high-pass form. Several common  $3 \times 3$  high-pass masks are given below (32-34).

**Mask 1:**

$$\mathbf{H} = \begin{bmatrix} 0 & -1 & 0 \\ -1 & 5 & -1 \\ 0 & -1 & 0 \end{bmatrix} \quad (10.4-1a)$$

**Mask 2:**

$$\mathbf{H} = \begin{bmatrix} -1 & -1 & -1 \\ -1 & 9 & -1 \\ -1 & -1 & -1 \end{bmatrix} \quad (10.4-1b)$$

**Mask 3:**

$$\mathbf{H} = \begin{bmatrix} 1 & -2 & 1 \\ -2 & 5 & -2 \\ 1 & -2 & 1 \end{bmatrix} \quad (10.4-1c)$$

These masks possess the property that the sum of their elements is unity, to avoid amplitude bias in the processed image. Figure 10.4-1 provides examples of edge crispening on a monochrome image with the masks of Eq. 10.4-1. Mask 2 appears to provide the best visual results.

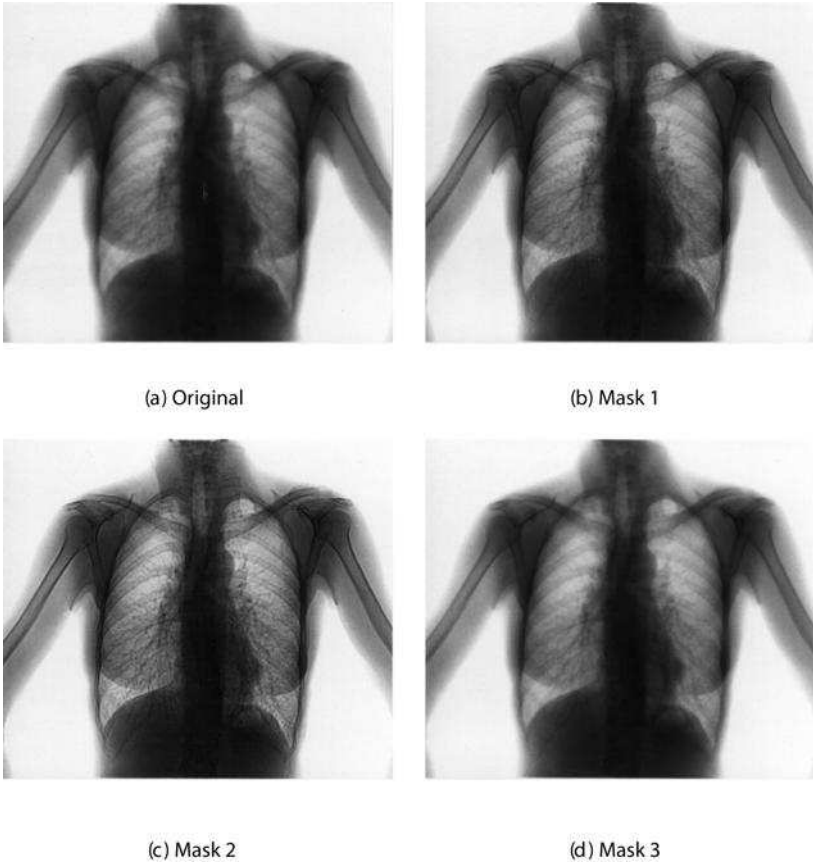


**FIGURE 10.4-1.** Edge crispening with  $3 \times 3$  masks on the chest\_xray image.

To obtain edge crispening on electronically scanned images, the scanner signal can be passed through an electrical filter with a high-frequency bandpass characteristic. Another possibility for scanned images is the technique of *unsharp masking* (35,36). In this process, the image is effectively scanned with two overlapping apertures, one at normal resolution and the other at a lower spatial resolution, which upon sampling produces normal and low-resolution images  $F(j, k)$  and  $F_L(j, k)$ , respectively. An unsharp masked image

$$G(j, k) = \frac{c}{2c-1} F(j, k) - \frac{1-c}{2c-1} F_L(j, k) \tag{10.4-2}$$

is then generated by forming the weighted difference between the normal and low-resolution images, where  $c$  is a weighting constant. Typically,  $c$  is in the range  $3/5$  to  $5/6$ , so that the ratio of normal to low-resolution components in the masked image is

from 1.5:1 to 5:1. Figure 10.4-2 illustrates typical scan signals obtained when scanning over an object edge. The masked signal has a longer-duration edge gradient as well as an overshoot and undershoot, as compared to the original signal. Subjectively, the apparent sharpness of the original image is improved. Figure 10.4-3 presents examples of unsharp masking in which the low-resolution image is obtained by convolution with a uniform  $L \times L$  impulse response array. The sharpening effect is stronger as  $L$  increases and  $c$  decreases.

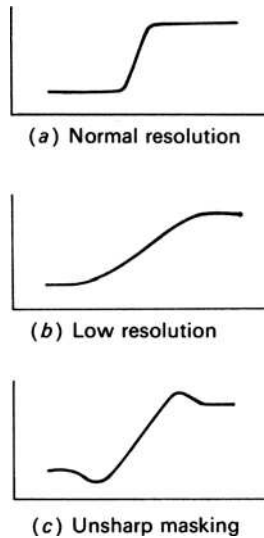


**FIGURE 10.4-2.** Waveforms in an unsharp masking image enhancement system.

Edge crispening using an unsharp masking operator is sensitive to image noise. Polesel et al. (37) have developed an adaptive unsharp masking filter in which contrast enhancement occurs in high detail regions of an image; little or no image sharpening occurs in smooth areas.

Linear edge crispening can be performed by Fourier domain filtering. A zonal high-pass filter with a transfer function given by Eq. 9.4-10 suppresses all spatial frequencies below the cutoff frequency except for the dc component, which is necessary to maintain the average amplitude of the filtered image. Figure 10.4-4 shows the result of zonal high-pass filtering of an image. Zonal high-pass filtering often causes *ringing* in a filtered image. Such ringing can be reduced significantly by utilization of a high-pass filter with a smooth cutoff response. One such filter is the Butterworth high-pass filter, whose transfer function is defined by Eq. 9.4-13.

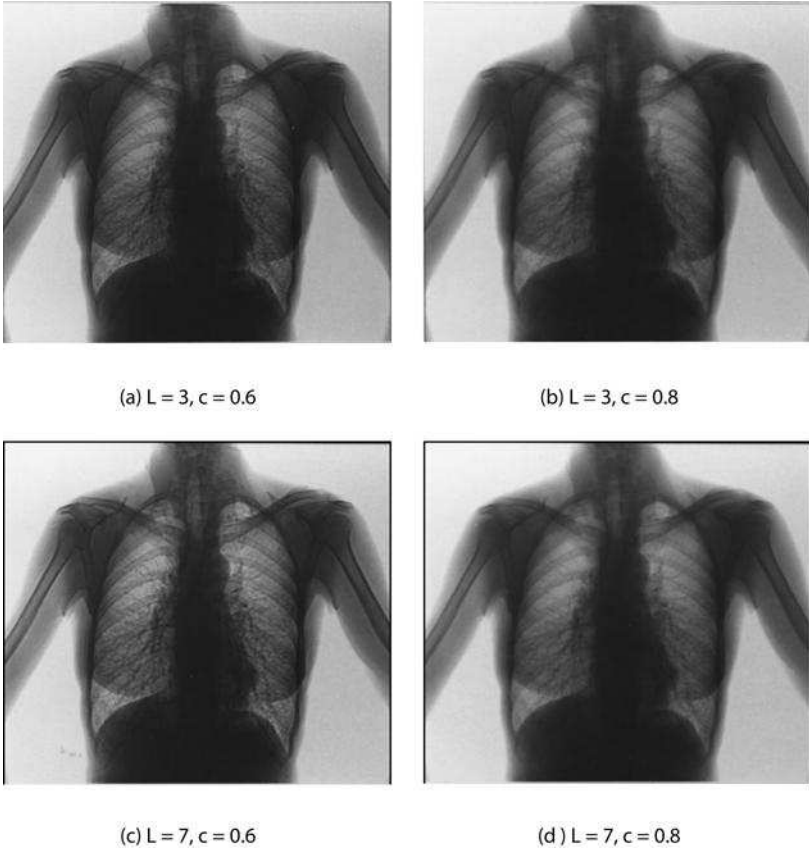


**FIGURE 10.4-3.** Unsharp mask processing for  $L \times L$  uniform low-pass convolution on the chest\_xray image.

Figure 10.4-4 shows the results of zonal and Butterworth high-pass filtering. In both examples, the filtered images are biased to a mid gray level for display.

**10.4.2. Statistical Differencing**

Another form of edge crispening, called *statistical differencing* (38, p. 100), involves the generation of an image by dividing each pixel value by its estimated standard deviation  $D(j, k)$  according to the basic relation

$$G(j, k) = \frac{F(j, k)}{D(j, k)} \tag{10.4-3}$$

where the estimated standard deviation

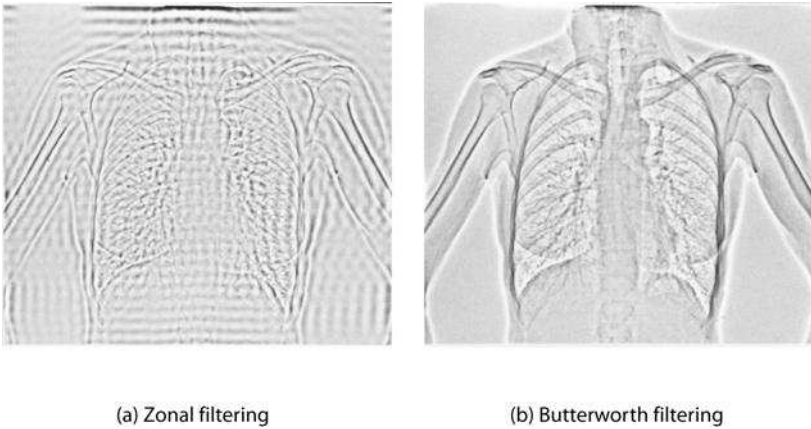


**FIGURE 10.4-4.** Zonal and Butterworth high-pass filtering on the chest\_xray image; cutoff frequency = 32.

$$D(j, k) = \frac{1}{W} \left[ \sum_{m=j-w}^{j+w} \sum_{n=k-w}^{k+w} [F(m, n) - M(m, n)]^2 \right]^{1/2} \quad (10.4-4)$$

is computed at each pixel over some  $W \times W$  neighborhood where  $W = 2w + 1$ . The function  $M(j, k)$  is the estimated mean value of the original image at point  $(j, k)$ , which is computed as

$$M(j, k) = \frac{1}{W^2} \sum_{m=j-w}^{j+w} \sum_{n=k-w}^{k+w} F(m, n). \quad (10.4-5)$$

The enhanced image  $G(j, k)$  is increased in amplitude with respect to the original at pixels that deviate significantly from their neighbors, and is decreased in relative amplitude elsewhere. The process is analogous to automatic gain control for an audio signal.

Wallis (39) has suggested a generalization of the statistical differencing operator in which the enhanced image is forced to a form with desired first- and second-order moments. The *Wallis operator* is defined by

$$G(j, k) = [F(j, k) - M(j, k)] \frac{A_{\max} D_d}{A_{\max} D(j, k) + D_d} + [pM_d + (1-p)M(j, k)] \quad (10.4-6)$$

where  $M_d$  and  $D_d$  represent desired average mean and standard deviation factors,  $A_{\max}$  is a maximum gain factor that prevents overly large output values when  $D(j, k)$  is small and  $0.0 \leq p \leq 1.0$  is a mean proportionality factor controlling the background flatness of the enhanced image.

The Wallis operator can be expressed in a more general form as

$$G(j, k) = [F(j, k) - M(j, k)]A(j, k) + B(j, k) \quad (10.4-7)$$

where  $A(j, k)$  is a spatially dependent gain factor and  $B(j, k)$  is a spatially dependent background factor. These gain and background factors can be derived directly from Eq. 10.4-6, or they can be specified in some other manner. For the Wallis operator, it is convenient to specify the desired average standard deviation  $D_d$  such that the spatial gain ranges between maximum  $A_{\max}$  and minimum  $A_{\min}$  limits. This can be accomplished by setting  $D_d$  to the value

$$D_d = \frac{A_{\min}A_{\max}D_{\max}}{A_{\max} - A_{\min}} \quad (10.4-8)$$

where  $D_{\max}$  is the maximum value of  $D(j, k)$ . The summations of Eqs. 10.4-4 and 10.4-5 can be implemented by convolutions with a uniform impulse array. But, overshoot and undershoot effects may occur. Better results are usually obtained with a pyramid or Gaussian-shaped array.

Figure 10.4-5 shows the mean, standard deviation, spatial gain and Wallis statistical differencing result on a monochrome image. Figure 10.4-6 presents a medical imaging example.

## 10.5. COLOR IMAGE ENHANCEMENT

The image enhancement techniques discussed previously have all been applied to monochrome images. This section considers the enhancement of natural color images and introduces the pseudocolor and false color image enhancement methods. In the literature, the terms pseudocolor and false color have often been used improperly. Pseudocolor produces a color image from a monochrome image, while false color produces an enhanced color image from an original natural color image or from multispectral image bands.

### 10.5.1. Natural Color Image Enhancement

The monochrome image enhancement methods described previously can be applied to natural color images by processing each color component individually. This comprises the class of intra-component processing algorithms. There is also a class of inter-component processing algorithms in which color pixels are combined on a pixel-by-pixel basis. Finally, there is a class of vector processing algorithms.



(a) Original



(b) Mean, 0.00 to 0.98



(c) Standard deviation, 0.01 to 0.26



(d) Background, 0.09 to 0.88



(e) Spatial gain, 0.75 to 2.35



(f) Wallis enhancement, - 0.07 to 1.12

**FIGURE 10.4-5.** Wallis statistical differencing on the bridge image for  $M_d = 0.45$ ,  $D_d = 0.28$ ,  $p = 0.20$ ,  $A_{\max} = 2.50$ ,  $A_{\min} = 0.75$  using a  $9 \times 9$  pyramid array.



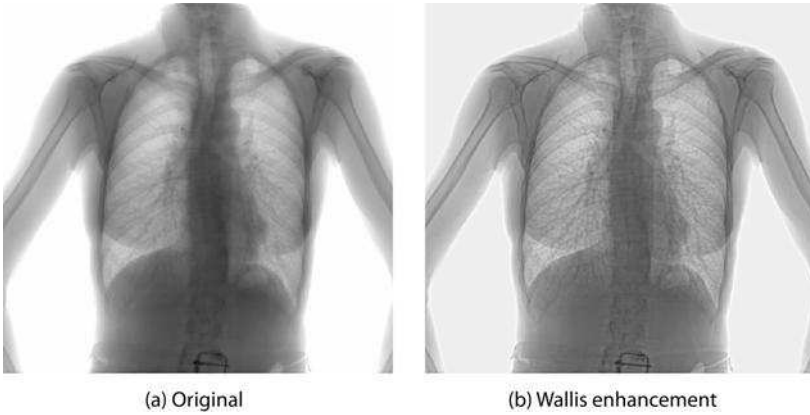


**FIGURE 10.4-6.** Wallis statistical differencing on the `chest_xray` image for  $M_d = 0.64$ ,  $D_d = 0.22$ ,  $p = 0.20$ ,  $A_{\max} = 2.50$ ,  $A_{\min} = 0.75$  using a  $11 \times 11$  pyramid array.

**Intra-component Processing.** Typically, color images are processed in the  $RGB$  color space. This approach works quite well for noise cleaning algorithms in which the noise is independent between the  $R$ ,  $G$  and  $B$  components. Edge crispening can also be performed on an intra-component basis, but better, and more efficient, results, are often obtained by processing in other color spaces. Contrast manipulation and histogram modification intra-component algorithms often result in severe shifts of the hue and saturation of color images. Hue preservation can be achieved by using a single point transformation for each of the three  $RGB$  components (40). For example, form a sum image  $S = R + G + B$ , and then compute a histogram equalization function, which is used for each  $RGB$  component.

For some image enhancement algorithms, there are computational advantages to processing in a luma-chroma space, such as  $YC_bC_r$ , or a lightness-chrominance space, such as  $L^*a^*b^*$ . As an example, if the objective is to perform edge crispening of a color image, it is usually only necessary to apply the enhancement method to the luma or lightness component. Because of the high-spatial-frequency response limitations of human vision, edge crispening of the chroma or chrominance components may not be perceptible.

Faugeras (41) has investigated color image enhancement in a perceptual space based on a color vision model similar to the model presented in Figure 2.5-3. The procedure is to transform a  $RGB$  tristimulus value original image according to the color vision model to produce a set of three perceptual space images that, ideally, are perceptually independent. Then, an image enhancement method is applied independently to the perceptual space images. Finally, the enhanced perceptual space images are subjected to steps that invert the color vision model and produce an enhanced color image represented in  $RGB$  color space.

**Inter-component Processing.** The intra-component processing algorithms previously discussed provide no means of modifying the hue and saturation of a processed image in a controlled manner. One means of doing so is to transform a source *RGB* image into a three component image, in which the three components form separate measures of the brightness, hue and saturation (*BHS*) of a color image. Ideally, the three components should be perceptually independent of one another. Once the *BHS* components are determined, they can be modified by amplitude scaling methods, as described, in Sec. 10.1.1.

The *IHS* color coordinate system defined by Eq. 3.5-20 has been proposed for non-standard color images. There are no standard colorimetric definitions for hue and saturation measures. However, the following ad hoc definition for the  $L^*a^*b^*$  color coordinate system of Eq. 3.5-6 can be utilized:

$$B = L^* \tag{10.5-1a}$$

$$H = \arctan \left\{ \frac{b^*}{a^*} \right\} \tag{10.5-1b}$$

$$S = [a^* + b^*]^{1/2} . \tag{10.5-1c}$$

**Color Vector Processing.** As shown in Figure 3.3-2, a color vector  $\mathbf{v} = [R, G, B]^T$  can be formed in three-dimensional color space based upon the *R*, *G* and *B* color components at each pixel  $(j, k)$ . Now consider a moving window about the  $(j, k)$  pixel, which contains a sequence of color vectors  $\mathbf{v}_1, \mathbf{v}_2, \dots, \mathbf{v}_N$ . For example, for a  $3 \times 3$  window, the neighborhood array is:

$$\begin{bmatrix} \mathbf{v}_1 & \mathbf{v}_2 & \mathbf{v}_3 \\ \mathbf{v}_4 & \mathbf{v}_5 & \mathbf{v}_6 \\ \mathbf{v}_7 & \mathbf{v}_8 & \mathbf{v}_9 \end{bmatrix}$$

For natural, noise-free images with a relatively small window, the vectors  $\mathbf{v}_n$  will be similar in magnitude and direction. For images subject to noise, some of the vectors may differ significantly from one another. Astola, Haavisto and Neuvo (42) have proposed a *vector median filter* (VMF) as a means of color image denoising. The vector in the window center is replaced by the median of all of the vectors in the window. References 42 to 44 discuss various sorting algorithms for computation of the VMF.

**10.5.2. Pseudocolor**

*Pseudocolor* (45–47) is a color mapping of a monochrome image array which is intended to enhance the detectability of detail within the image. The pseudocolor mapping of an array  $F(j, k)$  is defined as

$$R(j, k) = O_R\{F(j, k)\} \tag{10.5-2a}$$

$$G(j, k) = O_G\{F(j, k)\} \tag{10.5-2b}$$

$$B(j, k) = O_B\{F(j, k)\} \tag{10.5-2c}$$

where  $R(j, k)$ ,  $G(j, k)$ ,  $B(j, k)$  are display color components and  $O_R\{F(j, k)\}$ ,  $O_G\{F(j, k)\}$ ,  $O_B\{F(j, k)\}$  are linear or nonlinear functional operators. This mapping defines a path in three-dimensional color space parametrically in terms of the array  $F(j, k)$ . Figure 10.5-1 illustrates the *RGB* color space and two color mappings that originate at black and terminate at white. Mapping *A* represents the *achromatic* path through all shades of gray; it is the normal representation of a monochrome image. Mapping *B* is a spiral path through color space.

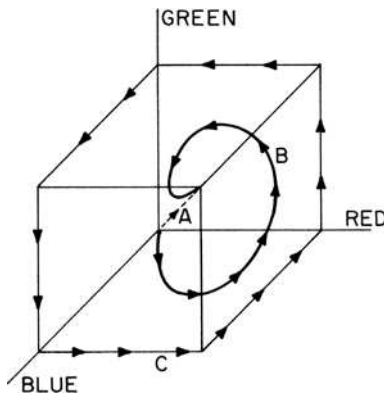
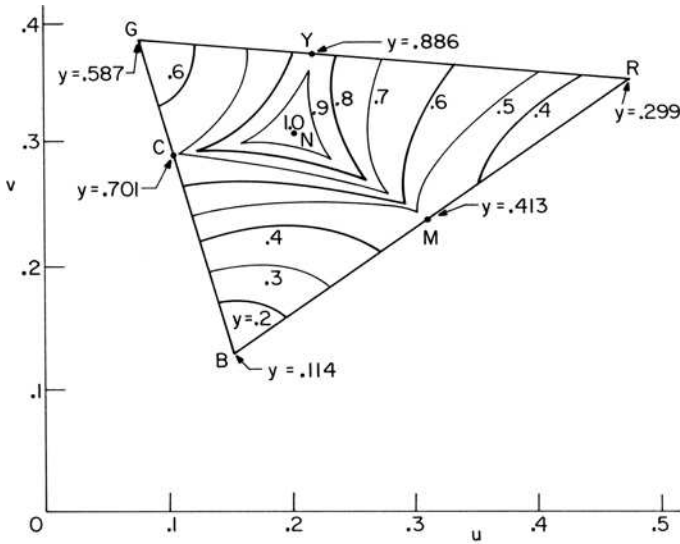
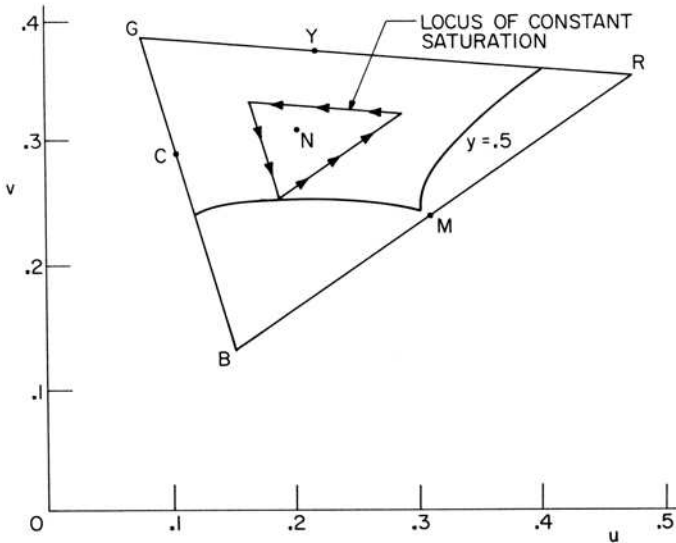


**FIGURE 10.5-1.** Black-to-white and *RGB* perimeter pseudocolor mappings.

Another class of pseudocolor mappings includes those mappings that exclude all shades of gray. Mapping *C*, which follows the edges of the *RGB* color cube, is such an example. This mapping follows the perimeter of the gamut of reproducible colors as depicted by the uniform chromaticity scale (UCS) chromaticity chart shown in Figure 10.5-2. The luminances of the colors red, green, blue, cyan, magenta and yellow that lie along the perimeter of reproducible colors are noted in the figure. It is seen that the luminance of the pseudocolor scale varies between a minimum of 0.114 for blue to a maximum of 0.886 for yellow. A maximum luminance of unity is reached only for white. In some applications, it may be desirable to fix the luminance of all displayed colors so that discrimination along the pseudocolor scale is by hue and saturation attributes of a color only. Loci of constant luminance are plotted in Figure 10.5-2.



(a) Loci of maximum luminance



(b) Locus of luminance  $Y = 0.5$

**FIGURE 10.5-2.** Luminance loci for NTSC colors.

Figure 10.5-2 also includes bounds for displayed colors of constant luminance. For example, if the *RGB* perimeter path is followed, the maximum luminance of any color must be limited to 0.114, the luminance of blue. At a luminance of 0.2, the *RGB* perimeter path can be followed except for the region around saturated

blue. At higher luminance levels, the gamut of constant luminance colors becomes severely limited. Figure 10.5-2b is a plot of the 0.5 luminance locus. Inscribed within this locus is the locus of those colors of largest constant saturation. A pseudocolor scale along this path would have the property that all points differ only in hue.

With a given pseudocolor path in color space, it is necessary to choose the scaling between the data plane variable and the incremental path distance. On the UCS chromaticity chart, incremental distances are subjectively almost equally noticeable.

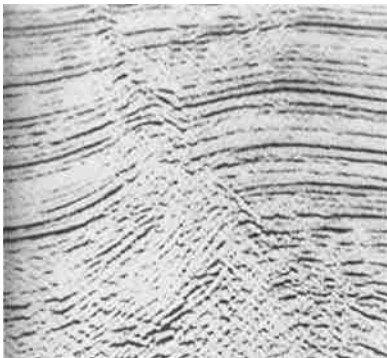
Therefore, it is reasonable to subdivide geometrically the path length into equal increments. Figure 10.5-3 shows examples of pseudocoloring of a gray scale chart image and a seismic image.



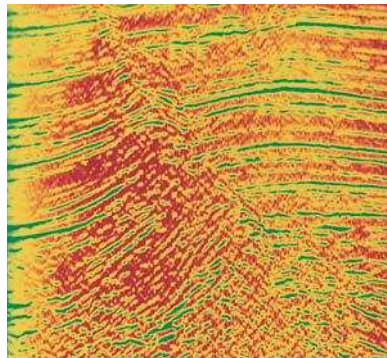
(a) Gray scale chart



(b) Pseudocolor of chart



(c) Seismic



(b) Pseudocolor of seismic

**FIGURE 10.5-3.** Pseudocoloring of the `gray_chart` and `seismic` images. For monochrome printers and displays, see the website for a color representation of this figure.

### 10.5.3. False Color

*False color* is a point-by-point mapping of an original color image, described by its three primary colors, or of a set of multispectral image planes of a scene, to a color space defined by display tristimulus values that are linear or nonlinear functions of the original image pixel values (48,49). A common intent is to provide a displayed image with objects possessing different or false colors from what might be expected. For example, blue sky in a normal scene might be converted to appear red, and green grass transformed to blue. One possible reason for such a color mapping is to place normal objects in a strange color world so that a human observer will pay more attention to the objects than if they were colored normally.

Another reason for false color mappings is the attempt to color a normal scene to match the color sensitivity of a human viewer. For example, it is known that the luminance response of cones in the retina peaks in the green region of the visible spectrum. Thus, if a normally red object is false colored to appear green, it may become more easily detectable. Another psychophysical property of color vision that can be exploited is the contrast sensitivity of the eye to changes in blue light. In some situations it may be worthwhile to map the normal colors of objects with fine detail into shades of blue.

A third application of false color is to produce a natural color representation of a set of multispectral images of a scene. Some of the multispectral images may even be obtained from sensors whose wavelength response is outside the visible wavelength range, for example, infrared or ultraviolet.

In a false color mapping, the red, green and blue display color components are related to natural or multispectral images  $F_i$  by

$$R_D = O_R\{F_1, F_2, \dots\} \tag{10.5-3a}$$

$$G_D = O_G\{F_1, F_2, \dots\} \tag{10.5-3b}$$

$$B_D = O_B\{F_1, F_2, \dots\} \tag{10.5-3c}$$

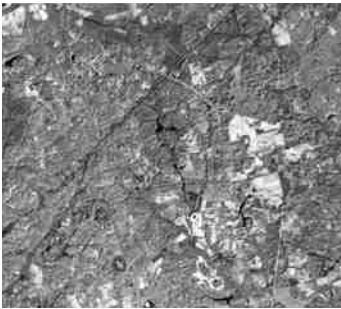
where  $O_R\{\cdot\}$ ,  $O_G\{\cdot\}$ ,  $O_B\{\cdot\}$  are general functional operators. As a simple example, the set of red, green and blue sensor tristimulus values ( $R_S = F_1$ ,  $G_S = F_2$ ,  $B_S = F_3$ ) may be interchanged according to the relation

$$\begin{bmatrix} R_D \\ G_D \\ B_D \end{bmatrix} = \begin{bmatrix} 0 & 1 & 0 \\ 0 & 0 & 1 \\ 1 & 0 & 0 \end{bmatrix} \begin{bmatrix} R_S \\ G_S \\ B_S \end{bmatrix}. \tag{10.5-4}$$

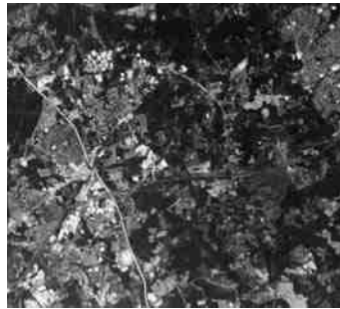
Green objects in the original will appear red in the display, blue objects will appear green and red objects will appear blue. A general linear false color mapping of natural color images can be defined as

$$\begin{bmatrix} R_D \\ G_D \\ B_D \end{bmatrix} = \begin{bmatrix} m_{11} & m_{12} & m_{13} \\ m_{21} & m_{22} & m_{21} \\ m_{23} & m_{32} & m_{33} \end{bmatrix} \begin{bmatrix} R_S \\ G_S \\ B_S \end{bmatrix} \quad (10.5-5)$$

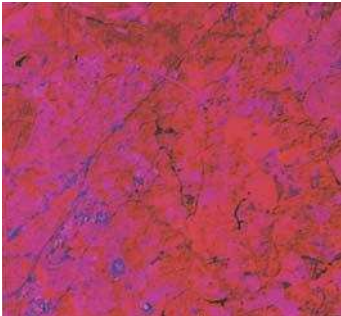
This color mapping should be recognized as a linear coordinate conversion of colors reproduced by the primaries of the original image to a new set of primaries. Figure 10.5-4 provides examples of false color mappings of a pair of images.



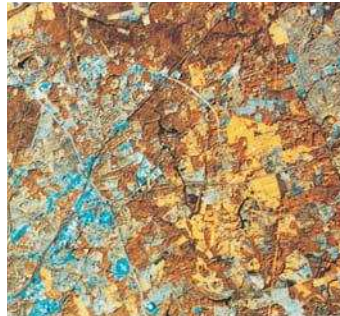
(a) Infrared band



(b) Blue band



(c) R = infrared, G = 0, B = blue



(d) R = infrared, G = 1/2 [infrared + blue], B = blue

**FIGURE 10.5-4.** False coloring of multispectral images. For monochrome printers and displays, see the website for a color representation of this figure.

### 10.6. MULTISPECTRAL IMAGE ENHANCEMENT

Enhancement procedures are often performed on multispectral image bands of a scene in order to accentuate salient features to assist in subsequent human interpretation or machine analysis (43-45). These procedures include individual image

band enhancement techniques, such as contrast stretching, noise cleaning and edge crispensing, as described earlier. Other methods, considered in this section, involve the joint processing of multispectral image bands.

Multispectral image bands can be subtracted in pairs according to the relation

$$D_{m,n}(j, k) = F_m(j, k) - F_n(j, k) \tag{10.6-1}$$

in order to accentuate reflectivity variations between the multispectral bands. An associated advantage is the removal of any unknown but common bias components that may exist. Another simple but highly effective means of multispectral image enhancement is the formation of ratios of the image bands. The ratio image between the  $m$ th and  $n$ th multispectral bands is defined as

$$R_{m,n}(j, k) = \frac{F_m(j, k)}{F_n(j, k)} \tag{10.6-2}$$

It is assumed that the image bands are adjusted to have nonzero pixel values. In many multispectral imaging systems, the image band  $F_n(j, k)$  can be modeled by the product of an object reflectivity function  $R_n(j, k)$  and an illumination function  $I(j, k)$  that is identical for all multispectral bands. Ratioing of such imagery provides an automatic compensation of the illumination factor. The ratio  $F_m(j, k)/[F_n(j, k) \pm \Delta(j, k)]$ , for which  $\Delta(j, k)$  represents a quantization level uncertainty, can vary considerably if  $F_n(j, k)$  is small. This variation can be reduced significantly by forming the logarithm of the ratios defined by

$$L_{m,n}(j, k) = \log\{R_{m,n}(j, k)\} = \log\{F_m(j, k)\} - \log\{F_n(j, k)\}. \tag{10.6-3}$$

There are a total of  $N(N - 1)$  different difference or ratio pairs that may be formed from  $N$  multispectral bands. To reduce the number of combinations to be considered, the differences or ratios are often formed with respect to an average image field:

$$A(j, k) = \frac{1}{N} \sum_{n=1}^N F_n(j, k). \tag{10.6-4}$$

Unitary transforms between multispectral planes have also been employed as a means of enhancement. For  $N$  image bands, a  $N \times 1$  vector

$$\mathbf{x} = \begin{bmatrix} F_1(j, k) \\ F_2(j, k) \\ \cdot \\ \cdot \\ F_N(j, k) \end{bmatrix} \tag{10.6-5}$$



is formed at each coordinate  $(j, k)$ . Then, a transformation

$$\mathbf{y} = \mathbf{A}\mathbf{x} \quad (10.6-6)$$

is formed where  $\mathbf{A}$  is a  $N \times N$  unitary matrix. A common transformation is the principal components decomposition, described in Appendix A1.2, in which the rows of the matrix  $\mathbf{A}$  are composed of the eigenvectors of the covariance matrix  $\mathbf{K}_x$  between the bands. The matrix  $\mathbf{A}$  performs a diagonalization of the covariance matrix  $\mathbf{K}_x$  such that the covariance matrix of the transformed imagery bands

$$\mathbf{K}_y = \mathbf{A}\mathbf{K}_x\mathbf{A}^T = \mathbf{\Lambda} \quad (10.6-7)$$

is a diagonal matrix  $\mathbf{\Lambda}$  whose elements are the eigenvalues of  $\mathbf{K}_x$  arranged in descending value. The principal components decomposition, therefore, results in a set of decorrelated data arrays whose energies are ranged in amplitude. This process, of course, requires knowledge of the covariance matrix between the multispectral bands. The covariance matrix must be either modeled, estimated or measured. If the covariance matrix is highly nonstationary, the principal components method becomes difficult to utilize.

Figure 10.6-1 contains a set of four multispectral images, and Figure 10.6-2 exhibits their corresponding log ratios (50). Principal components bands of these multispectral images are illustrated in Figure 10.6-3 (50).

## 10.7. IMAGE ENHANCEMENT EXERCISES

E10.1 Develop a program that displays the  $Q$  component of a  $YIQ$  color image over its full dynamic range. Steps:

- (a) Display the source monochrome  $RGB$  image.
- (b) Scale the  $RGB$  image to unit range and convert it to the  $YIQ$  space.
- (c) Extract the  $Q$  component image.
- (d) Compute the amplitude extrema.
- (e) Display the  $Q$  component.

The PIKS API executable `example_Q_display` performs this exercise.

E10.2 Develop a program to histogram equalize an unsigned integer, 8-bit, monochrome image. Steps:

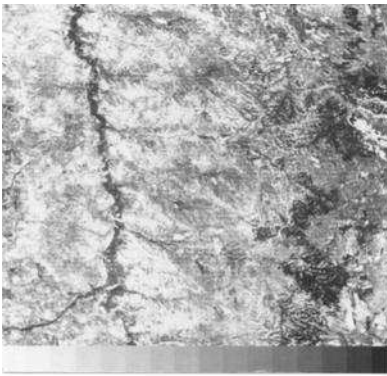
- (a) Display the source monochrome image.
- (b) Compute the image histogram.
- (c) Compute the image cumulative histogram.
- (d) Load the image cumulative histogram into a lookup table.

- (e) Pass the image through the lookup table.
- (f) Display the enhanced destination image.

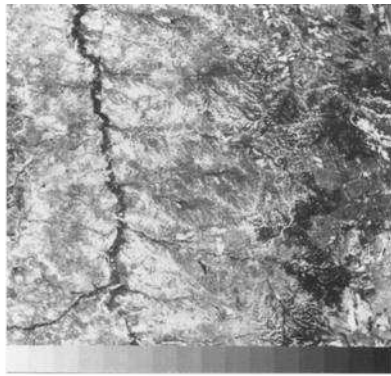
The PIKS API executable `example_histogram_equalization` performs this exercise.

E10.3 Develop a program to perform outlier noise cleaning of the unsigned integer, 8-bit, monochrome image `peppers_replacement_noise` following the algorithm of Figure 10.3-9. Steps:

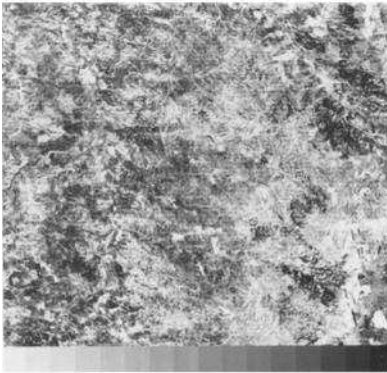
- (a) Display the source monochrome image.
- (b) Compute a  $3 \times 3$  neighborhood average image by convolution with a uniform impulse array.



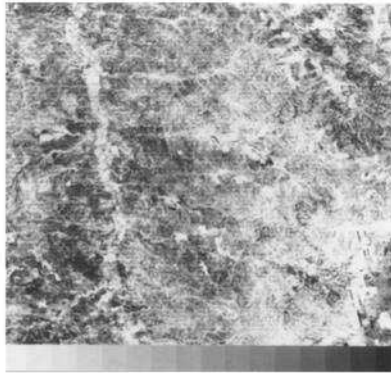
(a) Band 4 (green)



(b) Band 5 (red)

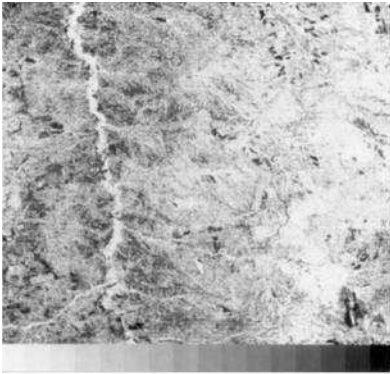


(c) Band 6 (infrared 1)

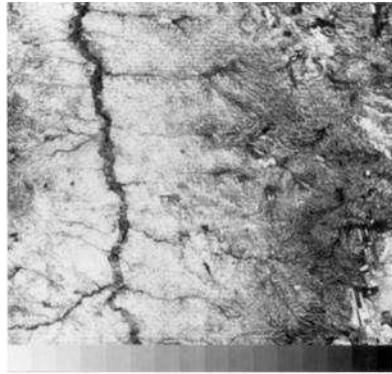


(d) Band 7 (infrared 2)

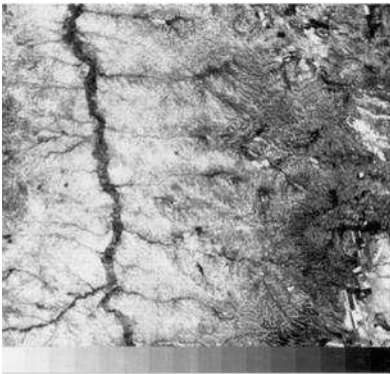
**FIGURE 10.6-1.** Multispectral images.



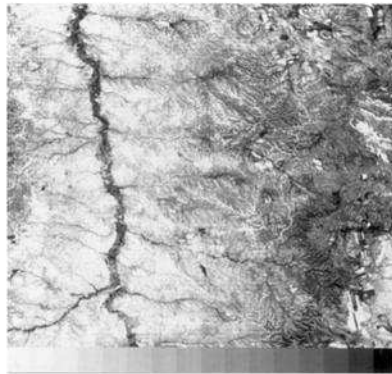
(a)  $\frac{\text{Band 4}}{\text{Band 5}}$



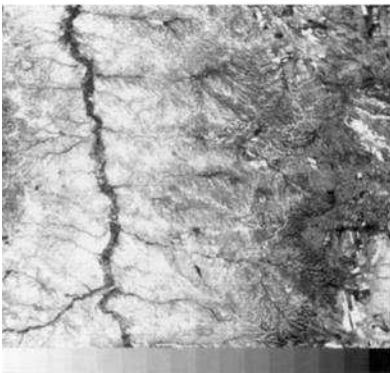
(b)  $\frac{\text{Band 4}}{\text{Band 6}}$



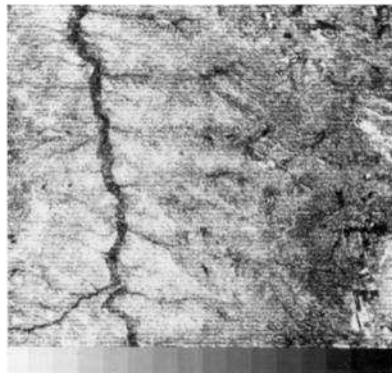
(c)  $\frac{\text{Band 4}}{\text{Band 7}}$



(d)  $\frac{\text{Band 5}}{\text{Band 6}}$



(e)  $\frac{\text{Band 5}}{\text{Band 7}}$



(f)  $\frac{\text{Band 6}}{\text{Band 7}}$

FIGURE 10.6-2. Logarithmic ratios of multispectral images.

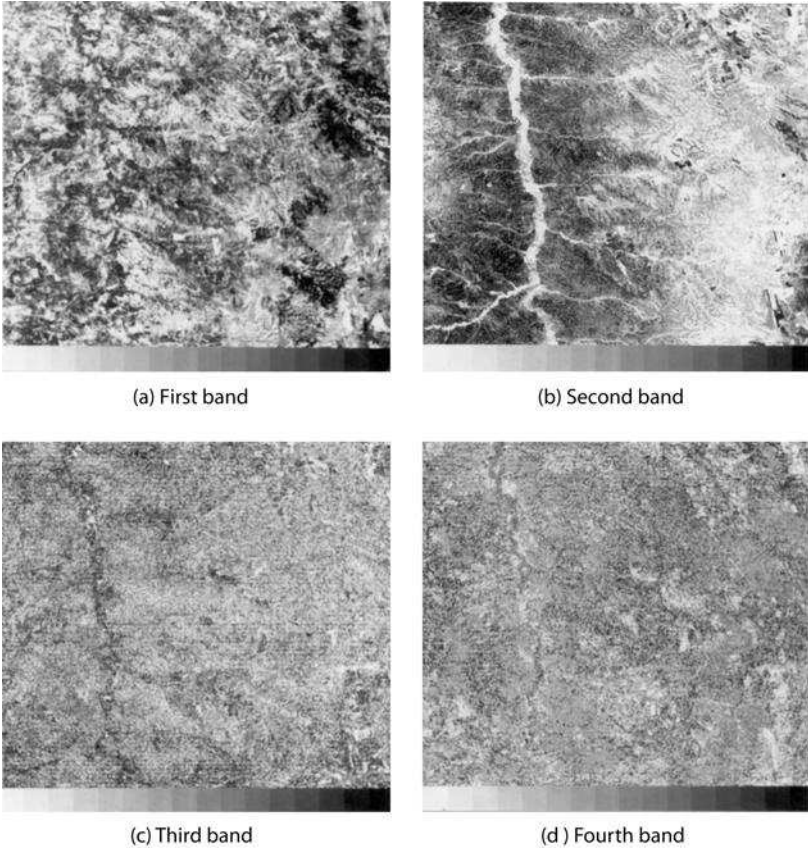


**FIGURE 10.6-3.** Principal components of multispectral images.

- (c) Display the neighborhood image.
- (d) Create a magnitude of the difference image between the source image and the neighborhood image.
- (e) Create a Boolean mask image which is TRUE if the magnitude difference image is greater than a specified error tolerance, e.g. 15%.
- (f) Convert the mask image to a ROI and use it to generate the outlier destination image.
- (g) Display the destination image.

The PIKS API executable `example_outlier` performs this exercise.

E10.4 Develop a program that performs linear edge crispening of an unsigned integer, 8-bit, color image by convolution. Steps:

- (a) Display the source color image.
- (b) Import the Mask 3 impulse response array defined by Eq.10.4-1c.
- (c) Convert the source image to 16-bit or larger integer or real datatype.
- (d) Convolve the color image with the impulse response array.
- (e) Clip the convolved image over the dynamic range of the source image to avoid amplitude undershoot and overshoot.
- (f) Display the clipped destination image.

The executable `example_edge_crispening` performs this exercise.

E10.5 Develop a program that performs  $7 \times 7$  plus-shape median filtering of the unsigned integer, 8-bit, monochrome image `peppers_replacement_noise`. Steps:

- (a) Display the source monochrome image.
- (b) Create a  $7 \times 7$  Boolean mask array.
- (c) Perform median filtering.
- (d) Display the destination image.

The PIKS API executable `example_filtering_median_plus7` performs this exercise.

E10.6 Develop a program that generates a pseudocolor display of the `ramp` image. Steps:

- (a) Display the source monochrome image.
- (b) Create the pseudocolor lookup table with six segments starting at blue and ending at magenta.
- (c) Pass the source image through the LUT.
- (d) Display the destination image.

The PIKS API executable `example_pseudocolor` performs this exercise.

E10.7 Develop a program that generates a false color display of an infrared image and a blue image. Steps:

- (a) Display the `landsat_ir` infrared band monochrome image.
- (b) Display the `landsat_blue` blue band monochrome image.
- (c) Copy the landsat infrared band to the red band of a false color image.
- (d) Copy the landsat blue band to the blue band of the false color image.

- (e) Create a hybrid image:  $0.5[\text{infrared} + \text{blue}]$ .
- (f) Copy the landsat hybrid image to the green band of the false color image.
- (g) Display the false color destination image.

The PIKS API executable `example_false_color` performs this exercise.

## REFERENCES

1. R. Nathan, "Picture Enhancement for the Moon, Mars and Man," in *Pictorial Pattern Recognition*, G. C. Cheng, Ed., Thompson, Washington, DC, 1968, 239–235.
2. F. Billingsley, "Applications of Digital Image Processing," *Applied Optics*, **9**, 2, February 1970, 289–299.
3. A. Pardo and G. Sapiro, "Visualization of High Dynamic Range Images," *IEEE Trans. Image Processing*, **12**, 6, June 2003, 639–647.
4. H. C. Andrews, A. G. Tescher and R. P. Kruger, "Image Processing by Digital Computer," *IEEE Spectrum*, **9**, 7, July 1972, 20–32.
5. E. L. Hall et al., "A Survey of Preprocessing and Feature Extraction Techniques for Radiographic Images," *IEEE Trans. Computers*, **C-20**, 9, September 1971, 1032–1044.
6. E. L. Hall, "Almost Uniform Distribution for Computer Image Enhancement," *IEEE Trans. Computers*, **C-23**, 2, February 1974, 207–208.
7. W. Frei, "Image Enhancement by Histogram Hyperbolization," *Computer Graphics and Image Processing*, **6**, 3, June 1977, 286–294.
8. D. J. Ketcham, "Real Time Image Enhancement Technique," *Proc. SPIE/OSA Conference on Image Processing*, Pacific Grove, CA, **74**, February 1976, 120–125.
9. R. A. Hummel, "Image Enhancement by Histogram Transformation," *Computer Graphics and Image Processing*, **6**, 2, 1977, 184–195.
10. S. M. Pizer et al., "Adaptive Histogram Equalization and Its Variations," *Computer Vision, Graphics and Image Processing*, **39**, 3, September 1987, 355–368.
11. J. A. Stark, "Adaptive Image Contrast Enhancement Using Generalizations of Histogram Equalization," *IEEE Trans. Image Processing*, **9**, 5, May 2000, 889–896.
12. G. P. Dineen, "Programming Pattern Recognition," *Proc. Western Joint Computer Conference*, March 1955, 94–100.
13. R. E. Graham, "Snow Removal: A Noise Stripping Process for Picture Signals," *IRE Trans. Information Theory*, **IT-8**, 1, February 1962, 129–144.
14. A. Rosenfeld, C. M. Park and J. P. Strong, "Noise Cleaning in Digital Pictures," *Proc. EASCON Convention Record*, October 1969, 264–273.
15. R. Nathan, "Spatial Frequency Filtering," in *Picture Processing and Psychopictorics*, B. S. Lipkin and A. Rosenfeld, Eds., Academic Press, New York, 1970, 151–164.
16. A. V. Oppenheim, R. W. Schaefer and T. G. Stockham, Jr., "Nonlinear Filtering of Multiplied and Convolved Signals," *Proc. IEEE*, **56**, 8, August 1968, 1264–1291.
17. G. A. Mastin, "Adaptive Filters for Digital Image Noise Smoothing: An Evaluation," *Computer Vision, Graphics and Image Processing*, **31**, 1, July 1985, 103–121.

18. L. S. Davis and A. Rosenfeld, "Noise Cleaning by Iterated Local Averaging," *IEEE Trans. Systems, Man and Cybernetics*, **SMC-7**, 1978, 705–710.
19. J.-S. Lee, "Digital Image Smoothing and the Sigma Filter," *Computer Vision, Graphics, and Image Processing*, **24**, 1983, 255–269.
20. C. Kenney et al., "Peer Group Image Enhancement," *IEEE Trans. Image Processing*, **10**, 2, February 2001, 326–334.
21. J. W. Tukey, *Exploratory Data Analysis*, Addison-Wesley, Reading, MA, 1971.
22. T. A. Nodes and N. C. Gallagher, Jr., "Median Filters: Some Manipulations and Their Properties," *IEEE Trans. Acoustics, Speech and Signal Processing*, **ASSP-30**, 5, October 1982, 739–746.
23. T. S. Huang, G. J. Yang and G. Y. Tang, "A Fast Two-Dimensional Median Filtering Algorithm," *IEEE Trans. Acoustics, Speech and Signal Processing*, **ASSP-27**, 1, February 1979, 13–18.
24. J. T. Astola and T. G. Campbell, "On Computation of the Running Median," *IEEE Trans. Acoustics, Speech and Signal Processing*, **37**, 4, April 1989, 572–574.
25. W. K. Pratt, T. J. Cooper and I. Kabir, "Pseudomedian Filter," *Proc. SPIE Conference*, Los Angeles, January 1984.
26. J. S. Walker, *A Primer on Wavelets and Their Scientific Applications*, Chapman & Hall CRC Press, Boca Raton, FL, 1999.
27. S. Mallat, *A Wavelet Tour of Signal Processing*, Academic Press, New York, 1998.
28. J. Zhong and R. Ning, "Image Denoising Based on Wavelets and Multifractals for Singularity Detection," *IEEE Trans. Image Processing*, **14**, 10, October 2005, 1435–1447.
29. E. J. Balster et al., "Feature-Based Wavelet Shrinkage Algorithm for Image Denoising," *IEEE Trans. Image Processing*, **14**, 12, December 2005, 2024–2039.
30. H.-L. Eng and K.-K. Ma, "Noise Adaptive Soft-Switching Median Filter," *IEEE Trans. Image Processing*, **10**, 2, February 2001, 242–251.
31. R. H. Chan et al., "Salt-and-Pepper Noise Removal by Median-Type Noise Detectors and Detail-Preserving Regularization," *IEEE Trans. Image Processing*, **14**, 10, October 2005, 1479–1485.
32. L. G. Roberts, "Machine Perception of Three-Dimensional Solids," in *Optical and Electro-Optical Information Processing*, J. T. Tippett et al., Eds., MIT Press, Cambridge, MA, 1965.
33. J. M. S. Prewitt, "Object Enhancement and Extraction," in *Picture Processing and Psychopictorics*, B. S. Lipkin and A. Rosenfeld, Eds., Academic Press, New York, 1970, 75–150.
34. A. Arcese, P. H. Mengert and E. W. Trombini, "Image Detection Through Bipolar Correlation," *IEEE Trans. Information Theory*, **IT-16**, 5, September 1970, 534–541.
35. W. F. Schreiber, "Wirephoto Quality Improvement by Unsharp Masking," *J. Pattern Recognition*, **2**, 1970, 111–121.
36. J.-S. Lee, "Digital Image Enhancement and Noise Filtering by Use of Local Statistics," *IEEE Trans. Pattern Analysis and Machine Intelligence*, **PAMI-2**, 2, March 1980, 165–168.
37. A. Polesel et al. "Image Enhancement via Adaptive Unsharp Masking," *IEEE Trans. Image Processing*, **9**, 3, March 2000, 505–510.
38. A. Rosenfeld, *Picture Processing by Computer*, Academic Press, New York, 1969.

39. R. H. Wallis, "An Approach for the Space Variant Restoration and Enhancement of Images," *Proc. Symposium on Current Mathematical Problems in Image Science*, Monterey, CA, November 1976.
40. S. K. Naik and C. A. Murthy, "Hue-Preserving Color Image Enhancement Without Gamut Problem," *IEEE Trans. Image Processing*, **12**, 12, December 2003, 1591–1598.
41. O. D. Faugeras, "Digital Color Image Processing Within the Framework of a Human Visual Model," *IEEE Trans. Acoustics, Speech, Signal Processing*, **ASSP-27**, 4, August 1979, 380–393.
42. J. Astola, P. Haavisto and Y. Neuvo, "Vector Median Filters," *Proc. IEEE*, **78**, 4, April 1990, 678–689.
43. C. S. Regazzoni and A. Teschioni, "A New Approach to Vector Median Filtering Based on Space Filling Curves," *IEEE Trans. Image Processing*, **6**, 7, July 1997, 1025–1037.
44. R. Lukac et al., "Vector Filtering for Color Imaging," *IEEE Signal Processing Magazine*, **22**, 1, January 2005, 74–86.
45. C. Gazley, J. E. Reibert and R. H. Stratton, "Computer Works a New Trick in Seeing Pseudo Color Processing," *Aeronautics and Astronautics*, **4**, April 1967, 56.
46. L. W. Nichols and J. Lamar, "Conversion of Infrared Images to Visible in Color," *Applied Optics*, **7**, 9, September 1968, 1757.
47. E. R. Kreins and L. J. Allison, "Color Enhancement of Nimbus High Resolution Infrared Radiometer Data," *Applied Optics*, **9**, 3, March 1970, 681.
48. A. F. H. Goetz et al., "Application of ERTS Images and Image Processing to Regional Geologic Problems and Geologic Mapping in Northern Arizona," Technical Report 32–1597, Jet Propulsion Laboratory, Pasadena, CA, May 1975.
49. W. Find, "Image Coloration as an Interpretation Aid," *Proc. SPIE/OSA Conference on Image Processing*, Pacific Grove, CA, February 1976, 74, 209–215.
50. G. S. Robinson and W. Frei, "Final Research Report on Computer Processing of ERTS Images," Report USCIPI 640, University of Southern California, Image Processing Institute, Los Angeles, September 1975.





---

# 11

---

## IMAGE RESTORATION

Image restoration may be viewed as an estimation process in which operations are performed on an observed or measured image field to estimate the ideal image field that would be observed if no image degradation were present in an imaging system. Mathematical models are described in the first section of this chapter for image degradation in general classes of imaging systems. These models are then utilized in the following sections as a basis for the development of image restoration techniques.

This chapter develops fundamental concepts for image restoration. Advanced image restoration techniques are described in Pratt(4Ed., 369-379).

### 11.1. IMAGE RESTORATION MODELS

In order effectively to design a digital image restoration system, it is necessary quantitatively to characterize the image degradation effects of the physical imaging system, the image digitizer and the image display. Basically, the procedure is to model the image degradation effects and then perform operations to undo the model to obtain a restored image. It should be emphasized that accurate image modeling is often the key to effective image restoration. There are two basic approaches to the modeling of image degradation effects: a priori modeling and a posteriori modeling. In the former case, measurements are made on the physical imaging system, digitizer and display to determine their response for an arbitrary image field. In some instances, it will be possible to model the system response deterministically, while in other situations it will only be possible to determine the system response in

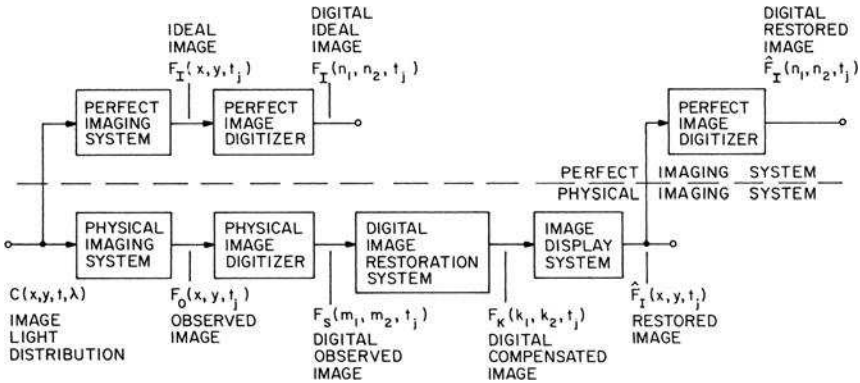


FIGURE 11.1-1. Digital image restoration model.

a stochastic sense. The a posteriori modeling approach is to develop the model for the image degradations based on measurements of a particular image to be restored. Basically, these two approaches differ only in the manner in which information is gathered to describe the character of the image degradation.

Figure 11.1-1 shows a general model of a digital imaging system and restoration process. In the model, a continuous image light distribution  $C(x, y, t, \lambda)$  dependent on spatial coordinates  $(x, y)$ , time  $(t)$  and spectral wavelength  $(\lambda)$  is assumed to exist as the driving force of a physical imaging system subject to point and spatial degradation effects and corrupted by deterministic and stochastic disturbances. Potential degradations include diffraction in the optical system, sensor nonlinearities, optical system aberrations, film nonlinearities, atmospheric turbulence effects, image motion blur and geometric distortion. Noise disturbances may be caused by electronic imaging sensors or film granularity. In this model, the physical imaging system produces a set of output image fields  $F_O^{(i)}(x, y, t_j)$  at time instant  $t_j$  described by the general relation

$$F_O^{(i)}(x, y, t_j) = O_P\{C(x, y, t, \lambda)\} \tag{11.1-1}$$

where  $O_P\{\cdot\}$  represents a general operator that is dependent on the space coordinates  $(x, y)$ , the time history  $(t)$ , the wavelength  $(\lambda)$  and the amplitude of the light distribution  $(C)$ . For a monochrome imaging system, there will only be a single output field, while for a natural color imaging system,  $F_O^{(i)}(x, y, t_j)$  may denote the red, green and blue tristimulus bands for  $i = 1, 2, 3$ , respectively. Multispectral imagery will also involve several output bands of data.

In the general model of Figure 11.1-1, each observed image field  $F_O^{(i)}(x, y, t_j)$  is digitized, following the techniques outlined in Part 2, to produce an array of image samples  $F_S^{(i)}(m_1, m_2, t_j)$  at each time instant  $t_j$ . The output samples of the digitizer are related to the input observed field by

$$F_S^{(i)}(m_1, m_2, t_j) = O_G\{F_O^{(i)}(x, y, t_j)\} \tag{11.1-2}$$

where  $O_G\{\cdot\}$  is an operator modeling the image digitization process.

A digital image restoration system that follows produces an output array  $F_K^{(i)}(k_1, k_2, t_j)$  by the transformation

$$F_K^{(i)}(k_1, k_2, t_j) = O_R\{F_S^{(i)}(m_1, m_2, t_j)\} \tag{11.1-3}$$

where  $O_R\{\cdot\}$  represents the designed restoration operator. Next, the output samples of the digital restoration system are interpolated by the image display system to produce a continuous image estimate  $\hat{F}_I^{(i)}(x, y, t_j)$ . This operation is governed by the relation

$$\hat{F}_I^{(i)}(x, y, t_j) = O_D\{F_K^{(i)}(k_1, k_2, t_j)\} \tag{11.1-4}$$

where  $O_D\{\cdot\}$  models the display transformation.

The function of the digital image restoration system is to compensate for degradations of the physical imaging system, the digitizer and the image display system to produce an estimate of a hypothetical ideal image field  $F_I^{(i)}(x, y, t_j)$  that would be displayed if all physical elements were perfect. The perfect imaging system would produce an ideal image field modeled by

$$F_I^{(i)}(x, y, t_j) = O_I\left\{\int_0^\infty \int_{t_j-T}^{t_j} C(x, y, t, \lambda) U_i(t, \lambda) dt d\lambda\right\} \tag{11.1-5}$$

where  $U_i(t, \lambda)$  is a desired temporal and spectral response function,  $T$  is the observation period and  $O_I\{\cdot\}$  is a desired point and spatial response function.

Usually, it will not be possible to restore perfectly the observed image such that the output image field is identical to the ideal image field. The design objective of the image restoration processor is to minimize some error measure between  $F_I^{(i)}(x, y, t_j)$  and  $\hat{F}_I^{(i)}(x, y, t_j)$ . The discussion here is limited, for the most part, to a consideration of techniques that minimize the mean-square error between the ideal and estimated image fields as defined by

$$\varepsilon_i = E\left\{[F_I^{(i)}(x, y, t_j) - \hat{F}_I^{(i)}(x, y, t_j)]^2\right\} \tag{11.1-6}$$

where  $E\{\cdot\}$  denotes the expectation operator. Often, it will be desirable to place side constraints on the error minimization, for example, to require that the image estimate be strictly positive if it is to represent light intensities that are positive.

Because the restoration process is to be performed digitally, it is often more convenient to restrict the error measure to discrete points on the ideal and estimated image fields. These discrete arrays are obtained by mathematical models of perfect image digitizers that produce the arrays

$$F_I^{(i)}(n_1, n_2, t_j) = F_I^{(i)}(x, y, t_j)\delta(x - n_1\Delta, y - n_2\Delta) \tag{11.1-7a}$$

$$\hat{F}_I^{(i)}(n_1, n_2, t_j) = \hat{F}_I^{(i)}(x, y, t_j)\delta(x - n_1\Delta, y - n_2\Delta). \tag{11.1-7b}$$

It is assumed that continuous image fields are sampled at a spatial period  $\Delta$  satisfying the Nyquist criterion. Also, quantization error is assumed negligible. It should be noted that the processes indicated by the blocks of Figure 11.1-1 above the dashed division line represent mathematical modeling and are not physical operations performed on physical image fields and arrays. With this discretization of the continuous ideal and estimated image fields, the corresponding mean-square restoration error becomes

$$\varepsilon_i = E\left\{ [F_I^{(i)}(n_1, n_2, t_j) - \hat{F}_I^{(i)}(n_1, n_2, t_j)]^2 \right\}. \tag{11.1-8}$$

With the relationships of Figure 11.1-1 quantitatively established, the restoration problem may be formulated as follows:

Given the sampled observation  $F_S^{(i)}(m_1, m_2, t_j)$  expressed in terms of the image light distribution  $C(x, y, t, \lambda)$ , determine the transfer function  $O_K\{ \cdot \}$  that minimizes the error measure between  $F_I^{(i)}(x, y, t_j)$  and  $\hat{F}_I^{(i)}(x, y, t_j)$  subject to desired constraints.

There are no general solutions for the restoration problem as formulated above because of the complexity of the physical imaging system. To proceed further, it is necessary to be more specific about the type of degradation and the method of restoration. The following sections describe models for the elements of the generalized imaging system of Figure 11.1-1.

This chapter began with an introduction to a general model of an imaging system and a digital restoration process. Now, the discussion turns to the development of several discrete image restoration models. In the development of these models, it is assumed that the spectral wavelength response and temporal response characteristics of the physical imaging system can be separated from the spatial and point characteristics. The following discussion considers only spatial and point characteristics.

After each element of the digital image restoration system of Figure 11.1-1 is modeled, following the techniques described previously, the restoration system may be conceptually distilled to three equations:

*Observed image:*

$$F_S(m_1, m_2) = O_M\{F_I(n_1, n_2), N_1(m_1, m_2), \dots, N_N(m_1, m_2)\} \tag{11.1-9a}$$

Compensated image:

$$F_K(k_1, k_2) = O_R\{F_S(m_1, m_2)\} \tag{11.1-9b}$$

Restored image:

$$\hat{F}_I(n_1, n_2) = O_D\{F_K(k_1, k_2)\} \tag{11.1-9c}$$

where  $F_S$  represents an array of observed image samples,  $F_I$  and  $\hat{F}_I$  are arrays of ideal image points and estimates, respectively,  $F_K$  is an array of compensated image points from the digital restoration system,  $N_i$  denotes arrays of noise samples from various system elements, and  $O_M\{\cdot\}$ ,  $O_R\{\cdot\}$ ,  $O_D\{\cdot\}$  represent general transfer functions of the imaging system, restoration processor and display system, respectively. Vector-space equivalents of Eq. 11.1-9 can be formed for purposes of analysis by column scanning of the arrays of Eq. 11.1-9. These relationships are given by

$$\mathbf{f}_S = O_M\{\mathbf{f}_p, \mathbf{n}_1, \dots, \mathbf{n}_N\} \tag{11.1-10a}$$

$$\mathbf{f}_K = O_R\{\mathbf{f}_S\} \tag{11.1-10b}$$

$$\hat{\mathbf{f}}_I = O_D\{\mathbf{f}_K\}. \tag{11.1-10c}$$

Several estimation approaches to the solution of 11.1-9 or 11.1-10 are described in the following sections. Unfortunately, general solutions have not been found; recourse must be made to specific solutions for less general models.

The most common digital restoration model is that of Figure 11.1-2a, in which a continuous image field is subjected to a linear blur, the electrical sensor responds nonlinearly to its input intensity, and the sensor amplifier introduces additive Gaussian noise independent of the image field. The physical image digitizer that follows may also introduce an effective blurring of the sampled image as the result of sampling with extended pulses. In this model, display degradation is ignored.

Figure 11.1-2b shows a restoration model for the imaging system. It is assumed that the imaging blur can be modeled as a superposition operation with an impulse response  $J(x, y)$  that may be space variant. The sensor is assumed to respond nonlinearly to the input field  $F_B(x, y)$  on a point-by-point basis, and its output is subject to an additive noise field  $N(x, y)$ . The effect of sampling with extended sampling pulses, which are assumed symmetric, can be modeled as a convolution of  $F_O(x, y)$  with each pulse  $P(x, y)$  followed by perfect sampling.

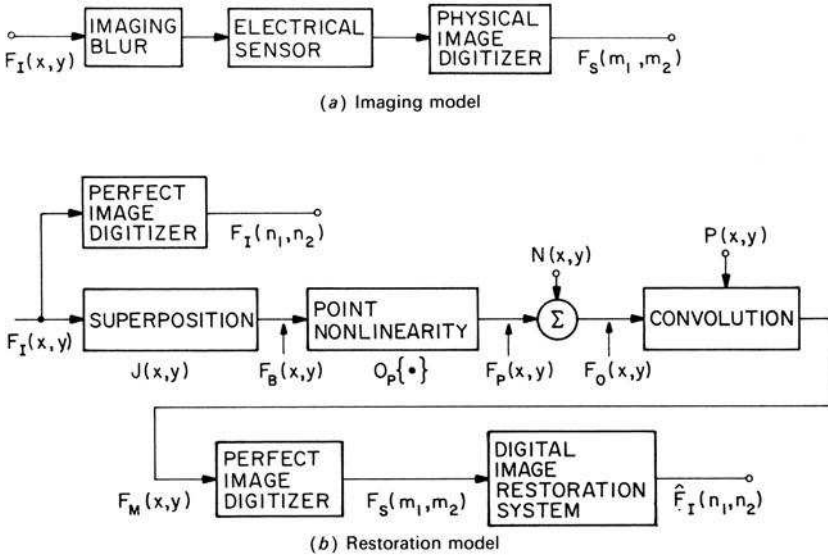


**FIGURE 11.1-2.** Imaging and restoration models for a sampled blurred image with additive noise.

The objective of the restoration is to produce an array of samples  $\hat{F}_I(n_1, n_2)$  that are estimates of points on the ideal input image field  $F_I(x, y)$  obtained by a perfect image digitizer sampling at a spatial period  $\Delta I$ . To produce a digital restoration model, it is necessary quantitatively to relate the physical image samples  $F_S(m_1, m_2)$  to the ideal image points  $F_I(n_1, n_2)$  following the techniques outlined in Section 7.2. This is accomplished by truncating the sampling pulse equivalent impulse response  $P(x, y)$  to some spatial limits  $\pm T_p$ , and then extracting points from the continuous observed field  $F_o(x, y)$  at a grid spacing  $\Delta P$ . The discrete representation must then be carried one step further by relating points on the observed image field  $F_o(x, y)$  to points on the image field  $F_p(x, y)$  and the noise field  $N(x, y)$ . The final step in the development of the discrete restoration model involves discretization of the superposition operation with  $J(x, y)$ . There are two potential sources of error in this modeling process: truncation of the impulse responses  $J(x, y)$  and  $P(x, y)$ , and quadrature integration errors. Both sources of error can be made negligibly small by choosing the truncation limits  $T_B$  and  $T_p$  large, and by choosing the quadrature spacings  $\Delta I$  and  $\Delta P$  small. This, of course, increases the sizes of the arrays, and eventually, the amount of storage and processing required. Actually, as is subsequently shown, the numerical stability of the restoration estimate may be impaired by improving the accuracy of the discretization process!

The relative dimensions of the various arrays of the restoration model are important. Figure 11.1-3 shows the nested nature of the arrays. The image array observed,  $F_o(k_1, k_2)$ , is smaller than the ideal image array,  $F_I(n_1, n_2)$ , by the half-width of the truncated impulse response  $J(x, y)$ . Similarly, the array of physical sample points

$F_S(m_1, m_2)$  is smaller than the array of image points observed,  $F_O(k_1, k_2)$ , by the half-width of the truncated impulse response  $P(x, y)$ .

It is convenient to form vector equivalents of the various arrays of the restoration model in order to utilize the formal structure of vector algebra in the subsequent restoration analysis. Again, following the techniques of Section 7.2, the arrays are reindexed so that the first element appears in the upper-left corner of each array. Next, the vector relationships between the stages of the model are obtained by column scanning of the arrays to give

$$\mathbf{f}_S = \mathbf{B}_P \mathbf{f}_O \tag{11.1-11a}$$

$$\mathbf{f}_O = \mathbf{f}_P + \mathbf{n} \tag{11.1-11b}$$

$$\mathbf{f}_P = O_P\{\mathbf{f}_B\} \tag{11.1-11c}$$

$$\mathbf{f}_B = \mathbf{B}_B \mathbf{f}_I. \tag{11.1-11d}$$

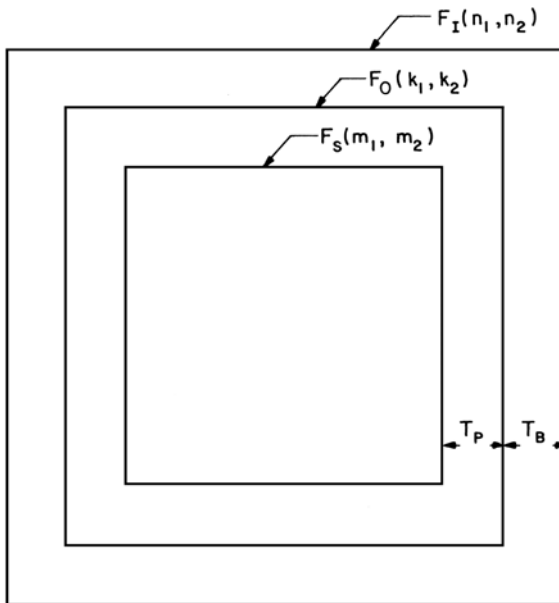


FIGURE 11.1-3. Relationships of sampled image arrays.

where the blur matrix  $\mathbf{B}_P$  contains samples of  $P(x, y)$  and  $\mathbf{B}_B$  contains samples of  $J(x, y)$ . The nonlinear operation of Eq. 11.1-11c is defined as a point-by-point nonlinear transformation. That is,

$$f_p(i) = O_P\{f_B(i)\}. \tag{11.1-12}$$



Equations 11.1-11a to 11.1-11d can be combined to yield a single equation for the observed physical image samples in terms of points on the ideal image:

$$\mathbf{f}_S = \mathbf{B}_p O_p\{\mathbf{B}_B \mathbf{f}_I\} + \mathbf{B}_p \mathbf{n}. \tag{11.1-13}$$

Several special cases of Eq. 11.1-13 will now be defined. First, if the point non-linearity is absent,

$$\mathbf{f}_S = \mathbf{B} \mathbf{f}_I + \mathbf{n}_B \tag{11.1-14}$$

where  $\mathbf{B} = \mathbf{B}_p \mathbf{B}_B$  and  $\mathbf{n}_B = \mathbf{B}_p \mathbf{n}$ . This is the classical discrete model consisting of a set of linear equations with measurement uncertainty. Another case that will be defined for later discussion occurs when the spatial blur of the physical image digitizer is negligible. In this case,

$$\mathbf{f}_S = O_p\{\mathbf{B} \mathbf{f}_I\} + \mathbf{n} \tag{11.1-15}$$

where  $\mathbf{B} = \mathbf{B}_B$  is defined by Eq. 7.2-15.

**Computer Simulation Image Model.** The following sections contain results for several image restoration experiments based on the restoration model defined by Eq. 11.1-14. An artificial image has been generated for these computer simulation experiments. The original image used for the analysis of under determined restoration techniques, shown in Figure 11.1-4a, consists of a  $4 \times 4$  pixel square of intensity 245 placed against an extended background of intensity 10 referenced to an intensity scale of 0 to 255. All images are zoomed for display purposes. The Gaussian-shaped impulse response function is defined as

$$H(l_1, l_2) = K \exp\left\{-\left(\frac{l_1^2}{2b_C^2} + \frac{l_2^2}{2b_R^2}\right)\right\}. \tag{11.1-16}$$

In the computer simulation restoration experiments, the observed blurred image model has been obtained by multiplying the column-scanned original image of Figure 11.1-4a by the blur matrix  $\mathbf{B}$ . Next, additive white Gaussian observation noise has been simulated by adding output variables from an appropriate random number generator to the blurred images. For display, all image points restored are clipped to the intensity range 0 to 255.

## 11.2. SENSOR AND DISPLAY POINT NONLINEARITY CORRECTION

A common defect in imaging systems is unwanted nonlinearities in the sensor and display systems. Post processing correction of sensor signals and pre-processing correction of display signals can reduce such degradations substantially (1). Such point restoration processing is usually relatively simple to implement. This section considers methods for compensation of point nonlinearities of sensors and displays.

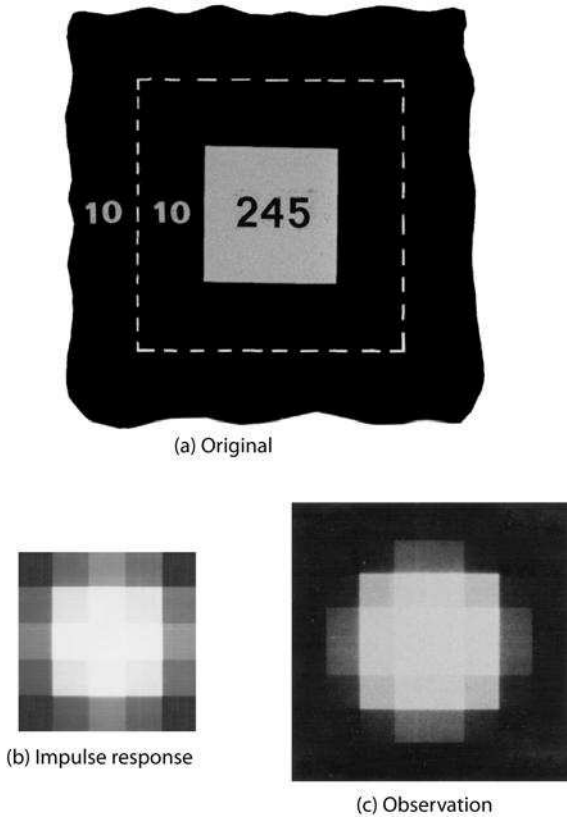


FIGURE 11.1-4. Image arrays for under determined model.

**11.2.1. Sensor Point Nonlinearity Correction**

In imaging systems in which the source degradation can be separated into cascaded spatial and point effects, it is often possible directly to compensate for the point degradation (2). Consider a physical imaging system that produces an observed image field  $F_O(x, y)$  according to the separable model

$$F_O(x, y) = O_O\{O_D\{C(x, y, \lambda)\}\} \tag{11.2-1}$$

where  $C(x, y, \lambda)$  is the spectral energy distribution of the input light field,  $O_O\{\cdot\}$  represents the point amplitude response of the sensor and  $O_D\{\cdot\}$  denotes the spatial and wavelength responses. Sensor luminance correction can then be accomplished

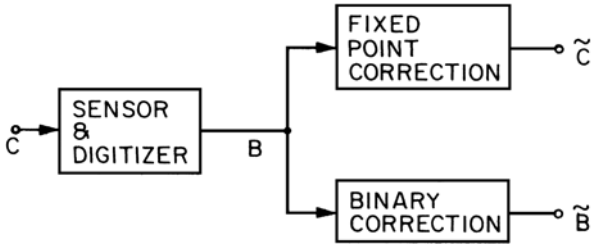


FIGURE 11.2-1. Point luminance correction for an image sensor.

by passing the observed image through a correction system with a point restoration operator  $O_R\{\cdot\}$  ideally chosen such that

$$O_R\{O_Q\{\cdot\}\} = 1. \tag{11.2-2}$$

For continuous images in optical form, it may be difficult to implement a desired point restoration operator if the operator is nonlinear. Compensation for images in analog electrical form can be accomplished with a nonlinear amplifier, while digital image compensation can be performed by arithmetic operators or by a table look-up procedure.

Figure 11.2-1 is a block diagram that illustrates the point luminance correction methodology. The sensor input is a point light distribution function  $C$  that is converted to a binary number  $B$  for eventual entry into a computer or digital processor. In some imaging applications, processing will be performed directly on the binary representation, while in other applications, it will be preferable to convert to a real fixed-point computer number linearly proportional to the sensor input luminance. In the former case, the binary correction unit will produce a binary number  $\tilde{B}$  that is designed to be linearly proportional to  $C$ , and in the latter case, the fixed-point correction unit will produce a fixed-point number  $\tilde{C}$  that is designed to be equal to  $C$ .

A typical measured response  $B$  versus sensor input luminance level  $C$  is shown in Figure 11.2-2a, while Figure 11.2-2b shows the corresponding compensated response that is desired. The measured response can be obtained by scanning a gray scale test chart of known luminance values and observing the digitized binary value  $B$  at each step. Repeated measurements should be made to reduce the effects of noise and measurement errors. For calibration purposes, it is convenient to regard the binary-coded luminance as a fixed-point binary number. As an example, if the luminance range is sliced into 4096 levels and coded with 12 bits, the binary representation would be

$$B = b_8 b_7 b_6 b_5 b_4 b_3 b_2 b_1 \cdot b_{-1} b_{-2} b_{-3} b_{-4} \tag{11.2-3}$$

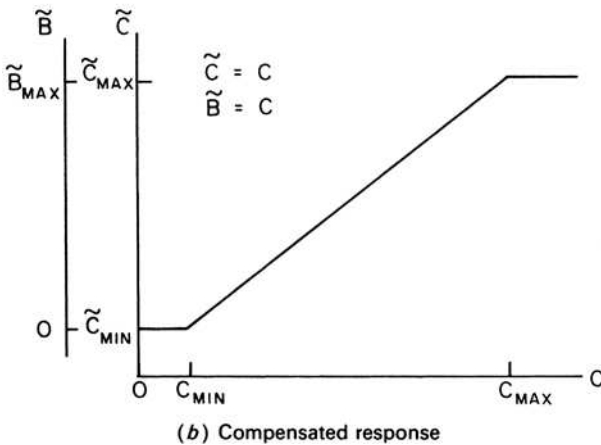
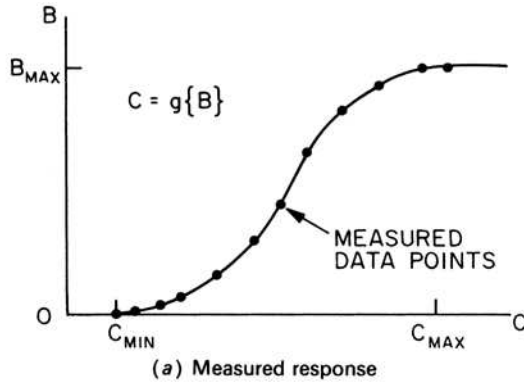


FIGURE 11.2-2. Measured and compensated sensor luminance response.

The whole-number part in this example ranges from 0 to 255, and the fractional part divides each integer step into 16 subdivisions. In this format, the scanner can produce output levels over the range

$$0.0 \leq B \leq 255.9375 \tag{11.2-4}$$

After the measured gray scale data points of Figure 11.2-2a have been obtained, a smooth analytic curve

$$C = g\{B\} \tag{11.2-5}$$

is fitted to the data. The desired luminance response in real number and binary number forms is

$$\tilde{C} = C \tag{11.2-6a}$$

$$\tilde{B} = B_{\max} \frac{C - C_{\min}}{C_{\max} - C_{\min}}. \tag{11.2-6b}$$

Hence, the required compensation relationships are

$$\tilde{C} = g\{B\} \tag{11.2-7a}$$

$$\tilde{B} = B_{\max} \frac{g\{B\} - C_{\min}}{C_{\max} - C_{\min}}. \tag{11.2-7b}$$

The limits of the luminance function are commonly normalized to the range 0.0 to 1.0.

To improve the accuracy of the calibration procedure, it is first wise to perform a rough calibration and then repeat the procedure as often as required to refine the correction curve. It should be observed that because  $B$  is a binary number, the corrected luminance value  $\tilde{C}$  will be a quantized real number. Furthermore, the corrected binary coded luminance  $\tilde{B}$  will be subject to binary roundoff of the right-hand side of Eq. 11.2-7b. As a consequence of the nonlinearity of the fitted curve  $C = g\{B\}$  and the amplitude quantization inherent to the digitizer, it is possible that some of the corrected binary-coded luminance values may be unoccupied. In other words, the image histogram of  $\tilde{B}$  may possess gaps. To minimize this effect, the number of output levels can be limited to less than the number of input levels. For example,  $B$  may be coded to 12 bits and  $\tilde{B}$  coded to only 8 bits. Another alternative is to add pseudorandom noise to  $\tilde{B}$  to smooth out the occupancy levels.

Many image scanning devices exhibit a variable spatial nonlinear point luminance response. Conceptually, the point correction techniques described previously could be performed at each pixel value using the measured calibrated curve at that point. Such a process, however, would be mechanically prohibitive. An alternative approach, called *gain correction*, that is often successful is to model the variable spatial response by some smooth normalized two-dimensional curve  $G(j, k)$  over the sensor surface. Then, the corrected spatial response can be obtained by the operation

$$\tilde{F}(j, k) = \frac{F(j, k)}{G(j, k)} \tag{11.2-8}$$

where  $F(j, k)$  and  $\tilde{F}(j, k)$  represent the raw and corrected sensor responses, respectively.

Figure 11.2-3 provides an example of adaptive gain correction of a charge coupled device (CCD) camera. Figure 11.2-3a is an image of a spatially flat light box surface obtained with the CCD camera. A line profile plot of a diagonal line through the original image is presented in Figure 11.2-3b. Figure 11.2-3c is the gain-corrected original, in which  $G(j, k)$  is obtained by Fourier domain low-pass filtering

of the original image. The line profile plot of Figure 11.2-3d shows the “flattened” result.

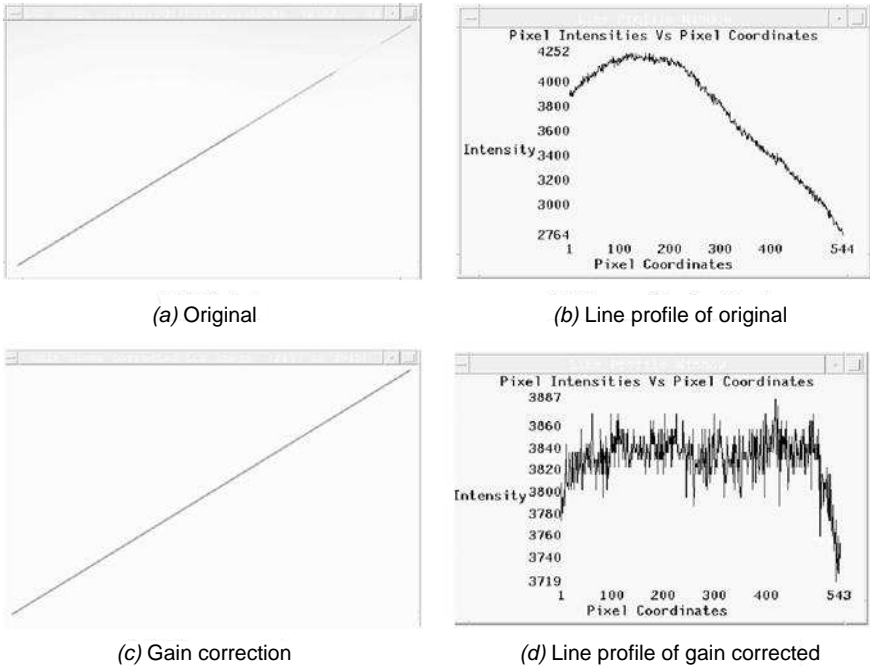


FIGURE 11.2-3. Gain correction of a CCD camera image.

### 11.2.2. Display Point Nonlinearity Correction

Correction of an image display for point luminance nonlinearities is identical in principle to the correction of point luminance nonlinearities of an image sensor. The procedure illustrated in Figure 11.2-4 involves distortion of the binary coded image luminance variable  $B$  to form a corrected binary coded luminance function  $\tilde{B}$  so that the displayed luminance  $\tilde{C}$  will be linearly proportional to  $B$ . In this formulation, the display may include a photographic record of a displayed light field. The desired overall response is

$$\tilde{C} = B \frac{\tilde{C}_{\max} - \tilde{C}_{\min}}{B_{\max}} + \tilde{C}_{\min} \tag{11.2-9}$$

Normally, the maximum and minimum limits of the displayed luminance function  $\tilde{C}$  are not absolute quantities, but rather are transmissivities or reflectivities normalized over a unit range. The measured response of the display and image reconstruction system is modeled by the nonlinear function

$$C = f\{B\} \tag{11.2-10}$$

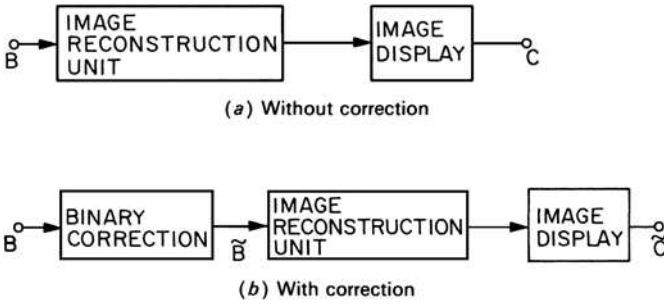


FIGURE 11.2-4. Point luminance correction of an image display.

Therefore, the desired linear response can be obtained by setting

$$\tilde{B} = g \left\{ B \frac{\tilde{C}_{\max} - \tilde{C}_{\min}}{B_{\max}} + \tilde{C}_{\min} \right\} \tag{11.2-11}$$

where  $g\{\cdot\}$  is the inverse function of  $f\{\cdot\}$ .

The experimental procedure for determining the correction function  $g\{\cdot\}$  will be described for the common example of producing a photographic print from an image display. The first step involves the generation of a digital gray scale step chart over the full range of the binary number  $B$ . Usually, about 16 equally spaced levels of  $B$  are sufficient. Next, the reflective luminance must be measured over each step of the developed print to produce a plot such as in Figure 11.2-5. The data points are then fitted by the smooth analytic curve  $B = g\{C\}$ , which forms the desired transformation of Eq. 11.2-10. It is important that enough bits be allocated to  $B$  so that the discrete mapping  $g\{\cdot\}$  can be approximated to sufficient accuracy. Also, the number of bits allocated to  $\tilde{B}$  must be sufficient to prevent gray scale contouring as the result of the nonlinear spacing of display levels. A 10-bit representation of  $B$  and an 8-bit representation of  $\tilde{B}$  should be adequate in most applications.

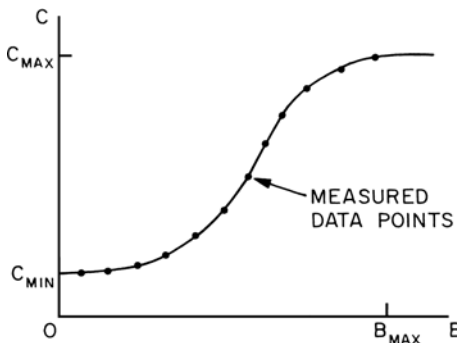


FIGURE 11.2-5. Measured image display response.

Image display devices such as cathode ray tube and liquid crystal displays often exhibit spatial luminance variation. Typically, a displayed image is brighter at the center of the display screen than at its periphery. Correction techniques, as described by Eq. 11.2-8, can be utilized for compensation of spatial luminance variations.

### 11.3. CONTINUOUS IMAGE SPATIAL FILTERING RESTORATION

For the class of imaging systems in which the spatial degradation can be modeled by a linear-shift-invariant impulse response and the noise is additive, restoration of continuous images can be performed by linear filtering techniques<sup>1</sup>. Figure 11.3-1 contains a block diagram for the analysis of such techniques. An ideal image  $F_I(x, y)$  passes through a linear spatial degradation system with an impulse response  $H_D(x, y)$  and is combined with additive noise  $N(x, y)$ . The noise is assumed to be uncorrelated with the ideal image. The image field observed can be represented by the convolution operation as

$$F_O(x, y) = \int_{-\infty}^{\infty} \int_{-\infty}^{\infty} F_I(\alpha, \beta) H_D(x - \alpha, y - \beta) d\alpha d\beta + N(x, y) \quad (11.3-1a)$$

or

$$F_O(x, y) = F_I(x, y) \otimes H_D(x, y) + N(x, y). \quad (11.3-1b)$$

The restoration system consists of a linear-shift-invariant filter defined by the impulse response  $H_R(x, y)$ . After restoration with this filter, the reconstructed image becomes

$$\hat{F}_I(x, y) = \int_{-\infty}^{\infty} \int_{-\infty}^{\infty} F_O(\alpha, \beta) H_R(x - \alpha, y - \beta) d\alpha d\beta \quad (11.3-2a)$$

or

$$\hat{F}_I(x, y) = F_O(x, y) \otimes H_R(x, y). \quad (11.3-2b)$$

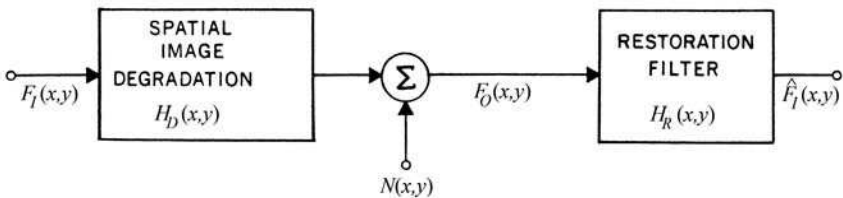


FIGURE 11.3-1. Continuous image restoration model.

1. References 3 to 7 contain surveys of spatial image restoration methods.



Substitution of Eq. 11.3-1b into Eq. 11.3-2b yields

$$\hat{F}_I(x, y) = \left[ F_I(x, y) \otimes H_D(x, y) + \hat{N}(x, y) \right] \otimes H_R(x, y). \quad (11.3-3)$$

It is analytically convenient to consider the reconstructed image in the Fourier transform domain. By the Fourier transform convolution theorem,

$$\hat{\mathcal{F}}_I(\omega_x, \omega_y) = [\mathcal{F}_I(\omega_x, \omega_y) \mathcal{K}_D(\omega_x, \omega_y) + \mathcal{N}(\omega_x, \omega_y)] \mathcal{K}_R(\omega_x, \omega_y) \quad (11.3-4)$$

where  $\mathcal{F}_I(\omega_x, \omega_y)$ ,  $\hat{\mathcal{F}}_I(\omega_x, \omega_y)$ ,  $\mathcal{N}(\omega_x, \omega_y)$ ,  $\mathcal{K}_D(\omega_x, \omega_y)$ ,  $\mathcal{K}_R(\omega_x, \omega_y)$  are the two-dimensional Fourier transforms of  $F_I(x, y)$ ,  $\hat{F}_I(x, y)$ ,  $N(x, y)$ ,  $H_D(x, y)$ ,  $H_R(x, y)$ , respectively.

The following sections describe various types of continuous image restoration filters.

### 11.3.1. Inverse Filter

The earliest attempts at image restoration were based on the concept of inverse filtering, in which the transfer function of the degrading system is inverted to yield a restored image (8–12). If the restoration *inverse filter* transfer function is chosen so that

$$\mathcal{K}_R(\omega_x, \omega_y) = \frac{1}{\mathcal{K}_D(\omega_x, \omega_y)} \quad (11.3-5)$$

then the spectrum of the reconstructed image becomes

$$\hat{\mathcal{F}}_I(\omega_x, \omega_y) = \mathcal{F}_I(\omega_x, \omega_y) + \frac{\mathcal{N}(\omega_x, \omega_y)}{\mathcal{K}_D(\omega_x, \omega_y)}. \quad (11.3-6)$$

Upon inverse Fourier transformation, the restored image field

$$\hat{F}_I(x, y) = F_I(x, y) + \frac{1}{4\pi^2} \int_{-\infty}^{\infty} \int_{-\infty}^{\infty} \frac{\mathcal{N}(\omega_x, \omega_y)}{\mathcal{K}_D(\omega_x, \omega_y)} \exp \{i(\omega_x x + \omega_y y)\} d\omega_x d\omega_y \quad (11.3-7)$$

is obtained. In the absence of source noise, a perfect reconstruction results, but if source noise is present, there will be an additive reconstruction error whose value can become quite large at spatial frequencies for which  $\mathcal{K}_D(\omega_x, \omega_y)$  is small. Typically,  $\mathcal{K}_D(\omega_x, \omega_y)$  and  $\mathcal{F}_I(\omega_x, \omega_y)$  are small at high spatial frequencies; hence image quality becomes severely impaired in high-detail regions of the reconstructed image. Figure 11.3-2 shows typical frequency spectra involved in inverse filtering.

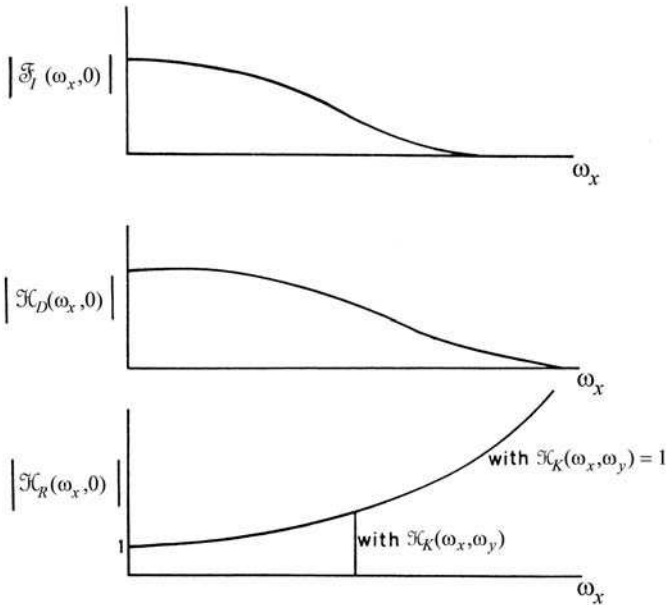


FIGURE 11.3-2. Typical spectra of an inverse filtering image restoration system.

The presence of noise may severely affect the uniqueness of a restoration estimate. That is, small changes in  $N(x, y)$  may radically change the value of the estimate  $\hat{F}_I(x, y)$ . For example, consider the dither function  $Z(x, y)$  added to an ideal image to produce a perturbed image

$$F_Z(x, y) = F_I(x, y) + Z(x, y). \tag{11.3-8}$$

There may be many dither functions for which

$$\left| \int_{-\infty}^{\infty} \int_{-\infty}^{\infty} Z(\alpha, \beta) H_D(x - \alpha, y - \beta) \, d\alpha \, d\beta \right| < |N(x, y)|. \tag{11.3-9}$$

For such functions, the perturbed image field  $F_Z(x, y)$  may satisfy the convolution integral of Eq. 11.3-1 to within the accuracy of the observed image field. Specifically, it can be shown that if the dither function is a high-frequency sinusoid of arbitrary amplitude, then in the limit

$$\lim_{n \rightarrow \infty} \left\{ \int_{-\infty}^{\infty} \int_{-\infty}^{\infty} \sin \{n(\alpha + \beta)\} H_D(x - \alpha, y - \beta) \, d\alpha \, d\beta \right\} = 0. \tag{11.3-10}$$

For image restoration, this fact is particularly disturbing, for two reasons. High-frequency signal components may be present in an ideal image, yet their presence may

be masked by observation noise. Conversely, a small amount of observation noise may lead to a reconstruction of  $F_I(x, y)$  that contains very large amplitude high-frequency components. If relatively small perturbations  $N(x, y)$  in the observation result in large dither functions for a particular degradation impulse response, the convolution integral of Eq. 11.3-1 is said to be unstable or *ill conditioned*. This potential instability is dependent on the structure of the degradation impulse response function.

There have been several ad hoc proposals to alleviate noise problems inherent to inverse filtering. One approach (10) is to choose a restoration filter with a transfer function

$$\mathcal{K}_R(\omega_x, \omega_y) = \frac{\mathcal{K}_K(\omega_x, \omega_y)}{\mathcal{K}_D(\omega_x, \omega_y)} \tag{11.3-11}$$

where  $\mathcal{K}_K(\omega_x, \omega_y)$  has a value of unity at spatial frequencies for which the expected magnitude of the ideal image spectrum is greater than the expected magnitude of the noise spectrum, and zero elsewhere. The reconstructed image spectrum is then

$$\hat{\mathcal{F}}_I(\omega_x, \omega_y) = \mathcal{F}_I(\omega_x, \omega_y) \mathcal{K}_K(\omega_x, \omega_y) + \frac{\mathcal{N}(\omega_x, \omega_y) \mathcal{K}_K(\omega_x, \omega_y)}{\mathcal{K}_D(\omega_x, \omega_y)}. \tag{11.3-12}$$

The result is a compromise between noise suppression and loss of high-frequency image detail.

Another fundamental difficulty with inverse filtering is that the transfer function of the degradation may have zeros in its passband. At such points in the frequency spectrum, the inverse filter is not physically realizable, and therefore the filter must be approximated by a large value response at such points.

### 11.3.2. Wiener Filter

It should not be surprising that inverse filtering performs poorly in the presence of noise because the filter design ignores the noise process. Improved restoration quality is possible with Wiener filtering techniques, which incorporate a priori statistical knowledge of the noise field (9–13).

In the general derivation of the *Wiener filter*, it is assumed that the ideal image  $F_I(x, y)$  and the observed image  $F_O(x, y)$  of Figure 11.3-1 are samples of two-dimensional, continuous stochastic fields with zero-value spatial means. The impulse response of the restoration filter is chosen to minimize the mean-square restoration error

$$\epsilon = E \left\{ [F_I(x, y) - \hat{F}_I(x, y)]^2 \right\}. \tag{11.3-13}$$

It can be shown Pratt(4Ed., 338-339) that the Wiener filter transfer function for the additive noise model of Figure 11.3-1 is

$$\mathcal{K}_R(\omega_x, \omega_y) = \frac{\mathcal{K}_D^*(\omega_x, \omega_y) \tilde{W}_{F_I}(\omega_x, \omega_y)}{|\mathcal{K}_D(\omega_x, \omega_y)|^2 \tilde{W}_{F_I}(\omega_x, \omega_y) + \tilde{W}_N(\omega_x, \omega_y)} \tag{11.3-14a}$$

or

$$\mathcal{K}_R(\omega_x, \omega_y) = \frac{\mathcal{K}_D^*(\omega_x, \omega_y)}{|\mathcal{K}_D(\omega_x, \omega_y)|^2 + \tilde{W}_N(\omega_x, \omega_y) / \tilde{W}_{F_I}(\omega_x, \omega_y)} \tag{11.3-14b}$$

where  $\tilde{W}_{F_I}(\omega_x, \omega_y)$  is the power spectrum of the ideal image and  $\tilde{W}_N(\omega_x, \omega_y)$  is the power spectrum of the additive noise. In the latter formulation, the transfer function of the restoration filter can be expressed in terms of the signal-to-noise power ratio

$$\text{SNR}(\omega_x, \omega_y) \equiv \frac{\tilde{W}_{F_I}(\omega_x, \omega_y)}{\tilde{W}_N(\omega_x, \omega_y)} \tag{11.3-15}$$

at each spatial frequency. Figure 11.3-3 shows cross-sectional sketches of a typical ideal image spectrum, noise spectrum, blur transfer function and the resulting Wiener filter transfer function. As noted from the figure, this version of the Wiener filter acts as a bandpass filter. It performs as an inverse filter at low spatial frequencies, and as a smooth roll off low-pass filter at high spatial frequencies.

Equation 11.3-14 is valid when the ideal image and observed image stochastic processes are zero mean. In this case, the reconstructed image Fourier transform is

$$\hat{\mathcal{F}}_I(\omega_x, \omega_y) = H_R(\omega_x, \omega_y) \mathcal{F}_O(\omega_x, \omega_y) \tag{11.3-16}$$

If the ideal image and observed image means are nonzero, the proper form of the reconstructed image Fourier transform is

$$\hat{\mathcal{F}}_I(\omega_x, \omega_y) = \mathcal{K}_R(\omega_x, \omega_y) [\mathcal{F}_O(\omega_x, \omega_y) - \mathcal{M}_O(\omega_x, \omega_y)] + \mathcal{M}_I(\omega_x, \omega_y) \tag{11.3-17a}$$

where

$$\mathcal{M}_O(\omega_x, \omega_y) = \mathcal{K}_D(\omega_x, \omega_y) \mathcal{M}_I(\omega_x, \omega_y) + \mathcal{M}_N(\omega_x, \omega_y) \tag{11.3-17b}$$

and  $\mathcal{M}_I(\omega_x, \omega_y)$  and  $\mathcal{M}_N(\omega_x, \omega_y)$  are the two-dimensional Fourier transforms of the means of the ideal image and noise, respectively. It should be noted that Eq. 11.3-17 accommodates spatially varying mean models. In practice, it is common to estimate the mean of the observed image by its spatial average  $M_O(x, y)$  and apply the Wiener filter of Eq. 11.3-14 to the observed image difference  $F_O(x, y) - M_O(x, y)$ , and then add back the ideal image mean  $M_I(x, y)$  to the Wiener filter result.

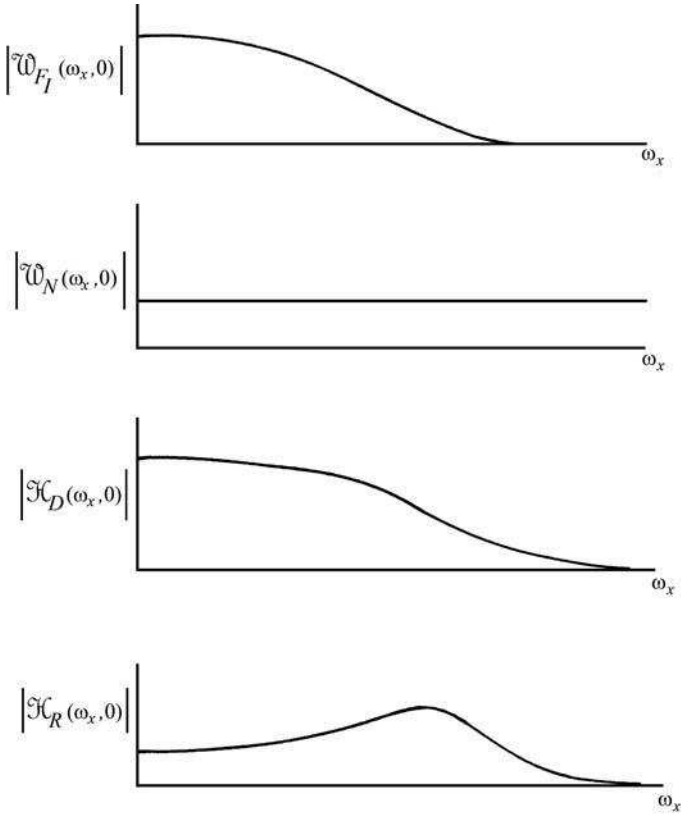


FIGURE 11.3-3. Typical spectra of a Wiener filtering image restoration system.

It is useful to investigate special cases of Eq. 11.3-14. If the ideal image is assumed to be uncorrelated with unit energy,  $W_{F_I}(\omega_x, \omega_y) = 1$ , and the Wiener filter becomes

$$\mathcal{K}_R(\omega_x, \omega_y) = \frac{\mathcal{K}_D^*(\omega_x, \omega_y)}{|\mathcal{K}_D(\omega_x, \omega_y)|^2 + \tilde{W}_N(\omega_x, \omega_y)}. \tag{11.3-18}$$

This version of the Wiener filter provides less noise smoothing than does the general case of Eq. 11.3-14. If there is no blurring of the ideal image,  $\mathcal{K}_D(\omega_x, \omega_y) = 1$ , and the Wiener filter becomes a noise smoothing filter with a transfer function

$$\mathcal{K}_R(\omega_x, \omega_y) = \frac{1}{1 + \tilde{W}_N(\omega_x, \omega_y)}. \tag{11.3-19}$$

In many imaging systems, the impulse response of the blur may not be fixed; rather, it may change shape in a random manner. A practical example is the blur caused by imaging through a turbulent atmosphere. Obviously, a Wiener filter applied to this problem would perform better if it could dynamically adapt to the changing blur impulse response. If this is not possible, a design improvement in the Wiener filter can be obtained by considering the impulse response to be a sample of a two-dimensional stochastic process with a known mean shape and with a random perturbation about the mean modeled by a known power spectral density. Transfer functions for this type of restoration filter have been developed by Slepian (14).

### 11.3.3. Parametric Estimation Filters

Several variations of the Wiener filter have been developed for image restoration. Some techniques are ad hoc, while others have a quantitative basis.

Cole (19) has proposed a restoration filter with a transfer function

$$\mathcal{K}_R(\omega_x, \omega_y) = \left[ \frac{\tilde{w}_{F_I}(\omega_x, \omega_y)}{|\mathcal{K}_D(\omega_x, \omega_y)|^2 \tilde{w}_{F_I}(\omega_x, \omega_y) + \tilde{w}_N(\omega_x, \omega_y)} \right]^{1/2} \quad (11.3-20)$$

The power spectrum of the filter output is

$$\tilde{w}_{F_I}(\omega_x, \omega_y) = |\mathcal{K}_R(\omega_x, \omega_y)|^2 \tilde{w}_{F_O}(\omega_x, \omega_y) \quad (11.3-21)$$

where  $\tilde{w}_{F_O}(\omega_x, \omega_y)$  represents the power spectrum of the observation, which is related to the power spectrum of the ideal image by

$$\tilde{w}_{F_O}(\omega_x, \omega_y) = |\mathcal{K}_D(\omega_x, \omega_y)|^2 \tilde{w}_{F_I}(\omega_x, \omega_y) + \tilde{w}_N(\omega_x, \omega_y). \quad (11.3-22)$$

Thus, it is easily seen that the power spectrum of the reconstructed image is identical to the power spectrum of the ideal image field. That is,

$$\tilde{w}_{F_I}(\omega_x, \omega_y) = \tilde{w}_{F_I}(\omega_x, \omega_y). \quad (11.3-23)$$

For this reason, the restoration filter defined by Eq. 11.3-20 is called the image *power spectrum filter*. In contrast, the power spectrum for the reconstructed image as obtained by the Wiener filter of Eq. 11.3-14 is

$$\tilde{w}_{F_I}(\omega_x, \omega_y) = \frac{|\mathcal{K}_D(\omega_x, \omega_y)|^2 [\tilde{w}_{F_I}(\omega_x, \omega_y)]^2}{|\mathcal{K}_D(\omega_x, \omega_y)|^2 \tilde{w}_{F_I}(\omega_x, \omega_y) + \tilde{w}_N(\omega_x, \omega_y)}. \quad (11.3-24)$$

In this case, the power spectra of the reconstructed and ideal images become identical only for a noise-free observation. Although equivalence of the power spectra of the ideal and reconstructed images appears to be an attractive feature of the image power spectrum filter, it should be realized that it is more important that the Fourier spectra (Fourier transforms) of the ideal and reconstructed images be identical because their Fourier transform pairs are unique, but power-spectra transform pairs are not necessarily unique. Furthermore, the Wiener filter provides a minimum mean-square error estimate, while the image power-spectrum filter may result in a large residual mean-square error.

Cole (15) has also introduced a *geometrical mean filter*, defined by the transfer function

$$\mathcal{K}_R(\omega_x, \omega_y) = [\mathcal{K}_D(\omega_x, \omega_y)]^{-S} \left[ \frac{\mathcal{K}_D^*(\omega_x, \omega_y) \mathcal{W}_{F_I}(\omega_x, \omega_y)}{|\mathcal{K}_D(\omega_x, \omega_y)|^2 \mathcal{W}_{F_I}(\omega_x, \omega_y) + \mathcal{W}_N(\omega_x, \omega_y)} \right]^{1-S} \tag{11.3-25}$$

where  $0 \leq S \leq 1$  is a design parameter. If  $S = 1/2$  and  $\mathcal{K}_D = \mathcal{K}_D^*$ , the geometrical mean filter reduces to the image power-spectrum filter as given in Eq. 11.3-20.

Hunt (16) has developed another parametric restoration filter, called the *constrained least-squares filter*, whose transfer function is of the form

$$\mathcal{K}_R(\omega_x, \omega_y) = \frac{\mathcal{K}_D^*(\omega_x, \omega_y)}{|\mathcal{K}_D(\omega_x, \omega_y)|^2 + \gamma |\mathcal{C}(\omega_x, \omega_y)|^2} \tag{11.3-26}$$

where  $\gamma$  is a design constant and  $\mathcal{C}(\omega_x, \omega_y)$  is a design spectral variable. If  $\gamma = 1$  and  $|\mathcal{C}(\omega_x, \omega_y)|^2$  is set equal to the reciprocal of the spectral signal-to-noise power ratio of Eq. 11.3-15, the constrained least-squares filter becomes equivalent to the Wiener filter of Eq. 11.3-14b. The spectral variable can also be used to minimize higher-order derivatives of the estimate.

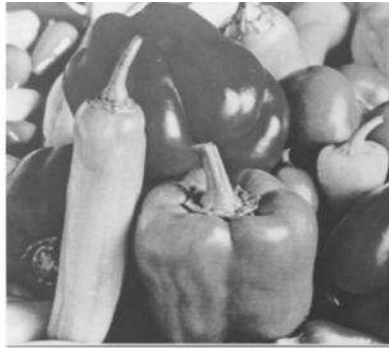
### 11.3.4. Application to Discrete Images

The inverse filtering, Wiener filtering and parametric estimation filtering techniques developed for continuous image fields are often applied to the restoration of discrete images. The common procedure has been to replace each of the continuous spectral functions involved in the filtering operation by its discrete two-dimensional Fourier transform counterpart. However, care must be taken in this conversion process so that the discrete filtering operation is an accurate representation of the continuous convolution process and that the discrete form of the restoration filter impulse response accurately models the appropriate continuous filter impulse response.

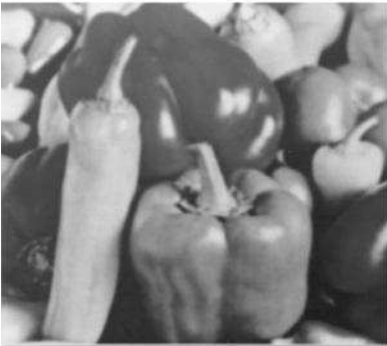
Figures 11.3-4 to 11.3-7 present examples of continuous image spatial filtering techniques by discrete Fourier transform filtering. The original image of Figure

11.3-4a has been blurred with a Gaussian-shaped impulse response with  $b = 2.0$  to obtain the blurred image of Figure 11.3-4b. White Gaussian noise has been added to the blurred image to give the noisy blurred image of Figure 11.3-4c, which has a signal-to-noise ratio of 10.0.

Figure 11.3-5 shows the results of inverse filter image restoration of the blurred and noisy-blurred images. In Figure 11.3-5a, the inverse filter transfer function follows Eq. 11.3-5 (i.e., no high-frequency cutoff). The restored image for the



(a) Original



(b) Blurred,  $b = 2.0$



(c) Blurred with noise, SNR = 10.0

**FIGURE 11.3-4.** Blurred test images.

noise-free observation is corrupted completely by the effects of computational error. The computation was performed using 32-bit floating-point arithmetic. In Figure 11.3-5c, the inverse filter restoration is performed with a circular cutoff inverse filter as defined by Eq. 11.3-11 with  $C = 200$  for the  $512 \times 512$  pixel



noise-free observation. Some faint artifacts are visible in the restoration. In Figure 11.3-5e, the cutoff frequency is reduced to  $C = 150$ . The restored image appears relatively sharp and free of artifacts. Figure 11.3-5b, d and f show the result of inverse filtering on the noisy-blurred observed image with varying cutoff frequencies. These restorations illustrate the trade-off between the level of artifacts and the degree of deblurring.

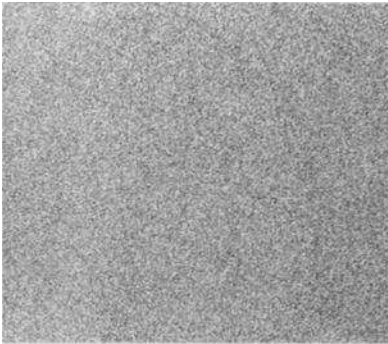
Figure 11.3-6 shows the results of Wiener filter image restoration. In all cases, the noise power spectral density is white and the signal power spectral density is circularly symmetric Markovian with a correlation factor  $\rho$ . For the noise-free observation, the Wiener filter provides restorations that are free of artifacts but only slightly sharper than the blurred observation. For the noisy observation, the restoration artifacts are less noticeable than for an inverse filter.

Figure 11.3-7 presents restorations using the power spectrum filter. For a noise-free observation, the power spectrum filter gives a restoration of similar quality to an inverse filter with a low cutoff frequency. For a noisy observation, the power spectrum filter restorations appear to be grainier than for the Wiener filter.

The continuous image field restoration techniques derived in this section are advantageous in that they are relatively simple to understand and to implement using Fourier domain processing. However, these techniques face several important limitations. First, there is no provision for aliasing error effects caused by physical under sampling of the observed image. Second, the formulation inherently assumes that the quadrature spacing of the convolution integral is the same as the physical sampling. Third, the methods only permit restoration for linear, space-invariant degradation. Fourth, and perhaps most important, it is difficult to analyze the effects of numerical errors in the restoration process and to develop methods of combatting such errors. For these reasons, it is necessary to turn to the discrete model of a sampled blurred image developed in Section 7.2, and then reformulate the restoration problem on a firm numeric basis. This is the subject of the remaining sections of the chapter.

#### 11.4. PSEUDOINVERSE SPATIAL IMAGE RESTORATION

The matrix pseudoinverse defined in Appendix 1 can be used for spatial image restoration of digital images when it is possible to model the spatial degradation as a vector-space operation on a vector of ideal image points yielding a vector of physical observed samples obtained from the degraded image (17–19).



(a) Noise-free, no cutoff



(b) Noisy,  $C = 100$



(c) Noise-free,  $C = 200$



(d) Noisy,  $C = 75$



(e) Noise-free,  $C = 150$



(f) Noisy,  $C = 50$

**FIGURE 11.3-5.** Inverse filter image restoration on the blurred test images.



(a) Noise-free,  $\rho = 0.9$



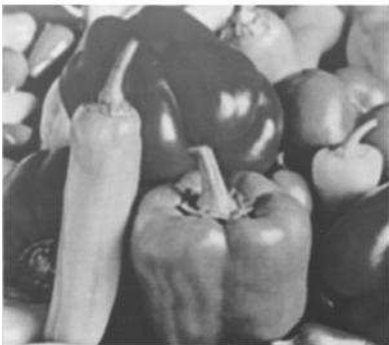
(b) Noisy,  $\rho = 0.9$



(c) Noise-free,  $\rho = 0.5$



(d) Noisy,  $\rho = 0.5$

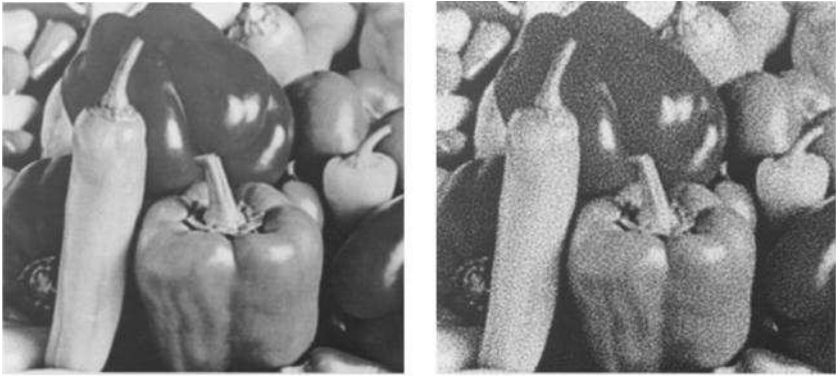


(e) Noise-free,  $\rho = 0.0$



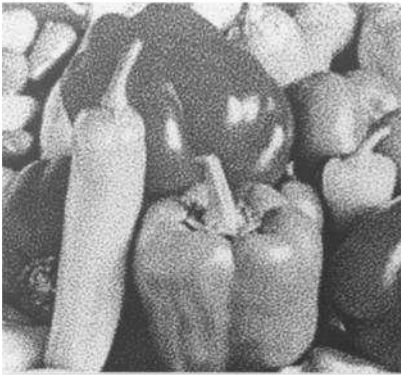
(f) Noisy,  $\rho = 0.0$

**FIGURE 11.3-6.** Wiener filter image restoration on the blurred test images; SNR = 10.0.

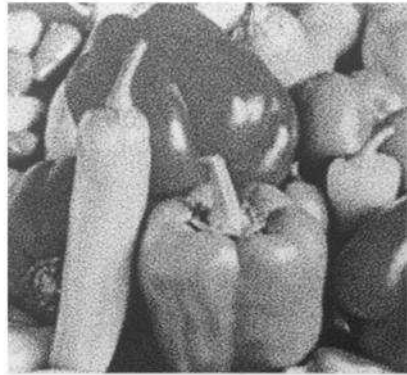


(a) Noise-free,  $\rho = 0.5$

(b) Noisy,  $\rho = 0.5$



(c) Noisy,  $\rho = 0.5$



(d) Noisy,  $\rho = 0.0$

**FIGURE 11.3-7.** Power spectrum filter image restoration on the blurred test images; SNR = 10.0.

### 11.4.1. Pseudoinverse: Image Blur

The first application of the pseudoinverse to be considered is that of the restoration of a blurred image described by the vector-space model

$$\mathbf{g} = \mathbf{B}\mathbf{f} \tag{11.4-1}$$

as derived in Eq. 11.1-14, where  $\mathbf{g}$  is a  $P \times 1$  vector ( $P = M^2$ ) containing the  $M \times M$  physical samples of the blurred image,  $\mathbf{f}$  is a  $Q \times 1$  vector ( $Q = N^2$ ) containing  $N \times N$  points of the ideal image and  $\mathbf{B}$  is the  $P \times Q$  matrix whose elements are points on the impulse function. If the physical sample period and the quadrature representation period are identical,  $P$  will be smaller than  $Q$ , and the system of

equations will be *under determined*. By oversampling the blurred image, it is possible to force  $P > Q$  or even  $P = Q$ . In either case, the system of equations is called *overdetermined*. An overdetermined set of equations can also be obtained if some of the elements of the ideal image vector can be specified through a priori knowledge. For example, if the ideal image is known to contain a limited size object against a black background (zero luminance), the elements of  $\mathbf{f}$  beyond the limits may be set to zero.

In discrete form, the restoration problem reduces to finding a solution  $\hat{\mathbf{f}}$  to Eq. 11.4-1 in the sense that

$$\mathbf{B}\hat{\mathbf{f}} = \mathbf{g} \tag{11.4-2}$$

Because the vector  $\mathbf{g}$  is determined by physical sampling and the elements of  $\mathbf{B}$  are specified independently by system modeling, there is no guarantee that a  $\hat{\mathbf{f}}$  even exists to satisfy Eq. 11.4-2. If there is a solution, the system of equations is said to be *consistent*; otherwise, the system of equations is *inconsistent*.

In Appendix 1, it is shown that inconsistency in the set of equations of Eq. 11.4-1 can be characterized as

$$\mathbf{g} = \mathbf{B}\mathbf{f} + \mathbf{e}\{\mathbf{f}\} \tag{11.4-3}$$

where  $\mathbf{e}\{\mathbf{f}\}$  is a vector of remainder elements whose value depends on  $\mathbf{f}$ . If the set of equations is inconsistent, a solution of the form

$$\hat{\mathbf{f}} = \mathbf{W}\mathbf{g} \tag{11.4-4}$$

is sought for which the linear operator  $\mathbf{W}$  minimizes the least-squares modeling error

$$\mathcal{E}_M = [\mathbf{e}\{\hat{\mathbf{f}}\}]^T [\mathbf{e}\{\hat{\mathbf{f}}\}] = [\mathbf{g} - \mathbf{B}\hat{\mathbf{f}}]^T [\mathbf{g} - \mathbf{B}\hat{\mathbf{f}}] \tag{11.4-5}$$

This error is shown, in Appendix 1, to be minimized when the operator  $\mathbf{W} = \mathbf{B}^S$  is set equal to the least-squares inverse of  $\mathbf{B}$ . The least-squares inverse is not necessarily unique. It is also proved in Appendix 1 that the generalized inverse operator  $\mathbf{W} = \mathbf{B}^-$ , which is a special case of the least-squares inverse, is unique, minimizes the least-squares modeling error, and simultaneously provides a minimum norm estimate. That is, the sum of the squares of  $\hat{\mathbf{f}}$  is a minimum for all possible minimum least-square error estimates. For the restoration of image blur, the generalized inverse provides a lowest-intensity restored image.

If Eq. 11.4-1 represents a consistent set of equations, one or more solutions may exist for Eq. 11.4-2. The solution commonly chosen is the estimate that minimizes the least-squares estimation error defined in the equivalent forms

$$\mathcal{E}_E = (\mathbf{f} - \hat{\mathbf{f}})^T (\mathbf{f} - \hat{\mathbf{f}}) \tag{11.4-6a}$$

$$\hat{\epsilon}_E = \text{tr}\{(\mathbf{f} - \hat{\mathbf{f}})(\mathbf{f} - \hat{\mathbf{f}})^T\}. \tag{11.4-6b}$$

In Appendix 1, it is proved that the estimation error is minimum for a *generalized inverse* ( $\mathbf{W} = \mathbf{B}^-$ ) estimate. The resultant residual estimation error then becomes

$$\hat{\epsilon}_E = \mathbf{f}^T [\mathbf{I} - [\mathbf{B}^- \mathbf{B}]] \mathbf{f} \tag{11.4-7a}$$

or

$$\hat{\epsilon}_E = \text{tr}\{\mathbf{f}\mathbf{f}^T [\mathbf{I} - [\mathbf{B}^- \mathbf{B}]]\}. \tag{11.4-7b}$$

The estimate is perfect, of course, if  $\mathbf{B}^- \mathbf{B} = \mathbf{I}$ .

Thus, it is seen that the generalized inverse is an optimal solution, in the sense defined previously, for both consistent and inconsistent sets of equations modeling image blur. From Appendix 1, the generalized inverse has been found to be algebraically equivalent to

$$\mathbf{B}^- = [\mathbf{B}^T \mathbf{B}]^{-1} \mathbf{B}^T \tag{11.4-8a}$$

if the  $P \times Q$  matrix  $\mathbf{B}$  is of rank  $Q$ . If  $\mathbf{B}$  is of rank  $P$ , then

$$\mathbf{B}^- = \mathbf{B}^T [\mathbf{B} \mathbf{B}^T]^{-1}. \tag{11.4-8b}$$

For a consistent set of equations and a rank  $Q$  generalized inverse, the estimate

$$\hat{\mathbf{f}} = \mathbf{B}^- \mathbf{g} = \mathbf{B}^- \mathbf{B} \mathbf{f} = [[\mathbf{B}^T \mathbf{B}]^{-1} \mathbf{B}^T] \mathbf{B} \mathbf{f} = \mathbf{f} \tag{11.4-9}$$

is obviously perfect. However, in all other cases, a residual estimation error may occur. Clearly, it would be desirable to deal with an overdetermined blur matrix of rank  $Q$  in order to achieve a perfect estimate. Unfortunately, this situation is rarely achieved in image restoration. Oversampling the blurred image can produce an overdetermined set of equations ( $P > Q$ ), but the rank of the blur matrix is likely to be much less than  $Q$  because the rows of the blur matrix will become more linearly dependent with finer sampling.

A major problem in application of the generalized inverse to image restoration is dimensionality. The generalized inverse is a  $Q \times P$  matrix where  $P$  is equal to the number of pixel observations and  $Q$  is equal to the number of pixels to be estimated in an image. It is usually not computationally feasible to use the generalized inverse operator, defined by Eq. 11.4-8, over large images because of difficulties in reliably computing the generalized inverse and the large number of vector multiplications associated with Eq. 11.4-4. Computational savings can be realized if the blur matrix  $\mathbf{B}$  is separable such that

$$\mathbf{B} = \mathbf{B}_C \otimes \mathbf{B}_R \tag{11.4-10}$$

where  $\mathbf{B}_C$  and  $\mathbf{B}_R$  are column and row blur operators. In this case, the generalized inverse is separable in the sense that

$$\mathbf{B}^- = \mathbf{B}_C^- \otimes \mathbf{B}_R^- \tag{11.4-11}$$

where  $\mathbf{B}_C^-$  and  $\mathbf{B}_R^-$  are generalized inverses of  $\mathbf{B}_C$  and  $\mathbf{B}_R$ , respectively. Thus when the blur matrix is of separable form, it becomes possible to form the estimate of the image by sequentially applying the generalized inverse of the row blur matrix to each row of the observed image array, and then using the column generalized inverse operator on each column of the array.

Figure 11.4-1a shows a blurred image based on the model of Figure 11.1-4. Figure 11.4-1b shows a restored image using generalized inverse image restoration. In this example, the observation is noise free and the blur impulse response function is Gaussian shaped, as defined in Eq. 11.1-15, with  $b_R = b_C = 1.2$ . Only the center  $8 \times 8$  region of the  $12 \times 12$  blurred picture is displayed, zoomed to an image size of  $256 \times 256$  pixels. The restored image appears to be visually improved compared to the blurred image, but the restoration is not identical to the original unblurred image of Figure 11.1-4a. The figure also gives the percentage least-squares error (PLSE) as defined in Appendix 2, between the blurred image and the original unblurred image, and between the restored image and the original. The restored image has less error than the blurred image.

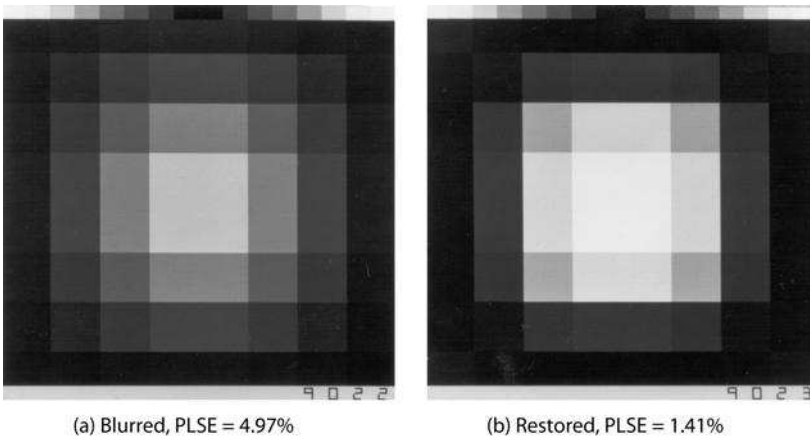


**FIGURE 11.4-1.** Pseudoinverse image restoration for test image blurred with Gaussian shape impulse response.  $M = 8, N = 12, L = 5; b_R = b_C = 1.2$ ; noise-free observation.

**11.4.2. Pseudoinverse: Image Blur Plus Additive Noise**

In many imaging systems, an ideal image is subject to both blur and additive noise; the resulting vector-space model takes the form

$$\mathbf{g} = \mathbf{Bf} + \mathbf{n} \tag{11.4-12}$$

where  $\mathbf{g}$  and  $\mathbf{n}$  are  $P \times 1$  vectors of the observed image field and noise field, respectively,  $\mathbf{f}$  is a  $Q \times 1$  vector of ideal image points, and  $\mathbf{B}$  is a  $P \times Q$  blur matrix. The vector  $\mathbf{n}$  is composed of two additive components: samples of an additive external noise process and elements of the vector difference  $(\mathbf{g} - \mathbf{B}\mathbf{f})$  arising from modeling errors in the formulation of  $\mathbf{B}$ . As a result of the noise contribution, there may be no vector solutions  $\mathbf{f}$  that satisfy Eq. 11.4-12. However, as indicated in Appendix 1, the generalized inverse  $\mathbf{B}^-$  can be utilized to determine a least-squares error, minimum norm estimate. In the absence of modeling error, the estimate

$$\hat{\mathbf{f}} = \mathbf{B}^- \mathbf{g} = \mathbf{B}^- \mathbf{B}\mathbf{f} + \mathbf{B}^- \mathbf{n} \tag{11.4-13}$$

differs from the ideal image because of the additive noise contribution  $\mathbf{B}^- \mathbf{n}$ . Also, for the under determined model,  $\mathbf{B}^- \mathbf{B}$  will not be an identity matrix. If  $\mathbf{B}$  is an over-determined rank  $Q$  matrix, as defined in Eq. 11.4-8a, then  $\mathbf{B}^- \mathbf{B} = \mathbf{I}$ , and the resulting estimate is equal to the original image vector  $\mathbf{f}$  plus a perturbation vector  $\Delta\mathbf{f} = \mathbf{B}^- \mathbf{n}$ . The perturbation error in the estimate can be measured as the ratio of the vector norm of the perturbation to the vector norm of the estimate. It can be shown (21, p. 52) that the relative error is subject to the bound

$$\frac{\|\Delta\mathbf{f}\|}{\|\mathbf{f}\|} < \|\mathbf{B}^- \|\cdot\|\mathbf{B}\| \frac{\|\mathbf{n}\|}{\|\mathbf{g}\|} . \tag{11.4-14}$$

The product  $\|\mathbf{B}^- \|\cdot\|\mathbf{B}\|$ , which is called the *condition number*  $C\{\mathbf{B}\}$  of  $\mathbf{B}$ , determines the relative error in the estimate in terms of the ratio of the vector norm of the noise to the vector norm of the observation. The condition number can be computed directly or found in terms of the ratio

$$C\{\mathbf{B}\} = \frac{W_1}{W_N} \tag{11.4-15}$$

of the largest  $W_1$  to smallest  $W_N$  singular values of  $\mathbf{B}$ . The noise perturbation error for the under determined matrix  $\mathbf{B}$  is also governed by Eqs. 11.4-14 and 11.4-15 if  $W_N$  is defined to be the smallest nonzero singular value of  $\mathbf{B}$  (21, p. 41). Obviously, the larger the condition number of the blur matrix, the greater will be the sensitivity to noise perturbations.

Figure 11.4-2 contains image restoration examples for a Gaussian-shaped blur function for several values of the blur standard deviation and a noise variance of 10.0 on an amplitude scale of 0.0 to 255.0. As expected, observation noise degrades the restoration. Also as expected, the restoration for a moderate degree of blur is worse than the restoration for less blur. However, this trend does not continue; the restoration for severe blur is actually better in a subjective sense than for moderate blur. This seemingly anomalous behavior, which results from spatial truncation of the point-spread function, can be explained in terms of the condition number of the blur matrix. Figure 11.4-3 is a plot of the condition number of the blur matrix of the previous examples as a function of the blur coefficient (17). For



small amounts of blur, the condition number is low. A maximum is attained for moderate blur, followed by a decrease in the curve for increasing values of the blur coefficient. The curve tends to stabilize as the blur coefficient approaches infinity. This curve provides an explanation for the previous experimental results. In the restoration operation, the blur impulse response is spatially truncated over a square region of  $5 \times 5$  quadrature points. As the blur coefficient increases, for fixed  $M$  and  $N$ , the blur impulse response becomes increasingly wider, and its tails become truncated to a greater extent. In the limit, the nonzero elements in the blur matrix become constant values, and the condition number assumes a constant level. For small values of the blur coefficient, the truncation effect is negligible, and the condition number curve follows an ascending path toward infinity with the asymptotic value obtained for a smoothly represented blur impulse response. As the blur factor increases, the number of nonzero elements in the blur matrix increases, and the condition number stabilizes to a constant value. In effect, a trade-off exists between numerical errors caused by ill-conditioning and modeling accuracy. Although this conclusion is formulated on the basis of a particular degradation model, the inference seems to be more general because the inverse of the integral operator that describes the blur is unbounded. Therefore, the closer the discrete model follows the continuous model, the greater the degree of ill-conditioning. A move in the opposite direction reduces singularity but imposes modeling errors. This inevitable dilemma can only be broken with the intervention of correct a priori knowledge about the original image.

**11.4.3. Pseudoinverse Computational Algorithms**

Efficient computational algorithms have been developed by Pratt and Davarian (18) for pseudoinverse image restoration for space-invariant blur. To simplify the explanation of these algorithms, consideration will initially be limited to a one-dimensional example.

Let the  $N \times 1$  vector  $\mathbf{f}_T$  and the  $M \times 1$  vector  $\mathbf{g}_T$  be formed by selecting the center portions of  $\mathbf{f}$  and  $\mathbf{g}$ , respectively. The truncated vectors are obtained by dropping  $L - 1$  elements at each end of the appropriate vector. Figure 11.4-4a illustrates the relationships of all vectors for  $N = 9$  original vector points,  $M = 7$  observations and an impulse response of length  $L = 3$ .

The elements  $\mathbf{f}_T$  and  $\mathbf{g}_T$  are entries in the *adjoint model*

$$\mathbf{q}_E = \mathbf{C}\mathbf{f}_E + \mathbf{n}_E \tag{11.4-16a}$$

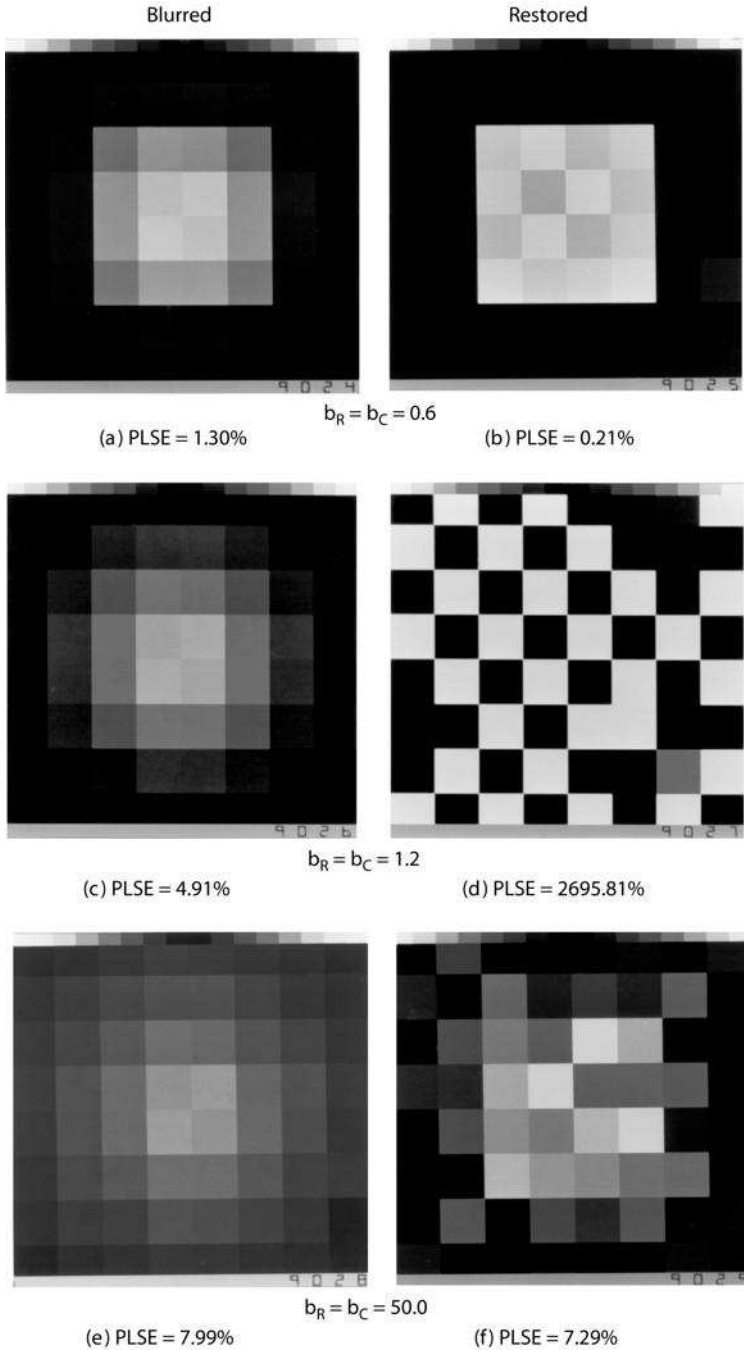


**FIGURE 11.4-2.** Pseudoinverse image restoration for test image blurred with Gaussian shape impulse response.  $M = 8$ ,  $N = 12$ ,  $L = 5$ ; noisy observation,  $\text{Var} = 10.0$ .

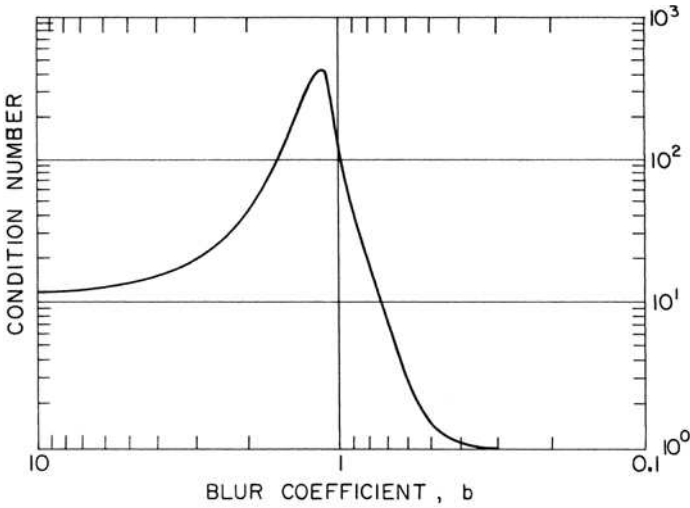


FIGURE 11.4-3. Condition number curve.

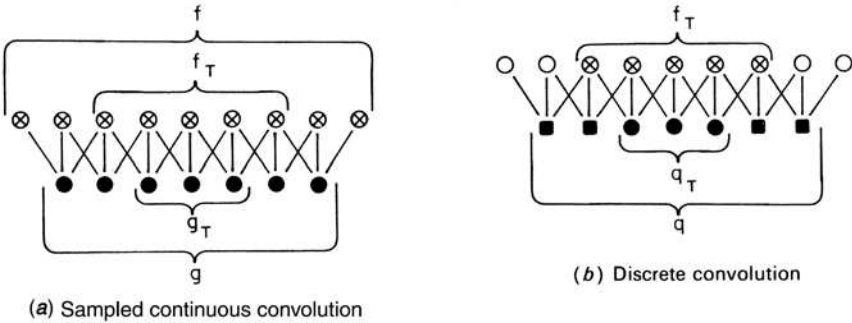


FIGURE 11.4-4. One-dimensional sampled continuous convolution and discrete convolution.

where the extended vectors  $\mathbf{q}_E$ ,  $\mathbf{f}_E$  and  $\mathbf{n}_E$  are defined in correspondence with

$$\begin{bmatrix} \mathbf{g} \\ \mathbf{0} \end{bmatrix} = \begin{bmatrix} \mathbf{C} \end{bmatrix} \begin{bmatrix} \mathbf{f}_T \\ \mathbf{0} \end{bmatrix} + \begin{bmatrix} \mathbf{n}_T \\ \mathbf{0} \end{bmatrix} \tag{11.4-16b}$$

where  $\mathbf{g}$  is a  $M \times 1$  vector,  $\mathbf{f}_T$  and  $\mathbf{n}_T$  are  $K \times 1$  vectors and  $\mathbf{C}$  is a  $J \times J$  matrix. As noted in Figure 11.4-4b, the vector  $\mathbf{q}$  is identical to the image observation  $\mathbf{g}$  over its  $R = M - 2(L - 1)$  center elements. The outer elements of  $\mathbf{q}$  can be approximated by

$$\mathbf{q} \approx \tilde{\mathbf{q}} = \mathbf{E}\mathbf{g} \tag{11.4-17}$$

where  $\mathbf{E}$ , called an *extraction weighting matrix*, is defined as

$$\mathbf{E} = \begin{bmatrix} \mathbf{a} & \mathbf{0} & \mathbf{0} \\ \mathbf{0} & \mathbf{I} & \mathbf{0} \\ \mathbf{0} & \mathbf{0} & \mathbf{b} \end{bmatrix} \tag{11.4-18}$$

where  $\mathbf{a}$  and  $\mathbf{b}$  are  $L \times L$  submatrices, which perform a windowing function similar to that described in Section 9.4.2 (18).

Combining Eqs. 11.4-17 and 11.4-18, an estimate of  $\mathbf{f}_T$  can be obtained from

$$\hat{\mathbf{f}}_E = \mathbf{C}^{-1}\hat{\mathbf{q}}_E \tag{11.4-19}$$

Equation 11.4-19 can be solved efficiently using Fourier domain convolution techniques, as described in Section 9.3. Computation of the pseudoinverse by Fourier processing requires on the order of  $J^2(1 + 4 \log_2 J)$  operations in two dimensions; spatial domain computation requires about  $M^2N^2$  operations. As an example, for  $M = 256$  and  $L = 17$ , the computational savings are nearly 1750:1 (18).

Figure 11.4-5 is a computer simulation example of the operation of the pseudoinverse image restoration algorithm for one-dimensional blur of an image. In the first step of the simulation, the center  $K$  pixels of the original image are extracted to form the set of truncated image vectors  $\mathbf{f}_T$  shown in Figure 11.4-5b. Next, the truncated image vectors are subjected to a simulated blur with a Gaussian-shaped impulse response with  $b_R = 1.5$  to produce the observation of Figure 11.4-5c. Figure 11.4-5d shows the result of the extraction operation on the observation. Restoration results without and with the extraction weighting operator  $\mathbf{E}$  are presented in Figure 11.4-5e and f, respectively.

These results graphically illustrate the importance of the extraction operation. Without weighting, errors at the observation boundary completely destroy the estimate in the boundary region, but with weighting the restoration is subjectively satisfying, and the restoration error is significantly reduced. Figure 11.4-6 shows simulation results for the experiment of Figure 11.4-5 when the degree of blur is increased by setting  $b_R = 2.0$ . The higher degree of blur greatly increases the ill-conditioning of the blur matrix, and the residual error in formation of the modified observation after weighting leads to the disappointing estimate of Figure 11.4-6b. Figure 11.4-6c and d illustrate the restoration improvement obtained with the pseudoinverse algorithm for horizontal image motion blur. In this example, the blur impulse response is constant, and the corresponding blur matrix is better conditioned than the blur matrix for Gaussian image blur. Reeves (20) has developed a similar method of FFT processing without boundary artifacts.

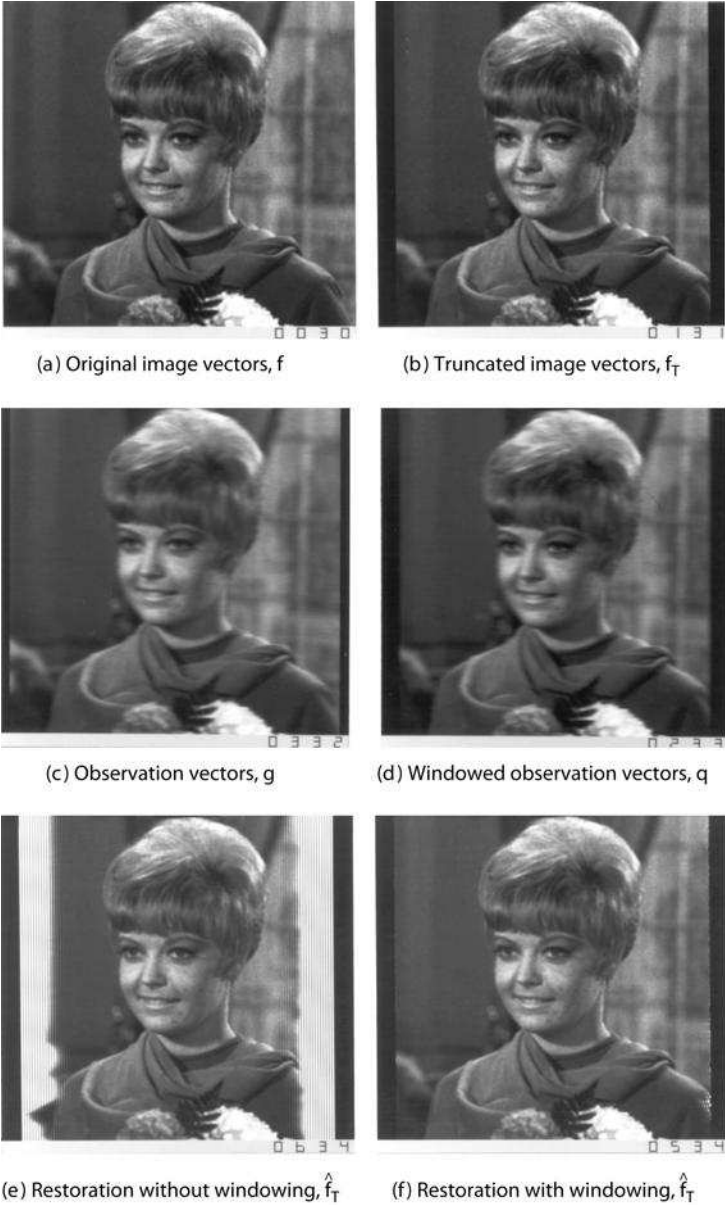


**FIGURE 11.4-5.** Pseudoinverse image restoration for small degree of horizontal blur,  $b_R = 1.5$ .



**FIGURE 11.4-6.** Pseudoinverse image restoration for moderate and high degrees of horizontal blur.

**11.4.4. SVD Pseudoinverse Spatial Image Restoration**

In Appendix 1, it is shown that any matrix can be decomposed into a series of eigenmatrices by the technique of singular value decomposition. For image restoration, this concept has been extended (21–26) to the eigen decomposition of blur matrices in the imaging model

$$g = Bf + n. \tag{11.4-20}$$

From Eq. A1.2-3, the blur matrix  $B$  may be expressed as

$$B = U\Lambda^{1/2}V^T \tag{11.4-21}$$

where the  $P \times P$  matrix  $\mathbf{U}$  and the  $Q \times Q$  matrix  $\mathbf{V}$  are unitary matrices composed of the eigenvectors of  $\mathbf{B}\mathbf{B}^T$  and  $\mathbf{B}^T\mathbf{B}$ , respectively and  $\mathbf{\Lambda}$  is a  $P \times Q$  matrix whose diagonal terms  $e(i) = \lambda(i)$  contain the eigenvalues of  $\mathbf{B}\mathbf{B}^T$  and  $\mathbf{B}^T\mathbf{B}$ . As a consequence of the orthogonality of  $\mathbf{U}$  and  $\mathbf{V}$ , it is possible to express the blur matrix in the series form

$$\mathbf{B} = \sum_{i=1}^R [\lambda(i)]^{1/2} \mathbf{u}_i \mathbf{v}_i^T \tag{11.4-22}$$

where  $\mathbf{u}_i$  and  $\mathbf{v}_i$  are the  $i$ th columns of  $\mathbf{U}$  and  $\mathbf{V}$ , respectively, and  $R$  is the rank of the matrix  $\mathbf{B}$ .

From Eq. 11.4-21, because  $\mathbf{U}$  and  $\mathbf{V}$  are unitary matrices, the generalized inverse of  $\mathbf{B}$  is

$$\mathbf{B}^- = \mathbf{V}\mathbf{\Lambda}^{1/2}\mathbf{U}^T = \sum_{i=1}^{\kappa} [\lambda(i)]^{-1/2} \mathbf{v}_i \mathbf{u}_i^T. \tag{11.4-23}$$

Figure 11.4-7 shows an example of the SVD decomposition of a blur matrix. The generalized inverse estimate can then be expressed as

$$\hat{\mathbf{f}} = \mathbf{B}^- \mathbf{g} = \mathbf{V}\mathbf{\Lambda}^{1/2}\mathbf{U}^T \mathbf{g} \tag{11.4-24a}$$

or, equivalently,

$$\hat{\mathbf{f}} = \sum_{i=1}^{\kappa} [\lambda(i)]^{-1/2} \mathbf{v}_i \mathbf{u}_i^T \mathbf{g} = \sum_{i=1}^{\kappa} [\lambda(i)]^{-1/2} [\mathbf{u}_i^T \mathbf{g}] \mathbf{v}_i \tag{11.4-24b}$$

recognizing the fact that the inner product  $\mathbf{u}_i^T \mathbf{g}$  is a scalar. Equation 11.4-24 provides the basis for sequential estimation; the  $k$ th estimate of  $\mathbf{f}$  in a sequence of estimates is equal to

$$\hat{\mathbf{f}}_k = \hat{\mathbf{f}}_{k-1} + [\lambda(k)]^{-1/2} [\mathbf{u}_k^T \mathbf{g}] \mathbf{v}_k. \tag{11.4-25}$$

One of the principal advantages of the sequential formulation is that problems of ill-conditioning generally occur only for higher-order singular values. Thus it is possible interactively to terminate the expansion before numerical problems occur.

Figure 11.4-8 shows an example of sequential SVD restoration for the under determined model example of Figure 11.1-4 with a poorly conditioned Gaussian blur matrix. A one-step pseudoinverse would have resulted in the final image estimate that is totally overwhelmed by numerical errors. The sixth step, which is the best subjective restoration, offers a considerable improvement over the blurred original, but the lowest least-squares error occurs for three singular values.

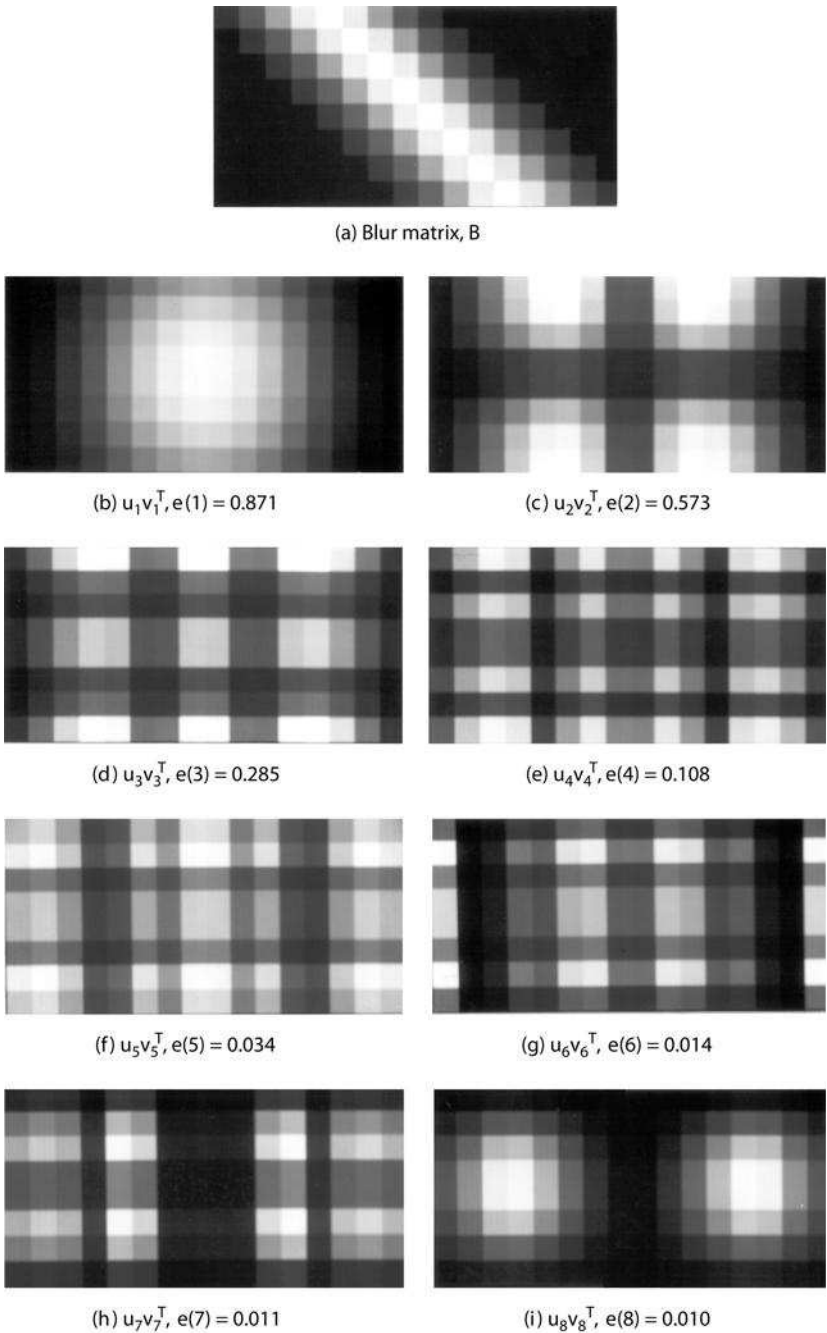


FIGURE 11.4-7. SVD decomposition of a blur matrix for  $b_R = 2.0, M = 8, N = 16, L = 9$ .



The major limitation of the SVD image restoration method formulation in Eqs. 11.4-25 and 11.4-26 is computational. The eigenvectors  $\mathbf{u}_i$  and  $\mathbf{v}_i$  must first be determined for the matrix  $\mathbf{B}\mathbf{B}^T$  and  $\mathbf{B}^T\mathbf{B}$ . Then the vector computations of Eq 11.4-25 or 11.4-26 must be performed. Even if  $\mathbf{B}$  is direct-product separable, permitting separable row and column SVD pseudo inversion, the computational task is staggering in the general case.

Pratt(4Ed., 361-364) has developed a fast computational algorithm for SVD pseudoinverse image restoration. Figure 11.4-9 shows an example of SVD pseudoinverse image restoration for one-dimensional Gaussian image blur with  $b_R = 3.0$ . It should be noted that the restoration attempt with the standard pseudoinverse shown in Figure 11.4-9b was subject to severe ill-conditioning errors at a blur spread of  $b_R = 2.0$ .

### 11.5. STATISTICAL ESTIMATION SPATIAL IMAGE RESTORATION

A fundamental limitation of pseudoinverse restoration techniques is that observation noise may lead to severe numerical instability and render the image estimate unusable. This problem can be alleviated in some instances by statistical restoration techniques that incorporate some a priori statistical knowledge of the observation noise (17).

#### 11.5.1. Wiener Estimation Spatial Image Restoration

With statistical techniques of spatial image restoration, the noise field is modeled as a sample of a two-dimensional random process with a known mean and covariance function. Wiener estimation techniques assume, in addition, that the ideal image is also a sample of a two-dimensional random process with known first and second moments (27,28).

**Wiener Estimation: General Case.** Consider the general discrete model of Figure 11.5-1 in which a  $Q \times 1$  image vector  $\mathbf{f}$  is subject to some unspecified type of point and spatial degradation resulting in the  $P \times 1$  vector of observations  $\mathbf{g}$ . An estimate of  $\mathbf{f}$  is formed by the linear operation

$$\hat{\mathbf{f}} = \mathbf{W}\mathbf{g} + \mathbf{b} \tag{11.5-1}$$

where  $\mathbf{W}$  is a  $Q \times P$  restoration matrix and  $\mathbf{b}$  is a  $Q \times 1$  bias vector. The objective of Wiener estimation is to choose  $\mathbf{W}$  and  $\mathbf{b}$  to minimize the mean-square restoration error, which may be defined as

$$E = E\{[\mathbf{f} - \hat{\mathbf{f}}]^T[\mathbf{f} - \hat{\mathbf{f}}]\} \tag{11.5-2a}$$

or

$$E = \text{tr}\{E\{[\mathbf{f} - \hat{\mathbf{f}}][\mathbf{f} - \hat{\mathbf{f}}]^T\}\}. \tag{11.5-2b}$$

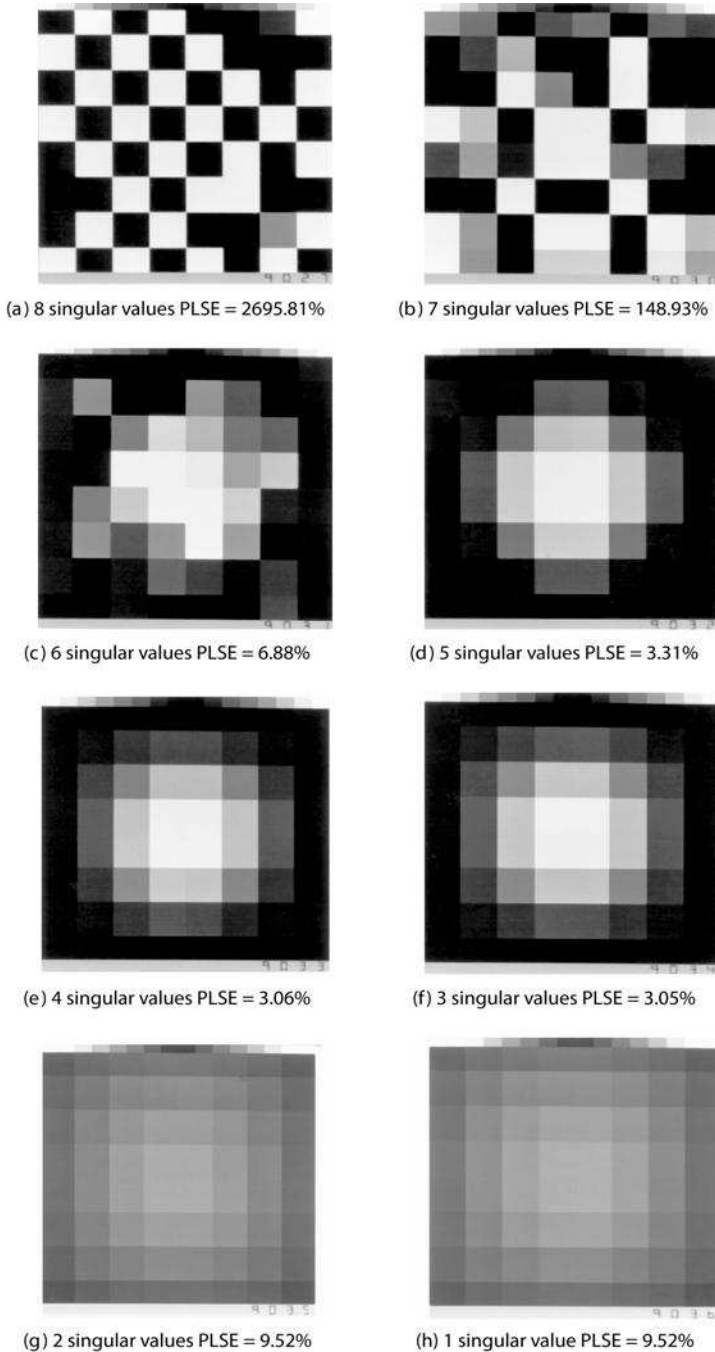


**FIGURE 11.4-8.** SVD restoration for test image blurred with a Gaussian-shaped impulse response.  $b_R = b_C = 1.2$ ,  $M = 8$ ,  $N = 12$ ,  $L = 5$ ; noisy observation,  $\text{Var} = 10.0$ .

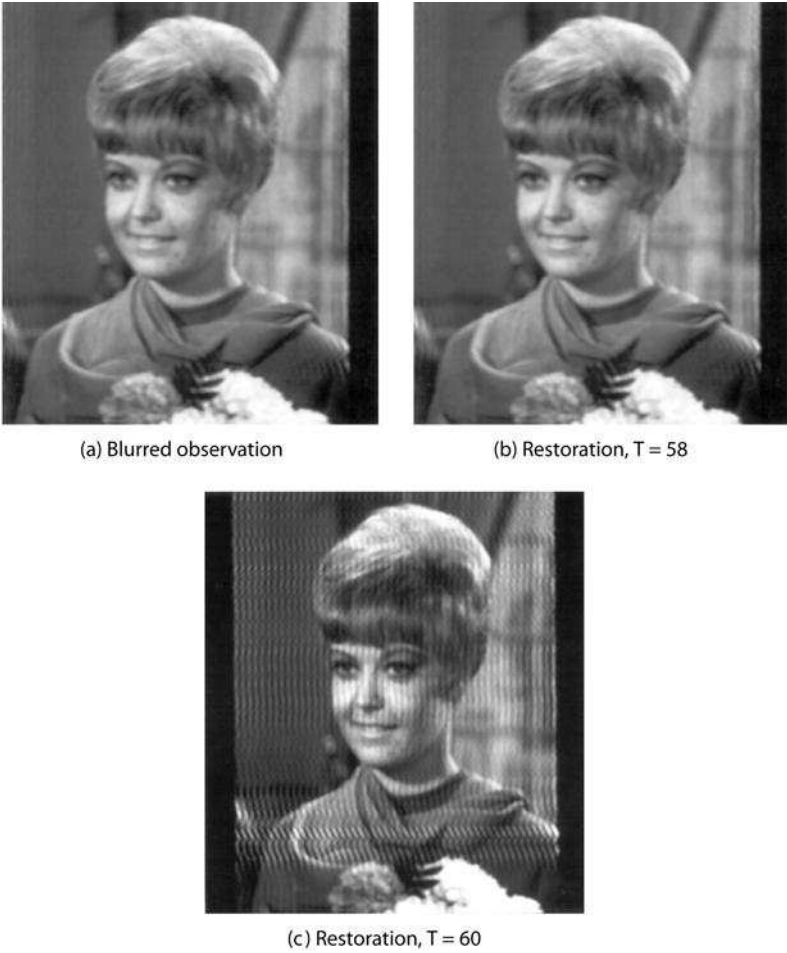


**FIGURE 11.4-9.** Sequential SVD pseudoinverse image restoration for horizontal Gaussian blur,  $b_R = 3.0$ ,  $L = 23$ ,  $J = 256$ .

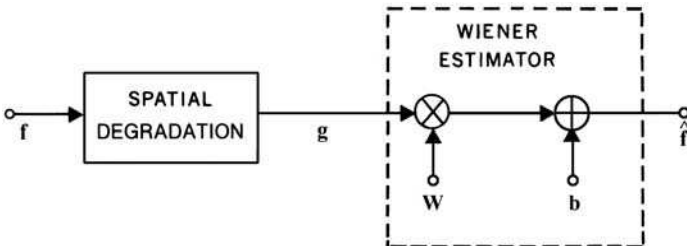


**FIGURE 11.5-1.** Wiener estimation for spatial image restoration.

Equation 11.5-2a expresses the error in inner-product form as the sum of the squares of the elements of the error vector  $[\mathbf{f} - \hat{\mathbf{f}}]$ , while Eq. 11.5-2b forms the covariance matrix of the error, and then sums together its variance terms (diagonal elements) by the trace operation. Minimization of Eq. 11.5-2 in either of its forms can be accomplished by differentiation of  $E$  with respect to  $\hat{\mathbf{f}}$ . An alternative approach, which is of quite general utility, is to employ the *orthogonality principle* (29, p. 219) to determine the values of  $\mathbf{W}$  and  $\mathbf{b}$  that minimize the mean-square error. In the context of image restoration, the orthogonality principle specifies two necessary and sufficient conditions for the minimization of the mean-square restoration error:

1. The expected value of the image estimate must equal the expected value of the image

$$E\{\hat{\mathbf{f}}\} = E\{\mathbf{f}\} \quad (11.5-3)$$

2. The restoration error must be orthogonal to the observation about its mean

$$E\{[\mathbf{f} - \hat{\mathbf{f}}][\mathbf{g} - E\{\mathbf{g}\}]^T\} = \mathbf{0}. \quad (11.5-4)$$

From condition 1, one obtains

$$\mathbf{b} = E\{\mathbf{f}\} - \mathbf{W}E\{\mathbf{g}\} \quad (11.5-5)$$

and from condition 2

$$E\{[\mathbf{W} + \mathbf{b} - \mathbf{f}][\mathbf{g} - E\{\mathbf{g}\}]^T\} = \mathbf{0}. \quad (11.5-6)$$

Upon substitution for the bias vector  $\mathbf{b}$  from Eq. 11.5-5 and simplification, Eq. 11.5-6 yields

$$\mathbf{W} = \mathbf{K}_{fg}[\mathbf{K}_{gg}]^{-1} \quad (11.5-7)$$

where  $\mathbf{K}_{gg}$  is the  $P \times P$  covariance matrix of the observation vector (assumed nonsingular) and  $\mathbf{K}_{fg}$  is the  $Q \times P$  cross-covariance matrix between the image and observation vectors. Thus the optimal bias vector  $\mathbf{b}$  and restoration matrix  $\mathbf{W}$  may be directly determined in terms of the first and second joint moments of the ideal image and observation vectors. It should be noted that these solutions apply for nonlinear and space-variant degradations. Subsequent sections describe applications of Wiener estimation to specific restoration models.

**Wiener Estimation: Image Blur with Additive Noise.** For the discrete model for a blurred image subjected to additive noise given by

$$\mathbf{g} = \mathbf{Bf} + \mathbf{n} \quad (11.5-8)$$

the Wiener estimator is composed of a bias term

$$\mathbf{b} = E\{\mathbf{f}\} - \mathbf{W}E\{\mathbf{g}\} = E\{\mathbf{f}\} - \mathbf{W}BE\{\mathbf{f}\} + \mathbf{W}E\{\mathbf{n}\} \tag{11.5-9}$$

and a matrix operator

$$\mathbf{W} = \mathbf{K}_{fg}[\mathbf{K}_{gg}]^{-1} = \mathbf{K}_f\mathbf{B}^T[\mathbf{B}\mathbf{K}_f\mathbf{B}^T + \mathbf{K}_n]^{-1} \tag{11.5-10}$$

If the ideal image field is assumed uncorrelated,  $\mathbf{K}_f = \sigma_f^2\mathbf{I}$  where  $\sigma_f^2$  represents the image energy. Equation 11.5-6 then reduces to

$$\mathbf{W} = \sigma_f^2\mathbf{B}^T[\sigma_f^2\mathbf{B}\mathbf{B}^T + \mathbf{K}_n]^{-1} \tag{11.5-11}$$

For a white-noise process with energy  $\sigma_n^2$ , the Wiener filter matrix becomes

$$\mathbf{W} = \mathbf{B}^T\left(\mathbf{B}\mathbf{B}^T + \frac{\sigma_n^2}{\sigma_f^2}\mathbf{I}\right)^{-1} \tag{11.5-12}$$

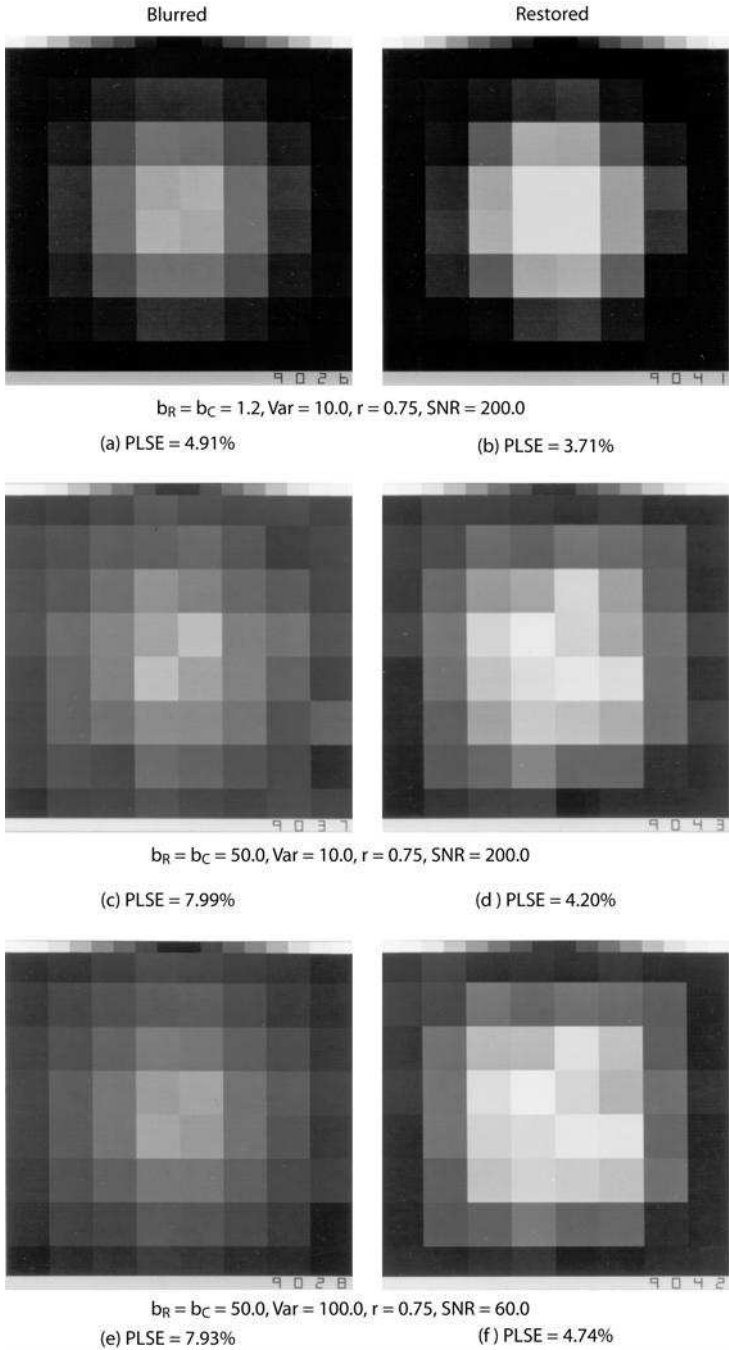
As the ratio of image energy to noise energy ( $\sigma_f^2/\sigma_n^2$ ) approaches infinity, the Wiener estimator of Eq. 11.5-1 becomes equivalent to the generalized inverse estimator.

Figure 11.5-2 shows restoration examples for the model of Figure 11.2-3 for a Gaussian-shaped blur function. Wiener restorations of large size images are given in Figure 11.5-3 using a fast computational algorithm developed by Pratt and Davarian (18). In the example of Figure 11.5-3a illustrating horizontal image motion blur, the impulse response is of rectangular shape of length  $L = 11$ . The center pixels have been restored and replaced within the context of the blurred image to show the visual restoration improvement. The noise level and blur impulse response of the electron microscope original image of Figure 11.5-3c were estimated directly from the photographic transparency using blind image restoration techniques described by Pratt(4Ed., 373-379). The parameters were then utilized to restore the center pixel region, which was then replaced in the context of the blurred original.

### 11.6. MULTI-PLANE IMAGE RESTORATION

A multi-plane image, also called a multi-channel image, consists of a set of two or more related pixel planes. Examples include:

- color image, e.g. *RGB*, *CMYK*, *YCbCr*,  $L^*a^*b^*$ ;
- multispectral image sequence;
- volumetric image, e.g. computerized tomography;
- temporal image sequence.



**FIGURE 11.5-2.** Wiener estimation for test image blurred with Gaussian-shaped impulse response.  $M = 8, N = 12, L = 5$ .

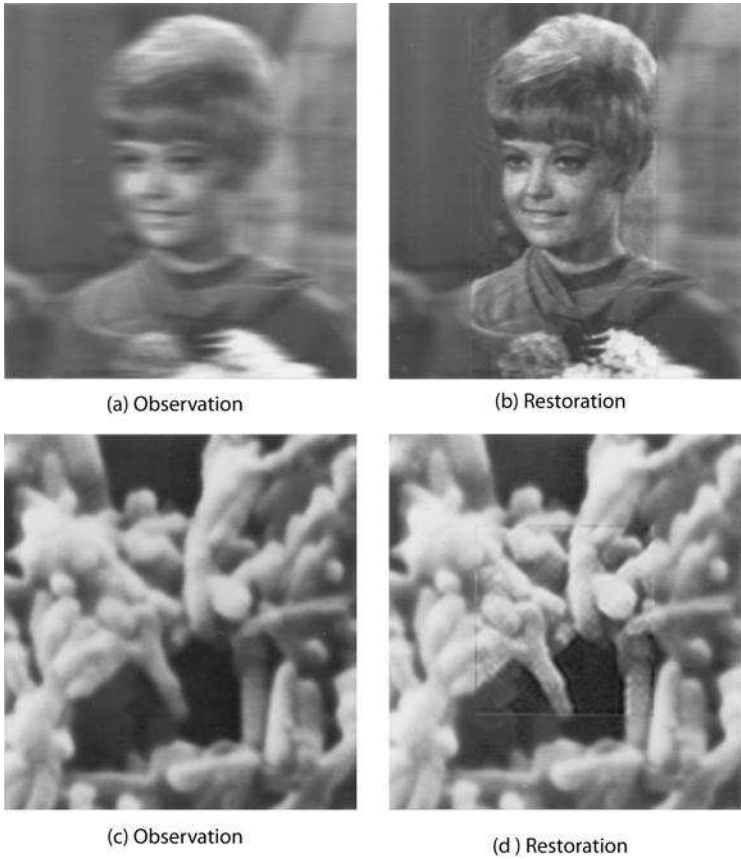


**FIGURE 11.5-3.** Wiener image restoration.

This classification is limited to three-dimensional images.<sup>1</sup>

The monochrome image restoration techniques previously discussed in this chapter can be applied independently to each pixel plane of a multi-plane image. However, with this strategy, the correlation between pixel planes is ignored; the restoration results, on a theoretical basis, will be sub-optimal compared to joint processing of all of the bands (30–33).

---

1. The PIKS image processing software application program interface defines a five-dimensional image space with indices  $x$ ,  $y$  for space,  $z$  for depth,  $t$  for time and  $b$  for spectral band.

### 11.6.1 Color Image Restoration Methods.

The multi-plane image restoration methods previously discussed can be applied to color images independently band-by-band. But such methods ignore the perceptual significance of the color planes.

If a multi-plane restoration method is to be applied to a *RGB* color image, care should be taken that the red, green and blue sensor signals are not gamma corrected. This is especially true when using a linear restoration filter, such as a Wiener filter, because the filter is designed to work on a linear blur plus additive noise model without point nonlinearities. If the gamma value is known, then inverse gamma processing following Eq. 12.7-2 can be performed directly; otherwise the gamma value can be estimated from the gamma corrected image using, for example, a method developed by Farid (34).

In their paper (30), Hunt and Kubler proposed the use of a Karhunen-Loeve (K-L) transformation across color image planes, to produce three bands  $K_1, K_2, K_3$ , which are spatially filtered independently. A problem with this approach is the amount of computation associated with the estimation of the inter-plane covariance matrix  $\mathbf{K}_p$  and the K-L transformation itself. Hunt and Kubler have substituted a *RGB* to *YIQ* luma/chroma transformation for the K-L transform. They found that the *YIQ* transformation was almost as good as the K-L transform in performing inter-plane decorrelation. They also obtained good experimental results by deblurring only the *Y* plane.

Altunbasak and Trussell (33) have performed a comprehensive evaluation of multi-plane Wiener filtering color image restoration for three, four and five color filter bands, various size blur impulse response arrays and a range of noise levels for K-L and independent color plane processing. Their experimental results indicate that the usage of more than three bands only achieves slight mean square error and visual improvement. Also, their studies showed that K-L processing was more effective than independent plane processing in terms of mean square error in *Lab* space.

**11.6.2. Temporal Averaging.** Temporal redundancy of scenes in real-time television systems can be exploited to perform image restoration indirectly. As an illustration, consider the *i*th continuous domain observed image frame

$$G_i(x, y) = F_I(x, y) + N_i(x, y) \quad (11.6-1)$$

of a video sequence in which  $F_I(x, y)$  is an ideal image and  $N_i(x, y)$  is an additive noise field independent of the ideal image. If the ideal image remains constant over a sequence of  $M$  frames, then temporal summation of the observed images yields the relation

$$F_I(x, y) = \frac{1}{M} \sum_{i=1}^M G_i(x, y) - \frac{1}{M} \sum_{i=1}^M N_i(x, y). \quad (11.6-2)$$



The value of the noise term on the right side will tend toward its ensemble average  $E\{N(x, y)\}$  for  $M$  large. In the common case of zero-mean white Gaussian noise, the ensemble average is zero at all  $(x, y)$ , and it is reasonable to form the estimate as

$$\hat{F}_I(x, y) = \frac{1}{M} \sum_{i=1}^M G_i(x, y) \quad (11.6-3)$$

## 11.7. IMAGE RESTORATION EXERCISES

E11.1 Develop a program that creates an unsigned integer, 8-bit, monochrome image with zero mean, additive, uniform noise with a signal-to-noise ratio of 10.0. The program should execute for arbitrary size source images. Steps:

- (a) Display the source monochrome image.
- (b) In application space, create a unit range noise image array using, for example, the C math.h function `rand`.
- (c) Import the noise image array.
- (d) Display the noise image array.
- (e) Scale the noise image array to produce a noise image array with zero mean and a SNR of 10.0.
- (f) Compute the mean and standard deviation of the noise image.
- (g) Read an unsigned integer, 8-bit monochrome image source image file and normalize it to unit range.
- (h) Add the noise image to the source image and clip to unit range.
- (i) Display the noisy source image.

The PIKS API executable `example_additive_noise` performs this exercise.

E11.2 Develop a program that creates an unsigned integer, 8-bit, monochrome image with replacement impulse noise. The program should execute for arbitrary size source images. Steps:

- (a) Display the source monochrome image.
- (b) In application space, create a unit range noise image array using, for example, the C math.h function `rand`.
- (c) Import the noise image array.
- (d) Read a source image file and normalize to unit range.

- (e) Replace each source image pixel with 0.0 if the noise pixel is less than 1.0%, and replace each source image pixel with 1.0 if the noise pixel is greater than 99%. The replacement operation can be implemented by image copying under ROI control.
- (f) Display the noisy source image.

The PIKS API executable `example_replacement_noise` performs this exercise.

E11.3 Develop a program that computes a  $512 \times 512$  Wiener filter transfer function for the blur impulse response array (Mask 3) of Eq. 10.3-2c and white noise with a SNR of 10.0. Steps:

- (a) Create the impulse response array  $H_D(x, y)$  or fetch it from a repository.
- (b) Convert the impulse response array to an image and embed it in a  $512 \times 512$  zero background array.
- (c) Compute the two-dimensional Fourier transform of the embedded impulse response array to obtain  $\mathcal{X}_D(\omega_x, \omega_y)$ .
- (d) Form the Wiener filter transfer function according to Eq. 11.2-18:

$$\mathcal{X}_R(\omega_x, \omega_y) = \frac{\mathcal{X}_D^*(\omega_x, \omega_y)}{|\mathcal{X}_D(\omega_x, \omega_y)|^2 + \bar{W}_N(\omega_x, \omega_y)}$$

- (e) Display the magnitude of the Wiener filter transfer function.

The PIKS API executable `example_wiener_filter` performs this exercise.

## REFERENCES

1. D. A. O'Handley and W. B. Green, "Recent Developments in Digital Image Processing at the Image Processing Laboratory at the Jet Propulsion Laboratory," *Proc. IEEE*, **60**, 7, July 1972, 821–828.
2. T. G. Stockham, Jr., "A–D and D–A Converters: Their Effect on Digital Audio Fidelity," in *Digital Signal Processing*, L. R. Rabiner and C. M. Rader, Eds., IEEE Press, New York, 1972, 484–496.
3. M. M. Sondhi, "Image Restoration: The Removal of Spatially Invariant Degradations," *Proc. IEEE*, **60**, 7, July 1972, 842–853.
4. H. C. Andrews, "Digital Image Restoration: A Survey," *IEEE Computer*, **7**, 5, May 1974, 36–45.
5. B. R. Hunt, "Digital Image Processing," *Proc. IEEE*, **63**, 4, April 1975, 693–708.
6. H. C. Andrews and B. R. Hunt, *Digital Image Restoration*, Prentice Hall, Englewood Cliffs, NJ, 1977.
7. B. R. Frieden, "Image Enhancement and Restoration," in *Picture Processing and Digital Filtering*, T. S. Huang, Ed., Springer-Verlag, New York, 1975.

8. A. Marechal, P. Croce and K. Dietzel, "Amelioration du Contrast des Details des Images Photographiques Par Filtrage des Fréquences Spatiales," *Optica Acta*, **5**, 1958, 256–262.
9. C. W. Helstrom, "Image Restoration by the Method of Least Squares," *J. Optical Society of America*, **57**, 3, March 1967, 297–303.
10. J. L. Harris, Sr., "Potential and Limitations of Techniques for Processing Linear Motion-Degraded Imagery," in *Evaluation of Motion Degraded Images*, US Government Printing Office, Washington DC, 1968, 131–138.
11. J. L. Homer, "Optical Spatial Filtering with the Least-Mean-Square-Error Filter," *J. Optical Society of America*, **51**, 5, May 1969, 553–558.
12. J. L. Homer, "Optical Restoration of Images Blurred by Atmospheric Turbulence Using Optimum Filter Theory," *Applied Optics*, **9**, 1, January 1970, 167–171.
13. B. L. Lewis and D. J. Sakrison, "Computer Enhancement of Scanning Electron Micrographs," *IEEE Trans. Circuits and Systems*, **CAS-22**, 3, March 1975, 267–278.
14. D. Slepian, "Restoration of Photographs Blurred by Image Motion," *Bell System Technical J.*, **XLVI**, 10, December 1967, 2353–2362.
15. E. R. Cole, "The Removal of Unknown Image Blurs by Homomorphic Filtering," Ph.D. dissertation, Department of Electrical Engineering, University of Utah, Salt Lake City, UT June 1973.
16. B. R. Hunt, "The Application of Constrained Least Squares Estimation to Image Restoration by Digital Computer," *IEEE Trans. Computers*, **C-23**, 9, September 1973, 805–812.
17. N. D. A. Mascarenhas and W. K. Pratt, "Digital Image Restoration Under a Regression Model," *IEEE Trans. Circuits and Systems*, **CAS-22**, 3, March 1975, 252–266.
18. W. K. Pratt and F. Davarian, "Fast Computational Techniques for Pseudoinverse and Wiener Image Restoration," *IEEE Trans. Computers*, **C-26**, 6, June 1977, 571–580.
19. W. K. Pratt, "Pseudoinverse Image Restoration Computational Algorithms," in *Optical Information Processing* Vol. 2, G. W. Stroke, Y. Nesterikhin and E. S. Barrekette, Eds., Plenum Press, New York, 1977.
20. S. J. Reeves, "Fast Image Restoration Without Boundary Artifacts," *IEEE Trans. Image Processing*, **14**, 10, October 2005, 1448–1453.
21. B. W. Rust and W. R. Burrus, *Mathematical Programming and the Numerical Solution of Linear Equations*, American Elsevier, New York, 1972.
22. A. Albert, *Regression and the Moore–Penrose Pseudoinverse*, Academic Press, New York, 1972.
23. H. C. Andrews and C. L. Patterson, "Outer Product Expansions and Their Uses in Digital Image Processing," *American Mathematical Monthly*, **1**, 82, January 1975, 1–13.
24. H. C. Andrews and C. L. Patterson, "Outer Product Expansions and Their Uses in Digital Image Processing," *IEEE Trans. Computers*, **C-25**, 2, February 1976, 140–148.
25. T. S. Huang and P. M. Narendra, "Image Restoration by Singular Value Decomposition," *Applied Optics*, **14**, 9, September 1975, 2213–2216.
26. H. C. Andrews and C. L. Patterson, "Singular Value Decompositions and Digital Image Processing," *IEEE Trans. Acoustics, Speech, and Signal Processing*, **ASSP-24**, 1, February 1976, 26–53.

27. T. O. Lewis and P. L. Odell, *Estimation in Linear Models*, Prentice Hall, Englewood Cliffs, NJ, 1971.
28. W. K. Pratt, "Generalized Wiener Filter Computation Techniques," *IEEE Trans. Computers*, **C-21**, 7, July 1972, 636–641.
29. A. Papoulis, *Probability Random Variables and Stochastic Processes, Third Edition*, McGraw-Hill, New York, 1991.
30. B. R. Hunt and O. Kubler, "Karhunen-Loeve Multispectral Image Restoration, Part 1: Theory," *IEEE Trans. Acoustics, Speech, Signal Processing*, **ASSP-32**, 3, June 1984, 592–600.
31. N. P. Galatsanos and R. T. Chin, "Digital Restoration of Multichannel Images," *IEEE Trans. Acoustics, Speech, Signal Processing*, **37**, 3, March 1989, 415–421.
32. N. P. Galatsanos et al., "Least Squares Restoration of Multichannel Images," *IEEE Trans. Signal Processing*, **39**, 10, October 1991, 2222–2236.
33. H. Altunbasak and H. J. Trussell, "Colorimetric Restoration of Digital Images," *IEEE Trans. Image Processing*, 10, 3, March 2001, 393–402.
34. H. Farid, "Blind Inverse Gamma Correction," *IEEE Trans. Image Processing*, **10**, 10, October 2001, 1428–1433.



---

# 12

---

## GEOMETRICAL IMAGE MODIFICATION

One of the most common image processing operations is geometrical modification in which an image is spatially translated, scaled in size, rotated or nonlinearly warped (1).

### 12.1. BASIC GEOMETRICAL METHODS

Image translation, size scaling and rotation can be analyzed from a unified standpoint. Let  $D(j, k)$  for  $0 \leq j \leq J-1$  and  $0 \leq k \leq K-1$  denote a discrete destination image that is created by geometrical modification of a discrete source image  $S(p, q)$  for  $0 \leq p \leq P-1$  and  $0 \leq q \leq Q-1$ . In this derivation, the source and destination images may be different in size. Geometrical image transformations are usually based on a Cartesian coordinate system representation in which pixels are of unit dimension, and the origin  $(0, 0)$  is at the center of the upper left corner pixel of an image array. The relationships between the Cartesian coordinate representations and the discrete image array of the destination image  $D(j, k)$  are illustrated in Figure 12.1-1. The destination image array indices are related to their Cartesian coordinates by

$$x_j = j + \frac{1}{2} \quad (12.1-1a)$$

$$y_k = k + \frac{1}{2}. \quad (12.1-1b)$$

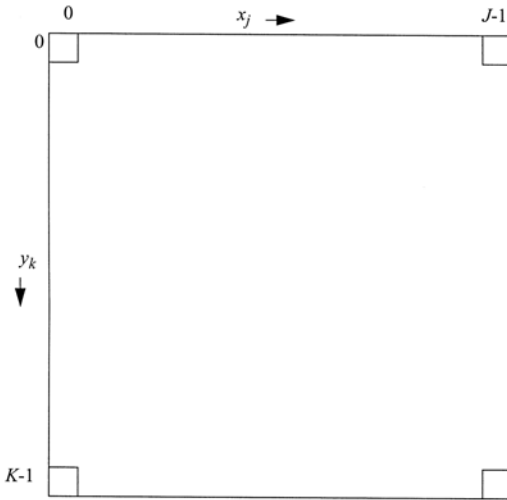


**FIGURE 12.1-1.** Relationship between discrete image array and Cartesian coordinate representation of a destination image  $D(j, k)$ .

Similarly, the source array relationship is given by

$$u_p = p + \frac{1}{2} \tag{12.1-2a}$$

$$v_q = q + \frac{1}{2}. \tag{12.1-2b}$$

**12.1.1. Translation**

Translation of  $S(p, q)$  with respect to its Cartesian origin to produce  $D(j, k)$  involves the computation of the relative offset addresses of the two images. The translation address relationships are

$$x_j = u_p + t_x \tag{12.1-3a}$$

$$y_k = v_q + t_y \tag{12.1-3b}$$

where  $t_x$  and  $t_y$  are translation offset constants. There are two approaches to this computation for discrete images: forward and reverse address computation. In the forward approach,  $u_p$  and  $v_q$  are computed for each source pixel  $(p, q)$  and substituted into Eq. 12.1-3 to obtain  $x_j$  and  $y_k$ . Next, the destination array addresses  $(j, k)$  are computed by inverting Eq. 12.1-1. The composite computation

reduces to

$$j' = p + t_x \quad (12.1-4a)$$

$$k' = q + t_y \quad (12.1-4b)$$

where the prime superscripts denote that  $j'$  and  $k'$  are not integers unless  $t_x$  and  $t_y$  are integers. If  $j'$  and  $k'$  are rounded to their nearest integer values, data voids can occur in the destination image. The reverse computation approach involves calculation of the source image addresses for integer destination image addresses. The composite address computation becomes

$$p' = j - t_x \quad (12.1-5a)$$

$$q' = k - t_y \quad (12.1-5b)$$

where again, the prime superscripts indicate that  $p'$  and  $q'$  are not necessarily integers. If they are not integers, it becomes necessary to interpolate pixel amplitudes of  $S(p, q)$  to generate a resampled pixel estimate  $\hat{S}(p, q)$ , which is transferred to  $D(j, k)$ . The geometrical resampling process is discussed in Section 12.3.

### 12.1.2. Scaling

Spatial size scaling of an image can be obtained by modifying the Cartesian coordinates of the source image according to the relations

$$x_j = s_x u_p \quad (12.1-6a)$$

$$y_k = s_y v_q \quad (12.1-6b)$$

where  $s_x$  and  $s_y$  are positive-valued scaling constants, but not necessarily integer valued. If  $s_x$  and  $s_y$  are each greater than unity, the address computation of Eq. 12.1-6 will lead to *magnification*. Conversely, if  $s_x$  and  $s_y$  are each less than unity, *minification* results. The reverse address relations for the source image address are found to be

$$p' = \frac{j + \frac{1}{2}}{s_x} - \frac{1}{2} \quad (12.1-7a)$$

$$q' = \frac{k + \frac{1}{2}}{s_y} - \frac{1}{2} \quad (12.1-7b)$$

As with generalized translation, it is necessary to interpolate  $S(p, q)$  to obtain  $D(j, k)$ .



**12.1.3. Rotation**

Rotation of an input image about its Cartesian origin can be accomplished by the address computation

$$x_k = u_q \cos \theta - v_p \sin \theta \tag{12.1-8a}$$

$$y_j = u_q \sin \theta + v_p \cos \theta \tag{12.1-8b}$$

where  $\theta$  is the counterclockwise angle of rotation with respect to the horizontal axis of the source image. Again, interpolation is required to obtain  $D(j, k)$ . Rotation of a source image about an arbitrary pivot point can be accomplished by translating the origin of the image to the pivot point, performing the rotation, and then translating back by the first translation offset. Equation 12.1-8 must be inverted and substitutions made for the Cartesian coordinates in terms of the array indices in order to obtain the reverse address indices  $(p', q')$ . This task is straightforward but results in a messy expression. A more elegant approach is to formulate the address computation as a vector-space manipulation.

**12.1.4. Generalized Linear Geometrical Transformations**

The vector-space representations for translation, scaling and rotation are given below.

*Translation:* 
$$\begin{bmatrix} x_j \\ y_k \end{bmatrix} = \begin{bmatrix} u_p \\ v_q \end{bmatrix} + \begin{bmatrix} t_x \\ t_y \end{bmatrix} \tag{12.1-9}$$

*Scaling:* 
$$\begin{bmatrix} x_j \\ y_k \end{bmatrix} = \begin{bmatrix} s_x & 0 \\ 0 & s_y \end{bmatrix} \begin{bmatrix} u_p \\ v_q \end{bmatrix} \tag{12.1-10}$$

*Rotation:* 
$$\begin{bmatrix} x_j \\ y_k \end{bmatrix} = \begin{bmatrix} \cos \theta & -\sin \theta \\ \sin \theta & \cos \theta \end{bmatrix} \begin{bmatrix} u_p \\ v_q \end{bmatrix} \tag{12.1-11}$$

Now, consider a compound geometrical modification consisting of translation, followed by scaling, followed by rotation. The address computations for this compound operation can be expressed as

$$\begin{bmatrix} x_j \\ y_k \end{bmatrix} = \begin{bmatrix} \cos \theta & -\sin \theta \\ \sin \theta & \cos \theta \end{bmatrix} \begin{bmatrix} s_x & 0 \\ 0 & s_y \end{bmatrix} \begin{bmatrix} u_p \\ v_q \end{bmatrix} + \begin{bmatrix} \cos \theta & -\sin \theta \\ \sin \theta & \cos \theta \end{bmatrix} \begin{bmatrix} s_x & 0 \\ 0 & s_y \end{bmatrix} \begin{bmatrix} t_x \\ t_y \end{bmatrix} \tag{12.1-12a}$$

or upon consolidation

$$\begin{bmatrix} x_j \\ y_k \end{bmatrix} = \begin{bmatrix} s_x \cos \theta & -s_y \sin \theta \\ s_x \sin \theta & s_y \cos \theta \end{bmatrix} \begin{bmatrix} u_p \\ v_q \end{bmatrix} + \begin{bmatrix} s_x t_x \cos \theta & -s_y t_y \sin \theta \\ s_x t_x \sin \theta & +s_y t_y \cos \theta \end{bmatrix}. \tag{12.1-12b}$$

Equation 12.1-12*b* is, of course, linear. It can be expressed as

$$\begin{bmatrix} x_j \\ y_k \end{bmatrix} = \begin{bmatrix} c_0 & c_1 \\ d_0 & d_1 \end{bmatrix} \begin{bmatrix} u_p \\ v_q \end{bmatrix} + \begin{bmatrix} c_2 \\ d_2 \end{bmatrix} \tag{12.1-13a}$$

in one-to-one correspondence with Eq. 12.1-12*b*. Equation 12.1-13*a* can be rewritten in the more compact form

$$\begin{bmatrix} x_j \\ y_k \end{bmatrix} = \begin{bmatrix} c_0 & c_1 & c_2 \\ d_0 & d_1 & d_2 \end{bmatrix} \begin{bmatrix} u_p \\ v_q \\ 1 \end{bmatrix}. \tag{12.1-13b}$$

As a consequence, the three address calculations can be obtained as a single linear address computation. It should be noted, however, that the three address calculations are not commutative. Performing rotation followed by minification followed by translation results in a mathematical transformation different than Eq. 12.1-12. The overall results can be made identical by proper choice of the individual transformation parameters.

To obtain the reverse address calculation, it is necessary to invert Eq. 12.1-13*b* to solve for  $(u_p, v_q)$  in terms of  $(x_j, y_k)$ . Because the matrix in Eq. 12.1-13*b* is not square, it does not possess an inverse. Although it is possible to obtain  $(u_p, v_q)$  by a pseudoinverse operation, as described in Appendix 1, it is convenient to augment the rectangular matrix as follows:

$$\begin{bmatrix} x_j \\ y_k \\ 1 \end{bmatrix} = \begin{bmatrix} c_0 & c_1 & c_2 \\ d_0 & d_1 & d_2 \\ 0 & 0 & 1 \end{bmatrix} \begin{bmatrix} u_p \\ v_q \\ 1 \end{bmatrix}. \tag{12.1-14}$$

This three-dimensional vector representation of a two-dimensional vector is a special case of a *homogeneous coordinates* representation (2–4).

The use of homogeneous coordinates enables a simple formulation of concatenated operators. For example, consider the rotation of an image by an angle  $\theta$  about a pivot point  $(x_c, y_c)$  in the image. This can be accomplished by

$$\begin{bmatrix} x_j \\ y_k \\ 1 \end{bmatrix} = \begin{bmatrix} 1 & 0 & x_c \\ 0 & 1 & y_c \\ 0 & 0 & 1 \end{bmatrix} \begin{bmatrix} \cos \theta & -\sin \theta & 0 \\ \sin \theta & \cos \theta & 0 \\ 0 & 0 & 1 \end{bmatrix} \begin{bmatrix} 1 & 0 & -x_c \\ 0 & 1 & -y_c \\ 0 & 0 & 1 \end{bmatrix} \begin{bmatrix} u_p \\ v_q \\ 1 \end{bmatrix} \tag{12.1-15}$$

which reduces to a single  $3 \times 3$  transformation:

$$\begin{bmatrix} x_j \\ y_k \\ 1 \end{bmatrix} = \begin{bmatrix} \cos\theta & -\sin\theta & -x_c \cos\theta + y_c \sin\theta + x_c \\ \sin\theta & \cos\theta & -x_c \sin\theta - y_c \cos\theta + y_c \\ 0 & 0 & 1 \end{bmatrix} \begin{bmatrix} u_p \\ v_q \\ 1 \end{bmatrix}. \quad (12.1-16)$$

The reverse address computation for the special case of Eq. 12.1-16, or the more general case of Eq. 12.1-13, can be obtained by inverting the  $3 \times 3$  transformation matrices by numerical methods. Another approach, which is more computationally efficient, is to initially develop the homogeneous transformation matrix in reverse order as

$$\begin{bmatrix} u_p \\ v_q \\ 1 \end{bmatrix} = \begin{bmatrix} a_0 & a_1 & a_2 \\ b_0 & b_1 & b_2 \\ 0 & 0 & 1 \end{bmatrix} \begin{bmatrix} x_j \\ y_k \\ 1 \end{bmatrix} \quad (12.1-17)$$

where for translation

$$a_0 = 1 \quad (12.1-18a)$$

$$a_1 = 0 \quad (12.1-18b)$$

$$a_2 = -t_x \quad (12.1-18c)$$

$$b_0 = 0 \quad (12.1-18d)$$

$$b_1 = 1 \quad (12.1-18e)$$

$$b_2 = -t_y \quad (12.1-18f)$$

and for scaling

$$a_0 = 1/s_x \quad (12.1-19a)$$

$$a_1 = 0 \quad (12.1-19b)$$

$$a_2 = 0 \quad (12.1-19c)$$

$$b_0 = 0 \quad (12.1-19d)$$

$$b_1 = 1/s_y \quad (12.1-19e)$$

$$b_2 = 0 \quad (12.1-19f)$$

and for rotation

$$a_0 = \cos\theta \quad (12.1-20a)$$

$$a_1 = \sin\theta \quad (12.1-20b)$$

$$a_2 = 0 \tag{12.1-20c}$$

$$b_0 = -\sin\theta \tag{12.1-20d}$$

$$b_1 = \cos\theta \tag{12.1-20e}$$

$$b_2 = 0 \tag{12.1-20f}$$

Address computation for a rectangular destination array  $D(j, k)$  from a rectangular source array  $S(p, q)$  of the same size results in two types of ambiguity: some pixels of  $S(p, q)$  will map outside of  $D(j, k)$ ; and some pixels of  $D(j, k)$  will not be mappable from  $S(p, q)$  because they will lie outside its limits. As an example, Figure 12.1-2 illustrates clockwise rotation of an image by  $45^\circ$  about its center. If the desire of the mapping is to produce a complete destination array  $D(j, k)$ , it is necessary to access a sufficiently large source image  $S(p, q)$  to prevent mapping voids in  $D(j, k)$ . This is accomplished in Figure 12.1-2d by embedding the original image of Figure 12.1-2a in a zero background that is sufficiently large to encompass the rotated original.

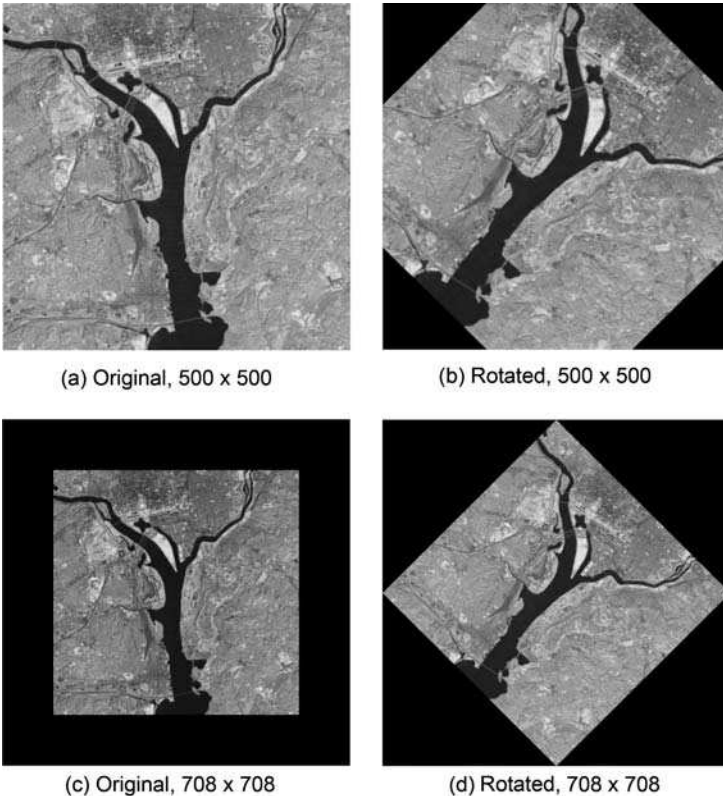


**FIGURE 12.1-2.** Image rotation by  $-45^\circ$  on the `washington_ir` image about its center.

### 12.1.5. Affine Transformation

The geometrical operations of translation, size scaling and rotation are special cases of a geometrical operator called an *affine transformation*. It is defined by Eq. 12.1-13b, in which the constants  $c_i$  and  $d_i$  are general weighting factors. The affine transformation is not only useful as a generalization of translation, scaling and rotation. It provides a means of image shearing in which the rows or columns are successively uniformly translated with respect to one another. Figure 12.1-3 illustrates image shearing of rows of an image. In this example,  $c_0 = d_1 = 1.0$ ,  $c_1 = 0.1$ ,  $d_0 = 0.0$  and  $c_2 = d_2 = 0.0$ .

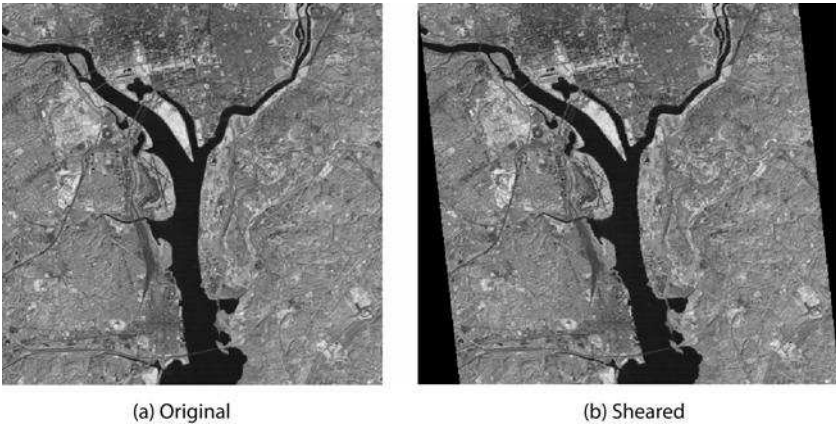


FIGURE 12.1-3. Horizontal image shearing on the `washington_ir` image.

### 12.1.6. Separable Rotation

The address mapping computations for translation and scaling are separable in the sense that the horizontal output image coordinate  $x_j$  depends only on  $u_p$ , and  $y_k$  depends only on  $v_q$ . Consequently, it is possible to perform these operations separably in two passes. In the first pass, a one-dimensional address translation is performed independently on each row of an input image to produce an intermediate array  $I(j, q)$ . In the second pass, columns of the intermediate array are processed independently to produce the final result  $D(j, k)$ .

Referring to Eq. 12.1-8, it is observed that the address computation for rotation is of a form such that  $x_j$  is a function of both  $u_p$  and  $v_q$ ; and similarly for  $y_k$ . One might then conclude that rotation cannot be achieved by separable row and column processing, but Catmull and Smith (5) have demonstrated otherwise. In the first pass of the Catmull and Smith procedure, each row of  $S(p, q)$  is mapped into

the corresponding row of the intermediate array  $I(j, q)$  using the standard row address computation of Eq. 12.1-8a. Thus,

$$x_j = u_q \cos \theta - v_q \sin \theta. \tag{12.1-21}$$

Then, each column of  $I(j, q)$  is processed to obtain the corresponding column of  $D(j, k)$  using the address computation

$$y_k = \frac{x_j \sin \theta + v_q}{\cos \theta}. \tag{12.1-22}$$

Substitution of Eq. 12.1-21 into Eq. 12.1-22 yields the proper composite  $y$ -axis transformation of Eq. 12.1-8b. The “secret” of this separable rotation procedure is the ability to invert Eq. 12.1-21 to obtain an analytic expression for  $u_p$  in terms of  $x_j$ . In this case,

$$u_p = \frac{x_j + v_q \sin \theta}{\cos \theta} \tag{12.1-23}$$

when substituted into Eq. 12.1-21, gives the intermediate column warping function of Eq. 12.1-22.

The Catmull and Smith two-pass algorithm can be expressed in vector-space form as

$$\begin{bmatrix} x_j \\ y_k \end{bmatrix} = \begin{bmatrix} 1 & 0 \\ \tan \theta & \frac{1}{\cos \theta} \end{bmatrix} \begin{bmatrix} \cos \theta & -\sin \theta \\ 0 & 1 \end{bmatrix} \begin{bmatrix} u_p \\ v_q \end{bmatrix}. \tag{12.1-24}$$

The separable processing procedure must be used with caution. In the special case of a rotation of  $90^\circ$ , all of the rows of  $S(p, q)$  are mapped into a single column of  $I(p, k)$ , and, hence, the second pass cannot be executed. This problem can be avoided by processing the columns of  $S(p, q)$  in the first pass. In general, the best overall results are obtained by minimizing the amount of spatial pixel movement. For example, if the rotation angle is  $+80^\circ$ , the original should be rotated by  $+90^\circ$  by conventional row–column swapping methods, and then that intermediate image should be rotated by  $-10^\circ$  using the separable method.

Figure 12.1-4 provides an example of separable rotation of an image by  $45^\circ$ . Figure 13.1-4a is the original, Figure 12.1-4b shows the result of the first pass and Figure 12.1-4c presents the final result.

Separable, two-pass rotation offers the advantage of simpler computation compared to one-pass rotation, but there are some disadvantages to two-pass rotation. Two-pass rotation causes loss of high spatial frequencies of an image because of the intermediate scaling step (6), as seen in Figure 12.1-4b. Also, there is the potential of increased aliasing error (6,7), as discussed in Section 12.3.

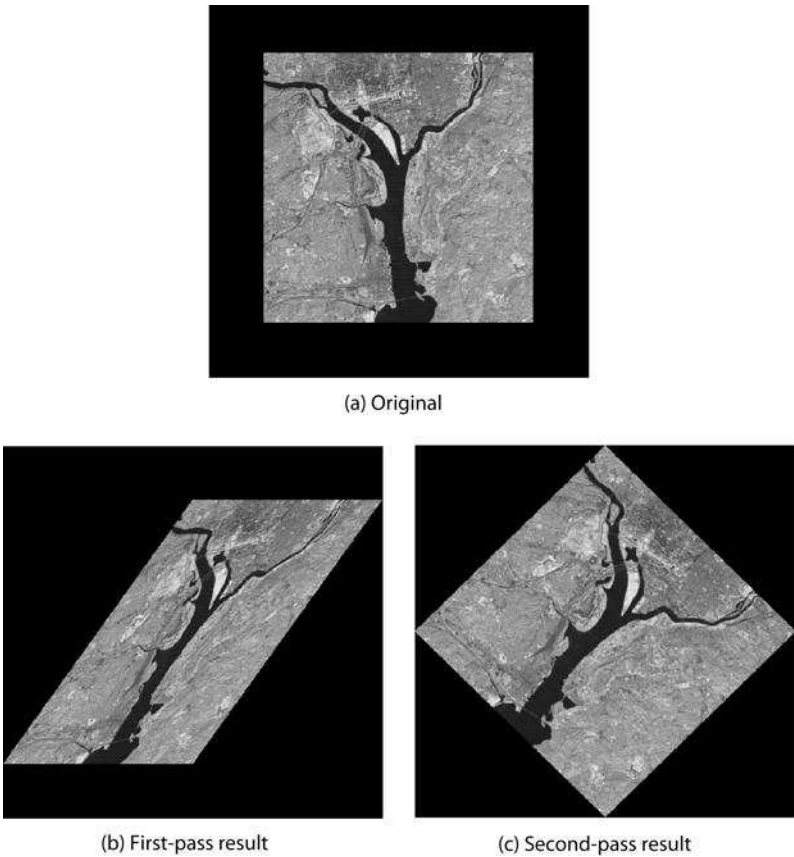


**FIGURE 12.1-4.** Separable two-pass image rotation on the `washington_ir` image.

Several authors (6,8,9) have proposed a three-pass rotation procedure in which there is no scaling step and, hence, no loss of high-spatial-frequency content with proper interpolation. The vector-space representation of this procedure is given by

$$\begin{bmatrix} x_j \\ y_k \end{bmatrix} = \begin{bmatrix} 1 & -\tan(\theta/2) \\ 0 & 1 \end{bmatrix} \begin{bmatrix} 1 & 0 \\ \sin \theta & 1 \end{bmatrix} \begin{bmatrix} 1 & -\tan(\theta/2) \\ 0 & 1 \end{bmatrix} \begin{bmatrix} u_p \\ v_q \end{bmatrix}. \tag{12.1-25}$$

This transformation is a series of image shearing operations without scaling. Figure 12.1-5 illustrates three-pass rotation for rotation by 45°.

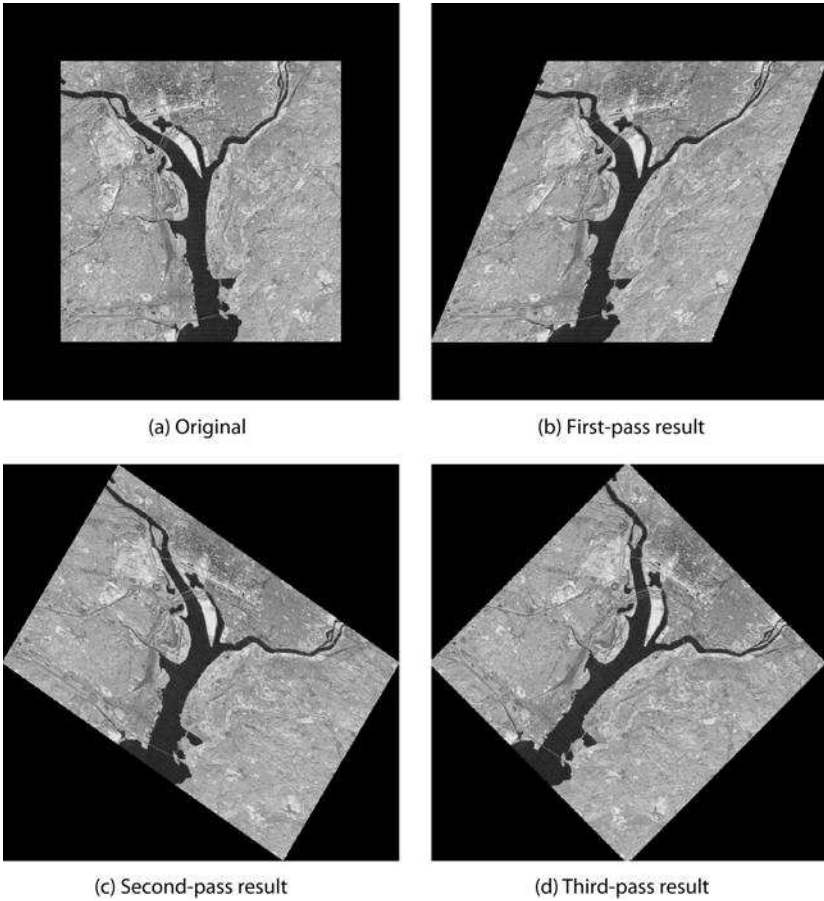


**FIGURE 12.1-5.** Separable three-pass image rotation on the `washington_ir` image.

## 12.2. SPATIAL WARPING

The address computation procedures described in the preceding section can be extended to provide nonlinear spatial warping of an image. In the literature, this process is often called *rubber-sheet stretching* (16,17). Let

$$x = X(u, v) \quad (12.2-1a)$$

$$y = Y(u, v) \quad (12.2-1b)$$



denote the generalized forward address mapping functions from an input image to an output image. The corresponding generalized reverse address mapping functions are given by

$$u = U(x, y) \tag{12.2-2a}$$

$$v = V(x, y) \tag{12.2-2b}$$

For notational simplicity, the  $(j, k)$  and  $(p, q)$  subscripts have been dropped from these and subsequent expressions. Consideration is given next to some examples and applications of spatial warping.

The reverse address computation procedure given by the linear mapping of Eq. 12.1-17 can be extended to higher dimensions. A second-order polynomial warp address mapping can be expressed as

$$u = a_0 + a_1x + a_2y + a_3x^2 + a_4xy + a_5y^2 \tag{12.2-3a}$$

$$v = b_0 + b_1x + b_2y + b_3x^2 + b_4xy + b_5y^2. \tag{12.2-3b}$$

In vector notation,

$$\begin{bmatrix} u \\ v \end{bmatrix} = \begin{bmatrix} a_0 & a_1 & a_2 & a_3 & a_4 & a_5 \\ b_0 & b_1 & b_2 & b_3 & b_4 & b_5 \end{bmatrix} \begin{bmatrix} 1 \\ x \\ y \\ x^2 \\ xy \\ y^2 \end{bmatrix}. \tag{12.2-3c}$$

For first-order address mapping, the weighting coefficients  $(a_i, b_i)$  can easily be related to the physical mapping as described in Section 12.1. There is no simple physical counterpart for second address mapping. Typically, second-order and higher-order address mapping are performed to compensate for spatial distortion caused by a physical imaging system. For example, Figure 12.2-1 illustrates the effects of imaging a rectangular grid with an electronic camera that is subject to nonlinear pincushion or barrel distortion.

Figure 12.2-2 presents a generalization of the problem. An ideal image  $S(j, k)$  is subject to an unknown physical spatial distortion. The observed image is measured over a rectangular array  $O(p, q)$ . The objective is to perform a spatial correction warp to produce a corrected image array  $S(j, k)$ . Assume that the address mapping from the ideal image space to the observation space is given by

$$u = O_u\{x, y\} \tag{12.2-4a}$$

$$v = O_v\{x, y\}. \tag{12.2-4b}$$

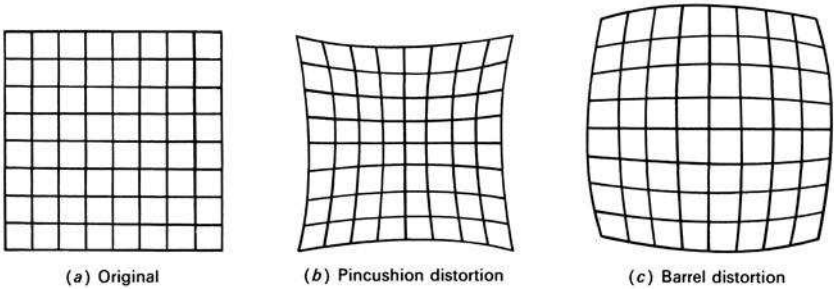


FIGURE 12.2-1. Geometric distortion.

where  $O_u\{x, y\}$  and  $O_v\{x, y\}$  are physical mapping functions. If these mapping functions are known, then Eq. 12.2-4 can, in principle, be inverted to obtain the proper corrective spatial warp mapping. If the physical mapping functions are not known, Eq. 12.2-3 can be considered as an estimate of the physical mapping functions based on the weighting coefficients  $(a_i, b_i)$ . These polynomial weighting coefficients are normally chosen to minimize the mean-square error between a set of observation coordinates  $(u_m, v_m)$  and the polynomial estimates  $(u, v)$  for a set  $(1 \leq m \leq M)$  of known data points  $(x_m, y_m)$  called *control points*.

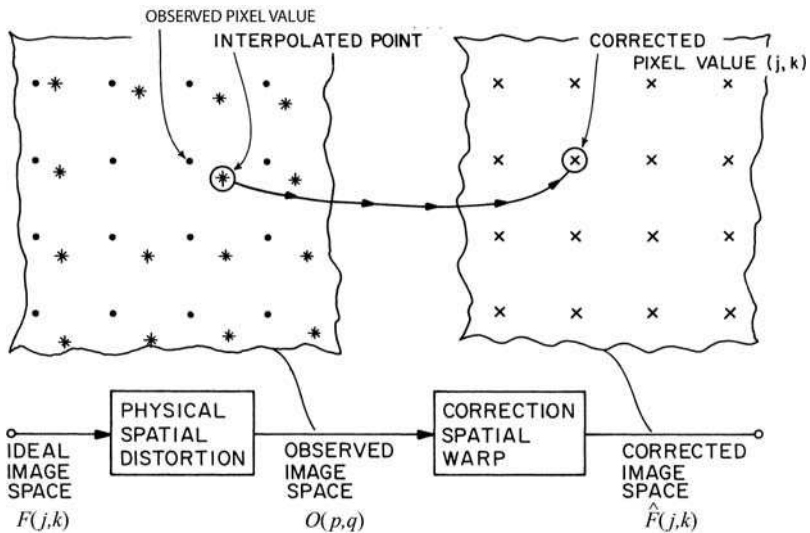


FIGURE 12.2-2. Spatial warping concept.

It is convenient to arrange the observation space coordinates into the vectors

$$\mathbf{u}^T = [u_1, u_2, \dots, u_M] \tag{12.2-5a}$$

$$\mathbf{v}^T = [v_1, v_2, \dots, v_M]. \tag{12.2-5b}$$

Similarly, let the second-order polynomial coefficients be expressed in vector form as

$$\mathbf{a}^T = [a_0, a_1, \dots, a_5] \tag{12.2-6a}$$

$$\mathbf{b}^T = [b_0, b_1, \dots, b_5]. \tag{12.2-6b}$$

The mean-square estimation error can be expressed in the compact form

$$E = (\mathbf{u} - \mathbf{Aa})^T(\mathbf{u} - \mathbf{Aa}) + (\mathbf{v} - \mathbf{Ab})^T(\mathbf{v} - \mathbf{Ab}) \tag{12.2-7}$$

where

$$\mathbf{A} = \begin{bmatrix} 1 & x_1 & y_1 & x_1^2 & x_1y_1 & y_1^2 \\ 1 & x_2 & y_2 & x_2^2 & x_2y_2 & y_2^2 \\ \vdots & \vdots & \vdots & \vdots & \vdots & \vdots \\ 1 & x_M & y_M & x_M^2 & x_My_M & y_M^2 \end{bmatrix} \tag{12.2-8}$$

From Appendix 1, it has been determined that the error will be minimum if

$$\mathbf{a} = \mathbf{A}^- \mathbf{u} \tag{12.2-9a}$$

$$\mathbf{b} = \mathbf{A}^- \mathbf{v} \tag{12.2-9b}$$

where  $\mathbf{A}^-$  is the generalized inverse of  $\mathbf{A}$ . If the number of control points is chosen greater than the number of polynomial coefficients, then

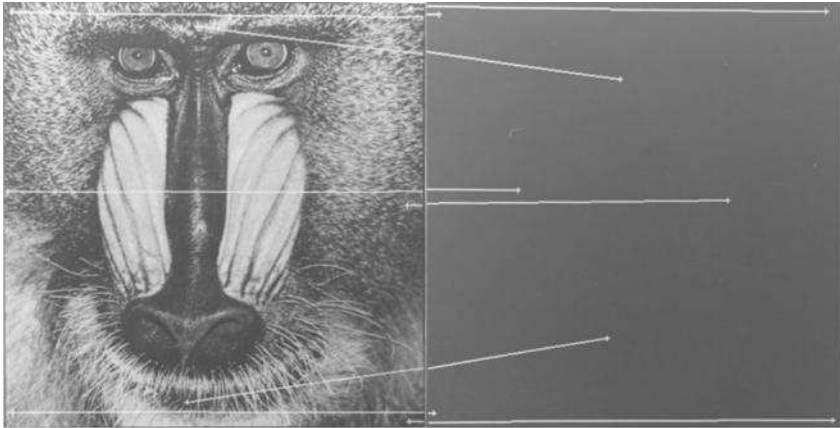
$$\mathbf{A}^- = [\mathbf{A}^T \mathbf{A}]^{-1} \mathbf{A} \tag{12.2-10}$$

provided that the control points are not linearly related. Following this procedure, the polynomial coefficients  $(a_i, b_i)$  can easily be computed, and the address mapping of Eq. 12.2-1 can be obtained for all  $(j, k)$  pixels in the corrected image. Of course, proper interpolation is necessary.

Equation 12.2-3 can be extended to provide a higher-order approximation to the physical mapping of Eq. 12.2-3. However, practical problems arise in computing the pseudoinverse accurately for higher-order polynomials. For most applications, second-order polynomial computation suffices. Figure 12.2-3 presents an example

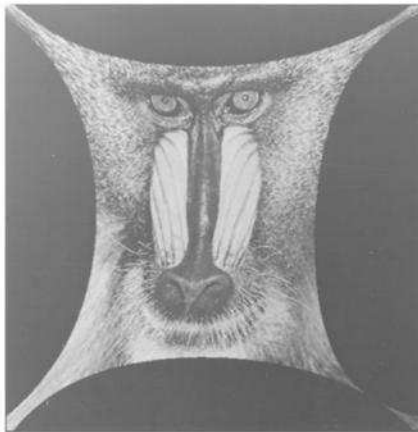
of second-order polynomial warping of an image. In this example, the mapping of control points is indicated by the graphics overlay.

The spatial warping techniques discussed in this section have application for two types of geometrical image manipulation: *image mosaicing* and *image blending*. Image mosaicing involves the spatial combination of a set of partially overlapped images to create a larger image of a scene. Image blending is a process of creating a set of images between a temporal pair of images such that the created images form a smooth spatial interpolation between the reference image pair. References 11 to 15 provide details of image mosaicing and image blending algorithms.



(a) Source control points

(b) Destination control points



(c) Warped

**FIGURE 12.2-3.** Second-order polynomial spatial warping on the mandrill\_mon image.

### 12.3. GEOMETRICAL IMAGE RESAMPLING

As noted in the preceding sections of this chapter, the reverse address computation process usually results in an address result lying between known pixel values of an input image. Thus, it is necessary to estimate the unknown pixel amplitude from its known neighbors. This process is related to the image reconstruction task, as described in Chapter 4, in which a space-continuous display is generated from an array of image samples. However, the geometrical resampling process is usually not spatially regular. Furthermore, the process is discrete to discrete; only one output pixel is produced for each input address.

In this section, consideration is given to the general geometrical resampling process in which output pixels are estimated by interpolation of input pixels. The special, but common, case of image magnification by an integer zooming factor is also discussed. In this case, it is possible to perform pixel estimation by convolution.

#### 12.3.1. Interpolation Methods

The simplest form of resampling interpolation is to choose the amplitude of an output image pixel to be the amplitude of the input pixel nearest to the reverse address. This process, called *nearest-neighbor interpolation*, can result in a spatial offset error by as much as  $1/\sqrt{2}$  pixel units. The resampling interpolation error can be significantly reduced by utilizing all four nearest neighbors in the interpolation. A common approach, called *bilinear interpolation*, is to interpolate linearly along each row of an image and then interpolate that result linearly in the columnar direction. Figure 12.3-1 illustrates the process. The estimated pixel is easily found to be

$$\hat{F}(p', q') = (1 - b)[(1 - a)F(p, q) + aF(p + 1, q)] + b[(1 - a)F(p, q + 1) + aF(p + 1, q + 1)] \tag{12.3-1}$$

where  $a = p' - p$  and  $b = q' - q$ . Although the horizontal and vertical interpolation operations are each linear, in general, their sequential application results in a nonlinear surface fit between the four neighboring pixels.

The expression for bilinear interpolation of Eq. 12.3-1 can be generalized for any interpolation function  $R\{x\}$  that is zero-valued outside the range of  $\pm 1$  sample spacing. With this generalization, interpolation can be considered as the summing of four weighted interpolation functions as given by

$$F(p', q') = F(p, q)R\{-b\}R\{a\} + F(p + 1, q)R\{-b\}R\{-(1 - a)\} + F(p, q + 1)R\{1 - b\}R\{a\} + F(p + 1, q + 1)R\{1 - b\}R\{-(1 - a)\}. \tag{12.3-2}$$

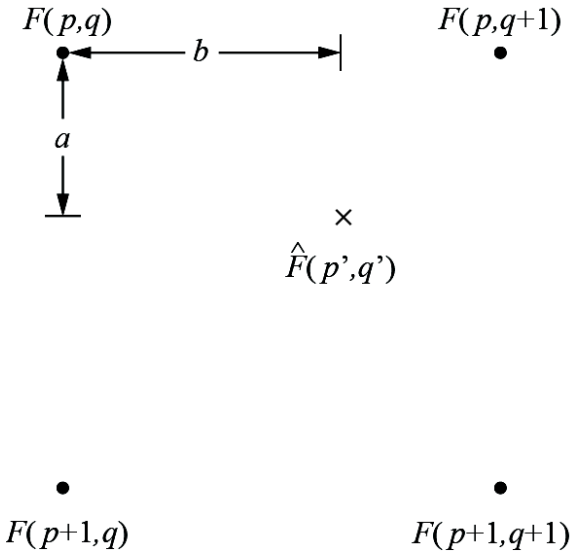


FIGURE 12.3-1. Bilinear interpolation.

In the special case of linear interpolation,  $R\{x\} = R_1\{x\}$ , where  $R_1\{x\}$  is defined in Eq. 4.3-2. Making this substitution, it is found that Eq. 12.3-2 is equivalent to the bilinear interpolation expression of Eq. 12.3-1.

Figure 12.3-2 defines a generalized interpolation neighborhood for support 2, 4 and 8 interpolation in which the pixel  $F(p, q)$  is the nearest neighbor to the pixel to be interpolated.

Typically, for reasons of computational complexity, resampling interpolation is limited to a  $4 \times 4$  pixel neighborhood. For this case, the interpolated pixel may be expressed in the compact form

$$F(p', q') = \sum_{m=-1}^2 \sum_{n=-1}^2 F(p+m, q+n) R_C\{(m-a)\} R_C\{-(n-b)\} \quad (12.3-3)$$

where  $R_C(x)$  denotes a bicubic interpolation function such as a cubic B-spline or cubic interpolation function, as defined in Section 4.3-2.

### 12.3.2. Convolution Methods

When an image is to be magnified by an integer zoom factor, pixel estimation can be implemented efficiently by convolution (18). As an example, consider image magni-

fication by a factor of 2:1. This operation can be accomplished in two stages. First, the input image is transferred to an array in which rows and columns of zeros are interleaved with the input image data as follows:

$$\begin{bmatrix} A & B \\ C & D \end{bmatrix} \qquad \begin{bmatrix} A & 0 & B \\ 0 & 0 & 0 \\ C & 0 & D \end{bmatrix}$$

input image                      zero-interleaved

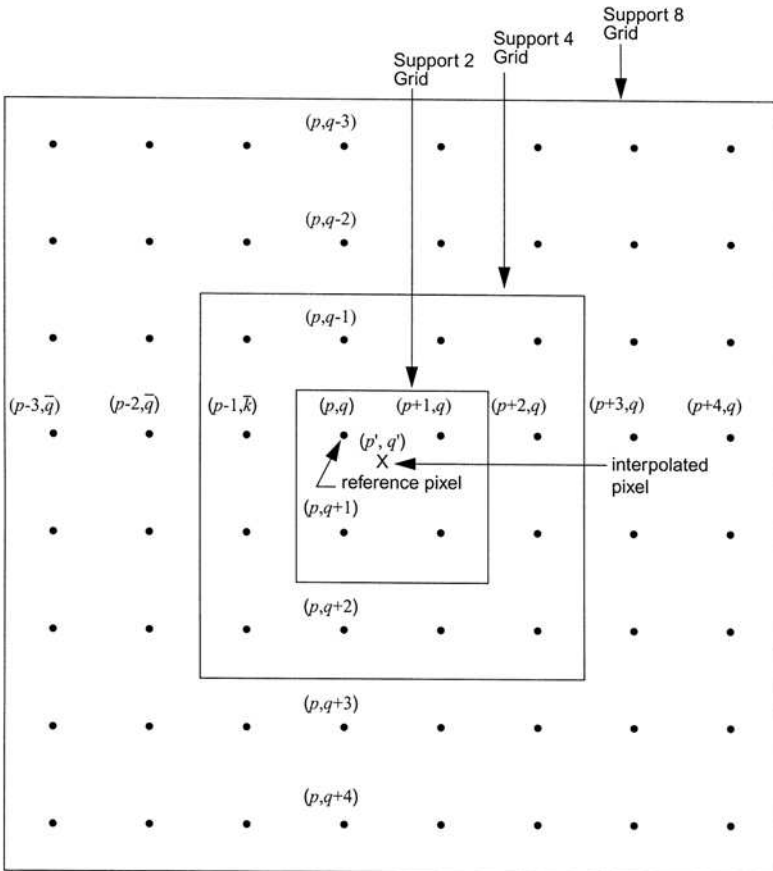


FIGURE 12.3-2. Support 2, 4 and 8 interpolation.

Next, the zero-interleaved neighborhood image is convolved with one of the discrete interpolation kernels listed in Figure 12.3-3. Figure 12.3-4 presents the magnification results for several interpolation kernels. The inevitable visual trade-off between the interpolation error (the jaggy line artifacts) and the loss of high spatial frequency detail in the image is apparent from the examples.

Peg

$$\begin{bmatrix} 1 & 1 \\ 1 & 1 \end{bmatrix}$$

Pyramid

$$\frac{1}{4} \begin{bmatrix} 1 & 2 & 1 \\ 2 & 4 & 2 \\ 1 & 2 & 1 \end{bmatrix}$$

Bell

$$\frac{1}{16} \begin{bmatrix} 1 & 3 & 3 & 1 \\ 3 & 9 & 9 & 3 \\ 3 & 9 & 9 & 3 \\ 1 & 3 & 3 & 1 \end{bmatrix}$$

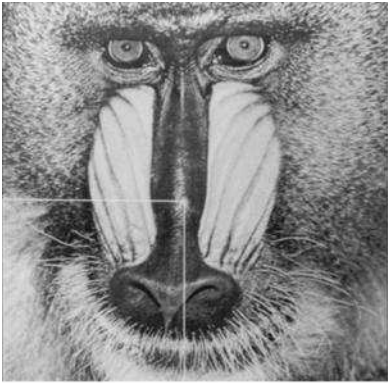
Cubic B-spline

$$\frac{1}{64} \begin{bmatrix} 1 & 4 & 6 & 4 & 1 \\ 4 & 16 & 24 & 16 & 4 \\ 6 & 24 & 36 & 24 & 6 \\ 4 & 16 & 24 & 16 & 4 \\ 1 & 4 & 6 & 4 & 1 \end{bmatrix}$$

FIGURE 12.3-3. Interpolation kernels for 2:1 magnification.

This discrete convolution operation can easily be extended to higher-order magnification factors. For  $N:1$  magnification, the core kernel is a  $N \times N$  peg array. For large kernels it may be more computationally efficient in many cases, to perform the interpolation indirectly by Fourier domain filtering rather than by convolution.





(a) Original



(b) Zero interleaved quadrant



(c) Peg



(d) Pyramid



(e) Bell



(f) Cubic B-spline

**FIGURE 12.3-4.** Image interpolation on the mandrill\_mon image for 2:1 magnification.

For color images, the geometrical image modification methods discussed in this chapter can be applied separately to the red, green and blue components of the color image. Vrhel (19) has proposed converting a color image to luma/chroma (or lightness/chrominance) color coordinates and performing the geometrical modification in the converted color space. Large support interpolation is then performed on the luma or lightness component, and nearest neighbor interpolation is performed on the luma/chrominance components. After the geometrical processing is completed, conversion to *RGB* space is performed. This type of processing takes advantage of the tolerance of the human visual system to chroma or chrominance errors compared to luma/lightness errors.

## 12.4. GEOMETRICAL IMAGE MODIFICATION EXERCISES

E12.1 Develop a program that minifies an unsigned integer, 8-bit, monochrome image by a factor of two and rotates the minified image by 45 degrees clockwise about its center using bilinear interpolation. Steps:

- (a) Display the source monochrome image
- (b) Minify the source image into the center of a zero valued work image of the same size as the source image using bilinear interpolation.
- (c) Rotate the work image clockwise about its center into a destination image using bilinear interpolation.
- (d) Display the destination image.

The PIKS API executable `example_minify_rotate` performs this exercise.

E12.2 Develop a program that performs shearing of the rows of an unsigned integer, 8-bit, monochrome image using bilinear interpolation such that the last image row is shifted 10% of the row width and all other rows are shifted proportionally. Steps:

- (a) Display the source monochrome image.
- (b) Shear the source image into a destination image using bilinear interpolation.
- (c) Display the destination image.

The PIKS API executable `example_shear` performs this exercise.

E12.3 Develop a program that performs clockwise rotation of an unsigned integer, 8-bit, monochrome image by 45 degrees using the Catmull and Smith two-pass algorithm. Steps:

- (a) Display the source monochrome image.
- (b) Perform shearing of each row of the source image into a work image using bilinear interpolation.

- (c) Perform shearing of each column of the work image into a destination image using bilinear interpolation.
- (d) Display the destination image.

The PIKS API executable `example_rotate_two-pass` performs this exercise.

E12.4 Develop a program that magnifies an unsigned integer, 8-bit, monochrome image source image by a factor of 2:1 using both nearest neighbor and bilinear interpolation. Compare the results. Steps:

- (a) Display the source monochrome image.
- (b) Magnify the source image by 2:1 into a work image using nearest neighbor interpolation.
- (c) Magnify the source image by 2:1 into a work image using bilinear interpolation.
- (d) Subtract the two magnified images and display the absolute value of the difference.

The PIKS API executable `example_magnify_interpolate` performs this exercise.

## REFERENCES

1. G. Wolberg, *Digital Image Warping*, IEEE Computer Society Press, Washington DC, 1990.
2. L. G. Roberts, "Machine Perception of Three-Dimensional Solids," in *Optical and Electro-Optical Information Processing*, J. T. Tippett et al., Eds., MIT Press, Cambridge, MA, 1965.
3. D. F. Rogers, *Mathematical Elements for Computer Graphics, Second Edition*, McGraw-Hill, New York, 1989.
4. J. D. Foley et al., *Computer Graphics: Principles and Practice in C, Second Edition*, Addison-Wesley, Reading, MA, 1996.
5. E. Catmull and A. R. Smith, "3-D Transformation of Images in Scanline Order," *Computer Graphics, SIGGRAPH '80 Proc.*, **14**, 3, July 1980, 279–285.
6. M. Unser, P. Thevenaz and L. Yaroslavsky, "Convolution-Based Interpolation for Fast, High-Quality Rotation of Images," *IEEE Trans. Image Processing*, **IP-4**, 10, October 1995, 1371–1381.
7. D. Fraser and R. A. Schowengerdt, "Avoidance of Additional Aliasing in Multipass Image Rotations," *IEEE Trans. Image Processing*, **IP-3**, 6, November 1994, 721–735.
8. A. W. Paeth, "A Fast Algorithm for General Raster Rotation," in *Proc. Graphics Interface '86-Vision Interface*, 1986, 77–81.
9. P. E. Danielson and M. Hammerin, "High Accuracy Rotation of Images," in *CVGIP: Graphical Models and Image Processing*, **54**, 4, July 1992, 340–344.

10. M. R. Spillage and J. Liu, *Schaum's Mathematical Handbook of Formulas and Tables, Second Edition*, McGraw-Hill 1998.
11. D. L. Milgram, "Computer Methods for Creating Photomosaics," *IEEE Trans. Computers*, **24**, 1975, 1113–1119.
12. D. L. Milgram, "Adaptive Techniques for Photomosaicking," *IEEE Trans. Computers*, **26**, 1977, 1175–1180.
13. S. Peleg, A. Rav-Acha and A. Zomet, "Mosaicing on Adaptive Manifolds," *IEEE Trans. Pattern Analysis and Machine Intelligence*, **22**, 10, October 2000, 1144–1154.
14. H. Nicolas, "New Methods for Dynamic Mosaicking," *IEEE Trans. Image Processing*, **10**, 8, August 2001, 1239–1251.
15. R. T. Whitaker, "A Level-Set Approach to Image Blending," *IEEE Trans. Image Processing*, **9**, 11, November 2000, 1849–1861.
16. R. Bernstein, "Digital Image Processing of Earth Observation Sensor Data," *IBM J. Research and Development*, **20**, 1, 1976, 40–56.
17. D. A. O'Handley and W. B. Green, "Recent Developments in Digital Image Processing at the Image Processing Laboratory of the Jet Propulsion Laboratory," *Proc. IEEE*, **60**, 7, July 1972, 821–828.
18. W. K. Pratt, "Image Processing and Analysis Using Primitive Computational Elements," in *Selected Topics in Signal Processing*, S. Haykin, Ed., Prentice Hall, Englewood Cliffs, NJ, 1989.
19. M. Vrhel, "Color Image Resolution Conversion," *IEEE Trans. Image Processing*, **14**, 3, March 2005, 328–333.



## **PART 5**

---

### **IMAGE ANALYSIS**

Image analysis is concerned with the extraction of measurements, data or information from an image by automatic or semiautomatic methods. In the literature, this field has been called image data extraction, scene analysis, image description, automatic photo interpretation, image understanding and a variety of other names.

Image analysis is distinguished from other types of image processing, such as coding, restoration and enhancement, in that the ultimate product of an image analysis system is usually numerical output rather than a picture. Image analysis also diverges from classical pattern recognition in that analysis systems, by definition, are not limited to the classification of scene regions to a fixed number of categories, but rather are designed to provide a description of complex scenes whose variety may be enormously large and ill-defined in terms of a priori expectation.



---

# 13

---

## MORPHOLOGICAL IMAGE PROCESSING

Morphological image processing is a type of processing in which the spatial form or structure of objects within an image are modified. Dilation, erosion and skeletonization are three fundamental morphological operations. With dilation, an object grows uniformly in spatial extent, whereas with erosion an object shrinks uniformly. Skeletonization results in a stick figure representation of an object.

The basic concepts of morphological image processing trace back to the research on spatial set algebra by Minkowski (1) and the studies of Matheron (2) on topology. Serra (3–5) developed much of the early foundation of the subject. Steinberg (6,7) was a pioneer in applying morphological methods to medical and industrial vision applications. This research work led to the development of the cytocomputer for high-speed morphological image processing (8,9).

In the following sections, morphological techniques are first described for binary images. Then these morphological concepts are extended to gray scale images.

### 13.1. BINARY IMAGE CONNECTIVITY

Binary image morphological operations are based on the geometrical relationship or *connectivity* of pixels that are deemed to be of the same class (10,11). In the binary image of Figure 13.1-1a, the ring of black pixels, by all reasonable definitions of connectivity, divides the image into three segments: the white pixels exterior to the ring, the white pixels interior to the ring and the black pixels of the ring itself. The pixels within each segment are said to be connected to one another. This concept of



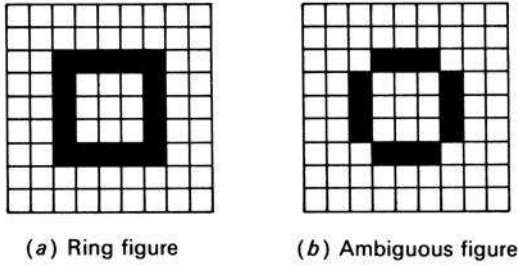


FIGURE 13.1-1. Connectivity.

connectivity is easily understood for Figure 13.1-1a, but ambiguity arises when considering Figure 13.1-1b. Do the black pixels still define a ring, or do they instead form four disconnected lines? The answers to these questions depend on the definition of connectivity.

Consider the following neighborhood pixel pattern:

$$\begin{array}{ccc}
 X_3 & X_2 & X_1 \\
 X_4 & X & X_0 \\
 X_5 & X_6 & X_7
 \end{array}$$

in which a binary-valued pixel  $F(j, k) = X$ , where  $X = 0$  (white) or  $X = 1$  (black) is surrounded by its eight nearest neighbors  $X_0, X_1, \dots, X_7$ . An alternative nomenclature is to label the neighbors by compass directions: north, northeast and so on:

$$\begin{array}{ccc}
 \text{NW} & \text{N} & \text{NE} \\
 \text{W} & \text{X} & \text{E} \\
 \text{SW} & \text{S} & \text{SE}
 \end{array}$$

Pixel  $X$  is said to be *four-connected* to a neighbor if it is a logical 1 and if its east, north, west or south ( $X_0, X_2, X_4, X_6$ ) neighbor is a logical 1. Pixel  $X$  is said to be *eight-connected* if it is a logical 1 and if its north, northeast, etc. ( $X_0, X_1, \dots, X_7$ ) neighbor is a logical 1.

The connectivity relationship between a center pixel and its eight neighbors can be quantified by the concept of a *pixel bond*, the sum of the bond weights between the center pixel and each of its neighbors. Each four-connected neighbor has a bond of two, and each eight-connected neighbor has a bond of one. In the following example, the pixel bond is seven.

$$\begin{array}{ccc}
 1 & 1 & 1 \\
 0 & X & 0 \\
 1 & 1 & 0
 \end{array}$$

0 0 0	0 0 0	0 0 0
0 1 1	0 1 1	0 1 0
0 1 0	0 0 1	0 0 0
<b>Four-connected</b>	<b>Eight-connected</b>	<b>Isolated</b>
<b>B = 4</b>	<b>B = 3</b>	<b>B = 0</b>
0 0 0	1 0 0	1 1 1
0 1 0	1 1 1	0 1 0
0 0 1	1 0 1	1 1 1
<b>Spur</b>	<b>Bridge</b>	<b>H-connected</b>
<b>B = 1</b>	<b>B = 7</b>	<b>B = 8</b>
0 0 0	0 1 1	0 1 1
0 1 1	1 1 1	0 1 1
0 1 1	1 1 1	0 1 1
<b>Corner</b>	<b>Interior</b>	<b>Exterior</b>
<b>B = 5</b>	<b>B = 1</b>	<b>B = 8</b>

**FIGURE 13.1-2.** Pixel neighborhood connectivity definitions.

Under the definition of four-connectivity, Figure 13.1-1b has four disconnected black line segments, but with the eight-connectivity definition, Figure 13.1-1b has a ring of connected black pixels. Note, however, that under eight-connectivity, all white pixels are connected together. Thus, a paradox exists. If the black pixels are to be eight-connected together in a ring, one would expect a division of the white pixels into pixels that are interior and exterior to the ring. To eliminate this dilemma, eight-connectivity can be defined for the black pixels of the object, and four-connectivity can be established for the white pixels of the background. Under this definition, a string of black pixels is said to be *minimally connected* if elimination of any black pixel results in a loss of connectivity of the remaining black pixels. Figure 13.1-2 provides definitions of several other neighborhood connectivity relationships between a center black pixel and its neighboring black and white pixels.

The preceding definitions concerning connectivity have been based on a discrete image model in which a continuous image field is sampled over a rectangular array of points. Golay (12) has utilized a hexagonal grid structure. With such a structure, many of the connectivity problems associated with a rectangular grid are eliminated. In a hexagonal grid, neighboring pixels are said to be *six-connected* if they are in the same set and share a common edge boundary. Algorithms have been developed for the linking of boundary points for many feature extraction tasks (13). However, two major drawbacks have hindered wide acceptance of the hexagonal grid. First, most image scanners are inherently limited to rectangular scanning. The second problem is that the hexagonal grid is not well suited to many spatial processing operations, such as convolution and Fourier transformation.

### 13.2. BINARY IMAGE HIT OR MISS TRANSFORMATIONS

The two basic morphological operations, dilation and erosion, plus many variants can be defined and implemented by a *hit-or-miss transformation* (3). The concept is quite simple. Conceptually, a small odd-sized mask, typically  $3 \times 3$ , is scanned over a binary image. If the binary-valued pattern of the mask matches the state of the pixels under the mask (hit), an output pixel in spatial correspondence to the center pixel of the mask is set to some desired binary state. For a pattern mismatch (miss), the output pixel is set to the opposite binary state. For example, to perform simple binary noise cleaning, if the isolated  $3 \times 3$  pixel pattern

$$\begin{matrix} 0 & 0 & 0 \\ 0 & 1 & 0 \\ 0 & 0 & 0 \end{matrix}$$

is encountered, the output pixel is set to zero; otherwise, the output pixel is set to the state of the input center pixel. In more complicated morphological algorithms, a large number of the  $2^9 = 512$  possible mask patterns may cause hits.

It is often possible to establish simple neighborhood logical relationships that define the conditions for a hit. In the isolated pixel removal example, the defining equation for the output pixel  $G(j, k)$  becomes

$$G(j, k) = X \cap (X_0 \cup X_1 \cup \dots \cup X_7) \tag{13.2-1}$$

where  $\cap$  denotes the *intersection* operation (logical AND) and  $\cup$  denotes the *union* operation (logical OR). For complicated algorithms, the logical equation method of definition can be cumbersome. It is often simpler to regard the hit masks as a collection of binary patterns.

Hit-or-miss morphological algorithms are often implemented in digital image processing hardware by a pixel stacker followed by a look-up table (LUT), as shown in Figure 13.2-1 (14). Each pixel of the input image is a positive integer, represented by a conventional binary code, whose most significant bit is a 1 (black) or a 0 (white). The pixel stacker extracts the bits of the center pixel  $X$  and its eight neighbors and puts them in a neighborhood pixel stack. Pixel stacking can be performed by convolution with the  $3 \times 3$  pixel kernel

$$\begin{bmatrix} 2^{-8} & 2^{-7} & 2^{-6} \\ 2^{-1} & 2^0 & 2^{-5} \\ 2^{-2} & 2^{-3} & 2^{-4} \end{bmatrix}.$$

The binary number state of the neighborhood pixel stack becomes the numeric input address of the LUT whose entry is  $Y$ . For isolated pixel removal, integer entry 256, corresponding to the neighborhood pixel stack state 100000000, contains  $Y = 0$ ; all other entries contain  $Y = X$ .

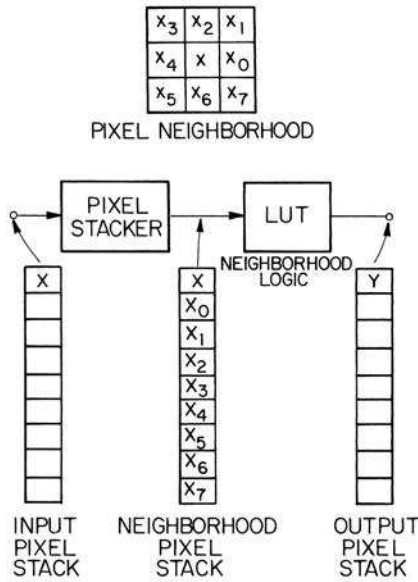


FIGURE 13.2-1. Look-up table flowchart for binary unconditional operations.

Several other 3x3 hit-or-miss operators are described in the following subsections.

### 13.2.1. Additive Operators

Additive hit-or-miss morphological operators cause the center pixel of a 3x3 pixel window to be converted from a logical 0 state to a logical 1 state if the neighboring pixels meet certain predetermined conditions. The basic operators are now defined.

**Interior Fill.** Create a black pixel if all four-connected neighbor pixels are black.

$$G(j, k) = X \cup [X_0 \cap X_2 \cap X_4 \cap X_6] \tag{13.2-2}$$

**Diagonal Fill.** Create a black pixel if creation eliminates the eight-connectivity of the background.

$$G(j, k) = X \cup [P_1 \cup P_2 \cup P_3 \cup P_4] \tag{13.2-3a}$$

where

$$P_1 = \bar{X} \cap X_0 \cap \bar{X}_1 \cap X_2 \tag{13.2-3b}$$

$$P_2 = \bar{X} \cap X_2 \cap \bar{X}_3 \cap X_4 \tag{13.2-3c}$$

$$P_3 = \bar{X} \cap X_4 \cap \bar{X}_5 \cap X_6 \tag{13.2-3d}$$

$$P_4 = \bar{X} \cap X_6 \cap \bar{X}_7 \cap X_0 \tag{13.2-3e}$$

In Eq. 13.2-3, the overbar denotes the logical *complement* of a variable.

**Bridge.** Create a black pixel if creation results in connectivity of previously unconnected neighboring black pixels.

$$G(j, k) = X \cup [P_1 \cup P_2 \cup \dots \cup P_6] \tag{13.2-4a}$$

where

$$P_1 = \bar{X}_2 \cap \bar{X}_6 \cap [X_3 \cup X_4 \cup X_5] \cap [X_0 \cup X_1 \cup X_7] \cap \bar{P}_Q \tag{13.2-4b}$$

$$P_2 = \bar{X}_0 \cap \bar{X}_4 \cap [X_1 \cup X_2 \cup X_3] \cap [X_5 \cup X_6 \cup X_7] \cap \bar{P}_Q \tag{13.2-4c}$$

$$P_3 = \bar{X}_0 \cap \bar{X}_6 \cap X_7 \cap [X_2 \cup X_3 \cup X_4] \tag{13.2-4d}$$

$$P_4 = \bar{X}_0 \cap \bar{X}_2 \cap X_1 \cap [X_4 \cup X_5 \cup X_6] \tag{13.2-4e}$$

$$P_5 = \bar{X}_2 \cap \bar{X}_4 \cap X_3 \cap [X_0 \cup X_6 \cup X_7] \tag{13.2-4f}$$

$$P_6 = \bar{X}_4 \cap \bar{X}_6 \cap X_5 \cap [X_0 \cup X_1 \cup X_2] \tag{13.2-4g}$$

and

$$P_Q = L_1 \cup L_2 \cup L_3 \cup L_4 \tag{13.2-4h}$$

$$L_1 = \bar{X} \cap \bar{X}_0 \cap X_1 \cap \bar{X}_2 \cap X_3 \cap \bar{X}_4 \cap \bar{X}_5 \cap \bar{X}_6 \cap \bar{X}_7 \tag{13.2-4i}$$

$$L_2 = \bar{X} \cap \bar{X}_0 \cap \bar{X}_1 \cap \bar{X}_2 \cap X_3 \cap \bar{X}_4 \cap X_5 \cap \bar{X}_6 \cap \bar{X}_7 \tag{13.2-4j}$$

$$L_3 = \bar{X} \cap \bar{X}_0 \cap \bar{X}_1 \cap \bar{X}_2 \cap \bar{X}_3 \cap \bar{X}_4 \cap X_5 \cap \bar{X}_6 \cap X_7 \tag{13.2-4k}$$

$$L_4 = \bar{X} \cap \bar{X}_0 \cap X_1 \cap \bar{X}_2 \cap \bar{X}_3 \cap \bar{X}_4 \cap \bar{X}_5 \cap \bar{X}_6 \cap X_7 \tag{13.2-4l}$$

The following is one of 119 qualifying patterns

```

1  0  0
1  0  1
0  0  1
    
```

A pattern such as

```

0  0  0
0  0  0
1  0  1
    
```

does not qualify because the two black pixels will be connected when they are on the middle row of a subsequent observation window if they are indeed unconnected.

**Eight-Neighbor Dilate.** Create a black pixel if at least one eight-connected neighbor pixel is black.

$$G(j, k) = X \cup X_0 \cup \dots \cup X_7 \tag{13.2-5}$$

This hit-or-miss definition of dilation is a special case of a generalized dilation operator that is introduced in Section 13.4. The dilate operator can be applied recursively. With each iteration, objects will grow by a single pixel width ring of exterior pixels. Figure 13.2-2 shows dilation for one and for three iterations for a binary image. In the example, the original pixels are recorded as black, the background pixels are white and the added pixels are mid gray.

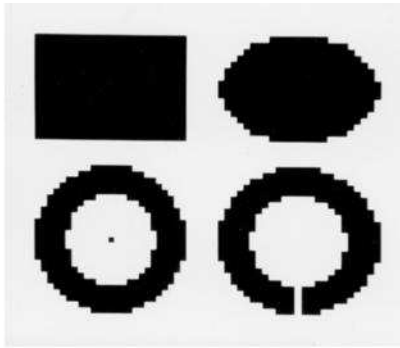
**Fatten.** Create a black pixel if at least one eight-connected neighbor pixel is black, provided that creation does not result in a bridge between previously unconnected black pixels in a  $3 \times 3$  neighborhood.

The following is an example of an input pattern in which the center pixel would be set black for the basic dilation operator, but not for the fatten operator.

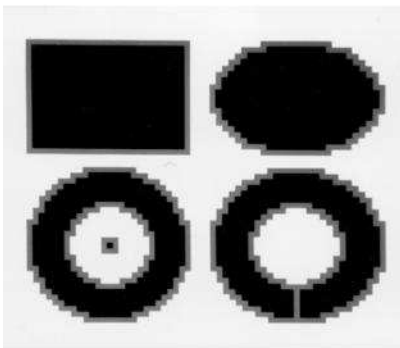
```

0  0  1
1  0  0
1  1  0
    
```

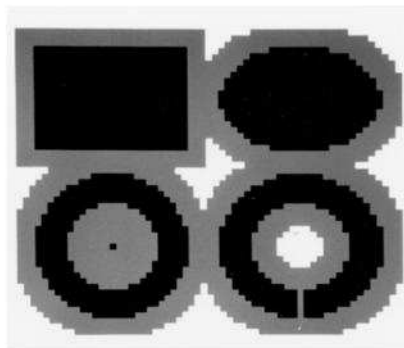
There are 132 such qualifying patterns. This stratagem will not prevent connection of two objects separated by two rows or columns of white pixels. A solution to this problem is considered in Section 13.3. Figure 13.2-3 provides an example of fattening.



(a) Original



(b) One iteration



(c) Three iterations

FIGURE 13.2-2. Dilation of a binary image.

### 13.2.2. Subtractive Operators

Subtractive hit-or-miss morphological operators cause the center pixel of a  $3 \times 3$  window to be converted from black to white if its neighboring pixels meet predetermined conditions. The basic subtractive operators are defined below.

**Isolated Pixel Remove.** Erase a black pixel with eight white neighbors.

$$G(j, k) = X \cap [X_0 \cup X_1 \cup \dots \cup X_7] \tag{13.2-6}$$

**Spur Remove.** Erase a black pixel with a single eight-connected neighbor.

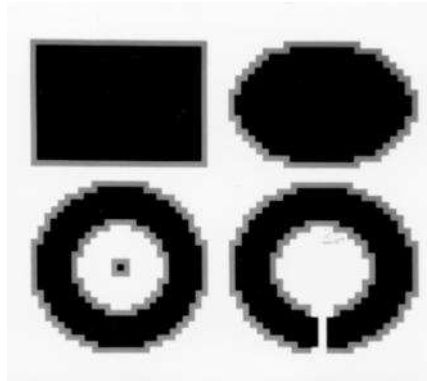


FIGURE 13.2-3. Fattening of a binary image.

The following is one of four qualifying patterns:

```

0  0  0
0  1  0
1  0  0
    
```

**Interior Pixel Remove.** Erase a black pixel if all four-connected neighbors are black.

$$G(j, k) = X \cap [\bar{X}_0 \cup \bar{X}_2 \cup \bar{X}_4 \cup \bar{X}_6] \tag{13.2-7}$$

There are 16 qualifying patterns.

**H-Break.** Erase a black pixel that is H-connected.

There are two qualifying patterns.

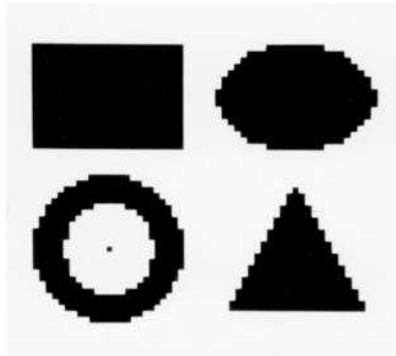
```

1  1  1      1  0  1
0  1  0      1  1  1
1  1  1      1  0  1
    
```

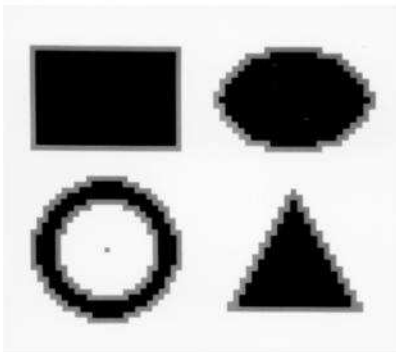
**Eight-Neighbor Erode.** Erase a black pixel if at least one eight-connected neighbor pixel is white.

$$G(j, k) = X \cap X_0 \cap \dots \cap X_7 \tag{13.2-8}$$

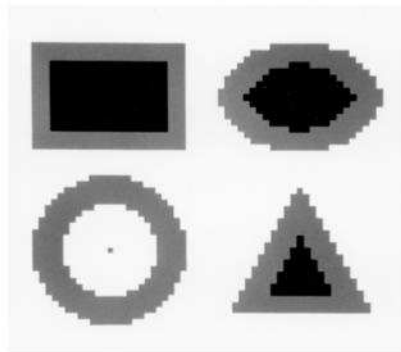




(a) Original



(b) One iteration



(c) Three iterations

**FIGURE 13.2-4.** Erosion of a binary image.

A generalized erosion operator is defined in Section 13.4. Recursive application of the erosion operator will eventually erase all black pixels. Figure 13.2-4 shows results for one and three iterations of the erode operator. The eroded pixels are mid gray. It should be noted that after three iterations, the ring is totally eroded.

### 13.2.3. Majority Black Operator

The following is the definition of the *majority black operator*:

**Majority Black.** Create a black pixel if five or more pixels in a  $3 \times 3$  window are black; otherwise, set the output pixel to white.

The majority black operator is useful for filling small holes in objects and closing short gaps in strokes. An example of its application to edge detection is given in Chapter 14.

### 13.3. BINARY IMAGE SHRINKING, THINNING, SKELETONIZING AND THICKENING

Shrinking, thinning, skeletonizing and thickening are forms of conditional erosion in which the erosion process is controlled to prevent total erasure and to ensure connectivity.

#### 13.3.1. Binary Image Shrinking

The following is a definition of *shrinking*:

**Shrink.** Erase black pixels such that an object without holes erodes to a single pixel at or near its center of mass, and an object with holes erodes to a connected ring lying midway between each hole and its nearest outer boundary.

A  $3 \times 3$  pixel object will be shrunk to a single pixel at its center. A  $2 \times 2$  pixel object will be arbitrarily shrunk, by definition, to a single pixel at its lower right corner.

It is not possible to perform shrinking using a single-stage  $3 \times 3$  pixel hit-or-miss transform of the type described in the previous section. The  $3 \times 3$  window does not provide enough information to prevent total erasure and to ensure connectivity. A  $5 \times 5$  hit-or-miss transform could provide sufficient information to perform proper shrinking. But such an approach would result in excessive computational complexity (i.e.,  $2^{25}$  possible patterns to be examined!). References 15 and 16 describe two-stage shrinking and thinning algorithms that perform a conditional marking of pixels for erasure in a first stage, and then examine neighboring marked pixels in a second stage to determine which ones can be unconditionally erased without total erasure or loss of connectivity. The following algorithm developed by Pratt and Kabir (17) is a pipeline processor version of the conditional marking scheme.

In the algorithm, two concatenated  $3 \times 3$  hit-or-miss transformations are performed to obtain indirect information about pixel patterns within a  $5 \times 5$  window. Figure 13.3-1 is a flowchart for the look-up table implementation of this algorithm. In the first stage, the states of nine neighboring pixels are gathered together by a pixel stacker, and a following look-up table generates a conditional mark  $M$  for possible erasures. Table 13.3-1 lists all patterns, as indicated by the letter  $S$  in the table column, which will be conditionally marked for erasure. In the second stage of the algorithm, the center pixel  $X$  and the conditional marks in a  $3 \times 3$  neighborhood centered about  $X$  are examined to create an output pixel. The shrinking operation can be expressed logically as

$$G(j, k) = X \cap [\bar{M} \cup P(M, M_0, \dots, M_7)] \tag{13.3-1}$$

where  $P(M, M_0, \dots, M_7)$  is an erasure inhibiting logical variable, as defined in Table 13.3-2. The first four patterns of the table prevent strokes of single pixel width from

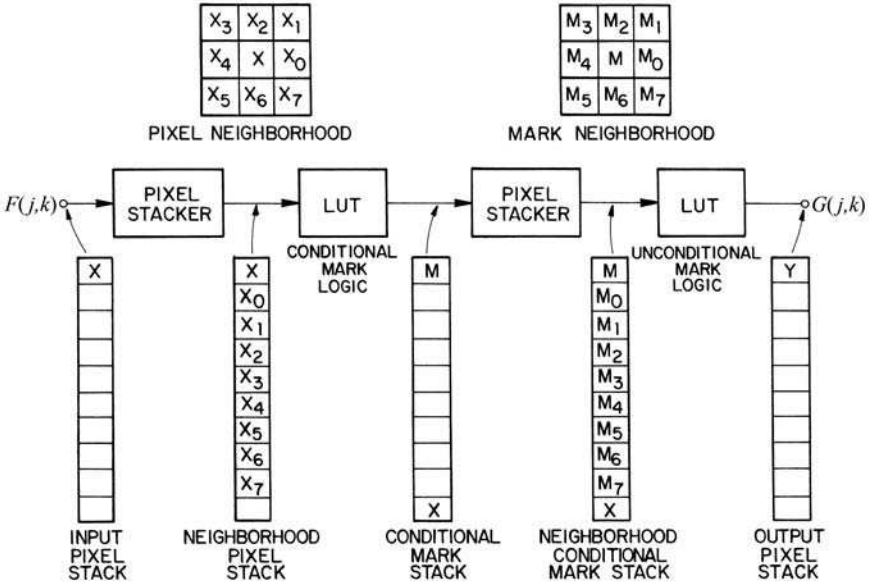


FIGURE 13.3-1. Look-up table flowchart for binary conditional mark operations.

being totally erased. The remaining patterns inhibit erasure that would break object connectivity. There are a total of 157 inhibiting patterns. This two-stage process must be performed iteratively until there are no further erasures. As an example, the  $2 \times 2$  square pixel object

$$\begin{matrix} 1 & 1 \\ 1 & 1 \end{matrix}$$

results in the following intermediate array of conditional marks

$$\begin{matrix} M & M \\ M & M \end{matrix}$$

The corner cluster pattern of Table 13.3-2 gives a hit only for the lower right corner mark. The resulting output is

$$\begin{matrix} 0 & 0 \\ 0 & 1 \end{matrix}$$

**TABLE 13.3-1. Shrink, Thin and Skeletonize Conditional Mark Patterns [ $M = 1$  if hit]**

Table	Bond	Pattern							
<i>S</i>	1	0 0 1	1 0 0	0 0 0	0 0 0				
		0 1 0	0 1 0	0 1 0	0 1 0				
		0 0 0	0 0 0	1 0 0	0 0 1				
<i>S</i>	2	0 0 0	0 1 0	0 0 0	0 0 0				
		0 1 1	0 1 0	1 1 0	0 1 0				
		0 0 0	0 0 0	0 0 0	0 1 0				
<i>S</i>	3	0 0 1	0 1 1	1 1 0	1 0 0	0 0 0	0 0 0	0 0 0	0 0 0
		0 1 1	0 1 0	0 1 0	1 1 0	1 1 0	0 1 0	0 1 0	0 1 1
		0 0 0	0 0 0	0 0 0	0 0 0	1 0 0	1 1 0	0 1 1	0 0 1
<i>TK</i>	4	0 1 0	0 1 0	0 0 0	0 0 0				
		0 1 1	1 1 0	1 1 0	0 1 1				
		0 0 0	0 0 0	0 1 0	0 1 0				
<i>STK</i>	4	0 0 1	1 1 1	1 0 0	0 0 0				
		0 1 1	0 1 0	1 1 0	0 1 0				
		0 0 1	0 0 0	1 0 0	1 1 1				
<i>ST</i>	5	1 1 0	0 1 0	0 1 1	0 0 1				
		0 1 1	0 1 1	1 1 0	0 1 1				
		0 0 0	0 0 1	0 0 0	0 1 0				
<i>ST</i>	5	0 1 1	1 1 0	0 0 0	0 0 0				
		0 1 1	1 1 0	1 1 0	0 1 1				
		0 0 0	0 0 0	1 1 0	0 1 1				
<i>ST</i>	6	1 1 0	0 1 1						
		0 1 1	1 1 0						
		0 0 1	1 0 0						
<i>STK</i>	6	1 1 1	0 1 1	1 1 1	1 1 0	1 0 0	0 0 0	0 0 0	0 0 1
		0 1 1	0 1 1	1 1 0	1 1 0	1 1 0	1 1 0	0 1 1	0 1 1
		0 0 0	0 0 1	0 0 0	1 0 0	1 1 0	1 1 1	1 1 1	0 1 1

(Continued)

TABLE 13.3-1. (Continued)

Table	Bond	Pattern							
STK	7	1 1 1	1 1 1	1 0 0	0 0 1				
		0 1 1	1 1 0	1 1 0	0 1 1				
		0 0 1	1 0 0	1 1 1	1 1 1				
STK	8	0 1 1	1 1 1	1 1 0	0 0 0				
		0 1 1	1 1 1	1 1 0	1 1 1				
		0 1 1	0 0 0	1 1 0	1 1 1				
STK	9	1 1 1	0 1 1	1 1 1	1 1 1	1 1 1	1 1 0	1 0 0	0 0 1
		0 1 1	0 1 1	1 1 1	1 1 1	1 1 0	1 1 0	1 1 1	1 1 1
		0 1 1	1 1 1	1 0 0	0 0 1	1 1 0	1 1 1	1 1 1	1 1 1
STK	10	1 1 1	1 1 1	1 1 1	1 0 1				
		0 1 1	1 1 1	1 1 0	1 1 1				
		1 1 1	1 0 1	1 1 1	1 1 1				
K	11	1 1 1	1 1 1	1 1 0	0 1 1				
		1 1 1	1 1 1	1 1 1	1 1 1				
		0 1 1	1 1 0	1 1 1	1 1 1				

Figure 13.3-2 shows an example of the shrinking of a binary image for four and 13 iterations of the algorithm. No further shrinking occurs for more than 13 iterations. At this point, the shrinking operation has become *idempotent* (i.e., reapplication evokes no further change). This shrinking algorithm does not shrink the symmetric original ring object to a ring that is also symmetric because of some of the conditional mark patterns of Table 13.3-2, which are necessary to ensure that objects of even dimension shrink to a single pixel. For the same reason, the shrunk ring is not minimally connected.

**13.3.2. Binary Image Thinning**

The following is a definition of *thinning*:

**Thin.** Erase black pixels such that an object without holes erodes to a minimally connected stroke located equidistant from its nearest outer boundaries, and an object with holes erodes to a minimally connected ring midway between each hole and its nearest outer boundary.

**TABLE 13.3-2. Shrink and Thin Unconditional Mark Patterns**

$[P(M, M_0, M_1, M_2, M_3, M_4, M_5, M_6, M_7) = 1 \text{ if hit}]^a$

Pattern							
Spur				Single 4-connection			
0 0 M	M 0 0	0 0 0	0 0 0	0 0 0	0 0 0	0 0 0	0 0 0
0 M 0	0 M 0	0 M 0	0 M 0	0 M M			
0 0 0	0 0 0	0 M 0	0 0 0				
L Cluster							
0 0 M	0 M M	M M 0	M 0 0	0 0 0	0 0 0	0 0 0	0 0 0
0 M M	0 M 0	0 M 0	M M 0	M M 0	0 M 0	0 M 0	0 M M
0 0 0	0 0 0	0 0 0	0 0 0	M 0 0	M M 0	0 M M	0 0 M
4-Connected offset							
0 M M	M M 0	0 M 0	0 0 M				
M M 0	0 M M	0 M M	0 M M				
0 0 0	0 0 0	0 0 M	0 M 0				
Spur corner cluster							
0 A M	M B 0	0 0 M	M 0 0				
0 M B	A M 0	A M 0	0 M B				
M 0 0	0 0 M	M B 0	0 A M				
Corner cluster							
M M D							
M M D							
D D D							
Tee branch							
D M 0	0 M D	0 0 D	D 0 0	D M D	0 M 0	0 M 0	D M D
M M M	M M M	M M M	M M M	M M 0	M M 0	0 M M	0 M M
D 0 0	0 0 D	0 M D	D M 0	0 M 0	D M D	D M D	0 M 0
Vee branch							
M D M	M D C	C B A	A D M				
D M D	D M B	D M D	B M D				
A B C	M D A	M D M	C D M				
Diagonal branch							
D M 0	0 M D	D 0 M	M 0 D				
0 M M	M M 0	M M 0	0 M M				
M 0 D	D 0 M	0 M D	D M 0				

<sup>a</sup> $A \cup B \cup C = 1 \quad D = 0 \cup 1 \quad A \cup B = 1.$

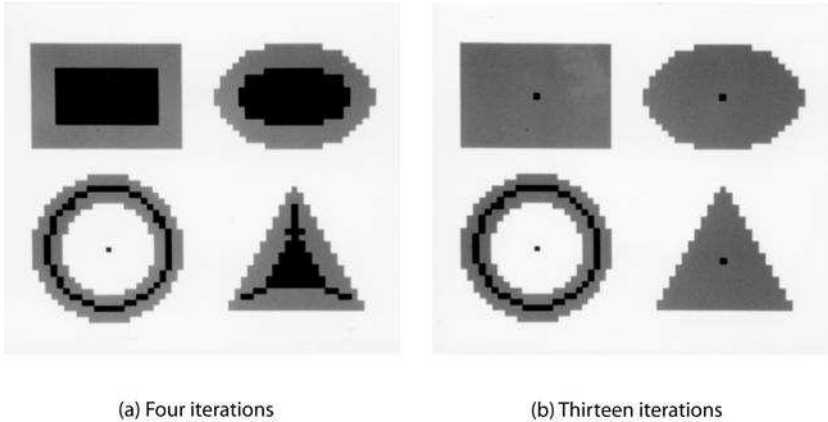


**FIGURE 13.3-2.** Shrinking of a binary image.

The following is an example of the thinning of a  $3 \times 5$  pixel object without holes

1	1	1	1	1	0	0	0	0	0
1	1	1	1	1	0	1	1	1	0
1	1	1	1	1	0	0	0	0	0
before					after				

A  $2 \times 5$  object is thinned as follows:

1	1	1	1	1	0	0	0	0	0
1	1	1	1	1	0	1	1	1	1
before					after				

Table 13.3-1 lists the conditional mark patterns, as indicated by the letter *T* in the table column, for thinning by the conditional mark algorithm of Figure 13.3-1. The shrink and thin unconditional patterns are identical, as shown in Table 13.3-2.

Figure 13.3-3 contains an example of the thinning of a binary image for four and eight iterations. Figure 13.3-4 provides an example of the thinning of an image of a printed circuit board in order to locate solder pads that have been deposited improperly and that do not have holes for component leads. The pads with holes erode to a minimally connected ring, while the pads without holes erode to a point.

Thinning can be applied to the background of an image containing several objects as a means of separating the objects. Figure 13.3-5 provides an example of the process. The original image appears in Figure 13.3-5a, and the background-reversed image is Figure 13.3-5b. Figure 13.3-5c shows the effect of thinning the background. The thinned strokes that separate the original objects are minimally

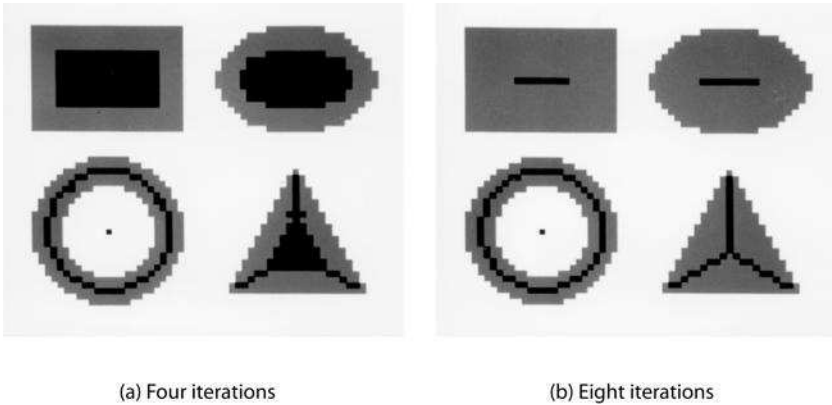


**FIGURE 13.3-3.** Thinning of a binary image.

connected, and, therefore, the background of the separating strokes is eight-connected throughout the image. This is an example of the connectivity ambiguity discussed in Section 13.1. To resolve this ambiguity, a diagonal fill operation can be applied to the thinned strokes. The result, shown in Figure 13.3-5d, is called the *exothin* of the original image. The name derives from the exoskeleton, discussed in the following section.

**13.3.3. Binary Image Skeletonizing**

A skeleton or stick figure representation of an object can be used to describe its structure. Thinned objects sometimes have the appearance of a skeleton, but they are not always uniquely defined. For example, in Figure 13.3-3, both the rectangle and ellipse thin to a horizontal line.

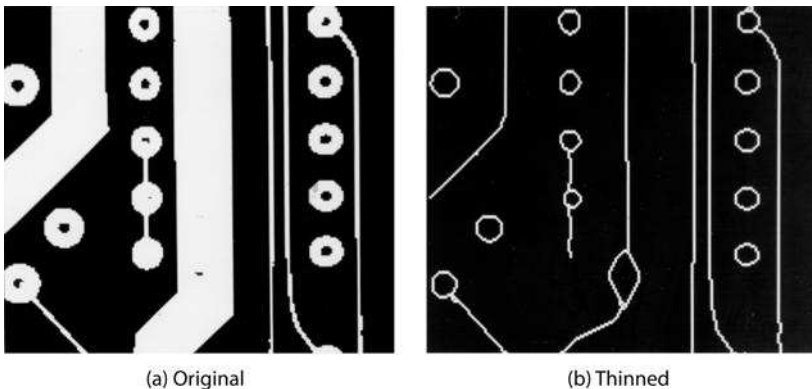


**FIGURE 13.3-4.** Thinning of a printed circuit board image.



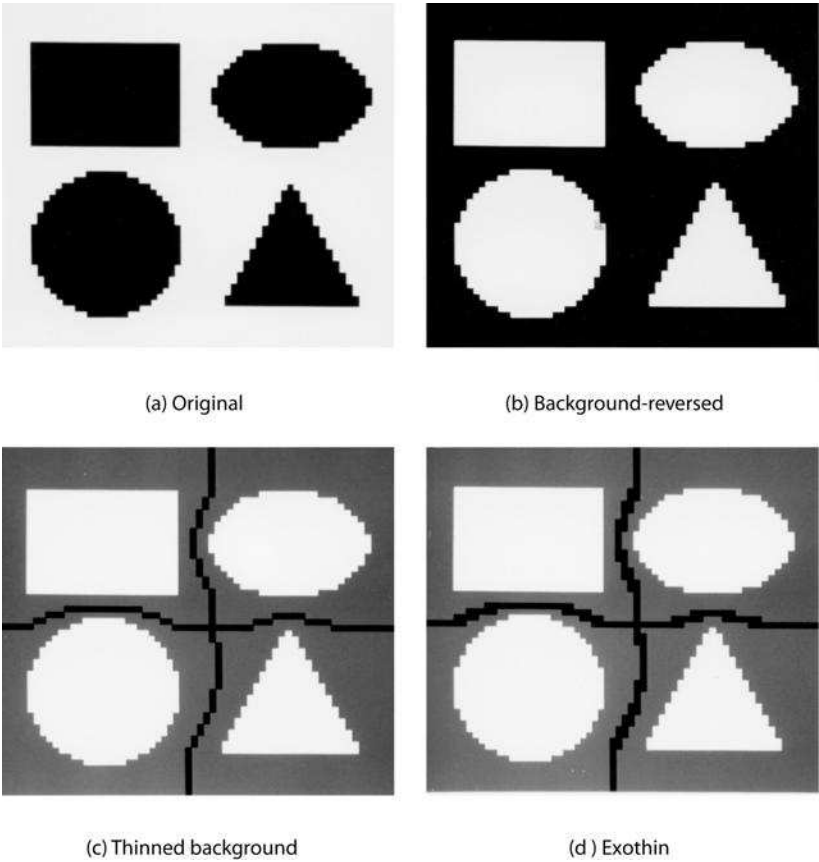
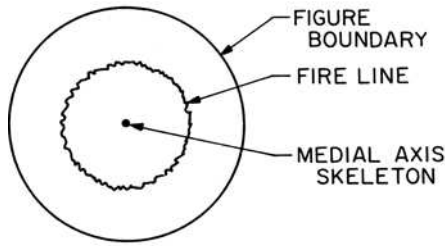
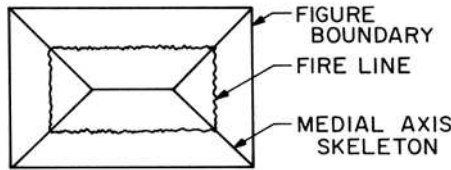


**FIGURE 13.3-5.** Exothinning of a binary image.

Blum (18) has introduced a skeletonizing technique called *medial axis transformation* that produces a unique skeleton for a given object. An intuitive explanation of the medial axis transformation is based on the *prairie fire* analogy (19–22). Consider the circle and rectangle regions of Figure 13.3-6 to be composed of dry grass on a bare dirt background. If a fire were to be started simultaneously on the perimeter of the grass, the fire would proceed to burn toward the center of the regions until all the grass was consumed. In the case of the circle, the fire would burn to the center point of the circle, which is the *quench point* of the circle. For the rectangle, the fire would proceed from each side. As the fire moved simultaneously from left and top, the fire lines would meet and quench the fire. The quench points or quench lines of a figure are called its *medial axis skeleton*. More generally, the medial axis skeleton consists of the set of points that are equally distant from two closest points of an object boundary. The minimal distance function is called the *quench distance* of the object. From the medial axis skeleton of an object and its quench distance, it is



(a) Circle



(b) Rectangle

**FIGURE 13.3-6.** Medial axis transforms.

possible to reconstruct the object boundary. The object boundary is determined by the union of a set of circular disks formed by circumscribing a circle whose radius is the quench distance at each point of the medial axis skeleton.

A reasonably close approximation to the medial axis skeleton can be implemented by a slight variation of the conditional marking implementation shown in Figure 13.3-1. In this approach, an image is iteratively eroded using conditional and unconditional mark patterns until no further erosion occurs. The conditional mark patterns for skeletonization are listed in Table 13.3-1 under the table indicator *K*. Table 13.3-3 lists the unconditional mark patterns. At the conclusion of the last iteration, it is necessary to perform a single iteration of bridging as defined by Eq. 13.2-4 to restore connectivity, which will be lost whenever the following pattern is encountered:

```

1 1 1 1 1
  1 1 1 1 1
    
```

Inhibiting the following mark pattern created by the bit pattern above:

```

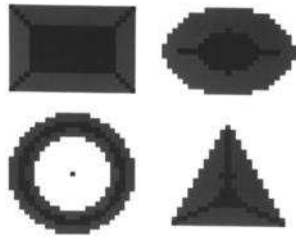
  M M
M M
    
```

will prevent elliptically shaped objects from being improperly skeletonized.

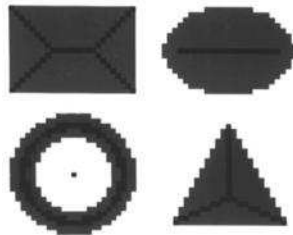
**TABLE 13.3-3. Skeletonize Unconditional Mark Patterns**  
 $[P(M, M_0, M_1, M_2, M_3, M_4, M_5, M_6, M_7) = 1 \text{ if hit}]^a$

Pattern											
Spur											
0	0	0	0	0	0	0	0	<i>M</i>	<i>M</i>	0	0
0	<i>M</i>	0	0	<i>M</i>	0	0	<i>M</i>	0	0	<i>M</i>	0
0	0	<i>M</i>	<i>M</i>	0	0	0	0	0	0	0	0
Single 4-connection											
0	0	0	0	0	0	0	0	0	0	<i>M</i>	0
0	<i>M</i>	0	0	<i>M</i>	<i>M</i>	<i>M</i>	<i>M</i>	0	0	<i>M</i>	0
0	<i>M</i>	0	0	0	0	0	0	0	0	0	0
L corner											
0	<i>M</i>	0	0	<i>M</i>	0	0	0	0	0	0	0
0	<i>M</i>	<i>M</i>	<i>M</i>	<i>M</i>	0	0	<i>M</i>	<i>M</i>	<i>M</i>	<i>M</i>	0
0	0	0	0	0	0	0	0	<i>M</i>	0	0	<i>M</i>
Corner cluster											
<i>M</i>	<i>M</i>	<i>D</i>	<i>D</i>	<i>D</i>	<i>D</i>						
<i>M</i>	<i>M</i>	<i>D</i>	<i>D</i>	<i>M</i>	<i>M</i>						
<i>D</i>	<i>D</i>	<i>D</i>	<i>D</i>	<i>M</i>	<i>M</i>						
Tee branch											
<i>D</i>	<i>M</i>	<i>D</i>	<i>D</i>	<i>M</i>	<i>D</i>	<i>D</i>	<i>D</i>	<i>D</i>	<i>D</i>	<i>M</i>	<i>D</i>
<i>M</i>	<i>M</i>	<i>M</i>	<i>M</i>	<i>M</i>	<i>D</i>	<i>M</i>	<i>M</i>	<i>M</i>	<i>D</i>	<i>M</i>	<i>M</i>
<i>D</i>	<i>D</i>	<i>D</i>	<i>D</i>	<i>M</i>	<i>D</i>	<i>D</i>	<i>M</i>	<i>D</i>	<i>D</i>	<i>M</i>	<i>D</i>
Vee branch											
<i>M</i>	<i>D</i>	<i>M</i>	<i>M</i>	<i>D</i>	<i>C</i>	<i>C</i>	<i>B</i>	<i>A</i>	<i>A</i>	<i>D</i>	<i>M</i>
<i>D</i>	<i>M</i>	<i>D</i>	<i>D</i>	<i>M</i>	<i>B</i>	<i>D</i>	<i>M</i>	<i>D</i>	<i>B</i>	<i>M</i>	<i>D</i>
<i>A</i>	<i>B</i>	<i>C</i>	<i>M</i>	<i>D</i>	<i>A</i>	<i>M</i>	<i>D</i>	<i>M</i>	<i>C</i>	<i>D</i>	<i>M</i>
Diagonal branch											
<i>D</i>	<i>M</i>	0	0	<i>M</i>	<i>D</i>	<i>D</i>	0	<i>M</i>	<i>M</i>	0	<i>D</i>
0	<i>M</i>	<i>M</i>	<i>M</i>	<i>M</i>	0	<i>M</i>	<i>M</i>	0	0	<i>M</i>	<i>M</i>
<i>M</i>	0	<i>D</i>	<i>D</i>	0	<i>M</i>	0	<i>M</i>	<i>D</i>	<i>D</i>	<i>M</i>	0

<sup>a</sup> $A \cup B \cup C = 1 \quad D = 0 \cup 1.$



(a) Four iterations



(b) Ten iterations

**FIGURE 13.3-7.** Skeletonizing of a binary image.

Figure 13.3-7 shows an example of the skeletonization of a binary image. The eroded pixels are mid gray. It should be observed that skeletonizing gives different results than thinning for many objects. Prewitt (23, p.136) has coined the term *exoskeleton* for the skeleton of the background of an object in a scene. The exoskeleton partitions each objects from neighboring object, as does the thinning of the background.

**13.3.4. Binary Image Thickening**

In Section 13.2.1, the fatten operator was introduced as a means of dilating objects such that objects separated by a single pixel stroke would not be fused. But the fatten operator does not prevent fusion of objects separated by a double width white stroke. This problem can be solved by iteratively thinning the background of an image, and then performing a diagonal fill operation. This process, called *thickening*, when taken to its idempotent limit, forms the exothin of the image, as discussed in Section 13.3.2. Figure 13.3-8 provides an example of thickening. The exothin operation is repeated three times on the background reversed version of the original image. Figure 13.3-8b shows the final result obtained by reversing the background of the exothinned image.

The binary thinning and skeletonizing methods presented in this section are based upon the conditional erosion concept. They are well suited for implementation on a pipeline processor because they can be computed by scanning an image with a  $3 \times 3$  pixel processing window (17). A drawback of the methods is that the processed images are not always minimally connected. Also, the thinned or skeletonized images are sometimes asymmetric even when the source image is symmetric. Chapter 18 presents some algorithms, which are based upon contour following of binary objects. These algorithms often avoid the problems associated with conditional erosion methods.

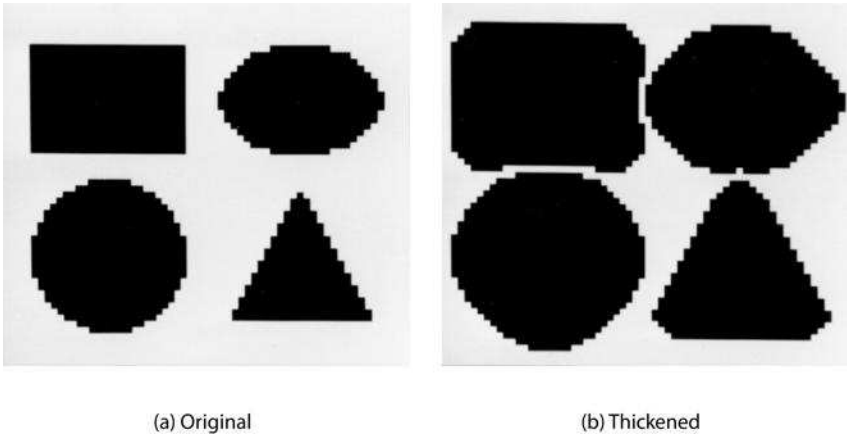


FIGURE 13.3-8. Thickening of a binary image.

### 13.4. BINARY IMAGE GENERALIZED DILATION AND EROSION

Dilation and erosion, as defined earlier in terms of hit-or-miss transformations, are limited to object modification by a single ring of boundary pixels during each iteration of the process. The operations can be generalized.

Before proceeding further, it is necessary to introduce some fundamental concepts of image set algebra that are the basis for defining the generalized dilation and erosions operators. Consider a binary-valued source image function  $F(j, k)$ . A pixel at coordinate  $(j, k)$  is a member of  $F(j, k)$ , as indicated by the symbol  $\in$ , if and only if it is a logical 1. A binary-valued image  $B(j, k)$  is a subset of a binary-valued image  $A(j, k)$ , as indicated by  $B(j, k) \subseteq A(j, k)$ , if for every spatial occurrence of a logical 1 of  $A(j, k)$ ,  $B(j, k)$  is a logical 1. The complement  $\bar{F}(j, k)$  of  $F(j, k)$  is a binary-valued image whose pixels are in the opposite logical state of those in  $F(j, k)$ . Figure 13.4-1 shows an example of the complement process and other image set algebraic operations on a pair of binary images. A reflected image  $\tilde{F}(j, k)$

is an image that has been flipped from left to right and from top to bottom. Figure 13.4-2 provides an example of image complementation. Translation of an image, as indicated by the function

$$G(j, k) = T_{r, c}\{F(j, k)\} \tag{13.4-1}$$

consists of spatially offsetting  $F(j, k)$  with respect to itself by  $r$  rows and  $c$  columns, where  $-R \leq r \leq R$  and  $-C \leq c \leq C$ . Figure 13.4-2 presents an example of the translation of a binary image.

0 0 0 0 0 0	0 0 0 0 0 0	1 1 1 1 1 1
0 0 1 1 0 0	0 0 0 0 0 0	1 1 0 0 1 1
0 0 1 1 0 0	0 1 1 1 1 0	1 1 0 0 1 1
0 0 1 1 0 0	0 1 1 1 1 0	1 1 0 0 1 1
0 0 1 1 0 0	0 0 0 0 0 0	1 1 0 0 1 1
0 0 0 0 0 0	0 0 0 0 0 0	1 1 1 1 1 1
<b>A</b>	<b>B</b>	<b><math>\bar{A}</math></b>
		complement
0 0 0 0 0 0	0 0 0 0 0 0	0 0 0 0 0 0
0 0 1 1 0 0	0 0 0 0 0 0	0 0 1 1 0 0
0 1 1 1 1 0	0 0 1 1 0 0	0 1 0 0 1 0
0 1 1 1 1 0	0 0 1 1 0 0	0 1 0 0 1 0
0 0 1 1 0 0	0 0 0 0 0 0	0 0 1 1 0 0
0 0 0 0 0 0	0 0 0 0 0 0	0 0 0 0 0 0
<b><math>A \cup B</math></b>	<b><math>A \cap B</math></b>	<b><math>A \text{ XOR } B</math></b>
union	intersection	exclusive-OR
OR	AND	XOR

**FIGURE 13.4-1.** Image set algebraic operations on binary arrays.

### 13.4.1. Generalized Dilation

*Generalized dilation* is expressed symbolically as

$$G(j, k) = F(j, k) \oplus H(j, k) \tag{13.4-2}$$

where  $F(j, k)$  for  $1 \leq j, k \leq N$  is a binary-valued image and  $H(j, k)$  for  $1 \leq j, k \leq L$ , where  $L$  is an odd integer, is a binary-valued array called a *structuring element*. For notational simplicity,  $F(j, k)$  and  $H(j, k)$  are assumed to be square arrays. Generalized dilation can be defined mathematically and implemented in several ways. The *Minkowski addition* definition (1) is

$$G(j, k) = \bigcup_{(r, c) \in H} T_{r,c}\{F(j, k)\} \tag{13.4-3}$$

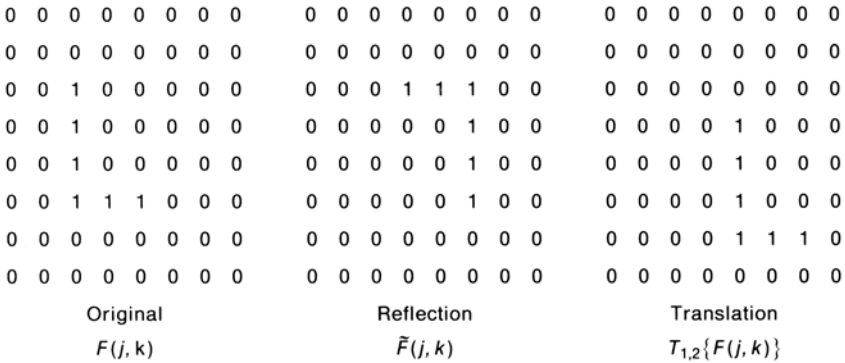


**FIGURE 13.4-2.** Reflection and translation of a binary array.

It states that  $G(j, k)$  is formed by the union of all translates of  $F(j, k)$  with respect to itself in which the translation distance is the row and column index of pixels of  $H(j, k)$  that is a logical 1. Figure 13.4-3 illustrates the concept. Equation 13.4-3 results in an  $M \times M$  output array  $G(j, k)$  that is justified with the upper left corner of the input array  $F(j, k)$ . The output array is of dimension  $M = N + L - 1$ , where  $L$  is the size of the structuring element. In order to register the input and output images properly,  $F(j, k)$  should be translated diagonally right by  $Q = (L - 1)/2$  pixels. Figure 13.4-3 shows the exclusive-OR difference between  $G(j, k)$  and the translate of  $F(j, k)$ . This operation identifies those pixels that have been added as a result of generalized dilation.

An alternative definition of generalized dilation is based on the scanning and processing of  $F(j, k)$  by the structuring element  $H(j, k)$ . With this approach, generalized dilation is formulated as (17)

$$G(j, k) = \bigcup_m \bigcup_n F(m, n) \cap H(j - m + 1, k - n + 1) \tag{13.4-4}$$

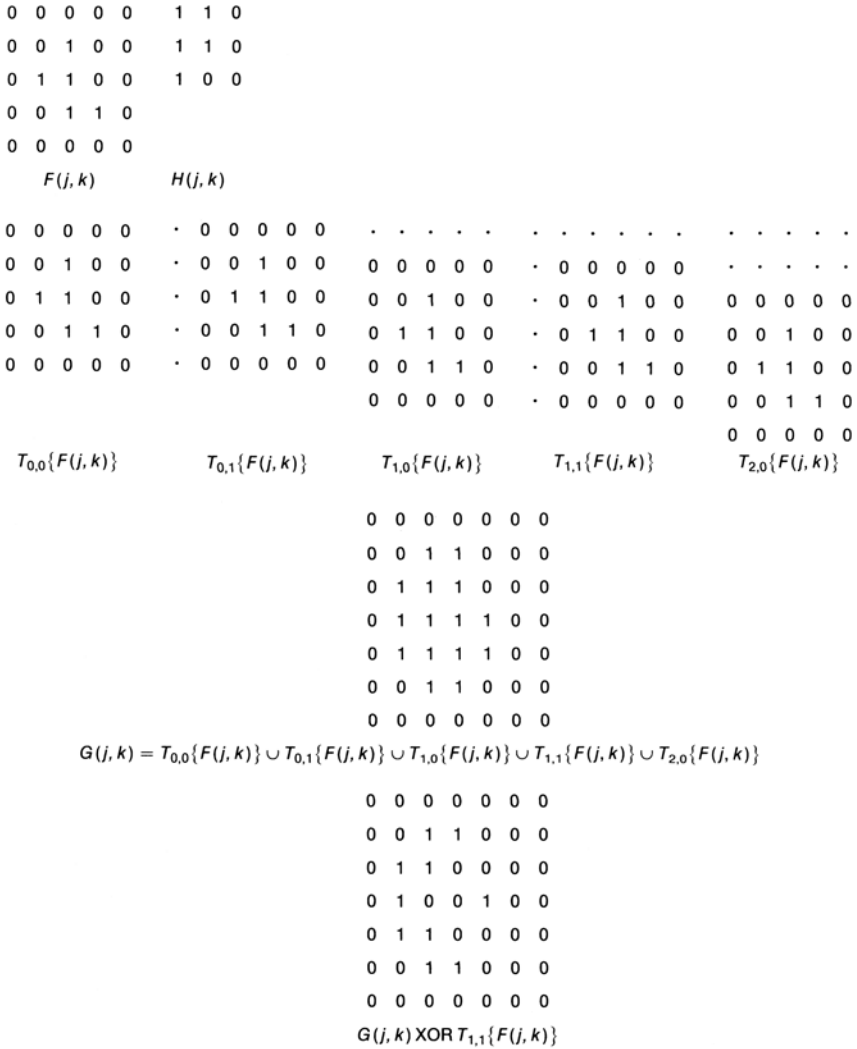


**FIGURE 13.4-3.** Generalized dilation computed by Minkowski addition.

With reference to Eq. 7.1-7, the spatial limits of the union combination are

$$\text{MAX}\{1, j - L + 1\} \leq m \leq \text{MIN}\{N, j\} \tag{13.4-5a}$$

$$\text{MAX}\{1, k - L + 1\} \leq n \leq \text{MIN}\{N, k\} \tag{13.4-5b}$$



Equation 13.4-4 provides an output array that is justified with the upper left corner of the input array. In image processing systems, it is often convenient to center the input and output images and to limit their size to the same overall dimension. This can be accomplished easily by modifying Eq. 13.4-4 to the form

$$G(j, k) = \bigcup_{m \dots} \bigcup_{n \dots} F(m, n) \cap H(j - m + S, k - n + S) \tag{13.4-6}$$

where  $S = (L - 1)/2$  and, from Eq. 7.1-10, the limits of the union combination are

$$\text{MAX}\{1, j - Q\} \leq m \leq \text{MIN}\{N, j + Q\} \tag{13.4-7a}$$

$$\text{MAX}\{1, k - Q\} \leq n \leq \text{MIN}\{N, k + Q\} \tag{13.4-7b}$$

where  $Q = (L - 1)/2$ . Equation 13.4-6 applies for  $S \leq j, k \leq N - Q$  and  $G(j, k) = 0$  elsewhere. The Minkowski addition definition of generalized dilation given in Eq. 13.4-2 can be modified to provide a centered result by taking the translations about the center of the structuring element. In the following discussion, only the centered definitions of generalized dilation will be utilized. In the special case for which  $L = 3$ , Eq. 13.4-6 can be expressed explicitly as

$$\begin{aligned} (G(j, k)) = & \\ & [H(3, 3) \cap F(j - 1, k - 1)] \cup [H(3, 2) \cap F(j - 1, k)] \cup [H(3, 1) \cap F(j - 1, K + 1)] \\ & \cup [H(2, 3) \cap F(j, k - 1)] \cup [H(2, 2) \cap F(j, k)] \cup [H(2, 1) \cap F(j, k + 1)] \\ & \cup [H(1, 3) \cap F(j + 1, k - 1)] \cup [H(1, 2) \cap F(j + 1, k)] \cup [H(1, 1) \cap F(j + 1, k + 1)] \end{aligned} \tag{13.4-8}$$

If  $H(j, k) = 1$  for  $1 \leq j, k \leq 3$ , then  $G(j, k)$ , as computed by Eq. 13.4-8, gives the same result as hit-or-miss dilation, as defined by Eq. 13.2-5.

It is interesting to compare Eqs. 13.4-6 and 13.4-8, which define generalized dilation, and Eqs. 7.1-14 and 7.1-15, which define convolution. In the generalized dilation equation, the union operations are analogous to the summation operations of convolution, while the intersection operation is analogous to point-by-point multiplication. As with convolution, dilation can be conceived as the scanning and processing of  $F(j, k)$  by  $H(j, k)$  rotated by  $180^\circ$ .

### 13.4.2. Generalized Erosion

*Generalized erosion* is expressed symbolically as

$$G(j, k) = F(j, k) \ominus H(j, k) \tag{13.4-9}$$

where again  $H(j, k)$  is an odd size  $L \times L$  structuring element. Serra (3) has adopted, as his definition for erosion, the dual relationship of Minkowski addition given by Eq. 13.4-1, which was introduced by Hadwiger (24). By this formulation, generalized erosion is defined to be

$$G(j, k) = \underbrace{\bigcap_{(r, c) \in H} T_{r, c} \{F(j, k)\}}_{(r, c) \in H} \tag{13.4-10}$$

The meaning of this relation is that erosion of  $F(j, k)$  by  $H(j, k)$  is the intersection of all translates of  $F(j, k)$  in which the translation distance is the row and column index of pixels of  $H(j, k)$  that are in the logical one state. Steinberg et al. (6,25) have adopted the subtly different formulation

$$G(j, k) = \underbrace{\bigcap_{(r, c) \in \tilde{H}} T_{r, c} \{F(j, k)\}}_{(r, c) \in \tilde{H}} \tag{13.4-11}$$

introduced by Matheron (2), in which the translates of  $F(j, k)$  are governed by the reflection  $\tilde{H}(j, k)$  of the structuring element rather than by  $H(j, k)$  itself.

Using the Steinberg definition,  $G(j, k)$  is a logical 1 if and only if the logical ones of  $H(j, k)$  form a subset of the spatially corresponding pattern of the logical ones of  $F(j, k)$  as  $H(j, k)$  is scanned over  $F(j, k)$ . It should be noted that the logical zeros of  $H(j, k)$  do not have to match the logical zeros of  $F(j, k)$ . With the Serra definition, the statements above hold when  $F(j, k)$  is scanned and processed by the reflection of the structuring element. Figure 13.4-4 presents a comparison of the erosion results for the two definitions of erosion. Clearly, the results are inconsistent.

Pratt (26) has proposed a relation, which is the dual to the generalized dilation expression of Eq. 13.4-6, as a definition of generalized erosion. By this formulation, generalized erosion in centered form is

$$G(j, k) = \bigcap_{\dots} \bigcap_{\dots} F(m, n) \cup \bar{H}(j - m + S, k - n + S) \tag{13.4-12}$$

where  $S = (L - 1)/2$ , and the limits of the intersection combination are given by Eq. 13.4-7. In the special case for which  $L = 3$ , Eq. 13.4-12 becomes

$$\begin{aligned} G(j, k) = & [\bar{H}(3, 3) \cup F(j - 1, k - 1)] \cap [\bar{H}(3, 2) \cup F(j - 1, k)] \cap [\bar{H}(3, 1) \cup F(j - 1, k + 1)] \\ & \cup [\bar{H}(2, 3) \cup F(j, k - 1)] \cap [\bar{H}(2, 2) \cup F(j, k)] \cap [\bar{H}(2, 1) \cup F(j, k + 1)] \\ & \cap [\bar{H}(1, 3) \cup F(j + 1, k - 1)] \cap [\bar{H}(1, 2) \cup F(j + 1, k)] \cap [H(1, 1) \cup F(j + 1, k + 1)] \end{aligned} \tag{13.4-13}$$

Sternberg definition of generalized erosion:

$$\begin{array}{ccccc}
 1 & 1 & 1 & 1 & 1 \\
 1 & 1 & 1 & 1 & 1 & 1 & 1 & 1 & 0 & 0 & 0 \\
 1 & 1 & 0 & 0 & 0 & \ominus & 1 & 0 & 0 & = & 1 & 1 & 0 \\
 1 & 1 & 1 & 1 & 1 & 1 & 1 & 1 & 0 & 0 & 0 \\
 1 & 1 & 1 & 1 & 1 & & & & & & & & \\
 & & F(j, k) & & H(j, k) & & G(j, k) & & & & & & 
 \end{array}$$

Serra definition of generalized erosion:

$$\begin{array}{ccccc}
 1 & 1 & 1 & 1 & 1 \\
 1 & 1 & 1 & 1 & 1 & 1 & 1 & 1 & 0 & 0 & 0 \\
 1 & 1 & 0 & 0 & 0 & \ominus & 1 & 0 & 0 & = & 0 & 0 & 0 \\
 1 & 1 & 1 & 1 & 1 & 1 & 1 & 1 & 0 & 0 & 0 \\
 1 & 1 & 1 & 1 & 1 & & & & & & & & \\
 & & F(j, k) & & H(j, k) & & G(j, k) & & & & & & 
 \end{array}$$

FIGURE 13.4-4. Comparison of erosion results for two definitions of generalized erosion.

If  $H(j, k) = 1$  for  $1 \leq j, k \leq 3$ , Eq. 13.4-13 gives the same result as hit-or-miss eight-neighbor erosion as defined by Eq. 13.2-8. Pratt's definition is the same as the Serra definition. However, Eq. 13.4-12 can easily be modified by substituting the reflection  $\tilde{H}(j, k)$  for  $H(j, k)$  to provide equivalency with the Steinberg definition. Unfortunately, the literature utilizes both definitions, which can lead to confusion. The definition adopted in this book is that of Hadwiger, Serra and Pratt, because the defining relationships (Eq. 13.4-1 or 13.4-12) are duals to their counterparts for generalized dilation (Eq. 13.4-3 or 13.4-6).

Figure 13.4-5 shows examples of generalized dilation and erosion for a symmetric  $5 \times 5$  structuring element.

### 13.4.3. Properties of Generalized Dilation and Erosion

Consideration is now given to several mathematical properties of generalized dilation and erosion. Proofs of these properties are found in Reference 25. For notational simplicity, in this subsection, the spatial coordinates of a set are dropped, i.e.,  $A(j, k) = A$ .

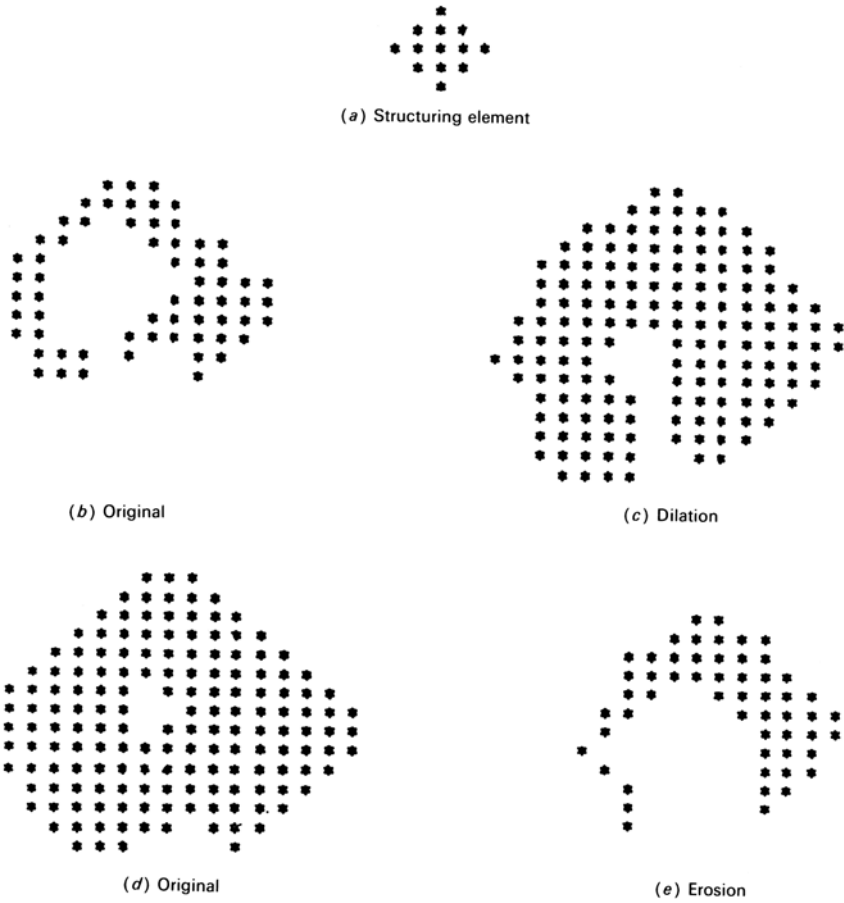


**FIGURE 13.4-5.** Generalized dilation and erosion for a 5 x 5 structuring element.

Dilation is commutative:

$$A \oplus B = B \oplus A \tag{13.4-14a}$$

But, in general, erosion is not commutative:

$$A \ominus B \neq B \ominus A \tag{13.4-14b}$$

Dilation and erosion are increasing operations in the sense that if  $A \subseteq B$ , then

$$A \oplus C \subseteq B \oplus C \tag{13.4-15a}$$

$$A \ominus C \subseteq B \ominus C . \tag{13.4-15b}$$

Dilation and erosion are opposite in effect; dilation of the background of an object behaves like erosion of the object. This statement can be quantified by the duality relationship

$$\overline{A \ominus B} = \bar{A} \oplus B . \tag{13.4-16}$$

For the Steinberg definition of erosion,  $B$  on the right-hand side of Eq. 13.4-16 should be replaced by its reflection  $\tilde{B}$ . Figure 13.4-6 contains an example of the duality relationship.

The dilation and erosion of the intersection and union of sets obey the following relations:

$$[A \cap B] \oplus C \subseteq [A \oplus C] \cap [B \oplus C] \tag{13.4-17a}$$

$$[A \cap B] \ominus C = [A \ominus C] \cap [B \ominus C] . \tag{13.4-17b}$$

$$[A \cup B] \oplus C = [A \oplus C] \cup [B \oplus C] \tag{13.4-17c}$$

$$[A \cup B] \ominus C \supseteq [A \ominus C] \cup [B \ominus C] \tag{13.4-17d}$$

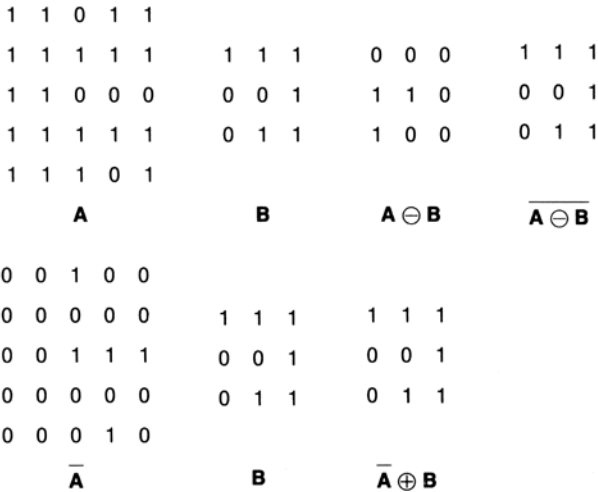


FIGURE 13.4-6. Duality relationship between dilation and erosion.

The dilation and erosion of a set by the intersection of two other sets satisfy these containment relations:

$$A \oplus [B \cap C] \subseteq [A \oplus B] \cap [A \oplus C] \tag{13.4-18a}$$

$$A \ominus [B \cap C] \supseteq [A \ominus B] \cup [A \ominus C]. \tag{13.4-18b}$$

On the other hand, dilation and erosion of a set by the union of a pair of sets are governed by the equality relations

$$A \oplus [B \cup C] = [A \oplus B] \cup [A \oplus C] \tag{13.4-19a}$$

$$A \ominus [B \cup C] = [A \ominus B] \cap [A \ominus C]. \tag{13.4-19b}$$

The following chain rules hold for dilation and erosion.

$$A \oplus [B \oplus C] = [A \oplus B] \oplus C \tag{13.4-20a}$$

$$A \ominus [B \oplus C] = [A \ominus B] \ominus C. \tag{13.4-20b}$$

### 13.5. BINARY IMAGE CLOSE AND OPEN OPERATIONS

Dilation and erosion are often applied to an image in concatenation. Dilation followed by erosion is called a *close operation*. It is expressed symbolically as

$$G(j, k) = F(j, k) \bullet H(j, k) \tag{13.5-1a}$$

where  $H(j, k)$  is a  $L \times L$  structuring element. In accordance with the Serra formulation of erosion, the close operation is defined as

$$G(j, k) = [F(j, k) \oplus H(j, k)] \ominus \tilde{H}(j, k) \tag{13.5-1b}$$

where it should be noted that erosion is performed with the reflection of the structuring element. Closing of an image with a compact structuring element without holes (zeros), such as a square or circle, smooths contours of objects, eliminates small holes in objects and fuses short gaps between objects.

An *open operation*, expressed symbolically as

$$G(j, k) = F(j, k) \circ H(j, k) \tag{13.5-2a}$$

consists of erosion followed by dilation. It is defined as

$$G(j, k) = [F(j, k) \ominus \tilde{H}(j, k)] \oplus H(j, k) \tag{13.5-2b}$$

where again, the erosion is with the reflection of the structuring element. Opening of an image smooths contours of objects, eliminates small objects and breaks narrow strokes.

The close operation tends to increase the spatial extent of an object, while the open operation decreases its spatial extent. In quantitative terms

$$F(j, k) \bullet H(j, k) \supseteq F(j, k) \tag{13.5-3a}$$

$$F(j, k) \circ H(j, k) \subseteq F(j, k) . \tag{13.5-3b}$$

It can be shown that the close and open operations are stable in the sense that (25)

$$[F(j, k) \bullet H(j, k)] \bullet H(j, k) = F(j, k) \bullet H(j, k) \tag{13.5-4a}$$

$$[F(j, k) \circ H(j, k)] \circ H(j, k) = F(j, k) \circ H(j, k) . \tag{13.5-4b}$$

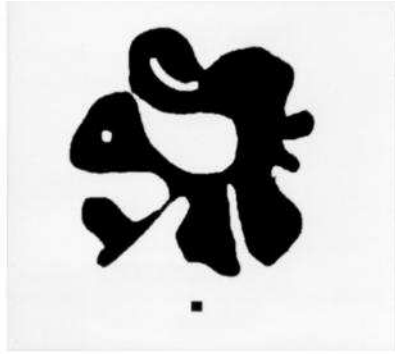
Also, it can be easily shown that the open and close operations satisfy the following duality relationship:

$$\overline{F(j, k) \bullet H(j, k)} = \overline{F(j, k)} \circ H(j, k) . \tag{13.5-5}$$

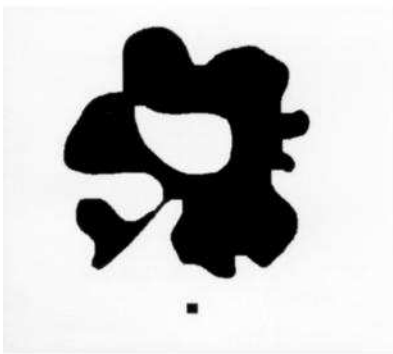
Figure 13.5-1 presents examples of the close and open operations on a binary image.

### 13.6. GRAY SCALE IMAGE MORPHOLOGICAL OPERATIONS

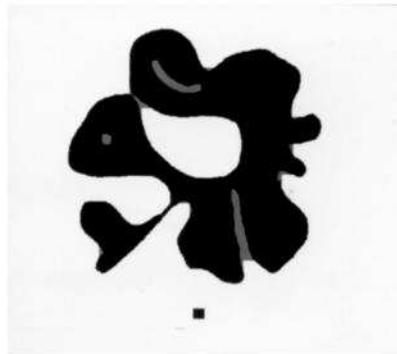
Morphological concepts can be extended to gray scale images, but the extension often leads to theoretical issues and to implementation complexities. When applied to a binary image, dilation and erosion operations cause an image to increase or decrease in spatial extent, respectively. To generalize these concepts to a gray scale image, it is assumed that the image contains visually distinct gray scale objects set against a gray background. Also, it is assumed that the objects and background are both relatively spatially smooth. Under these conditions, it is reasonable to ask: Why not just threshold the image and perform binary image morphology? The reason for not taking this approach is that the thresholding operation often introduces significant error in segmenting objects from the background. This is especially true when the gray scale image contains shading caused by nonuniform scene illumination.



(a) Original



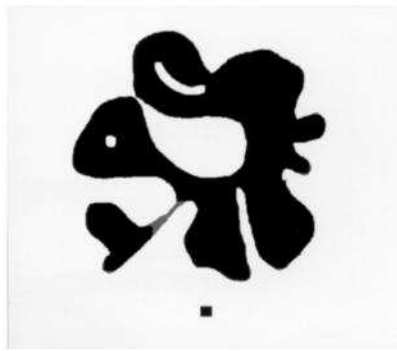
(b) Close



(c) Overlay of original and close



(d) Open



(e) Overlay of original and open

**FIGURE 13.5-1.** Close and open operations on a binary image.



### 13.6.1. Gray Scale Image Dilation and Erosion

Dilation or erosion of an image could, in principle, be accomplished by hit-or-miss transformations in which the quantized gray scale patterns are examined in a  $3 \times 3$  window and an output pixel is generated for each pattern. This approach is, however, not computationally feasible. For example, if a look-up table implementation were to be used, the table would require  $2^{72}$  entries for 256-level quantization of each pixel! The common alternative is to use gray scale extremum operations over a  $3 \times 3$  pixel neighborhoods.

Consider a gray scale image  $F(j, k)$  quantized to an arbitrary number of gray levels. According to the extremum method of gray scale image dilation, the dilation operation is defined as

$$G(j, k) = \text{MAX}\{F(j, k), F(j, k + 1), F(j - 1, k + 1), \dots, F(j + 1, k + 1)\} \quad (13.6-1)$$

where  $\text{MAX}\{S_1, \dots, S_9\}$  generates the largest-amplitude pixel of the nine pixels in the neighborhood. If  $F(j, k)$  is quantized to only two levels, Eq. 13.6-1 provides the same result as that using binary image dilation as defined by Eq. 13.2-5.

By the extremum method, gray scale image erosion is defined as

$$G(j, k) = \text{MIN}\{F(j, k), F(j, k + 1), F(j - 1, k + 1), \dots, F(j + 1, k + 1)\} \quad (13.6-2)$$

where  $\text{MIN}\{S_1, \dots, S_9\}$  generates the smallest-amplitude pixel of the nine pixels in the  $3 \times 3$  pixel neighborhood. If  $F(j, k)$  is binary-valued, then Eq. 13.6-2 gives the same result as hit-or-miss erosion as defined in Eq. 13.2-8.

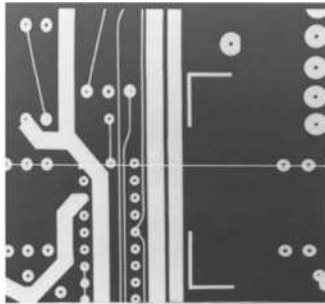
In Chapter 10, when discussing the pseudomedian, it was shown that the MAX and MIN operations can be computed sequentially. As a consequence, Eqs. 13.6-1 and 13.6-2 can be applied iteratively to an image. For example, three iterations gives the same result as a single iteration using a  $7 \times 7$  moving-window MAX or MIN operator. By selectively excluding some of the terms  $S_1, \dots, S_9$  of Eq. 13.6-1 or 13.6-2 during each iteration, it is possible to synthesize large non square gray scale structuring elements in the same manner as illustrated in Figure 13.4-7 for binary structuring elements. However, no systematic decomposition procedure has yet been developed.

Figures 13.6-1 and 13.6-2 show the amplitude profile of a row of a gray scale image of a printed circuit board (PCB) after several dilation and erosion iterations. The row selected is indicated by the white horizontal line in Figure 13.6-1a. In Figure 13.6-2, two-dimensional gray scale dilation and erosion are performed on the PCB image.

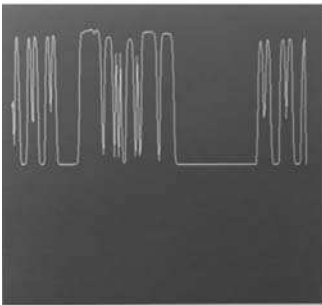
### 13.6.2. Gray Scale Image Close and Open Operators

The close and open operations introduced in Section 13.5 for binary images can easily be extended to gray scale images. Gray scale closing is realized by first performing gray scale dilation with a gray scale structuring element, then gray scale erosion with the same structuring element. Similarly, gray scale opening is accomplished by

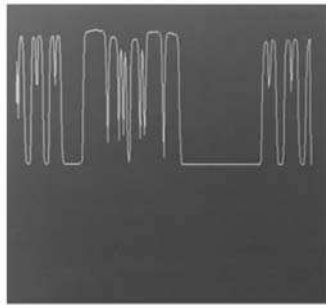
gray scale erosion followed by gray scale dilation. Figures 13.6-3a and b give examples of gray scale image closing and opening.



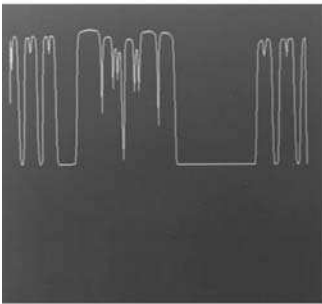
(a) Original



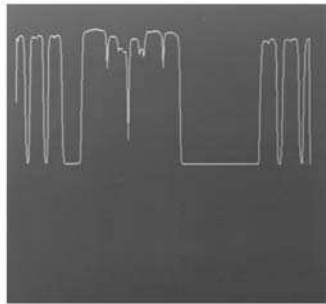
(b) Original profile



(c) One iteration

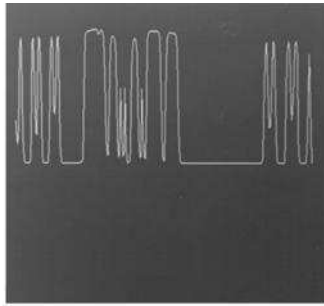


(d) Two iterations

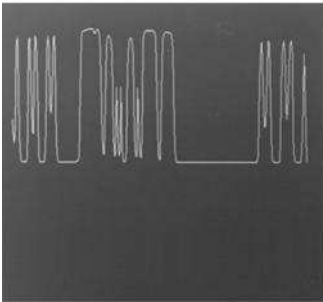


(e) Three iterations

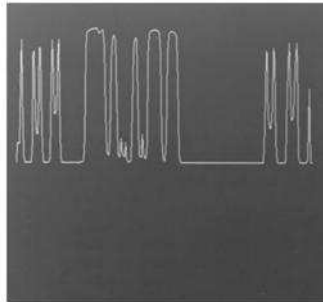
**FIGURE 13.6-1.** One-dimensional gray scale image dilation on a printed circuit board image.



(a) One iteration



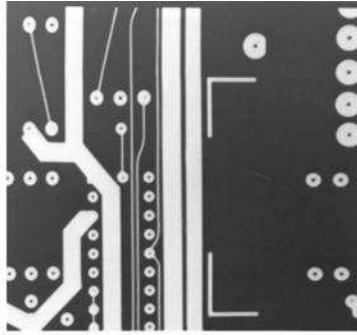
(b) Two iterations



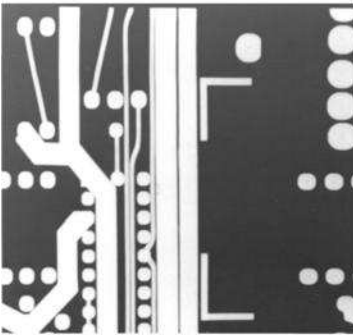
(c) Three iterations

**FIGURE 13.6-2.** One-dimensional gray scale image erosion on a printed circuit board image.

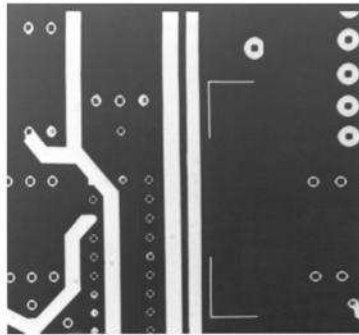
Steinberg (26) has introduced the use of three-dimensional structuring elements for gray scale image closing and opening operations. Although the concept is well defined mathematically, it is simpler to describe in terms of a structural image model. Consider a gray scale image to be modeled as an array of closely packed square pegs, each of which is proportional in height to the amplitude of a corresponding pixel. Then a three-dimensional structuring element, for example a sphere, is placed over each peg. The bottom of the structuring element, as it is translated over the peg array, forms another spatially discrete surface, which is the close array of the original image. A spherical structuring element will touch pegs at peaks of the original peg array, but will not touch pegs at the bottom of steep valleys. Consequently, the close surface “fills in” dark spots in the original image. The opening of a gray scale image can be conceptualized in a similar manner. An original image is modeled as a peg array in which the height of each peg is inversely proportional to the amplitude of each corresponding pixel (i.e., the gray scale is subtractively



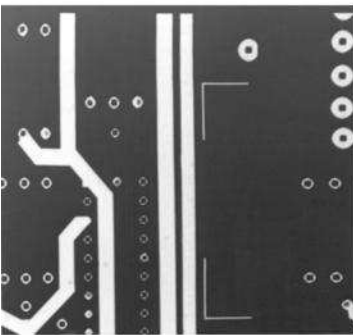
(a) Original



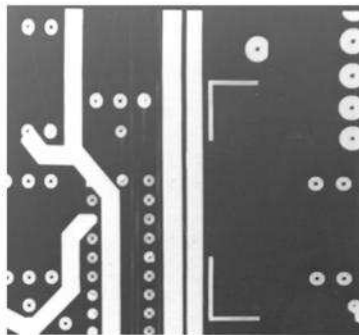
(b) Dilation



(c) Erosion



(d) Close



(e) Open

**FIGURE 13.6-3.** Two-dimensional gray scale image dilation, erosion, close and open on a printed circuit board image.

inverted). The translated structuring element then forms the open surface of the original image. For a spherical structuring element, bright spots in the original image are made darker.

### 13.6.3. Conditional Gray Scale Image Morphological Operators

There have been attempts to develop morphological operators for gray scale images that are analogous to binary image shrinking, thinning, skeletonizing and thickening. The stumbling block to these extensions is the lack of a definition for connectivity of neighboring gray scale pixels. Serra (4) has proposed approaches based on topographic mapping techniques. Another approach is to iteratively perform the basic dilation and erosion operations on a gray scale image, and then use a binary thresholded version of the resultant image to determine connectivity at each iteration.

## 13.7. MORPHOLOGICAL IMAGE PROCESSING EXERCISES

E13.1 Develop a program that reads the  $64 \times 64$ , Boolean test image `boolean_test` and dilates it by one and two iterations with a  $3 \times 3$  structuring element. Steps:

- (a) Read the source image and zoom it by a factor of 8:1.
- (b) Create a  $3 \times 3$  structuring element array.
- (c) Dilate the source image with one iteration.
- (d) Display the zoomed destination image.
- (e) Dilate the source image with two iterations.
- (f) Display the zoomed destination image.

The PIKS API executable `example_boolean_dilation` performs this exercise.

E13.2 Develop a program that reads the  $64 \times 64$ , Boolean test image `boolean_test` and erodes it by one and two iterations with a  $3 \times 3$  structuring element. Steps:

- (a) Read the source image and zoom it by a factor of 8:1.
- (b) Create a  $3 \times 3$  structuring element array.
- (c) Erode the source image with one iteration.
- (d) Display the zoomed destination image.
- (e) Erode the source image with two iterations.
- (f) Display the zoomed destination image.

The PIKS API executable `example_boolean_erosion` performs this exercise.

E13.3 Develop a program that performs gray scale dilation on an unsigned integer, 8-bit, monochrome image with a  $5 \times 5$  zero-value structuring element and a  $5 \times 5$  TRUE state mask. Steps:

- (a) Display the source image.
- (b) Create a  $5 \times 5$  Boolean mask.
- (c) Perform gray scale dilation on the source image.
- (d) Display the destination image.

The PIKS API executable `example_dilation_grey_ND` performs this exercise.

E13.4 Develop a program that performs gray scale erosion on an unsigned integer, 8-bit, monochrome image with a  $5 \times 5$  zero-value structuring element and a  $5 \times 5$  TRUE state mask. Steps:

- (a) Display the source image.
- (b) Create a  $5 \times 5$  Boolean mask.
- (c) Perform gray scale erosion on the source image.
- (d) Display the destination image.

The PIKS API executable `example_erosion_grey_ND` performs this exercise.

## REFERENCES

1. H. Minkowski, "Volumen und Oberfiläche," *Mathematische Annalen*, **57**, 1903, 447–459.
2. G. Matheron, *Random Sets and Integral Geometry*, John Wiley and Sons, New York, 1975.
3. J. Serra, *Image Analysis and Mathematical Morphology*, Vol. 1, Academic Press, London, 1982.
4. J. Serra, *Image Analysis and Mathematical Morphology: Theoretical Advances*, Vol. 2, Academic Press, London, 1988.
5. J. Serra, "Introduction to Mathematical Morphology," *Computer Vision, Graphics and Image Processing*, **35**, 3, September 1986, 283–305.
6. S. R. Steinberg, "Parallel Architectures for Image Processing," *Proc. 3rd International IEEE Compsac*, Chicago, 1981.
7. S. R. Steinberg, "Biomedical Image Processing," *IEEE Computer*, January 1983, 22–34.
8. S. R. Steinberg, "Automatic Image Processor," US patent 4,167,728.

9. R. M. Lougheed and D. L. McCubbrey, "The Cytocomputer: A Practical Pipelined Image Processor," *Proc. 7th Annual International Symposium on Computer Architecture*, 1980.
10. A. Rosenfeld, "Connectivity in Digital Pictures," *J. Association for Computing Machinery*, **17**, 1, January 1970, 146–160.
11. A. Rosenfeld, *Picture Processing by Computer*, Academic Press, New York, 1969.
12. M. J. E. Golay, "Hexagonal Pattern Transformation," *IEEE Trans. Computers*, **C-18**, 8, August 1969, 733–740.
13. K. Preston, Jr., "Feature Extraction by Golay Hexagonal Pattern Transforms," *IEEE Trans. Computers*, **C-20**, 9, September 1971, 1007–1013.
14. F. A. Gerritsen and P. W. Verbeek, "Implementation of Cellular Logic Operators Using 3 x 3 Convolutions and Lookup Table Hardware," *Computer Vision, Graphics and Image Processing*, **27**, 1, 1984, 115–123.
15. A. Rosenfeld, "A Characterization of Parallel Thinning Algorithms," *Information and Control*, **29**, 1975, 286–291.
16. T. Pavlidis, "A Thinning Algorithm for Discrete Binary Images," *Computer Graphics and Image Processing*, **13**, 2, 1980, 142–157.
17. W. K. Pratt and I. Kabir, "Morphological Binary Image Processing with a Local Neighborhood Pipeline Processor," *Computer Graphics*, Tokyo, 1984.
18. H. Blum, "A Transformation for Extracting New Descriptors of Shape," in *Symposium Models for Perception of Speech and Visual Form*, W. Whaten-Dunn, Ed., MIT Press, Cambridge, MA, 1967.
19. R. O. Duda and P. E. Hart, *Pattern Classification and Scene Analysis*, Wiley-Interscience, New York, 1973.
20. L. Calabi and W. E. Harnett, "Shape Recognition, Prairie Fires, Convex Deficiencies and Skeletons," *American Mathematical Monthly*, **75**, 4, April 1968, 335–342.
21. J. C. Mott-Smith, "Medial Axis Transforms," in *Picture Processing and Psychopictorics*, B. S. Lipkin and A. Rosenfeld, Eds., Academic Press, New York, 1970.
22. C. Arcelli and G. Sanniti Di Baja, "On the Sequential Approach to Medial Line Thinning Transformation," *IEEE Trans. Systems, Man and Cybernetics*, **SMC-8**, 2, 1978, 139–144.
23. J. M. S. Prewitt, "Object Enhancement and Extraction," in *Picture Processing and Psychopictorics*, B. S. Lipkin and A. Rosenfeld, Eds., Academic Press, New York, 1970.
24. H. Hadwiger, *Vorlesungen über Inhalt, Oberfläche und Isoperimetrie*, Springer-Verlag, Berlin, 1957.
25. R. M. Haralick, S. R. Steinberg and X. Zhuang, "Image Analysis Using Mathematical Morphology," *IEEE Trans. Pattern Analysis and Machine Intelligence*, **PAMI-9**, 4, July 1987, 532–550.
26. S. R. Steinberg, "Grayscale Morphology," *Computer Vision, Graphics and Image Processing*, **35**, 3, September 1986, 333–355.

---

# 14

---

## EDGE DETECTION

Changes or discontinuities in an image amplitude attribute such as luminance or tristimulus value are fundamentally important primitive characteristics of an image because they often provide an indication of the physical extent of objects within the image. Local discontinuities in image luminance from one level to another are called *luminance edges*. Global luminance discontinuities, called *luminance boundary segments*, are considered in Section 16.4. In this chapter, the definition of a luminance edge is limited to image amplitude discontinuities between reasonably smooth regions. Discontinuity detection between textured regions is considered in Section 16.5. This chapter also considers edge detection in color images, as well as the detection of lines and spots within an image.

### 14.1. EDGE, LINE AND SPOT MODELS

Figure 14.1-1a is a sketch of a continuous domain, one-dimensional *ramp edge* modeled as a ramp increase in image amplitude from a low to a high level, or vice versa. The edge is characterized by its height, slope angle and horizontal coordinate of the slope midpoint. An edge exists if the edge height is greater than a specified value. An ideal edge detector should produce an edge indication localized to a single pixel located at the midpoint of the slope. If the slope angle of Figure 14.1-1a is  $90^\circ$ , the resultant edge is called a *step edge*, as shown in Figure 14.1-1b. In a digital imaging system, step edges usually exist only for artificially generated images such as test patterns and bi-level graphics data. Digital images, resulting from digitization



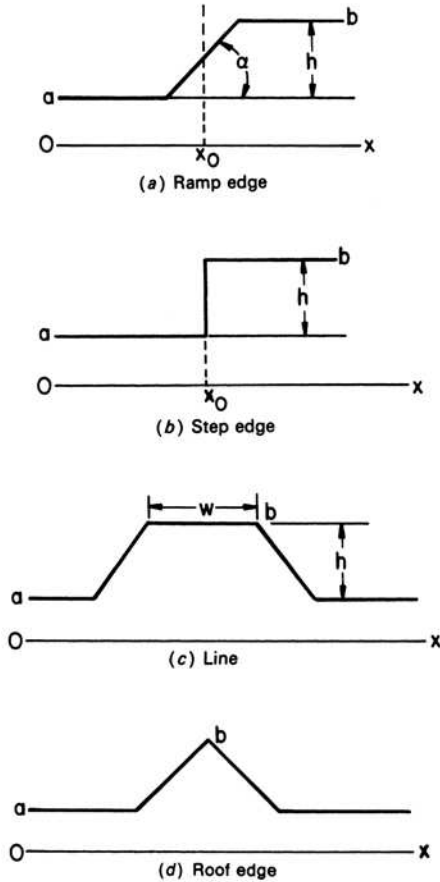


**FIGURE 14.1-1.** One-dimensional, continuous domain edge and line models.

of optical images of real scenes, generally do not possess step edges because the anti-aliasing low-pass filtering prior to digitization reduces the edge slope in the digital image caused by any sudden luminance change in the scene. The one-dimensional profile of a *line* is shown in Figure 14.1-1c. In the limit, as the line width  $w$  approaches zero, the resultant amplitude discontinuity is called a *roof edge*.

Continuous domain, two-dimensional models of edges and lines assume that the amplitude discontinuity remains constant in a small neighborhood orthogonal to the edge or line profile. Figure 14.1-2a is a sketch of a two-dimensional edge. In addition to the edge parameters of a one-dimensional edge, the orientation of the edge slope with respect to a reference axis is also important. Figure 14.1-2b defines the edge orientation nomenclature for edges of an octagonally shaped object whose amplitude is higher than its background.

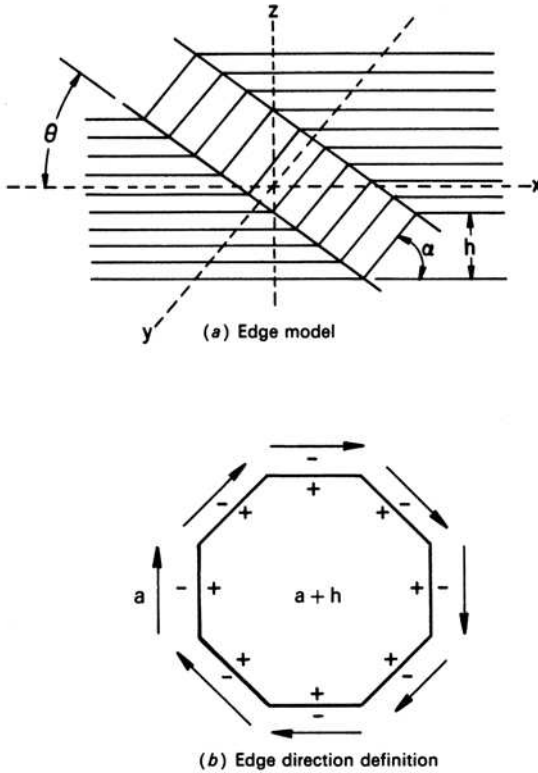


**FIGURE 14.1-2.** Two-dimensional, continuous domain edge model.

Figure 14.1-3 contains step and unit width ramp edge models in the discrete domain. The vertical ramp edge model in the figure contains a single transition pixel whose amplitude is at the mid value of its neighbors. This edge model can be obtained by performing a  $2 \times 2$  pixel moving window average on the vertical step edge model. The figure also contains two versions of a diagonal ramp edge. The single-pixel transition model contains a single mid value transition pixel between the regions of high-amplitude and low-amplitude; the smoothed transition model is generated by a  $2 \times 2$  pixel moving window average of the diagonal step edge model. Figure 14.1-3 also presents models for a discrete step and ramp corner edge. The edge location for discrete step edges is usually marked at the higher-amplitude side of an edge transition. For the single-pixel transition model and the smoothed transition vertical and corner edge models, the proper edge location is at the transition pixel. The smoothed transition diagonal ramp edge model has a pair of adjacent pixels in its transition zone. The edge is usually marked at the higher-amplitude pixel of the pair. In Figure 14.1-3, the edge pixels are italicized.

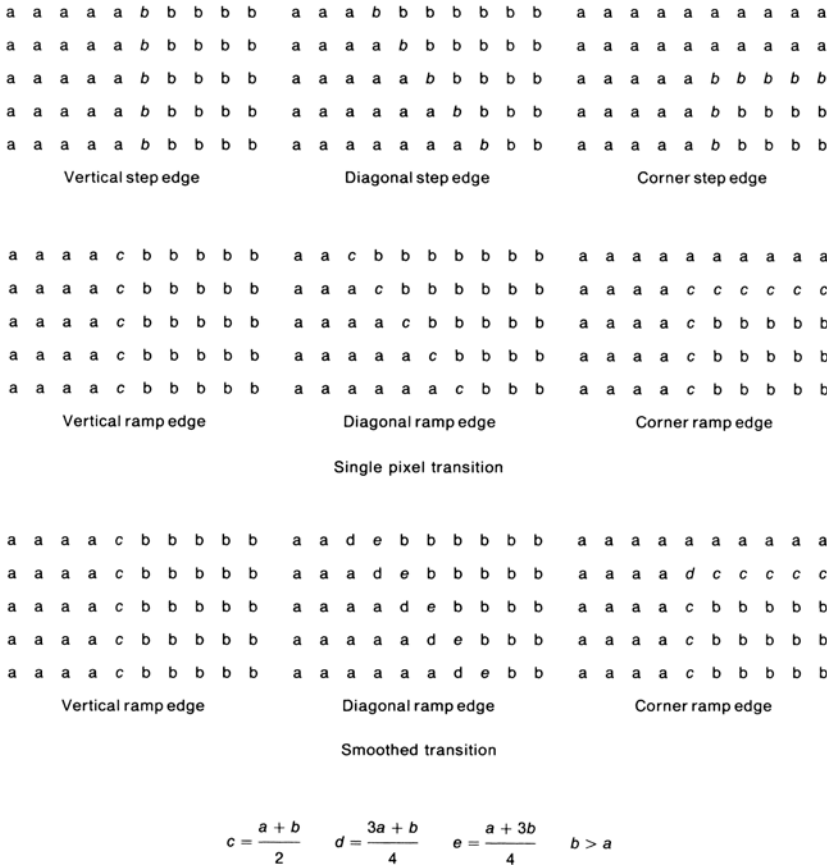
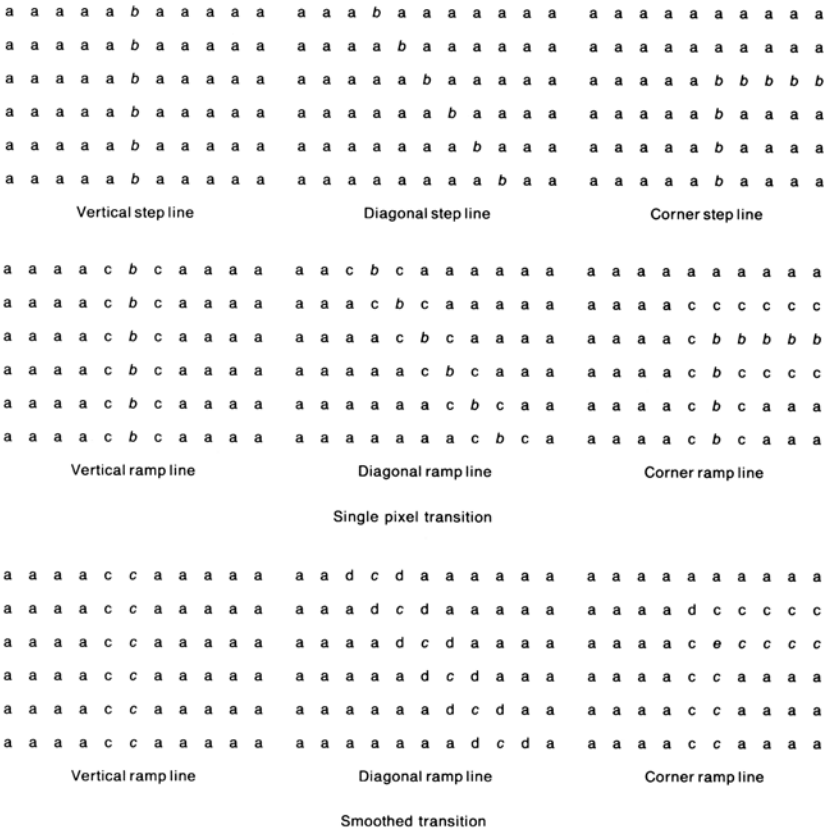


FIGURE 14.1-3. Two-dimensional, discrete domain edge models.

Discrete two-dimensional single-pixel line models are presented in Figure 14.1-4 for step lines and unit width ramp lines. The single-pixel transition model has a mid value transition pixel inserted between the high-value of the line plateau and the low-value background. The smoothed transition model is obtained by performing a  $2 \times 2$  pixel moving window average on the step line model.

A *spot*, which can only be defined in two dimensions, consists of a plateau of high amplitude against a lower amplitude background, or vice versa. Figure 14.1-5 presents single-pixel spot models in the discrete domain.

There are two generic approaches to the detection of edges, lines and spots in a luminance image: differential detection and model fitting. With the differential detection approach, as illustrated in Figure 14.1-6, spatial processing is performed on an original image  $F(j, k)$  to produce a differential image  $G(j, k)$  with accentuated spatial amplitude changes. Next, a differential detection operation is executed to determine the pixel locations of significant differentials. The second general approach to



**FIGURE 14.1-4.** Two-dimensional, discrete domain line models.

edge, line or spot detection involves fitting of a local region of pixel values to a model of the edge, line or spot, as represented in Figures 14.1-1 to 14.1-5. If the fit is sufficiently close, an edge, line or spot is said to exist, and its assigned parameters are those of the appropriate model. A binary indicator *edge map*  $E(j, k)$  is often generated to indicate the position of edges, lines or spots within an image. Typically, edge, line and spot locations are specified by black pixels against a white background.

There are two major classes of differential edge detection: first- and second-order derivative. For the first-order class, some form of spatial first-order differentiation is performed, and the resulting edge gradient is compared to a threshold value. An edge is judged present if the gradient exceeds the threshold. For the second-order derivative class of differential edge detection, an edge is judged present if there is a significant spatial change in the polarity of the second derivative.



$$c = \frac{a + b}{2} \quad d = \frac{3a + b}{4} \quad b > a$$

FIGURE 14.1-5. Two-dimensional, discrete domain single pixel spot models.

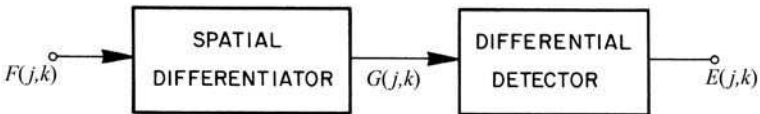


FIGURE 14.1-6. Differential edge, line and spot detection.

Sections 14.2 and 14.3 discuss the first-order and second-order derivative forms of edge detection, respectively. Edge fitting methods of edge detection are considered in Section 14.4.

## 14.2. FIRST-ORDER DERIVATIVE EDGE DETECTION

There are two fundamental methods for generating first-order derivative edge gradients. One method involves generation of gradients in two orthogonal directions in an image; the second utilizes a set of directional derivatives.

### 14.2.1. Orthogonal Gradient Generation

An edge in a continuous domain edge segment  $F(x, y)$ , such as the one depicted in Figure 14.1-2a, can be detected by forming the continuous one-dimensional gradient  $G(x, y)$  along a line normal to the edge slope, which is at an angle  $\theta$  with respect to the horizontal axis. If the gradient is sufficiently large (i.e., above some threshold value), an edge is deemed present. The gradient along the line normal to the edge slope can be computed in terms of the derivatives along orthogonal axes according to the following: (1, p. 106)

$$G(x, y) = \frac{\partial F(x, y)}{\partial x} \cos \theta + \frac{\partial F(x, y)}{\partial y} \sin \theta. \quad (14.2-1)$$

Figure 14.2-1 describes the generation of an *edge gradient*  $G(x, y)$  in the discrete domain<sup>1</sup> in terms of a *row gradient*  $G_R(j, k)$  and a *column gradient*  $G_C(j, k)$ . The spatial gradient amplitude is given by

$$G(j, k) = [[G_R(j, k)]^2 + [G_C(j, k)]^2]^{1/2}. \quad (14.2-2)$$

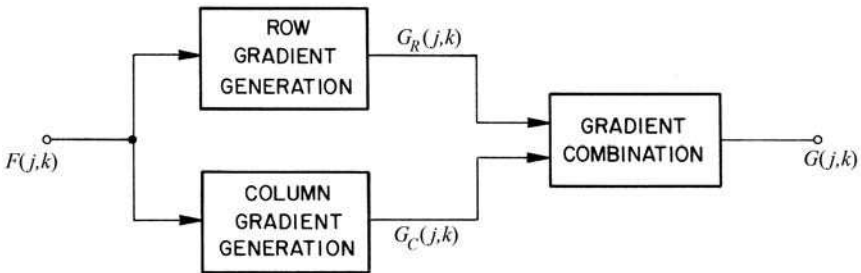


FIGURE 14.2-1. Orthogonal gradient generation.

1. The array nomenclature employed in this chapter places the origin in the upper left corner of the array with  $j$  increasing horizontally and  $k$  increasing vertically.

For computational efficiency, the gradient amplitude is sometimes approximated by the magnitude combination

$$G(j, k) = |G_R(j, k)| + |G_C(j, k)|. \tag{14.2-3}$$

The orientation of the spatial gradient with respect to the row axis is

$$\theta(j, k) = \arctan \left\{ \frac{G_C(j, k)}{G_R(j, k)} \right\}. \tag{14.2-4}$$

The remaining issue for discrete domain orthogonal gradient generation is to choose a good discrete approximation to the continuous differentials of Eq. 14.2-1.

**Small Neighborhood Gradient Operators.** The simplest method of discrete gradient generation is to form the running difference of pixels along rows and columns of the image. The row gradient is defined as

$$G_R(j, k) = F(j, k) - F(j - 1, k) \tag{14.2-5a}$$

and the column gradient is<sup>2</sup>

$$G_C(j, k) = F(j, k) - F(j, k + 1) \tag{14.2-5b}$$

As an example of the response of a pixel difference edge detector, the following is the row gradient along the center row of the vertical step edge model of Figure 14.1-3:

$$0 \quad 0 \quad 0 \quad 0 \quad h \quad 0 \quad 0 \quad 0 \quad 0$$

In this sequence,  $h = b - a$  is the step edge height. The row gradient for the vertical ramp edge model is

$$0 \quad 0 \quad 0 \quad 0 \quad \frac{h}{2} \quad \frac{h}{2} \quad 0 \quad 0 \quad 0$$

For ramp edges, the running difference edge detector cannot localize the edge to a single pixel. Figure 14.2-2 provides examples of horizontal and vertical differencing absolute value gradients of the monochrome peppers image. In this and subsequent gradient display photographs, the gradient range has been scaled over the full contrast range of the photograph. It is visually apparent from the photograph that the

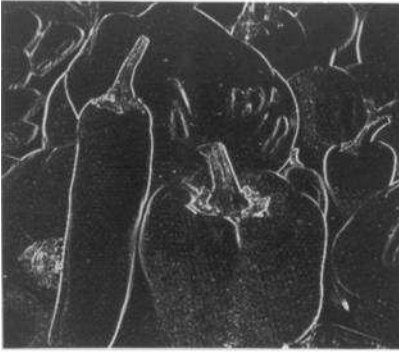
---

2. These definitions of row and column gradients, and subsequent extensions, are chosen such that  $G_R$  and  $G_C$  are positive for an edge that increases in amplitude from left to right and from bottom to top in an image.

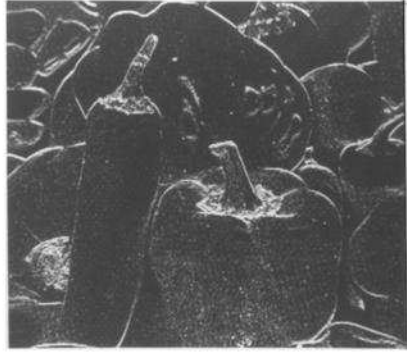
running difference technique is highly susceptible to small fluctuations in image luminance and that the object boundaries are not well delineated.



(a) Original



(b) Horizontal magnitude



(c) Vertical magnitude

**FIGURE 14.2-2.** Horizontal and vertical differencing gradients of the peppers\_mon image.

Diagonal edge gradients can be obtained by forming running differences of diagonal pairs of pixels. This is the basis of the Roberts (2) cross-difference operator, which is defined in magnitude form as

$$G(j, k) = |G_1(j, k)| + |G_2(j, k)| \quad (14.2-6a)$$

and in square-root form as

$$G(j, k) = \left[ [G_1(j, k)]^2 + [G_2(j, k)]^2 \right]^{1/2} \quad (14.2-6b)$$



where

$$G_1(j, k) = F(j, k) - F(j - 1, k + 1) \quad (14.2-6c)$$

$$G_2(j, k) = F(j, k) - F(j + 1, k + 1). \quad (14.2-6d)$$

The edge orientation with respect to the row axis is

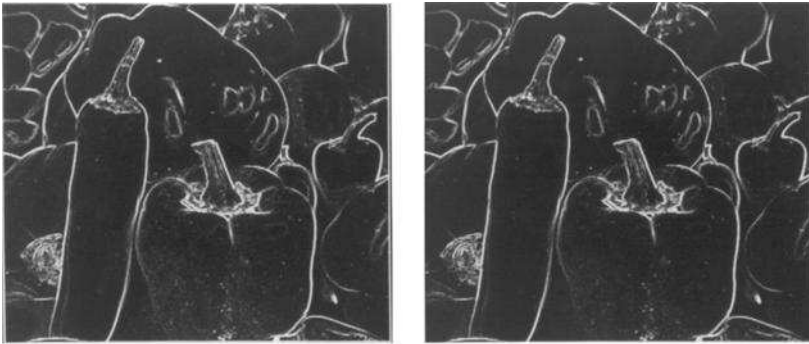
$$\theta(j, k) = \frac{\pi}{4} + \arctan\left\{\frac{G_2(j, k)}{G_1(j, k)}\right\}. \quad (14.2-7)$$

Figure 14.2-3 presents the edge gradients of the peppers image for the *Roberts operators*. Visually, the objects in the image appear to be slightly better distinguished with the Roberts square-root gradient than with the magnitude gradient. In Section 14.5, a quantitative evaluation of edge detectors confirms the superiority of the square-root combination technique.

The pixel difference method of gradient generation can be modified to localize the edge center of the ramp edge model of Figure 14.1-3 by forming the pixel difference separated by a null value. The row and column gradients then become

$$G_R(j, k) = F(j + 1, k) - F(j - 1, k) \quad (14.2-8a)$$

$$G_C(j, k) = F(j, k - 1) - F(j, k + 1). \quad (14.2-8b)$$



(a) Magnitude

(b) Square root

**FIGURE 14.2-3.** Roberts gradients of the peppers\_mon image.

$A_0$	$A_1$	$A_2$
$A_7$	$F(j,k)$	$A_3$
$A_6$	$A_5$	$A_4$

**FIGURE 14.2-4.** Numbering convention for  $3 \times 3$  edge detection operators.

The row gradient response for a vertical ramp edge model is then

$$0 \ 0 \ \frac{h}{2} \ h \ \frac{h}{2} \ 0 \ 0$$

Although the ramp edge is properly localized, the separated pixel difference gradient generation method remains highly sensitive to small luminance fluctuations in the image. This problem can be alleviated by using two-dimensional gradient formation operators that perform differentiation in one coordinate direction and spatial averaging in the orthogonal direction simultaneously.

Prewitt (1, p. 108) has introduced a  $3 \times 3$  pixel edge gradient operator described by the pixel numbering convention of Figure 14.2-4. The *Prewitt operator* square root edge gradient is defined as

$$G(j, k) = [[G_R(j, k)]^2 + [G_C(j, k)]^2]^{1/2} \quad (14.2-9a)$$

with

$$G_R(j, k) = \frac{1}{K+2} [(A_2 + KA_3 + A_4) - (A_0 + KA_7 + A_6)] \quad (14.2-9b)$$

$$G_C(j, k) = \frac{1}{K+2} [(A_0 + KA_1 + A_2) - (A_6 + KA_5 + A_4)]. \quad (14.2-9c)$$

where  $K = 1$ . In this formulation, the row and column gradients are normalized to provide unit-gain positive and negative weighted averages about a separated edge position. The *Sobel operator* edge detector (3, p. 271) differs from the Prewitt edge detector in that the values of the north, south, east and west pixels are doubled (i.e.,  $K = 2$ ). The motivation for this weighting is to give equal importance to each pixel in terms of its contribution to the spatial gradient. Frei and Chen (4) have proposed north, south, east and west weightings by  $K = \sqrt{2}$  so that the gradient is the same for horizontal, vertical and diagonal edges. The edge gradient  $G(j, k)$  for these three

operators along a row through the single pixel transition vertical ramp edge model of Figure 14.1-3 is:

$$0 \quad 0 \quad \frac{h}{2} \quad h \quad \frac{h}{2} \quad 0 \quad 0$$

Along a row through the single transition pixel diagonal ramp edge model, the gradient is

$$0 \quad \frac{h}{\sqrt{2}(2+K)} \quad \frac{h}{\sqrt{2}} \quad \frac{\sqrt{2}(1+K)h}{2+K} \quad \frac{h}{\sqrt{2}} \quad \frac{h}{\sqrt{2}(2+K)} \quad 0$$

In the *Frei-Chen operator*, with  $K = \sqrt{2}$ , the edge gradient is the same at the edge center for the single-pixel transition vertical and diagonal ramp edge models. The Prewitt gradient for a diagonal edge is 0.94 times that of a vertical edge. The corresponding factor for a Sobel edge detector is 1.06. Consequently, the Prewitt operator is more sensitive to horizontal and vertical edges than to diagonal edges; the reverse is true for the Sobel operator. The gradients along a row through the smoothed transition diagonal ramp edge model are different for vertical and diagonal edges for all three of the  $3 \times 3$  edge detectors. None of them are able to localize the edge to a single pixel.

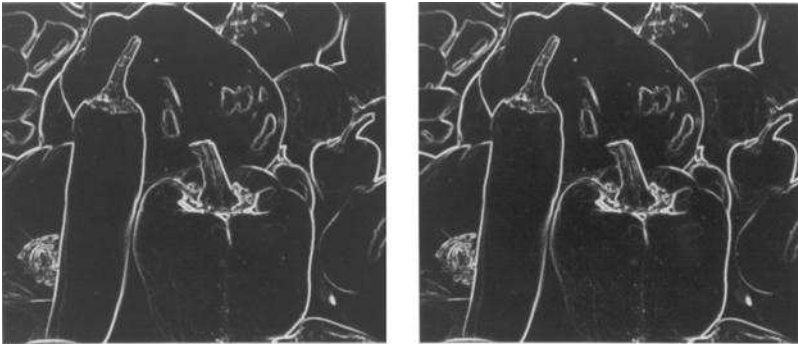
Figure 14.2-5 shows examples of the Prewitt, Sobel and Frei-Chen gradients of the peppers image. The reason that these operators visually appear to better delineate object edges than the Roberts operator is attributable to their larger size, which provides averaging of small luminance fluctuations.

The row and column gradients for all the edge detectors mentioned previously in this subsection involve a linear combination of pixels within a small neighborhood. Consequently, the row and column gradients can be computed by the convolution relationships

$$G_R(j, k) = F(j, k) \otimes H_R(j, k) \tag{14.2-10a}$$

$$G_C(j, k) = F(j, k) \otimes H_C(j, k) \tag{14.2-10b}$$

where  $H_R(j, k)$  and  $H_C(j, k)$  are  $3 \times 3$  row and column impulse response arrays, respectively, as defined in Figure 14.2-6. It should be noted that this specification of the gradient impulse response arrays takes into account the  $180^\circ$  rotation of an impulse response array inherent to the definition of convolution in Eq. 7.1-14.



(a) Prewitt

(b) Sobel



(c) Frei-Chen

**FIGURE 14.2-5.** Prewitt, Sobel and Frei–Chen gradients of the `peppers_mon` image.

**Large Neighborhood Gradient Operators.** A limitation common to the edge gradient generation operators previously defined is their inability to detect accurately edges in high-noise environments. This problem can be alleviated by properly extending the size of the neighborhood operators over which the differential gradients are computed. As an example, a Prewitt-type  $7 \times 7$  operator has a row gradient impulse response of the form

Operator	Row gradient	Column gradient
Pixel difference	$\begin{bmatrix} 0 & 0 & 0 \\ 0 & 1 & -1 \\ 0 & 0 & 0 \end{bmatrix}$	$\begin{bmatrix} 0 & -1 & 0 \\ 0 & 1 & 0 \\ 0 & 0 & 0 \end{bmatrix}$
Separated pixel difference	$\begin{bmatrix} 0 & 0 & 0 \\ 1 & 0 & -1 \\ 0 & 0 & 0 \end{bmatrix}$	$\begin{bmatrix} 0 & -1 & 0 \\ 0 & 0 & 0 \\ 0 & 1 & 0 \end{bmatrix}$
Roberts	$\begin{bmatrix} 0 & 0 & -1 \\ 0 & 1 & 0 \\ 0 & 0 & 0 \end{bmatrix}$	$\begin{bmatrix} -1 & 0 & 0 \\ 0 & 1 & 0 \\ 0 & 0 & 0 \end{bmatrix}$
Prewitt	$\frac{1}{3} \begin{bmatrix} 1 & 0 & -1 \\ 1 & 0 & -1 \\ 1 & 0 & -1 \end{bmatrix}$	$\frac{1}{3} \begin{bmatrix} -1 & -1 & -1 \\ 0 & 0 & 0 \\ 1 & 1 & 1 \end{bmatrix}$
Sobel	$\frac{1}{4} \begin{bmatrix} 1 & 0 & -1 \\ 2 & 0 & -2 \\ 1 & 0 & -1 \end{bmatrix}$	$\frac{1}{4} \begin{bmatrix} -1 & -2 & -1 \\ 0 & 0 & 0 \\ 1 & 2 & 1 \end{bmatrix}$
Frei-Chen	$\frac{1}{2 + \sqrt{2}} \begin{bmatrix} 1 & 0 & -1 \\ \sqrt{2} & 0 & -\sqrt{2} \\ 1 & 0 & -1 \end{bmatrix}$	$\frac{1}{2 + \sqrt{2}} \begin{bmatrix} -1 & -\sqrt{2} & -1 \\ 0 & 0 & 0 \\ 1 & \sqrt{2} & 1 \end{bmatrix}$

FIGURE 14.2-6. Impulse response arrays for 3 × 3 orthogonal differential gradient edge operators.

$$\mathbf{H}_R = \frac{1}{21} \begin{bmatrix} 1 & 1 & 1 & 0 & -1 & -1 & -1 \\ 1 & 1 & 1 & 0 & -1 & -1 & -1 \\ 1 & 1 & 1 & 0 & -1 & -1 & -1 \\ 1 & 1 & 1 & 0 & -1 & -1 & -1 \\ 1 & 1 & 1 & 0 & -1 & -1 & -1 \\ 1 & 1 & 1 & 0 & -1 & -1 & -1 \\ 1 & 1 & 1 & 0 & -1 & -1 & -1 \end{bmatrix} \quad (14.2-11)$$

An operator of this type is called a *boxcar operator*. Figure 14.2-7 presents the boxcar gradient of a 7 × 7 array.



(a) 7x7 boxcar



(b) 9x9 truncated pyramid

(c) 11x11 Argyle,  $s = 2.0$ (d) 11x11 Macleod,  $s = 2.0$ (e) 11x11 FDOG,  $s = 2.0$ 

**FIGURE 14.2-7.** Boxcar, truncated pyramid, Argyle, Macleod and FDOG gradients of the peppers\_mon image.

Abdou (5) has suggested a *truncated pyramid operator* that gives a linearly decreasing weighting to pixels away from the center of an edge. The row gradient impulse response array for a  $7 \times 7$  truncated pyramid operator is given by

$$\mathbf{H}_R = \frac{1}{34} \begin{bmatrix} 1 & 1 & 1 & 0 & -1 & -1 & -1 \\ 1 & 2 & 2 & 0 & -2 & -2 & -1 \\ 1 & 2 & 3 & 0 & -3 & -2 & -1 \\ 1 & 2 & 3 & 0 & -3 & -2 & -1 \\ 1 & 2 & 3 & 0 & -3 & -2 & -1 \\ 1 & 2 & 2 & 0 & -2 & -2 & -1 \\ 1 & 1 & 1 & 0 & -1 & -1 & -1 \end{bmatrix}. \tag{14.2-12}$$

Argyle (6) and Macleod (7,8) have proposed large neighborhood Gaussian-shaped weighting functions as a means of noise suppression. Let

$$g(x, s) = [2\pi s^2]^{-1/2} \exp\{-1/2(x/s)^2\} \tag{14.2-13}$$

denote a continuous domain Gaussian function with standard deviation  $s$ . Utilizing this notation, the *Argyle operator* horizontal coordinate impulse response array can be expressed as a sampled version of the continuous domain impulse response

$$H_R(j, k) = \begin{cases} -2g(x, s)g(y, t) & \text{for } x \geq 0 \\ 2g(x, s)g(y, t) & \text{for } x < 0 \end{cases} \tag{14.2-14a}$$

where  $s$  and  $t$  are spread parameters. The vertical impulse response function can be expressed similarly. The *Macleod operator* horizontal gradient impulse response function is given by

$$H_R(j, k) = [g(x + s, s) - g(x - s, s)]g(y, t). \tag{14.2-15}$$

The Argyle and Macleod operators, unlike the boxcar operator, give decreasing importance to pixels far removed from the center of the neighborhood. Figure 14.2-7 provides examples of the Argyle and Macleod gradients.

Extended-size differential gradient operators can be considered to be compound operators in which a smoothing operation is performed on a noisy image followed by a differentiation operation. The compound gradient impulse response can be written as

$$H(j, k) = H_G(j, k) \otimes H_S(j, k) \tag{14.2-16}$$

where  $H_G(j, k)$  is one of the gradient impulse response operators of Figure 14.2-6 and  $H_S(j, k)$  is a low-pass filter impulse response. For example, if  $H_S(j, k)$  is the  $3 \times 3$  Prewitt row gradient operator and  $H_S(j, k) = 1/9$ , for all  $(j, k)$ , is a  $3 \times 3$  uni-

form smoothing operator, the resultant  $5 \times 5$  row gradient operator, after normalization to unit positive and negative gain, becomes

$$\mathbf{H}_R = \frac{1}{18} \begin{bmatrix} 1 & 1 & 0 & -1 & -1 \\ 2 & 2 & 0 & -2 & -2 \\ 3 & 3 & 0 & -3 & -3 \\ 2 & 2 & 0 & -2 & -2 \\ 1 & 1 & 0 & -1 & -1 \end{bmatrix}. \tag{14.2-17}$$

The decomposition of Eq. 14.2-16 applies in both directions.

A well-known example of a compound gradient operator is the *first derivative of Gaussian* (FDOG) operator, in which Gaussian-shaped smoothing is followed by differentiation (9). The FDOG continuous domain horizontal impulse response is

$$H_R(j, k) = \frac{-\partial[g(x, s)g(y, t)]}{\partial x} \tag{14.2-18a}$$

which upon differentiation yields

$$H_R(j, k) = \frac{-xg(x, s)g(y, t)}{s^2} \tag{14.2-18b}$$

Figure 14.2-7e presents an example of the FDOG gradient.

**Canny Gradient Operators.** All of the differential edge enhancement operators presented previously in this subsection have been derived heuristically. Canny (9) has taken an analytic approach to the design of such operators. Canny's development is based on a one-dimensional continuous domain model of a step edge of amplitude  $s$  plus additive white Gaussian noise with standard deviation  $\sigma_n$ . It is assumed that edge detection is performed by convolving a one-dimensional continuous domain noisy edge signal  $f(x)$  with an anti-symmetric impulse response function  $h(x)$ , which is of zero amplitude outside the range  $[-W, W]$ . An edge is marked at the local maximum of the convolved gradient  $f(x) \otimes h(x)$ . The *Canny operator* continuous domain impulse response  $h(x)$  is chosen to satisfy the following three criteria.

1. *Good detection.* The amplitude signal-to-noise ratio (SNR) of the gradient is maximized to obtain a low probability of failure to mark real edge points and a low probability of falsely marking non-edge points. The SNR for the model is (9)

$$\text{SNR} = \frac{\left| \int_{-W}^W h(x)f(-x)dx \right|}{\sigma_n \sqrt{\int_{-W}^W [h(x)]^2 dx}} \tag{14.2-19a}$$



which reduces to (10)

$$SNR = \frac{s \int_{-W}^0 h(x) dx}{\sigma_n \int_{-W}^W [h(x)]^2 dx} \tag{14.2-19b}$$

- 2. *Good localization.* Edge points marked by the operator should be as close to the center of the edge as possible. The localization factor is defined as (9)

$$LOC = \frac{\left| \int_{-W}^W h'(x) f(-x) dx \right|}{\sigma_n \sqrt{\int_{-W}^W [h'(x)]^2 dx}} \tag{14.2-20a}$$

which reduces to (10)

$$LOC = \frac{s|h'(0)|}{\sigma_n \sqrt{\int_{-W}^W [h'(x)]^2 dx}} \tag{14.2-20b}$$

where  $h'(x)$  is the derivative of  $h(x)$ .

- 3. *Single response.* There should be only a single response to a true edge. The distance between peaks of the gradient when only noise is present, denoted as  $x_m$ , is set to some fraction  $k$  of the operator width factor  $W$ . Thus

$$x_m = kW \tag{14.2-21}$$

Canny has combined these three criteria by maximizing the product of SNR and LOC subject to the constraint of Eq. 14.2-21. Because of the complexity of the formulation, no analytic solution has been found, but a variational approach has been developed. Figure 14.2-8 contains plots of the Canny impulse response functions in terms of  $x_m$ . As noted from the figure, for low values of  $x_m$ , the Canny function resembles a boxcar function, while for  $x_m$  large, the Canny function is closely approximated by a FDOG impulse response function. Demigny and Kamle (10) have developed a discrete version of Canny’s three criteria.

Tagare and deFugueiredo (11) have questioned the validity of Canny’s approximations leading to the localization measure LOC of Eq. 14.2-20. Koplowitz and Greco (12) and Demigny and Kamle (10) have also investigated the accuracy of the Canny localization measure. Tagare and deFugueiredo (11) have derived the following localization measure.

$$L = \frac{\int_{-W}^W x^2 [h(x)]^2 dx}{\int_{-W}^W [h'(x)]^2 dx} \tag{14.2-22}$$

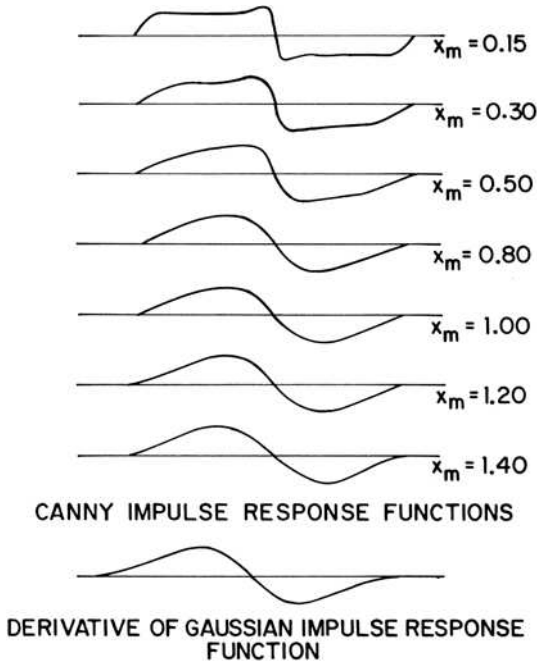


**FIGURE 14.2-8.** Comparison of Canny and first derivative of Gaussian impulse response functions.

Using this measure, they have determined that the first derivative of Gaussian impulse response function is optimal for gradient edge detection of step edges.

There have been a number of extensions of Canny's concept of edge detection. Bao, Zhang and Wu (13) have used Canny's impulse response functions at two or more scale factors, and then formed products of the resulting gradients before thresholding. They found that this approach improved edge localization with only a small loss in detection capability. Petrou and Kittler (14) have applied Canny's methodology to the detection of ramp edges. Demigny (15) has developed discrete impulse response function versions of Canny's detection and localization criteria for the detection of pulse edges.

Discrete domain versions of the large operators defined in the continuous domain can be obtained by sampling their continuous impulse response functions over some  $W \times W$  window. The window size should be chosen sufficiently large that truncation of the impulse response function does not cause high-frequency artifacts.

**14.2.2. Edge Template Gradient Generation**

With the orthogonal differential edge enhancement techniques discussed previously, edge gradients are computed in two orthogonal directions, usually along rows and columns, and then the edge direction is inferred by computing the vector sum of the gradients. Another approach is to compute gradients in a large number of directions by convolution of an image with a set of template gradient impulse response arrays. The edge template gradient is defined as

$$G(j, k) = \text{MAX}\{|G_1(j, k)|, \dots, |G_m(j, k)|, \dots, |G_M(j, k)|\} \quad (14.2-22a)$$

where

$$G_m(j, k) = F(j, k) \otimes H_m(j, k) \quad (14.2-22b)$$

is the gradient in the  $m$ th equi-spaced direction obtained by convolving an image with a gradient impulse response array  $H_m(j, k)$ . The edge angle is determined by the direction of the largest gradient.

Figure 14.2-9 defines eight gain-normalized compass gradient impulse response arrays suggested by Prewitt (1, p. 111). The compass names indicate the slope direction of maximum response. Kirsch (16) has proposed a directional gradient defined by

$$G(j, k) = \text{MAX}_{i=0}^7 \left\{ \left| 5S_i - 3T_i \right| \right\} \quad (14.2-23a)$$

where

$$S_i = A_i + A_{i+1} + A_{i+2} \quad (14.2-23b)$$

$$T_i = A_{i+3} + A_{i+4} + A_{i+5} + A_{i+5} + A_{i+6} \quad (14.2-23c)$$

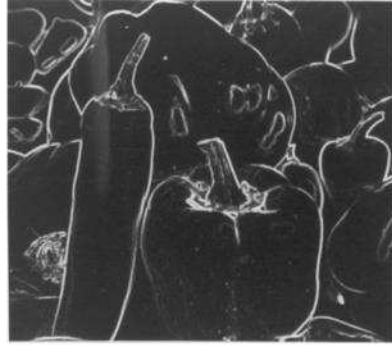
The subscripts of  $A_i$  are evaluated modulo 8. It is possible to compute the Kirsch gradient by convolution as in Eq. 14.2-22b. Figure 14.2-9 specifies the gain-normalized *Kirsch operator* impulse response arrays. This figure also defines two other sets of gain-normalized impulse response arrays proposed by Robinson (17), called the *Robinson three-level operator* and the *Robinson five-level operator*, which are derived from the Prewitt and Sobel operators, respectively. Figure 14.2-10 provides a comparison of the edge gradients of the peppers image for the four  $3 \times 3$  template gradient operators.

Gradient direction	Prewitt compass gradient	Kirsch	Robinson 3-level	Robinson 5-level
East $H_1$	$\begin{bmatrix} 1 & 1 & -1 \\ 1 & -2 & -1 \\ 1 & 1 & -1 \end{bmatrix}$	$\begin{bmatrix} 5 & -3 & -3 \\ 5 & 0 & -3 \\ 5 & -3 & -3 \end{bmatrix}$	$\begin{bmatrix} 1 & 0 & -1 \\ 1 & 0 & -1 \\ 1 & 0 & -1 \end{bmatrix}$	$\begin{bmatrix} 1 & 0 & -1 \\ 2 & 0 & -2 \\ 1 & 0 & -1 \end{bmatrix}$
Northeast $H_2$	$\begin{bmatrix} 1 & -1 & -1 \\ 1 & -2 & -1 \\ 1 & 1 & 1 \end{bmatrix}$	$\begin{bmatrix} -3 & -3 & -3 \\ 5 & 0 & -3 \\ 5 & 5 & -3 \end{bmatrix}$	$\begin{bmatrix} 0 & -1 & -1 \\ 1 & 0 & -1 \\ 1 & 1 & 0 \end{bmatrix}$	$\begin{bmatrix} 0 & -1 & -2 \\ 1 & 0 & -1 \\ 2 & 1 & 0 \end{bmatrix}$
North $H_3$	$\begin{bmatrix} -1 & -1 & -1 \\ 1 & -2 & 1 \\ 1 & 1 & 1 \end{bmatrix}$	$\begin{bmatrix} -3 & -3 & -3 \\ -3 & 0 & -3 \\ 5 & 5 & 5 \end{bmatrix}$	$\begin{bmatrix} -1 & -1 & -1 \\ 0 & 0 & 0 \\ 1 & 1 & 1 \end{bmatrix}$	$\begin{bmatrix} -1 & -2 & -1 \\ 0 & 0 & 0 \\ 1 & 2 & 1 \end{bmatrix}$
Northwest $H_4$	$\begin{bmatrix} -1 & -1 & 1 \\ -1 & -2 & 1 \\ 1 & 1 & 1 \end{bmatrix}$	$\begin{bmatrix} -3 & -3 & -3 \\ -3 & 0 & 5 \\ -3 & 5 & 5 \end{bmatrix}$	$\begin{bmatrix} -1 & -1 & 0 \\ -1 & 0 & 1 \\ 0 & 1 & 1 \end{bmatrix}$	$\begin{bmatrix} -2 & -1 & 0 \\ -1 & 0 & 1 \\ 0 & 1 & 2 \end{bmatrix}$
West $H_5$	$\begin{bmatrix} -1 & 1 & 1 \\ -1 & -2 & 1 \\ -1 & 1 & 1 \end{bmatrix}$	$\begin{bmatrix} -3 & -3 & 5 \\ -3 & 0 & 5 \\ -3 & -3 & 5 \end{bmatrix}$	$\begin{bmatrix} -1 & 0 & 1 \\ -1 & 0 & 1 \\ -1 & 0 & 1 \end{bmatrix}$	$\begin{bmatrix} -1 & 0 & 1 \\ -2 & 0 & 2 \\ -1 & 0 & 1 \end{bmatrix}$
Southwest $H_6$	$\begin{bmatrix} 1 & 1 & 1 \\ -1 & -2 & 1 \\ -1 & -1 & 1 \end{bmatrix}$	$\begin{bmatrix} -3 & 5 & 5 \\ -3 & 0 & 5 \\ -3 & -3 & -3 \end{bmatrix}$	$\begin{bmatrix} 0 & 1 & 1 \\ -1 & 0 & 1 \\ -1 & -1 & 0 \end{bmatrix}$	$\begin{bmatrix} 0 & 1 & 2 \\ -1 & 0 & 1 \\ -2 & -1 & 0 \end{bmatrix}$
South $H_7$	$\begin{bmatrix} 1 & 1 & 1 \\ 1 & -2 & 1 \\ -1 & -1 & -1 \end{bmatrix}$	$\begin{bmatrix} 5 & 5 & 5 \\ -3 & 0 & -3 \\ -3 & -3 & -3 \end{bmatrix}$	$\begin{bmatrix} 1 & 1 & 1 \\ 0 & 0 & 0 \\ -1 & -1 & -1 \end{bmatrix}$	$\begin{bmatrix} 1 & 2 & 1 \\ 0 & 0 & 0 \\ -1 & -2 & -1 \end{bmatrix}$
Southeast $H_8$	$\begin{bmatrix} 1 & 1 & 1 \\ 1 & -2 & -1 \\ 1 & -1 & -1 \end{bmatrix}$	$\begin{bmatrix} 5 & 5 & -3 \\ 5 & 0 & -3 \\ -3 & -3 & -3 \end{bmatrix}$	$\begin{bmatrix} 1 & 1 & 0 \\ 1 & 0 & -1 \\ 0 & -1 & -1 \end{bmatrix}$	$\begin{bmatrix} 2 & 1 & 0 \\ 1 & 0 & -1 \\ 0 & -1 & -2 \end{bmatrix}$
Scale factor	$\frac{1}{5}$	$\frac{1}{15}$	$\frac{1}{3}$	$\frac{1}{4}$

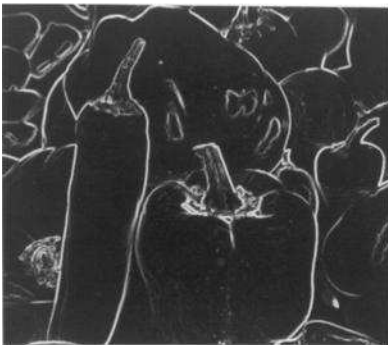
FIGURE 14.2-9. Template gradient 3 x 3 impulse response arrays.



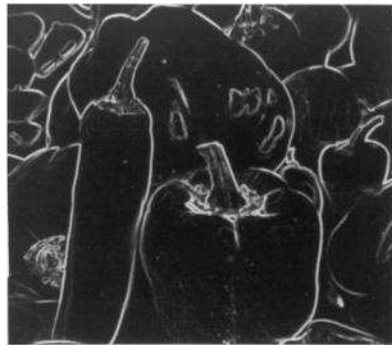
(a) Prewitt compass gradient



(b) Kirsch



(c) Robinson three-level



(d) Robinson five-level

**FIGURE 14.2-10.**  $3 \times 3$  template gradients of the peppers\_mon image.

Nevatia and Babu (18) have developed an edge detection technique in which the gain-normalized  $5 \times 5$  masks defined in Figure 14.2-11 are utilized to detect edges in  $30^\circ$  increments. Figure 14.2-12 shows the template gradients for the peppers image. Larger template masks will provide both a finer quantization of the edge orientation angle and a greater noise immunity, but the computational requirements increase. Paplinski (19) has developed a design procedure for  $n$ -directional template masks of arbitrary size.

### 14.2.3. Threshold Selection

After the edge gradient is formed for the differential edge detection methods, the gradient is compared to a threshold to determine if an edge exists. The threshold value determines the sensitivity of the edge detector. For noise-free images, the

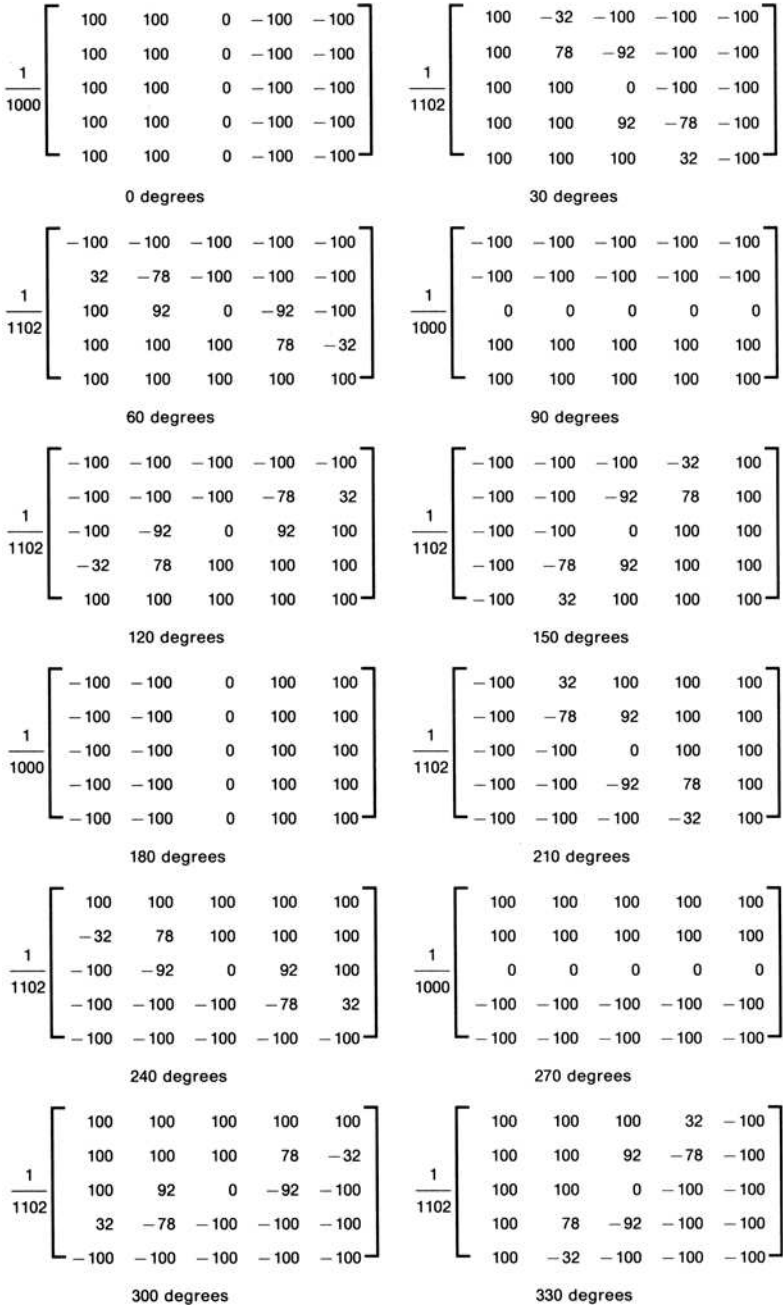


FIGURE 14.2-11. Nevatia-Babu template gradient impulse response arrays.



FIGURE 14.2-12. Nevatia-Babu gradient of the peppers\_mon image.

threshold can be chosen such that all amplitude discontinuities of a minimum contrast level are detected as *edges*, and all others are called *non-edges*. With noisy images, threshold selection becomes a trade-off between missing valid edges and creating noise-induced false edges.

Edge detection can be regarded as a hypothesis-testing problem to determine if an image region contains an edge or contains no edge (20). Let  $P(\text{edge})$  and  $P(\text{no-edge})$  denote the a priori probabilities of these events. Then the edge detection process can be characterized by the probability of correct edge detection,

$$P_D = \int_t^\infty p(G|\text{edge}) dG \tag{14.2-24a}$$

and the probability of false detection,

$$P_F = \int_t^\infty p(G|\text{no-edge}) dG \tag{14.2-24b}$$

where  $t$  is the edge detection threshold and  $p(G|\text{edge})$  and  $p(G|\text{no-edge})$  are the conditional probability densities of the edge gradient  $G(j, k)$ . Figure 14.2-13 is a sketch of typical edge gradient conditional densities. The probability of edge misclassification error can be expressed as

$$P_E = (1 - P_D)P(\text{edge}) + (P_F)P(\text{no-edge}) \tag{14.2-25}$$

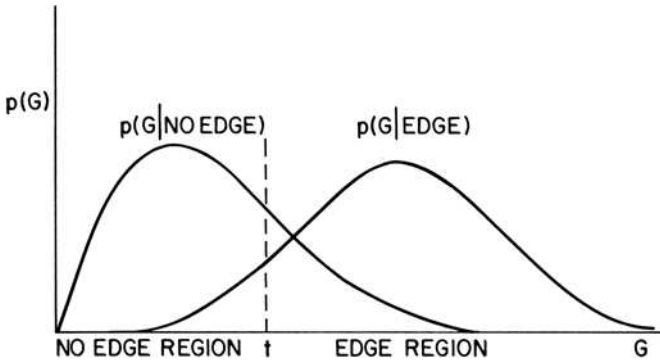


FIGURE 14.2-13. Typical edge gradient conditional probability densities.

This error will be minimum if the threshold is chosen such that an edge is deemed present when

$$\frac{p(G|\text{edge})}{p(G|\text{no-edge})} \geq \frac{P(\text{no-edge})}{P(\text{edge})} \quad (14.2-26)$$

and the no-edge hypothesis is accepted otherwise. Equation 14.2-26 defines the well-known *maximum likelihood ratio* test associated with the *Bayes minimum error* decision rule of classical decision theory (21). Another common decision strategy, called the *Neyman-Pearson test*, is to choose the threshold  $t$  to minimize  $P_F$  for a fixed acceptable  $P_D$  (21).

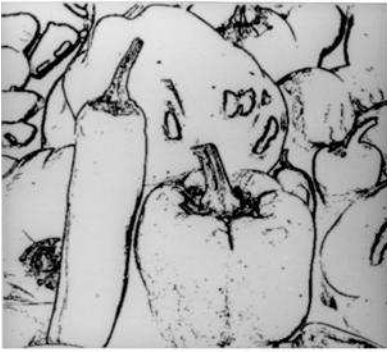
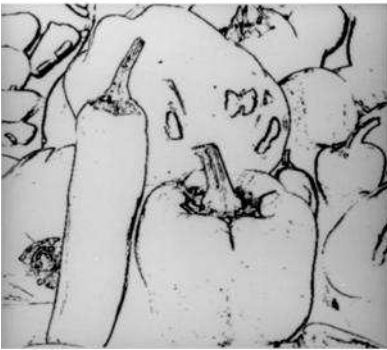
Application of a statistical decision rule to determine the threshold value requires knowledge of the a priori edge probabilities and the conditional densities of the edge gradient. The a priori probabilities can be estimated from images of the class under analysis. Alternatively, the a priori probability ratio can be regarded as a sensitivity control factor for the edge detector. The conditional densities can be determined, in principle, for a statistical model of an ideal edge plus noise. Abdou (5) has derived these densities for  $2 \times 2$  and  $3 \times 3$  edge detection operators for the case of a ramp edge of width  $w = 1$  and additive Gaussian noise. Henstock and Chelberg (22) have used gamma densities as models of the conditional probability densities.

There are two difficulties associated with the statistical approach of determining the optimum edge detector threshold: reliability of the stochastic edge model and analytic difficulties in deriving the edge gradient conditional densities. Another approach, developed by Abdou and Pratt (5,20), which is based on pattern recognition techniques, avoids the difficulties of the statistical method. The pattern recognition method involves creation of a large number of prototype noisy image regions, some of which contain edges and some without edges. These prototypes are then used as a training set to find the threshold that minimizes the classification error. Details of the design procedure are found in Reference 5.



**TABLE 14.2-1. Threshold Levels and Associated Edge Detection Probabilities for  $3 \times 3$  Edge Detectors as Determined by the Abdou and Pratt Pattern Recognition Design Procedure**

Operator	Vertical Edge						Diagonal Edge					
	SNR = 1			SNR = 10			SNR = 1			SNR = 10		
	$t_N$	$P_D$	$P_F$	$t_N$	$P_D$	$P_F$	$t_N$	$P_D$	$P_F$	$t_N$	$P_D$	$P_F$
Roberts orthogonal gradient	1.36	0.559	0.400	0.67	0.892	0.105	1.74	0.551	0.469	0.78	0.778	0.221
Prewitt orthogonal gradient	1.16	0.608	0.384	0.66	0.912	0.480	1.19	0.593	0.387	0.64	0.931	0.064
Sobel orthogonal gradient	1.18	0.600	0.395	0.66	0.923	0.057	1.14	0.604	0.376	0.63	0.947	0.053
Prewitt compass template gradient	1.52	0.613	0.466	0.73	0.886	0.136	1.51	0.618	0.472	0.71	0.900	0.153
Kirsch template gradient	1.43	0.531	0.341	0.69	0.898	0.058	1.45	0.524	0.324	0.79	0.825	0.023
Robinson three-level template gradient	1.16	0.590	0.369	0.65	0.926	0.038	1.16	0.587	0.365	0.61	0.946	0.056
Robinson five-level template gradient	1.24	0.581	0.361	0.66	0.924	0.049	1.22	0.593	0.374	0.65	0.931	0.054

(a) Sobel,  $t = 0.06$ (b) FDOG,  $t = 0.08$ (c) Sobel,  $t = 0.08$ (d) FDOG,  $t = 0.10$ (e) Sobel,  $t = 0.10$ (f) FDOG,  $t = 0.12$ 

**FIGURE 14.2-14.** Edge map threshold sensitivity of the Sobel and first derivative of Gaussian edge detectors for the `peppers_mon` image.

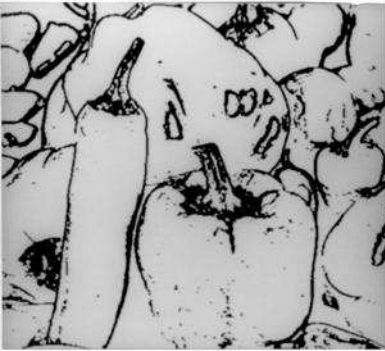
Table 14.2-1 provides a tabulation of the optimum threshold for several  $2 \times 2$  and  $3 \times 3$  edge detectors for an experimental design with an evaluation set of 250 prototypes not in the training set (20). The table also lists the probability of correct and false edge detection as defined by Eq. 14.2-24 for theoretically derived gradient conditional densities. In the table, the threshold is normalized such that  $t_N = t/G_M$ , where  $G_M$  is the maximum amplitude of the gradient in the absence of noise. The power signal-to-noise ratio is defined as  $SNR = (h/\sigma_n)^2$  where  $h$  is the edge height and  $\sigma_n$  is the noise standard deviation. In most of the cases of Table 14.2-1, the optimum threshold results in approximately equal error probabilities (i.e.,  $P_F = 1 - P_D$ ). This is the same result that would be obtained by the Bayes design procedure when edges and non-edges are equally probable. The tests associated with Table 14.2-1 were conducted with relatively low signal-to-noise ratio images. Section 14.5 provides examples of such images. For high signal-to-noise ratio images, the optimum threshold is much lower. As a rule of thumb, under the condition that  $P_F = 1 - P_D$ , the edge detection threshold can be scaled linearly with signal-to-noise ratio. Hence, for an image with  $SNR = 100$ , the threshold is about 10% of the peak gradient value.

Figure 14.2-14 shows the edge map generation threshold sensitivity for the  $3 \times 3$  Sobel and the  $11 \times 11$  FDOG edge detectors for the peppers image, which is a relatively high signal-to-noise ratio image. For both edge detectors, variation of the threshold provides a trade-off between delineation of strong edges and definition of weak edges.

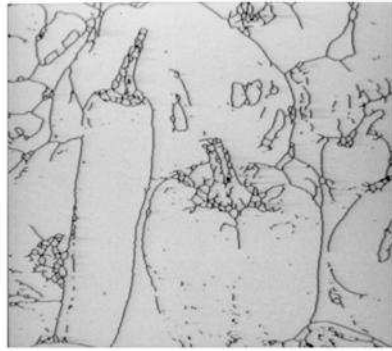
The threshold selection techniques described in this subsection are spatially invariant. Rakesh et al. (23) have proposed a spatially adaptive threshold selection method in which the threshold at each pixel depends upon the statistical variability of the row and column gradients. They report improved performance with a variety of non-adaptive edge detectors.

#### 14.2.4. Morphological Post Processing

It is possible to improve edge delineation of first-derivative edge detectors by applying morphological operations on their edge maps. Figure 14.2-15 provides examples for the  $3 \times 3$  Sobel and  $11 \times 11$  FDOG edge detectors. In the Sobel example, the threshold is lowered slightly to improve the detection of weak edges. Then the morphological majority black operation is performed on the edge map to eliminate noise-induced edges. This is followed by the thinning operation to thin the edges to minimally connected lines. In the FDOG example, the majority black noise smoothing step is not necessary.

(a) Sobel,  $t = 0.07$ 

(b) Sobel majority black



(c) Sobel thinned

(d) FDOG,  $t = 0.11$ 

(e) FDOG thinned

**FIGURE 14.2-15.** Morphological thinning of edge maps for the peppers\_mon image.

### 14.3. SECOND-ORDER DERIVATIVE EDGE DETECTION

Second-order derivative edge detection techniques employ some form of spatial second-order differentiation to accentuate edges. An edge is marked if a significant spatial change occurs in the second derivative. Two types of second-order derivative methods are considered: Laplacian and directed second derivative.

#### 14.3.1. Laplacian Generation

The edge Laplacian of an image function  $F(x, y)$  in the continuous domain is defined as

$$G(x, y) = -\nabla^2\{F(x, y)\} \tag{14.3-1a}$$

where, from Eq. 1.2-17, the *Laplacian* is

$$\nabla^2 = \frac{\partial^2}{\partial x^2} + \frac{\partial^2}{\partial y^2}. \tag{14.3-1b}$$

The Laplacian  $G(x, y)$  is zero if  $F(x, y)$  is constant or changing linearly in amplitude. If the rate of change of  $F(x, y)$  is greater than linear,  $G(x, y)$  exhibits a sign change at the point of inflection of  $F(x, y)$ . The zero crossing of  $G(x, y)$  indicates the presence of an edge. The negative sign in the definition of Eq. 14.3-1a is present so that the zero crossing of  $G(x, y)$  has a positive slope for an edge whose amplitude increases from left to right or bottom to top in an image.

Torre and Poggio (24) have investigated the mathematical properties of the Laplacian of an image function. They have found that if  $F(x, y)$  meets certain smoothness constraints, the zero crossings of  $G(x, y)$  are closed curves.

In the discrete domain, the simplest approximation to the continuous Laplacian is to compute the difference of slopes along each axis:

$$G(j, k) = [F(j, k) - F(j - 1, k)] - [F(j + 1, k) - F(j, k)] \\ + [F(j, k) - F(j, k + 1)] - [F(j, k - 1) - F(j, k)]. \tag{14.3-2}$$

This four-neighbor Laplacian (1, p. 111) can be generated by the convolution operation

$$G(j, k) = F(j, k) \otimes H(j, k) \tag{14.3-3}$$

with

$$\mathbf{H} = \begin{bmatrix} 0 & 0 & 0 \\ -1 & 2 & -1 \\ 0 & 0 & 0 \end{bmatrix} + \begin{bmatrix} 0 & -1 & 0 \\ 0 & 2 & 0 \\ 0 & -1 & 0 \end{bmatrix} \tag{14.3-4a}$$

or

$$\mathbf{H} = \begin{bmatrix} 0 & -1 & 0 \\ -1 & 4 & -1 \\ 0 & -1 & 0 \end{bmatrix} \quad (14.3-4b)$$

where the two arrays of Eq. 14.3-4a correspond to the second derivatives along image rows and columns, respectively, as in the continuous Laplacian of Eq. 14.3-1b. The four-neighbor Laplacian is often normalized to provide unit-gain averages of the positive weighted and negative weighted pixels in the  $3 \times 3$  pixel neighborhood. The gain-normalized four-neighbor Laplacian impulse response is defined by

$$\mathbf{H} = \frac{1}{4} \begin{bmatrix} 0 & -1 & 0 \\ -1 & 4 & -1 \\ 0 & -1 & 0 \end{bmatrix}. \quad (14.3-5)$$

Prewitt (1, p. 111) has suggested an eight-neighbor Laplacian defined by the gain-normalized impulse response array

$$\mathbf{H} = \frac{1}{8} \begin{bmatrix} -1 & -1 & -1 \\ -1 & 8 & -1 \\ -1 & -1 & -1 \end{bmatrix}. \quad (14.3-6)$$

This array is not separable into a sum of second derivatives, as in Eq. 14.3-4a. A separable eight-neighbor Laplacian can be obtained by the construction

$$\mathbf{H} = \begin{bmatrix} -1 & 2 & -1 \\ -1 & 2 & -1 \\ -1 & 2 & -1 \end{bmatrix} + \begin{bmatrix} -1 & -1 & -1 \\ 2 & 2 & 2 \\ -1 & -1 & -1 \end{bmatrix} \quad (14.3-7)$$

in which the difference of slopes is averaged over three rows and three columns. The gain-normalized version of the separable eight-neighbor Laplacian is given by

$$\mathbf{H} = \frac{1}{8} \begin{bmatrix} -2 & 1 & -2 \\ 1 & 4 & 1 \\ -2 & 1 & -2 \end{bmatrix}. \quad (14.3-8)$$

It is instructive to examine the Laplacian response to the edge models of Figure 14.1-3. As an example, the separable eight-neighbor Laplacian corresponding to the center row of the vertical step edge model is

$$0 \quad \frac{-3h}{8} \quad \frac{3h}{8} \quad 0$$

where  $h = b - a$  is the edge height. The Laplacian response of the vertical ramp edge model is

$$0 \quad \frac{-3h}{16} \quad 0 \quad \frac{3h}{16} \quad 0$$

For the vertical edge ramp edge model, the edge lies at the zero crossing pixel between the negative- and positive-value Laplacian responses. In the case of the step edge, the zero crossing lies midway between the neighboring negative and positive response pixels; the edge is correctly marked at the pixel to the right of the zero crossing. The Laplacian response for a single-transition-pixel diagonal ramp edge model is

$$0 \quad \frac{-h}{8} \quad \frac{-h}{8} \quad 0 \quad \frac{h}{8} \quad \frac{h}{8} \quad 0$$

and the edge lies at the zero crossing at the center pixel. The Laplacian response for the smoothed transition diagonal ramp edge model of Figure 14.1-3 is

$$0 \quad \frac{-h}{16} \quad \frac{-h}{8} \quad \frac{-h}{16} \quad \frac{h}{16} \quad \frac{h}{8} \quad \frac{h}{16} \quad 0$$

In this example, the zero crossing does not occur at a pixel location. The edge should be marked at the pixel to the right of the zero crossing. Figure 14.3-1 shows the Laplacian response for the two ramp corner edge models of Figure 14.1-3. The edge transition pixels are indicated by line segments in the figure. A zero crossing exists at the edge corner for the smoothed transition edge model, but not for the single-pixel transition model. The zero crossings adjacent to the edge corner do not occur at pixel samples for either of the edge models. From these examples, it can be concluded that zero crossings of the Laplacian do not always occur at pixel samples. But for these edge models, marking an edge at a pixel with a positive response that has a neighbor with a negative response identifies the edge correctly.

Figure 14.3-2 shows the Laplacian responses of the peppers image for the three types of  $3 \times 3$  Laplacians. In these photographs, negative values are depicted as dimmer than mid gray and positive values are brighter than mid gray.

Marr and Hildrith (25) have proposed the *Laplacian of Gaussian* (LOG) edge detection operator in which Gaussian-shaped smoothing is performed prior to application of the Laplacian. The continuous domain LOG gradient is

$$G(x, y) = -\nabla^2 \{ F(x, y) \otimes H_S(x, y) \} \tag{14.3-9a}$$

where

$$G(x, y) = g(x, s)g(y, s). \tag{14.3-9b}$$

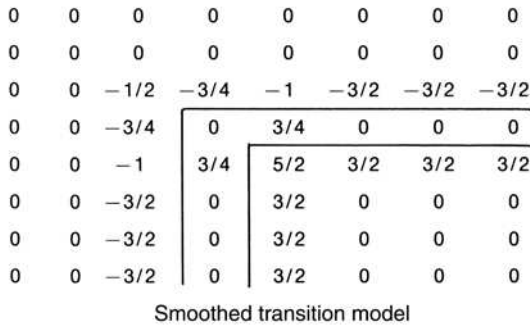
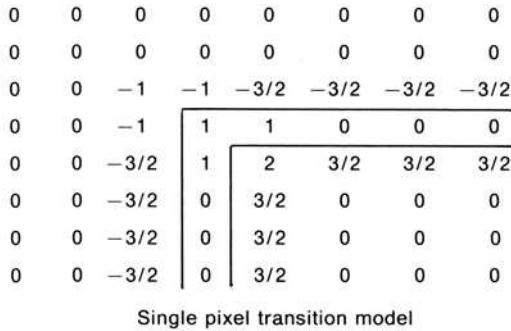


**FIGURE 14.3-1.** Separable eight-neighbor Laplacian responses for ramp corner models; all values should be scaled by  $h/8$ .

is the impulse response of the Gaussian smoothing function as defined by Eq. 14.2-13. As a result of the linearity of the second derivative operation and of the linearity of convolution, it is possible to express the LOG response as

$$G(j, k) = F(j, k) \otimes H(j, k) \tag{14.3-10a}$$

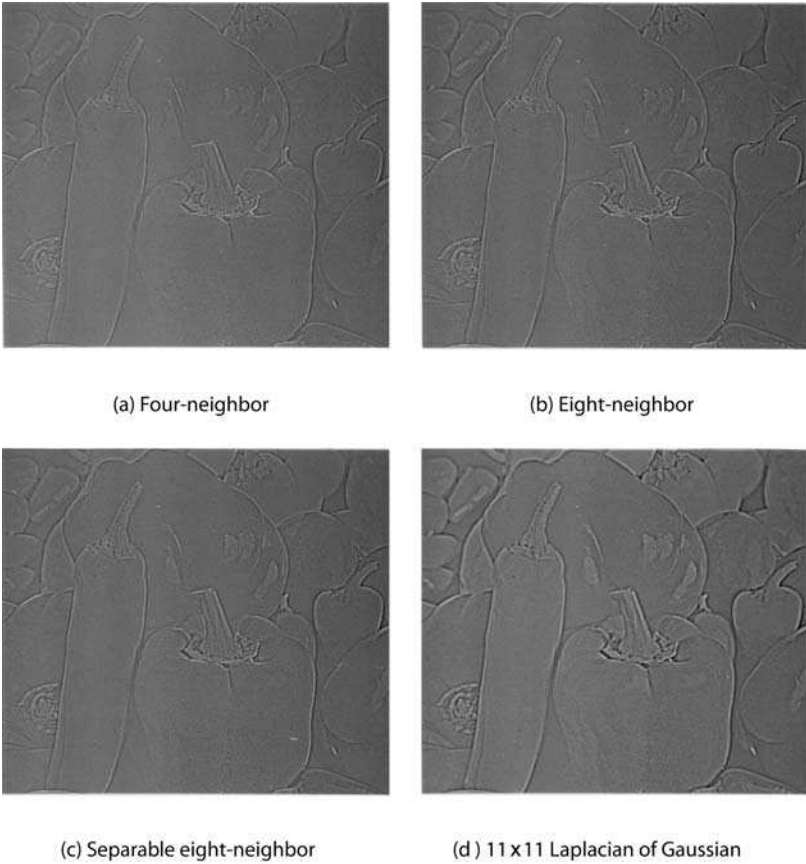
where

$$H(x, y) = -\nabla^2\{g(x, s)g(y, s)\}. \tag{14.3-10b}$$

Upon differentiation, one obtains

$$H(x, y) = \frac{1}{\pi s^4} \left( 1 - \frac{x^2 + y^2}{2s^2} \right) \exp \left\{ -\frac{x^2 + y^2}{2s^2} \right\}. \tag{14.3-11}$$





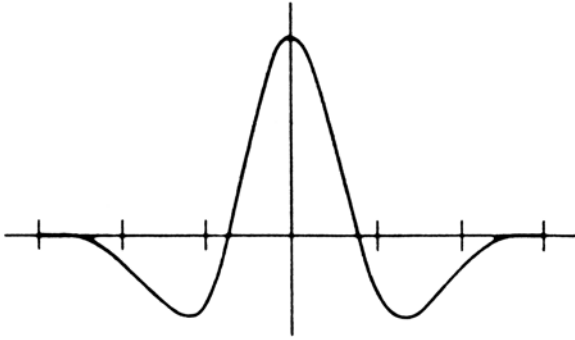
**FIGURE 14.3-2.** Laplacian responses of the peppers\_mon image.

Figure 14.3-3 is a cross-sectional view of the LOG continuous domain impulse response. In the literature, it is often called the *Mexican hat filter*. It can be shown (26,27) that the LOG impulse response can be expressed as

$$H(x, y) = \frac{1}{\pi s^2} \left( 1 - \frac{y^2}{s^2} \right) g(x, s)g(y, s) + \frac{1}{\pi s^2} \left( 1 - \frac{x^2}{s^2} \right) g(x, s)g(y, s) \quad .(14.3-12)$$

Consequently, the convolution operation can be computed separably along rows and columns of an image. It is possible to approximate the LOG impulse response closely by a *difference of Gaussians* (DOG) operator. The resultant impulse response is

$$H(x, y) = g(x, s_1)g(y, s_1) - g(x, s_2)g(y, s_2) \quad .(14.3-13)$$



**FIGURE 14.3-3.** Cross section of continuous domain Laplacian of Gaussian impulse response.

where  $s_1 < s_2$ . Marr and Hildrith (25) have found that the ratio  $s_2/s_1 = 1.6$  provides a good approximation to the LOG.

A discrete domain version of the LOG operator can be obtained by sampling the continuous domain impulse response function of Eq. 14.3-11 over a  $W \times W$  window. To avoid deleterious truncation effects, the size of the array should be set such that  $W = 3c$ , or greater, where  $c = 2\sqrt{2}s$  is the width of the positive center lobe of the LOG function (27). Figure 14.3-2d shows the LOG response of the peppers image for a  $11 \times 11$  operator.

### 14.3.2. Laplacian Zero-Crossing Detection

From the discrete domain Laplacian response examples of the preceding section, it has been shown that zero crossings do not always lie at pixel sample points. In fact, for real images subject to luminance fluctuations that contain ramp edges of varying slope, zero-valued Laplacian response pixels are unlikely.

A simple approach to Laplacian zero-crossing detection in discrete domain images is to form the maximum of all positive Laplacian responses and to form the minimum of all negative-value responses in a  $3 \times 3$  window. If the magnitude of the difference between the maxima and the minima exceeds a threshold, an edge is judged present.

Huertas and Medioni (27) have developed a systematic method for classifying  $3 \times 3$  Laplacian response patterns in order to determine edge direction. Figure 14.3-4 illustrates a somewhat simpler algorithm. In the figure, plus signs denote positive-value Laplacian responses, and negative signs denote negative Laplacian responses. The algorithm can be implemented efficiently using morphological image processing techniques.

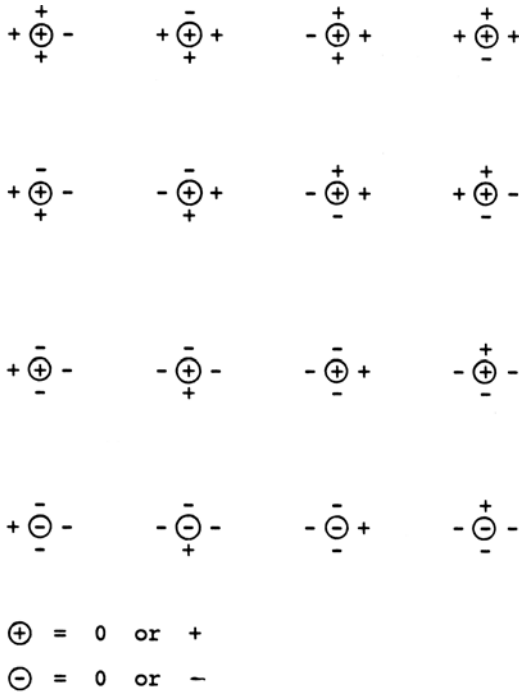


FIGURE 14.3-4. Laplacian zero-crossing patterns.

### 14.3.3. Directed Second-Order Derivative Generation

Laplacian edge detection techniques employ rotationally invariant second-order differentiation to determine the existence of an edge. The direction of the edge can be ascertained during the zero-crossing detection process. An alternative approach is first to estimate the edge direction and then compute the one-dimensional second-order derivative along the edge direction. A zero crossing of the second-order derivative specifies an edge.

The directed second-order derivative of a continuous domain image  $F(x, y)$  along a line at an angle  $\theta$  with respect to the horizontal axis is given by

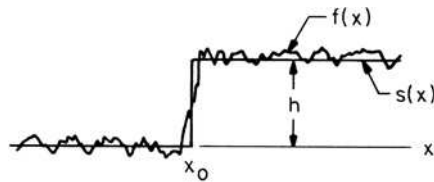
$$F''(x, y) = \frac{\partial^2 F(x, y)}{\partial x^2} \cos^2 \theta + \frac{\partial^2 F(x, y)}{\partial x \partial y} \cos \theta \sin \theta + \frac{\partial^2 F(x, y)}{\partial y^2} \sin^2 \theta. \quad (14.3-14)$$

It should be noted that, unlike the Laplacian, the directed second-order derivative is a nonlinear operator. Convoluting a smoothing function with  $F(x, y)$  prior to differentiation is not equivalent to convoluting the directed second derivative of  $F(x, y)$  with the smoothing function.

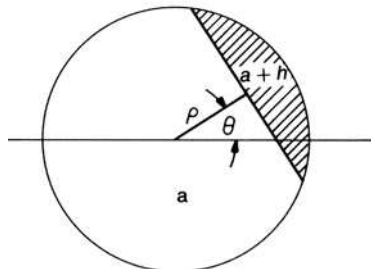
A key factor in the utilization of the directed second-order derivative edge detection method is the ability to determine its suspected edge direction accurately. One approach is to employ some first-order derivative edge detection method to estimate the edge direction, and then compute a discrete approximation to Eq. 14.3-14. Another approach, proposed by Haralick (28), called *facet modeling*, involves approximating  $F(x, y)$  by a two-dimensional *Chebyshev polynomial*, from which the directed second-order derivative can be determined analytically. Pratt(4Ed., 500-506) describes this technique.

#### 14.4. EDGE-FITTING EDGE DETECTION

Ideal edges may be viewed as one- or two-dimensional edges of the form sketched in Figure 14.1-1. Actual image data can then be matched against, or fitted to, the ideal edge models. If the fit is sufficiently accurate at a given image location, an edge is assumed to exist with the same parameters as those of the ideal edge model.



(a) One dimensional



(b) Two dimensional

**FIGURE 14.4-1.** One- and two-dimensional edge fitting.

In the one-dimensional edge-fitting case described in Figure 14.4-1, the image signal  $f(x)$  is fitted to a step function

$$s(x) = \begin{cases} a & \text{for } x < x_0 \\ a + h & \text{for } x \geq x_0. \end{cases} \tag{14.4-1a}$$

$$\tag{14.4-1b}$$

An edge is assumed present if the mean-square error

$$\mathcal{E} = \int_{x_0-L}^{x_0+L} [f(x) - s(x)]^2 dx \tag{14.4-2}$$

is below some threshold value. In the two-dimensional formulation, the ideal step edge is defined as

$$s(x) = \begin{cases} a & \text{for } x \cos \theta + y \sin \theta < \rho \\ a + h & \text{for } x \cos \theta + y \sin \theta \geq \rho \end{cases} \tag{14.4-3a}$$

$$\tag{14.4-3b}$$

where  $\theta$  and  $\rho$  jointly specify the polar distance from the center of a circular test region to the normal point of the edge. The edge-fitting error is

$$\mathcal{E} = \iint [F(x, y) - S(x, y)]^2 dx dy \tag{14.4-4}$$

where the integration is over the circle in Figure 14.4-1.

Hueckel (29) has developed a procedure for two-dimensional edge fitting in which the pixels within the circle of Figure 14.4-1 are expanded in a set of two-dimensional basis functions by a Fourier series in polar coordinates. Let  $B_i(x, y)$  represent the basis functions. Then, the weighting coefficients for the expansions of the image and the ideal step edge become

$$f_i = \iint B_i(x, y) F(x, y) dx dy \tag{14.4-5a}$$

$$s_i = \iint B_i(x, y) S(x, y) dx dy. \tag{14.4-5b}$$

In Hueckel's algorithm, the expansion is truncated to eight terms for computational economy and to provide some noise smoothing. Minimization of the mean-square-error difference of Eq. 14.4-4 is equivalent to minimization of  $(f_i - s_i)^2$  for all coefficients. Hueckel has performed this minimization, invoking some simplifying approximations, and has formulated a set of nonlinear equations expressing the estimated edge parameter set in terms of the expansion coefficients  $f_i$ .

Nalwa and Binford (30) have proposed an edge-fitting scheme in which the edge angle is first estimated by a sequential least-squares fit within a  $5 \times 5$  region. Then, the image data along the edge direction is fit to a hyperbolic tangent function

$$\tanh \rho = \frac{e^{\rho} - e^{-\rho}}{e^{\rho} + e^{-\rho}} \quad (14.4-6)$$

as shown in Figure 14.4-2.

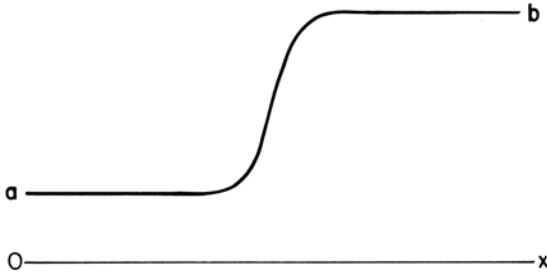


FIGURE 14.4-2. Hyperbolic tangent edge model.

## 14.5. LUMINANCE EDGE DETECTOR PERFORMANCE

Relatively few comprehensive studies of edge detector performance have been reported in the literature (15,31-35). A performance evaluation is difficult because of the large number of methods proposed, problems in determining the optimum parameters associated with each technique and the lack of definitive performance criteria.

In developing performance criteria for an edge detector, it is wise to distinguish between mandatory and auxiliary information to be obtained from the detector. Obviously, it is essential to determine the pixel location of an edge. Other information of interest includes the height and slope angle of the edge as well as its spatial orientation. Another useful item is a confidence factor associated with the edge decision, for example, the closeness of fit between actual image data and an idealized model. Unfortunately, few edge detectors provide this full gamut of information.

The next sections discuss several performance criteria. No attempt is made to provide a comprehensive comparison of edge detectors.

### 14.5.1. Edge Detection Probability

The probability of correct edge detection  $P_D$  and the probability of false edge detection  $P_F$ , as specified by Eq. 14.2-24, are useful measures of edge detector performance. The trade-off between  $P_D$  and  $P_F$  can be expressed parametrically in terms of the detection threshold. Figure 14.5-1 presents analytically derived plots of  $P_D$  versus  $P_F$  for several differential operators for vertical and diagonal edges and a signal-to-noise ratio of 1.0 and 10.0 (20). From these curves, it is apparent that the Sobel and Prewitt  $3 \times 3$  operators are superior to the Roberts  $2 \times 2$  operators. The Prewitt operator is better than the Sobel operator for a vertical edge. But for a diagonal edge, the Sobel operator is supe-

rior. In the case of template-matching operators, the Robinson three-level and five-level operators exhibit almost identical performance, which is superior to the Kirsch and Prewitt compass gradient operators. Finally, the Sobel and Prewitt differential operators perform slightly better than the Robinson three-level and Robinson five-level operators. It has not been possible to apply this statistical approach to any of the larger operators because of analytic difficulties in evaluating the detection probabilities.

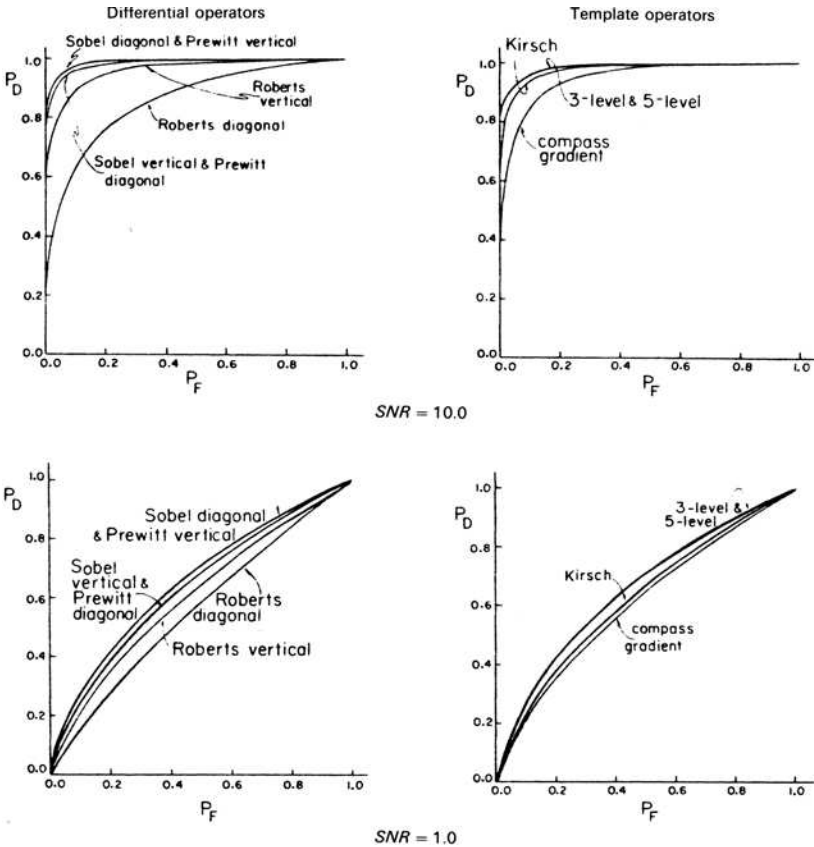


**FIGURE 14.5-1.** Probability of detection versus probability of false detection for  $2 \times 2$  and  $3 \times 3$  operators.

### 14.5.2. Edge Detection Orientation

An important characteristic of an edge detector is its sensitivity to edge orientation. Abdou and Pratt (20) have analytically determined the gradient response of  $3 \times 3$  template matching edge detectors and  $2 \times 2$  and  $3 \times 3$  orthogonal gradient edge detectors for square-root and magnitude combinations of the orthogonal gradients. Figure 14.5-2 shows plots of the edge gradient as a function of actual edge orientation for a unit-width ramp edge model. The figure clearly shows that magnitude combination of orthogonal gradients is inferior to square-root combination.

Figure 14.5-3 is a plot of the detected edge angle as a function of the actual orientation of an edge. The Sobel operator provides the most linear response. Laplacian edge detectors are rotationally symmetric operators, and, hence, are invariant to edge orientation. The edge angle can be determined to within  $45^\circ$  increments during the  $3 \times 3$  pixel zero-crossing detection process.

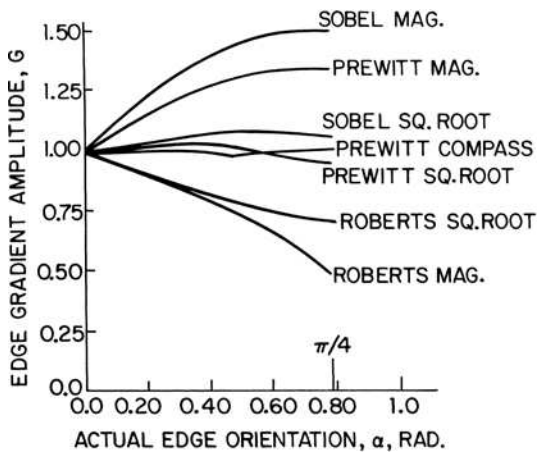


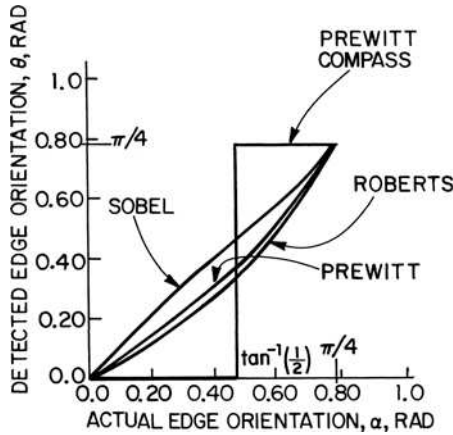
**FIGURE 14.5-2.** Edge gradient response as a function of edge orientation for  $2 \times 2$  and  $3 \times 3$  first derivative operators.

### 14.5.3. Edge Detection Localization

Another important property of an edge detector is its ability to localize an edge. Abdou and Pratt (20) have analyzed the edge localization capability of several first derivative operators for unit width ramp edges. Figure 14.5-4 shows edge models in which the sampled continuous ramp edge is displaced from the center of the operator.

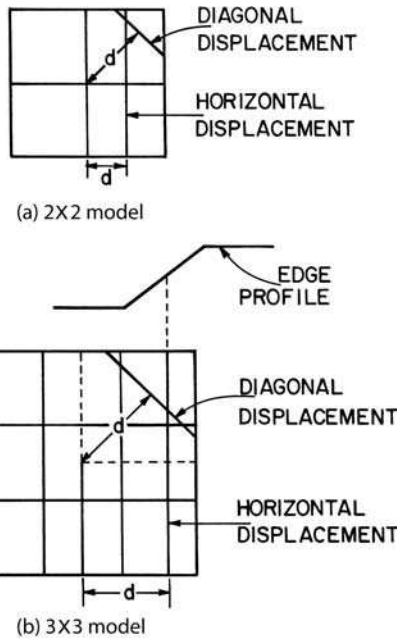
Figure 14.5-5 shows plots of the gradient response as a function of edge displacement for vertical and diagonal edges for  $2 \times 2$  and  $3 \times 3$  orthogonal gradient and  $3 \times 3$  template matching edge detectors. All of the detectors, with the exception of the Kirsch operator, exhibit a desirable monotonically decreasing response as a function of edge displacement. If the edge detection threshold is set at one-half the edge height, or greater, an edge will be properly localized in a noise-



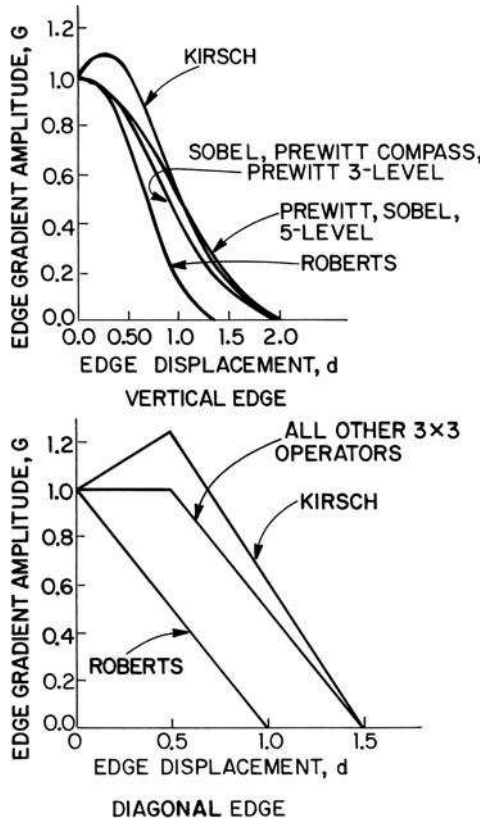


**FIGURE 14.5-3.** Detected edge orientation as a function of actual edge orientation for  $2 \times 2$  and  $3 \times 3$  first derivative operators.

free environment for all of the operators, with the exception of the Kirsch operator, for which the threshold must be slightly higher.



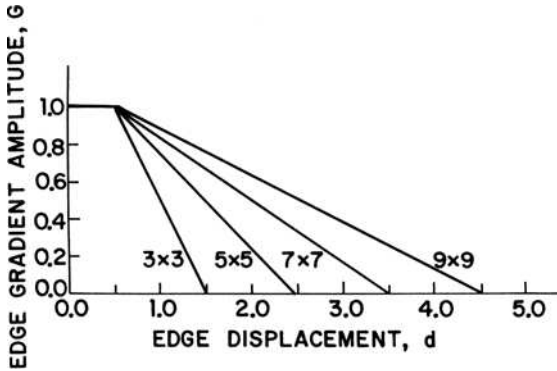
**FIGURE 14.5-4.** Edge models for edge localization analysis.



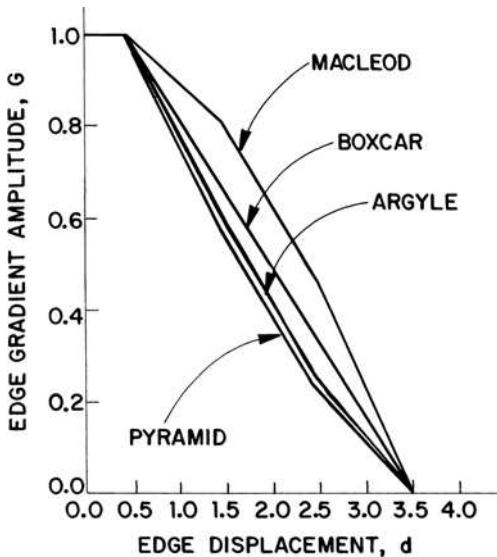
**FIGURE 14.5-5.** Edge gradient response as a function of edge displacement distance for  $2 \times 2$  and  $3 \times 3$  first derivative operators.

Figure 14.5-6 illustrates the gradient response of boxcar operators as a function of their size (5). A gradient response comparison of  $7 \times 7$  orthogonal gradient operators is presented in Figure 14.5-7. For such large operators, the detection threshold must be set relatively high to prevent smeared edge markings. Setting a high threshold will, of course, cause low-amplitude edges to be missed.

Ramp edges of extended width can cause difficulties in edge localization. For first-derivative edge detectors, edges are marked along the edge slope at all points for which the slope exceeds some critical value. Raising the threshold results in the missing of low-amplitude edges. Second derivative edge detection methods are often able to eliminate smeared ramp edge markings. In the case of a unit width ramp edge, a zero crossing will occur only at the midpoint of the edge slope. Extended-width ramp edges will also exhibit a zero crossing at the ramp midpoint provided that the size of the Laplacian operator exceeds the slope width. Figure 14.5-8 illustrates Laplacian of Gaussian (LOG) examples (27).



**FIGURE 14.5-6.** Edge gradient response as a function of edge displacement distance for variable-size boxcar operators.



**FIGURE 14.5-7** Edge gradient response as a function of edge displacement distance for several  $7 \times 7$  orthogonal gradient operators.

Berzins (36) has investigated the accuracy to which the LOG zero crossings locate a step edge. Figure 14.5-9 shows the LOG zero crossing in the vicinity of a corner step edge. A zero crossing occurs exactly at the corner point, but the zero-crossing curve deviates from the step edge adjacent to the corner point. The maximum deviation is about  $0.3s$ , where  $s$  is the standard deviation of the Gaussian smoothing function.

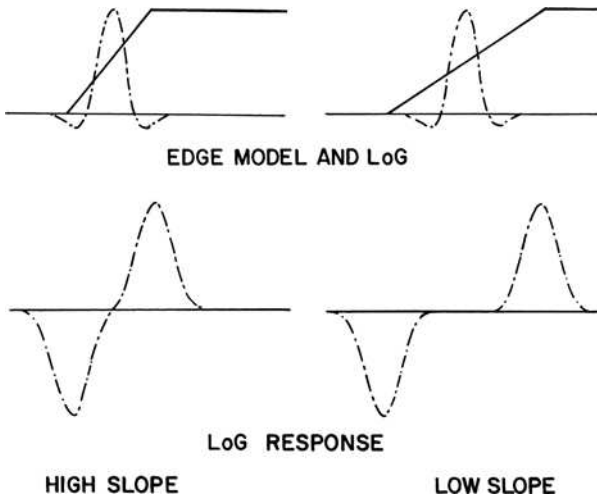


**FIGURE 14.5-8.** Laplacian of Gaussian response of continuous domain for high- and low-slope ramp edges.

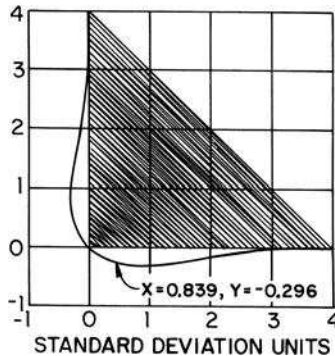


**FIGURE 14.5-9.** Locus of zero crossings in vicinity of a corner edge for a continuous Laplacian of Gaussian edge detector.

**14.5.4. Edge Detector Figure of Merit**

There are three major types of error associated with determination of an edge: (1) missing valid edge points, (2) failure to localize edge points and (3) classification of noise fluctuations as edge points. Figure 14.5-10 illustrates a typical edge segment in a discrete image, an ideal edge representation and edge representations subject to various types of error.

A common strategy in signal detection problems is to establish some bound on the probability of false detection resulting from noise and then attempt to maximize the probability of true signal detection. Extending this concept to edge detection

simply involves setting the edge detection threshold at a level such that the probability of false detection resulting from noise alone does not exceed some desired value. The probability of true edge detection can readily be evaluated by a coincidence comparison of the edge maps of an ideal and an actual edge detector. The penalty for non-localized edges is somewhat more difficult to access. Edge detectors that provide a smeared edge location should clearly be penalized; however, credit should be given to edge detectors whose edge locations are localized but biased by a small amount. Pratt (37) has introduced a figure of merit that balances these three types of error. The figure of merit is defined by

$$R = \frac{1}{I_N} \sum_{i=1}^{I_A} \frac{1}{1 + ad^2} \tag{14.5-1}$$

where  $I_N = \text{MAX}\{I_I, I_A\}$  and  $I_I$  and  $I_A$  represent the number of ideal and actual edge map points,  $a$  is a scaling constant and  $d$  is the separation distance of an actual edge point normal to a line of ideal edge points. The rating factor is normalized so

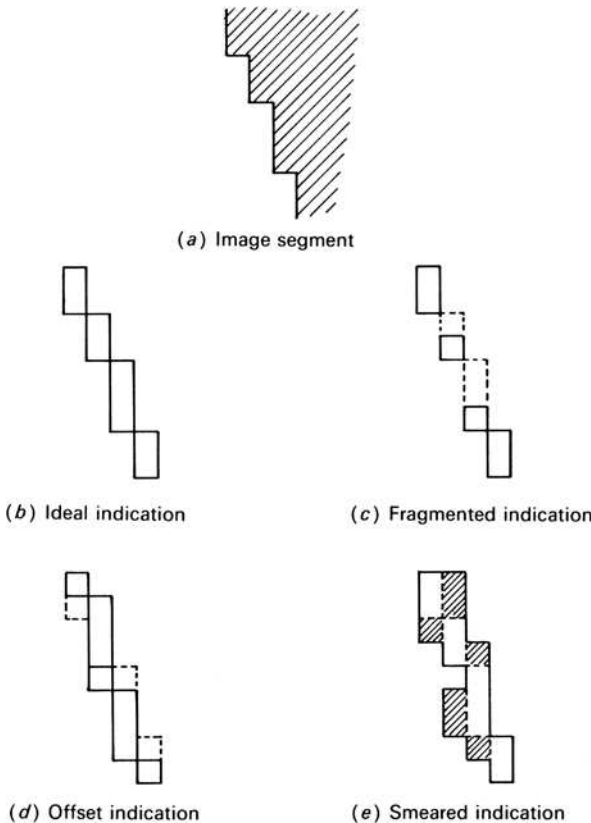


**FIGURE 14.5-10.** Indications of edge location.

that  $R = 1$  for a perfectly detected edge. The scaling factor may be adjusted to penalize edges that are localized but offset from the true position. Normalization by the maximum of the actual and ideal number of edge points ensures a penalty for smeared or fragmented edges. As an example of performance, if  $a = 1/9$ , the rating of a vertical detected edge offset by one pixel becomes  $R = 0.90$ , and a two-pixel offset gives a rating of  $R = 0.69$ . With  $a = 1/9$ , a smeared edge of three pixels width centered about the true vertical edge yields a rating of  $R = 0.93$ , and a five-pixel-wide smeared edge gives  $R = 0.84$ . A higher rating for a smeared edge than for an offset edge is reasonable because it is possible to thin the smeared edge by morphological postprocessing.

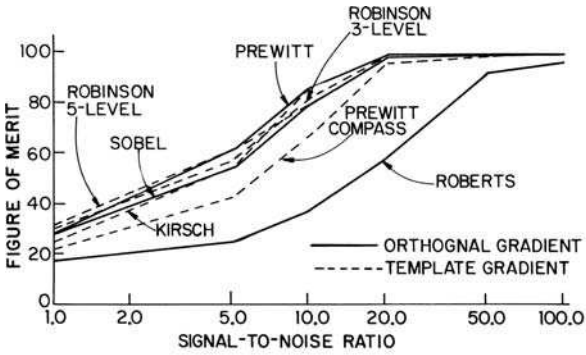
The figure-of-merit criterion described above has been applied to the assessment of some of the edge detectors discussed previously, using a test image consisting of a  $64 \times 64$  pixel array with a vertically oriented edge of variable contrast and slope placed at its center. Independent Gaussian noise of standard deviation  $\sigma_n$  has been added to the edge image. The signal-to-noise ratio is defined as  $\text{SNR} = (h/\sigma_n)^2$  where  $h$  is the edge height scaled over the range 0.0 to 1.0. Because the purpose of the testing is to compare various edge detection methods, for fairness it is important that each edge detector be tuned to its best capabilities. Consequently, each edge detector has been permitted to train both on random noise fields without edges and the actual test images before evaluation. For each edge detector, the threshold parameter has been set to achieve the maximum figure-of-merit subject to the maximum allowable false detection rate.

Figure 14.5-11 shows plots of the figure of merit for a vertical ramp edge as a function of signal-to-noise ratio for several edge detectors (5). The figure of merit is also plotted in Figure 14.5-12 as a function of edge width. The figure-of-merit curves in the figures follow expected trends: low for wide and noisy edges; and high in the opposite case. Some of the edge detection methods are universally superior to others for all test images. As a check on the subjective validity of the edge location figure of merit, Figures 14.5-13 and 14.5-14 present the edge maps obtained for several high- and low-ranking edge detectors. These figures tend to corroborate the utility of the figure of merit. A high figure-of-merit generally corresponds to a well-located edge upon visual scrutiny, and vice versa.

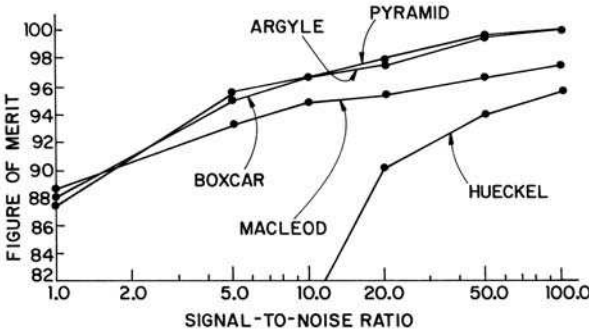
### 14.5.5. Subjective Assessment

In many, if not most applications in which edge detection is performed to outline objects in a real scene, the only performance measure of ultimate importance is how well edge detector markings match with the visual perception of object boundaries. A human observer is usually able to discern object boundaries in a scene quite accurately in a perceptual sense. However, most observers have difficulty recording their observations by tracing object boundaries. Nevertheless, in the evaluation of edge detectors, it is useful to assess them in terms of how well they produce outline drawings of a real scene that are meaningful to a human observer.

The peppers image of Figure 14.2-2 has been used for the subjective assessment of edge detectors. The peppers in the image are visually distinguishable objects, but shadows and nonuniform lighting create a challenge to edge detectors, which by



(a) 3X3 edge detectors



(b) Larger size edge detectors

**FIGURE 14.5-11.** Edge location figure of merit for a vertical ramp edge as a function of signal-to-noise ratio for  $h = 0.1$  and  $w = 1$ .

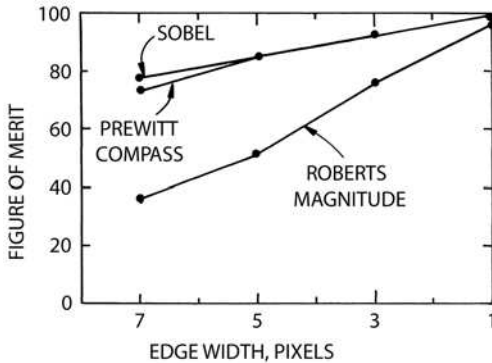


**FIGURE 14.5-12.** Edge location figure of merit for a vertical ramp edge as a function of signal-to-noise ratio for  $h = 0.1$  and  $SNR = 100$ .

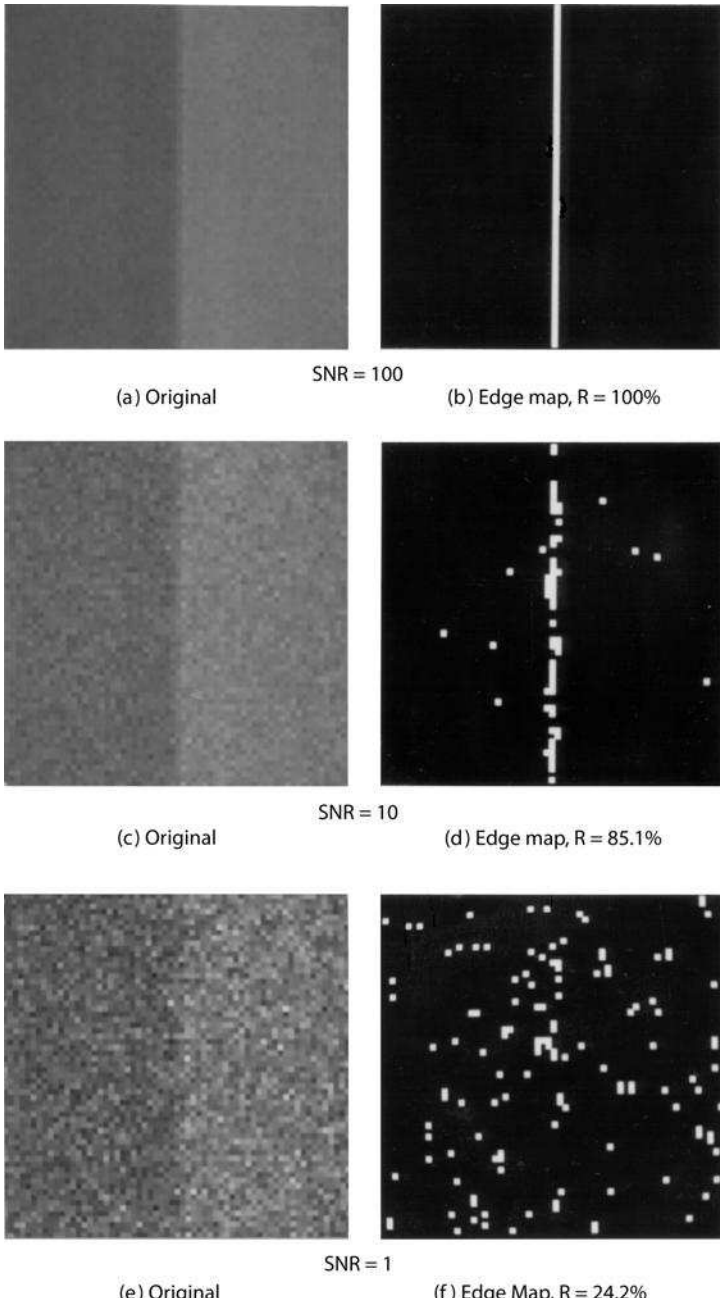
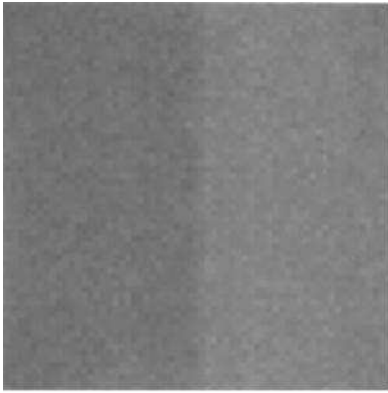
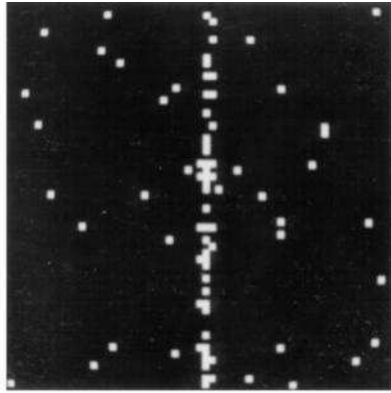


**FIGURE 14.5-13.** Edge location performance of Sobel edge detector as a function of signal-to-noise ratio,  $h = 0.1$ ,  $w = 1$ ,  $a = 1/9$ .

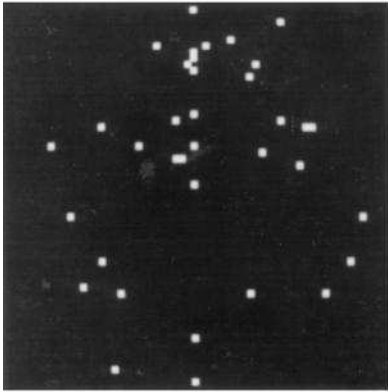




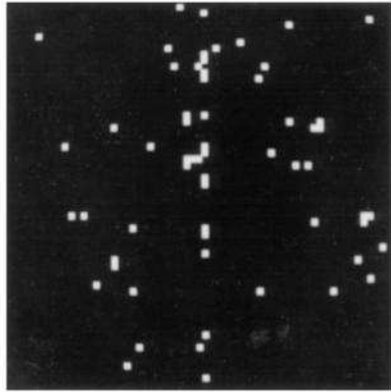
(a) Original



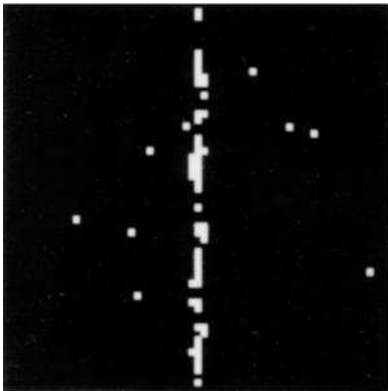
(b) East compass,  $R = 66.1\%$



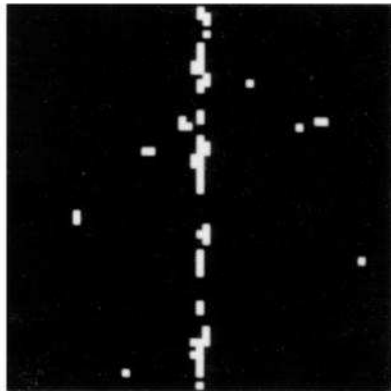
(c) Roberts magnitude,  $R = 31.5\%$



(d) Roberts square root,  $R = 37.0\%$



(e) Sobel,  $R = 85.1\%$



(f) Kirsch,  $R = 80.8\%$

**FIGURE 14.5-14.** Edge location performance of several edge detectors for  $SNR = 10$ ,  $h = 0.1$ ,  $w = 1$ ,  $a = 1/9$ .

definition do not utilize higher-order perceptive intelligence. Figures 14.5-15 and 14.5-16 present edge maps of the peppers image for several edge detectors. The



(a) 2X2 Roberts,  $t = 0.08$



(b) 3X3 Prewitt,  $t = 0.08$



(c) 3X3 Sobel,  $t = 0.09$



(d) 3X3 Robinson five-level



(e) 5X5 Nevatia-Babu,  $t = 0.05$



(f) 3X3 Laplacian

**FIGURE 14.5-15.** Edge maps of the peppers\_mon image for several small edge detectors.

parameters of the various edge detectors have been chosen to produce the best visual delineation of objects.



(a) 7X7 boxcar,  $t = 0.10$



(b) 9X9 truncated pyramid,  $t = 0.10$



(c) 11X11 Argyle,  $t = 0.05$



(d) 11X11 Macleod,  $t = 0.10$



(e) 11X11 derivative of Gaussian,  $t = 0.11$



(f) 11X11 Laplacian of Gaussian

**FIGURE 14.5-16.** Edge maps of the peppers\_mon image for several large edge detectors.

Heath et al. (34) have performed extensive visual testing of several complex edge detection algorithms, including the Canny and Nalwa–Binford methods, for a number of natural images. The judgment criterion was a numerical rating as to how well the edge map generated by an edge detector allows for easy, quick and accurate recognition of objects within a test image.

### 14.6. COLOR EDGE DETECTION

In Chapter 3, it was established that color images may be described quantitatively at each pixel by a set of three tristimulus values  $T_1, T_2, T_3$ , which are proportional to the amount of red, green and blue primary lights required to match the pixel color. The luminance of the color is a weighted sum  $Y = a_1T_1 + a_2T_2 + a_3T_3$  of the tristimulus values, where the  $a_i$  are constants that depend on the spectral characteristics of the primaries.

Several definitions of a color edge have been proposed (38,39). An edge in a color image can be said to exist if and only if its luminance representation contains a monochrome edge. This definition ignores discontinuities in hue and saturation that occur in regions of constant luminance. Figure 2 of reference 39 shows an artificial image, which consists of a checkerboard grid of three different color squares of identical luminance but differing hue and saturation. The color squares are visually distinct but the color image contains no luminance edges.

Another definition is to judge a color edge present if an edge exists in any of its constituent tristimulus components. A third definition is based on forming the sum of the magnitudes

$$G(j, k) = |G_1(j, k)| + |G_2(j, k)| + |G_3(j, k)| \tag{14.6-1a}$$

or the vector sum

$$G(j, k) = [[G_1(j, k)]^2 + [G_2(j, k)]^2 + [G_3(j, k)]^2]^{1/2} \tag{14.6-1b}$$

of the gradients  $G_i(j, k)$  of the three tristimulus values or some linear or nonlinear color components. A color edge exists if the gradient  $G(j, k)$  exceeds a threshold.

With the tri-component definitions of color edges, results are dependent on the particular color coordinate system chosen for representation. Figure 14.6-1 is a color photograph of the peppers image and monochrome photographs of its red, green and blue components. The  $YIQ$  and  $L^*a^*b^*$  coordinates are shown in Figure 14.6-2. Edge maps of the individual  $RGB$  components are shown in Figure 14.6-3 for Sobel edge detection. This figure also shows the logical OR of the  $RGB$  edge maps plus the edge maps of the gradient sum and the vector sum. The  $RGB$  gradient vector sum edge map provides slightly better visual edge delineation than that provided by the gradient sum edge map; the logical OR edge map tends to produce thick edges and numerous isolated edge points. Sobel edge maps for the  $YIQ$  and the  $L^*a^*b^*$



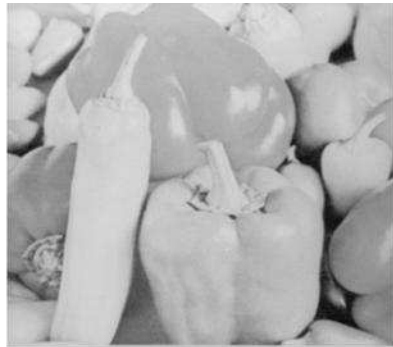
**FIGURE 14.6-1.** The `peppers_gamma` color image and its *RGB* color components. For monochrome printers and displays, see the web site for a color representation of this figure.

color components are presented in Figures 14.6-4 and 14.6-5. The *YIQ* gradient vector sum edge map gives the best visual edge delineation, but it does not delineate edges quite as well as the *RGB* vector sum edge map. Edge detection results for the *L\*a\*b\** coordinate system are quite poor because the *a\** component is very noise sensitive.

Koschan and Abidi (39) have reviewed the investigation, performed by Kanade (40), for using the Canny operator for color edge detection. The first step in this application is to determine the best row and column impulse response functions that satisfy the three Canny criteria for each color component. These functions are then applied to each component to determine the edge direction and edge magnitude. Then the color gradient is found using Eq. 14.6-1 or some other combination function. Finally, the color gradient is thresholded to create a composite edge map. Kanade observed that the color edges better describe the visual object geometry than the luminance edges.



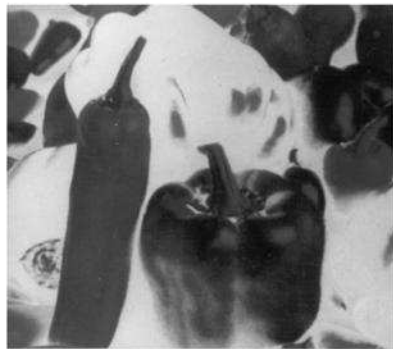
(a) Y component



(b) L\* component



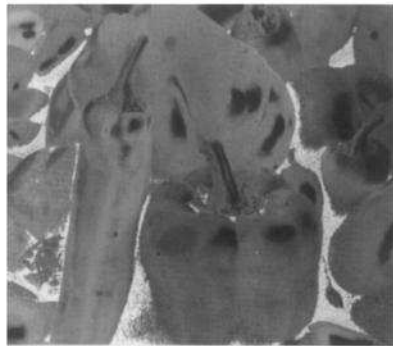
(c) I component



(d) a\* component



(e) Q component

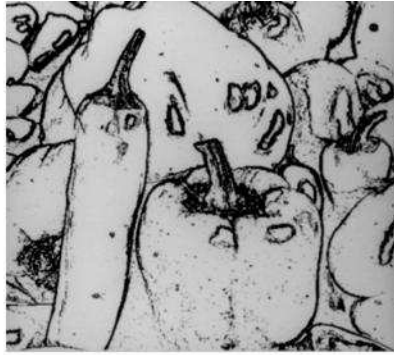


(f) b\* component

**FIGURE 14.6-2.**  $YIQ$  and  $L^*a^*b^*$  color components of the peppers\_gamma image.



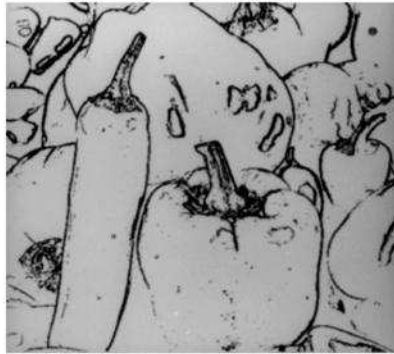
(a) Red edge map



(b) Logical OR of RGB edges



(c) Green edge map



(d) RGB sum edge map



(e) Blue edge map

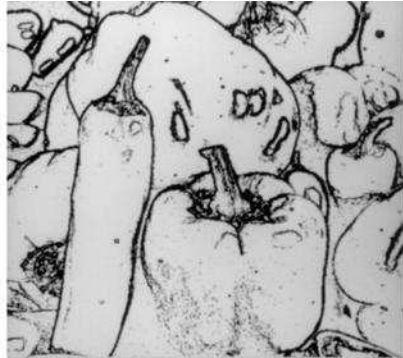


(f) RGB vector sum edge map

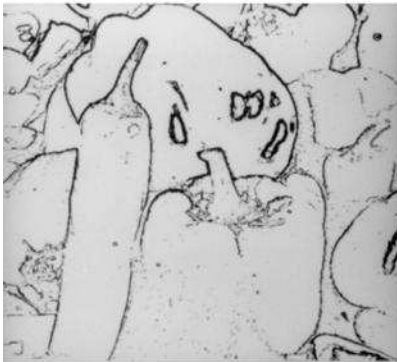
**FIGURE 14.6-3.** Sobel edge maps for edge detection using the *RGB* color components of the *peppers\_gamma* image.



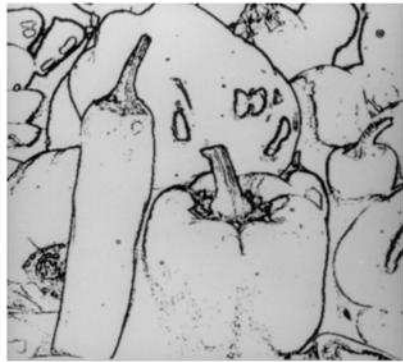
(a) Y edge map



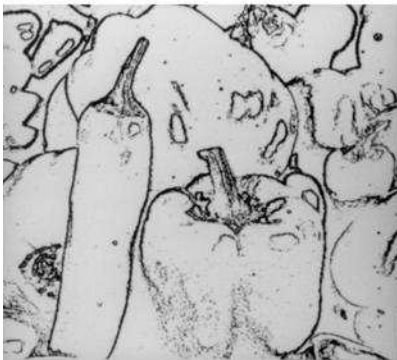
(b) Logical OR of YIQ edges



(c) I edge map



(d) YIQ sum edge map



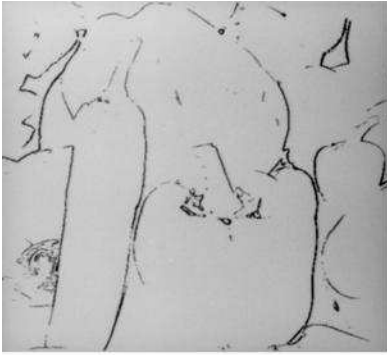
(e) Q edge map



(f) YIQ vector sum edge map

**FIGURE 14.6-4.** Sobel edge maps for edge detection using the *YIQ* color components of the *peppers\_gamma* image.

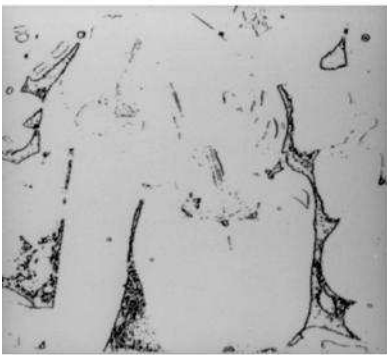




(a)  $L^*$  edge map



(b) Logical OR of  $L^*a^*b^*$  edges



(c)  $a^*$  edge map



(d)  $L^*a^*b^*$  sum edge map



(e)  $b^*$  edge map



(f)  $L^*a^*b^*$  vector sum edge map

**FIGURE 14.6-5.** Sobel edge maps for edge detection using the  $L^*a^*b^*$  color components of the peppers\_gamma image.

### 14.7. LINE AND SPOT DETECTION

A line in an image could be considered to be composed of parallel, closely spaced edges. Similarly, a spot could be considered to be a closed contour of edges. This method of line and spot detection involves the application of scene analysis techniques to spatially relate the constituent edges of the lines and spots. The approach taken in this chapter is to consider only small-scale models of lines and edges and to apply the detection methodology developed previously for edges.

Figure 14.1-4 presents several discrete models of lines. For the unit-width line models, line detection can be accomplished by threshold detecting a line gradient

$$G(j, k) = \text{MAX}_{m=1}^4 \left\{ F(j, k) \otimes H_m(j, k) \right\} \tag{14.7-1}$$

where  $H_m(j, k)$  is a  $3 \times 3$  line detector impulse response array corresponding to a specific line orientation. Figure 14.7-1 contains two sets of line detector impulse response arrays, weighted and unweighted, which are analogous to the Prewitt and Sobel template matching edge detector impulse response arrays. The detection of ramp lines, as modeled in Figure 14.1-4, requires  $5 \times 5$  pixel templates.

	Unweighted line	Weighted line
$H_1$	$\begin{bmatrix} -1 & 2 & -1 \\ -1 & 2 & -1 \\ -1 & 2 & -1 \end{bmatrix}$	$\begin{bmatrix} -1 & 2 & -1 \\ -2 & 4 & -2 \\ -1 & 2 & -1 \end{bmatrix}$
$H_2$	$\begin{bmatrix} -1 & -1 & -1 \\ 2 & 2 & 2 \\ -1 & -1 & -1 \end{bmatrix}$	$\begin{bmatrix} -1 & -2 & -1 \\ 2 & 4 & 2 \\ -1 & -2 & -1 \end{bmatrix}$
$H_3$	$\begin{bmatrix} -1 & -1 & 2 \\ -1 & 2 & -1 \\ 2 & -1 & -1 \end{bmatrix}$	$\begin{bmatrix} -2 & -1 & 2 \\ -1 & 4 & -1 \\ 2 & -1 & -2 \end{bmatrix}$
$H_4$	$\begin{bmatrix} 2 & -1 & -1 \\ -1 & 2 & -1 \\ -1 & -1 & 2 \end{bmatrix}$	$\begin{bmatrix} 2 & -1 & -2 \\ -1 & 4 & -1 \\ -2 & -1 & 2 \end{bmatrix}$
Scale factor	$\frac{1}{6}$	$\frac{1}{8}$

FIGURE 14.7-1. Line detector  $3 \times 3$  impulse response arrays.

Unit-width step spots can be detected by thresholding a spot gradient

$$G(j, k) = F(j, k) \otimes H(j, k) \quad (14.7-2)$$

where  $H(j, k)$  is an impulse response array chosen to accentuate the gradient of a unit-width spot. One approach is to use one of the three types of  $3 \times 3$  Laplacian operators defined by Eq. 14.3-5, 14.3-6 or 14.3-8, which are discrete approximations to the sum of the row and column second derivatives of an image. The gradient responses to these impulse response arrays for the unit-width spot model of Figure 14.1-6a are simply replicas of each array centered at the spot, scaled by the spot height  $h$  and zero elsewhere. It should be noted that the Laplacian gradient responses are thresholded for spot detection, whereas the Laplacian responses are examined for sign changes (zero crossings) for edge detection. The disadvantage to using Laplacian operators for spot detection is that they evoke a gradient response for edges, which can lead to false spot detection in a noisy environment. This problem can be alleviated by the use of a  $3 \times 3$  operator that approximates the continuous cross second derivative  $\partial^2/\partial x^2\partial y^2$ . Prewitt (1, p. 126) has suggested the following discrete approximation:

$$\mathbf{H} = \frac{1}{8} \begin{bmatrix} 1 & -2 & 1 \\ -2 & 4 & -2 \\ 1 & -2 & 1 \end{bmatrix}. \quad (14.7-3)$$

The advantage of this operator is that it evokes no response for horizontally or vertically oriented edges, however, it does generate a response for diagonally oriented edges. The detection of unit-width spots modeled by the ramp model of Figure 14.1-5 requires a  $5 \times 5$  impulse response array. The *cross second derivative* operator of Eq. 14.7-3 and the separable eight-connected Laplacian operator are deceptively similar in appearance; often, they are mistakenly exchanged with one another in the literature. It should be noted that the cross second derivative is identical to within a scale factor with the ninth Chebyshev polynomial impulse response array described by Pratt(4Ed., 503).

Cook and Rosenfeld (41) and Zucker et al. (42) have suggested several algorithms for detection of large spots. In one algorithm, an image is first smoothed with a  $W \times W$  low-pass filter impulse response array. Then the value of each point in the averaged image is compared to the average value of its north, south, east and west neighbors spaced  $W$  pixels away. A spot is marked if the difference is sufficiently large. A similar approach involves formation of the difference of the average pixel amplitude in a  $W \times W$  window and the average amplitude in a surrounding ring region of width  $W$ .

Chapter 18 considers the general problem of detecting objects within an image by template matching. Such templates can be developed to detect large spots.

## 14.8. EDGE DETECTION EXERCISES

E14.1 Develop a program that generates the Sobel edge gradient according to Figure 14.2-1 using a square root sum of squares gradient combination. Steps:

- (a) Display the source image.
- (b) Generate the horizontal and vertical Sobel impulse response arrays or fetch them from a repository.
- (c) Convolve the source image with the horizontal Sobel.
- (d) Display the Sobel horizontal gradient.
- (e) Convolve the source image with the vertical Sobel.
- (f) Display the Sobel vertical gradient.
- (g) Form the square root sum of squares of the gradients.
- (h) Display the Sobel gradient.

The PIKS API executable `example_sobel_gradient` performs this exercise.

E14.2 Develop a program that generates the Laplacian of Gaussian gradient for a  $11 \times 11$  impulse response array and a standard deviation of 2.0. Steps:

- (a) Display the source image.
- (b) Generate the Laplacian of Gaussian impulse response array.
- (c) Convolve the source image with the Laplacian of Gaussian impulse response array.
- (d) Display the Laplacian of Gaussian gradient.

The PIKS API executable `example_Log_gradient` performs this exercise.

## REFERENCES

1. J. M. S. Prewitt, "Object Enhancement and Extraction," in *Picture Processing and Psychopictorics*, B. S. Lipkin and A. Rosenfeld, Eds., Academic Press, New York, 1970.
2. L. G. Roberts, "Machine Perception of Three-Dimensional Solids," in *Optical and Electro-Optical Information Processing*, J. T. Tippett et al., Eds., MIT Press, Cambridge, MA, 1965, 159–197.
3. R. O. Duda and P. E. Hart, *Pattern Classification and Scene Analysis*, John Wiley and Sons, New York, 1973.
4. W. Frei and C. Chen, "Fast Boundary Detection: A Generalization and a New Algorithm," *IEEE Trans. Computers*, **C-26**, 10, October 1977, 988–998.
5. I. Abdou, "Quantitative Methods of Edge Detection," USCIP Report 830, Image Processing Institute, University of Southern California, Los Angeles, 1973.
6. E. Argyle, "Techniques for Edge Detection," *Proc. IEEE*, **59**, 2, February 1971, 285–287.

7. I. D. G. Macleod, "On Finding Structure in Pictures," in *Picture Processing and Psychopictorics*, B. S. Lipkin and A. Rosenfeld, Eds., Academic Press, New York, 1970.
8. I. D. G. Macleod, "Comments on Techniques for Edge Detection," *Proc. IEEE*, **60**, 3, March 1972, 344.
9. J. Canny, "A Computational Approach to Edge Detection," *IEEE Trans. Pattern Analysis and Machine Intelligence*, **PAMI-8**, 6, November 1986, 679–698.
10. H. D. Tagare and R. J. P. deFigueiredo, "On the Localization Performance Measure and Optimal Edge Detection," *IEEE Trans. Pattern Analysis and Machine Intelligence*, **12**, 12, December 1990, 1186–1190.
11. J. Koplowitz and V. Greco, "On the Edge Location Error for Local Maximum and Zero-Crossing Edge Detectors," *IEEE Trans. Pattern Analysis and Machine Intelligence*, **16**, 12, December 1994, 1207–1212.
12. D. Demigny and T. Kamle, "A Discrete Expression of Canny's Criteria for Step Edge Detector Performances Evaluation," *IEEE Trans. Pattern Analysis and Machine Intelligence*, **PAMI-19**, 11, November 1997, 1199–1211.
13. P. Bao, L. Zhang and X. Wu, "Canny Edge Detection Enhancement by Scale Multiplication," *IEEE Trans. Pattern Analysis and Machine Intelligence*, **27**, 9, September 2005, 1485–1490.
14. M. Petrou and J. Kittler, "Optimal Edge Detectors for Ramp Edges," *IEEE Trans. Pattern Analysis and Machine Intelligence*, **13**, 5, May 1991, 483–491.
15. D. Demigny, "On Optimal Linear Filtering for Edge Detection," *IEEE Trans. Image Processing*, **11**, 7, July 2002, 728–737.
16. R. Kirsch, "Computer Determination of the Constituent Structure of Biomedical Images," *Computers and Biomedical Research*, **4**, 3, 1971, 315–328.
17. G. S. Robinson, "Edge Detection by Compass Gradient Masks," *Computer Graphics and Image Processing*, **6**, 5, October 1977, 492–501.
18. R. Nevatia and K. R. Babu, "Linear Feature Extraction and Description," *Computer Graphics and Image Processing*, **13**, 3, July 1980, 257–269.
19. A. P. Paplinski, "Directional Filtering in Edge Detection," *IEEE Trans. Image Processing*, **IP-7**, 4, April 1998, 611–614.
20. I. E. Abdou and W. K. Pratt, "Quantitative Design and Evaluation of Enhancement/Thresholding Edge Detectors," *Proc. IEEE*, **67**, 5, May 1979, 753–763.
21. K. Fukunaga, *Introduction to Statistical Pattern Recognition*, Academic Press, New York, 1972.
22. P. V. Henstock and D. M. Chelberg, "Automatic Gradient Threshold Determination for Edge Detection," *IEEE Trans. Image Processing*, **IP-5**, 5, May 1996, 784–787.
23. R. R. Rakesh, P. Chaudhuri and C. A. Murthy, "Thresholding in Edge Detection: A Statistical Approach," *IEEE Trans. Image Processing*, **13**, 7, July 2004, 927–936.
24. V. Torre and T. A. Poggio, "On Edge Detection," *IEEE Trans. Pattern Analysis and Machine Intelligence*, **PAMI-8**, 2, March 1986, 147–163.
25. D. Marr and E. Hildrith, "Theory of Edge Detection," *Proc. Royal Society of London*, **B207**, 1980, 187–217.
26. J. S. Wiejak, H. Buxton and B. F. Buxton, "Convolution with Separable Masks for Early Image Processing," *Computer Vision, Graphics and Image Processing*, **32**, 3, December 1985, 279–290.

27. A. Huertas and G. Medioni, "Detection of Intensity Changes Using Laplacian-Gaussian Masks," *IEEE Trans. Pattern Analysis and Machine Intelligence*, **PAMI-8**, 5, September 1986, 651–664.
28. R. M. Haralick, "Digital Step Edges from Zero Crossing of Second Directional Derivatives," *IEEE Trans. Pattern Analysis and Machine Intelligence*, **PAMI-6**, 1, January 1984, 58–68.
29. M. Hueckel, "An Operator Which Locates Edges in Digital Pictures," *J. Association for Computing Machinery*, **18**, 1, January 1971, 113–125.
30. V. S. Nalwa and T. O. Binford, "On Detecting Edges," *IEEE Trans. Pattern Analysis and Machine Intelligence*, **PAMI-6**, November 1986, 699–714.
31. J. R. Fram and E. S. Deutsch, "On the Evaluation of Edge Detection Schemes and Their Comparison with Human Performance," *IEEE Trans. Computers*, **C-24**, 6, June 1975, 616–628.
32. L. Kitchen and A. Rosenfeld, "Edge Evaluation Using Local Edge Coherence," *IEEE Trans. Systems, Man, Cybernetics*, **SMC-11**, 9, September 1981, 597–605.
33. T. Kanungo, M. Y. Jaisimha, J. Palmer and R. M. Haralick, "A Methodology for Quantitative Performance Evaluation of Detection Algorithms," *IEEE Trans. Image Processing*, **4**, 12, December 1995, 1667–1674.
34. M. D. Heath, S. Sarkar, T. Sanocki and K. W. Boyer., "A Robust Visual Method for Assessing the Relative Performance of Edge-Detection Algorithms," *IEEE Trans. Pattern Analysis and Machine Intelligence*, **PAMI-19**, 12, December 1997, 1338–1359.
35. K. Bowyer, C. Kranenburg and S. Dougherty, "Edge Detector Evaluation Using Empirical ROC Curves," *Computer Vision and Image Understanding*, **84**, 1, October 2001, 77–103.
36. V. Berzins, "Accuracy of Laplacian Edge Detectors," *Computer Vision, Graphics and Image Processing*, **27**, 2, August 1984, 195–210.
37. W. K. Pratt, *Digital Image Processing*, Wiley-Interscience, New York, 1978, 497–499.
38. G. S. Robinson, "Color Edge Detection," *Proc. SPIE Symposium on Advances in Image Transmission Techniques*, **87**, San Diego, CA, August 1976.
39. A. Koschan and M. Abidi, "Detection and Classification of Edges in Color Images," *IEEE Signal Processing Magazine*, **22**, 1, January 2005, 64–73.
40. T. Kanade, "Image Understanding Research at CMU," *Proc. Image Understanding Workshop*, **II**, 1987, 32–40.
41. C. M. Cook and A. Rosenfeld, "Size Detectors," *Proc. IEEE Letters*, **58**, 12, December 1970, 1956–1957.
42. S. W. Zucker, A. Rosenfeld and L. S. Davis, "Picture Segmentation by Texture Discrimination," *IEEE Trans. Computers*, **C-24**, 12, December 1975, 1228–1233.



---

# 15

---

## IMAGE FEATURE EXTRACTION

An *image feature* is a distinguishing primitive characteristic or attribute of an image. Some features are natural in the sense that such features are defined by the visual appearance of an image, while other, so called, artificial features result from specific manipulations of an image. Natural features include the luminance of a region of pixels and gray scale textural regions. Image amplitude histograms and spatial frequency spectra are examples of artificial features.

Image features are of major importance in the isolation of regions of common property within an image (*image segmentation*) and subsequent identification or labeling of such regions (*image classification*). Image segmentation is discussed in Chapter 16. References 1 to 4 provide information on image classification techniques.

This chapter describes several types of image features that have been proposed for image segmentation and classification. Before introducing them, however, methods of evaluating their performance are discussed.

### 15.1. IMAGE FEATURE EVALUATION

There are two quantitative approaches to the evaluation of image features: prototype performance and figure-of-merit. In the prototype performance approach for image classification, a prototype image with regions (segments) that have been independently categorized is classified by a classification procedure using various image features to be evaluated. The classification error is then measured for each feature



set. The best set of features is, of course, that which results in the least classification error. The prototype performance approach for image segmentation is similar in nature. A prototype image with independently identified regions is segmented by a segmentation procedure using a test set of features. Then, the detected segments are compared to the known segments, and the segmentation error is evaluated. The problems associated with the prototype performance methods of feature evaluation are the integrity of the prototype data and the fact that the performance indication is dependent not only on the quality of the features but also on the classification or segmentation ability of the classifier or segmenter.

The figure-of-merit approach to feature evaluation involves the establishment of some functional distance measurements between sets of image features such that a large distance implies a low classification error, and vice versa. Faugeras and Pratt (5) have utilized the *Bhattacharyya distance* (3) figure-of-merit for texture feature evaluation. The method is extensible for other features as well. The Bhattacharyya distance (*B-distance* for simplicity) is a scalar function of the probability densities of features of a pair of classes defined as

$$B(S_1, S_2) = -\ln \left\{ \int [p(\mathbf{x}|S_1)p(\mathbf{x}|S_2)]^{1/2} d\mathbf{x} \right\} \tag{15.1-1}$$

where  $\mathbf{x}$  denotes a vector containing individual image feature measurements with conditional density  $p(\mathbf{x}|S_i)$ . It can be shown (3) that the *B-distance* is related monotonically to the *Chernoff bound* for the probability of classification error using a Bayes classifier. The bound on the error probability is

$$P \leq [P(S_1)P(S_2)]^{1/2} \exp \{-B(S_1, S_2)\} \tag{15.1-2}$$

where  $P(S_i)$  represents the a priori class probability. For future reference, the Chernoff error bound is tabulated in Table 15.1-1 as a function of *B-distance* for equally likely feature classes.

For Gaussian densities, the *B-distance* becomes

$$B(S_1, S_2) = \frac{1}{8}(\mathbf{u}_1 - \mathbf{u}_2)^T \left( \frac{\boldsymbol{\Sigma}_1 + \boldsymbol{\Sigma}_2}{2} \right)^{-1} (\mathbf{u}_1 - \mathbf{u}_2) + \frac{1}{2} \ln \left\{ \frac{\frac{1}{2}|\boldsymbol{\Sigma}_1 + \boldsymbol{\Sigma}_2|}{|\boldsymbol{\Sigma}_1|^{1/2}|\boldsymbol{\Sigma}_2|^{1/2}} \right\} \tag{15.1-3}$$

where  $\mathbf{u}_i$  and  $\boldsymbol{\Sigma}_i$  represent the feature mean vector and the feature covariance matrix of the classes, respectively. Calculation of the *B-distance* for other densities is generally difficult. Consequently, the *B-distance* figure of merit is applicable only for Gaussian-distributed feature data, which fortunately is the common case. In practice, features to be evaluated by Eq. 15.1-3 are measured in regions whose class has been determined independently. Sufficient feature measurements need be taken so that the feature mean vector and covariance can be estimated accurately.

**TABLE 15.1-1. Relationship of Bhattacharyya Distance and Chernoff Error Bound**

$B(S_1, S_2)$	Error Bound
1	$1.84 \times 10^{-1}$
2	$6.77 \times 10^{-2}$
4	$9.16 \times 10^{-3}$
6	$1.24 \times 10^{-3}$
8	$1.68 \times 10^{-4}$
10	$2.27 \times 10^{-5}$
12	$2.07 \times 10^{-6}$

### 15.2. AMPLITUDE FEATURES

The most basic of all image features is some measure of image amplitude in terms of luminance, tristimulus value, spectral value or other units. There are many degrees of freedom in establishing image amplitude features. Image variables such as luminance or tristimulus values may be utilized directly, or alternatively, some linear, nonlinear, or perhaps non-invertible transformation can be performed to generate variables in a new amplitude space. Amplitude measurements may be made at specific image points, e.g., the amplitude  $F(j, k)$  at pixel coordinate  $(j, k)$ , or over a neighborhood centered at  $(j, k)$ . For example, the average or mean image amplitude in a  $W \times W$  pixel neighborhood is given by

$$M(j, k) = \frac{1}{W^2} \sum_{m=-w}^w \sum_{n=-w}^w F(j+m, k+n) \tag{15.2-1}$$

where  $W = 2w + 1$ . An advantage of a neighborhood, as opposed to a point measurement, is a diminishing of noise effects because of the averaging process. A disadvantage is that object edges falling within the neighborhood can lead to erroneous measurements.

The median of pixels within a  $W \times W$  neighborhood can be used as an alternative amplitude feature to the mean measurement of Eq. 15.2-1, or as an additional feature. The *median* is defined to be that pixel amplitude in the window for which one-half of the pixels are equal or smaller in amplitude, and one-half are equal or greater in amplitude. Another useful image amplitude feature is the neighborhood standard deviation, which can be computed as

$$S(j, k) = \frac{1}{W} \left[ \sum_{m=-w}^w \sum_{n=-w}^w [F(j+m, k+n) - M(j+m, k+n)]^2 \right]^{1/2} . \tag{15.2-2}$$

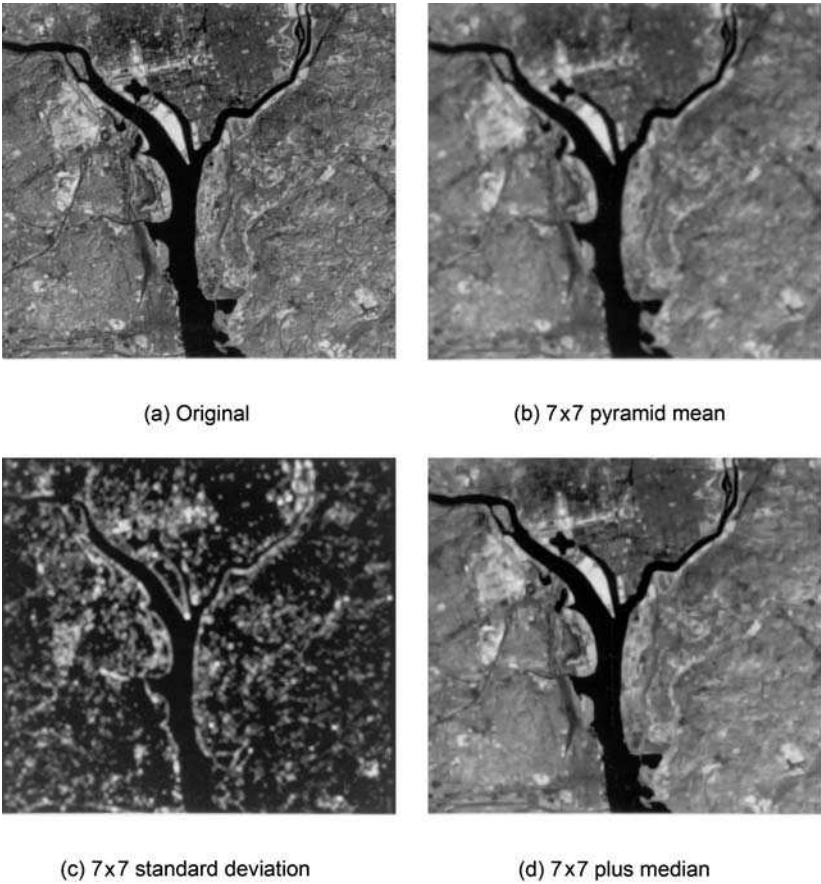


**FIGURE 15.2-1.** Image amplitude features of the washington\_ir image.

In the literature, the standard deviation image feature is sometimes called the *image dispersion*. Figure 15.2-1 shows an original image and the mean, median and standard deviation of the image computed over a small neighborhood.

The mean and standard deviation of Eqs. 15.2-1 and 15.2-2 can be computed indirectly in terms of the histogram of image pixels within a neighborhood. This leads to a class of image amplitude *histogram features*. Referring to Section 5.4, the first-order probability distribution of the amplitude of a quantized image may be defined as

$$P(b) = P_R [F(j, k) = r_b] \tag{15.2-3}$$

where  $r_b$  denotes the quantized amplitude level for  $0 \leq b \leq L - 1$ . The first-order histogram estimate of  $P(b)$  is simply

$$P(b) \approx \frac{N(b)}{M} \quad (15.2-4)$$

where  $M$  represents the total number of pixels in a neighborhood window centered about  $(j, k)$ , and  $N(b)$  is the number of pixels of amplitude  $r_b$  in the same window.

The shape of an image histogram provides many clues as to the character of the image. For example, a narrowly distributed histogram indicates a low-contrast image. A bimodal histogram often suggests that the image contains an object with a narrow amplitude range against a background of differing amplitude. The following measures have been formulated as quantitative shape descriptions of a first-order histogram (6).

*Mean:*

$$S_M \equiv \bar{b} = \sum_{b=0}^{L-1} bP(b) \quad (15.2-5)$$

*Standard deviation:*

$$S_D \equiv \sigma_b = \left[ \sum_{b=0}^{L-1} (b - \bar{b})^2 P(b) \right]^{1/2} \quad (15.2-6)$$

*Skewness:*

$$S_S = \frac{1}{\sigma_b^3} \sum_{b=0}^{L-1} (b - \bar{b})^3 P(b) \quad (15.2-7)$$

*Kurtosis:*

$$S_K = \frac{1}{\sigma_b^4} \sum_{b=0}^{L-1} (b - \bar{b})^4 P(b) - 3 \quad (15.2-8)$$

*Energy:*

$$S_N = \sum_{b=0}^{L-1} [P(b)]^2 \quad (15.2-9)$$

*Entropy:*

$$S_E = - \sum_{b=0}^{L-1} P(b) \log_2 \{P(b)\} \quad (15.2-10)$$

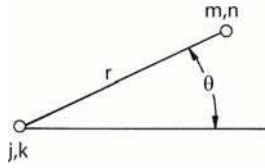


FIGURE 15.2-2. Relationship of pixel pairs.

The factor of 3 inserted in the expression for the Kurtosis measure normalizes  $S_K$  to zero for a zero-mean, Gaussian-shaped histogram. Another useful histogram shape measure is the *histogram mode*, which is the pixel amplitude corresponding to the histogram peak (i.e., the most commonly occurring pixel amplitude in the window). If the histogram peak is not unique, the pixel at the peak closest to the mean is usually chosen as the histogram shape descriptor.

Second-order histogram features are based on the definition of the joint probability distribution of pairs of pixels. Consider two pixels  $F(j, k)$  and  $F(m, n)$  that are located at coordinates  $(j, k)$  and  $(m, n)$ , respectively, and, as shown in Figure 15.2-2, are separated by  $r$  radial units at an angle  $\theta$  with respect to the horizontal axis. The joint distribution of image amplitude values is then expressed as

$$P(a, b) = P_R [F(j, k) = r_a, F(m, n) = r_b] \tag{15.2-11}$$

where  $r_a$  and  $r_b$  represent quantized pixel amplitude values. As a result of the discrete rectilinear representation of an image, the separation parameters  $(r, \theta)$  may assume only certain discrete values. The histogram estimate of the second-order distribution is

$$P(a, b) \approx \frac{N(a, b)}{M} \tag{15.2-12}$$

where  $M$  is the total number of pixels in the measurement window and  $N(a, b)$  denotes the number of occurrences for which  $F(j, k) = r_a$  and  $F(m, n) = r_b$ .

If the pixel pairs within an image are highly correlated, the entries in  $P(a, b)$  will be clustered along the diagonal of the array. Various measures, listed below, have been proposed (6,7) as measures that specify the energy spread about the diagonal of  $P(a, b)$ .

*Autocorrelation:*

$$S_A = \sum_{a=0}^{L-1} \sum_{b=0}^{L-1} abP(a, b) \tag{15.2-13}$$

*Covariance:*

$$S_C = \sum_{a=0}^{L-1} \sum_{b=0}^{L-1} (a - \bar{a})(b - \bar{b})P(a, b) \quad (15.2-14a)$$

where

$$\bar{a} = \sum_{a=0}^{L-1} \sum_{b=0}^{L-1} aP(a, b) \quad (15.2-14b)$$

$$\bar{b} = \sum_{a=0}^{L-1} \sum_{b=0}^{L-1} bP(a, b) \quad (15.2-14c)$$

*Inertia:*

$$S_I = \sum_{a=0}^{L-1} \sum_{b=0}^{L-1} (a-b)^2 P(a, b) \quad (15.2-15)$$

*Absolute value:*

$$S_V = \sum_{a=0}^{L-1} \sum_{b=0}^{L-1} |a-b| P(a, b) \quad (15.2-16)$$

*Inverse difference:*

$$S_F = \sum_{a=0}^{L-1} \sum_{b=0}^{L-1} \frac{P(a, b)}{1 + (a-b)^2} \quad (15.2-17)$$

*Energy:*

$$S_G = \sum_{a=0}^{L-1} \sum_{b=0}^{L-1} [P(a, b)]^2 \quad (15.2-18)$$

*Entropy:*

$$S_T = - \sum_{a=0}^{L-1} \sum_{b=0}^{L-1} P(a, b) \log_2 \{P(a, b)\} \quad (15.2-19)$$

The utilization of second-order histogram measures for texture analysis is considered in Section 15.6.

### 15.3. TRANSFORM COEFFICIENT FEATURES

The coefficients of a two-dimensional transform of a luminance image specify the amplitude of the luminance patterns (two-dimensional *basis functions*) of a transform such that the weighted sum of the luminance patterns is identical to the image. By this characterization of a transform, the coefficients may be considered to indicate the degree of correspondence of a particular luminance pattern with an image field. If a *basis pattern* is of the same spatial form as a feature to be detected within the image, image detection can be performed simply by monitoring the value of the transform coefficient. The problem, in practice, is that objects to be detected within an image are often of complex shape and luminance distribution, and hence do not correspond closely to the more primitive luminance patterns of most image transforms.

Lendaris and Stanley (8) have investigated the application of the continuous two-dimensional Fourier transform of an image, obtained by a coherent optical processor, as a means of image feature extraction. The optical system produces an electric field radiation pattern proportional to

$$\mathcal{F}(\omega_x, \omega_y) = \int_{-\infty}^{\infty} \int_{-\infty}^{\infty} F(x, y) \exp \{-i(\omega_x x + \omega_y y)\} dx dy \tag{15.3-1}$$

where  $(\omega_x, \omega_y)$  are the image spatial frequencies. An optical sensor produces an output

$$\mathcal{N}(\omega_x, \omega_y) = |\mathcal{F}(\omega_x, \omega_y)|^2 \tag{15.3-2}$$

proportional to the intensity of the radiation pattern. It should be observed that  $\mathcal{F}(\omega_x, \omega_y)$  and  $F(x, y)$  are unique transform pairs, but  $\mathcal{N}(\omega_x, \omega_y)$  is not uniquely related to  $F(x, y)$ . For example,  $\mathcal{N}(\omega_x, \omega_y)$  does not change if the origin of  $F(x, y)$  is shifted. In some applications, the translation invariance of  $\mathcal{N}(\omega_x, \omega_y)$  may be a benefit. Angular integration of  $\mathcal{N}(\omega_x, \omega_y)$  over the spatial frequency plane produces a spatial frequency feature that is invariant to translation and rotation. Representing  $\mathcal{N}(\omega_x, \omega_y)$  in polar form, this feature is defined as

$$\mathcal{N}(\rho) = \int_0^{2\pi} \mathcal{N}(\rho, \theta) d\theta \tag{15.3-3}$$

where  $\theta = \arctan\{\omega_x/\omega_y\}$  and  $\rho^2 = \omega_x^2 + \omega_y^2$ . Invariance to changes in scale is an attribute of the feature

$$P(\theta) = \int_0^{\infty} \mathcal{N}(\rho, \theta) d\rho \tag{15.3-4}$$

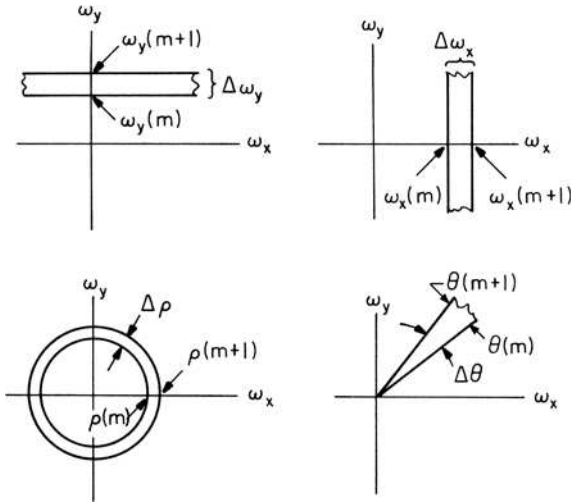


FIGURE 15.3-1. Fourier transform feature masks.

The Fourier domain intensity pattern  $\mathcal{N}(\omega_x, \omega_y)$  is normally examined in specific regions to isolate image features. As an example, Figure 15.3-1 defines regions for the following Fourier features:

*Horizontal slit:*

$$S_1(m) = \int_{-\infty}^{\infty} \int_{\omega_y(m)}^{\omega_y(m+1)} \mathcal{N}(\omega_x, \omega_y) d\omega_x d\omega_y \tag{15.3-5}$$

*Vertical slit:*

$$S_2(m) = \int_{\omega_x(m)}^{\omega_x(m+1)} \int_{-\infty}^{\infty} \mathcal{N}(\omega_x, \omega_y) d\omega_x d\omega_y \tag{15.3-6}$$

*Ring:*

$$S_3(m) = \int_{\rho(m)}^{\rho(m+1)} \int_0^{2\pi} \mathcal{N}(\rho, \theta) d\rho d\theta \tag{15.3-7}$$

*Sector:*

$$S_4(m) = \int_0^{\theta(m+1)} \int_{\theta(m)}^{\infty} \mathcal{N}(\rho, \theta) d\rho d\theta \tag{15.3-8}$$



For a discrete image array  $F(j, k)$ , the discrete Fourier transform

$$\mathcal{F}(u, v) = \frac{1}{N} \sum_{j=0}^{N-1} \sum_{k=0}^{N-1} F(j, k) \exp\left\{\frac{-2\pi i}{N}(ux + vy)\right\} \quad (15.3-9)$$

for  $u, v = 0, \dots, N-1$  can be examined directly for feature extraction purposes. Horizontal slit, vertical slit, ring and sector features can be defined analogous to Eqs. 15.3-5 to 15.3-8. This concept can be extended to other unitary transforms, such as the Hadamard and Haar transforms.

#### 15.4. TEXTURE CHARACTERIZATION

Many portions of images of natural scenes are devoid of sharp edges over large areas. In these areas, the scene can often be characterized as exhibiting a consistent structure analogous to the texture of cloth. Image texture measurements can be used to segment an image and classify its segments.

Several authors have attempted qualitatively to define *texture*. Pickett (9) states that “texture is used to describe two-dimensional arrays of variations... The elements and rules of spacing or arrangement may be arbitrarily manipulated, provided a characteristic repetitiveness remains.” Hawkins (10) has provided a more detailed description of texture: “The notion of texture appears to depend upon three ingredients: (1) some local ‘order’ is repeated over a region which is large in comparison to the order’s size, (2) the order consists in the nonrandom arrangement of elementary parts and (3) the parts are roughly uniform entities having approximately the same dimensions everywhere within the textured region.” Although these descriptions of texture seem perceptually reasonable, they do not immediately lead to simple quantitative textural measures in the sense that the description of an edge discontinuity leads to a quantitative description of an edge in terms of its location, slope angle and height.

Texture is often qualitatively described by its *coarseness* in the sense that a patch of wool cloth is coarser than a patch of silk cloth under the same viewing conditions. The coarseness index is related to the spatial repetition period of the local structure. A large period implies a coarse texture; a small period implies a fine texture. This perceptual coarseness index is clearly not sufficient as a quantitative texture measure, but can at least be used as a guide for the slope of texture measures; that is, small numerical texture measures should imply fine texture, and large numerical measures should indicate coarse texture. It should be recognized that texture is a neighborhood property of an image point. Therefore, texture measures are inherently dependent on the size of the observation neighborhood. Because texture is a spatial property, measurements should be restricted to regions of relative uniformity. Hence it is necessary to establish the boundary of a uniform

textural region by some form of image segmentation before attempting texture measurements.

Texture may be classified as being artificial, natural or stochastic. Artificial textures consist of arrangements of symbols, such as line segments, dots and stars placed against a neutral background. Several examples of artificial texture are presented in Figure 15.4-1 (9). As the name implies, natural textures are images of natural scenes containing semi-repetitive arrangements of pixels. Examples include photographs of brick walls, terrazzo tile, sand and grass. Brodatz (11) has published an album of photographs of naturally occurring textures. Figure 15.4-2 shows several natural texture examples obtained by digitizing photographs from the Brodatz album.

A discrete stochastic field is an array of numbers that are randomly distributed in amplitude and governed by some joint probability density (12,13). When converted to light intensities, such fields can be made to approximate natural textures surprisingly well by control of the generating probability density. This technique is useful for generating realistic appearing artificial scenes for applications such as airplane flight simulators. Stochastic texture fields are also an extremely useful tool for investigating human perception of texture as a guide to the development of texture feature extraction methods.

In the early 1960s, Julesz (14) attempted to determine the parameters of stochastic texture fields of perceptual importance. This study was extended later by Julesz et al. (15–17). Further extensions of Julesz's work have been made by Pollack (18) Purks and Richards (19) and Pratt et al. (13,20). These studies have provided valuable insight into the mechanism of human visual perception and have led to some useful quantitative texture measurement methods.

Figure 15.4-1 is a model for stochastic texture generation. In this model, an array of independent, identically distributed random variables  $W(j, k)$  passes through a linear or nonlinear spatial operator  $O\{\cdot\}$  to produce a stochastic texture array  $F(j, k)$ . By controlling the form of the generating probability density  $p(W)$  and the spatial operator, it is possible to create texture fields with specified statistical properties. Consider a continuous amplitude pixel  $x_0$  at some coordinate  $(j, k)$  in  $F(j, k)$ . Let the set  $\{z_1, z_2, \dots, z_J\}$  denote neighboring pixels but not necessarily nearest geometric neighbors, raster scanned in a conventional top-to-bottom, left-to-right fashion. The conditional probability density of  $x_0$  conditioned on the state of its neighbors is given by

$$p(x_0|z_1, \dots, z_J) = \frac{p(x_0, z_1, \dots, z_J)}{p(z_1, \dots, z_J)}. \quad (15.4-1)$$

The first-order density  $p(x_0)$  employs no conditioning, the second-order density  $p(x_0|z_1)$  implies that  $J = 1$ , the third-order density implies that  $J = 2$ , and so on.

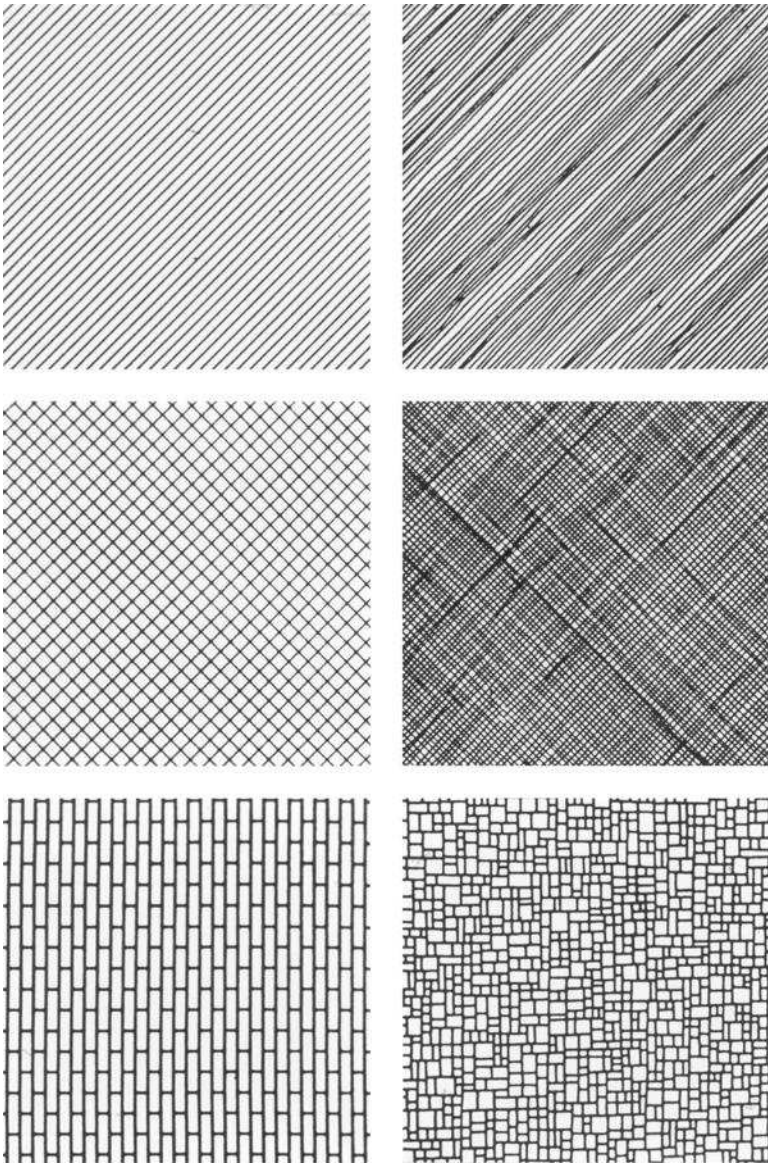


**FIGURE 15.4-1.** Artificial texture.

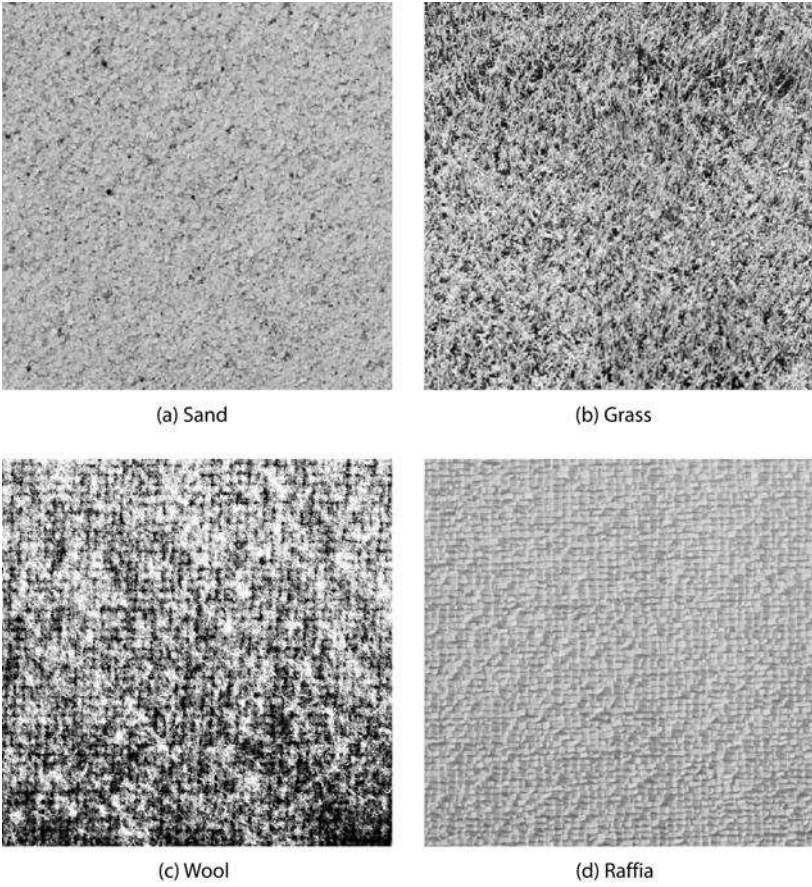


FIGURE 15.4-2. Brodatz texture fields.

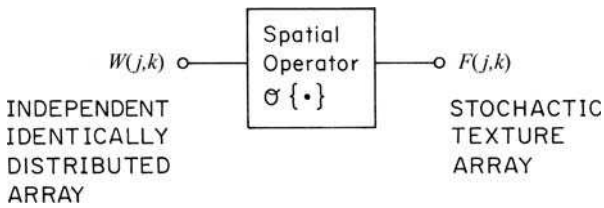


FIGURE 15.4-3. Stochastic texture field generation model.

**15.4.1. Julesz Texture Fields**

In his pioneering texture discrimination experiments, Julesz utilized Markov process state methods to create stochastic texture arrays independently along rows of the array. The family of Julesz stochastic textures are described in Pratt(4Ed., 548-549).

Figure 15.4-4 contains several examples of Julesz texture field discrimination tests performed by Pratt et al. (20). In these tests, the textures were generated according to the presentation format of Figure 15.4-5. In these and subsequent visual texture discrimination tests, the perceptual differences are often small. Proper discrimination testing should be performed using high-quality photographic transparencies, prints or electronic displays. The following moments were used as simple indicators of differences between generating distributions and densities of the stochastic fields.

$$\eta = E\{x_0\} \tag{15.4-2a}$$

$$\sigma^2 = E\{[x_0 - \eta]^2\} \tag{15.4-2b}$$

$$\alpha = \frac{E\{[x_0 - \eta][x_1 - \eta]\}}{\sigma^2} \tag{15.4-2c}$$

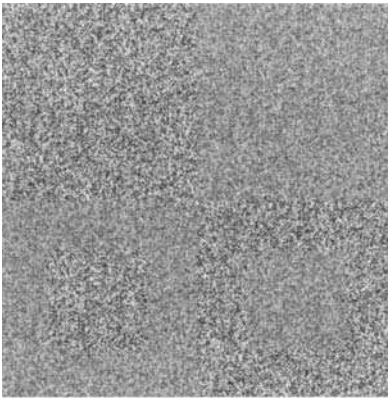
$$\theta = \frac{E\{[x_0 - \eta][x_1 - \eta][x_2 - \eta]\}}{\sigma^3} \tag{15.5-2d}$$

The examples of Figure 15.4-4a and b indicate that texture field pairs differing in their first- and second-order distributions can be discriminated. The example of Figure 15.4-4c supports the conjecture, attributed to Julesz, that differences in third-order, and presumably, higher-order distribution texture fields cannot be perceived provided that their first-order and second-order distributions are pairwise identical.

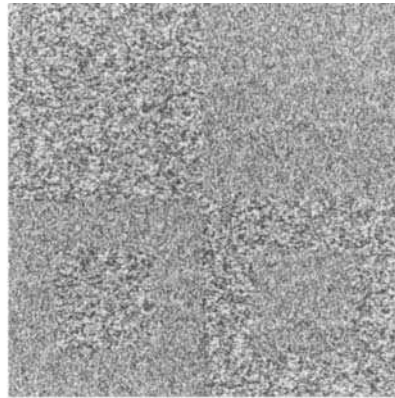
**15.4.2. Pratt, Faugeras and Gagalowicz Texture Fields**

Pratt et al. (20) have extended the work of Julesz et al. (14–17) in an attempt to study the discrimination ability of spatially correlated stochastic texture fields. A class of Gaussian fields was generated according to the conditional probability density of Eq. 15.4-1 where the covariance matrix of the Gaussian process is of the parametric form

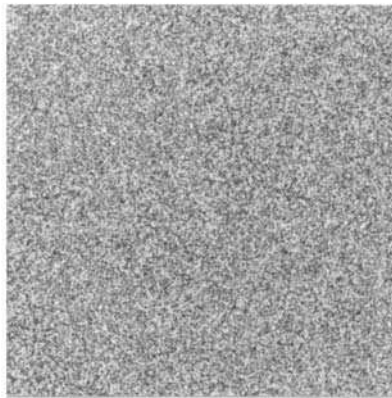
$$\mathbf{K}_{J+1} = \begin{bmatrix} 1 & \alpha & \beta & \gamma & \cdots \\ \alpha & & & & \\ \beta & & \sigma^{-2}\mathbf{K}_J & & \\ \gamma & & & & \\ \vdots & & & & \end{bmatrix} \tag{15.4-3}$$



(a) Different first order  
 $\sigma_A = 0.289, \sigma_B = 0.204$



(b) Different second order  
 $\sigma_A = 0.289, \sigma_B = 0.289$   
 $\alpha_A = 0.250, \alpha_B = -0.250$



(c) Different third order  
 $\sigma_A = 0.289, \sigma_B = 0.289$   
 $\alpha_A = 0.000, \alpha_B = 0.000$   
 $\theta_A = 0.058, \theta_B = -0.058$

**FIGURE 15.4-4.** Field comparison of Julesz stochastic fields;  $\eta_A = \eta_B = 0.500$ .

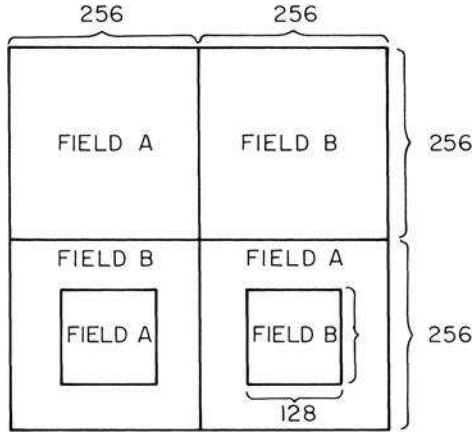
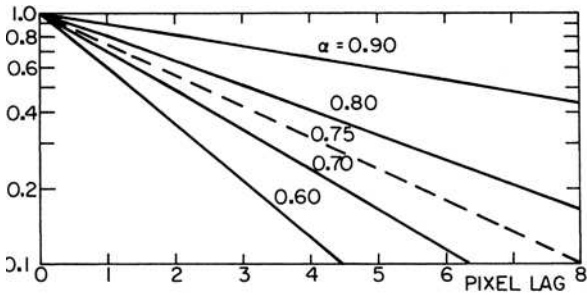
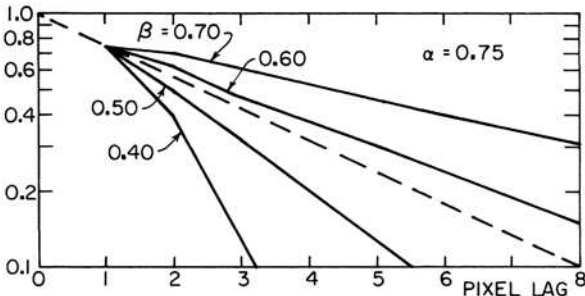


FIGURE 15.4-5. Presentation format for visual texture discrimination experiments.



(a) Constrained second-order density



(b) Constrained third-order density

FIGURE 15.4-6. Row correlation factors for stochastic field generation. Dashed line, field A; solid line, field B.

where  $\alpha, \beta, \gamma, \dots$  denote correlation lag terms. Figure 15.4-6 presents an example of the row correlation functions used in the texture field comparison tests described below.

Figures 15.4-7 and 15.4-8 contain examples of Gaussian texture field comparison tests. In Figure 15.4-7, the first-order densities are set equal, but the second-order nearest neighbor conditional densities differ according to the covariance function plot of Figure 15.4-6a. Visual discrimination can be made in Figure 15.4-7, in which the correlation parameter differs by 20%. Visual discrimination has been found to be marginal when the correlation factor differs by less than 10% (20). The first- and second-order densities of each field are fixed in Figure 15.4-8, and the third-order

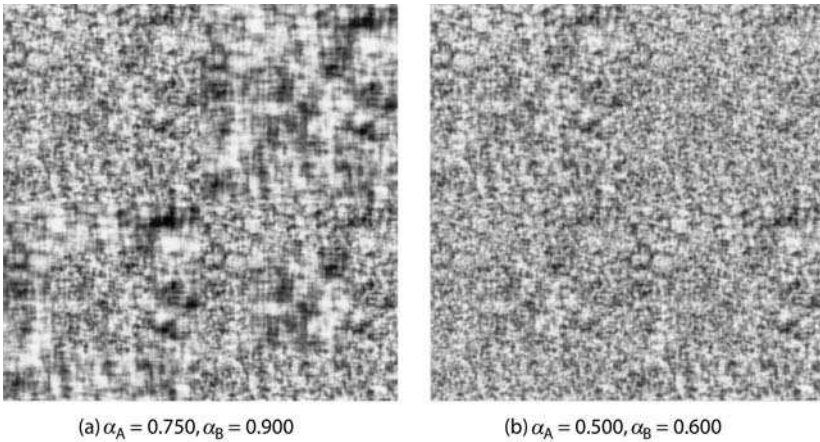


**FIGURE 15.4-7.** Field comparison of Gaussian stochastic fields with different second-order nearest neighbor densities;  $\eta_A = \eta_B = 0.500, \sigma_A = \sigma_B = 0.167$ .

conditional densities differ according to the plan of Figure 15.4-6b. Visual discrimination is possible. The test of Figure 15.4-8 seemingly provides a counterexample to the Julesz conjecture. In this test,  $[p^A(x_0) = p^B(x_0)]$  and  $p^A(x_0, x_1) = p^B(x_0, x_1)$ , but  $p^A(x_0, x_1, x_2) \neq p^B(x_0, x_1, x_2)$ . However, the general second-order density pairs  $p^A(x_0, z_j)$  and  $p^B(x_0, z_j)$  are not necessarily equal for an arbitrary neighbor  $z_j$ , and therefore the conditions necessary to disprove Julesz's conjecture are violated.

To test the Julesz conjecture for realistically appearing texture fields, it is necessary to generate a pair of fields with identical first-order densities, identical Markovian type second-order densities, and differing third-order densities for every pair of similar observation points in both fields. An example of such a pair of fields is presented in Figure 15.4-9 for a non-Gaussian generating process (19). In this example, the texture appears identical in both fields, thus supporting the Julesz conjecture.



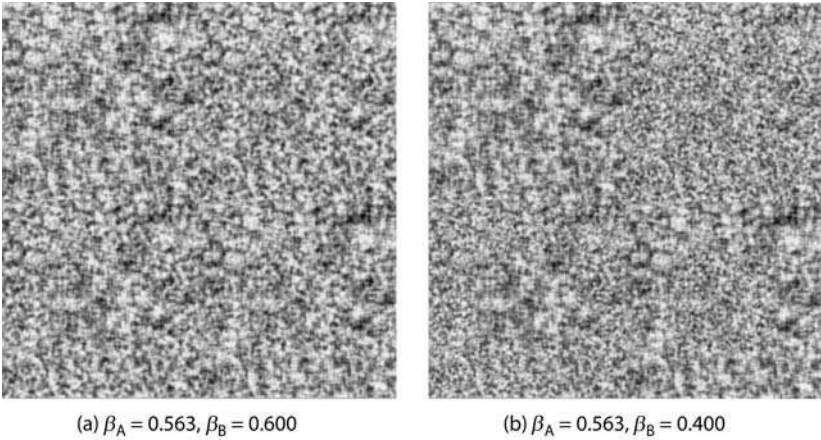


**FIGURE 15.4-8.** Field comparison of Gaussian stochastic fields with different third-order nearest neighbor densities;  $\eta_A = \eta_B = 0.500$ ,  $\sigma_A = \sigma_B = 0.167$ ,  $\alpha_A = \alpha_B = 0.750$ .

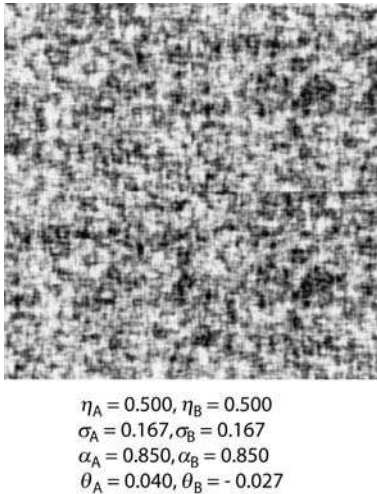


**FIGURE 15.4-9.** Field comparison of correlated Julesz stochastic fields with identical first- and second-order densities, but different third-order densities.

Gagalowicz has succeeded in generating a pair of texture fields that disprove the Julesz conjecture (21). However, the counterexample, shown in Figure 15.4-10, is not very realistic in appearance. Thus, it seems likely that if a statistically based

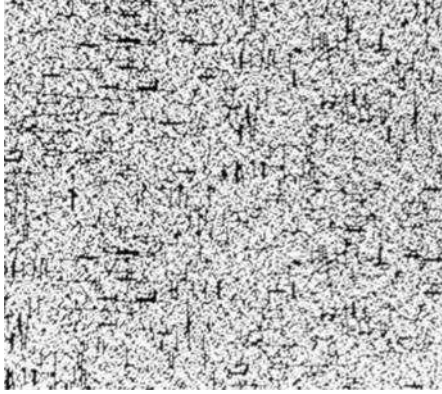
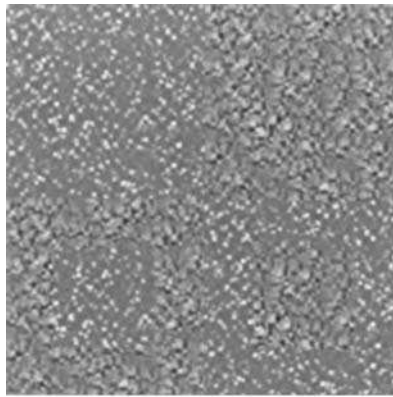


**FIGURE 15.4-10.** Galagowicz counterexample.



$$\begin{aligned}\eta_A &= 0.413, \eta_B = 0.412 \\ \sigma_A &= 0.078, \sigma_B = 0.078 \\ \alpha_A &= 0.915, \alpha_B = 0.917 \\ \theta_A &= 1.512, \theta_B = 0.006\end{aligned}$$

**FIGURE 15.4-11.** Field comparison of correlated stochastic fields with identical means, variances and autocorrelation functions, but different  $n$ th-order probability densities generated by different processing of the same input field. Input array consists of uniform random variables raised to the 256th power. Moments are computed.

texture measure can be developed, it need not utilize statistics greater than second-order.

Because a human viewer is sensitive to differences in the mean, variance and autocorrelation function of the texture pairs, it is reasonable to investigate the sufficiency of these parameters in terms of texture representation. Figure 15.4-11 presents examples of the comparison of texture fields with identical means, vari-

ances and autocorrelation functions, but different  $n$ th-order probability densities. Visual discrimination is readily accomplished between the fields. This leads to the conclusion that these low-order moment measurements, by themselves, are not always sufficient to distinguish texture fields.

## 15.5. TEXTURE FEATURES

As noted in Section 15.4, there is no commonly accepted quantitative definition of visual texture. As a consequence, researchers seeking a quantitative texture measure have been forced to search intuitively for texture features, and then attempt to evaluate their performance by techniques such as those presented in Section 15.1. The following subsections describe several texture features of historical and practical importance. References 22 to 24 provide surveys on image texture feature extraction. Randen and Husoy (25) have performed a comprehensive study of many texture feature extraction methods.

### 15.5.1. Fourier Spectra Methods

Several studies (8,26,27) have considered textural analysis based on the Fourier spectrum of an image region, as discussed in Section 15.2. Because the degree of texture coarseness is proportional to its spatial period, a region of coarse texture should have its Fourier spectral energy concentrated at low spatial frequencies. Conversely, regions of fine texture should exhibit a concentration of spectral energy at high spatial frequencies. Although this correspondence exists to some degree, difficulties often arise because of spatial changes in the period and phase of texture pattern repetitions. Experiments (10) have shown that there is considerable spectral overlap of regions of distinctly different natural texture, such as urban, rural and woodland regions extracted from aerial photographs. On the other hand, Fourier spectral analysis has proved successful (28,29) in the detection and classification of coal miner's black lung disease, which appears as diffuse textural deviations from the norm.

### 15.5.2. Edge Detection Methods

Rosenfeld and Troy (30) have proposed a measure of the number of edges in a neighborhood as a textural measure. As a first step in their process, an edge map array  $E(j, k)$  is produced by some edge detector such that  $E(j, k) = 1$  for a detected edge and  $E(j, k) = 0$  otherwise. Usually, the detection threshold is set lower than the normal setting for the isolation of boundary points. This texture measure is defined as

$$T(j, k) = \frac{1}{W^2} \sum_{m=-w}^w \sum_{n=-w}^w E(j+m, k+n) \quad (15.5-1)$$

where  $W = 2w + 1$  is the dimension of the observation window. A variation of this approach is to substitute the edge gradient  $G(j, k)$  for the edge map array in Eq. 15.5-1. A generalization of this concept is presented in Section 15.5.4.

### 15.5.3. Autocorrelation Methods

The autocorrelation function has been suggested as the basis of a texture measure (30). Although it has been demonstrated in the preceding section that it is possible to generate visually different stochastic fields with the same autocorrelation function, this does not necessarily rule out the utility of an autocorrelation feature set for natural images. The *autocorrelation function* is defined as

$$A_F(m, n) = \sum_j \sum_k F(j, k)F(j - m, k - n) \tag{15.5-2}$$

for computation over a  $W \times W$  window with  $-T \leq m, n \leq T$  pixel lags. Presumably, a region of coarse texture will exhibit a higher correlation for a fixed shift  $(m, n)$  than will a region of fine texture. Thus texture coarseness should be proportional to the spread of the autocorrelation function. Faugeras and Pratt (5) have proposed the following set of autocorrelation spread measures:

$$S(u, v) = \sum_{m=0}^T \sum_{n=-T}^T (m - \eta_m)^u (n - \eta_n)^v A_F(m, n) \tag{15.5-3a}$$

where

$$\eta_m = \sum_{m=0}^T \sum_{n=-T}^T mA_F(m, n) \tag{15.5-3b}$$

$$\eta_n = \sum_{m=0}^T \sum_{n=-T}^T nA_F(m, n). \tag{15.5-3c}$$

In Eq. 15.5-3, computation is only over one-half of the autocorrelation function because of its symmetry. Features of potential interest include the profile spreads  $S(2, 0)$  and  $S(0, 2)$ , the cross-relation  $S(1, 1)$  and the second-degree spread  $S(2, 2)$ .

Figure 15.5-1 shows perspective views of the autocorrelation functions of the four Brodatz texture examples (5). Bhattacharyya distance measurements of these texture fields, performed by Faugeras and Pratt (5), are presented in Table 15.5-1. These  $B$ -distance measurements indicate that the autocorrelation shape features are marginally adequate for the set of four shape features, but unacceptable for fewer features. Tests by Faugeras and Pratt (5) verify that the  $B$ -distances are low for

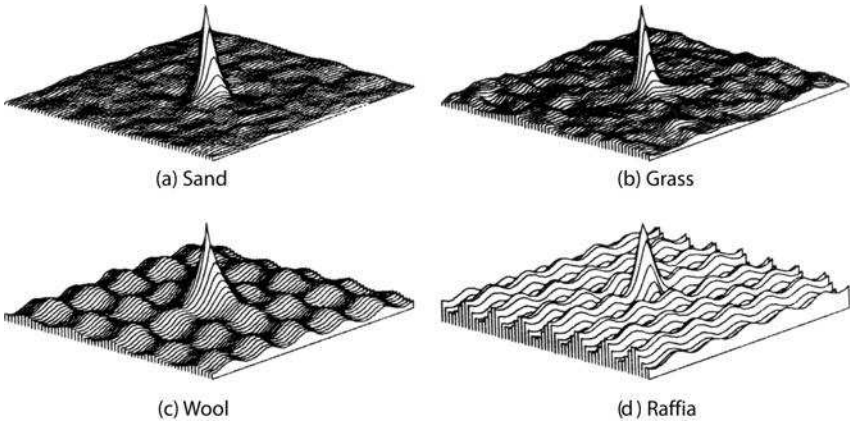


FIGURE 15.5-1. Perspective views of autocorrelation functions of Brodatz texture fields.

TABLE 15.5-1. Bhattacharyya Distance of Texture Feature Sets for Prototype Texture Fields: Autocorrelation Features

Field Pair	Set 1 <sup>a</sup>	Set 2 <sup>b</sup>	Set 3 <sup>c</sup>
Grass – sand	5.05	4.29	2.92
Grass – raffia	7.07	5.32	3.57
Grass – wool	2.37	0.21	0.04
Sand – raffia	1.49	0.58	0.35
Sand – wool	6.55	4.93	3.14
Raffia – wool	8.70	5.96	3.78
Average	5.21	3.55	2.30

<sup>a</sup>1: S(2, 0), S(0, 2), S(1, 1), S(2,2).

<sup>b</sup>2: S(1,1), S(2,2).

<sup>c</sup>3: S(2,2).

the stochastic field pairs of Figure 15.4-119, which have the same autocorrelation functions but are visually distinct.

### 15.5.4. Decorrelation Methods

Stochastic texture fields generated by the model of Figure 15.4-3 can be described quite compactly by specification of the spatial operator  $O\{\cdot\}$  and the stationary

first-order probability density  $p(W)$  of the independent, identically distributed generating process  $W(j, k)$ . This observation has led to a texture feature extraction procedure, developed by Faugeras and Pratt (5), in which an attempt has been made to invert the model and estimate its parameters. Figure 15.5-2 is a block diagram of their decorrelation method of texture feature extraction. In the first step of the method, the spatial autocorrelation function  $A_F(m, n)$  is measured over a texture field to be analyzed. The autocorrelation function is then used to develop a whitening filter, with an impulse response  $H_W(j, k)$ , using techniques described in Section 18.2. The *whitening filter* is a special type of *decorrelation operator*. It is used to generate the whitened field

$$\hat{W}(j, k) = F(j, k) \otimes H_W(j, k). \tag{15.5-4}$$

This whitened field, which is spatially uncorrelated, can be utilized as an estimate of the independent generating process  $W(j, k)$  by forming its first-order histogram. If  $W(j, k)$  were known exactly, then, in principle, it could be used to identify  $O\{\cdot\}$  from the texture observation  $F(j, k)$ . But, the whitened field estimate  $\hat{W}(j, k)$  can only be used to identify the autocorrelation function, which, of course, is already known. As a consequence, the texture generation model cannot be inverted. However, the shape of the histogram of  $\hat{W}(j, k)$  augmented by the shape of the autocorrelation function have proved to be useful texture features.

Figure 15.5-3 shows the whitened texture fields of the Brodatz test images. Figure 15.5-4 provides plots of their histograms. The whitened fields are observed to be visually distinctive; their histograms are also different from one another. Tables 15.5-2 and 15.5-3 list, respectively, the  $B$ -distance measurements for histogram shape features alone, and histogram and autocorrelation shape features. The  $B$ -distance is relatively low for some of the test textures for histogram-only features. A combination of the autocorrelation shape and histogram shape features provides good results, as noted in Table 15.5-3.

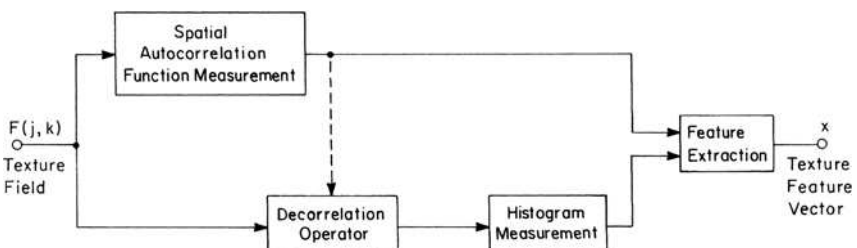
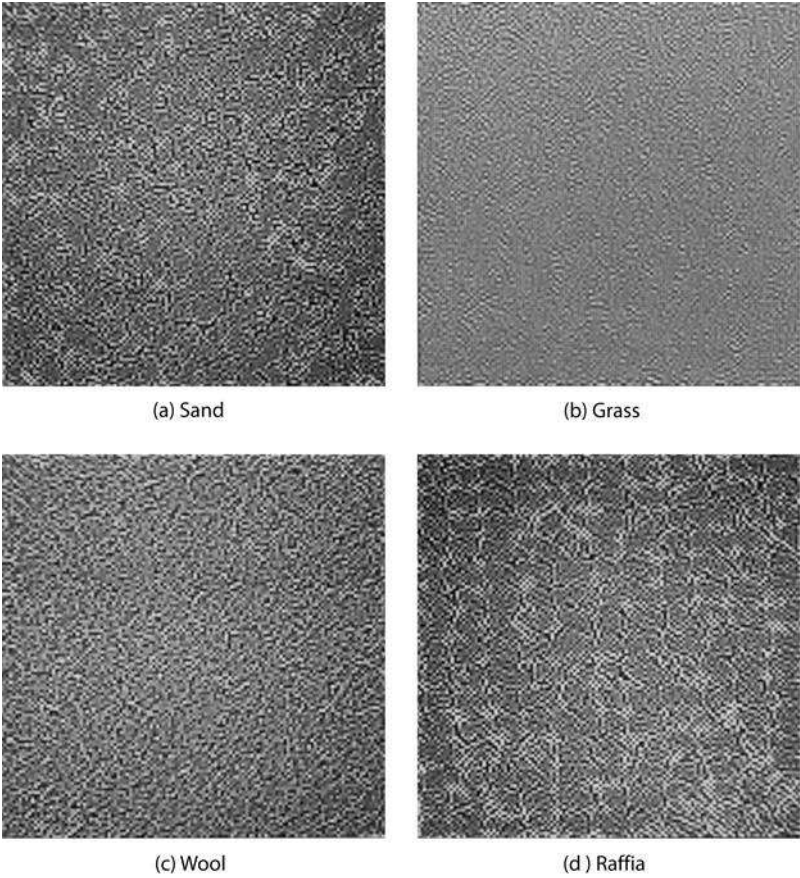


FIGURE 15.5-2. Decorrelation method of texture feature extraction.



**FIGURE 15.5-3.** Whitened Brodatz texture fields.

An obvious disadvantage of the decorrelation method of texture measurement, as just described, is the large amount of computation involved in generating the whitening operator. An alternative is to use an approximate decorrelation operator. Two candidates, investigated by Faugeras and Pratt (5), are the Laplacian and Sobel gradients. Figure 15.5-5 shows the resultant decorrelated fields for these operators. The  $B$ -distance measurements using the Laplacian and Sobel gradients are presented in Tables 15.5-2 and 15.5-3. These tests indicate that the whitening operator is superior, on average, to the Laplacian operator. But the Sobel operator yields the largest average and largest minimum  $B$ -distances.

15.5.5. Dependency Matrix Methods

Haralick et al. (7) have proposed a number of textural features based on the joint amplitude histogram of pairs of pixels. If an image region contains fine texture, the two-dimensional histogram of pixel pairs will tend to be uniform, and for coarse texture, the histogram values will be skewed toward the diagonal of the histogram. Consider the pair of pixels  $F(j, k)$  and  $F(m, n)$  that are separated by  $r$  radial units at an angle  $\theta$  with respect to the horizontal axis. Let  $P(a, b; j, k, r, \theta)$  represent the two-dimensional histogram measurement of an image over some  $W \times W$  window where each pixel is quantized over a range  $0 \leq a, b \leq L - 1$ . The two-dimensional histogram can be considered as an estimate of the joint probability distribution

$$P(a, b; j, k, r, \theta) \approx P_R[F(j, k) = a, F(m, n) = b]. \tag{15.5-5}$$

For each member of the parameter set  $(j, k, r, \theta)$ , the two-dimensional histogram may be regarded as a  $L \times L$  array of numbers relating the measured statistical dependency of pixel pairs. Such arrays have been called a *gray scale dependency matrix* or a *co-occurrence matrix*. Because a  $L \times L$  histogram array must be accumulated for each image point  $(j, k)$  and separation set  $(r, \theta)$  under consideration, it is usually computationally necessary to restrict the angular and radial separation to a limited number of values. Figure 15.5-6 illustrates geometrical relationships of histogram measurements made for four radial separation points and angles of  $\theta = 0, \pi/4, \pi/2, 3\pi/4$  radians under the assumption of angular symmetry.

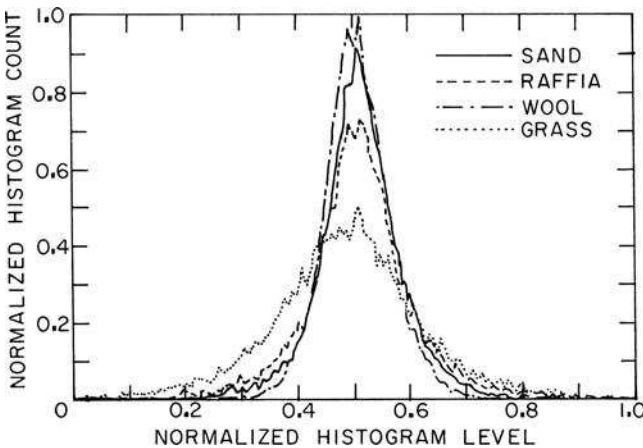


FIGURE 15.5-4. First-order histograms of whitened Brodatz texture fields.



**TABLE 15.5-2. Bhattacharyya Distance of Texture Feature Sets for Prototype Texture Fields: Histogram Features**

Field Pair	Texture Feature											
	Whitening				Laplacian				Sobel			
	Set 1 <sup>a</sup>	Set 2 <sup>b</sup>	Set 3 <sup>c</sup>	Set 4 <sup>d</sup>	Set 1	Set 2	Set 3	Set 4	Set 1	Set 2	Set 3	Set 4
Grass – sand	4.61	4.52	4.04	0.77	1.29	1.28	0.19	0.66	9.90	7.15	4.41	2.31
Grass – raffia	1.15	1.04	0.51	0.52	3.48	3.38	0.55	1.87	2.20	1.00	0.27	0.02
Grass – wool	1.68	1.59	1.07	0.14	2.23	2.19	1.76	0.13	2.98	1.67	1.01	1.46
Sand – raffia	12.76	12.60	10.93	0.24	2.23	2.14	1.57	0.28	5.09	4.79	3.51	2.30
Sand – wool	12.61	12.55	8.24	2.19	7.73	7.65	7.42	1.40	9.98	5.01	1.67	0.56
Raffia – wool	4.20	3.87	0.39	1.47	4.59	4.43	1.53	3.13	7.73	2.31	0.41	1.41
Average	6.14	6.03	4.20	0.88	3.59	3.51	2.17	1.24	6.31	3.66	1.88	1.35

<sup>a</sup>Set 1: S<sub>M</sub>, S<sub>D</sub>, S<sub>S</sub>, S<sub>K</sub>.

<sup>b</sup>Set 2: S<sub>S</sub>, S<sub>K</sub>.

<sup>c</sup>Set 3: S<sub>S</sub>.

<sup>d</sup>Set 4: S<sub>K</sub>.

**TABLE 15.5-3. Bhattacharyya Distance of Texture Feature Sets for Prototype Texture Fields: Autocorrelation and Histogram Features**

Field Pair	Texture Feature											
	Whitening				Laplacian				Sobel			
	Set 1 <sup>a</sup>	Set 2 <sup>b</sup>	Set 3 <sup>c</sup>	Set 4	Set 1	Set 2	Set 3	Set 4	Set 1	Set 2	Set 3	Set 4
Grass – sand	9.80	9.72	8.94	7.48	6.39	6.37	5.61	4.21	15.34	12.34	11.48	10.12
Grass – raffia	8.47	8.34	6.56	4.66	10.61	10.49	8.74	6.95	9.46	8.15	6.33	4.59
Grass – wool	4.17	4.03	1.87	1.70	4.64	4.59	2.48	2.31	5.62	4.05	1.87	1.72
Sand – raffia	15.26	15.08	13.22	12.98	3.85	3.76	2.74	2.49	6.75	6.40	5.39	5.13
Sand – wool	19.14	19.08	17.43	15.72	14.43	14.38	12.72	10.86	18.75	12.3	10.52	8.29
Raffia – wool	13.29	13.14	10.32	7.96	13.93	13.75	10.90	8.47	17.28	11.19	8.24	6.08
Average	11.69	11.57	9.72	8.42	8.98	8.89	7.20	5.88	12.20	9.08	7.31	5.99

<sup>a</sup>Set 1:  $S_M, S_D, S_S, S_K, S(2,0), S(0,2), S(1,1), S(2,2)$ .

<sup>b</sup>Set 2:  $S_S, S_K, S(2,0), S(0,2), S(1,1), S(2,2)$ .

<sup>c</sup>Set 3:  $S_S, S_K, S(1,1), S(2,2)$ .

<sup>d</sup>Set 4:  $S_S, S_K, S(2,2)$ .

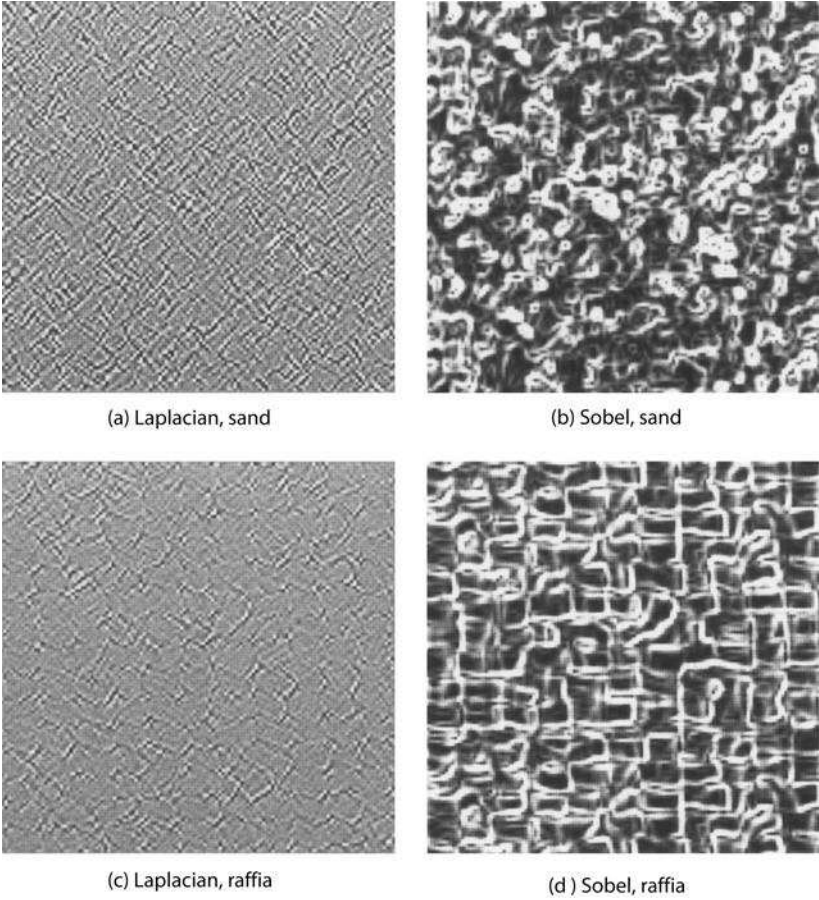


FIGURE 15.5-5. Laplacian and Sobel gradients of Brodatz texture fields.

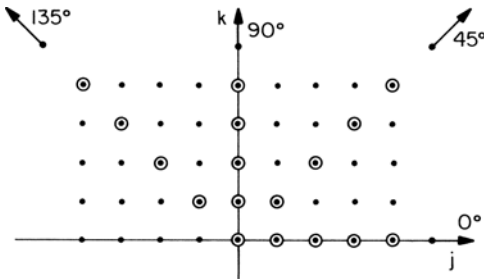


FIGURE 15.5-6. Geometry for measurement of gray scale dependency matrix.

To obtain statistical confidence in estimation of the joint probability distribution, the histogram must contain a reasonably large average occupancy level. This can be achieved either by restricting the number of amplitude quantization levels or by utilizing a relatively large measurement window. The former approach results in a loss of accuracy in the measurement of low-amplitude texture, while the latter approach causes errors if the texture changes over the large window. A typical compromise is to use 16 gray levels and a window of about 30 to 50 pixels on each side. Perspective views of joint amplitude histograms of two texture fields are presented in Figure 15.5-7.

For a given separation set  $(r, \theta)$ , the histogram obtained for fine texture tends to be more uniformly dispersed than the histogram for coarse texture. Texture coarseness can be measured in terms of the relative spread of histogram occupancy cells about the main diagonal of the histogram. Haralick et al. (7) have proposed a number of spread indicators for texture measurement. Several of these have been presented in Section 15.2. As an example, the inertia function of Eq. 15.2-15 results in a texture measure of the form

$$T(j, k, r, \theta) = \sum_{a=0}^{L-1} \sum_{b=0}^{L-1} (a-b)^2 P(a, b; j, k, r, \theta). \tag{15.5-6}$$

If the textural region of interest is suspected to be angularly invariant, it is reasonable to average over the measurement angles of a particular measure to produce the mean textural measure (23)

$$M_T(j, k, r) = \frac{1}{N_\theta} \sum_{\theta} T(j, k, r, \theta) \tag{15.5-7}$$

where the summation is over the angular measurements, and  $N_\theta$  represents the number of such measurements. Similarly, an angular-independent texture variance may be defined as

$$V_T(j, k, r) = \frac{1}{N_\theta} \sum_{\theta} [T(j, k, r, \theta) - M_T(j, k, r)]^2. \tag{15.5-8}$$

Another useful measurement is the angular independent spread defined by

$$S(j, k, r) = \text{MAX}_{\theta} \{T(j, k, r, \theta)\} - \text{MIN}_{\theta} \{T(j, k, r, \theta)\} \tag{15.5-9}$$

**15.5.6. Microstructure Methods**

Examination of the whitened, Laplacian and Sobel gradient texture fields of Figures 15.5-3 and 15.5-5 reveals that they appear to accentuate the microstructure of the texture. This observation was the basis of a texture feature extraction scheme developed by Laws (31), and described in Figure 15.5-8. Laws proposed that the set of nine  $3 \times 3$  pixel impulse response arrays  $H_i(j, k)$  shown in Figure 15.5-9, be convolved with a texture field to accentuate its microstructure. The  $i$ th microstructure array is defined as

$$M_i(j, k) = F(j, k) \otimes H_i(j, k). \tag{15.6-10}$$

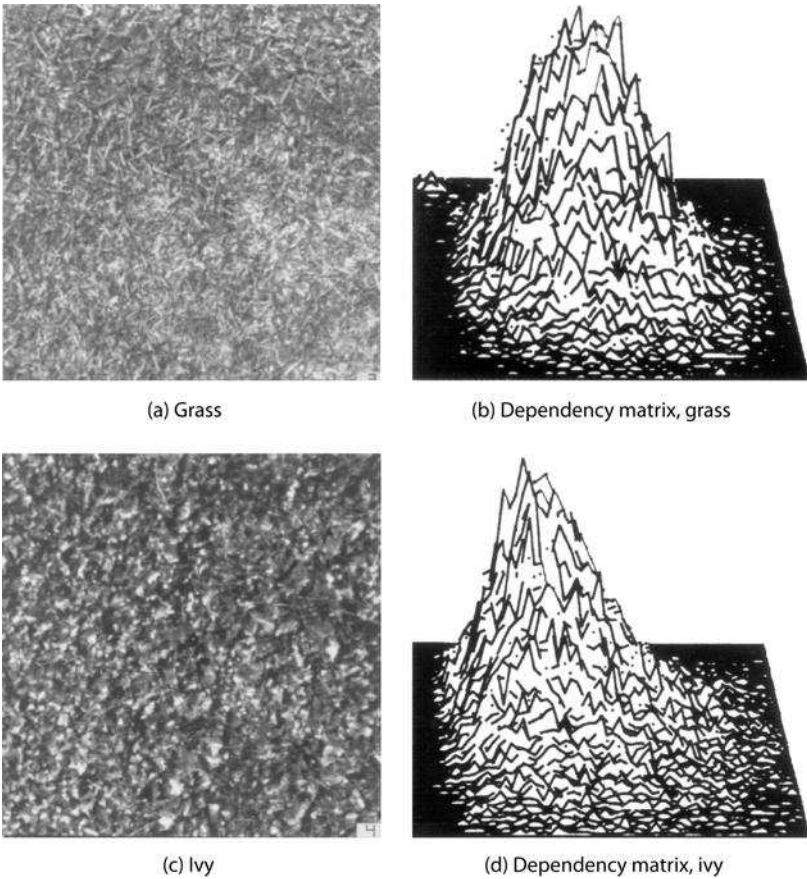


**FIGURE 15.5-7.** Perspective views of gray scale dependency matrices for  $r = 4, \theta = 0$ .

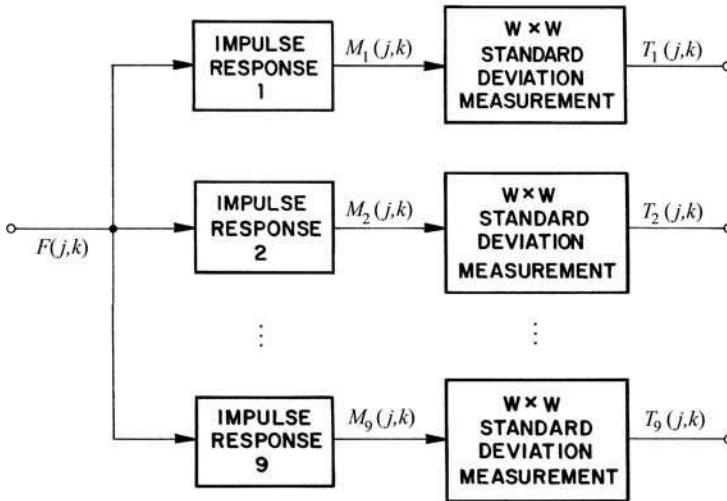


FIGURE 15.5-8. Laws microstructure texture feature extraction method.

Then, the energy of these microstructure arrays is measured by forming their moving window standard deviation  $T_i(j, k)$  according to Eq. 15.2-2, over a window that contains a few cycles of the repetitive texture.

$\frac{1}{36} \begin{bmatrix} 1 & 2 & 1 \\ 2 & 4 & 2 \\ 1 & 2 & 1 \end{bmatrix}$	$\frac{1}{12} \begin{bmatrix} 1 & 0 & -1 \\ 2 & 0 & -2 \\ 1 & 0 & -1 \end{bmatrix}$	$\frac{1}{12} \begin{bmatrix} -1 & 2 & -1 \\ -2 & 4 & -2 \\ -1 & 2 & -1 \end{bmatrix}$
Laws 1	Laws 2	Laws 3
$\frac{1}{12} \begin{bmatrix} -1 & -2 & -1 \\ 0 & 0 & 0 \\ 1 & 2 & 1 \end{bmatrix}$	$\frac{1}{4} \begin{bmatrix} 1 & 0 & -1 \\ 0 & 0 & 0 \\ -1 & 0 & 1 \end{bmatrix}$	$\frac{1}{4} \begin{bmatrix} -1 & 2 & -1 \\ 0 & 0 & 0 \\ 1 & -2 & 1 \end{bmatrix}$
Laws 4	Laws 5	Laws 6
$\frac{1}{12} \begin{bmatrix} -1 & -2 & -1 \\ 2 & 4 & 2 \\ -1 & -2 & -1 \end{bmatrix}$	$\frac{1}{4} \begin{bmatrix} -1 & 0 & 1 \\ 2 & 0 & -2 \\ -1 & 0 & 1 \end{bmatrix}$	$\frac{1}{4} \begin{bmatrix} 1 & -2 & 1 \\ -2 & 4 & -2 \\ 1 & -2 & 1 \end{bmatrix}$
Laws 7	Laws 8	Laws 9

FIGURE 15.5-9. Laws microstructure impulse response arrays.

Figure 15.5-10 shows a mosaic of several Brodatz texture fields that have been used to test the Laws feature extraction method. Note that some of the texture fields appear twice in the mosaic. Figure 15.5-11 illustrates the texture arrays  $T_i(j, k)$ . In classification tests of the Brodatz textures performed by Laws (31), the correct texture was identified in nearly 90% of the trials.

Many of the microstructure detection operators of Figure 15.5-9 have been encountered previously in this book: the pyramid average, the Sobel horizontal and vertical gradients, the weighted line horizontal and vertical gradients and the cross second derivative.

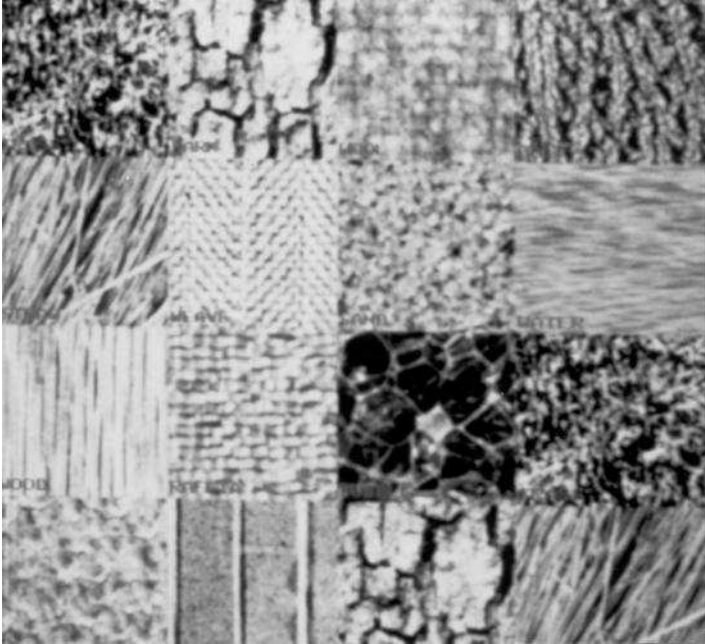
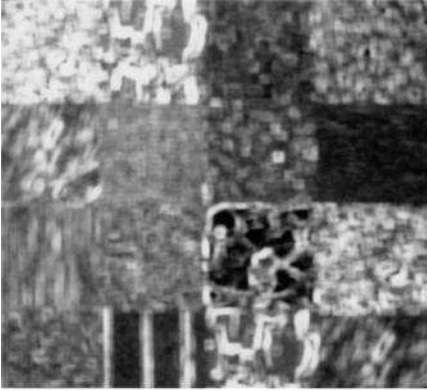
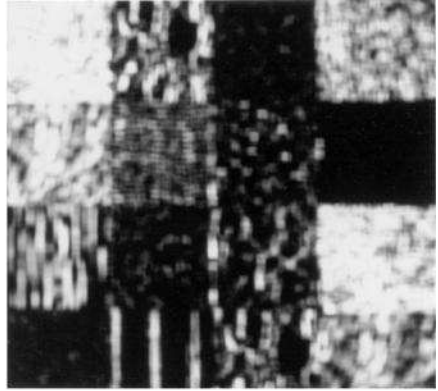


**FIGURE 15.5-10.** Mosaic of Brodatz texture fields.

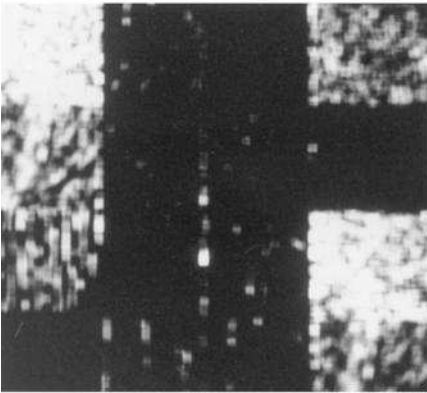
Ade (34) has suggested a microstructure texture feature extraction procedure similar in nature to the Laws method, which is based on a principal components transformation of a texture sample. Manian et al. (36) have also developed a variant of the Laws microstructure.



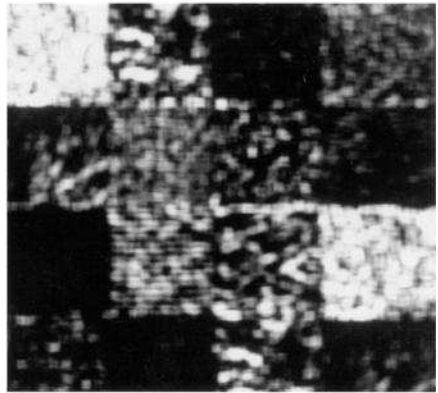
(a) Laws no. 1



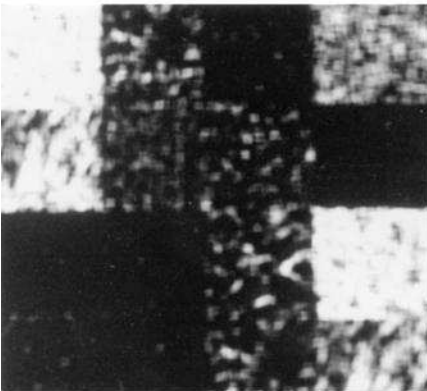
(b) Laws no. 2



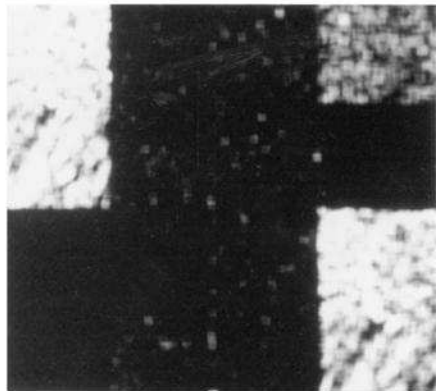
(c) Laws no. 3



(d) Laws no. 4



(e) Laws no. 5



(f) Laws no. 6

**FIGURE 15.5-11.** Laws microstructure texture features.



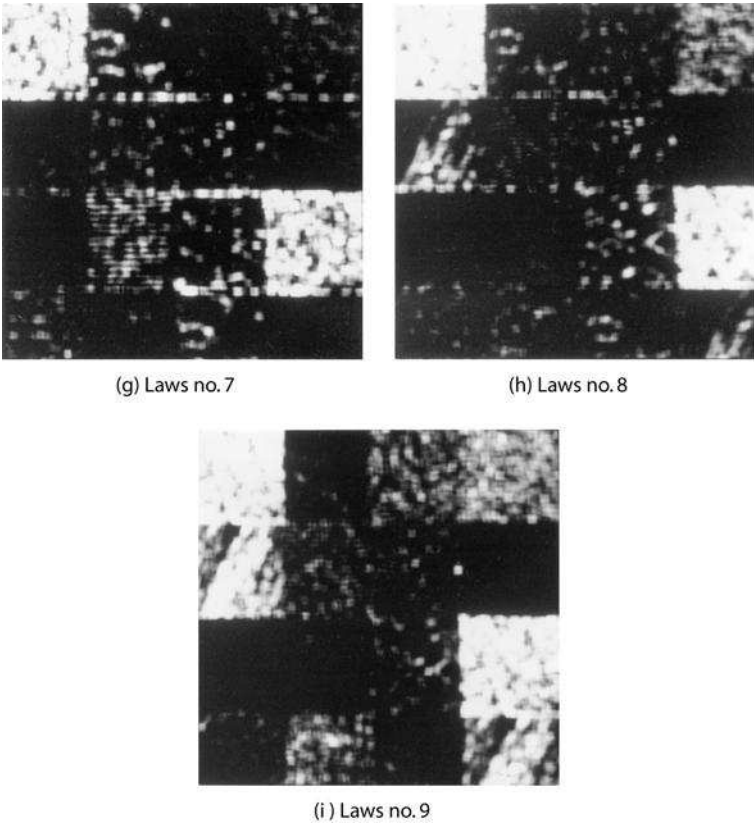


FIGURE 15.5-11. (continued) Laws microstructure texture features.

### 15.5.7. Gabor Filter Methods

The microstructure method of texture feature extraction is not easily scalable. Microstructure arrays must be derived to match the inherent periodicity of each texture to be characterized. Bovik et al. (37–39) have utilized Gabor filters (40) as an efficient means of scaling the impulse response function arrays of Figure 15.5-8 to the texture periodicity.

A two-dimensional *Gabor filter* is a complex field sinusoidal grating that is modulated by a two-dimensional Gaussian function in the spatial domain (38). Gabor filters have tunable orientation and radial frequency passbands and tunable center frequencies. A special case of the Gabor filter is the *daisy petal filter*, in which the filter lobes radiate from the origin of the spatial frequency domain. The continuous domain impulse response function of the daisy petal Gabor filter is given by (38)

$$H(x, y) = G(x', y') \exp \{2\pi i F x'\} \quad (15.5-11)$$

where  $F$  is a scaling factor and  $i = \sqrt{-1}$ . The Gaussian component is

$$G(x, y) = \frac{1}{2\pi\lambda\sigma^2} \exp \left\{ -\frac{(x/\lambda)^2 + y^2}{2\sigma^2} \right\} \quad (15.5-12)$$

where  $\sigma$  is the Gaussian spread factor and  $\lambda$  is the aspect ratio between the  $x$  and  $y$  axes. The rotation of coordinates is specified by

$$(x', y') = (x \cos \phi + y \sin \phi, -x \sin \phi + y \cos \phi) \quad (15.5-13)$$

where  $\phi$  is the orientation angle with respect to the  $x$  axis. The continuous domain filter transfer function is given by (38)

$$\mathcal{H}(u, v) = \exp \{-2\pi^2 \sigma^2 [(u' - F)^2 + (v')^2]\}. \quad (15.5-14)$$

Figure 15.5-14 shows the relationship between the real and imaginary components of the impulse response array and the magnitude of the transfer function (38). The impulse response array is composed of sine-wave gratings within the elliptical region. The half energy profile of the transfer function is shown in gray.

Grigorescu et al. (41) have performed a comprehensive comparison of Gabor filter texture features. In the comparative study of texture classification methods by Randen and Husoy (25), the Gabor filter method, like many other methods, gave mixed results. It performed well on some texture samples, but poorly on others.

### 15.5.8. Transform and Wavelet Methods

The Fourier spectra method of texture feature extraction can be generalized to other unitary transforms. The concept is straightforward. A  $N \times N$  texture sample is subdivided into  $M \times M$  pixel arrays, and a unitary transform is performed for each array yielding a  $M^2 \times 1$  feature vector. The window size needs to be large enough to contain several cycles of the texture periodicity.

Mallat (42) has used the discrete wavelet transform, based on Haar wavelets (see Section 8.4.2) as a means of generating texture feature vectors. Improved results have been obtained by Unser (43), who has used a complete Haar-based wavelet transform for a  $8 \times 8$  window. In their comparative study of texture classification, Randen and Husoy (25) used several types of Daubechies transforms up to size 10 (see Section 8.4.4).

The transform and wavelet methods provide reasonably good classification for many texture samples (25). However, the computational requirement is high for large windows.

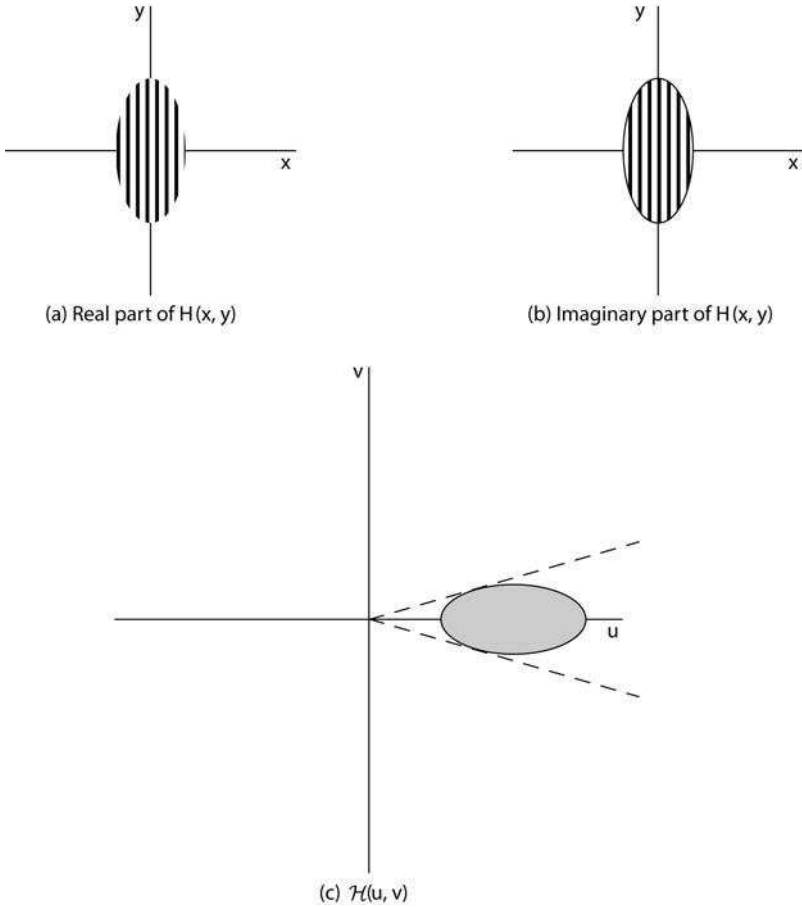


**FIGURE 15.5-14.** Relationship between impulse response array and transfer function of a Gabor filter.

**15.5.9. Singular-Value Decomposition Methods**

Ashjari (44) has proposed a texture measurement method based on the singular-value decomposition of a texture sample. In this method, a  $N \times N$  texture sample is treated as a  $N \times N$  matrix  $\mathbf{X}$ , and the amplitude-ordered set of singular values  $s(n)$  for  $n = 1, 2, \dots, N$  is computed, as described in Appendix A1.2. If the elements of  $\mathbf{X}$  are spatially unrelated to one another, the singular values tend to be uniformly distributed in amplitude. On the other hand, if the elements of  $\mathbf{X}$  are highly structured, the singular-value distribution tends to be skewed such that the lower-order singular values are much larger than the higher-order ones.

Figure 15.5-15 contains measurements of the singular-value distributions of the four Brodatz textures performed by Ashjari (44). In this experiment, the  $512 \times 512$

pixel texture originals were first subjected to a statistical rescaling process to produce four normalized texture images whose first-order distributions were Gaussian with identical moments. Next, these normalized texture images were subdivided into 196 non-overlapping  $32 \times 32$  pixel blocks, and a SVD transformation was taken of each block. Figure 15.5-14 is a plot of the average value of each singular value. The shape of the singular-value distributions can be quantified by the one-dimensional shape descriptors defined in Section 15.2. Table 15.5-4 lists Bhattacharyya distance measurements obtained by Ashjari (44) for the mean, standard deviation, skewness and kurtosis shape descriptors. For this experiment, the *B*-distances are relatively high, and therefore good classification results should be expected.

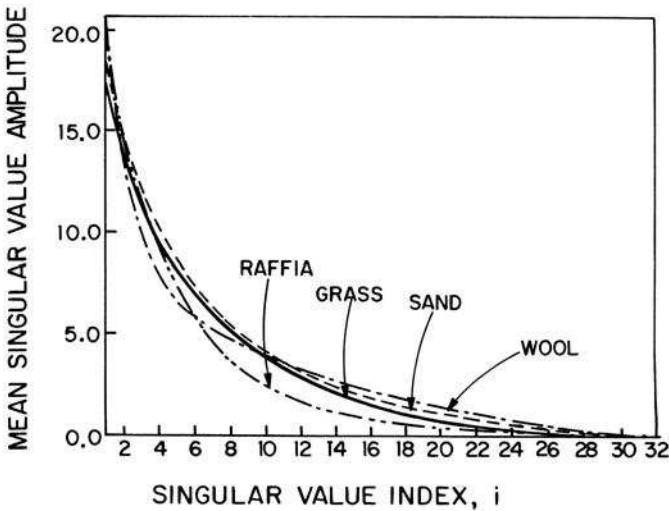


FIGURE 15.5-15. Singular-value distributions of Brodatz texture fields.

TABLE 15.5-4. Bhattacharyya Distance of SVD Texture Feature Sets for Prototype Texture Fields: SVD Features

Field Pair	B-distance
Grass – sand	1.25
Grass – raffia	2.42
Grass – wool	3.31
Sand – raffia	6.33
Sand – wool	2.56
Raffia – wool	9.24
Average	4.19

## 15.6. SCALE-INVARIANT FEATURES

Many sophisticated computer vision applications, such as object recognition, image stitching and video tracking, require the matching of an image pair, which is subject to differences in translation, scale and rotation. Chapter 18 describes methods to accommodate these differences singularly. This Section discusses methods in which all mismatches are jointly handled through the use of scale invariant features.

In 1999, Lowe (45-47) developed an algorithm called *Space-Invariant Feature Transform* (SIFT), which can be used to match image pairs for all three spatial differences. Surf (48) has been developed as a faster version of SIFT.

SIFT is a relatively complex algorithm, which is beyond the scope of this book. Reference 47 provides details of its implementation. The following is a summary of its structure.

### SIFT Algorithm Steps

1. Construct an image scale space, which consists of a first octave, one-dimensional array  $L(x, y, k\sigma)$  of an original image  $I(x, y)$  convolved with  $K$  (typically 5) Gaussian shape impulse blur functions  $G(x, y, k\sigma)$ . Minify the original image by one-half its height, and create  $S$  images with increasing Gaussian blur. This produces the second array octave. Repeat the procedure for, typically, four octaves.
2. Perform Difference of Gaussians on image scale space along each octave.

$$D(x, y, \sigma) = L(x, y, k_i\sigma) - L(x, y, k_j\sigma)$$

where  $k_i$  and  $k_j$  are scale factors.

3. Find keypoints of DoG images, which are their maxima and minima.
4. Eliminate keypoints of strong edges and low contrast regions.
5. Assign keypoints orientation.
6. Generate key point features.

## 15.7. IMAGE FEATURE EXTRACTION EXERCISES

E15.1 Develop a program that generates the  $7 \times 7$  moving window mean and standard deviation features of an unsigned integer, 8-bit, monochrome image. Steps:

- (a) Display the source image.
- (b) Scale the source image to unit range.

- (c) Create a  $7 \times 7$  uniform impulse response array.
- (d) Compute the moving window mean with the uniform impulse response array.
- (e) Display the moving window mean image.
- (f) Compute the moving window standard deviation with the uniform impulse response array.
- (g) Display the moving window standard deviation image.

The PIKS API executable `example_amplitude_features` performs this exercise.

E15.2 Develop a program that computes the mean, standard deviation, skewness, kurtosis, energy, and entropy first-order histogram features of an unsigned integer, 8-bit, monochrome image. Steps:

- (a) Display the source image.
- (b) Compute the histogram of the source image.
- (c) Export the histogram and compute the histogram features.

The PIKS API executable `example_histogram_features` performs this exercise.

E15.3 Develop a program that computes the nine Laws texture features of an unsigned integer, 8-bit, monochrome image. Use a  $7 \times 7$  moving window to compute the standard deviation. Steps:

- (a) Display the source image.
- (b) Generate the nine Laws impulse response arrays or fetch them from a repository.
- (c) For each Laws array:
  - convolve the source image with the Laws array.
  - compute the moving window mean of the Laws convolution.
  - compute the moving window standard deviation of the Laws convolution image.
  - display the Laws texture features.

The PIKS API executable `example_laws_features` performs this exercise.

## REFERENCES

1. H. C. Andrews, *Introduction to Mathematical Techniques in Pattern Recognition*, Wiley-Interscience, New York, 1972.

2. R. O. Duda, P. E. Hart and D. G. Stork, *Pattern Classification, Second Edition*, Wiley-Interscience, New York, 2001.
3. K. Fukunaga, *Introduction to Statistical Pattern Recognition, Second Edition*, Academic Press, New York, 1990.
4. W. S. Meisel, *Computer-Oriented Approaches to Pattern Recognition*, Academic Press, New York, 1972.
5. O. D. Faugeras and W. K. Pratt, "Decorrelation Methods of Texture Feature Extraction," *IEEE Trans. Pattern Analysis and Machine Intelligence*, **PAMI-2**, 4, July 1980, 323–332.
6. R. O. Duda, "Image Data Extraction," unpublished notes, July 1975.
7. R. M. Haralick, K. Shanmugan and I. Dinstein, "Texture Features for Image Classification," *IEEE Trans. Systems, Man and Cybernetics*, **SMC-3**, November 1973, 610–621.
8. G. G. Lendaris and G. L. Stanley, "Diffraction Pattern Sampling for Automatic Pattern Recognition," *Proc. IEEE*, **58**, 2, February 1970, 198–215.
9. R. M. Pickett, "Visual Analysis of Texture in the Detection and Recognition of Objects," in *Picture Processing and Psychopictorics*, B. C. Lipkin and A. Rosenfeld, Eds., Academic Press, New York, 1970, 289–308.
10. J. K. Hawkins, "Textural Properties for Pattern Recognition," in *Picture Processing and Psychopictorics*, B. C. Lipkin and A. Rosenfeld, Eds., Academic Press, New York, 1970, 347–370.
11. P. Brodatz, *Texture: A Photograph Album for Artists and Designers*, Dover Publications, New York, 1956.
12. J. W. Woods, "Two-Dimensional Discrete Markov Random Fields," *IEEE Trans. Information Theory*, **IT-18**, 2, March 1972, 232–240.
13. W. K. Pratt, O. D. Faugeras and A. Gagalowicz, "Applications of Stochastic Texture Field Models to Image Processing," *Proc. IEEE*, **69**, 5, May 1981, 542–551.
14. B. Julesz, "Visual Pattern Discrimination," *IRE Trans. Information Theory*, **IT-8**, 1, February 1962, 84–92.
15. B. Julesz et al., "Inability of Humans to Discriminate Between Visual Textures That Agree in Second-Order Statistics Revisited," *Perception*, **2**, 1973, 391–405.
16. B. Julesz, *Foundations of Cyclopean Perception*, University of Chicago Press, Chicago, 1971.
17. B. Julesz, "Experiments in the Visual Perception of Texture," *Scientific American*, **232**, 4, April 1975, 2–11.
18. I. Pollack, *Perceptual Psychophysics*, **13**, 1973, 276–280.
19. S. R. Purks and W. Richards, "Visual Texture Discrimination Using Random-Dot Patterns," *J. Optical Society America*, **67**, 6, June 1977, 765–771.
20. W. K. Pratt, O. D. Faugeras and A. Gagalowicz, "Visual Discrimination of Stochastic Texture Fields," *IEEE Trans. Systems, Man and Cybernetics*, **SMC-8**, 11, November 1978, 796–804.
21. A. Gagalowicz, "Stochastic Texture Fields Synthesis from a priori Given Second Order Statistics," *Proc. IEEE Computer Society Conf. Pattern Recognition and Image Processing*, Chicago, August 1979, 376–381.

22. E. L. Hall et al., "A Survey of Preprocessing and Feature Extraction Techniques for Radiographic Images," *IEEE Trans. Computers*, **C-20**, 9, September 1971, 1032–1044.
23. R. M. Haralick, "Statistical and Structural Approach to Texture," *Proc. IEEE*, **67**, 5, May 1979, 786–804.
24. T. R. Reed and J. M. H. duBuf, "A Review of Recent Texture Segmentation and Feature Extraction Techniques," *CVGIP: Image Understanding*, **57**, May 1993, 358–372.
25. T. Randen and J. H. Husoy, "Filtering for Classification: A Comparative Study," *IEEE Trans. Pattern Analysis and Machine Intelligence*, **PAMI 21**, 4, April 1999, 291–310.
26. A. Rosenfeld, "Automatic Recognition of Basic Terrain Types from Aerial Photographs," *Photogrammic Engineering*, **28**, 1, March 1962, 115–132.
27. J. M. Coggins and A. K. Jain, "A Spatial Filtering Approach to Texture Analysis," *Pattern Recognition Letters*, **3**, 3, 1985, 195–203.
28. R. P. Kruger, W. B. Thompson and A. F. Turner, "Computer Diagnosis of Pneumoconiosis," *IEEE Trans. Systems, Man and Cybernetics*, **SMC-4**, 1, January 1974, 40–49.
29. R. N. Sutton and E. L. Hall, "Texture Measures for Automatic Classification of Pulmonary Disease," *IEEE Trans. Computers*, **C-21**, July 1972, 667–676.
30. A. Rosenfeld and E. B. Troy, "Visual Texture Analysis," *Proc. UMR–Mervin J. Kelly Communications Conference*, University of Missouri–Rolla, Rolla, MO, October 1970, Sec. 10–1.
31. K. I. Laws, "Textured Image Segmentation," USCIP Report 940, University of Southern California, Image Processing Institute, Los Angeles, January 1980.
32. R. M. Haralick, "Digital Step Edges from Zero Crossing of Second Directional Derivatives," *IEEE Trans. Pattern Analysis and Machine Intelligence*, **PAMI-6**, 1, January 1984, 58–68.
33. M. Unser and M. Eden, "Multiresolution Feature Extraction and Selection for Texture Segmentation," *IEEE Trans. Pattern Analysis and Machine Intelligence*, **PAMI-11**, 7, July 1989, 717–728.
34. F. Ade, "Characterization of Textures by Eigenfilters," *Signal Processing*, September 1983.
35. F. Ade, "Application of Principal Components Analysis to the Inspection of Industrial Goods," *Proc. SPIE International Technical Conference/Europe*, Geneva, April 1983.
36. V. Manian, R. Vasquez and P. Katiyar, "Texture Classification Using Logical Operators," *IEEE Trans. Image Processing*, **9**, 10, October 2000, 1693–1703.
37. M. Clark and A. C. Bovik, "Texture Discrimination Using a Model of Visual Cortex," *Proc. IEEE International Conference on Systems, Man and Cybernetics*, Atlanta, GA, 1986.
38. A. C. Bovik, M. Clark and W. S. Geisler, "Multichannel Texture Analysis Using Localized Spatial Filters," *IEEE Trans. Pattern Analysis and Machine Intelligence*, **PAMI-12**, 1, January 1990, 55–73.
39. A. C. Bovik, "Analysis of Multichannel Narrow-Band Filters for Image Texture Segmentation," *IEEE Trans. Signal Processing*, **39**, 9, September 1991, 2025–2043.
40. D. Gabor, "Theory of Communication," *J. Institute of Electrical Engineers*, **93**, 1946, 429–457.



41. S. Grigorescu, N. Petkov and P. Kruizinga, "Comparison of Texture Features Based on Gabor Filters," *IEEE Trans. Image Processing*, **11**, 10, October 2002, 1160–1167.
42. S. G. Mallat, "A Theory for Multiresolution Signal Decomposition: The Wavelet Representation," *IEEE Trans. Pattern Analysis and Machine Intelligence*, **PAMI-11**, 7, July 1989, 674–693.
43. M. Unser, "Texture Classification and Segmentation Using Wavelet Frames," *IEEE Trans. Image Processing*, **IP-4**, 11, November 1995, 1549–1560.
44. B. Ashjari, "Singular Value Decomposition Texture Measurement for Image Classification," Ph.D. dissertation, University of Southern California, Department of Electrical Engineering, Los Angeles, February 1982.
45. D. G. Lowe, "Object Recognition from Local Scale-Invariant Features," *International Conference on Computer Vision*, Corfu, Greece, September 1999, 1150-1157.
46. D. G. Lowe, "Method and Apparatus for Identifying Scale Invariant Features in an Image and Use of Same for Locating an Object in an image," *U.S. Patent No. 6,711,293*, March 23, 2004.
47. D. G. Lowe, "Distinctive Features from Scale-Invariant Keypoints," *International Journal of Computer Vision*, **60**, 2, 2004, 91-110.
48. B. H. Yuytelaars and T. Gool, "SURF: Speeded Up Robust features," *Proc. of the Ninth European Conf. Computer Vision*, May 2006.

---

# 16

---

## IMAGE SEGMENTATION

Segmentation of an image entails the division or separation of the image into regions of similar attribute. The most basic attribute for segmentation is image luminance amplitude for a monochrome image and color components for a color image. Image edges and texture are also useful attributes for segmentation.

The definition of segmentation adopted in this chapter is deliberately restrictive; no contextual information is utilized in the segmentation. Furthermore, segmentation does not involve classifying each segment. The segmenter only subdivides an image; it does not attempt to recognize the individual segments or their relationships to one another.

There is no theory of image segmentation. As a consequence, no single standard method of image segmentation has emerged. Rather, there are a collection of ad hoc methods that have received some degree of popularity. Because the methods are ad hoc, it would be useful to have some means of assessing their performance. Haralick and Shapiro (1) have established the following qualitative guideline for a good image segmentation: “Regions of an image segmentation should be uniform and homogeneous with respect to some characteristic such as gray tone or texture. Region interiors should be simple and without many small holes. Adjacent regions of a segmentation should have significantly different values with respect to the characteristic on which they are uniform. Boundaries of each segment should be simple, not ragged, and must be spatially accurate.” Unfortunately, no quantitative image segmentation performance metric has been developed.

Several generic methods of image segmentation are described in the following sections. Because of their complexity, it is not feasible to describe all the details of

the various algorithms. Early surveys of image segmentation methods are given in References 2 to 8.

## 16.1. AMPLITUDE SEGMENTATION

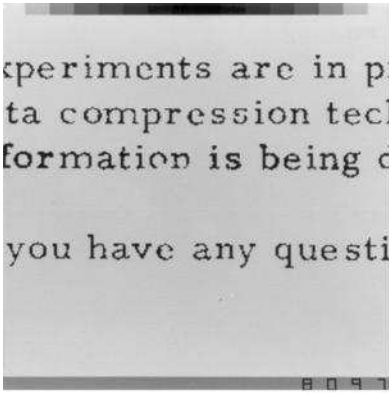
This section considers several image segmentation methods based on the thresholding of luminance or color components of an image. An amplitude projection segmentation technique is also discussed.

### 16.1.1. Bilevel Luminance Thresholding

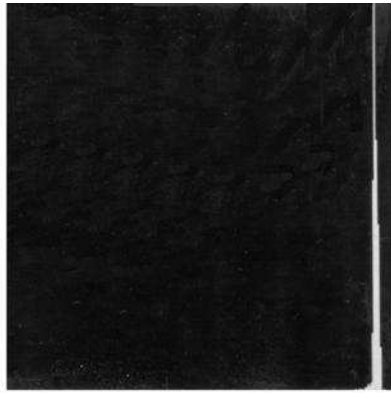
Many images can be characterized as containing some object of interest of reasonably uniform brightness placed against a background of differing brightness. Typical examples include handwritten and typewritten text, microscope biomedical samples and airplanes on a runway. For such images, luminance is a distinguishing feature that can be utilized to segment the object from its background. If an object of interest is white against a black background, or vice versa, it is a trivial task to set a mid gray threshold to segment the object from the background. Practical problems occur, however, when the observed image is subject to noise and when both the object and background assume some broad range of gray scales. Another frequent difficulty is that the background may be nonuniform.

Figure 16.1-1*a* shows a digitized typewritten text consisting of dark letters against a lighter background. A gray scale histogram of the text is presented in Figure 16.1-1*b*. The expected bimodality of the histogram is masked by the relatively large percentage of background pixels. Figure 16.1-1*c* to *e* are threshold displays in which all pixels brighter than the threshold are mapped to unity display luminance and all the remaining pixels below the threshold are mapped to the zero level of display luminance. The photographs illustrate a common problem associated with image thresholding. If the threshold is set too low, portions of the letters are deleted (the stem of the letter “p” is fragmented). Conversely, if the threshold is set too high, object artifacts result (the loop of the letter “e” is filled in).

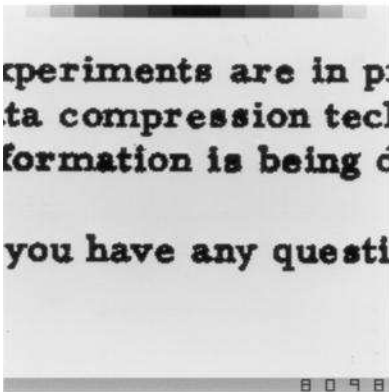
Several analytic approaches to the setting of a luminance threshold have been proposed (3,9). One method is to set the gray scale threshold at a level such that the cumulative gray scale count matches an a priori assumption of the gray scale probability distribution (10). For example, it may be known that black characters cover 25% of the area of a typewritten page. Thus, the threshold level on the image might be set such that the quartile of pixels with the lowest luminance are judged to be black. Another approach to luminance threshold selection is to set the threshold at the minimum point of the histogram between its bimodal peaks (11). Determination of the minimum is often difficult because of the jaggedness



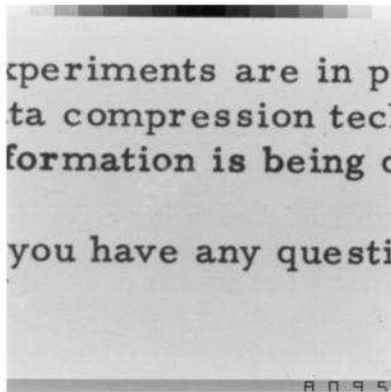
(a) Gray scale text



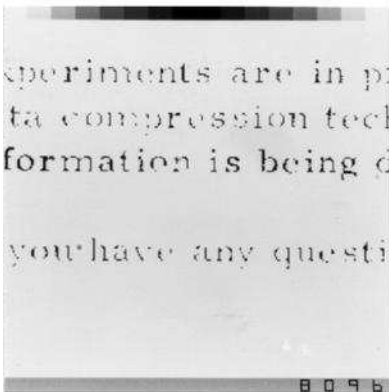
(b) Histogram



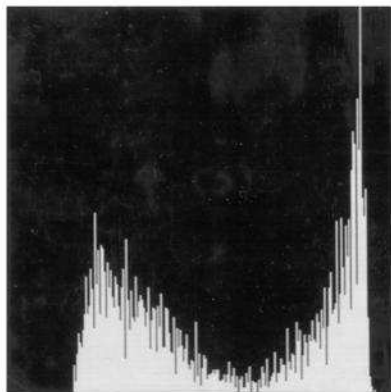
(c) High threshold,  $T = 0.67$



(d) Medium threshold,  $T = 0.50$



(e) Low threshold,  $T = 0.10$



(f) Histogram, Laplacian mask

FIGURE 16.1-1. Luminance thresholding segmentation of typewritten text.

of the histogram. A solution to this problem is to fit the histogram values between the peaks with some analytic function, and then obtain its minimum by differentiation. For example, let  $y$  and  $x$  represent the histogram ordinate and abscissa, respectively. Then the quadratic curve

$$y = ax^2 + bx + c \quad (16.1-1)$$

where  $a$ ,  $b$ , and  $c$  are constants provides a simple histogram approximation in the vicinity of the histogram valley. The minimum histogram valley occurs for  $x = -b/2a$ . Papamarkos and Gatos (12) have extended this concept for threshold selection.

A global threshold can be determined by minimization of some difference measure between an image to be segmented and its test segments. Otsu (13) has developed a thresholding algorithm using the Euclidean difference. Sahoo et al. (6) have reported that the Otsu method is the best global thresholding technique among those that they tested.

Weska et al. (14) have suggested the use of a Laplacian operator to aid in luminance threshold selection. As defined in Eq. 15.3-1, the Laplacian forms the spatial second partial derivative of an image. Consider an image region in the vicinity of an object in which the luminance increases from a low plateau level to a higher plateau level in a smooth ramp like fashion. In the flat regions and along the ramp, the Laplacian is zero. Large positive values of the Laplacian will occur in the transition region from the low plateau to the ramp; large negative values will be produced in the transition from the ramp to the high plateau. A gray scale histogram formed of only those pixels of the original image that lie at coordinates corresponding to very high or low values of the Laplacian tends to be bimodal with a distinctive valley between the peaks. Figure 16.1-1f shows the histogram of the text image of Figure 16.1-1a after the Laplacian mask operation.

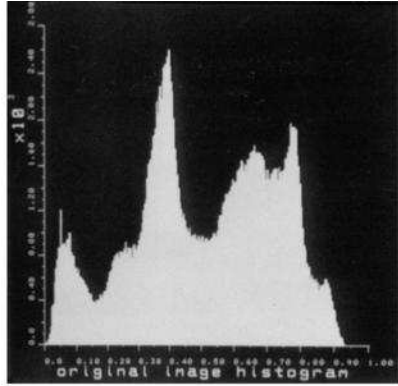
If the background of an image is nonuniform, it often is necessary to adapt the luminance threshold to the mean luminance level (15,16). This can be accomplished by subdividing the image into small blocks and determining the best threshold level for each block by the methods discussed previously. Threshold levels for each pixel may then be determined by interpolation between the block centers. Yankowitz and Bruckstein (17) have proposed an adaptive thresholding method in which a threshold surface is obtained by interpolating an image only at points where its gradient is large.

### 16.1.2. Multilevel Luminance Thresholding

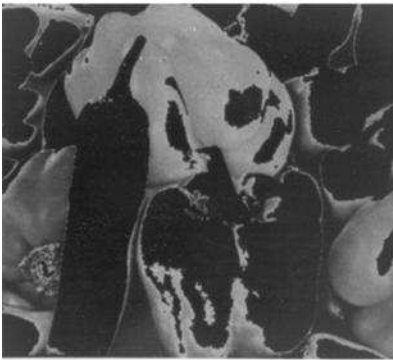
Effective segmentation can be achieved in some classes of images by a recursive *multilevel thresholding* method suggested by Tomita et al. (18). In the first stage of the process, the image is thresholded to separate brighter regions from darker



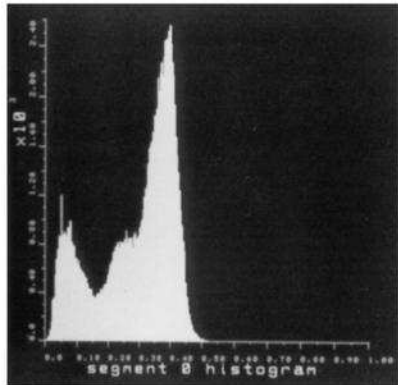
(a) Original



(b) Original histogram



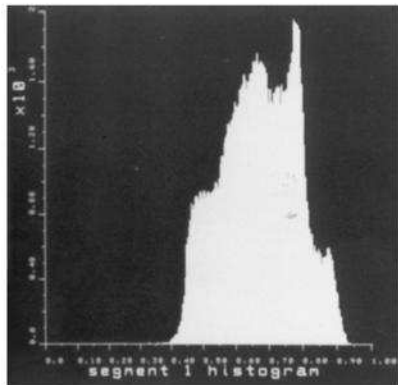
(c) Segment 0



(d) Segment 0 histogram



(e) Segment 1

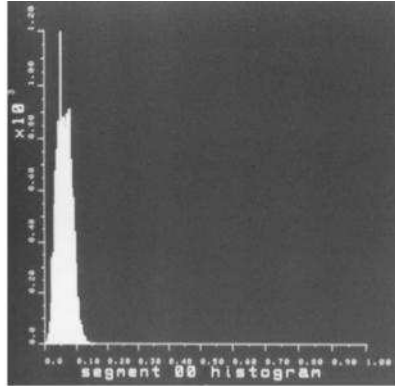


(f) Segment 1 histogram

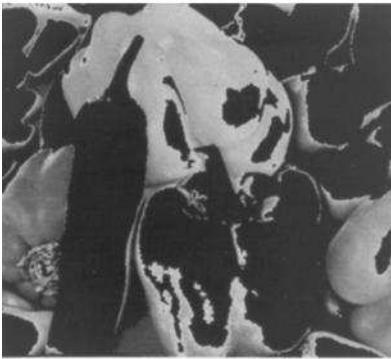
**FIGURE 16.1-2.** Multilevel luminance thresholding image segmentation of the peppers\_ mon image; first-level segmentation.



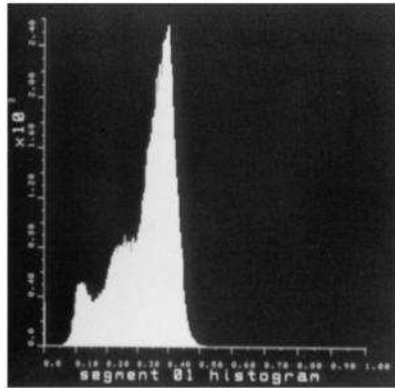
(a) Segment 00



(b) Segment 00 histogram



(c) Segment 01



(d) Segment 01 histogram

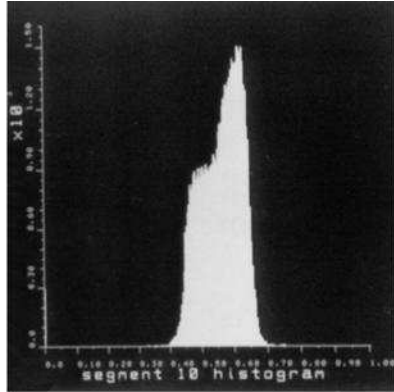
**FIGURE 16.1-3.** Multilevel luminance thresholding image segmentation of the peppers\_ mon image; second-level segmentation, 0 branch.

regions by locating a minimum between luminance modes of the histogram. Then, histograms are formed of each of the segmented parts. If these histograms are not uni-modal, the parts are thresholded again. The process continues until the histogram of a part becomes unimodal. Figures 16.1-2 to 16.1-4 provide an example of this form of amplitude segmentation in which the peppers image is segmented into four gray scale segments.

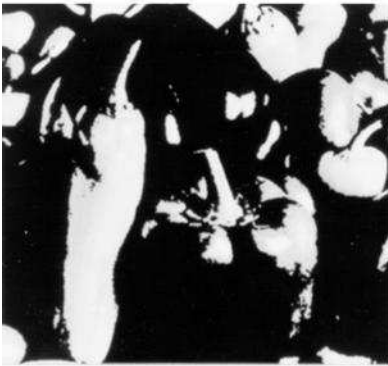
Several methods have been proposed for the selection of multilevel thresholds. The methods of Reddi et al. (19) and Kapur et al. (20) are based upon image histograms. References 21 to 23 are more recent proposals for threshold selection.



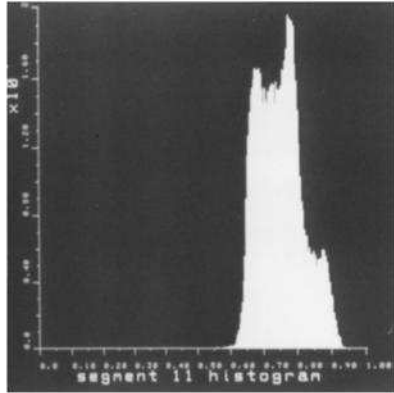
(a) Segment 10



(b) Segment 10 histogram



(c) Segment 11



(d) Segment 11 histogram

**FIGURE 16.1-4.** Multilevel luminance thresholding image segmentation of the `peppers_mon` image; second-level segmentation, 1 branch.

### 16.1.3. Multilevel Color Component Thresholding

The multilevel luminance thresholding concept can be extended to the segmentation of color and multispectral images. Ohlander et al. (24,25) have developed a segmentation scheme for natural color images based on multi-dimensional thresholding of color images represented by their *RGB* color components, their *luma/chroma YIQ* components and by a set of nonstandard color components, loosely called intensity, hue and saturation. Figure 16.1-5 provides an example of the *property histograms* of these nine color components for a scene. The histograms, have been measured over those parts of the original scene that are relatively devoid of texture: the non-busy parts of the scene. This important step of the segmentation process is necessary to avoid false segmentation of homogeneous textured regions into many isolated parts. If the property histograms are not all unimodal, an ad hoc procedure is



invoked to determine the best property and the best level for thresholding of that property. The first candidate is image intensity. Other candidates are selected on a priority basis, depending on contrast level and location of the histogram modes. After a threshold level has been determined, the image is subdivided into its segmented parts. The procedure is then repeated on each part until the resulting property histograms become unimodal or the segmentation reaches a reasonable stage of separation under manual surveillance. Ohlander's segmentation technique using multidimensional thresholding aided by texture discrimination has proved quite effective in simulation tests. However, a large part of the segmentation control has been performed by a human operator; human judgment, predicated on trial threshold setting results, is required for guidance.

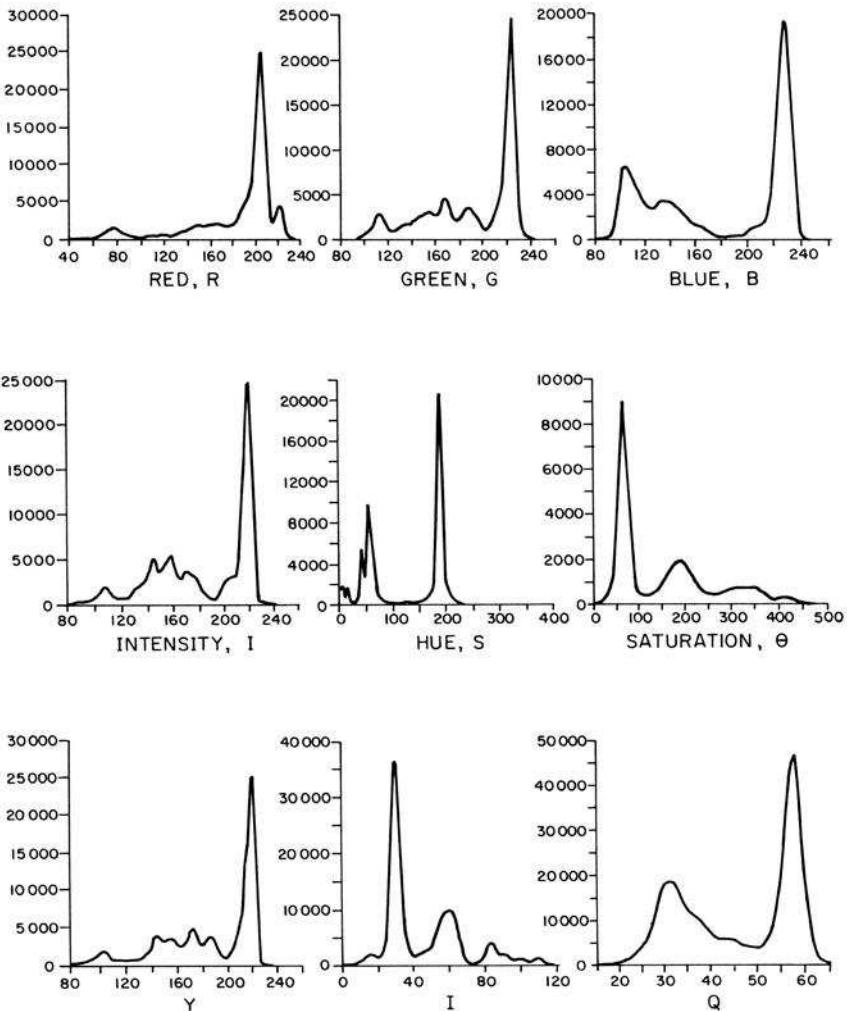


FIGURE 16.1-5. Typical property histograms for color image segmentation.

In Ohlander's segmentation method, the nine property values are obviously interdependent. The  $YIQ$  and intensity components are linear combinations of  $RGB$ ; the hue and saturation measurements are nonlinear functions of  $RGB$ . This observation raises several questions. What types of linear and nonlinear transformations of  $RGB$  are best for segmentation? Ohta et al. (26) suggest an approximation to the spectral Karhunen–Loeve transform. How many property values should be used? What is the best form of property thresholding? Perhaps answers to these last two questions may be forthcoming from a study of clustering techniques in pattern recognition (27).

Property value histograms are really the marginal histograms of a joint histogram of property values. Clustering methods can be utilized to specify multidimensional decision boundaries for segmentation. This approach permits utilization of all the property values for segmentation and inherently recognizes their respective cross correlation. The following section discusses clustering methods of image segmentation.

#### 16.1.4. Amplitude Projection

Image segments can sometimes be effectively isolated by forming the average *amplitude projections* of an image along its rows and columns (28,29). The horizontal (row) and vertical (column) projections are defined as

$$H(k) = \frac{1}{J} \sum_{j=1}^J F(j, k) \quad (16.1-2)$$

and

$$V(j) = \frac{1}{K} \sum_{k=1}^K F(j, k). \quad (16.1-3)$$

Figure 16.1-6 illustrates an application of gray scale projection segmentation of an image. The rectangularly shaped segment can be further delimited by taking projections over oblique angles.

### 16.2. CLUSTERING SEGMENTATION

One of the earliest examples of image segmentation, by Haralick and Kelly (30) using data clustering, was the subdivision of multispectral aerial images of agricultural land into regions containing the same type of land cover. The clustering segmentation concept is simple; however, it is usually computationally intensive.

Consider a vector  $\mathbf{x} = [x_1, x_2, \dots, x_N]^T$  of measurements at each pixel coordinate  $(j, k)$  in an image. The measurements could be point multispectral values, point color components or derived color components, as in the Ohlander approach

described previously, or they could be neighborhood feature measurements such as the moving window mean, standard deviation and mode, as discussed in Section 16.2. If the measurement set is to be effective for image segmentation, data collected at various pixels within a segment of common attribute should be similar. That is, the data should be tightly clustered in an  $N$ -dimensional measurement space. If this condition holds, the segmenter design task becomes one of subdividing the  $N$ -dimensional measurement space into mutually exclusive compartments, each of which envelops typical data clusters for each image segment. Figure 16.2-1 illustrates the concept for two features. In the segmentation process, if a measurement vector for a pixel falls within a measurement space compartment, the pixel is assigned the segment name or label of that compartment.

Coleman and Andrews (31) have developed a robust and relatively efficient image segmentation clustering algorithm. Figure 16.2-2 is a flowchart that describes a simplified version of the algorithm for segmentation of monochrome images.

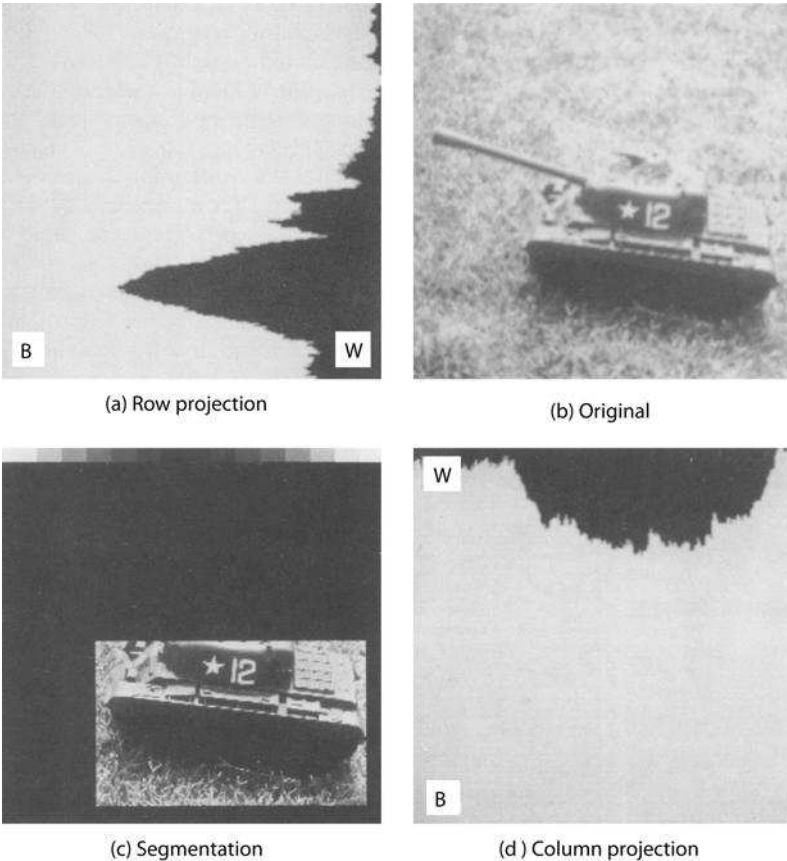


**FIGURE 16.1-6.** Gray scale projection image segmentation of a toy tank image.

The first stage of the algorithm involves feature computation. In one set of experiments, Coleman and Andrews used 12 mode measurements in square windows of size 1, 3, 7 and 15 pixels. The next step in the algorithm is the clustering stage, in which the optimum number of clusters is determined along with the feature space center of each cluster. In the segmenter, a given feature vector is assigned to its closest cluster center.

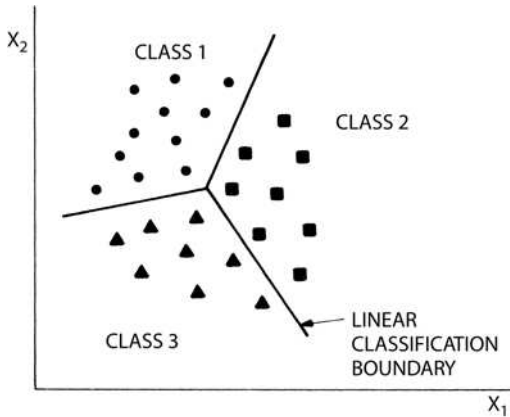


FIGURE 16.2-1. Data clustering for two feature measurements.

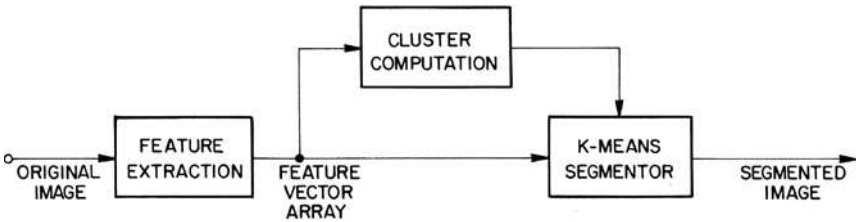


FIGURE 16.2-2. Simplified version of Coleman–Andrews clustering image segmentation method.

The cluster computation algorithm begins by establishing two initial trial cluster centers. All feature vectors of an image are assigned to their closest cluster center. Next, the number of cluster centers is successively increased by one, and a clustering quality factor  $\beta$  is computed at each iteration until the maximum value of  $\beta$  is determined. This establishes the optimum number of clusters. When the number of clusters is incremented by one, the new cluster center becomes the feature vector that is farthest from its closest cluster center. The  $\beta$  factor is defined as

$$\beta = \text{tr}\{\mathbf{S}_W\} \text{tr}\{\mathbf{S}_B\} \quad (16.2-1)$$

where  $\mathbf{S}_W$  and  $\mathbf{S}_B$  are the within-cluster and between-cluster *scatter matrices*, respectively, and  $\text{tr}\{\cdot\}$  denotes the trace of a matrix. The within-cluster scatter matrix is computed as

$$S_W = \frac{1}{K} \sum_{k=1}^K \frac{1}{M_k} \sum_{\mathbf{x}_i \in S_k} (\mathbf{x}_i - \mathbf{u}_k)(\mathbf{x}_i - \mathbf{u}_k)^T \tag{16.2-2}$$

where  $K$  is the number of clusters,  $M_k$  is the number of vector elements in the  $k$ th cluster,  $\mathbf{x}_i$  is a vector element in the  $k$ th cluster,  $\mathbf{u}_k$  is the mean of the  $k$ th cluster and  $S_k$  is the set of elements in the  $k$ th cluster. The between-cluster scatter matrix is defined as

$$S_B = \frac{1}{K} \sum_{k=1}^K (\mathbf{u}_k - \mathbf{u}_0)(\mathbf{u}_k - \mathbf{u}_0)^T \tag{16.2-3}$$

where  $\mathbf{u}_0$  is the mean of all of the feature vectors as computed by

$$\mathbf{u}_0 = \frac{1}{M} \sum_{i=1}^M \mathbf{x}_i \tag{16.2-4}$$

where  $M$  denotes the number of pixels to be clustered. Coleman and Andrews (31) have obtained subjectively good results for their clustering algorithm in the segmentation of monochrome and color images.

### 16.3. REGION SEGMENTATION

The amplitude and clustering methods described in the preceding sections are based on point properties of an image. The logical extension, as first suggested by Muerle and Allen (32), is to utilize spatial properties of an image for segmentation.

#### 16.3.1. Region Growing

*Region growing* is one of the conceptually simplest approaches to image segmentation; neighboring pixels of similar amplitude are grouped together to form a segmented region. However, in practice, constraints, some of which are reasonably complex, must be placed on the growth pattern to achieve acceptable results.

Brice and Fenema (33) have developed a region-growing method based on a set of simple growth rules. In the first stage of the process, pairs of pixels are combined together in groups called *atomic regions* if they are of the same amplitude and are four-connected. Two heuristic rules are next invoked to dissolve weak boundaries between atomic boundaries. Referring to Figure 16.3-1, let  $R_1$  and  $R_2$  be two adjacent regions with perimeters  $P_1$  and  $P_2$ , respectively, which have previously been merged. After the initial stages of region growing, a region may contain previously merged subregions of different amplitude values. Also, let  $C$  denote the length of the common boundary and let  $D$  represent the length of that portion of  $C$  for which the amplitude difference  $Y$  across the boundary is smaller than a significance factor  $\epsilon_1$ . The regions  $R_1$  and  $R_2$  are then merged if

$$\frac{D}{\text{MIN}\{P_1, P_2\}} > \epsilon_2 \tag{16.3-1}$$

where  $\epsilon_2$  is a constant typically set at  $\epsilon_2 = 1/2$ . This heuristic prevents merger of adjacent regions of the same approximate size, but permits smaller regions to be absorbed into larger regions. The second rule merges weak common boundaries remaining after application of the first rule. Adjacent regions are merged if

$$\frac{D}{C} > \epsilon_3 \tag{16.3-2}$$

where  $\epsilon_3$  is a constant set at about  $\epsilon_3 = 3/4$ . Application of only the second rule tends to overmerge regions.

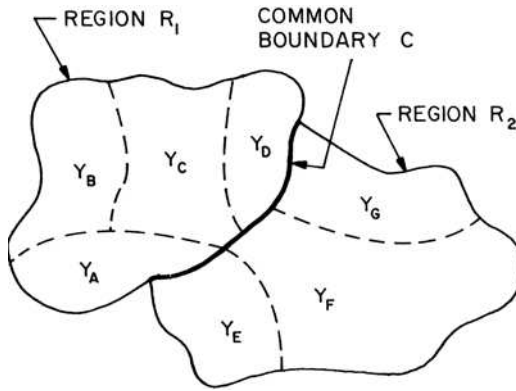


FIGURE 16.3-1. Region-growing geometry.

The Brice and Fenema region growing method provides reasonably accurate segmentation of simple scenes with few objects and little texture (33-35) but, does not perform well on more complex scenes. Yakimovsky (36) has attempted to improve the region-growing concept by establishing merging constraints based on estimated Bayesian probability densities of feature measurements of each region.

Adams and Bischof (37) have proposed a seeded region growing algorithm in which a user manually selects a set of seeds  $s_1, s_2, \dots, s_n$  that are placed in areas of visual homogeneity. The seeds can be single pixels for nearly noise free-images, or they can be small clusters of pixels to provide some degree of noise tolerance for noisy images. Then, conventional region growing proceeds with one new pixel added to each of the  $n$  seeded regions. The process proceeds until adjacent regions meet at a common boundary.

An adaptive region growing algorithm has been developed by Chang and Li (38). With this algorithm, an unspecified feature histogram analysis is performed on each pair of regions, which are candidates for merging. If the feature means of the candidate regions are within a dynamic tolerance range, the candidates are merged.

Hojjatoleslami and Kittler (39) have proposed a novel region growing method in which a single unassigned pixel is added to an existing region if a pair of contrast measures are satisfied. Consider an existing region, which is surrounded by unassigned pixels or pixels from some other region. The *internal boundary* of the region is the set of connected outermost pixels of the region. The *current boundary* is the set of connected pixels adjacent to the internal boundary. In Figure 16.3-2, the internal boundary is formed by connected pixels just inside the solid line while the current boundary is formed by connected pixels just outside the solid line. The *average contrast* measure is defined to be the difference between the average grey level of the region and the average of its current boundary pixels. The *peripheral contrast* measure is defined as the difference of the grey level average of the internal boundary and the average of the current boundary. Together, these two contrast measures determine if a pixel is to be included into the current region. A single border pixel will be subsumed into the current region if it is the maximum of its nearest neighbors and if the last local maximum of the peripheral contrast occurs before the maximum of the average contrast measure.

Most region growing techniques have an inherent dependence upon the location of seeds for each region. As a consequence, the segmented result is sensitive to the location and ordering of seeds. Wan and Higgins (40) have proposed a set of region growing algorithms, called *symmetric region growing*, which are insensitive to the location of seeds.

### 16.3.2. Split and Merge

*Split and merge* image segmentation techniques (41) are based on a quad tree data representation whereby a square image segment is broken (split) into four quadrants if the original image segment is nonuniform in attribute. If four neighboring squares are found to be uniform, they are replaced (merge) by a single square composed of the four adjacent squares.

In principle, the split and merge process could start at the full image level and initiate split operations. This approach tends to be computationally intensive. Conversely, beginning at the individual pixel level and making initial merges has the drawback that region uniformity measures are limited at the single pixel level. Initializing the split and merge process at an intermediate level enables the use of more powerful uniformity tests without excessive computation.

The simplest uniformity measure is to compute the difference between the largest and smallest pixels of a segment. Fukada (42) has proposed the segment variance as a uniformity measure. Chen and Pavlidis (43) suggest more complex statistical measures of uniformity. The basic split and merge process tends to produce rather blocky segments because of the rule that square blocks are either split or merged.





There are two basic algorithmic approaches to the computation of the watershed of an image: rainfall and flooding.

In the *rainfall* approach, local minima are found throughout the image. Each local minima is given a unique tag. Adjacent local minima are combined with a unique tag. Next, a conceptual water drop is placed at each un tagged pixel. The drop moves to its lower-amplitude neighbor until it reaches a tagged pixel, at which time it assumes the tag value. Figure 16.3-2 illustrates a section of a digital image encompassing a watershed in which the local minimum pixel is black and the dashed line indicates the path of a water drop to the local minimum.

In the *flooding* approach, conceptual single pixel holes are pierced at each local minima, and the amplitude surface is lowered into a large body of water. The water enters the holes and proceeds to fill each catchment basin. If a basin is about to overflow, a conceptual dam is built on its surrounding ridge line to a height equal to the highest altitude ridge point. Figure 16.3-3 shows a profile of the filling process of a catchment basin (50). Figure 16.3-4 is an example of watershed segmentation provided by Moga and Gabbouj (51).

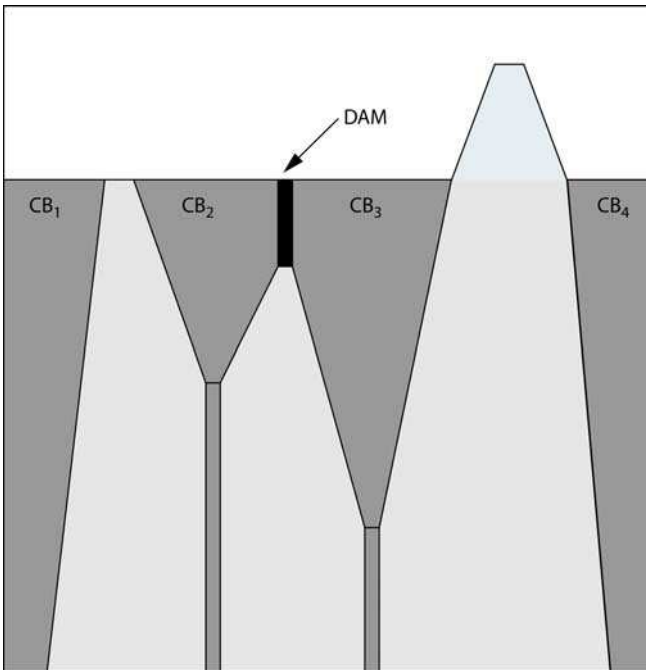
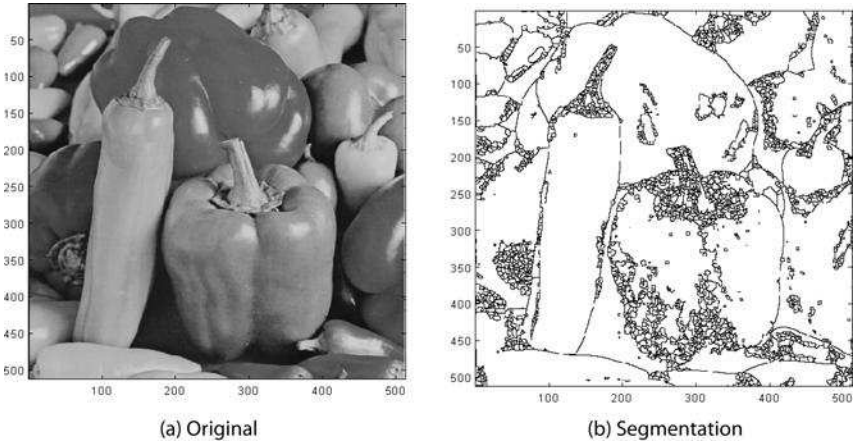


FIGURE 16.3-3. Profile of catchment basin filling.



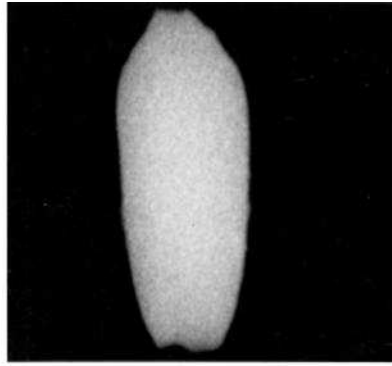
**FIGURE 16.3-4.** Watershed image segmentation of the `peppers_mon` image. Courtesy of Alina N. Moga and M. Gabbouj, Tampere University of Technology, Finland.

Simple watershed algorithms tend to produce results that are over segmented (52). Najman and Schmitt (50,53,54) have applied morphological methods in their watershed algorithm to reduce over segmentation. Wright and Acton (55) have performed watershed segmentation on a pyramid of different spatial resolutions to avoid over segmentation. Jackway (56) has investigated gradient watersheds. References 57 to 61 describe extensions and improvements to the basic watershed image segmentation method.

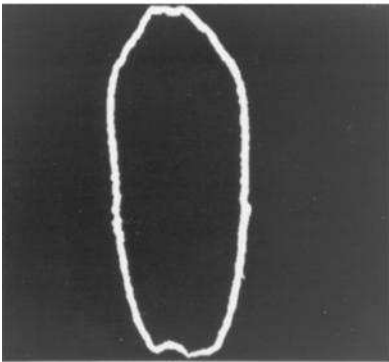
## 16.4. BOUNDARY SEGMENTATION

It is possible to segment an image into regions of common attribute by detecting the boundary of each region for which there is a significant change in attribute across the boundary. Boundary detection can be accomplished by means of edge detection as described in Chapter 15. Figure 16.4-1 illustrates the segmentation of a projectile from its background. In this example, a  $11 \times 11$  derivative of Gaussian detector is used to generate the edge map of Figure 16.4-1b. Morphological thinning of this edge map results in Figure 16.4-1c. The resulting boundary appears visually to be correct when overlaid on the original image. If an image is noisy or if its region attributes differ by only a small amount between regions, a detected boundary may often be broken. *Edge linking* techniques can be employed to bridge short gaps in such a region boundary.

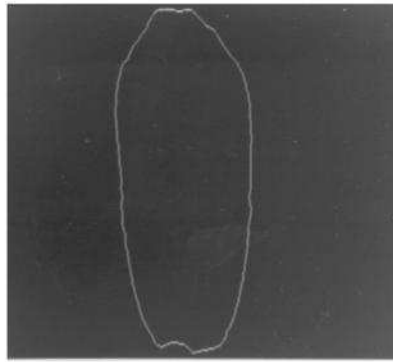
The following sections describe a number of boundary segmentation techniques.



(a) Original



(b) Edge map



(c) Thinned edge map

FIGURE 16.4-1. Boundary detection image segmentation of the projectile image.

### 16.4.1. Curve-Fitting Edge Linking

In some instances, edge map points of a broken segment boundary can be linked together to form a closed contour by curve-fitting methods. If a priori information is available as to the expected shape of a region in an image (e.g., a rectangle or a circle), the fit may be made directly to that closed contour. For more complex-shaped regions, as illustrated in Figure 16.4-2, it is usually necessary to break up the supposed closed contour into chains with broken links. One such chain, shown in Figure 16.4-2 starting at point *A* and ending at point *B*, contains a single broken link. Classical curve-fitting methods (41) such as *Bezier polynomial* or *spline fitting* can be used to fit the broken chain.

In their book, Duda and Hart (62) credit Forsen as being the developer of a simple piecewise linear curve-fitting procedure called the *iterative endpoint fit*. In the

first stage of the algorithm, illustrated in Figure 16.4-3, data endpoints  $A$  and  $B$  are connected by a straight line. The point of greatest departure from the straight-line (point  $C$ ) is examined. If the separation of this point is too large, the point becomes an anchor point for two straight-line segments ( $A$  to  $C$  and  $C$  to  $B$ ). The procedure then continues until the data points are well fitted by line segments. The principal advantage of the algorithm is its simplicity; its disadvantage is error caused by incorrect data points. Ramer (63) has used a technique similar to the iterated end-point procedure to determine a polynomial approximation to an arbitrary-shaped closed curve. Pavlidis and Horowitz (64) have developed related algorithms for polygonal curve fitting.

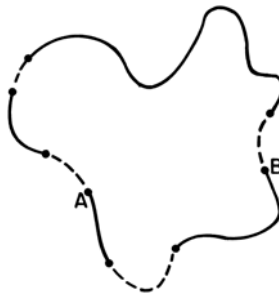


**FIGURE 16.4-2.** Region boundary with missing links indicated by dashed lines.

Wang et al. (65) have developed a complex, but effective, method of gap filling of edge fragments. The method, called *ratio contour*, involves three steps:

preprocess an edge detector output to produce a set of topologically unconnected edge fragments;

smooth the edge fragments to minimize noise effects;

estimate a curved gap filling segment between pairs of fragments.

The third step is accomplished by minimizing the following boundary cost function (65)

$$\Gamma(B) = \frac{W(B)}{L(B)} \quad (16.4-1)$$

where  $W(B)$  is a weighted sum of the total gap length and curvature along a boundary  $B$  and  $L(B)$  is the length of the boundary  $B$ . The minimization is accomplished using a spline-based curve smoothing algorithm (65). Wang et al.

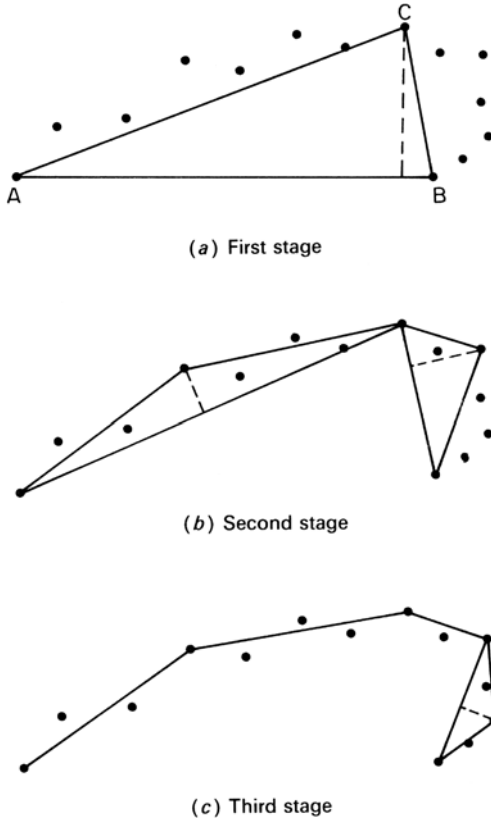


FIGURE 16.4-3. Iterative endpoint curve fitting.

have compared their gap filling method to related algorithms (66-68) for numerous test images, and determined that the ratio contour approach achieves as good or better than the alternate approaches (65).

The curve-fitting method is reasonably effective for simply structured objects. Difficulties occur when an image contains many overlapping objects and its corresponding edge map contains branch structures.

### 16.4.2. Heuristic Edge-Linking Methods

The edge segmentation technique developed by Roberts (69) is typical of the philosophy of many heuristic edge-linking methods. In Roberts' method, edge gradients are examined in  $4 \times 4$  pixels blocks. The pixel whose magnitude gradient is largest is declared a tentative edge point if its magnitude is greater than a threshold value. Then north-, east-, south- and west-oriented lines of length 5 are fitted to the gradient

data about the tentative edge point. If the ratio of the best fit to the worst fit, measured in terms of the fit correlation, is greater than a second threshold, the tentative edge point is declared valid, and it is assigned the direction of the best fit. Next, straight lines are fitted between pairs of edge points if they are in adjacent  $4 \times 4$  blocks and if the line direction is within  $\pm 23$  degrees of the edge direction of either edge point. Those points failing to meet the linking criteria are discarded. A typical boundary at this stage, shown in Figure 16.4-4a, will contain gaps and multiply connected edge points. Small triangles are eliminated by deleting the longest side; small

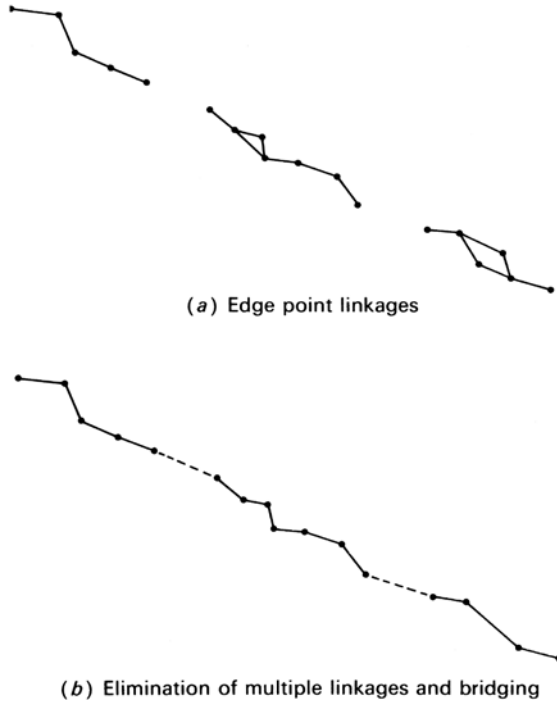


**FIGURE 16.4-4.** Roberts edge linking.

rectangles are replaced by their longest diagonal, as indicated in Figure 16.4-4b. Short spur lines are also deleted. At this stage, short gaps are bridged by straight-line connection. This form of edge linking can be used with a wide variety of edge detectors. Nevatia (70) has used a similar method for edge linking of edges produced by a Heuckel edge detector.

Robinson (71) has suggested a simple but effective edge-linking algorithm in which edge points from an edge detector providing eight edge compass directions are examined in  $3 \times 3$  blocks as indicated in Figure 16.4-5. The edge point in the center of the block is declared a valid edge if it possesses directional neighbors in

the proper orientation. Extensions to larger windows should be beneficial, but the number of potential valid edge connections will grow rapidly with window size.

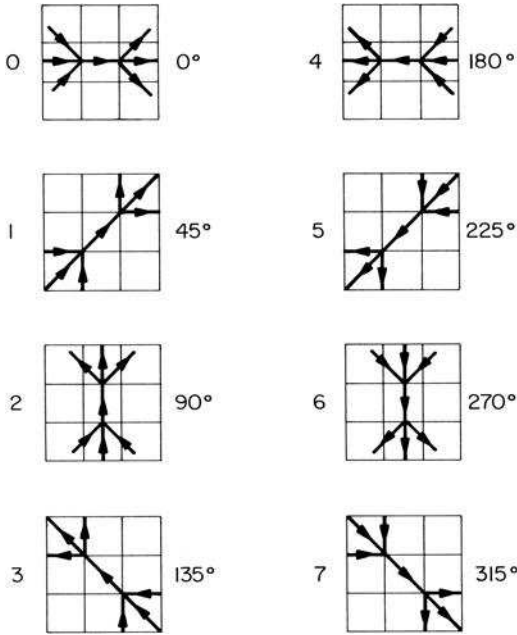


FIGURE 16.4-5. Edge linking rules.

### 16.4.3. Hough Transform Edge Linking

The *Hough transform* (72–74) can be used as a means of edge linking. The Hough transform involves the transformation of a line in Cartesian coordinate space to a point in polar coordinate space. With reference to Figure 16.4-6a, a straight line can be described parametrically as

$$\rho = x \cos \theta + y \sin \theta \tag{16.4-1}$$

where  $\rho$  is the normal distance of the line from the origin and  $\theta$  is the angle of the origin with respect to the  $x$  axis. The Hough transform of the line is simply a point at coordinate  $(\rho, \theta)$  in the polar domain as shown in Figure 16.4-6b. A family of lines passing through a common point, as shown in Figure 16.4-6c, maps into the connected set of  $\rho$ - $\theta$  points of Figure 16.4-6d. Now, consider the three colinear points of Figure 16.4-6e. The Hough transform of the family of curves passing through the three points results in the set of three parametric curves in the  $\rho$ - $\theta$  space of Figure 16.4-6f. These three curves cross at a single point  $(\rho_0, \theta_0)$  corresponding to the dashed line passing through the colinear points.

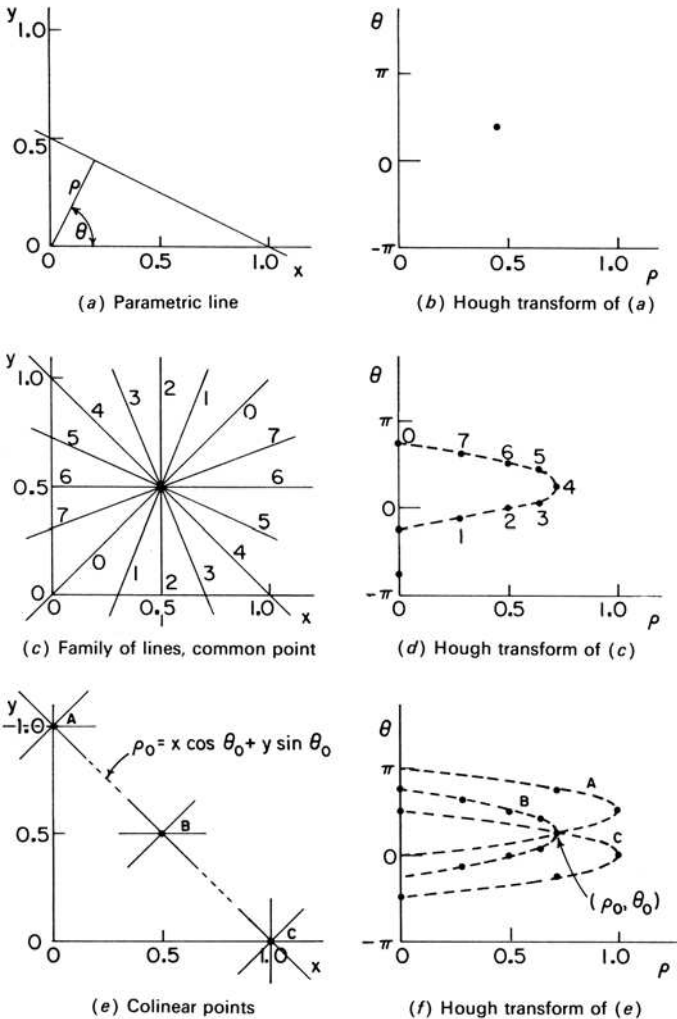


FIGURE 16.4-6. Hough transform.

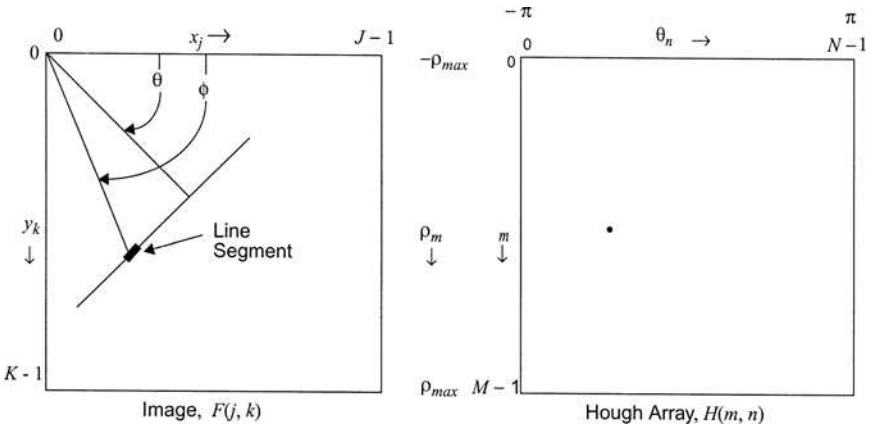
**Duda and Hart Version.** Duda and Hart (73) have adapted the Hough transform technique for line and curve detection in discrete binary images. Each nonzero data point in the image domain is transformed to a curve in the  $\rho$ - $\theta$  domain, which is quantized into cells. If an element of a curve falls in a cell, that particular cell is incremented by one count. After all data points are transformed, the  $\rho$ - $\theta$  cells are examined. Large cell counts correspond to colinear data points that may be fitted by a straight line with the appropriate  $\rho$ - $\theta$  parameters. Small counts in a cell generally indicate isolated data points that can be deleted.



Figure 16.4-7a presents the geometry utilized for the development of an algorithm for the Duda and Hart version of the Hough transform. Following the notation adopted in Section 13.1, the origin of the image is established at the upper left corner of the image. The discrete Cartesian coordinates of the image point  $(j, k)$  are

$$x_j = j + \frac{1}{2} \tag{16.4-3a}$$

$$y_k = k + \frac{1}{2} \tag{16.4-3b}$$



**FIGURE 16.4-7.** Geometry for Hough transform computation.

Consider a line segment in a binary image  $F(j, k)$ , which contains a point at coordinate  $(j, k)$  that is at an angle  $\phi$  with respect to the horizontal reference axis. When the line segment is projected, it intersects a normal line of length  $\rho$  emanating from the origin at an angle  $\theta$  with respect to the horizontal axis. The Hough array  $H(m, n)$  consists of cells of the quantized variables  $\rho_m$  and  $\theta_n$ . It can be shown that

$$-\frac{\rho_{\max}}{2} \leq \rho_m \leq \rho_{\max} \tag{16.4-4a}$$

$$-\frac{\pi}{2} \leq \theta_n \leq \pi \tag{16.4-4b}$$

where

$$\rho_{\max} = [(x_j)^2 + (y_k)^2]^{1/2}. \tag{16.4-4c}$$

For ease of interpretation, it is convenient to adopt the symmetrical limits of Figure 16.4-7b and to set  $M$  and  $N$  as odd integers so that the center cell of the Hough array represents  $\rho_m = 0$  and  $\theta_n = 0$ . The Duda and Hart (D & H) Hough transform algorithm follows.

1. Initialize the Hough array to zero.
2. For each  $(j, k)$  for which  $F(j, k) = 1$ , compute

$$\rho(n) = x_j \cos \theta_n + y_k \sin \theta_n \tag{16.4-5a}$$

where

$$\theta_n = \pi - \frac{2\pi(N-n)}{N-1} \tag{16.4-5b}$$

is incremented over the range  $1 \leq n \leq N$  under the restriction that

$$\phi - \frac{\pi}{2} \leq \theta_n \leq \phi + \frac{\pi}{2} \tag{16.4-6}$$

where

$$\phi = \arctan \left\{ \frac{y_k}{x_j} \right\} \tag{16.4-7}$$

3. Determine the  $m$  index of the quantized rho value.

$$m = \left[ M - \frac{[\rho_{\max} - \rho(n)](M-1)}{2\rho_{\max}} \right]_N \tag{16.4-8}$$

where  $[\cdot]_N$  denotes the nearest integer value of its argument.

4. Increment the Hough array.

$$H(m, n) = H(m, n) + 1. \tag{16.4-9}$$

It is important to observe the restriction of Eq. 16.4-6; not all  $\rho-\theta$  combinations are legal for a given pixel coordinate  $(j, k)$ .

Computation of the Hough array requires on the order of  $N$  evaluations of Eqs. 16.4-4 to 16.4-9 for each nonzero pixel of  $F(j, k)$ . The size of the Hough array is not strictly dependent on the size of the image array. However, as the image size increases, the Hough array size should also be increased accordingly to maintain computational accuracy of rho and theta. In most applications, the Hough array size should be set at least one quarter the image size to obtain reasonably accurate results.

Figure 16.4-8 presents several examples of the D & H version of the Hough transform. In these examples,  $M = N = 127$  and  $J = K = 512$ . The Hough arrays

have been flipped bottom to top for display purposes so that the positive rho and positive theta quadrant is in the normal Cartesian first quadrant (i.e., the upper right quadrant).

**O’Gorman and Clowes Version.** O’Gorman and Clowes (75) have proposed a modification of the Hough transformation for linking edge points in an image. In their procedure, the angle  $\theta$  for entry in  $\rho-\theta$  space is obtained from the gradient direction of an edge. The corresponding  $\rho$  value is then computed from Eq. 16.4-4 for an edge coordinate  $(j, k)$ . However, instead of incrementing the  $(\rho, \theta)$  cell by unity, the cell is incremented by the edge gradient magnitude in order to give greater importance to strong edges than weak edges.

The following is an algorithm for computation of the O’Gorman and Clowes (O & C) version of the Hough transform. Figure 16.4-7a defines the edge angles referenced in the algorithm.

1. Initialize the Hough array to zero.
2. Given a gray scale image  $F(j, k)$ , generate a first-order derivative edge gradient array  $G(j, k)$  and an edge gradient angle array  $\gamma(j, k)$  using one of the edge detectors described in Section 15.2.1.
3. For each  $(j, k)$  for which  $G(j, k) > T$ , where  $T$  is the edge detector threshold value, compute

$$\rho(j, k) = x_j \cos \{ \theta(j, k) \} + y_k \sin \{ \theta(j, k) \} \tag{16.4-10}$$

where

$$\theta = \begin{cases} \psi + \frac{\pi}{2} & \text{for } \psi < \phi \\ \psi + \frac{\pi}{2} & \text{for } \psi \geq \phi \end{cases} \tag{16.4-11a}$$

$$\tag{16.4-11b}$$

with

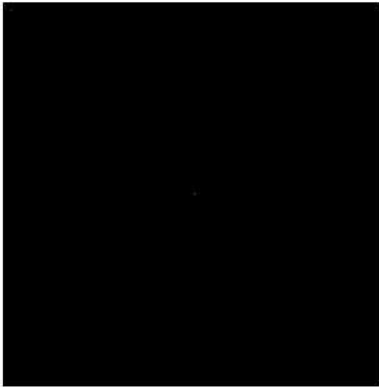
$$\phi = \arctan \left\{ \frac{y_k}{x_j} \right\} \tag{16.4-12}$$

and

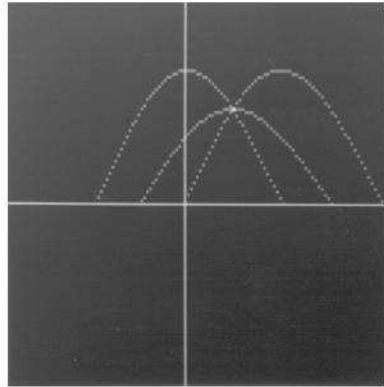
$$\psi = \begin{cases} \gamma + \frac{3\pi}{2} & \text{for } -\pi \leq \gamma < -\frac{\pi}{2} \\ \gamma + \frac{\pi}{2} & \text{for } -\frac{\pi}{2} \leq \gamma < \frac{\pi}{2} \\ \gamma - \frac{\pi}{2} & \text{for } \frac{\pi}{2} \leq \gamma < \pi \end{cases} \tag{16.4-13a}$$

$$\tag{16.4-13b}$$

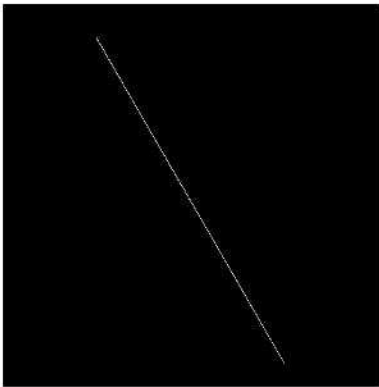
$$\tag{16.4-13c}$$



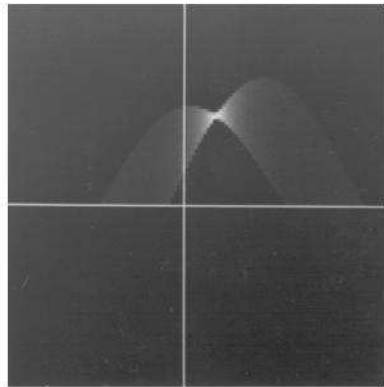
(a) Three dots: upper left, center, lower right



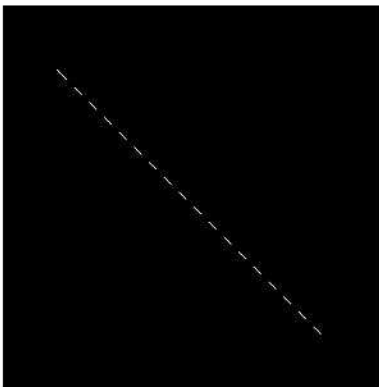
(b) Hough transform of dots



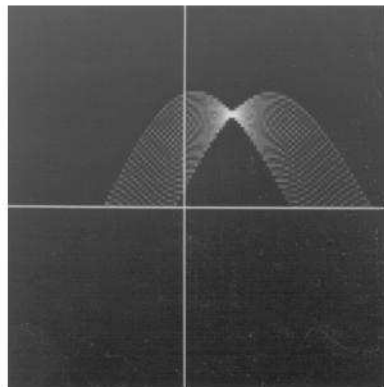
(c) Straight line



(d) Hough transform of line



(e) Straight dashed line



(f) Hough transform of dashed line

**FIGURE 16.4-8.** Duda and Hart version of the Hough transform.

- Determine the  $m$  and  $n$  indices of the quantized rho and theta values.

$$m = \left\lfloor M - \frac{[\rho_{\max} - \rho(j, k)](M - 1)}{2\rho_{\max}} \right\rfloor_N \tag{16.4-14a}$$

$$n = \left\lfloor N - \frac{[\pi - \theta](N - 1)}{2\pi} \right\rfloor_N \tag{16.4-14b}$$

- Increment the Hough array.

$$H(m, n) = H(m, n) + G(j, k). \tag{16.4-15}$$

Figure 16.4-9 gives an example of the O’Gorman and Clowes version of the Hough transform. The original image is  $512 \times 512$  pixels, and the Hough array is of size  $511 \times 511$  cells. The Hough array has been flipped bottom to top for display.

Kesidis and Papamarkos (76) have developed an algorithm for computing an inverse Hough transform (IHT) of a binary image. The algorithm detects peaks of the sinusoidal curves in the Hough transform (HT) space and decomposes each sinusoid to produce an image identical to the original image except for relatively minor quantization error effects. They propose filtering in the HT space as a means of extracting image edges on the basis of their size, orientation and location.

The task of detecting straight lines in a gray scale image has been formulated by Aggarwal and Karl (77) as an inverse problem. This formulation, based upon an inverse Radon transformation,<sup>1</sup> relates the location and orientation of image lines to the input image such that constraints can be established to suppress image noise.

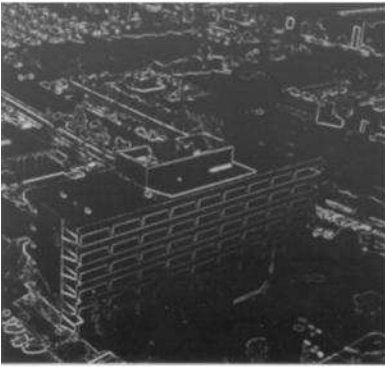
**Hough Transform Edge Linking.** The Hough transform can be used for edge linking in the following manner. Each  $(\rho, \theta)$  cell whose magnitude is sufficiently large defines a straight line that passes through the original image. If this line is overlaid with the image edge map, it should cover the missing links of straight-line edge segments, and therefore, it can be used as a mask to fill-in the missing links using some heuristic method, such as those described in the preceding section. Another approach, described below, is to use the line mask as a spatial control function for morphological image processing.

---

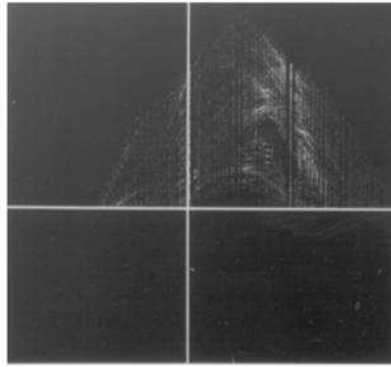
1. S. R. Deans (78) has proved that a Hough transform can be computed as a special case of the Radon transform.



(a) Original



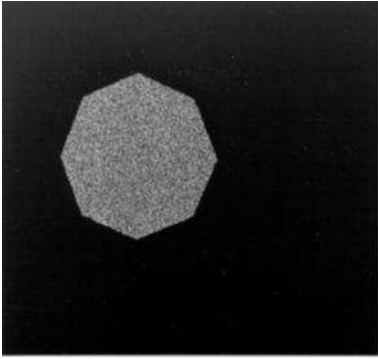
(b) Sobel edge gradient



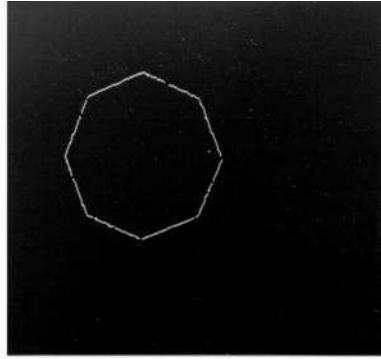
(c) Hough array

**FIGURE 16.4-9.** O’Gorman and Clowes version of the Hough transform of the building image.

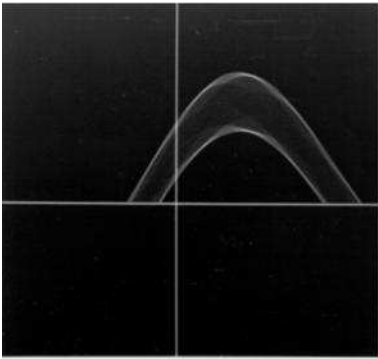
Figure 16.4-10 presents an example of Hough transform morphological edge linking. Figure 16.4-10a is an original image of a noisy octagon, and Figure 16.4-10b shows an edge map of the original image obtained by Sobel edge detection followed by morphological thinning, as defined in Section 14.3. Although this form of edge detection performs reasonably well, there are gaps in the contour of the object caused by image noise. Figure 16.4-10c shows the D & H version of the Hough transform. The eight largest cells in the Hough array have been used to generate the eight Hough lines shown as gray lines overlaid on the original image in Figure 16.4-10d. These Hough lines have been widened to a width of 3 pixels and used as a *region-of-interest* (ROI) mask that controls the edge linking morphological processing such that the processing is performed only on edge map pixels within the ROI. Edge map pixels outside the ROI are left unchanged. The morphological processing consists of three iterations of  $3 \times 3$  pixel dilation followed by five iterations of  $3 \times 3$  pixel thinning. The linked edge map is presented in Figure 16.4-10f.



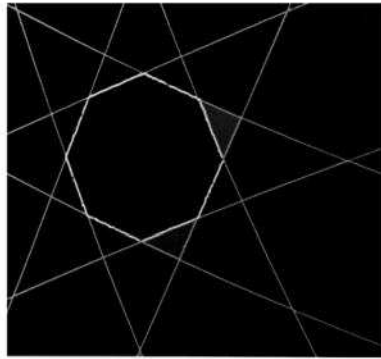
(a) Original



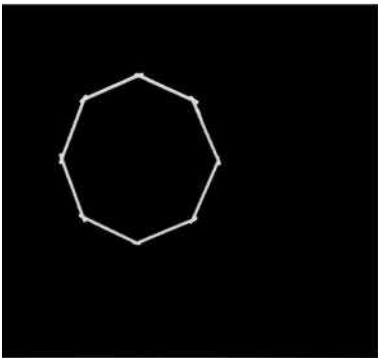
(b) Sobel edge map after thinning



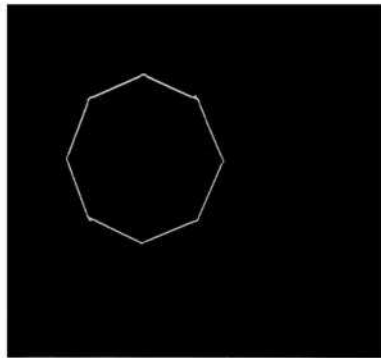
(c) D & H Hough array



(d) Hough line overlays



(e) Edge map after ROI dilation



(f) Linked edge map

**FIGURE 16.4-10.** Hough transform morphological edge linking.

### 16.4.4. Snakes Boundary Detection

*Snakes*, developed by Kass et al. (79), is a method of molding a closed contour to the boundary of an object in an image. The snake model is a controlled continuity closed contour that deforms under the influence of internal forces, image forces and external constraint forces. The internal contour forces provide a piecewise smoothness constraint. The image forces manipulate the contour toward image edges. The external forces are the result of the initial positioning of the contour by some a priori means.

Let  $\mathbf{v}(s) = [x(s), y(s)]$  denote a parametric curve in the continuous domain where  $s$  is the arc length of the curve. The continuous domain snake energy is defined as (79)

$$E_S = \int_0^1 E_N\{\mathbf{v}(s)\} ds + \int_0^1 E_I\{\mathbf{v}(s)\} ds + \int_0^1 E_T\{\mathbf{v}(s)\} ds \tag{16.4-16}$$

where  $E_N$  denotes the internal energy of the contour due to bending or discontinuities,  $E_I$  represents the image energy and  $E_T$  is the constraint energy. In the discrete domain, the snake energy is

$$E_S = \sum_{n=1}^N E_N\{\mathbf{v}_n\} + \sum_{n=1}^N E_I\{\mathbf{v}_n\} + \sum_{n=1}^N E_T\{\mathbf{v}_n\} \tag{16.4-17}$$

where  $\mathbf{v}_n = [x_n, y_n]$  for  $n = 0, 1, \dots, N$  represents the discrete contour. The location of a snake corresponds to the local minima of the energy functional of Eq. 16.4-16.

Kass et al. (79) have derived a set of  $N$  differential equations whose solution minimizes the snake energy. Samadani (80) has investigated the stability of these snake model solutions. The *greedy algorithm* (81,82) expresses the internal snake energy in terms of its continuity energy  $E_C$  and curvature energy  $E_K$  as

$$E_N = \alpha(n)E_C\{\mathbf{v}_n\} + \beta(n)E_K\{\mathbf{v}_n\} \tag{16.4-18}$$

where  $\alpha(n)$  and  $\beta(n)$  control the elasticity and rigidity of the snake model. The continuity energy is defined as

$$E_C = \frac{d - |\mathbf{v}_n - \mathbf{v}_{n-1}|}{\text{MAX}\{d - |\mathbf{v}_n(j) - \mathbf{v}_{n-1}|\}} \tag{16.4-19}$$

and the curvature energy is defined as

$$E_K = \frac{|\mathbf{v}_{n-1} - 2\mathbf{v}_n + \mathbf{v}_{n+1}|^2}{\text{MAX}\{|\mathbf{v}_{n-1} - 2\mathbf{v}_n(j) + \mathbf{v}_{n+1}|^2\}} \tag{16.4-19}$$



where  $d$  is the average curve length and  $\mathbf{v}_n(j)$  represents the eight neighbors of a point  $\mathbf{v}_n$  for  $j = 1, 2, \dots, 8$ .

The conventional snake model algorithms suffer from the inability to mold a contour to severe object concavities. Another problem is the generation of false contours due to the creation of unwanted contour loops. Ji and Yan (83) have developed a loop-free snake model segmentation algorithm that overcomes these problems. Figure 16.4-11 illustrates the performance of their algorithm. Figure 16.4-11*a* shows the initial contour around the pliers object, Figure 16.4-11*b* is the segmentation using the greedy algorithm and Figure 16.4-11*c* is the result with the loop-free algorithm.

Brigger, Hoeg and Unser (84) and Sakalli, Lam and Yan (85) have proposed refinements that improve the speed of the snakes algorithm. A problem with the basic snake algorithm is that it sometimes converges to a local minima, which is not on the true boundary of an object. Park and Keller (86) have combined the snake method with watershed segmentation as a means of avoiding local minima. Nguyn, Worring and van den Boomgaard (87) have also combined the snake algorithm with watershed segmentation to obtain smoother contours of segmented objects. Xie and Mirmehdi (88) have combined the snake algorithm with a form of region segmentation to create a segmentation method, which is more tolerant to weak edges and image noise.

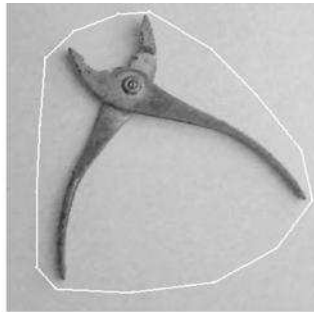
## 16.5. TEXTURE SEGMENTATION

It has long been recognized that texture should be a valuable feature for image segmentation. Putting this proposition to practice, however, has been hindered by the lack of a reliable and computationally efficient means of texture measurement.

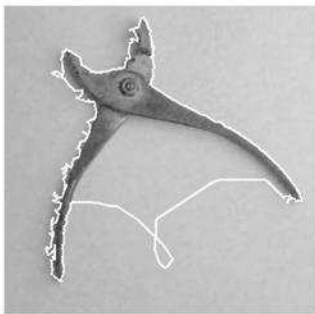
One approach to texture segmentation, fostered by Rosenfeld et al. (89–91), is to compute some texture coarseness measure at all image pixels and then detect changes in the coarseness of the texture measure. In effect, the original image is pre-processed to convert texture to an amplitude scale for subsequent amplitude segmentation. A major problem with this approach is that texture is measured over a window area, and therefore, texture measurements in the vicinity of the boundary between texture regions represent some average texture computation. As a result, it becomes difficult to locate a texture boundary accurately.

Another approach to texture segmentation is to detect the transition between regions of differing texture. The basic concept of texture edge detection is identical to that of luminance edge detection; the dissimilarity between textured regions is enhanced over all pixels in an image, and then the enhanced array is thresholded to locate texture discontinuities. Thompson (92) has suggested a means of texture enhancement analogous to the Roberts gradient presented in Section 15.2. Texture measures are computed in each of four adjacent  $W \times W$  pixel subregions scanned over the image, and the sum of the cross-difference magnitudes is formed and thresholded to locate significant texture changes. This method can be generalized to include computation in adjacent windows arranged in  $3 \times 3$  groups. Then, the result-

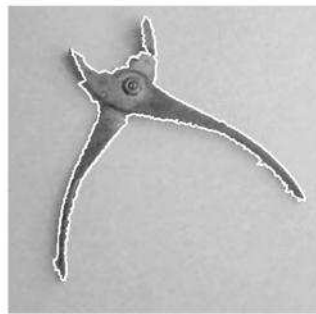
ing texture measures of each window can be combined in some linear or nonlinear manner analogous to the  $3 \times 3$  luminance edge detection methods of Section 14.2.



(a) Original with initial contour



(b) Segmentation with greedy algorithm



(c) Segmentation with loop-free algorithm

**FIGURE 16.4-11.** Snakes image segmentation of the pliers image. Courtesy of Lilian Ji and Hong Yan, University of Sydney, Australia.

Zucker et al. (93) have proposed a histogram thresholding method of texture segmentation based on a texture analysis technique developed by Tsuji and Tomita (94). In this method, a texture measure is computed at each pixel by forming the spot gradient followed by a dominant neighbor suppression algorithm. Then a histogram is formed over the resultant modified gradient data. If the histogram is multimodal, thresholding of the gradient at the minimum between histogram modes should provide a segmentation of textured regions. The process is repeated on the separate parts until segmentation is complete.

Section 16.6.7 has discussed the utilization of tunable Gabor filters as a means of texture analysis. Bovik et al. (95) have proposed using a bank of Gabor filters of multiple narrow spatial frequency and orientation for texture segmentation. Boundaries between adjacent textural regions can be detected by comparing changes in the channel amplitude responses (95). Dunn and Higgins (96) have

developed a design procedure for determining optimal Gabor filter parameters for texture segmentation.

Texture feature extraction using a wavelet transform has been introduced in Section 16.6.8. Unser (97) has suggested a method of texture segmentation using wavelets in which the wavelet variances are estimated. Hsin (98) has proposed a modulated wavelet transform as an improvement of the basic wavelet transform.

Rushing et al. (99) have developed a novel texture segmentation method based upon association rules. In data mining applications, association rules are used to determine relationships between items in large data sets. For example, items might be books of a certain topic that a buyer orders from an internet bookstore. If a buyer purchases a book of that topic (Digital Image Processing), the buyer is likely to buy another book of that topic. Rushing et al. have developed association rules that capture frequently occurring local intensity variations in textural images. There have been several proposals for hybrid texture segmentation schemes, which utilize some combination of edge, amplitude boundary, texture gradient, Gabor filter or active contours methods. Ma and Manjunath (100) have proposed a method, called Edge-Flow, in which the direction of change in amplitude and texture at each pixel is used to guide the segmentation. Hill et al. (101) have developed a hybrid method in which a wavelet transform is used to obtain a texture gradient. A watershed transform is applied to the texture gradient to obtain a segmentation. Sagiv et al. (102) have used Gabor filters to generate feature vectors, which are processed by a geodesic active contours algorithm. All three schemes have reported good texture segmentation, but on different data sets; so that a performance comparison is not possible.

The texture segmentation methods, previously presented, have all been applied to gray scale images. They can be applied to color images, simplistically, by combining the red, green and blue components to form a luminance-like image, and then segmenting the luminance image. Alternatively, texture segmentation can be performed separately on the *RGB* components, and the three segmentations can be combined in some heuristic manner. In the following, three non-simplistic color texture segmentation methods are described at a high (non detailed) level.

Mirmehdi and Petrou (103) have developed a complex, but effective, color texture segmentation algorithm. Its key point is that the *RGB* image to be segmented is linearly transformed to obtain three color components that represent the luminance, the red-green and the blue-yellow content of the image. In subsequent steps, the three color components are processed in parallel. The next step is to smooth the color components to several levels of coarse to fine resolution. The red-green and blue-yellow components are blurred more than the luminance component. The remaining steps in the algorithm, described in detail in reference 103, consist of clustering segmentation at different blur levels followed by multi scale probabilistic relaxation.

Deng and Manjunath have proposed an algorithm that first performs a gross color re-quantization that produces color class maps. Region growing is performed on the class maps to effect the segmentation.

Chen et al. (104) have developed an algorithm in which a luminance component is derived from a *RGB* image. Gray scale feature extraction is then per-

formed on the luminance image. In parallel, a small set of dominant color features are extracted from the *RGB* image. Then a crude segmentation is performed using the two sets of features. Finally, an iterative border process is performed to refine the segmentation. See reference 103 for details. All three color texture segmentation algorithms perform well on experimental images. As with the gray level methods, the test data sets are different. So a relative performance assessment is not possible.

In summary, a relatively large number of heuristic texture segmentation methods have been described in order from simple to complex. As might be expected, the simpler methods do not perform very well on cluttered images. The more complex methods fare better on cluttered images, but they require considerable computation.

## 16.6. SEGMENT LABELING

The result of any successful image segmentation is the unique labeling of each pixel that lies within a specific distinct segment. One means of labeling is to append to each pixel of an image the label number or index of its segment. A more succinct method is to specify the closed contour of each segment. If necessary, contour filling techniques (41) can be used to label each pixel within a contour. The following describes two common techniques of contour following.

The contour following approach to image segment representation is commonly called *bug following*. In the binary image example of Figure 16.6-1, a conceptual bug begins marching from the white background to the black pixel region indicated by the closed contour. When the bug crosses into a black pixel, it makes a left turn

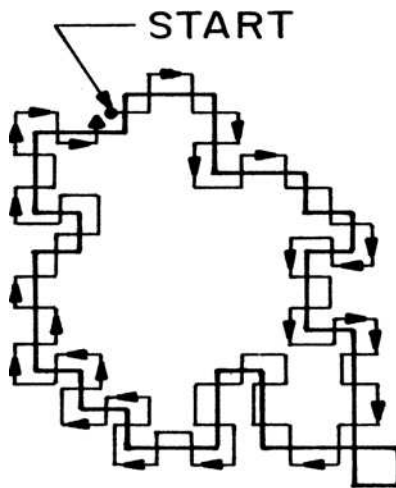


FIGURE 16.6-1. Contour following.

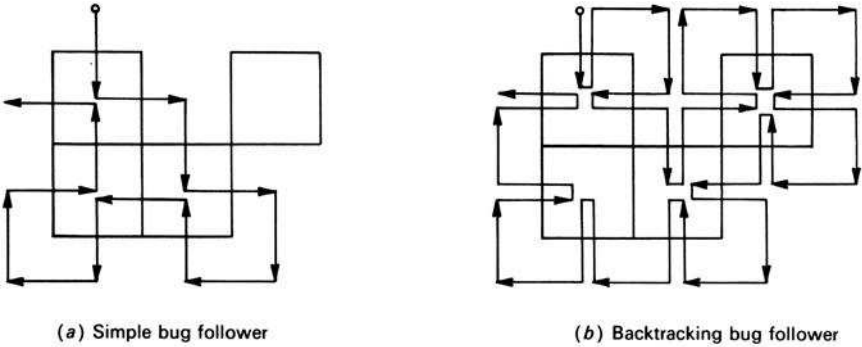


FIGURE 16.6-2. Comparison of bug follower algorithms.

and proceeds to the next pixel. If that pixel is black, the bug again turns left, and if the pixel is white, the bug turns right. The procedure continues until the bug returns to the starting point. This simple bug follower may miss spur pixels on a boundary. Figure 16.6-2a shows the boundary trace for such an example. This problem can be overcome by providing the bug with some memory and intelligence that permit the bug to remember its past steps and backtrack if its present course is erroneous.

Figure 16.6-2b illustrates the boundary trace for a *backtracking bug follower*. In this algorithm, if the bug makes a white-to-black pixel transition, it returns to its previous starting point and makes a right turn. The bug makes a right turn whenever it makes a white-to-white transition. Because of the backtracking, this bug follower takes about twice as many steps as does its simpler counterpart.

While the bug is following a contour, it can create a list of the pixel coordinates of each boundary pixel. Alternatively, the coordinates of some reference pixel on the boundary can be recorded, and the boundary can be described by a relative movement code. One such simple code is the *crack code* (106), which is generated for each side  $p$  of a pixel on the boundary such that  $C(p) = 0, 1, 2, 3$  for movement to the right, down, left, or up, respectively, as shown in Figure 16.6-3. The crack code for the object of Figure 16.6-2 is as follows:

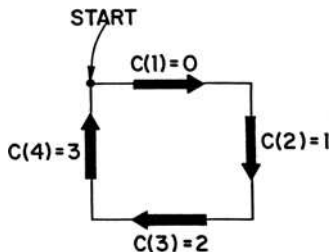


FIGURE 16.6-3. Crack code definition.

$p:$	1	2	3	4	5	6	7	8	9	10	11	12
$C(p):$	0	1	0	3	0	1	2	1	2	2	3	3

Upon completion of the boundary trace, the value of the index  $p$  is the perimeter of the segment boundary. Section 18.2 describes a method for computing the enclosed area of the segment boundary during the contour following.

Freeman (107,108) has devised a method of boundary coding, called *chain coding*, in which the path from the centers of connected boundary pixels are represented by an eight-element code. Figure 16.6-4 defines the chain code and provides an example of its use. Freeman has developed formulas for perimeter and area calculation based on the chain code of a closed contour.

Zingaretti et al. (109) have developed a fast, single pass algorithm for the coding of region boundaries.

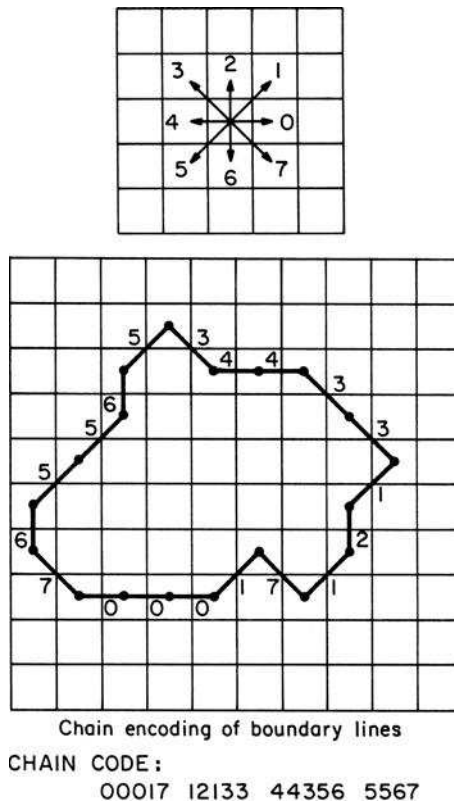


FIGURE 16.6-4. Chain coding contour coding.

## 16.7. IMAGE SEGMENTATION EXERCISES

E16.1 Develop a program that thresholds the monochrome image `parts` and displays the thresholded image. Determine the threshold value that provides the best visual segmentation. Steps:

- (a) Display the source image.
- (b) Threshold the source image into a Boolean destination image.
- (c) Display the destination image.

The PIKS API executable `example_threshold` performs this exercise.

E16.2 Develop a program that locates and tags the watershed segmentation local minima in the monochrome image `segmentation_test`. Steps:

- (a) Display the source image.
- (b) Generate a  $3 \times 3$  Boolean mask.
- (c) Erode the source image into a work image with the Boolean mask.
- (d) Compute the local minima of the work image.
- (e) Display the local minima image.

The PIKS API executable `example_watershed` performs this exercise.

## REFERENCES

1. R. M. Haralick and L. G. Shapiro, "Image Segmentation Techniques," *Computer Vision, Graphics and Image Processing*, **29**, 1, January 1985, 100–132.
2. E. M. Riseman and M. A. Arbib, "Computational Techniques in the Visual Segmentation of Static Scenes," *Computer Graphics and Image Processing*, **6**, 3, June 1977, 221–276.
3. J. S. Weska, "A Survey of Threshold Selection Techniques," *Computer Graphics and Image Processing*, **7**, 2, April 1978, 259–265.
4. T. Kanade, "Region Segmentation: Signal vs. Semantics," *Computer Graphics and Image Processing*, **13**, 4, August 1980, 279–297.
5. K. S. Fu and J. K. Mui, "A Survey on Image Segmentation," *Pattern Recognition*, **13**, 1981, 3–16.
6. P. K. Sahoo, S. Soltani and A. K. C. Wong, "SURVEY: A Survey of Thresholding Techniques," *Computer Graphics Image Processing*, **41**, 1988, 233–260.
7. N. R. Pal and S. K. Pal, "A Review of Image Segmentation Techniques," *Pattern Recognition*, **26**, 9, 1993, 1277–1294.
8. C. A. Glasbey, "An Analysis of Histogram-Based Thresholding Algorithms," *Computer Vision Image Processing*, **55**, 1993, 532–537.

9. B. Sankur, A. T. Abak and U. Baris, "Assessment of Thresholding Algorithms for Document Processing," *Proc. IEEE International Conference on Image Processing*, Kobe, Japan, October 1999, **1**, 580–584.
10. W. Doyle, "Operations Useful for Similarity-Invariant Pattern Recognition," *J. Association for Computing Machinery*, **9**, 2, April 1962, 259–267.
11. J. M. S. Prewitt and M. L. Mendelsohn, "The Analysis of Cell Images," *Ann. New York Academy of Science*, **128**, 1966, 1036–1053.
12. N. Papamarkos and B. Gatos, "A New Approach for Multilevel Threshold Selection," *CVGIP: Graphical Models and Image Processing*, **56**, 5, September 1994, 357–370.
13. N. Otsu, "A Threshold Selection Method from Gray-Level Histograms," *IEEE Trans. Systems, Man, Cybernetics*, **SMC-9**, 1, January 1979, 62–66.
14. J. S. Weska, R. N. Nagel and A. Rosenfeld, "A Threshold Selection Technique," *IEEE Trans. Computers*, **C-23**, 12, December 1974, 1322–1326.
15. M. R. Bartz, "The IBM 1975 Optical Page Reader, II: Video Thresholding System," *IBM J. Research and Development*, **12**, September 1968, 354–363.
16. C. K. Chow and T. Kaneko, "Boundary Detection of Radiographic Images by a Threshold Method," in *Frontiers of Pattern Recognition*, S. Watanabe, Ed., Academic Press, New York, 1972.
16. S. D. Yankowitz and A. M. Bruckstein, "A New Method for Image Segmentation," *Computer Vision, Graphics and Image Processing*, **46**, 1, April 1989, 82–95.
18. F. Tomita, M. Yachida and S. Tsuji, "Detection of Homogeneous Regions by Structural Analysis," *Proc. International Joint Conference on Artificial Intelligence*, Stanford, CA, August 1973, 564–571.
19. S. S. Reddi, S. F. Rudin and H. R. Keshavan, "An Optimal Multiple Threshold Scheme for Image Segmentation," *IEEE Trans. Systems, Man, Cybernetics*, **SMC-14**, 4, January 1984, 661–665.
20. J. N. Kapur, P. K. Sahoo and A. K. Wong, "A New Method for Gray-Level Picture Thresholding Using the Entropy of the Histogram," *Computer Vision Graphics and Image Processing*, **29**, 3, 1985, 273–285.
21. P. K. Saha and J. K. Udupa, "Optimum Image Thresholding via Class Uncertainty and Region Homogeneity," *IEEE Trans. Pattern Analysis and Machine Intelligence*, **23**, 7, July 2001, 689–706.
22. O. J. Tobias and R. Seara, "Image Segmentation by Histogram Thresholding Using Fuzzy Sets," *IEEE Trans. Image Processing*, **11**, 12, December 2002, 1457–1465.
23. Q. Hu, Z. Hou and W. L. Nowinski, "Supervised Range-Constrained Thresholding," *IEEE Trans. Image Processing*, **15**, 1, January 2006, 228–240.
24. R. B. Ohlander, "Analysis of Natural Scenes," Ph.D. dissertation, Carnegie-Mellon University, Department of Computer Science, Pittsburgh, PA, April 1975.
25. R. B. Ohlander, K. Price and D. R. Ready, "Picture Segmentation Using a Recursive Region Splitting Method," *Computer Graphics and Image Processing*, **8**, 3, December 1978, 313–333.
26. Y. Ohta, T. Kanade and T. Saki, "Color Information for Region Segmentation," *Computer Graphics and Image Processing*, **13**, 3, July 1980, 222–241.
27. R. O. Duda, P. E. Hart and D. G. Stork, *Pattern Classification, Second Edition*, Wiley-Interscience, New York, 2001.



28. H. C. Becker et al., "Digital Computer Determination of a Medical Diagnostic Index Directly from Chest X-ray Images," *IEEE Trans. Biomedical Engineering.*, **BME-11**, 3, July 1964, 67–72.
29. R. P. Kruger et al., "Radiographic Diagnosis via Feature Extraction and Classification of Cardiac Size and Shape Descriptors," *IEEE Trans. Biomedical Engineering*, **BME-19**, 3, May 1972, 174–186.
30. R. M. Haralick and G. L. Kelly, "Pattern Recognition with Measurement Space and Spatial Clustering for Multiple Images," *Proc. IEEE*, **57**, 4, April 1969, 654–665.
31. G. B. Coleman and H. C. Andrews, "Image Segmentation by Clustering," *Proc. IEEE*, **67**, 5, May 1979, 773–785.
32. J. L. Muerle and D. C. Allen, "Experimental Evaluation of Techniques for Automatic Segmentation of Objects in a Complex Scene," in *Pictorial Pattern Recognition*, G. C. Cheng et al., Eds., Thompson, Washington, DC, 1968, 3–13.
33. C. R. Brice and C. L. Fenema, "Scene Analysis Using Regions," *Artificial Intelligence*, **1**, 1970, 205–226.
34. C. R. Brice and C. L. Fenema, "Scene Analysis Using Regions," in *Computer Methods in Image Analysis*, J. K. Aggarwal, R. O. Duda and A. Rosenfeld, IEEE Press, New York, 1977.
35. H. G. Barrow and R. J. Popplestone, "Relational Descriptions in Picture Processing," in *Machine Intelligence*, Vol. 6, B. Meltzer and D. Michie, Eds., University Press, Edinburgh, 1971, 377–396.
36. Y. Yakimovsky, "Scene Analysis Using a Semantic Base for Region Growing," Report AIM-209, Stanford University, Stanford, CA., 1973.
37. R. Adams and L. Bischof, "Seeded Region Growing," *IEEE Trans. Pattern Analysis and Machine Intelligence*, **16**, 6, June 1994, 641–647.
38. Y.-L. Chang and X. Li, "Adaptive Image Region-Growing," *IEEE Trans. Image Processing*, **3**, 6, November 1994, 868–872.
39. S. A. Hojjatoleslami and J. Kittler, "Region Growing: A New Approach," *IEEE Trans. Image Processing*, **7**, 7, July 1998, 1079–1084.
40. S.-Y. Wan and W. E. Higgins, "Symmetric Region Growing," *IEEE Trans. Image Processing*, **12**, 9, September 2003, 1007–1015.
41. T. Pavlidis, *Algorithms for Graphics and Image Processing*, Computer Science Press, Rockville, MD, 1982.
42. Y. Fukada, "Spatial Clustering Procedures for Region Analysis," *Pattern Recognition*, **12**, 1980, 395–403.
43. P. C. Chen and T. Pavlidis, "Image Segmentation as an Estimation Problem," *Computer Graphics and Image Processing*, **12**, 2, February 1980, 153–172.
44. S. L. Horowitz and T. Pavlidis, "Picture Segmentation by a Tree Transversal Algorithm," *J. Association for Computing Machinery*, **23**, 1976, 368–388.
45. A. Tyagi and M. A. Bayoumi, "Image Segmentation on a 2-D Array by a Directed Split and Merge Procedure," *IEEE Trans. Signal Processing*, **40**, 11, November 1992, 2804–2813.
46. R. M. Haralick, "Ridges and Valleys on Digital Images," *Computer Vision, Graphics and Image Processing*, **22**, 10, April 1983, 28–38.

47. S. Beucher and C. Lantuejoul, "Use of Watersheds in Contour Detection," *Proc. International Workshop on Image Processing, Real Time Edge and Motion Detection/Estimation*, Rennes, France, September 1979.
48. S. Beucher and F. Meyer, "The Morphological Approach to Segmentation: The Watershed Transformation," in *Mathematical Morphology in Image Processing*, E. R. Dougherty, Ed., Marcel Dekker, New York, 1993.
49. L. Vincent and P. Soille, "Watersheds in Digital Spaces: An Efficient Algorithm Based on Immersion Simulations," *IEEE Trans. Pattern Analysis and Machine Intelligence*, **PAMI-13**, 6, June 1991, 583–598.
50. L. Najman and M. Schmitt, "Geodesic Saliency of Watershed Contours and Hierarchical Segmentation," *IEEE Trans. Pattern Analysis and Machine Intelligence*, **PAMI-18**, 12, December 1996.
51. A. N. Morga and M. Gabbouj, "Parallel Image Component Labeling with Watershed Transformation," *IEEE Trans. Pattern Analysis and Machine Intelligence*, **PAMI-19**, 5, May 1997, 441–440.
52. A. M. Lopez et al., "Evaluation of Methods for Ridge and Valley Detection," *IEEE Trans. Pattern Analysis and Machine Intelligence*, **PAMI-21**, 4, April 1999, 327–335.
53. C. Lemarechal et al., "Comments on "Geodesic Saliency of Watershed Contours and Hierarchical Segmentation,"" *IEEE Trans. Pattern Analysis and Machine Intelligence*, **20**, 7, July 1998, 764–766.
54. M. Schmitt, "Response to the Comment on "Geodesic Saliency of Watershed Contours and Hierarchical Segmentation,"" *IEEE Trans. Pattern Analysis and Machine Intelligence*, **20**, 7, July 1998, 762–763.
55. A. S. Wright and S. T. Acton, "Watershed Pyramids for Edge Detection," *Proc. 1997 International Conference on Image Processing*, **II**, Santa Barbara, CA, 1997, 578–581.
56. P. T. Jackway, "Gradient Watersheds in Morphological Scale-Space," *IEEE Trans. Image Processing*, **5**, 6, June 1996, 913–921.
57. K. Haris et al., "Hybrid Image Segmentation Using Watersheds and Fast Region Merging," *IEEE Trans. Image Processing*, **7**, 12, December 1998, 1684–1699.
58. M. W. Hansen and W. E. Higgins, "Watershed-Based Maximum-Homogeneity Filtering," *IEEE Trans. Image Processing*, **8**, 7, July 1999, 982–988.
59. I. Pitas and C. I. Cotsaces, "Memory Efficient Propagation-Based Watershed and Influence Zone Algorithms for Large Images," *IEEE Trans. Image Processing*, **9**, 7, July 2000, 1185–1199.
60. I. Vanhamel, I. Pratikakis and H. Sahli, "Multiscale Gradient Watersheds of Color Images," *IEEE Trans. Image Processing*, **12**, 6, June 2003, 617–626.
61. Y-C Lin et al. "Comparison Between Immersion-Based and Toboggan-Based Watershed Image Segmentation," *IEEE Trans. Image Processing*, **15**, 3, March 2006, 632–640.
62. R. O. Duda and P. E. Hart, *Pattern Classification and Scene Analysis*, Wiley-Interscience, New York, 1973.
63. U. Ramer, "An Iterative Procedure for the Polygonal Approximation of Plane Curves," *Computer Graphics and Image Processing*, **1**, 3, November 1972, 244–256.
64. T. Pavlidis and S. L. Horowitz, "Segmentation of Plane Curves," *IEEE Trans. Computers*, **C-23**, 8, August 1974, 860–870.
65. S. Wong et al., "Salient Closed Boundary Extraction with Ratio Contour," *IEEE Trans. Pattern Analysis and Machine Intelligence*, **27**, 4, April 2005, 546–561.

66. J. Elder and S. Zucker, "Computing Contour Closure," *Proc. European Conf. Computer Vision*, 1996, 399–412.
67. L. Williams and K. K. Thornber, "A Comparison of Measures for Detecting Natural Shapes in Cluttered Background," *Int'l. Journal Computer Vision*, **34**, 2/3, 2000, 81–96.
68. S. Mahamud et al., "Segmentation of Multiple Salient Closed Contours from Real Images," *IEEE Trans. Pattern Analysis and Machine Intelligence*, **25**, 4, April 2003, 433–444.
69. L. G. Roberts, "Machine Perception of Three Dimensional Solids," in *Optical and Electro-Optical Information Processing*, J. T. Tippett et al., Eds., MIT Press, Cambridge, MA, 1965.
70. R. Nevatia, "Locating Object Boundaries in Textured Environments," *IEEE Trans. Computers*, **C-25**, 11, November 1976, 1170–1175.
71. G. S. Robinson, "Detection and Coding of Edges Using Directional Masks," *Proc. SPIE Conference on Advances in Image Transmission Techniques*, San Diego, CA, August 1976.
72. P. V. C. Hough, "Method and Means for Recognizing Complex Patterns," U.S. patent 3,069,654, December 18, 1962.
73. R. O. Duda and P. E. Hart, "Use of the Hough Transformation to Detect Lines and Curves in Pictures," *Communication of the ACM*, **15**, 1, January 1972, 11–15.
74. J. Illingworth and J. Kittler, "A Survey of the Hough Transform," *Computer Vision, Graphics and Image Processing*, **44**, 1, October 1988, 87–116.
75. F. O'Gorman and M. B. Clowes, "Finding Picture Edges Through Colinearity of Feature Points," *IEEE Trans. Computers*, **C-25**, 4, April 1976, 449–456.
76. A. L. Kesidis and N. Papamarkos, "On the Inverse Hough Transform," *IEEE Trans. Pattern Analysis and Machine Intelligence*, **21**, 12, December 1999, 1329–1343.
77. N. Aggarwal and W. C. Karl, "Line Detection in Images Through Regularized Hough Transform," *IEEE Trans. Image Processing*, **15**, 3, March 2006, 582–591.
78. S. R. Deans, "Hough Transform from Radon Transform," *IEEE Trans. Pattern Analysis and Machine Intelligence*, **PAMI-3**, 2, March 1981, 185–188.
79. M. Kass, A. Witkin and D. Terzopoulos, "Snakes: Active Contour Models," *International J. Computer Vision*, **1**, 4, 1987, 321–331.
80. R. Samadani, "Adaptive Snakes: Control of Damping and Material Parameters," *Proc. SPIE Conference, on Geometric Methods in Computer Vision*, **1570**, San Diego, CA, 202–213.
81. D. J. Williams and M. Shah, "A Fast Algorithm for Active Contours and Curve Estimation," *CVGIP: Image Understanding*, **55**, 1, 1992, 14–26.
82. K.-H. Lam and H. Yan, "Fast Greedy Algorithm for Active Contours," *Electronic Letters*, **30**, 1, January 1994, 21–23.
83. L. Ji and H. Yan, "Loop-Free Snakes for Image Segmentation," *Proc. 1999 International Conference on Image Processing*, **3**, Kobe, Japan, 1999, 193–197.
84. P. Brigger, J. Hoeg and M. Unser, "B-Spline Snakes: A Flexible Tool for Parametric Contour Detection," *IEEE Trans. Image Processing*, **9**, 9, September 2000, 1484–1496.
85. M. Sakalli, K.-M. Lam and H. Yan, "A Faster Converging Snake Algorithm to Locate Object Boundaries," *IEEE Trans. Image Processing*, **15**, 5, May 2006, 1182–1191.

86. J. Park and J. Keller, "Snakes on the Watershed," *IEEE Trans. Pattern Analysis and Machine Intelligence*, **23**, 10, October 2001, 1201–1205.
87. H. T. Nguyen, M. Worrning and R. van den Boomgaard, "Watersnakes: Energy-Driven Watershed Segmentation," *IEEE Trans. Pattern Analysis and Machine Intelligence*, **25**, 3, March 2003, 330–342.
88. X. Xie and M. Mirmehdi, "RAGS: Region-Aided Geometric Snake," *IEEE Trans. Image Processing*, **13**, 5, May 2004, 640–652.
89. A. Rosenfeld and M. Thurston, "Edge and Curve Detection for Visual Scene Analysis," *IEEE Trans. Computers*, **C-20**, 5, May 1971, 562–569.
90. A. Rosenfeld, M. Thurston and Y. H. Lee, "Edge and Curve Detection: Further Experiments," *IEEE Trans. Computers*, **C-21**, 7, July 1972, 677–715.
91. K. C. Hayes, Jr., A. N. Shah and A. Rosenfeld, "Texture Coarseness: Further Experiments," *IEEE Trans. Systems, Man and Cybernetics (Correspondence)*, **SMC-4**, 5, September 1974, 467–472.
92. W. B. Thompson, "Textural Boundary Analysis," Report USCIPI 620, University of Southern California, Image Processing Institute, Los Angeles, September 1975, 124–134.
93. S. W. Zucker, A. Rosenfeld and L. S. Davis, "Picture Segmentation by Texture Discrimination," *IEEE Trans. Computers*, **C-24**, 12, December 1975, 1228–1233.
94. S. Tsuji and F. Tomita, "A Structural Analyzer for a Class of Textures," *Computer Graphics and Image Processing*, **2**, 3/4, December 1973, 216–231.
95. A. C. Bovik, M. Clark and W. S. Geisler, "Multichannel Texture Analysis Using Localized Spatial Filters," *IEEE Trans. Pattern Analysis and Machine Intelligence*, **12**, 1, January 1990, 55–73.
96. D. Dunn and W. E. Higgins, "Optimal Gabor Filters for Texture Segmentation," *IEEE Trans. Image Processing*, **4**, 7, July 1995, 9472–964.
97. M. Unser, "Texture Classification and Segmentation Using Wavelet Frames," *IEEE Trans. Image Processing*, **4**, 11, November 1995, 1549–1560.
98. H.-C. Hsin, "Texture Segmentation Using Modulated Wavelet Transform," *IEEE Trans. Image Processing*, **9**, 7, July 2000, 1299–1302.
99. J. A. Rushing et al., "Image Segmentation Using Association Rule Features," *IEEE Trans. Image Processing*, **11**, 5, May 2002, 558–567.
100. W. Y. Ma and B. S. Manjunath, "EdgeFlow: A Technique for Boundary Detection and Image Segmentation," *IEEE Trans. Image Processing*, **9**, 8, August 2000, 1375–1388.
101. P. R. Hill, C. N. Canagarajah and D. R. Bull, "Image Segmentation Using a Texture Gradient Base Watershed Transform," *IEEE Trans. Image Processing*, **12**, 12, December 2003, 1618–1633.
102. C. Sagiv, N. A. Sochen and Y. Y. Zeevi, "Integrated Active Contours for Texture Segmentation," *IEEE Trans. Image Processing*, 2006.
103. M. Mirmehdi and M. Petrou, "Segmentation of Color Textures," *IEEE Trans. Pattern Analysis and Machine Intelligence*, **22**, 2, February 2000, 142–159.
104. Y. Deng and B. S. Manjunath, "Unsupervised Segmentation of Color-Texture Regions in Images and Video," *IEEE Trans. Pattern Analysis and Machine Intelligence*, **23**, 8, August 2001, 800–810.

105. J. Chen et al. "Adaptive Perceptual Color-Texture Image Segmentation," *IEEE Trans. Image Processing*, **14**, 10, October 2005, 1524–1536.
106. Z. Kulpa, "Area and Perimeter Measurements of Blobs in Discrete Binary Pictures," *Computer Graphics and Image Processing*, **6**, 4, December 1977, 434–451.
107. H. Freeman, "On the Encoding of Arbitrary Geometric Configurations," *IRE Trans. Electronic Computers*, **EC-10**, 2, June 1961, 260–268.
108. H. Freeman, "Boundary Encoding and Processing," in *Picture Processing and Psychopictorics*, B. S. Lipkin and A. Rosenfeld, Eds., Academic Press, New York, 1970, 241–266.
109. P. Zingaretti, M. Gasparroni and L. Vecci, "Fast Chain Coding of Region Boundaries," *IEEE Trans. Pattern Analysis and Machine Intelligence*, **20**, 4, April 1998, 407–415.

---

# 17

---

## SHAPE ANALYSIS

Several qualitative and quantitative techniques have been developed for characterizing the shape of objects within an image. These techniques are useful for classifying objects in a pattern recognition system, and for symbolically describing objects in an image understanding system. Some of the techniques apply only to binary-valued images; others can be extended to gray level images.

### 17.1. TOPOLOGICAL ATTRIBUTES

Topological shape attributes are properties of a shape that are invariant under *rubber-sheet* transformation (1–3). Such a transformation or mapping can be visualized as the stretching of a rubber sheet containing the image of an object of a given shape to produce some spatially distorted object. Mappings that require cutting of the rubber sheet or connection of one part to another are not permissible. Metric distance is clearly not a topological attribute because distance can be altered by rubber-sheet stretching. Also, the concepts of perpendicularity and parallelism between lines are not topological properties. Connectivity is a topological attribute. Figure 17.1-1a is a binary-valued image containing two connected object components. Figure 17.1-1b is a spatially stretched version of the same image. Clearly, there are no stretching operations that can either increase or decrease the connectivity of the objects in the stretched image. Connected components of an object may contain holes, as illustrated in Figure 17.1-1c. The number of holes is obviously unchanged by a topological mapping.

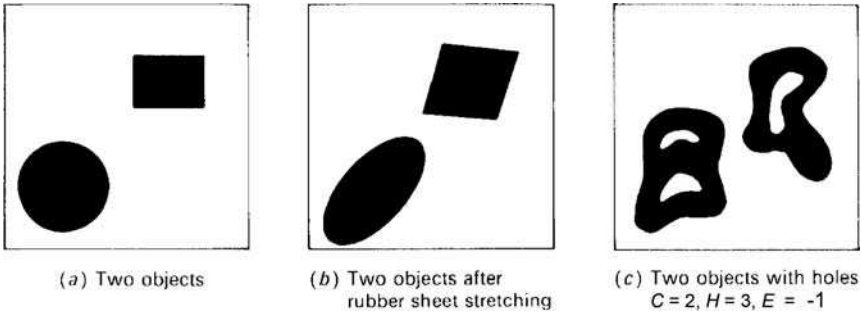


FIGURE 17.1-1. Topological attributes.

There is a fundamental relationship between the number of connected object components  $C$  and the number of object holes  $H$  in an image called the *Euler number*, as defined by

$$E = C - H. \quad (17.1-1)$$

The Euler number is also a topological property because  $C$  and  $H$  are topological attributes.

Irregularly shaped objects can be described by their topological constituents. Consider the tubular-shaped object letter R of Figure 17.1-2a, and imagine a rubber band stretched about the object. The region enclosed by the rubber band is called the *convex hull* of the object. The set of points within the convex hull, which are not in the object, form the *convex deficiency* of the object. There are two types of convex deficiencies: regions totally enclosed by the object, called *lakes*; and regions lying between the convex hull perimeter and the object, called *bays*. In some applications, it is simpler to describe an object indirectly in terms of its convex hull and convex deficiency. For objects represented over rectilinear grids, the definition of the convex hull must be modified slightly to remain meaningful. Objects such as discretized circles and triangles clearly should be judged as being convex even though their boundaries are jagged. This apparent difficulty can be handled by considering a rubber band to be stretched about the discretized object. A pixel lying totally within the rubber band, but not in the object, is a member of the convex deficiency. Sklansky et al. (4,5) have developed practical algorithms for computing the convex attributes of discretized objects.

## 17.2. DISTANCE, PERIMETER AND AREA MEASURES

This section develops shape analysis measures based upon distance measurements.



FIGURE 17.1-2. Definitions of convex shape descriptors.

**17.2.1. Distance Measures**

Distance is a real-valued function  $d\{(j_1, k_1), (j_2, k_2)\}$  of two image points  $(j_1, k_1)$  and  $(j_2, k_2)$  satisfying the following properties (6):

$$d\{(j_1, k_1), (j_2, k_2)\} \geq 0 \tag{17.2-1a}$$

$$d\{(j_1, k_1), (j_2, k_2)\} = d\{(j_2, k_2), (j_1, k_1)\} \tag{17.2-1b}$$

$$d\{(j_1, k_1), (j_2, k_2)\} + d\{(j_2, k_2), (j_3, k_3)\} \geq d\{(j_1, k_1), (j_3, k_3)\}. \tag{17.2-1c}$$

There are a number of distance functions that satisfy the defining properties. The most common measures encountered in image analysis are the *Euclidean distance*,

$$d_E = [(j_1 - j_2)^2 + (k_1 - k_2)^2]^{1/2} \tag{17.2-2a}$$

the *magnitude distance* also called the *city block distance*,

$$d_M = |j_1 - j_2| + |k_1 - k_2| \tag{17.2-2b}$$

and the *maximum value distance* also called the *chessboard distance*,

$$d_X = \text{MAX}\{|j_1 - j_2|, |k_1 - k_2|\}. \tag{17.2-2c}$$

In discrete images, the coordinate differences  $(j_1 - j_2)$  and  $(k_1 - k_2)$  are integers, but the Euclidean distance is usually not an integer.

**Voronoi Tessellation.** *Voronoi tessellation* is an important tool in image analysis (7). The Voronoi tessellation process accepts a zero background value image, which contains feature seeds of unit amplitude scattered throughout its area. The placing of the seeds is determined by some other means. All background pixels are assigned to the nearest seed in a geometric distance sense except for the skeleton of nearly equi-distant region border pixels. The result of the tessellation process is the production of a *Voronoi diagram* in which all pixels are uniquely



labeled. Rosenfeld and Pfaltz (8) are credited with the first Voronoi tessellation algorithm. Breu et al. (9) and Guan and Ma (10) have developed more efficient algorithms. Most Voronoi tessellation algorithms use the Euclidean distance measure because the separating skeleton is rotation invariant. It is possible to use morphological dilation algorithms, such as the thickening operator defined in Section 14.3.4, to create a Voronoi diagram. Using a rhombus structuring element in the dilation process is equivalent to using a city block distance measure. Likewise use of a square structuring element gives the same result as with a chessboard distance measure. Figure 17.2-1 contains a combined Voronoi diagram and a distance transform of an image containing 50 randomly placed seeds. In the figure, the white lines delineate the Voronoi regions.

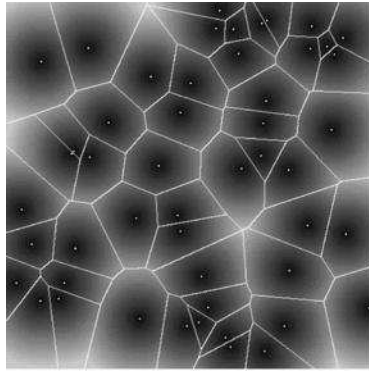


**FIGURE 17.2-1.** Example of a Voronoi diagram and a distance transform. Courtesy of S. Ma.

**Distance Transform.** The *distance transform*, also called the *distance map*, is another useful distance measuring tool (11, p 489). Consider a binary image for which the Voronoi diagram exists. At each pixel within a Voronoi region, the distance to the nearest seed pixel is recorded in a distance map image at the corresponding pixel (8). In the example of Figure 17.2-1, the brightness of a pixel is proportional to the distance to the nearest seed. Computing the Euclidean distance at each pixel is time consuming. Danielsson (12) has developed an efficient, but approximate, distance transform algorithm based upon neighborhood measurements. Maurer (13) has proposed a sequential algorithm base upon a partial Voronoi construction, which operates in linear time.

### 17.2.2. Perimeter and Area Measures

Perimeter and area measurements are meaningful only for binary images. Consider a discrete binary image containing one or more objects, where  $F(j, k) = 1$  if a pixel is part of the object and  $F(j, k) = 0$  for all non-object or background pixels.

The perimeter of each object is the count of the number of pixel sides traversed around the boundary of the object starting at an arbitrary initial boundary pixel and returning to the initial pixel. The area of each object within the image is simply the count of the number of pixels in the object for which  $F(j, k) = 1$ . As an example, for a  $2 \times 2$  pixel square, the object area is  $A_O = 4$  and the object perimeter is  $P_O = 8$ . An object formed of three diagonally connected pixels possesses  $A_O = 3$  and  $P_O = 12$ .

The enclosed area of an object is defined to be the total number of pixels for which  $F(j, k) = 0$  or 1 within the outer perimeter boundary  $P_E$  of the object. The enclosed area can be computed during a boundary-following process while the perimeter is being computed (14,15). Assume that the initial pixel in the boundary-following process is the first black pixel encountered in a raster scan of the image. Then, proceeding in a clockwise direction around the boundary, a crack code  $C(p)$ , as defined in Section 17.6, is generated for each side  $p$  of the object perimeter such that  $C(p) = 0, 1, 2, 3$  for directional angles  $0, 90, 180, 270^\circ$ , respectively. The enclosed area is

$$A_E = \sum_{p=1}^{P_E} j(p-1) \Delta k(p) \tag{17.2-3a}$$

where  $P_E$  is the perimeter of the enclosed object and

$$j(p) = \sum_{i=1}^p \Delta j(i) \tag{17.2-3b}$$

with  $j(0) = 0$ . The delta terms are defined by

$$\Delta j(p) = \begin{cases} 1 & \text{if } C(p) = 1 & (17.2-4a) \\ 0 & \text{if } C(p) = 0 \text{ or } 2 & (17.2-4b) \\ -1 & \text{if } C(p) = 3 & (17.2-4c) \end{cases}$$

$$\Delta k(p) = \begin{cases} 1 & \text{if } C(p) = 0 & (17.2-4d) \\ 0 & \text{if } C(p) = 1 \text{ or } 3 & (17.2-4e) \\ -1 & \text{if } C(p) = 2. & (17.2-4f) \end{cases}$$

Table 17.2-1 gives an example of computation of the enclosed area of the following four-pixel object:

$$\begin{matrix}
 0 & 0 & 0 & 0 & 0 \\
 0 & 1 & 0 & 1 & 0 \\
 0 & 1 & 1 & 0 & 0 \\
 0 & 0 & 0 & 0 & 0
 \end{matrix}$$

**TABLE 17.2-1. Example of Perimeter and Area Computation**

$p$	$C(p)$	$\Delta j(p)$	$\Delta k(p)$	$j(p)$	$A(p)$
1	0	0	1	0	0
2	3	-1	0	-1	0
3	0	0	1	-1	-1
4	1	1	0	0	-1
5	0	0	1	0	-1
6	3	-1	0	-1	-1
7	2	0	-1	-1	0
8	3	-1	0	-2	0
9	2	0	-1	-2	2
10	2	0	-1	-2	4
11	1	1	0	-1	4
12	1	1	0	0	4

**17.2.3. Bit Quads**

Gray (16) has devised a systematic method of computing the area and perimeter of binary objects based on matching the logical state of regions of an image to binary patterns. Let  $n\{Q\}$  represent the count of the number of matches between image pixels and the pattern  $Q$  within the curly brackets. By this definition, the object area is then

$$A_O = n\{1\}. \tag{17.2-5}$$

If the object is enclosed completely by a border of white pixels, its perimeter is equal to

$$P_O = 2n\{0\ 1\} + 2n\left\{ \begin{matrix} 0 \\ 1 \end{matrix} \right\}. \tag{17.2-6}$$

Now, consider the following set of  $2 \times 2$  pixel patterns called *bit quads* defined in Figure 17.2-2. The object area and object perimeter of an image can be expressed in terms of the number of bit quad counts in the image as

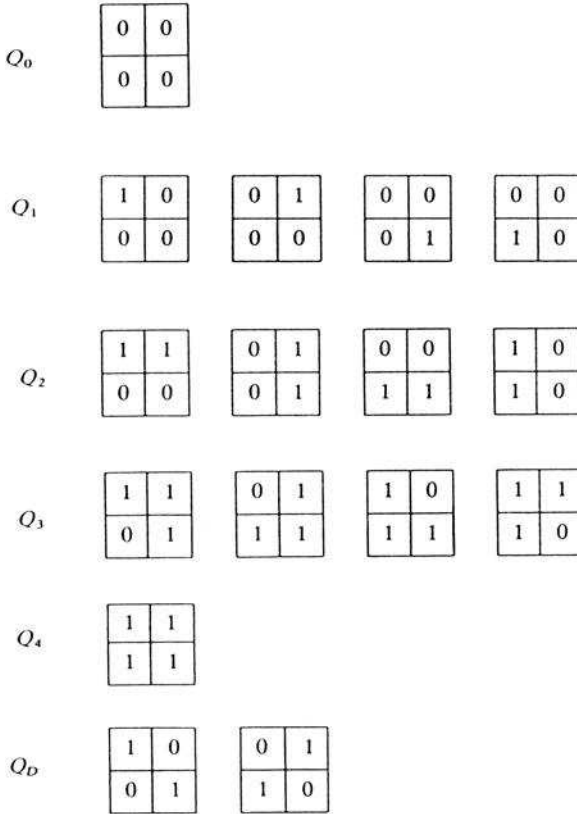


**FIGURE 17.2-2.** Bit quad patterns.

$$A_O = \frac{1}{4}[n\{Q_1\} + 2n\{Q_2\} + 3n\{Q_3\} + 4n\{Q_4\} + 2n\{Q_D\}] \quad (17.2-7a)$$

$$P_O = n\{Q_1\} + n\{Q_2\} + n\{Q_3\} + 2n\{Q_D\}. \quad (17.2-7b)$$

These area and perimeter formulas may be in considerable error if they are utilized to represent the area of a continuous object that has been coarsely discretized. More accurate formulas for such applications have been derived by Duda (17):

$$A_O = \frac{1}{4}n\{Q_1\} + \frac{1}{2}n\{Q_2\} + \frac{7}{8}n\{Q_3\} + n\{Q_4\} + \frac{3}{4}n\{Q_D\} \quad (17.2-8a)$$

$$P_O = n\{Q_2\} + \frac{1}{\sqrt{2}}[n\{Q_1\} + n\{Q_3\} + 2n\{Q_D\}]. \tag{17.2-8b}$$

Bit quad counting provides a very simple means of determining the Euler number of an image. Gray (16) has determined that under the definition of four-connectivity, the Euler number can be computed as

$$E = \frac{1}{4}[n\{Q_1\} - n\{Q_3\} + 2n\{Q_D\}] \tag{17.2-9a}$$

and for eight-connectivity

$$E = \frac{1}{4}[n\{Q_1\} - n\{Q_3\} - 2n\{Q_D\}]. \tag{17.2-9b}$$

It should be noted that although it is possible to compute the Euler number  $E$  of an image by local neighborhood computation, neither the number of connected components  $C$  nor the number of holes  $H$ , for which  $E = C - H$ , can be separately computed by local neighborhood computation.

**17.2.4. Geometric Attributes**

With the establishment of distance, area and perimeter measurements, various geometric attributes of objects can be developed. In the following, it is assumed that the number of holes with respect to the number of objects is small (i.e.,  $E$  is approximately equal to  $C$ ).

The *circularity* of an object is defined as

$$C_O = \frac{4\pi A_O}{(P_O)^2}. \tag{17.2-10}$$

This attribute is also called the *thinness ratio*. A circle-shaped object has a circularity of unity; oblong-shaped objects possess a circularity of less than 1.

If an image contains many components but few holes, the Euler number can be taken as an approximation of the number of components. Hence, the average area and perimeter of connected components, for  $E > 0$ , may be expressed as (16)

$$A_A = \frac{A_O}{E} \tag{17.2-11}$$

$$P_A = \frac{P_O}{E}. \tag{17.2-12}$$

For images containing thin objects, such as typewritten or script characters, the average object length and width can be approximated by

$$L_A = \frac{P_A}{2} \tag{17.2-13}$$

$$W_A = \frac{2A_A}{P_A} \tag{17.2-14}$$

These simple measures are useful for distinguishing gross characteristics of an image. For example, does it contain a multitude of small point like objects, or fewer blob like objects of larger size; are the objects fat or thin? Figure 17.2-3 contains images of playing card symbols. Table 17.2-2 lists the geometric attributes of these objects.

**TABLE 17.2-2. Geometric Attributes of Playing Card Symbols**

Attribute	Spade	Heart	Diamond	Club
Outer perimeter	652	512	548	668
Enclosed area	8,421	8,681	8,562	8,820
Average area	8,421	8,681	8,562	8,820
Average perimeter	652	512	548	668
Average length	326	256	274	334
Average width	25.8	33.9	31.3	26.4
Circularity	0.25	0.42	0.36	0.25

### 17.3. SPATIAL MOMENTS

From probability theory, the  $(m, n)$ th moment of the joint probability density  $p(x, y)$  is defined as

$$M(m, n) = \int_{-\infty}^{\infty} \int_{-\infty}^{\infty} x^m y^n p(x, y) dx dy \tag{17.3-1}$$

The central moment is given by

$$U(m, n) = \int_{-\infty}^{\infty} \int_{-\infty}^{\infty} (x - \eta_x)^m (y - \eta_y)^n p(x, y) dx dy \tag{17.3-2}$$

where  $\eta_x$  and  $\eta_y$  are the marginal means of  $p(x, y)$ . These classical relationships of probability theory have been applied to shape analysis by Hu (18) and Alt (19). The concept is quite simple. The joint probability density  $p(x, y)$  of Eqs. 17.3-1 and 17.3-2 is replaced by the continuous image function  $F(x, y)$ . Object shape is

characterized by a few of the low-order moments. Abu-Mostafa and Psaltis (20,21) have investigated the performance of spatial moments as features for shape analysis.

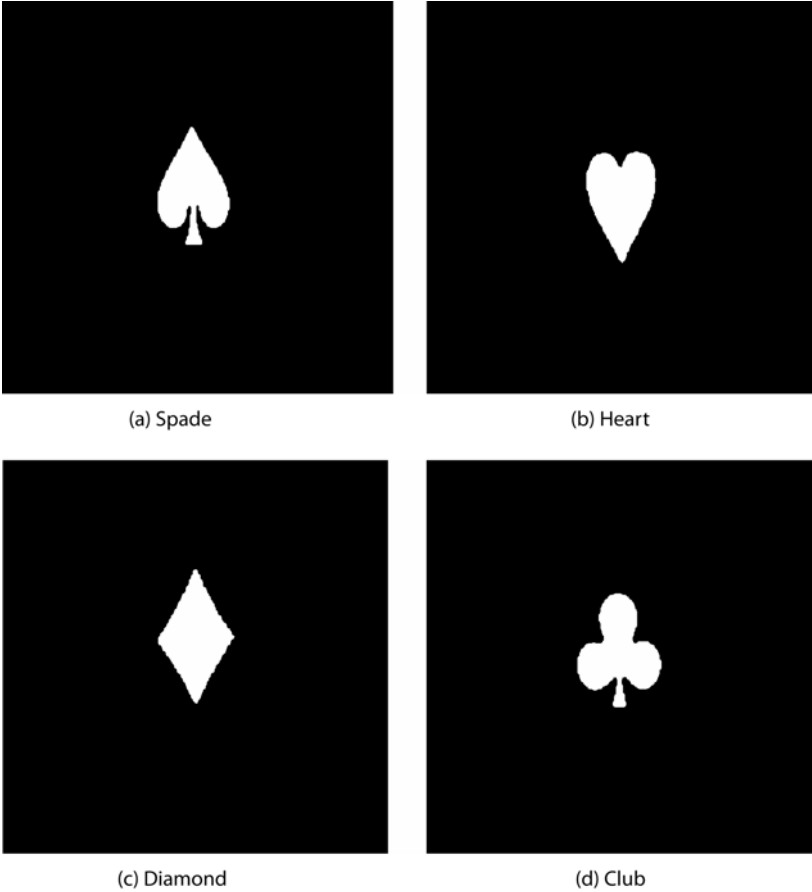


FIGURE 17.2-3. Playing card symbol images.

### 17.3.1. Discrete Image Spatial Moments

The spatial moment concept can be extended to discrete images by forming spatial summations over a discrete image function  $F(j, k)$ . The literature (22–24) is notationally inconsistent on the discrete extension because of the differing relationships defined between the continuous and discrete domains. Following the notation established in Chapter 12, the  $(m, n)$ th spatial *geometric moment* is defined as

$$M_U(m, n) = \sum_{j=1}^J \sum_{k=1}^K (x_j)^m (y_k)^n F(j, k) \quad (17.3-3)$$

where, with reference to Figure 12.1-1, the scaled coordinates are

$$x_j = j + \frac{1}{2} \quad (17.3-4a)$$

$$y_k = k + \frac{1}{2}. \quad (17.3-4b)$$

The origin of the coordinate system is the upper left corner of the image. This formulation results in moments that are extremely scale dependent; the ratio of second-order ( $m + n = 2$ ) to zero-order ( $m = n = 0$ ) moments can vary by several orders of magnitude (25). The spatial moments can be restricted in range by spatially scaling the image array over a unit range in each dimension. The  $(m, n)$ th scaled spatial geometric moment is then defined as

$$M(m, n) = \frac{1}{J^m K^n} \sum_{j=1}^J \sum_{k=1}^K (x_j)^m (y_k)^n F(j, k). \quad (17.3-5)$$

Clearly,

$$M(m, n) = \frac{M_U(m, n)}{J^m K^n}. \quad (17.3-6)$$

It is instructive to explicitly identify the lower-order spatial moments. The zero-order moment

$$M(0, 0) = \sum_{j=1}^J \sum_{k=1}^K F(j, k) \quad (17.3-7)$$

is the sum of the pixel values of an image. It is called the *image surface*. If  $F(j, k)$  is a binary image, its surface is equal to its area. The *first-order row moment* is

$$M(1, 0) = \frac{1}{J} \sum_{j=1}^J \sum_{k=1}^K x_j F(j, k) \quad (17.3-8)$$

and the *first-order column moment* is

$$M(0, 1) = \frac{1}{K} \sum_{j=1}^J \sum_{k=1}^K y_k F(j, k). \quad (17.3-9)$$



Table 17.3-1 lists the scaled spatial moments of several test images. These images include unit-amplitude gray scale versions of the playing card symbols of Figure 17.2-2, several rotated, minified and magnified versions of these symbols, as shown in Figure 17.3-1, as well as an elliptically shaped gray scale object shown in Figure 17.3-2. The ratios

$$\bar{x}_j = \frac{M(1, 0)}{M(0, 0)} \tag{17.3-10a}$$

$$\bar{y}_k = \frac{M(0, 1)}{M(0, 0)} \tag{17.3-10b}$$

of first-order to zero-order spatial moments define the *image centroid*. The centroid, called the *center of gravity*, is the balance point of the image function  $F(j, k)$  such that the mass of  $F(j, k)$  left and right of  $\bar{x}_j$  and above and below  $\bar{y}_k$  is equal.

With the centroid established, it is possible to define the scaled spatial central moments of a discrete image, in correspondence with Eq. 17.3-2, as

$$U(m, n) = \frac{1}{J^m K^n} \sum_{j=1}^J \sum_{k=1}^K (x_j - \bar{x}_j)^m (y_k - \bar{y}_k)^n F(j, k). \tag{17.3-11}$$

For future reference, the  $(m, n)$ th unscaled spatial central moment is defined as

$$U_U(m, n) = \sum_{j=1}^J \sum_{k=1}^K (x_j - \tilde{x}_j)^m (y_k - \tilde{y}_k)^n F(j, k) \tag{17.3-12}$$

where

$$\tilde{x}_j = \frac{M_U(1, 0)}{M_U(0, 0)} \tag{17.3-13a}$$

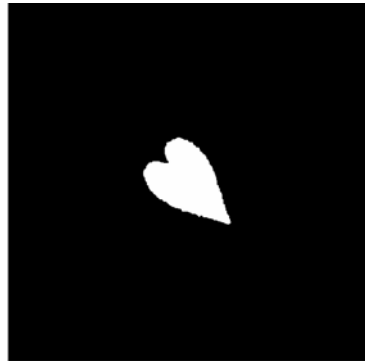
$$\tilde{y}_k = \frac{M_U(0, 1)}{M_U(0, 0)} \tag{17.3-13b}$$

**TABLE 17.3-1. Scaled Spatial Moments of Test Images**

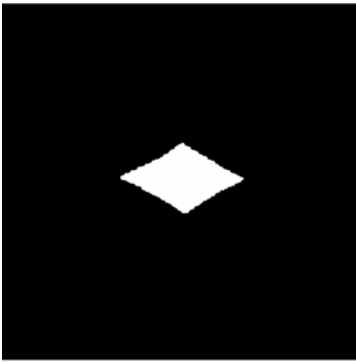
Image	$M(0,0)$	$M(1,0)$	$M(0,1)$	$M(2,0)$	$M(1,1)$	$M(0,2)$	$M(3,0)$	$M(2,1)$	$M(1,2)$	$M(0,3)$
Spade	8,219.98	4,013.75	4,281.28	1,976.12	2,089.86	2,263.11	980.81	1,028.31	1,104.36	1,213.73
Rotated spade	8,215.99	4,186.39	3,968.30	2,149.35	2,021.65	1,949.89	1,111.69	1,038.04	993.20	973.53
Heart	8,616.79	4,283.65	4,341.36	2,145.90	2,158.40	2,223.79	1,083.06	1,081.72	1,105.73	1,156.35
Rotated heart	8,613.79	4,276.28	4,337.90	2,149.18	2,143.52	2,211.15	1,092.92	1,071.95	1,008.05	1,140.43
Magnified heart	34,523.13	17,130.64	17,442.91	8,762.68	8,658.34	9,402.25	4,608.05	4,442.37	4,669.42	5,317.58
Miniified heart	2,104.97	1,047.38	1,059.44	522.14	527.16	535.38	260.78	262.82	266.41	271.61
Diamond	8,561.82	4,349.00	4,704.71	2,222.43	2,390.10	2,627.42	1,142.44	1,221.53	1,334.97	1,490.26
Rotated diamond	8,562.82	4,294.89	4,324.09	2,196.40	2,168.00	2,196.97	1,143.83	1,108.30	1,101.11	1,122.93
Club	8,781.71	4,323.54	4,500.10	2,150.47	2,215.32	2,344.02	1,080.29	1,101.21	1,153.76	1,241.04
Rotated club	8,787.71	4,363.23	4,220.96	2,196.08	2,103.88	2,057.66	1,120.12	1,062.39	1,028.90	1,017.60
Ellipse	8,721.74	4,326.93	4,377.78	2,175.86	2,189.76	2,226.61	1,108.47	1,109.92	1,122.62	1,146.97



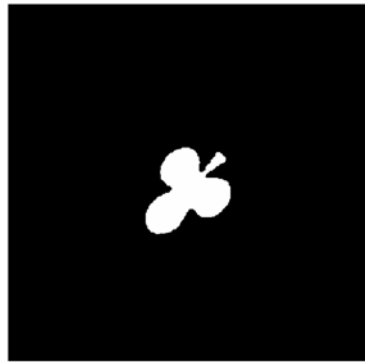
(a) Rotated spade



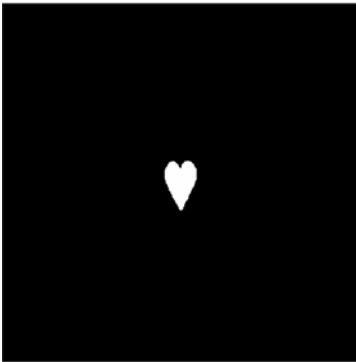
(b) Rotated heart



(c) Rotated diamond



(d) Rotated club



(e) Minified heart



(f) Magnified heart

**FIGURE 17.3-1.** Rotated, magnified and minified playing card symbol images.

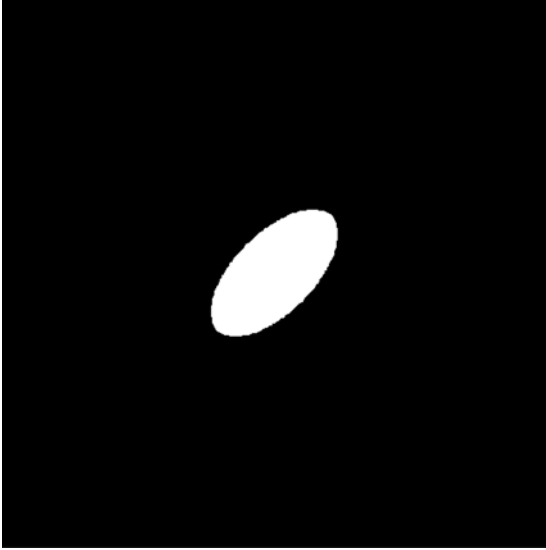


**FIGURE 17.3-2.** Elliptically shaped object image.

It is easily shown that

$$U(m, n) = \frac{U_U(m, n)}{J^m K^n} \tag{17.3-14}$$

The three second-order scaled central moments are the *row moment of inertia*,

$$U(2, 0) = \frac{1}{J^2} \sum_{j=1}^J \sum_{k=1}^K (x_j - \bar{x}_j)^2 F(j, k) \tag{17.3-15}$$

the *column moment of inertia*,

$$U(0, 2) = \frac{1}{K^2} \sum_{j=1}^J \sum_{k=1}^K (y_k - \bar{y}_k)^2 F(j, k) \tag{17.3-16}$$

and the *row-column cross moment of inertia*,

$$U(1, 1) = \frac{1}{JK} \sum_{j=1}^J \sum_{k=1}^K (x_j - \bar{x}_j)(y_k - \bar{y}_k) F(j, k). \tag{17.3-17}$$

The central moments of order 3 can be computed directly from Eq. 17.3-11 for  $m + n = 3$ , or indirectly according to the following relations:

$$U(3, 0) = M(3, 0) - 3\bar{y}_k M(2, 0) + 2(\bar{y}_k)^2 M(1, 0) \tag{17.3-18a}$$

$$U(2, 1) = M(2, 1) - 2\bar{y}_k M(1, 1) - \bar{x}_j M(2, 0) + 2(\bar{y}_k)^2 M(0, 1) \tag{17.3-18b}$$

$$U(1, 2) = M(1, 2) - 2\bar{x}_j M(1, 1) - \bar{y}_k M(0, 2) + 2(\bar{x}_j)^2 M(1, 0) \tag{17.3-18c}$$

$$U(0, 3) = M(0, 3) - 3\bar{x}_j M(0, 2) + 2(\bar{x}_j)^2 M(0, 1). \tag{17.3-18d}$$

Table 17.3-2 presents the horizontal and vertical centers of gravity and the scaled central spatial moments of the test images.

The three second-order moments of inertia defined by Eqs. 17.3-15, 17.3-16 and 17.3-17 can be used to create the moment of inertia covariance matrix,

$$\mathbf{U} = \begin{bmatrix} U(2, 0) & U(1, 1) \\ U(1, 1) & U(0, 2) \end{bmatrix}. \tag{17.3-19}$$

Performing a singular-value decomposition of the covariance matrix results in the diagonal matrix

$$\mathbf{E}^T \mathbf{U} \mathbf{E} = \mathbf{\Lambda} \tag{17.3-20}$$

where the columns of

$$\mathbf{E} = \begin{bmatrix} e_{11} & e_{12} \\ e_{21} & e_{22} \end{bmatrix} \tag{17.3-21}$$

are the eigenvectors of  $\mathbf{U}$  and

$$\mathbf{\Lambda} = \begin{bmatrix} \lambda_1 & 0 \\ 0 & \lambda_2 \end{bmatrix} \tag{17.3-22}$$

contains the eigenvalues of  $\mathbf{U}$ . Expressions for the eigenvalues can be derived explicitly. They are

$$\lambda_1 = \frac{1}{2}[U(2, 0) + U(0, 2)] + \frac{1}{2}[U(2, 0)^2 + U(0, 2)^2 - 2U(2, 0)U(0, 2) + 4U(1, 1)^2]^{1/2}$$

(17.3-23a)

$$\lambda_2 = \frac{1}{2}[U(2, 0) + U(0, 2)] - \frac{1}{2}[U(2, 0)^2 + U(0, 2)^2 - 2U(2, 0)U(0, 2) + 4U(1, 1)^2]^{1/2}.$$

(17.3-23b)

Let  $\lambda_M = \text{MAX}\{\lambda_1, \lambda_2\}$  and  $\lambda_N = \text{MIN}\{\lambda_1, \lambda_2\}$ , and let the *orientation angle*  $\theta$  be defined as

$$\theta = \begin{cases} \arctan\left\{\frac{e_{21}}{e_{11}}\right\} & \text{if } \lambda_M = \lambda_1 \end{cases} \quad (17.3-24a)$$

$$\theta = \begin{cases} \arctan\left\{\frac{e_{22}}{e_{12}}\right\} & \text{if } \lambda_M = \lambda_2 \end{cases} \quad (17.3-24b)$$

The orientation angle can be expressed explicitly as

$$\theta = \arctan\left\{\frac{\lambda_M - U(0, 2)}{U(1, 1)}\right\}. \quad (17.3-24c)$$

The eigenvalues  $\lambda_M$  and  $\lambda_N$  and the orientation angle  $\theta$  define an ellipse, as shown in Figure 17.3-2, whose major axis is  $\lambda_M$  and whose minor axis is  $\lambda_N$ . The major axis of the ellipse is rotated by the angle  $\theta$  with respect to the horizontal axis. This elliptically shaped object has the same moments of inertia along the horizontal and vertical axes and the same moments of inertia along the principal axes as does an actual object in an image. The ratio

$$R_A = \frac{\lambda_N}{\lambda_M} \quad (17.3-25)$$

of the minor-to-major axes is a useful shape feature.

Table 17.3-3 provides moment of inertia data for the test images. It should be noted that the orientation angle can only be determined to within plus or minus  $\pi/2$  radians.

**TABLE 17.3-2. Centers of Gravity and Scaled Spatial Central Moments of Test Images**

Image	Horizontal COG		Vertical COG		$U(2,0)$	$U(1,1)$	$U(0,2)$	$U(3,0)$	$U(2,1)$	$U(1,2)$	$U(0,3)$
Spade	0.488	0.510	0.521	0.483	16.240	-0.653	33.261	0.026	-0.285	-0.017	0.363
Rotated spade	0.510	0.488	0.483	0.521	16.207	-0.366	33.215	-0.013	0.284	-0.002	-0.357
Heart	0.497	0.504	0.504	0.497	16.380	0.194	36.506	-0.012	0.371	0.027	-0.831
Rotated heart	0.496	0.504	0.504	0.496	26.237	-10.009	26.584	-0.077	-0.438	0.411	0.122
Magnified heart	0.496	0.505	0.505	0.496	262.321	3.037	589.162	0.383	11.991	0.886	-27.284
Minified heart	0.498	0.503	0.503	0.498	0.984	0.013	2.165	0.000	0.011	0.000	-0.025
Diamond	0.508	0.508	0.549	0.508	13.337	0.324	42.186	-0.002	-0.026	0.005	0.136
Rotated diamond	0.502	0.505	0.505	0.502	42.198	-0.853	13.366	-0.158	0.009	0.029	-0.005
Club	0.492	0.512	0.512	0.492	21.834	-0.239	37.979	0.037	-0.545	-0.039	0.950
Rotated club	0.497	0.480	0.480	0.497	29.675	8.116	30.228	0.268	-0.505	-0.557	0.216
Ellipse	0.496	0.502	0.502	0.496	29.236	17.913	29.236	0.000	0.000	0.000	0.000

**TABLE 17.3-3. Moment of Inertia Data of Test Images**

Image	Largest Eigenvalue	Smallest Eigenvalue	Orientation (radians)	Eigenvalue Ratio
Spade	33.286	16.215	-0.153	0.487
Rotated spade	33.223	16.200	-1.549	0.488
Heart	36.508	16.376	1.561	0.449
Rotated heart	36.421	16.400	-0.794	0.450
Magnified heart	589.190	262.290	1.562	0.445
Minified heart	2.165	0.984	1.560	0.454
Diamond	42.189	13.334	1.560	0.316
Rotated diamond	42.223	13.341	-0.030	0.316
Club	37.982	21.831	-1.556	0.575
Rotated club	38.073	21.831	0.802	0.573
Ellipse	47.149	11.324	0.785	0.240

**17.3.2. Hu’s Invariant Moments**

Hu (18) has proposed a normalization of the unscaled central moments, defined by Eq. 17.3-12, according to the relation

$$V(m, n) = \frac{U_V(m, n)}{[M(0, 0)]^\alpha} \tag{17.3-26a}$$

where

$$\alpha = \frac{m+n}{2} + 1 \tag{17.3-26b}$$

for  $m + n = 2, 3, \dots$  These normalized central moments have been used by Hu to develop a set of seven compound spatial moments that are invariant in the continuous image domain to translation, rotation and scale change. The *Hu invariant moments* are defined below.

$$h_1 = V(2, 0) + V(0, 2) \tag{17.3-27a}$$

$$h_2 = [V(2, 0) - V(0, 2)]^2 + 4[V(1, 1)]^2 \tag{17.3-27b}$$

$$h_3 = [V(3, 0) - 3V(1, 2)]^2 + [V(0, 3) - 3V(2, 1)]^2 \tag{17.3-27c}$$

$$h_4 = [V(3, 0) + V(1, 2)]^2 + [V(0, 3) - V(2, 1)]^2 \tag{17.3-27d}$$



$$\begin{aligned}
 h_5 = & [V(3, 0) - 3V(1, 2)][V(3, 0) + V(1, 2)][[V(3, 0) + V(1, 2)]^2 - 3[V(0, 3) + V(2, 1)]^2] \\
 & + [3V(2, 1) - V(0, 3)][V(0, 3) + V(2, 1)][3[V(3, 0) + V(1, 2)]^2 \\
 & - [V(0, 3) + V(2, 1)]^2] \tag{17.3-27e}
 \end{aligned}$$

$$\begin{aligned}
 h_6 = & [V(2, 0) - V(0, 2)][[V(3, 0) + V(1, 2)]^2 - [V(0, 3) + V(2, 1)]^2] \\
 & + 4V(1, 1)[V(3, 0) + V(1, 2)][V(0, 3) + V(2, 1)] \tag{17.3-27f}
 \end{aligned}$$

$$\begin{aligned}
 h_7 = & [3V(2, 1) - V(0, 3)][V(3, 0) + V(1, 2)][[V(3, 0) + V(1, 2)]^2 - 3[V(0, 3) + V(2, 1)]^2] \\
 & + [3V(1, 2) - V(3, 0)][V(0, 3) + V(2, 1)][3[V(3, 0) + V(1, 2)]^2 \\
 & - [V(0, 3) + V(2, 1)]^2] \tag{17.3-27g}
 \end{aligned}$$

Table 17.3-4 lists the moment invariants of the test images. As desired, these moment invariants are in reasonably close agreement for the geometrically modified versions of the same object, but differ between objects. The relatively small degree of variability of the moment invariants for the same object is due to the spatial discretization of the objects.

The terms of Eq. 17.3-27 contain differences of relatively large quantities, and therefore, are sometimes subject to significant roundoff error. Liao and Pawlak (26) have investigated the numerical accuracy of geometric spatial moment measures.

**TABLE 17.3-4. Invariant Moments of Test Images**

Image	$h_1 \times 10^1$	$h_2 \times 10^3$	$h_3 \times 10^3$	$h_4 \times 10^5$	$h_5 \times 10^9$	$h_6 \times 10^6$	$h_7 \times 10^1$
Spade	1.920	4.387	0.715	0.295	0.123	0.185	-14.159
Rotated spade	1.919	4.371	0.704	0.270	0.097	0.162	-11.102
Heart	1.867	5.052	1.435	8.052	27.340	5.702	-15.483
Rotated heart	1.866	5.004	1.434	8.010	27.126	5.650	-14.788
Magnified heart	1.873	5.710	1.473	8.600	30.575	6.162	0.559
Minified heart	1.863	4.887	1.443	8.019	27.241	5.583	0.658
Diamond	1.986	10.648	0.018	0.475	0.004	0.490	0.004
Rotated diamond	1.987	10.663	0.024	0.656	0.082	0.678	-0.020
Club	2.033	3.014	2.313	5.641	20.353	3.096	10.226
Rotated club	2.033	3.040	2.323	5.749	20.968	3.167	13.487
Ellipse	2.015	15.242	0.000	0.000	0.000	0.000	0.000

### 17.3.3. Non-Geometric Spatial Moments

Teage (27) has introduced a family of orthogonal spatial moments based upon orthogonal polynomials. The family includes Legendre, Zernike and pseudo Zernike moments as defined in reference 28 in the continuous domain. Khotanzad and Hong (29) and Lia and Pawlak (30) have investigated Zernike spatial moments for spatial invariance. Teh and Chin (28) have analyzed these orthogonal spatial moments along with rotational and complex spatial moments as candidates for invariant moments. They concluded that the Zernike and pseudo Zernike moments out performed the others in terms of noise sensitivity and information redundancy.

The polynomials previously discussed for spatial moment computation are defined in the continuous domain. To use them for digital images requires that the polynomials be discretized. This introduces quantization error, which limits their usage. Mukundan, Ong and Lee (31) have proposed the use of Tchebichef polynomials, which are directly defined in the discrete domain, and therefore, are not subject to quantization error. Yap, Paramesran and Ong (32) have suggested the use of Krawtchouk polynomials, which also are defined in the discrete domain. Their studies show that the Krawtchouk moments are superior to moments based upon the Zernike, Legendre and Tchebichef moments.

## 17.4. SHAPE ORIENTATION DESCRIPTORS

The spatial orientation of an object with respect to a horizontal reference axis is the basis of a set of orientation descriptors developed at the Stanford Research Institute (33). These descriptors, defined below, are described in Figure 17.4-1.

1. *Image-oriented bounding box*: the smallest rectangle oriented along the rows of the image that encompasses the object
2. *Image-oriented box height*: dimension of box height for image-oriented box
3. *Image-oriented box width*: dimension of box width for image-oriented box

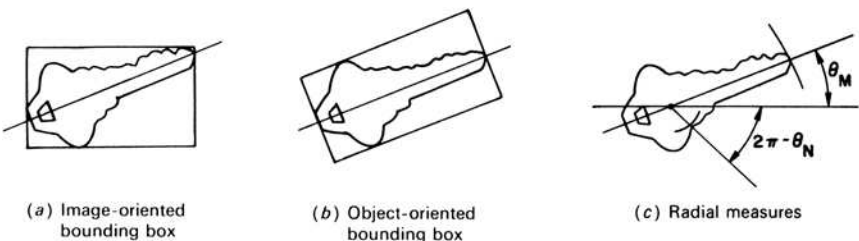


FIGURE 17.4-1. Shape orientation descriptors.

4. *Image-oriented box area*: area of image-oriented bounding box
5. *Image oriented box ratio*: ratio of box area to enclosed area of an object for an image-oriented box
6. *Object-oriented bounding box*: the smallest rectangle oriented along the major axis of the object that encompasses the object
7. *Object-oriented box height*: dimension of box height for object-oriented box
8. *Object-oriented box width*: dimension of box width for object-oriented box
9. *Object-oriented box area*: area of object-oriented bounding box
10. *Object-oriented box ratio*: ratio of box area to enclosed area of an object for an object-oriented box
11. *Minimum radius*: the minimum distance between the centroid and a perimeter pixel
12. *Maximum radius*: the maximum distance between the centroid and a perimeter pixel
13. *Minimum radius angle*: the angle of the minimum radius vector with respect to the horizontal axis
14. *Maximum radius angle*: the angle of the maximum radius vector with respect to the horizontal axis
15. *Radius ratio*: ratio of minimum radius angle to maximum radius angle

Table 17.4-1 lists the orientation descriptors of some of the playing card symbols.

**TABLE 17.4-1. Shape Orientation Descriptors of the Playing Card Symbols**

Descriptor	Spade	Rotated Heart	Rotated Diamond	Rotated Club
Row-bounding box height	155	122	99	123
Row-bounding box width	95	125	175	121
Row-bounding box area	14,725	15,250	17,325	14,883
Row-bounding box ratio	1.75	1.76	2.02	1.69
Object-bounding box height	94	147	99	148
Object-bounding box width	154	93	175	112
Object-bounding box area	14,476	13,671	17,325	16,576
Object-bounding box ratio	1.72	1.57	2.02	1.88
Minimum radius	11.18	38.28	38.95	26.00
Maximum radius	92.05	84.17	88.02	82.22
Minimum radius angle	-1.11	0.35	1.06	0.00
Maximum radius angle	-1.54	-0.76	0.02	0.85

## 17.5. FOURIER DESCRIPTORS

The perimeter of an arbitrary closed curve can be represented by its instantaneous curvature at each perimeter point. Consider the continuous closed curve drawn on the complex plane of Figure 17.5-1, in which a point on the perimeter is measured by its polar position  $z(s)$  as a function of arc length  $s$ . The complex function  $z(s)$  may be expressed in terms of its real part  $x(s)$  and imaginary part  $y(s)$  as

$$z(s) = x(s) + iy(s). \quad (17.5-1)$$

The tangent angle defined in Figure 17.5-1 is given by

$$\Phi(s) = \arctan \left\{ \frac{dy(s)/ds}{dx(s)/ds} \right\} \quad (17.5-2)$$

and the curvature is the real function

$$k(s) = \frac{d\Phi(s)}{ds} \quad (17.5-3)$$

The coordinate points  $[x(s), y(s)]$  can be obtained from the curvature function by the reconstruction formulas

$$x(s) = x(0) + \int_0^s k(\alpha) \cos \{ \Phi(\alpha) \} d\alpha \quad (17.5-4a)$$

$$y(s) = y(0) + \int_0^s k(\alpha) \sin \{ \Phi(\alpha) \} d\alpha \quad (17.5-4b)$$

where  $x(0)$  and  $y(0)$  are the starting point coordinates.

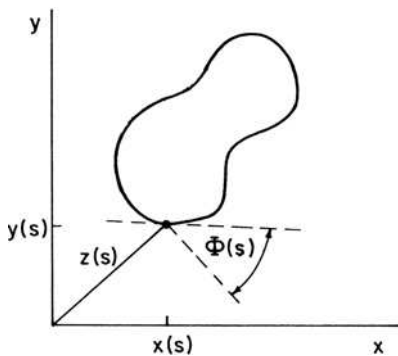


FIGURE 17.5-1. Geometry for curvature definition.

Because the *curvature function* is periodic over the perimeter length  $P$ , it can be expanded in a Fourier series as

$$k(s) = \sum_{n=-\infty}^{\infty} c_n \exp\left\{\frac{2\pi i n s}{P}\right\} \tag{17.5-5a}$$

where the coefficients  $c_n$  are obtained from

$$c_n = \frac{1}{P} \int_0^P k(s) \exp\left\{-\frac{2\pi i n s}{P}\right\} ds \tag{17.5-5b}$$

This result is the basis of an analysis technique developed by Cosgriff (34) and Brill (35) in which the Fourier expansion of a shape is truncated to a few terms to produce a set of Fourier descriptors. These Fourier descriptors are then utilized as a symbolic representation of shape for subsequent recognition.

If an object has sharp discontinuities (e.g., a rectangle), the curvature function is undefined at these points. This analytic difficulty can be overcome by the utilization of a cumulative shape function

$$\theta(s) = \int_0^s k(\alpha) d\alpha - \frac{2\pi s}{P} \tag{17.5-6}$$

proposed by Zahn and Roskies (36). This function is also periodic over  $P$  and can therefore be expanded in a Fourier series for a shape description.

Bennett and MacDonald (37) have analyzed the discretization error associated with the curvature function defined on discrete image arrays for a variety of connectivity algorithms. The discrete definition of curvature is given by

$$z(s_j) = x(s_j) + iy(s_j) \tag{17.5-7a}$$

$$\Phi(s_j) = \arctan\left\{\frac{y(s_j) - y(s_{j-1})}{x(s_j) - x(s_{j-1})}\right\} \tag{17.5-7b}$$

$$k(s_j) = \Phi(s_j) - \Phi(s_{j-1}) \tag{17.5-7c}$$

where  $s_j$  represents the  $j$ th step of arc position. Figure 17.5-2 contains results of the Fourier expansion of the discrete curvature function.

Bartolini et al. (38) have developed a Fourier descriptor-based shape matching technique called WARP in which a dynamic time warping distance is used for shape comparison.

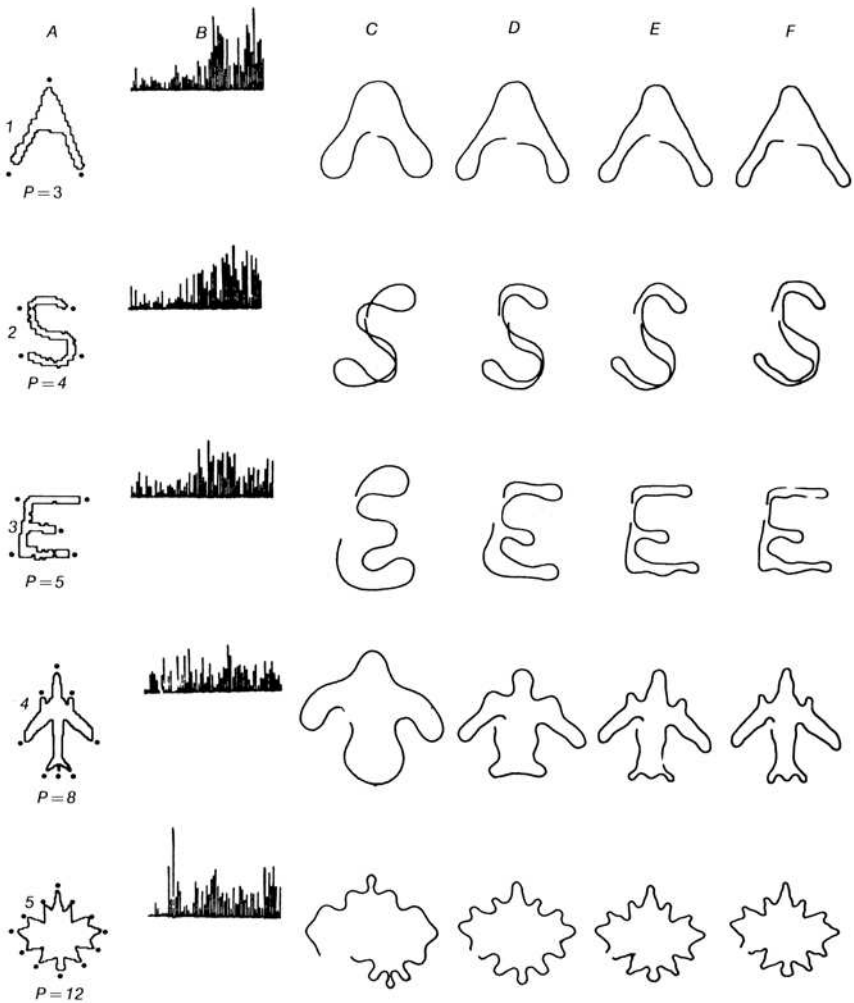


FIGURE 17.5-2. Fourier expansions of curvature function.

17.6. THINNING AND SKELETONIZING

Sections 13.3.2 and 13.3.3 have previously discussed the usage of morphological conditional erosion as a means of thinning or skeletonizing, respectively, a binary object to obtain a stick figure representation of the object. There are other non-morphological methods of thinning and skeletonizing. Some of these methods create thinner, minimally connected stick figures. Others are more computationally efficient.

Thinning and skeletonizing algorithms can be classified as sequential or parallel (39,40). In a sequential algorithm, pixels are examined for deletion (erasure) in a fixed sequence over several iterations of an algorithm. The erasure of a pixel in the  $n$ th iteration depends on all previous operations performed in the  $(n-1)$ th iteration plus all pixels already processed in the incomplete  $n$ th iteration. In a parallel algorithm, erasure of a pixel in the  $n$ th iteration only depends upon the result of the  $(n-1)$ th iteration. Sequential operators are, of course, designed for sequential computers or pipeline processors, while parallel algorithms take advantage of parallel processing architectures.

Sequential algorithms can be classified as raster scan or contour following. The morphological conditional erosion operators (41) described in Sections 14.3.2 and 14.3.3 are examples of raster scan operators. With these operators, pixels are examined in a  $3 \times 3$  window, and are marked for erasure or not for erasure. In a second pass, the conditionally marked pixels are sequentially examined in a  $3 \times 3$  window. Conditionally marked pixels are erased if erasure does not result in the breakage of a connected object into two or more objects.

In the contour following algorithms, an image is first raster scanned to identify each binary object to be processed. Then, each object is traversed about its periphery by a contour following algorithm, and the outer ring of pixels is conditionally marked for erasure. This is followed by a connectivity test to eliminate erasures that would break connectivity of an object. Rosenfeld (42) and Arcelli and di Bija (43) have developed some of the first connectivity tests for contour following thinning and skeletonizing.

More than one hundred papers have been published on thinning and skeletonizing algorithms. No attempt has been made to analyze these algorithms; rather, the following references are provided. Lam et al. (39) have published a comprehensive survey of thinning algorithms. The same authors (40) have evaluated a number of skeletonization algorithms. Lam and Suen (44) have evaluated parallel thinning algorithms. Leung et al. (45) have evaluated several contour following algorithms. R. Kimmel et al. (46) have used distance maps for skeletonization. References 47 and 48 describe a rotation-invariant, rule-based thinning method.

## 17.6. SHAPE ANALYSIS EXERCISES

E17.1 Develop a program that computes the scaled second-order central moments of the monochrome image `ellipse`. Steps:

- (a) Display the source image.
- (b) Normalize the source image to unit range.
- (c) Export the source image and perform the computation in application space in double precision.

The PIKS API executable `example_spatial_moments` performs this exercise.

E17.2 Develop a program that computes the crack code of the binarized monochrome image `ellipse`. Steps:

- (a) Display the source image.
- (b) Threshold the source image to binary range.
- (c) Compute the crack code and enclosed perimeter of the binary format `ellipse`.

The PIKS API executable `example_ellipse_perimeter` performs this exercise.

## REFERENCES

1. R. O. Duda and P. E. Hart, *Pattern Classification and Scene Analysis*, Wiley-Interscience, New York, 1973.
2. E. C. Greanis et al., "The Recognition of Handwritten Numerals by Contour Analysis," *IBM J. Research and Development*, **7**, 1, January 1963, 14–21.
3. M. A. Fischler, "Machine Perception and Description of Pictorial Data," *Proc. International Joint Conference on Artificial Intelligence*, D. E. Walker and L. M. Norton, Eds., May 1969, 629–639.
4. J. Sklansky, "Recognizing Convex Blobs," *Proc. International Joint Conference on Artificial Intelligence*, D. E. Walker and L. M. Norton, Eds., May 1969, 107–116.
5. J. Sklansky, L. P. Cordella and S. Levialdi, "Parallel Detection of Concavities in Cellular Blobs," *IEEE Trans. Computers*, **C-25**, 2, February 1976, 187–196.
6. A. Rosenfeld and J. L. Pfaltz, "Distance Functions on Digital Pictures," *Pattern Recognition*, **1**, July 1968, 33–62.
7. I. Pitas, *Digital Image Processing Algorithms and Applications*, Wiley-Interscience, New York, 2000.
8. A. Rosenfeld and J. Pfaltz, "Sequential Operations in Digital Picture Processing," *Journal ACM*, **13**, 4, 1966, 471–494.
9. H. Breu et al., "Linear Time Euclidean Distance Transform Algorithms," *IEEE Trans. Pattern Analysis and Machine Intelligence*, **17**, 5, May 1995, 529–533.
10. W. Guan and S. Ma, "A List-Processing Approach to Compute Voronoi Diagrams and the Euclidean Distance Transform," *IEEE Trans. Pattern Analysis and Machine Intelligence*, **20**, 7, July 1998, 757–761.
11. J. C. Russ, *The Image Processing Handbook, Third Edition*, CRC Press, Boca Raton, Florida, 1999.
12. P. E. Danielsson, "Euclidean Distance Mapping," *Computer Graphics, Image Processing*, **14**, 1980, 227–248.
13. C. R. Maurer, Jr., R. Qi and V. Raghavan, "A Linear Time Algorithm for Computing Exact Euclidean Distance Transforms of Binary Images in Arbitrary Dimensions," *IEEE Trans. Pattern Analysis and Machine Intelligence*, **25**, 2, February 2003, 265–270.



14. Z. Kulpa, "Area and Perimeter Measurements of Blobs in Discrete Binary Pictures," *Computer Graphics and Image Processing*, **6**, 5, October 1977, 434–451.
15. G. Y. Tang, "A Discrete Version of Green's Theorem," *IEEE Trans. Pattern Analysis and Machine Intelligence*, **PAMI-7**, 3, May 1985, 338–344.
16. S. B. Gray, "Local Properties of Binary Images in Two Dimensions," *IEEE Trans. Computers*, **C-20**, 5, May 1971, 551–561.
17. R. O. Duda, "Image Segmentation and Description," unpublished notes, 1975.
18. M. K. Hu, "Visual Pattern Recognition by Moment Invariants," *IRE Trans. Information Theory*, **IT-8**, 2, February 1962, 179–187.
19. F. L. Alt, "Digital Pattern Recognition by Moments," *J. Association for Computing Machinery*, **9**, 2, April 1962, 240–258.
20. Y. S. Abu-Mostafa and D. Psaltis, "Recognition Aspects of Moment Invariants," *IEEE Trans. Pattern Analysis and Machine Intelligence*, **PAMI-6**, 6, November 1984, 698–706.
21. Y. S. Abu-Mostafa and D. Psaltis, "Image Normalization by Complex Moments," *IEEE Trans. Pattern Analysis and Machine Intelligence*, **PAMI-7**, 6, January 1985, 46–55.
22. S. A. Dudani et al., "Aircraft Identification by Moment Invariants," *IEEE Trans. Computers*, **C-26**, February 1962, 179–187.
23. F. W. Smith and M. H. Wright, "Automatic Ship Interpretation by the Method of Moments," *IEEE Trans. Computers*, **C-20**, 1971, 1089–1094.
24. R. Wong and E. Hall, "Scene Matching with Moment Invariants," *Computer Graphics and Image Processing*, **8**, 1, August 1978, 16–24.
25. A. Goshtasby, "Template Matching in Rotated Images," *IEEE Trans. Pattern Analysis and Machine Intelligence*, **PAMI-7**, 3, May 1985, 338–344.
26. S. X. Liao and M. Pawlak, "On Image Analysis by Moments," *IEEE Trans. Pattern Analysis and Machine Intelligence*, **PAMI-18**, 3, March 1996, 254–266.
27. M. R. Teague, "Image Analysis Via the General Theory of Moments," *J. Optical Society America*, **70**, 9, August 1980, 920–930.
28. C.-H. Teh and R. T. Chin, "On Image Analysis by the Methods of Moments," *IEEE Trans. Pattern Analysis and Machine Intelligence*, **10**, 4, July 1988, 496–513.
29. A. Khotanzad and Y. H. Hong, "Invariant Image Recognition by Zernike Moments," *IEEE Trans. Pattern Analysis and Machine Intelligence*, **12**, 5, May 1990, 489–497.
30. S. X. Liao and M. Pawlak, "On Image Analysis by Moments," *IEEE Trans. Pattern Analysis and Machine Intelligence*, **18**, 3, March 1996, 254–266.
31. R. Mukundan, S.-H. Ong and P. A. Lee, "Image Analysis by Tchebichef Moments," *IEEE Trans. Image Processing*, **10**, 9, September 2001, 1357–1364.
32. P.-T. Yap, R. Paramesran and S.-H. Ong, "Image Analysis by Krawtchouk Moments," *IEEE Trans. Image Processing*, **12**, 11, November 2003, 1367–1377.
33. Stanford Research Institute, unpublished notes.
34. R. L. Cosgriff, "Identification of Shape," Report 820-11, ASTIA AD 254 792, Ohio State University Research Foundation, Columbus, OH, December 1960.
35. E. L. Brill, "Character Recognition via Fourier Descriptors," *WESCON Convention Record*, Paper 25/3, Los Angeles, 1968.
36. C. T. Zahn and R. Z. Roskies, "Fourier Descriptors for Plane Closed Curves," *IEEE Trans. Computers*, **C-21**, 3, March 1972, 269–281.

37. J. R. Bennett and J. S. MacDonald, "On the Measurement of Curvature in a Quantized Environment," *IEEE Trans. Computers*, **C-25**, 8, August 1975, 803–820.
38. I. Bartolini, P. Ciacci and M. Patella, "WARP: Accurate Retrieval of Shapes Using Phase of Fourier Descriptors and Time Warping Distance," *IEEE Trans. Pattern Analysis and Machine Intelligence*, **27**, 1, January 2005, 142–147.
39. L. Lam, S.-W. Lee and C. Y. Suen, "Thinning Methodologies—A Comprehensive Survey," *IEEE Trans. Pattern Analysis and Machine Intelligence*, **14**, 9, September 1992, 869–885.
40. S.-W. Lee, L. Lam and C. Y. Suen, "A Systematic Evaluation of Skeletonization Algorithms," *Int'l J. Pattern Recognition and Artificial Intelligence*, **7**, 5, 1993, 203–225.
41. W. K. Pratt and I. Kabir, "Morphological Binary Image Processing with a Local Neighborhood Pipeline Processor," *Computer Graphics*, Tokyo, 1984.
42. A. Rosenfeld, "Connectivity in Digital Pictures," *J. ACM*, **17**, 1, January 1970, 146–160.
43. C. Arcelli and G. S. di Baja, "On the Sequential Approach to Medial Line Transformation," *IEEE Trans. Systems, Man Cybernetics*, **SMC-8**, 2, 1978, 139–144.
44. L. Lam and C. Y. Suen, "An Evaluation of Parallel Thinning Algorithms for Character Recognition," *IEEE Trans. Pattern Analysis and Machine Intelligence*, **17**, 9, September 1995, 914–919.
45. W.-N. Leung, C. M. Ng and P. C. Yu, "Contour Following Parallel Thinning for Simple Binary Images," *IEEE International Conf. Systems, Man and Cybernetics*, 3, October 2000, 1650–1655.
46. R. Kimmel et al., "Skeletonization via Distance Maps and Level Sets," *Computer Vision and Image Understanding*, **62**, 3, November 1995, 382–391.
47. M. Ahmed and R. Ward, "A Rotation Invariant Rule-Based Thinning Algorithm for Character Recognition," *IEEE Trans. Pattern Analysis and Machine Intelligence*, **24**, 12, December 2002, 1672–1678.
48. P. I. Rockett, "An Improved Rotation-Invariant Thinning Algorithm," *IEEE Trans. Pattern Analysis and Machine Intelligence*, **27**, 10, October 2005, 1671–1674.



---

# 18

---

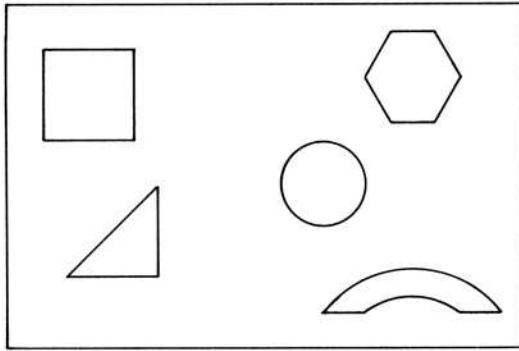
## IMAGE DETECTION AND REGISTRATION

This chapter covers two related image analysis tasks: detection and registration. Image detection is concerned with the determination of the presence or absence of objects suspected of being in an image. Image registration involves the spatial alignment of a pair of views of a scene.

### 18.1. TEMPLATE MATCHING

One of the most fundamental means of object detection within an image field is by *template matching*, in which a replica of an object of interest is compared to all unknown objects in the image field (1–4). If the template match between an unknown object and the template is sufficiently close, the unknown object is labeled as the template object.

As a simple example of the template-matching process, consider the set of binary black line figures against a white background as shown in Figure 18.1-1*a*. In this example, the objective is to detect the presence and location of right triangles in the image field. Figure 18.1-1*b* contains a simple template for localization of right triangles that possesses unit value in the triangular region and zero elsewhere. The width of the legs of the triangle template is chosen as a compromise between localization accuracy and size invariance of the template. In operation, the template is sequentially scanned over the image field, and the common region between the template and image field is compared for similarity.



(a) Array of objects



(b) Triangle template

**FIGURE 18.1-1.** Template-matching example.

A template match is rarely ever exact because of image noise, spatial and amplitude quantization effects and a priori uncertainty as to the exact shape and structure of an object to be detected. Consequently, a common procedure is to produce a difference measure  $D(m, n)$  between the template and the image field at all points of the image field where  $-M \leq m \leq M$  and  $-N \leq n \leq N$  denote the trial offset. An object is deemed to be matched wherever the difference is smaller than some established level  $L_D(m, n)$ . Normally, the threshold level is constant over the image field. The usual difference measure is the mean-square difference or error as defined by

$$D(m, n) = \sum_i \sum_k [F(j, k) - T(j - m, k - n)]^2 \tag{18.1-1}$$

where  $F(j, k)$  denotes the image field to be searched and  $T(j, k)$  is the template. The search, of course, is restricted to the overlap region between the translated template and the image field. A template match is then said to exist at coordinate  $(m, n)$  if

$$D(m, n) < L_D(m, n) . \tag{18.1-2}$$

Now, let Eq. 18.1-1 be expanded to yield

$$D(m, n) = D_1(m, n) - 2D_2(m, n) + D_3(m, n) \tag{18.1-3}$$

where

$$D_1(m, n) = \sum_i \sum_k [F(j, k)]^2 \tag{18.1-4a}$$

$$D_2(m, n) = \sum_i \sum_k [F(j, k)T(j - m, k - n)] \tag{18.1-4b}$$

$$D_3(m, n) = \sum_i \sum_k [T(j - m, k - n)]^2. \tag{18.1-4c}$$

The term  $D_3(m, n)$  represents a summation of the template energy. It is constant valued and independent of the coordinate  $(m, n)$ . The image energy over the window area represented by the first term  $D_1(m, n)$  generally varies rather slowly over the image field. The second term should be recognized as the cross correlation  $R_{FT}(m, n)$  between the image field and the template. At the coordinate location of a template match, the cross correlation should become large to yield a small difference. However, the magnitude of the cross correlation is not always an adequate measure of the template difference because the image energy term  $D_1(m, n)$  is position variant. For example, the cross correlation can become large, even under a condition of template mismatch, if the image amplitude over the template region is high about a particular coordinate  $(m, n)$ . This difficulty can be avoided by comparison of the normalized cross correlation

$$\tilde{R}_{FT}(m, n) = \frac{D_2(m, n)}{D_1(m, n)} = \frac{\sum_j \sum_k [F(j, k)T(j - m, k - n)]}{\sum_i \sum_k [F(j, k)]^2} \tag{18.1-5}$$

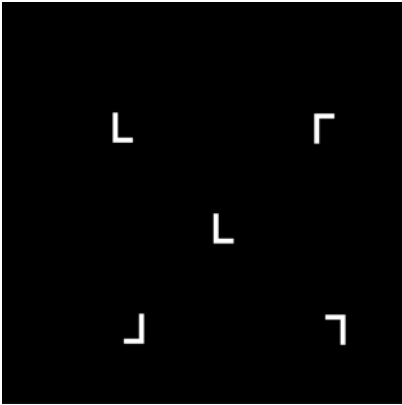
to a threshold level  $L_R(m, n)$ . A template match is said to exist if

$$\tilde{R}_{FT}(m, n) > L_R(m, n) \tag{18.1-6}$$

The normalized cross correlation has a maximum value of unity that occurs if and only if the image function under the template exactly matches the template. Figure 18.1-2 provides an example of normalized cross-correlation template matching of a binary image containing a L-shaped object, which is translated and rotated.

Rosenfeld (5) has proposed using the following absolute value difference as a template matching difference measure.

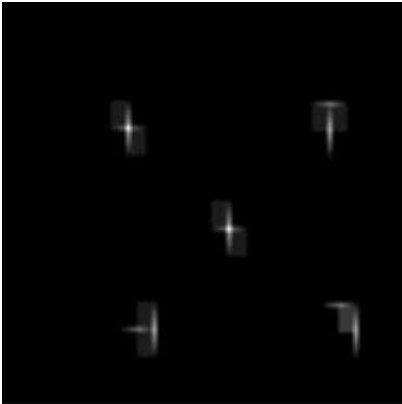
$$D(m, n) = \sum_j \sum_k |F(j, k) - T(j - m, k - n)|. \tag{18.1-7}$$



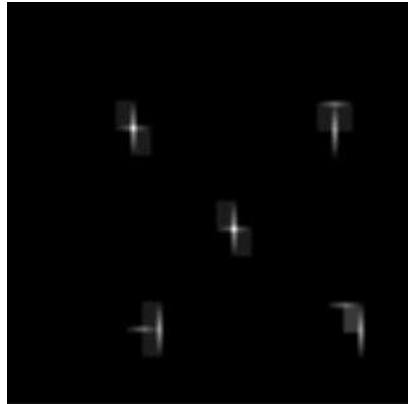
(a) Source image



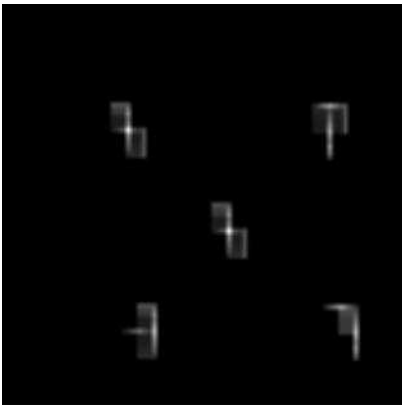
(b) Template image



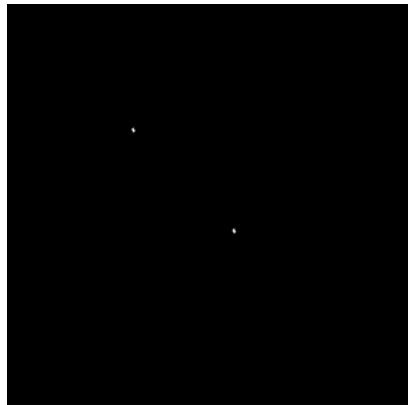
(c) Numerator image



(d) Denominator image



(e) Cross-correlation image



(f) Thresholded c-c image,  $T = 0.78$

**FIGURE 18.1-2.** Normalized cross-correlation template matching of the  $L_{source}$  image.

For some computing systems, the absolute difference computes faster than the squared difference. Rosenfeld (5) also has suggested comparing the difference measure of Eq. 18.1-7 to a relatively high threshold value during its computation. If the threshold is exceeded, the summation is terminated. Nagel and Rosenfeld (6) have proposed to vary the order in which template data is accessed rather than the conventional row by row access. The template data fetching they proposed is determined by a probability estimate of  $D(m, n)$ . Atallah (7) has developed a Monte Carlo algorithm for the computation of the absolute value difference, which is faster than brute force computation.

One of the major limitations of template matching is that an enormous number of templates must often be test matched against an image field to account for changes in rotation and magnification of template objects. For this reason, template matching is usually limited to smaller local features, which are more invariant to size and shape variations of an object. Such features, for example, include edges joined in a Y or T arrangement.

## 18.2. MATCHED FILTERING OF CONTINUOUS IMAGES

Matched filtering, implemented by electrical circuits, is widely used in one-dimensional signal detection applications such as radar and digital communication (8–10). It is also possible to detect objects within images by a two-dimensional version of the matched filter (11–15).

In the context of image processing, the *matched filter* is a spatial filter that provides an output measure of the spatial correlation between an input image and a reference image. This correlation measure may then be utilized, for example, to determine the presence or absence of a given input image, or to assist in the spatial registration of two images. This section considers matched filtering of deterministic and stochastic images.

### 18.2.1. Matched Filtering of Deterministic Continuous Images

As an introduction to the concept of the matched filter, consider the problem of detecting the presence or absence of a known continuous, deterministic signal or reference image  $F(x, y)$  in an unknown or input image  $F_U(x, y)$  corrupted by additive, stationary noise  $N(x, y)$  independent of  $F(x, y)$ . Thus,  $F_U(x, y)$  is composed of the signal image plus noise

$$F_U(x, y) = F(x, y) + N(x, y) \quad (18.2-1a)$$

or noise alone

$$F_U(x, y) = N(x, y). \quad (18.2-1b)$$



The unknown image is spatially filtered by a matched filter with impulse response  $H(x, y)$  and transfer function  $\mathcal{H}(\omega_x, \omega_y)$  to produce an output

$$F_O(x, y) = F_U(x, y) \otimes H(x, y) \tag{18.2-2}$$

The matched filter is designed so that the ratio of the signal image energy to the noise field energy at some point  $(\epsilon, \eta)$  in the filter output plane is maximized.

The instantaneous signal image energy at point  $(\epsilon, \eta)$  of the filter output in the absence of noise is given by

$$|S(\epsilon, \eta)|^2 = |F(x, y) \otimes H(x, y)|^2 \tag{18.2-3}$$

with  $x = \epsilon$  and  $y = \eta$ . By the convolution theorem,

$$|S(\epsilon, \eta)|^2 = \left| \int_{-\infty}^{\infty} \int_{-\infty}^{\infty} \mathcal{F}(\omega_x, \omega_y) \mathcal{H}(\omega_x, \omega_y) \exp\{i(\omega_x \epsilon + \omega_y \eta)\} d\omega_x d\omega_y \right|^2 \tag{18.2-4}$$

where  $\mathcal{F}(\omega_x, \omega_y)$  is the Fourier transform of  $F(x, y)$ . The additive input noise component  $N(x, y)$  is assumed to be stationary, independent of the signal image, and described by its noise power-spectral density  $\mathcal{W}_N(\omega_x, \omega_y)$ . From Eq. 1.4-24, the total noise power at the filter output is

$$N = \int_{-\infty}^{\infty} \int_{-\infty}^{\infty} \mathcal{W}_N(\omega_x, \omega_y) |\mathcal{H}(\omega_x, \omega_y)|^2 d\omega_x d\omega_y. \tag{18.2-5}$$

Then, forming the signal-to-noise ratio, one obtains

$$\frac{|S(\epsilon, \eta)|^2}{N} = \frac{\left| \int_{-\infty}^{\infty} \int_{-\infty}^{\infty} \mathcal{F}(\omega_x, \omega_y) \mathcal{H}(\omega_x, \omega_y) \exp\{i(\omega_x \epsilon + \omega_y \eta)\} d\omega_x d\omega_y \right|^2}{\int_{-\infty}^{\infty} \int_{-\infty}^{\infty} \mathcal{W}_N(\omega_x, \omega_y) |\mathcal{H}(\omega_x, \omega_y)|^2 d\omega_x d\omega_y}. \tag{18.2-6}$$

This ratio is found to be maximized when the filter transfer function is of the form (8,11)

$$\mathcal{H}(\omega_x, \omega_y) = \frac{\mathcal{F}^*(\omega_x, \omega_y) \exp\{-i(\omega_x \epsilon + \omega_y \eta)\}}{\mathcal{W}_N(\omega_x, \omega_y)}. \tag{18.2-7}$$

If the input noise power-spectral density is white with a flat spectrum,  $\mathcal{W}_N(\omega_x, \omega_y) = n_w/2$ , the matched filter transfer function reduces to

$$\mathcal{H}(\omega_x, \omega_y) = \frac{2}{n_w} \mathcal{F}^*(\omega_x, \omega_y) \exp\{-i(\omega_x \epsilon + \omega_y \eta)\} \tag{18.2-8}$$

and the corresponding filter impulse response becomes

$$H(x, y) = \frac{2}{n_w} F^*(\epsilon - x, \eta - y) \tag{18.2-9}$$

In this case, the matched filter impulse response is an amplitude scaled version of the complex conjugate of the signal image rotated by 180°.

For the case of white noise, the filter output can be written as

$$F_O(x, y) = \frac{2}{n_w} F_U(x, y) \otimes F^*(\epsilon - x, \eta - y) \tag{18.2-10a}$$

or

$$F_O(x, y) = \frac{2}{n_w} \int_{-\infty}^{\infty} \int_{-\infty}^{\infty} F_U(\alpha, \beta) F^*(\alpha + \epsilon - x, \beta + \eta - y) d\alpha d\beta \tag{18.2-10b}$$

If the matched filter offset  $(\epsilon, \eta)$  is chosen to be zero, the filter output

$$F_O(x, y) = \frac{2}{n_w} \int_{-\infty}^{\infty} \int_{-\infty}^{\infty} F_U(\alpha, \beta) F^*(\alpha - x, \beta - y) d\alpha d\beta \tag{18.2-11}$$

is then seen to be proportional to the mathematical correlation between the input image and the complex conjugate of the signal image. Ordinarily, the parameters  $(\epsilon, \eta)$  of the matched filter transfer function are set to be zero so that the origin of the output plane becomes the point of no translational offset between  $F_U(x, y)$  and  $F(x, y)$ .

If the unknown image  $F_U(x, y)$  consists of the signal image translated by distances  $(\Delta x, \Delta y)$  plus additive noise as defined by

$$F_U(x, y) = F(x + \Delta x, y + \Delta y) + N(x, y) \tag{18.2-12}$$

the matched filter output for  $\epsilon = 0, \eta = 0$  will be

$$F_O(x, y) = \frac{2}{n_w} \int_{-\infty}^{\infty} \int_{-\infty}^{\infty} [F(\alpha + \Delta x, \beta + \Delta y) + N(x, y)] F^*(\alpha - x, \beta - y) d\alpha d\beta \tag{18.2-13}$$

A correlation peak will occur at  $x = \Delta x, y = \Delta y$  in the output plane, thus indicating the translation of the input image relative to the reference image. Hence, the matched filter is translation invariant. It is, however, not invariant to rotation of the image to be detected.

The basic limitation of the normal matched filter, as defined by Eq. 18.2-7, is that the correlation output between an unknown image and an image signal to be detected is primarily dependent on the energy of the images rather than their spatial structure. For example, consider a signal image in the form of a bright hexagonally

shaped object against a black background. If the unknown image field contains a circular disk of the same brightness and area as the hexagonal object, the correlation function resulting will be very similar to the correlation function produced by a perfect match. In general, the normal matched filter provides relatively poor discrimination between objects of different, but of similar size or energy content. This drawback of the normal matched filter is overcome somewhat with the *derivative matched filter* (11), which makes use of the edge structure of an object to be detected. The transfer function of the  $p$ th-order derivative matched filter is given by

$$\mathcal{H}_p(\omega_x, \omega_y) = \frac{(\omega_x^2 + \omega_y^2)^p \mathcal{F}^*(\omega_x, \omega_y) \exp\{-i(\omega_x \varepsilon + \omega_y \eta)\}}{\mathcal{W}_N(\omega_x, \omega_y)} \tag{18.2-14}$$

where  $p$  is an integer. If  $p = 0$ , the normal matched filter

$$\mathcal{H}_0(\omega_x, \omega_y) = \frac{\mathcal{F}^*(\omega_x, \omega_y) \exp\{-i(\omega_x \varepsilon + \omega_y \eta)\}}{\mathcal{W}_N(\omega_x, \omega_y)} \tag{18.2-15}$$

is obtained. With  $p = 1$ , the resulting filter

$$\mathcal{H}_1(\omega_x, \omega_y) = (\omega_x^2 + \omega_y^2) \mathcal{H}_0(\omega_x, \omega_y) \tag{18.2-16}$$

is called the *Laplacian matched filter*. Its impulse response function is

$$H_1(x, y) = \left( \frac{\partial}{\partial x^2} + \frac{\partial}{\partial y^2} \right) \otimes H_0(x, y). \tag{18.2-17}$$

The  $p$ th-order derivative matched filter transfer function is

$$\mathcal{H}_p(\omega_x, \omega_y) = (\omega_x^2 + \omega_y^2)^p \mathcal{H}_0(\omega_x, \omega_y). \tag{18.2-18}$$

Hence, the derivative matched filter may be implemented by cascaded operations consisting of a generalized derivative operator whose function is to enhance the edges of an image, followed by a normal matched filter.

### 18.2.2. Matched Filtering of Stochastic Continuous Images

In the preceding section, the ideal image  $F(x, y)$  to be detected in the presence of additive noise was assumed to be deterministic. If the state of  $F(x, y)$  is not known exactly, but only statistically, the matched filtering concept can be extended to the detection of a stochastic image in the presence of noise (16). Even if  $F(x, y)$  is known deterministically, it is often useful to consider it as a random field with a mean  $E\{F(x, y)\} = F(x, y)$ . Such a formulation provides a mechanism for incorporating a priori knowledge of the spatial correlation of an image in its detection. Con-

ventional matched filtering, as defined by Eq. 18.2-7, completely ignores the spatial relationships between the pixels of an observed image.

For purposes of analysis, let the observed unknown field

$$F_U(x, y) = F(x, y) + N(x, y) \tag{18.2-19a}$$

or noise alone

$$F_U(x, y) = N(x, y) \tag{18.2-19b}$$

be composed of an ideal image  $F(x, y)$ , which is a sample of a two-dimensional stochastic process with known moments, plus noise  $N(x, y)$  independent of the image, or be composed of noise alone. The unknown field is convolved with the matched filter impulse response  $H(x, y)$  to produce an output modeled as

$$F_O(x, y) = F_U(x, y) \otimes H(x, y). \tag{18.2-20}$$

The stochastic matched filter is designed so that it maximizes the ratio of the average squared signal energy without noise to the variance of the filter output. This is simply a generalization of the conventional signal-to-noise ratio of Eq. 18.2-6. In the absence of noise, the expected signal energy at some point  $(\epsilon, \eta)$  in the output field is

$$|S(\epsilon, \eta)|^2 = |E\{F(x, y)\} \otimes H(x, y)|^2. \tag{18.2-21}$$

By the convolution theorem and linearity of the expectation operator,

$$|S(\epsilon, \eta)|^2 = \left| \int_{-\infty}^{\infty} \int_{-\infty}^{\infty} E\{\mathcal{F}(\omega_x, \omega_y)\} \mathcal{H}(\omega_x, \omega_y) \exp\{i(\omega_x \epsilon + \omega_y \eta)\} d\omega_x d\omega_y \right|^2. \tag{18.2-22}$$

The variance of the matched filter output, under the assumption of stationarity and signal and noise independence, is

$$N = \int_{-\infty}^{\infty} \int_{-\infty}^{\infty} [\tilde{w}_F(\omega_x, \omega_y) + \tilde{w}_N(\omega_x, \omega_y)] |\mathcal{H}(\omega_x, \omega_y)|^2 d\omega_x d\omega_y \tag{18.2-23}$$

where  $\tilde{w}_F(\omega_x, \omega_y)$  and  $\tilde{w}_N(\omega_x, \omega_y)$  are the image signal and noise power spectral densities, respectively. The generalized signal-to-noise ratio of the two equations above, which is of similar form to the specialized case of Eq. 18.2-6, is maximized when

$$\mathcal{H}(\omega_x, \omega_y) = \frac{E\{\mathcal{F}^*(\omega_x, \omega_y)\} \exp\{-i(\omega_x \epsilon + \omega_y \eta)\}}{\tilde{w}_F(\omega_x, \omega_y) + \tilde{w}_N(\omega_x, \omega_y)}. \tag{18.2-24}$$

Note that when  $F(x, y)$  is deterministic, Eq. 18.2-24 reduces to the matched filter transfer function of Eq. 18.2-7.

The stochastic matched filter is often modified by replacement of the mean of the ideal image to be detected by a replica of the image itself. In this case, for  $\epsilon = \eta = 0$ ,

$$\mathcal{H}(\omega_x, \omega_y) = \frac{\mathcal{F}^*(\omega_x, \omega_y)}{\mathcal{W}_F(\omega_x, \omega_y) + \mathcal{W}_N(\omega_x, \omega_y)}. \tag{18.2-25}$$

A special case of common interest occurs when the noise is white,  $\mathcal{W}_N(\omega_x, \omega_y) = n_W/2$ , and the ideal image is regarded as a first-order nonseparable Markov process, as defined by Eq. 1.4-16, with power spectrum

$$\mathcal{W}_F(\omega_x, \omega_y) = \frac{2}{\alpha^2 + \omega_x^2 + \omega_y^2} \tag{18.2-26}$$

where  $\exp\{-\alpha\}$  is the adjacent pixel correlation. For such processes, the resultant modified matched filter transfer function becomes

$$\mathcal{H}(\omega_x, \omega_y) = \frac{2(\alpha^2 + \omega_x^2 + \omega_y^2)\mathcal{F}^*(\omega_x, \omega_y)}{4 + n_W(\alpha^2 + \omega_x^2 + \omega_y^2)}. \tag{18.2-27}$$

At high spatial frequencies and low noise levels, the modified matched filter defined by Eq. 18.2-27 becomes equivalent to the Laplacian matched filter of Eq. 18.2-16.

A matched filter for object detection can be defined for discrete as well as continuous images. One approach is to perform discrete linear filtering using a discretized version of the matched filter transfer function of Eq. 18.2-7 following the techniques outlined in Section 9.4. Alternatively, the discrete matched filter can be developed by a vector-space formulation (16,17). The latter approach is described by Pratt (18).

### 18.3. IMAGE REGISTRATION

In many image processing applications, it is necessary to form a pixel-by-pixel comparison of two images of the same object field obtained from different sensors, or of two images of an object field taken from the same sensor at different times. To form this comparison, it is necessary to spatially register the images and, thereby, to correct for relative translation shifts, rotational differences, scale differences and even perspective view differences. Often, it is possible to eliminate or minimize many of these sources of misregistration by proper static calibration of an image sensor. However, in many cases, a posteriori misregistration detection and subsequent correction must be performed. Chapter 12 considered the task of spatially warping an

image to compensate for physical spatial distortion mechanisms. This section considers means of detecting the parameters of misregistration.

Consideration is given first to the common problem of detecting the translational misregistration of two images. Techniques developed for the solution to this problem are then extended to other forms of misregistration.

### 18.3.1. Translational Misregistration Detection

The classical technique for registering a pair of images subject to unknown translational differences is to: (a) form the normalized cross correlation function between the image pair; (b) determine the translational offset coordinates of the correlation function peak; and (c) translate one of the images with respect to the other by the offset coordinates (19,20). This subsection considers the generation of the basic cross correlation function and several of its derivatives as means of detecting the translational differences between a pair of images.

**Basic Correlation Function.** Let  $F_1(j, k)$  and  $F_2(j, k)$  for  $1 \leq j \leq J$  and  $1 \leq k \leq K$ , represent two discrete images to be registered.  $F_1(j, k)$  is considered to be the reference image, and

$$F_2(j, k) = F_1(j - j_o, k - k_o) \tag{18.3-1}$$

is a translated version of  $F_1(j, k)$  where  $(j_o, k_o)$  are the offset coordinates of the translation. The normalized cross correlation between the image pair is defined as

$$R(m, n) = \frac{\sum_j \sum_k F_1(j, k) F_2(j - m + (M + 1)/2, k - n + (N + 1)/2)}{\left[ \sum_i \sum_k [F_1(j, k)]^2 \right]^{\frac{1}{2}} \left[ \sum_i \sum_k [F_2(j - m + (M + 1)/2, k - n + (N + 1)/2)]^2 \right]^{\frac{1}{2}}} \tag{18.3-2}$$

for  $m = 1, 2, \dots, M$  and  $n = 1, 2, \dots, N$ , where  $M$  and  $N$  are odd integers. This formulation, which is a generalization of the template matching cross correlation expression, as defined by Eq. 18.1-5, utilizes an upper left corner-justified definition for all of the arrays. The dashed-line rectangle of Figure 18.3-1 specifies the bounds of the correlation function region over which the upper left corner of  $F_2(j, k)$  moves in space with respect to  $F_1(j, k)$ . The bounds of the summations of Eq. 18.3-2 are

$$\text{MAX}\{1, m - (M - 1)/2\} \leq j \leq \text{MIN}\{J, J + m - (M + 1)/2\} \tag{18.3-3a}$$

$$\text{MAX}\{1, n - (N - 1)/2\} \leq k \leq \text{MIN}\{K, K + n - (N + 1)/2\}. \tag{18.3-3b}$$

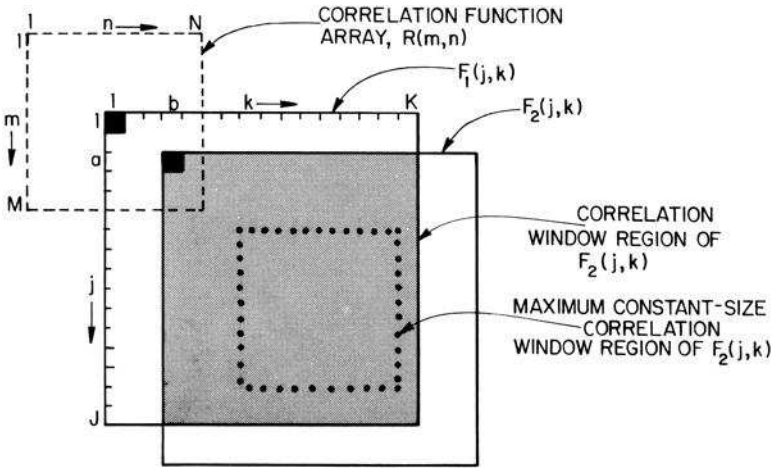


**FIGURE 18.3-1.** Geometrical relationships between arrays for the cross correlation of an image pair.

These bounds are indicated by the shaded region in Figure 18.3-1 for the trial offset  $(a, b)$ . This region is called the *window region* of the correlation function computation. The computation of Eq. 18.3-2 is often restricted to a constant-size window area less than the overlap of the image pair in order to reduce the number of calculations. This  $P \times Q$  constant-size window region, called a *template region*, is defined by the summation bounds

$$m \leq j \leq m + J - M \tag{18.3-4a}$$

$$n \leq k \leq n + K - N \tag{18.3-4b}$$

The dotted lines in Figure 18.3-1 specify the maximum constant-size template region, which lies at the center of  $F_2(j, k)$ . The sizes of the  $M \times N$  correlation function array, the  $J \times K$  search region and the  $P \times Q$  template region are related by

$$M = J - P + 1 \tag{18.3-5a}$$

$$N = K - Q + 1. \tag{18.3-5b}$$

For the special case in which the correlation window is of constant size, the correlation function of Eq. 18.3-2 can be reformulated as a template search process. Let  $S(u, v)$  denote a  $U \times V$  search area within  $F_1(j, k)$  whose upper left corner is at the offset coordinate  $(j_s, k_s)$ . Let  $T(p, q)$  denote a  $P \times Q$  template region extracted from  $F_2(j, k)$  whose upper left corner is at the offset coordinate  $(j_t, k_t)$ . Figure 18.3-2

relates the template region to the search area. Clearly,  $U > P$  and  $V > Q$ . The normalized cross correlation function can then be expressed as

$$R(m, n) = \frac{\sum_u \sum_v S(u, v)T(u - m + 1, v - n + 1)}{\left[ \sum_u \sum_v [S(u, v)]^2 \right]^{\frac{1}{2}} \left[ \sum_u \sum_v [T(u - m + 1, v - n + 1)]^2 \right]^{\frac{1}{2}}} \quad (18.3-6)$$

for  $m = 1, 2, \dots, M$  and  $n = 1, 2, \dots, N$  where

$$M = U - P + 1 \quad (18.3-7a)$$

$$N = V - Q + 1 \quad (18.3-7b)$$

The summation limits of Eq. 18.3-6 are

$$m \leq u \leq m + P - 1 \quad (18.3-8a)$$

$$n \leq v \leq n + Q - 1. \quad (18.3-8b)$$

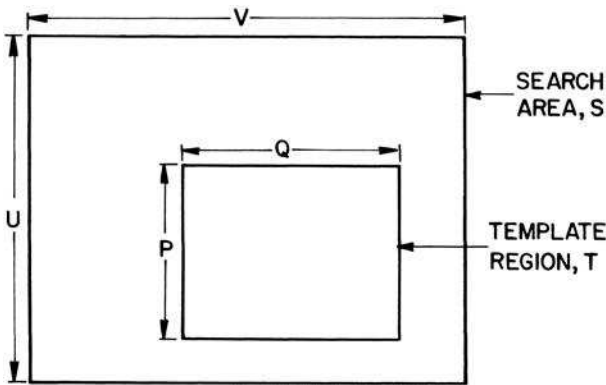


FIGURE 18.3-2. Relationship of template region and search area.

Computation of the numerator of Eq. 18.3-6 is equivalent to raster scanning the template  $T(p, q)$  over the search area  $S(u, v)$  such that the template always resides within  $S(u, v)$ , and then forming the sum of the products of the template and the search area under the template. The left-hand denominator term is the square root of the sum of the terms  $[S(u, v)]^2$  within the search area defined by the template position. The right-hand denominator term is simply the square root of the sum of the template terms  $[T(p, q)]^2$  independent of  $(m, n)$ . It should be recognized that the numerator of Eq. 18.3-6 can be computed by convolution of  $S(u, v)$  with an impulse



response function consisting of the template  $T(p, q)$  spatially rotated by  $180^\circ$ . Similarly, the left-hand term of the denominator can be implemented by convolving the square of  $S(u, v)$  with a  $P \times Q$  uniform impulse response function. For large templates, it may be more computationally efficient to perform the convolutions indirectly by Fourier domain filtering.

**Statistical Correlation Function.** There are two problems associated with the basic correlation function of Eq. 18.3-2. First, the correlation function may be rather broad, making detection of its peak difficult. Second, image noise may mask the peak correlation. Both problems can be alleviated by extending the correlation function definition to consider the statistical properties of the pair of image arrays.

The statistical correlation function (17) is defined as

$$R_S(m, n) = \frac{\sum_j \sum_k G_1(j, k) G_2(j - m + 1, k - n + 1)}{\left[ \sum_j \sum_k [G_1(j, k)]^2 \right]^{1/2} \left[ \sum_j \sum_k [G_2(j - m + 1, k - n + 1)]^2 \right]^{1/2}} \tag{18.3-9}$$

The arrays  $G_i(j, k)$  are obtained by the convolution operation

$$G_i(j, k) = [F_i(j, k) - \bar{F}_i(j, k)] \otimes D_i(j, k) \tag{18.3-10}$$

where  $\bar{F}_i(j, k)$  is the spatial average of  $F_i(j, k)$  over the correlation window. The impulse response functions  $D_i(j, k)$  are chosen to maximize the peak correlation when the pair of images is in best register. The design problem can be solved by recourse to the theory of matched filtering of discrete arrays developed by Pratt (18).

Computation of the statistical correlation function requires calculation of two sets of eigenvectors and eigenvalues of the covariance matrices of the two images to be registered. If the window area contains  $P \cdot Q$  pixels, the covariance matrices  $\mathbf{K}_1$  and  $\mathbf{K}_2$  will each be  $(P \cdot Q) \times (P \cdot Q)$  matrices. For example, if  $P = Q = 16$ , the covariance matrices  $\mathbf{K}_1$  and  $\mathbf{K}_2$  are each of dimension  $256 \times 256$ . Computation of the eigenvectors and eigenvalues of such large matrices is numerically difficult. However, in special cases, the computation can be simplified appreciably (17). For example, if the images are modeled as separable Markov process sources, and there is no observation noise, the convolution operators of Eq. 18.3-10 reduce to the statistical mask operator

$$\mathbf{D}_i = \frac{1}{(1 + \rho^2)^2} \begin{bmatrix} \rho^2 & -\rho(1 + \rho^2) & \rho^2 \\ -\rho(1 + \rho^2) & (1 + \rho^2)^2 & -\rho(1 + \rho^2) \\ \rho^2 & -\rho(1 + \rho^2) & \rho^2 \end{bmatrix} \tag{18.3-11}$$

where  $\rho$  denotes the adjacent pixel correlation (21). If the images are spatially uncorrelated, then  $\rho = 0$ , and the correlation operation is not required. At the other extreme, if  $\rho = 1$ , then

$$\mathbf{D}_i = \frac{1}{4} \begin{bmatrix} 1 & -2 & 1 \\ -2 & 4 & -2 \\ 1 & -2 & 1 \end{bmatrix} \quad (18.3-12)$$

This operator is an orthonormally scaled version of the cross second derivative spot detection operator of Eq. 14.7-3. In general, when an image is highly spatially correlated, the statistical correlation operators  $\mathbf{D}_i$  produce outputs that are large in magnitude only in regions of an image for which its amplitude changes significantly in both coordinate directions simultaneously.

Figure 18.3-3 provides computer simulation results of the performance of the statistical correlation measure for registration of the toy tank image of Figure 16.1-6b. In the simulation, the reference image  $F_1(j, k)$  has been spatially offset horizontally by three pixels and vertically by four pixels to produce the translated image  $F_2(j, k)$ . The pair of images has then been correlated in a window area of  $16 \times 16$  pixels over a search area of  $32 \times 32$  pixels. The curves in Figure 18.3-3 represent the normalized statistical correlation measure taken through the peak of the correlation function. It should be noted that for  $\rho = 0$ , corresponding to the basic correlation measure, it is relatively difficult to distinguish the peak of  $R_S(m, n)$ . For  $\rho = 0.9$  or greater,  $R(m, n)$  peaks sharply at the correct point.

The correlation function methods of translation offset detection defined by Eqs. 18.3-2 and 18.3-9 are capable of estimating any translation offset to an accuracy of  $\pm 1/2$  pixel. It is possible to improve the accuracy of these methods to subpixel levels by interpolation techniques (22). One approach (23) is to spatially interpolate the correlation function and then search for the peak of the interpolated correlation function. Another approach is to spatially interpolate each of the pair of images and then correlate the higher-resolution pair.

A common criticism of the correlation function method of image registration is the great amount of computation that must be performed if the template region and the search areas are large. Several computational methods that attempt to overcome this problem are presented next.

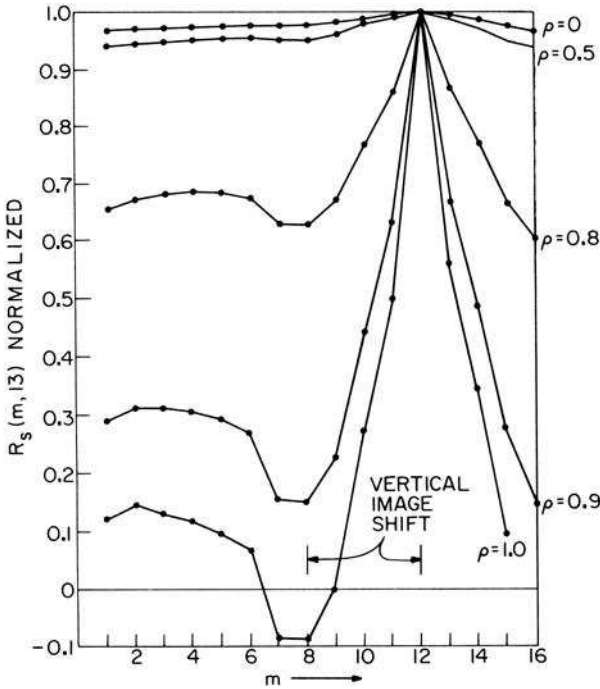


FIGURE 18.3-3. Statistical correlation misregistration detection.

**Two-State Methods.** Rosenfeld and Vandenburg (24,25) have proposed two efficient two-stage methods of translation offset detection. In one of the methods, called *coarse-fine matching*, each of the pair of images is reduced in resolution by conventional techniques (low-pass filtering followed by subsampling) to produce coarse representations of the images. Then the coarse images are correlated and the resulting correlation peak is determined. The correlation peak provides a rough estimate of the translation offset, which is then used to define a spatially restricted search area for correlation at the fine resolution of the original image pair. The other method, suggested by Vandenburg and Rosenfeld (25), is to use a subset of the pixels within the window area to compute the correlation function in the first stage of the two-stage process. This can be accomplished by restricting the size of the window area or by performing subsampling of the images within the window area. Goshtasby et al. (26) have proposed random rather than deterministic subsampling. The second stage of the process is the same as that of the coarse-fine method; correlation is performed over the full window at fine resolution. Two-stage methods can provide a significant reduction in computation, but they can produce false results.

**Sequential Search Method.** With the correlation measure techniques, no decision can be made until the correlation array is computed for all  $(m, n)$  elements. Furthermore, the amount of computation of the correlation array is the same for all degrees of misregistration. These deficiencies of the standard correlation measures have led to the search for efficient sequential search algorithms.

An efficient sequential search method has been proposed by Barnea and Silverman (27). The basic form of this algorithm is deceptively simple. The absolute value difference error

$$\varepsilon_S = \sum_i \sum_k |F_1(j, k) - F_2(j - m, k - n)| \tag{18.3-13}$$

is accumulated for pixel values in a window area. If the error exceeds a predetermined threshold value before all  $P \cdot Q$  pixels in the window area are examined, it is assumed that the test has failed for the particular offset  $(m, n)$ , and a new offset is checked. If the error grows slowly, the number of pixels examined when the threshold is finally exceeded is recorded as a rating of the test offset. Eventually, when all test offsets have been examined, the offset with the largest rating is assumed to be the proper misregistration offset.

**Phase Correlation Method.** Consider a pair of continuous domain images

$$F_2(x, y) = F_1(x - x_o, y - y_o) \tag{18.3-14}$$

that are translated by an offset  $(x_o, y_o)$  with respect to one another. By the Fourier transform shift property of Eq. 1.3-13a, the Fourier transforms of the images are related by

$$\mathcal{F}_2(\omega_x, \omega_y) = \mathcal{F}_1(\omega_x, \omega_y) \exp\{-i(\omega_x x_o + \omega_y y_o)\}. \tag{18.3-15}$$

The exponential phase shift factor can be computed by the *cross-power spectrum* (28) of the two images as given by

$$\mathcal{G}(\omega_x, \omega_y) \equiv \frac{\mathcal{F}_1(\omega_x, \omega_y) \mathcal{F}_2^*(\omega_x, \omega_y)}{|\mathcal{F}_1(\omega_x, \omega_y) \mathcal{F}_2(\omega_x, \omega_y)|} = \exp\{i(\omega_x x_o + \omega_y y_o)\}. \tag{18.3-16}$$

Taking the inverse Fourier transform of Eq. 18.3-16 yields the spatial offset in the space domain.

$$G(x, y) = \delta(x - x_o, y - y_o). \tag{18.3-17}$$

The cross-power spectrum approach can be applied to discrete images by utilizing discrete Fourier transforms in place of the continuous Fourier transforms in Eq. 18.3-16. However, care must be taken to prevent wraparound error. Figure 18.3-4 presents an example of translational misregistration detection using the phase correlation method. Figure 18.3-4a and b show translated portions of a scene embedded

in a zero background. The scene in Figure 18.3-4a was obtained by extracting the first 480 rows and columns of the  $500 \times 500$  `washington_ir` source image. The scene in Figure 18.3-4b consists of the last 480 rows and columns of the source image. Figure 18.4-4c and *d* are the logarithm magnitudes of the Fourier transforms of the two images, and Figure 18.3-4e is the inverse Fourier transform of the cross-power spectrum of the pair of images. The white pixel in the upper left corner of Figure 18.3-4e, located at coordinate (20,20), is the correlation peak.

**18.3.2. Scale and Rotation Misregistration Detection**

The phase correlation method for translational misregistration detection has been extended to scale and rotation misregistration detection (28,29). Consider a pair of images in which a second image is translated by an offset  $(x_o, y_o)$  and rotated by an angle  $\theta_o$  with respect to the first image. Then,

$$F_2(x, y) = F_1(x \cos \theta_o + y \sin \theta_o - x_o, -x \sin \theta_o + y \cos \theta_o - y_o). \quad (18.3-18)$$

Taking Fourier transforms of both sides of Eq. 18.3-18, one obtains the relationship (28)

$$\mathcal{F}_2(\omega_x, \omega_y) = \mathcal{F}_1(\omega_x \cos \theta_o + \omega_y \sin \theta_o, -\omega_x \sin \theta_o + \omega_y \cos \theta_o) \exp\{-i(\omega_x x_o + \omega_y y_o)\}. \quad (18.3-19)$$

The rotation component can be isolated by taking the magnitudes  $\mathcal{M}_1(\omega_x, \omega_y)$  and  $\mathcal{M}_2(\omega_x, \omega_y)$  of both sides of Eq. 18.3-15. By representing the frequency variables in polar form,

$$\mathcal{M}_2(\rho, \theta) = \mathcal{M}_1(\rho, \theta - \theta_o) \quad (18.3-20)$$

the phase correlation method can be used to determine the rotation angle  $\theta_o$ .

If a second image is a size-scaled version of a first image with scale factors  $(a, b)$ , then from the Fourier transform scaling property of Eq. 1.3-12,

$$\mathcal{F}_2(\omega_x, \omega_y) = \frac{1}{|ab|} \mathcal{F}_1\left(\frac{\omega_x}{a}, \frac{\omega_y}{b}\right). \quad (18.3-21)$$

By converting the frequency variables to a logarithmic scale, scaling can be converted to a translational movement. Then

$$\mathcal{F}_2(\log \omega_x, \log \omega_y) = \frac{1}{|ab|} \mathcal{F}_1(\log \omega_x - \log a, \log \omega_y - \log b). \quad (18.3-22)$$

Now, the phase correlation method can be applied to determine the unknown scale factors  $(a,b)$ .

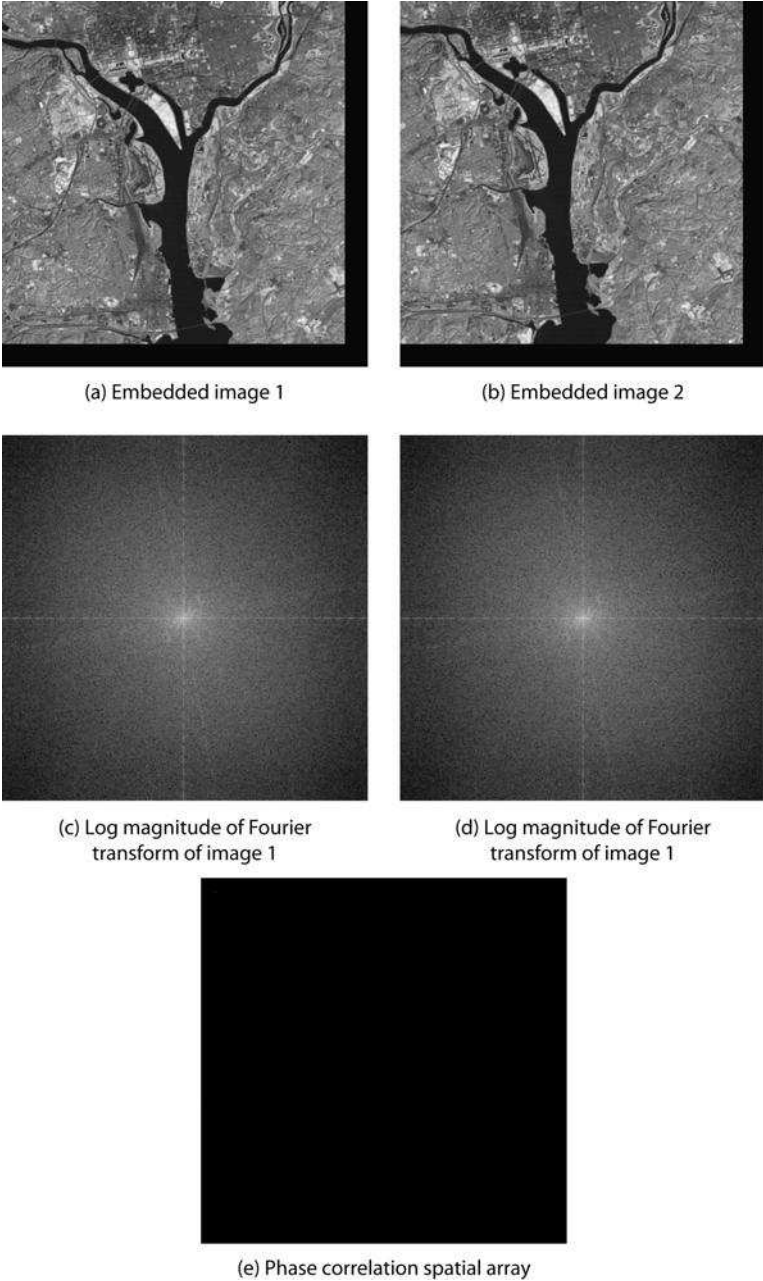


**FIGURE 18.3-4.** Translational misregistration detection on the `washington_ir1` and `washington_ir2` images using the phase correlation method. There is a dim white pixel in the upper left corner of (e).

**18.4. IMAGE DETECTION AND REGISTRATION EXERCISES**

E18.1 Develop a program that performs normalized cross-correlation template matching of the monochrome source image `L_source` and the monochrome template image `L_template` using the convolution operator as a means of correlation array computation. Steps:

- (a) Display the source image.
- (b) Display the template image.
- (c) Rotate the template image 180 degrees and convert it to an impulse response array.
- (d) Convolve the source image with the impulse response array to form the numerator of the cross-correlation array.
- (e) Display the numerator image.
- (f) Square the source image and compute its moving window average energy by convolution with a rectangular impulse response array to form the denominator of the cross-correlation array.
- (g) Display the denominator image.
- (h) Form the cross-correlation array image.
- (i) Display the cross-correlation array image.
- (j) Threshold the cross-correlation array image.
- (k) Display the thresholded cross-correlation array image.

Note, it is necessary to properly scale the source and template images to obtain valid results. The PIKS API executable `example_template` performs this exercise.

E18.2 Develop a program that executes the cross-correlation operator on the monochrome source image `washington_ir1` and the monochrome source image `washington_ir2` using the cross-correlation operator. Steps:

- (a) Display the first source image.
- (b) Display the second source image.
- (c) Execute the cross-correlation operator.
- (d) Convert the cross-correlation to a destination image.
- (e) Display the destination image.

The PIKS API executable `example_cross_correlation` performs this exercise.

## REFERENCES

1. R. O. Duda and P. E. Hart, *Pattern Classification and Scene Analysis*, Wiley-Interscience, New York, 1973.
2. W. H. Highleyman, "An Analog Method for Character Recognition," *IRE Trans. Electronic Computers*, EC-10, 3, September 1961, 502–510.
3. L. N. Kanal and N. C. Randall, "Recognition System Design by Statistical Analysis," *Proc. ACM National Conference*, 1964.
4. J. H. Munson, "Experiments in the Recognition of Hand-Printed Text, I. Character Recognition," *Proc. Fall Joint Computer Conference*, December 1968, 1125–1138.
5. A. Rosenfeld, *Picture Processing by Computer*, Academic Press, New York, 1969.
6. R. N. Nagel and A. Rosenfeld, "Ordered Search Techniques in Template Matching," *Proc. IEEE*, February 1972, 242–244.
7. M. J. Atallah, "Faster Image Template Matching in the Sum of the Absolute Value of Difference Measure," *IRE Trans. Image Processing*, 10, 4, April 2001, 659–663.
8. G. L. Turin, "An Introduction to Matched Filters," *IRE Trans. Information Theory*, IT-6, 3, June 1960, 311–329.
9. C. E. Cook and M. Bernfeld, *Radar Signals*, Academic Press, New York, 1965.
10. J. B. Thomas, *An Introduction to Statistical Communication Theory*, John Wiley and Sons, New York, 1965, 187–218.
11. H. C. Andrews, *Computer Techniques in Image Processing*, Academic Press, New York, 1970, 55–71.
12. L. J. Cutrona, E. N. Leith, C. J. Palermo and L. J. Porcello, "Optical Data Processing and Filtering Systems," *IRE Trans. Information Theory*, IT-6, 3, June 1960, 386–400.
13. A. Vander Lugt, F. B. Rotz and A. Kloester, Jr., "Character-Reading by Optical Spatial Filtering," in *Optical and Electro-Optical Information Processing*, J. Tippett et al., Eds., MIT Press, Cambridge, MA, 1965, 125–141.
14. A. Vander Lugt, "Signal Detection by Complex Spatial Filtering," *IEEE Trans. Information Theory*, IT-10, 2, April 1964, 139–145.
15. A. Kozma and D. L. Kelly, "Spatial Filtering for Detection of Signals Submerged in Noise," *Applied Optics*, 4, 4, April 1965, 387–392.
16. A. Arcese, P. H. Mengert and E. W. Trombini, "Image Detection Through Bipolar Correlation," *IEEE Trans. Information Theory*, IT-16, 5, September 1970, 534–541.
17. W. K. Pratt, "Correlation Techniques of Image Registration," *IEEE Trans. Aerospace and Electronic Systems*, AES-10, 3, May 1974, 353–358.
18. W. K. Pratt, *Digital Image Processing, Fourth Edition*, Wiley-Interscience, New York.
19. W. Meyer-Eppler and G. Darius, "Two-Dimensional Photographic Autocorrelation of Pictures and Alphabet Letters," *Proc. 3rd London Symposium on Information Theory*, C. Cherry, Ed., Academic Press, New York, 1956, 34–36.
20. P. F. Anuta, "Digital Registration of Multispectral Video Imagery," *SPIE J.*, 7, September 1969, 168–178.
21. J. M. S. Prewitt, "Object Enhancement and Extraction," in *Picture Processing and Psychopictorics*, B. S. Lipkin and A. Rosenfeld, Eds., Academic Press, New York, 1970.
22. Q. Tian and M. N. Huhns, "Algorithms for Subpixel Registration," *Computer Graphics, Vision and Image Processing*, 35, 2, August 1986, 220–233.



23. P. F. Anuta, "Spatial Registration of Multispectral and Multitemporal Imagery Using Fast Fourier Transform Techniques," *IEEE Trans. Geoscience and Electronics*, **GE-8**, 1970, 353–368.
24. A. Rosenfeld and G. J. Vandenburg, "Coarse–Fine Template Matching," *IEEE Trans. Systems, Man and Cybernetics*, **SMC-2**, February 1977, 104–107.
25. G. J. Vandenburg and A. Rosenfeld, "Two-Stage Template Matching," *IEEE Trans. Computers*, **C-26**, 4, April 1977, 384–393.
26. A. Goshtasby, S. H. Gage and J. F. Bartolic, "A Two-Stage Cross-Correlation Approach to Template Matching," *IEEE Trans. Pattern Analysis and Machine Intelligence*, **PAMI-6**, 3, May 1984, 374–378.
27. D. I. Barnea and H. F. Silverman, "A Class of Algorithms for Fast Image Registration," *IEEE Trans. Computers*, **C-21**, 2, February 1972, 179–186.
28. B. S. Reddy and B. N. Chatterji, "An FFT-Based Technique for Translation, Rotation and Scale-Invariant Image Registration," *IEEE Trans. Image Processing*, **IP-5**, 8, August 1996, 1266–1271.
29. E. De Castro and C. Morandi, "Registration of Translated and Rotated Images Using Finite Fourier Transforms," *IEEE Trans. Pattern Analysis and Machine Intelligence*, **PAMI-9**, 5, September 1987, 700–703.

## **PART 6**

---

# **IMAGE AND VIDEO COMPRESSION**

During the past fifty years there have been significant, and largely successful, efforts toward the development of efficient digital still image and video coding systems. The design objective of these, so called, compression systems, generally, has been the representation of images with acceptable fidelity and as small a number of coded bits as possible. For still images, reducing the number of coded bits permits more compact image storage. For video, bit rate reduction allows video image frames to be transmitted faster and permits more parallel channels to be transmitted over a communication link.

Chapters 19 and 20 provide descriptions of still image compression methods including the JPEG standards, while Chapter 21 describes video compression systems including the MPEG family of video compression standards. Appendix 3 provides a summary of the capability of the JPEG and MPEG standards and their development history.



---

# 19

---

## POINT PROCESSING IMAGE COMPRESSION

This chapter covers still image compression using coding methods for monochrome and color images, which are based upon point processing. In the early days of still image coding research, techniques were limited to point processing because of implementation restrictions. As will be seen, point processing by itself does not provide significant bit rate compression. However, these techniques have been proven to be important sub systems for spatial processing methods to be discussed in the following chapters. References 1 to 8 provide useful historical background information on the subject of image and video data compression.

### 19.1. PULSE CODE MODULATION CODING OF MONOCHROME IMAGES

In a basic pulse code modulation (PCM) image coding system, a continuous amplitude image signal is sampled and quantized. Each quantized sample is then assigned a constant-length group of bits, called a code word. A bit rate reduction can be achieved by reducing the number of quantization levels. For an imaging system whose quality is assessed by some analytic measure, the number of quantization levels is taken as the smallest value that satisfies the measure of image quality. The number of quantization levels must be kept large enough to prevent a noticeable gray scale contouring effect caused by a jump in the reconstructed image luminance between quantization levels in a region where the original image is slowly changing in amplitude. For monochrome images, 50 or more levels are usually required to

prevent noticeable gray scale contouring. Consequentially, in a PCM image coder, the image luminance is usually quantized from 64 to 256 levels corresponding to a 6 to 8 bit per pixel code (9-11).

## 19.2. STATISTICAL CODING OF MONOCHROME IMAGES

Statistical measurements of the pixel amplitude distribution of digital images indicates that natural images contain a large amount of redundancy. In this context, redundancy can be defined as the total number of PCM code bits minus the theoretical coding limit, called the *entropy*, of the coding process.

### 19.2.1. Single Pixel Coding.

The simplest type of statistical coder is one in which each pixel is individually assigned a code group from a code book based upon its quantized amplitude. For efficient coding, the code assignment should be such that pixel values with a high likelihood of occurrence should be assigned code groups with a small number of bits. Conversely, rarely occurring pixel values should be assigned longer code groups. If this process is performed efficiently, the average length of a code group will be equal to the single pixel entropy of the image.

As a starting point for the code development, it is necessary to model, estimate or measure the probability of occurrence of each pixel value for the class of images to be encoded. Suppose that the probability that a quantized pixel amplitude is equal to the  $i$ th reconstruction level  $r_i$  is given by

$$p_i = Pr\{F(j, k) = r_i\}. \quad (19.2-1)$$

In the coding process, a code word of  $b_i$  bits is assigned to each quantized level resulting in an *average code length*

$$L_c = \sum_{i=0}^{Q-1} p_i b_i \quad (19.2-2)$$

for  $Q$  quantization levels. The single pixel entropy is defined as

$$H = - \sum_{i=0}^{Q-1} p_i \log_2(p_i) \quad (19.2-3)$$

where the logarithm is taken to the base of 2.

Huffman (12) has developed a coding method, which results in a minimal length code book for a given set of symbol probabilities. Table 19.2-1 provides a compari-

son between PCM coding and Huffman coding for 8-level gray scale quantization. Appendix 4 describes the generation of this code book. The average code length for this example is  $L_c = 2.70$  and the entropy for the probability set is  $H = 2.68$ .

**Table 19.2-1. Comparison of PCM and Huffman codes**

Amplitude Index	Probability	PCM code	Huffman code
0	0.20	000	00
1	0.20	001	10
2	0.25	010	01
3	0.15	011	011
4	0.10	100	0111
5	0.05	101	01111
6	0.03	110	011111
7	0.02	111	111111

In general, Huffman codes are variable in length. Thus, it becomes necessary to provide data buffer storage to collect the variable bit rate code bits and transmit or store them at some slower average rate. There is another problem associated with the use of statistical source codes. The codes are matched to an assumed set of source probabilities. If the actual source probabilities differ from the assumed source probabilities, the coder performance can be degraded drastically. In fact, a mismatched coder can result in an increased bit requirement compared to PCM coding.

For typical natural monochrome images, the single pixel entropy ranges from about 5 to 7 bits per pixel. This relatively small amount of redundancy compared to PCM coding is seldom worth the penalty of increased implementation requirements.

**19.2.2 Previous Pixel Coding.**

Because adjacent pixels along an image row are highly correlated in natural images, there is a high degree of redundancy between pixel pairs along an image row. A statistical coder to take advantage of the previous pixel redundancy is simple in principle. For each of the  $Q$  quantized levels of a previous pixel, there is an associated conditional probability distribution  $P(j|k)$  and a corresponding code word. Thus, in operation, the coder selects one of  $Q^2$  codes. For 256 quantization levels, the code book would contain 65,536 entries.

A simpler variant of previous pixel coding is to code the differences in pixel values after the first pixel along a row (13,14). If each pixel is quantized to  $Q$  levels, then the pixel difference may assume  $2Q - 1$  values. Because the probability of occurrence of large differences is relatively small, it is possible to simplify the coder considerably without a great loss in performance. The coding strategy is as follows: small differences receive individual code words; if the difference exceeds some specified level, the actual pixel value is coded and appended to a prefix code that distinguishes the total code word from the coded differences. Table 19.21-2 illustrates a pixel difference code book.

**Table 19.2-2. Example of pixel difference coding**

Difference, $D$	Code
0	1
+1	0100
-1	0101
+2	0110
-2	0111
+3	00100
-3	00101
+4	00110
-4	00111
$ D  \Rightarrow 5$	0000 + 8 bit pixel

**19.3. PREDICTIVE CODING OF MONOCHROME IMAGES**

In a predictive coding system, as shown in Figure 19.3-1, the value of each raster scanned pixel is predicted based upon some previous history of scanned pixels. Then, the predicted estimate is subtracted from the present pixel value. The difference signal is then quantized and coded. At the decoder, the quantized difference signal is used to form a reconstruction of the image. A bandwidth reduction is possible by coarsely quantizing the difference signal.

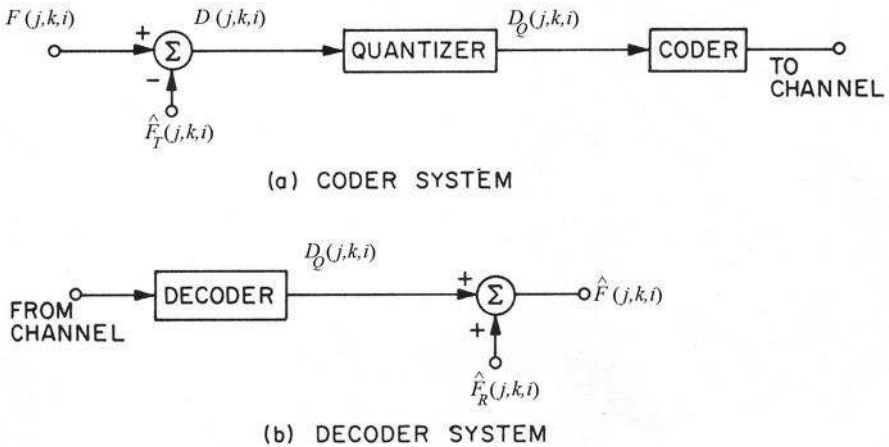


FIGURE 19.3-1. Predictive image coding system.

### 19.3.1 Differential Pulse Code Modulation Coding

The general concept of linear predictive coding has developed from an invention by Cutler (13) of the differential pulse code modulation (DPCM) system. In Cutler's original 1952 patent, it was proposed that integrators be employed to predict the present sample based upon the previous sample value along a scan line, and that the difference between the present sample and its estimate be quantized and coded for transmission or storage.

Figure 19.3-2 contains a block diagram of a DPCM image coding system. In such a system, the continuous image signal is sampled, and the difference between an actual pixel and its estimate is quantized and coded for transmission or storage. Usually the difference signal is quantized to eight levels and coded with a three bit code (14,15). Thus the bandwidth reduction is from the 6 to 8 bits per pixel of conventional PCM to 3 bits per pixel for DPCM. In a basic DPCM coder, the prediction is based upon the quantized difference signal of the previously scanned pixel along an image row. At the decoder, the decoded difference is reconstructed and combined with an estimate from a predictor identical to the one at the coder to provide a reconstruction of the source image.



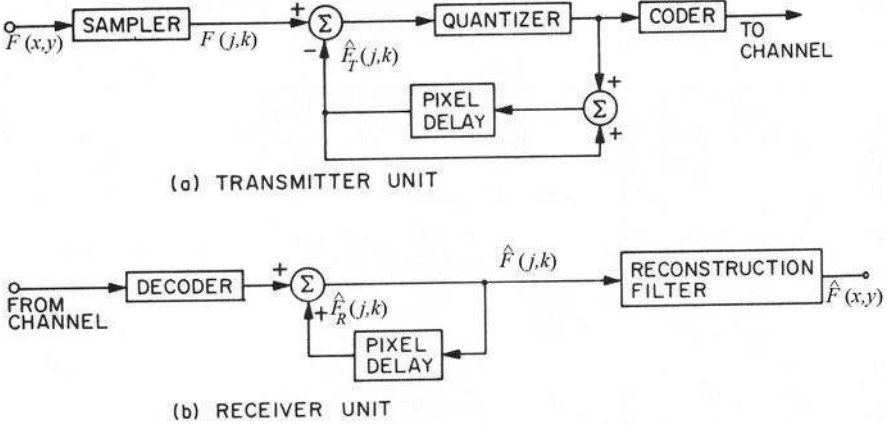
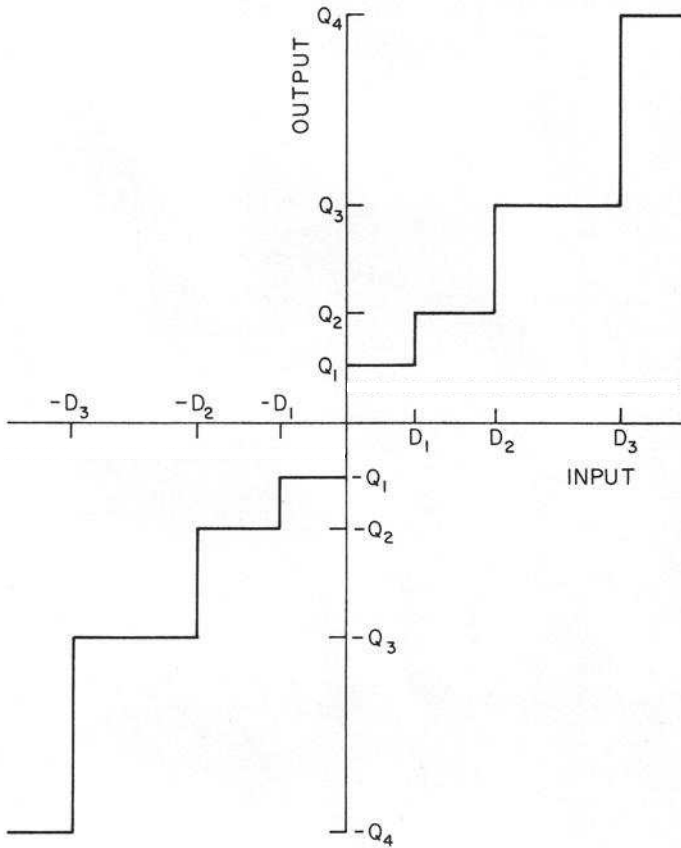


FIGURE 19.3-2. DPCM image coding system

In 1958, Graham (16) proposed the use of a tapered quantizer scale in which the quantization levels are placed nonlinearly as shown in Figure 19.4-3. With a tapered quantizer, the subjective quality of the reconstructed image is improved substantially. However, in most applications, it has been found that at least eight quantization levels are still required.

Harrison (17), in 1952, extended the basic DPCM concept by forming the prediction signal from a linear combination of several previously scanned pixels along a row and from previous rows. Both theoretical and experimental studies have found that the mean square error measure subjective quality can be improved by utilizing more information in the prediction (18,19). Figure 19.3-4 contains a generalized block diagram for a spatial predictive coding system. A standard DPCM coder, which utilizes the previously scanned pixel ( $S_1$ ) along an image row as the basis of its prediction of  $S_0$  is often referred to as a first-order predictor. Following this nomenclature, a second-order predictor would utilize the two previously scanned pixels along a row ( $S_1$  and  $S_2$ ) or perhaps the previous pixel along the row ( $S_1$ ) and the nearest pixel from the previous row ( $S_2$ ). A third order predictor might employ ( $S_1, S_2, S_4$ ) as the basis for its prediction. Pixel  $S_6$  is often used for prediction because  $S_6$  provides a good indication of vertical edge structure.



**FIGURE 19.3-3.** Tapered DPCM quantizer scale.

Pratt (20) has developed a design procedure for linear predictive image coders. This procedure concludes, not surprisingly, that the neighboring pixel values used in the prediction should have the highest correlation with the pixel to be predicted. Also, it was found that the prediction difference variance diminishes rapidly beyond a third-order prediction system.

**19.4. POINT PROCESSING COLOR IMAGE CODING**

The point processing image coding techniques previously described for monochrome images can be applied individually to the red, green and blue components of a color image. This straight forward approach results in a coding rate that is three times that of a monochrome image. It is possible to perform a point-wise linear or

nonlinear transformation of a color image to a colorimetric color space such as  $L^*a^*b^*$  or to a video color space such as  $YIQ$ , as defined in Chapter 3. Experiments (21-23) indicate that the chromaticity or chrominance color components can be more coarsely quantized than the luminance or luma color components. This results in a somewhat lower coding rate than  $RGB$  coding. However, in order to exploit the spatial frequency limitations of human vision, it is necessary to perform spatial processing forms of image coding, as described in the next chapter.

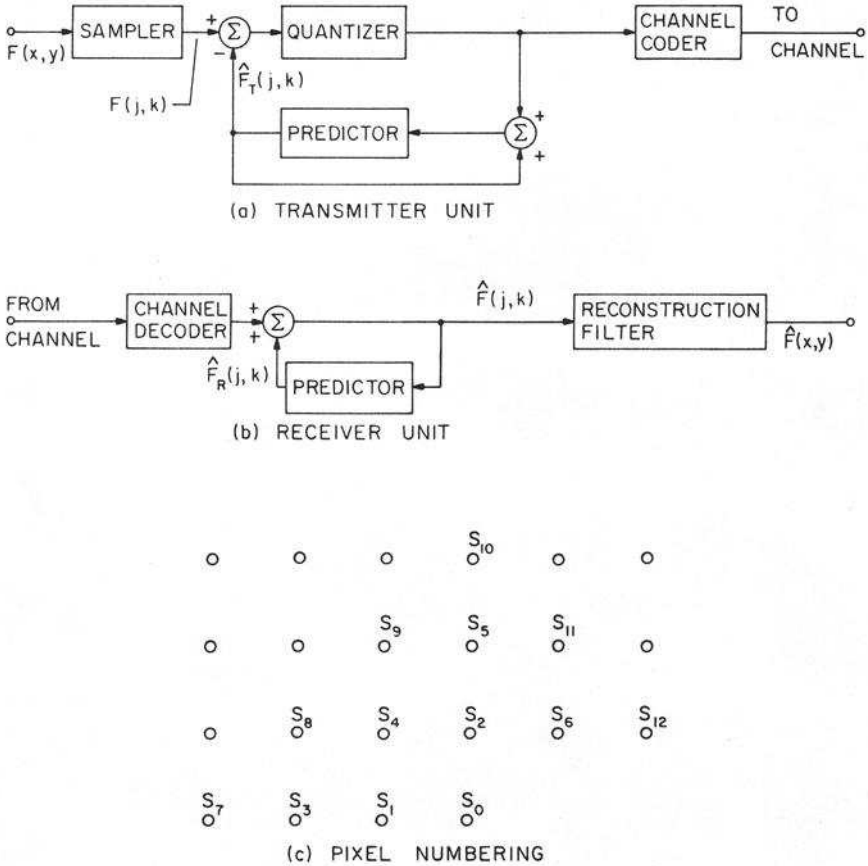


FIGURE 19.3-4. Spatial predictive image coding system.

19.5. JPEG LOSSLESS IMAGE CODING

As described in Appendix 3, the JPEG still image coding standard supports four operational modes, one of which is a point processing lossless image coder (24, 25).

In this context, lossless image coding means, quite simply, that the image to be coded and the resultant image reconstruction are identical at the bit level.

Figure 19.4-1 is a simplified block diagram of the JPEG lossless encoder. In operation, a pixel  $F(j, k)$  enters a predictor element, which produces a prediction of the present scanned pixel based upon the previously predicted pixels  $A$ ,  $B$  and  $C$ , as shown below.

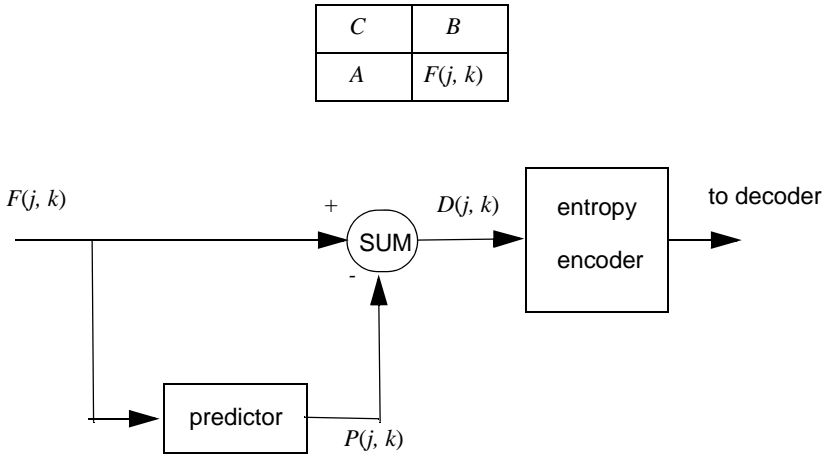


**FIGURE 19.4-1.** JPEG lossless image encoder.

A prediction difference  $D(j, k)$  is formed between  $F(j, k)$  and its predicted value  $P(j, k)$ , which enters an entropy encoder. Huffman and arithmetic encoders (25) are supported by the standard. JPEG lossless supports seven prediction rules, as defined in Table 19.4-1. The prediction rule is sent to the decoder in a session header.

**TABLE 19.4-1. Prediction Options**

Option	Prediction Rule
1	$A$
2	$B$
3	$C$
4	$A + B - C$
5	$A + (B - C)/2$
6	$B + (A - C)/2$
7	$(A + B)/2$

The JPEG lossless standard accommodates source pixel values in the precision range of 2 to 16 bits. In the standard, arithmetic operations are of 16-bit precision such that the reconstructed image has the same amplitude value as the source image i.e. no computational errors occur. Direct entropy coding of  $D(j, k)$  at full arithmetic precision would require an extremely large entropy code table. The JPEG lossless standard has adopted a clever code assignment procedure. The code table is divided into 17 categories, called SSSS in the standard document. As shown in Table 19.4-2, each category provides a pointer to a nested set of difference values. For example, category 3 specifies the set of prediction difference code symbols values:

$$-7, -6, -5, -4, +4, +5, +6, +7$$

one of which is selected for encoding. The category values are encoded by an arithmetic or Huffman encoder. The difference value of the category is binary encoded and appended to the category code.

On typical gray scale images, the JPEG lossless coder achieves about a 2:1 compression ratio compared to PCM coding. In comparison, the JPEG baseline lossy algorithm discussed in the next chapter provides about a 20:1 compression ratio (25, p. 78).

## 19.6. POINT PROCESSING IMAGE COMPRESSION EXERCISES

E19.1 Develop a program that generates the Huffman code book for a set of eight symbols. See Appendix 4. Steps:

- (a) Read a user generated set of symbol probabilities.
- (b) Compute the Huffman code word corresponding to each symbol using the code tree algorithm of Appendix 4.
- (c) Print the Huffman code table.
- (d) Compute the code book average code length and entropy.

The PIKS API executable `example_huffman_code_table` performs this exercise for the example of Appendix 4.

E19.2 Develop a program that computes the entropy of the `lena_mon` image. Steps:

- (a) Display the source image.
- (b) Compute the histogram of the source image.
- (c) Estimate the grey level probabilities for an eight-level re-quantization of the source image based upon its histogram.
- (d) Compute the entropy of the re-quantized source image.

The PIKS API executable `example_lena_entropy` performs this exercise.

E19.3 Develop a program that emulates the DPCM image coding system of Figure 19.3-2 using an 8 level tapered quantizer implemented by a lookup table. Process the `lena_mon` image with the emulated coding system. Steps:

- (a) Display the source image.
- (b) Generate the quantizer lookup table with decision levels of: 0, 8, 16 and 32 and quantization levels of: 4, 12, 24 and 48.
- (c) Create the destination image with the emulator.
- (d) Display the destination image.

The PIKS API executable `example_DPCM` performs this exercise.

**TABLE 19.4-2. JPEG lossless coding difference symbol codes**

SSSS	$D(j,k)$					
0	0					
1	-1	1				
2	-3	-2	2	3		
3	-7	.....	-4	4	.....	7
4	-15	.....	-8	8	.....	15
5	-31	.....	-16	16	.....	31
6	-63	.....	-32	32	.....	63
7	-127	.....	-64	64	.....	127
8	-255	.....	-128	128	.....	255
9	-511	.....	-256	256	.....	511
10	-1023	.....	-512	512	.....	1023
11	-2047	.....	-1024	1024	.....	2047
12	-4095	.....	-2048	2048	.....	4095
13	-8191	.....	-4096	4096	.....	8191
14	-16383	.....	-8192	8192	.....	16383
15	-32767	.....	-16384	16384	.....	32767
16	32768					

## REFERENCES

1. T. S. Huang, PCM Picture Transmission, *IEEE Spectrum*, **2**, 2, December 1965, 57-60.
2. Special Issue on Redundancy Reduction, *Proc. IEEE*, **55**, 3, March 1967.
3. T. S. Huang, W. F. Schreiber and O. J. Tretiak, "Image Processing," *Proc. IEEE*, **59**, 11, November 1971, 1586-1609.
4. Special Issue on Signal Processing for Digital Communications, *IEEE Trans. Communications Technology*, **COM-19**, 6, Part 1, December 1971.
5. Special Issue on Digital Picture Processing, *Proc. IEEE*, **60**, 7, July 1972.
6. T. S. Huang and O. J. Tretiak, Eds., *Picture Bandwidth Compression*, Gordon and Breach, New York, 1972.
7. A. Habibi and G. S. Robinson, "A Survey of Digital Picture Coding," *IEEE Computer*, **7**, 5, May 1974, 21-34.
8. R. Forchheimer, "Video Coding Past, Present and Future," *Picture Coding Symposium Record*, May 2009, Chicago.
9. W. M. Goodall, "Video Transmission by Pulse Code Modulation." *Bell Systems Technical Journal*, **30**, January 1951, 33-49.
10. R. L. Cabrey, "Video Transmission over Telephone Cable Pairs by Pulse Code Modulation," *Proc. IEEE*, **48**, 9, September 1960, 1546-1561.
11. L. H. Harper, "PCM Picture Transmissions," *IEEE Spectrum*, **3**, June 1966, 146.
11. F. Kretz, "Subjectively Optimal Quantization of Pictures," *IEEE Trans. Communications*, **COM-23**, 11, November 1975, 1288-1292.
12. D. A. Huffman, "A Method for the Construction of Minimum-Redundancy Codes," *Proc. IRE*, **40**, 9, September 1952, 1098-1101.
13. C. C. Cutler, "Differential Quantization of Communication Signals," U. S. Patent 2,605,361, July 1952.
14. J. B. Millard and H. I. Maunsell, "Digital Encoding of Video Signals," *Bell Systems Technical Journal*, **50**, 2, February 1971, 459-479.
15. R. P. Abbott, "A Differential Pulse-Code-Modulation Coder for Videotelephony Using Four Bits per Sample," *IEEE Trans. Communications Technology*, **COM-19**, 6, December 1971, 907-913.
16. R. E. Graham, "Predictive Quantizing of Television Signals," *IRE WESCON Convention Record*, Part 4, 1958, 142-157.
17. C. W. Harrison, "Experiments with Linear Prediction in Television," *Bell Systems Technical Journal*, **31**, 4, July 1952, 746-783.
18. J. B. O'Neal, "Predictive Quantizing Systems (Differential Pulse Code Modulation) for the Transmission of Television Signals," *Bell Systems Technical Journal*, **45**, 5, May-June 1966, 689-721.
19. D. J. Connor, R. F. W. Pease and W. G. Scholes, "Television Coding Using Two-Dimensional Spatial Prediction," *Bell Systems Technical Journal*, **50**, March 1971, 1049-1063.
20. W. K. Pratt, *Digital Image Processing*, John Wiley and Sons, New York, 1978, 650-657.
21. A. K. Bhushan, "Transmission and Coding of Color Pictures," in *Picture Bandwidth Compression*, T. S. Huang and O. J. Tretiak, Eds., Gordon and Breach, New York, 1972, 697-725.

22. J. O. Limb, C. B. Rubenstein and K. A. Walsh, "Digital Coding of Color Picturephone Signals by Element-Differential Quantization," *IEEE Trans. Communications technology*, **COM-19**, 6, December 1971, 992-1006.
23. A. Habibi, "Deltamodulation and DPCM Coding of Color Signals," *Proc. International Telemetering Conference*, Los Angeles, Vol. 8, October 197, 333-343.
24. ISO/IEC JTC1 1098-1 Rec. T.81, *Information Technology - Digital Compression and Coding of Continuous-Tone Still Images: Requirements and Guidelines*, 1994.
25. W. B. Pennebaker and J. L. Mitchell, *JPEG Still Image Data Compression Standard*, Nostrand Reinhold, New York, 1993.
26. R. B. Arps, "Binary Image Compression," W. K. Pratt, Ed., *Image Transmission Techniques*, Academic Press, New York, 1979, 219-276.





---

# 20

---

## SPATIAL PROCESSING IMAGE COMPRESSION

This chapter covers still image compression using coding methods for monochrome and color images, which are based upon spatial processing of image bands. The chapter also describes two international standards for still image compression: the JPEG baseline coding system based upon the Discrete Cosine Transform (DCT) and the JPEG 2000 coding system based upon wavelet coding.

### 20.1. RUN CODING OF MONOCHROME IMAGES

*Run coding* (1-8) is a relatively simple coding technique in which the amplitudes of adjacent pixels along an image row are compared. If a significant change in amplitude (an edge) occurs, a run is said to exist. Either a function of the amplitude of the pixel at the end of the run, or a function of the amplitude of the difference of adjacent pixels is coded along with an indication of the location of the run end. If the location of the end of a run is determined by counting the number of pixels from the beginning of the row to the occurrence of the end of the run, the coding system is called *run end coding*. The location of the end of a run can also be specified in terms of the relative distance from the previous end. This coding system is called *run length coding*.

The run end coding system has the disadvantage of requiring a large fixed number of bits to describe each run position. The run length coding system requires shorter groups of bits to specify the position of a run on average. However, the variable length of the position code presents some implementation problems in terms of

long position code words. A variation of the position encoding method is to limit the length of the position code describing the run length to a uniform fixed length. If no natural run ends occur within the maximum run length interval, a “pseudo” run is formed and coded. The pseudo run signifies a run of zero amplitude (i.e. no run end). This technique has the disadvantage of requiring a larger number of runs to code an image. However, a judicious choice of the length of the maximum run length based upon image statistics can minimize the coding system redundancy. Figure 20.1-1 illustrates the theoretical performance of a run length coding system for  $A = 3$  pixel amplitude bits and a pseudo run length of  $M$  pixels (7).

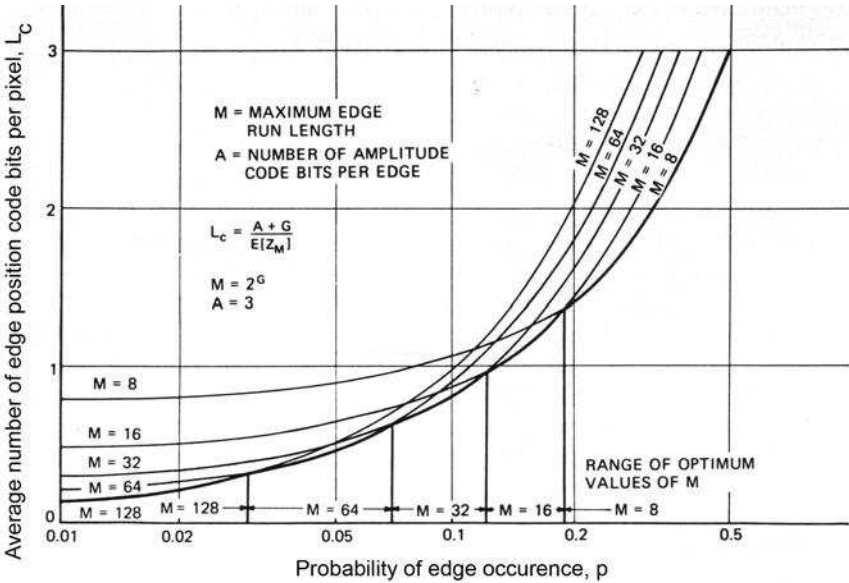


**FIGURE 20.1-1.** Theoretical run length coding performance for a monochrome image.

Run length coding is most practical for images with few gray scales. For black or white facsimile images, it is only necessary to code the changes in amplitude level after the first pixel along an image row is coded. Compression ratios of about 8:1 have been achieved for facsimile images (9). For monochrome images, the compromise between gray scale fidelity and coding performance is not favorable compared to alternate coding methods to be described subsequently. However, the run length coding concept has been very successful as a sub system coder for transform image coding.

20.2. INTERPOLATION CODING OF MONOCHROME IMAGES

Interpolative coding systems are based on numerical representation or approximation techniques whereby a sequence or plane of pixel values is “fitted” by continuous functions. In an interpolative coding system, the amplitude values of an image are approximated by continuous functions within some permissible error band (10-14). Interpolation may be performed along a row or over areas of an image.

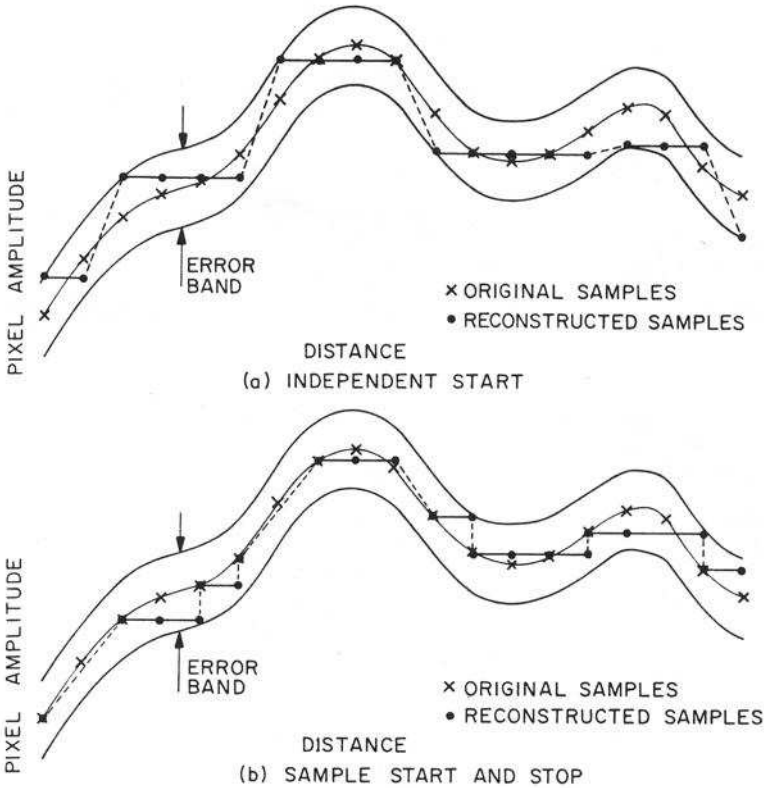


FIGURE 20.2-1. Zero-order interpolation.

Figure 20.2-1a illustrates the operation of a zero-order interpolator. In this example, an error tolerance band is established about each pixel value, and maximal length horizontal line segments are fitted within the error band without any constraints as to the start and stop coordinates. Each pixel is spanned by a horizontal line segment. The vertical coordinate and sample spacing length of each horizontal line segment is then coded. At the decoder, pixel values are reconstructed to the amplitude of the horizontal line segment. This type of interpolation permits the greatest amount of freedom possible in fitting the horizontal line segments to the image data, and thus provides the most efficient representation in terms of minimiz-

ing the horizontal line lengths. However, the computation involved in the line fitting process is often excessive. Figure 20.2-1b describes a simplified zero-order interpolator in which the horizontal line segments are restricted to begin at a pixel sample value and to end at a sample time. This simplified form of a zero-order interpolator is equivalent to a run length encoder.

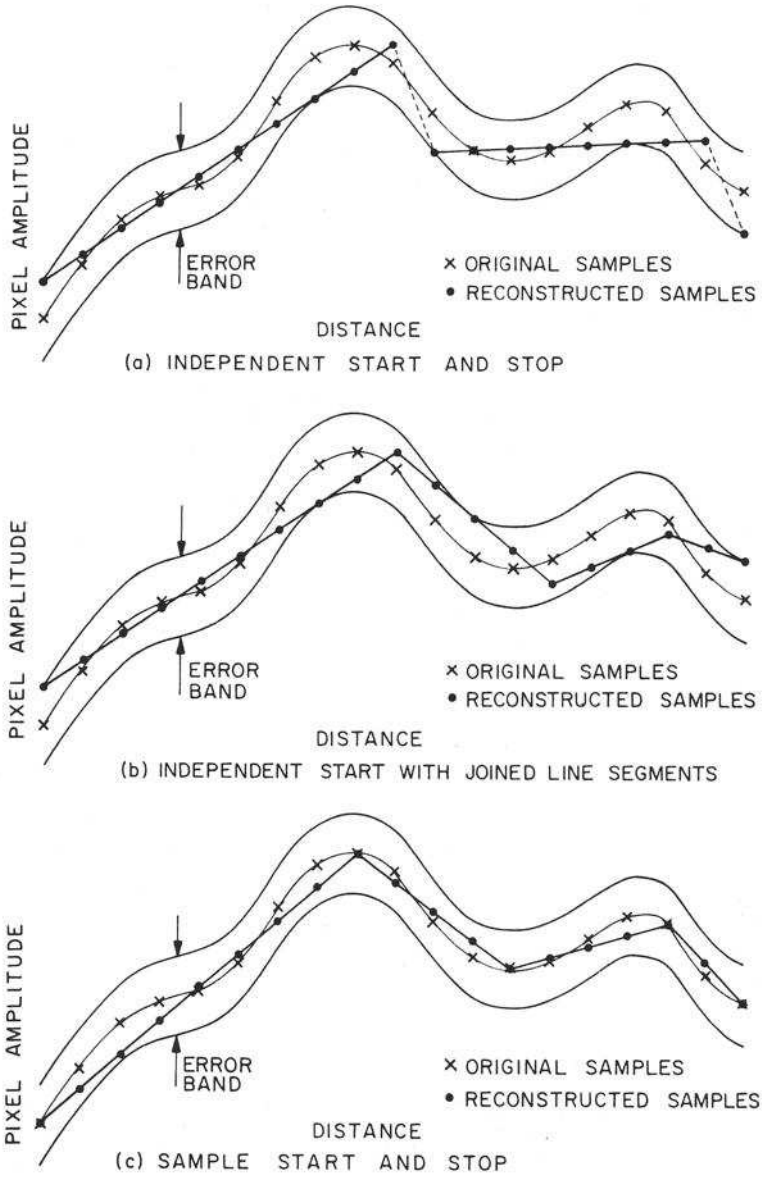


FIGURE 20.2-2. First-order interpolation.

The operation of several first-order interpolators is presented in Figure 20.2-2. In the interpolator of Figure 20.2-2a, straight line segments spanning all pixel values are fitted within the error tolerance without restrictions as to the start and stop coordinates of the line segments. The computational task of line segment fitting can be simplified somewhat by anchoring the starting point of a line segment to the stopping point of the previous line segment, as shown in Figure 20.2-2b. A still simpler version, described in Figure 20.2-2c, restricts the start and stop line segment coordinates to pixel values. This type of interpolator is often called a *fan interpolator*.

Higher-order polynomial functions, such as cubic spline functions, can be utilized for interpolative coding, but the computation involved in the interpolation process grows rapidly with the degree of the fitting polynomial. Two-dimensional versions of zero-order and first-order interpolators can also be formulated. But again, the attendant implementation task is formidable.

There have been some analytical studies (15,16) of zero-order and first-order interpolation for very simple interpolation algorithms. However, analysis for the general algorithms with few constraints is a formidable task. Simulation studies (11,12) indicate that monochrome image coding down to about 1.0 bits per pixel with a relatively low peak error can be achieved with first-order interpolation, but the coding systems are generally quite complex.

### 20.3. UNITARY TRANSFORM CODING OF MONOCHROME IMAGES

Transform image coding represents a radical departure from the classical forms of image coding such as DPCM, predictive coding, run length coding and interpolative coding in which the image signal is directly coded. The unitary transform image coding process is indirect. A unitary mathematical transform is performed on the image data to produce a set of transform coefficients, which are then quantized and coded for transmission or storage. Transform coding has proved to be an effective and practical means of coding for monochrome, color and multispectral images for both still images and real-time video.

In 1968, the concept of coding the two-dimensional Fourier transform of a monochrome image, rather than the image itself, was introduced by Andrews and Pratt (17). The basic concept of the Fourier transform coding process is that, for most natural images, many of the transform coefficients are of relatively low magnitude. These coefficients often can be discarded entirely, or coded with a small number of code symbols with only negligible image distortion (18). Pratt, Andrews and Kane (19) found, in 1969, that the Hadamard transform could be utilized in place of the Fourier transform with a considerable decrease in computational requirements for many applications (20,21). Investigations then began into application of other unitary transforms such as the discrete Karhunen-Loeve (22) and Haar transforms for image coding (23,24). The Karhunen-Loeve transform, also known as the Hoetelling transform, provides minimum mean-square error coding performance, but unfortunately requires statistical knowledge of the image source. Also, it does not

possess a fast computational algorithm. On the other hand, the Haar transform has the attribute of an extremely efficient computational algorithm, but usually results in a relatively large coding error. Shibata and Enomoto introduced orthogonal transforms containing a slant basis vector for data of vector lengths of four and eight in 1971 (25). The slant vector, a discrete sawtooth waveform decreasing in uniform steps over its length, is suitable for efficiently representing gradual brightness changes in an image line. Ahmed, et al. (26) have shown that the cosine transform, which possesses a fast algorithm, approaches the efficiency of the Karhunen-Loeve transform for Markov process image data. Jain has suggested a sine transform with similar properties (27).

The basic premise of a monochrome image transform coding system is that the two-dimensional transform of an image has an energy distribution more suitable for coding than the spatial domain representation (28,29). As a result of the inherent pixel-to-pixel correlation of natural monochrome images, the energy in the transform domain tends to be clustered into a relatively small number of transform samples. To achieve a coding compression, low-magnitude transform samples can be discarded or grossly quantized without introducing serious image degradation.

One of the drawbacks of transform coding of a monochrome image is the large size of the transform domain array — the size of the spatial domain image itself. Habibi and Wintz (22) and Woods and Huang (21) have proposed the division of a source image into small blocks, e.g. the  $8 \times 8$  block size in the JPEG baseline standard (23). As will be seen, the coding compression quality is compromised by the restriction to small blocks. However, the smaller size blocks are amenable to adaptive coding schemes.

Figure 20.3-1 contains a block diagram of a transform coding system for monochrome images. In operation, a two-dimensional transform is taken of the image pixels over the entire image, or repeatedly over subsections of the image called blocks. Let  $F(j, k)$  denote a  $N \times N$  block of pixels. For a two dimensional unitary transform that is orthogonally separable, the transform coefficients are described by

$$\mathcal{F}(u, v) = \sum_{j=1}^N \sum_{k=1}^N F(j, k) A_C(j, u) A_R(k, v) \tag{20.3-1}$$

where  $A_R(k, v)$  and  $A_C(j, u)$  represent the row and column kernels, respectively, and  $\mathcal{F}(u, v)$  is a  $N \times N$  array of transform coefficients. Next, the transform domain samples are operated on by a sample selector that decides which samples are to be coded. For a digital communication link or digital storage unit, the selected samples are quantized and coded in binary form. At the decoder, the incoming data is decoded, and an inverse transform is performed to reconstruct the original image.

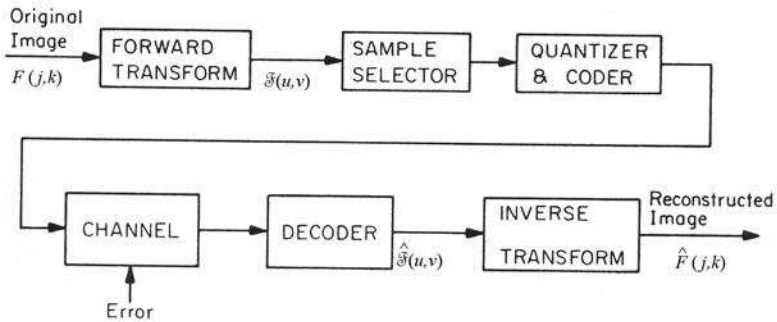


**Figure 20.3-1.** Monochrome image transform image coding system.

There are two basic strategies of sample selection: zonal sampling and threshold sampling (28). In zonal sampling, the reconstruction is made with a subset of transform samples lying in certain pre-specified geometric zones, usually the low-frequency coefficients. Each component in a zone is quantized and assigned a binary code word. The number of quantization levels is usually made proportional to the estimated variance of the component, and the number of code bits made proportional to its expected probability of occurrence. With threshold sampling, the image reconstruction is made with a subset of the samples that are larger than a specified threshold.

### 20.3.1. Zonal Sampling.

The sample selection process for two zones can be analyzed conveniently by defining a transform domain sampling function  $\mathcal{S}(u, v)$ , which takes on the value unity for samples to be transmitted and zero for samples to be discarded. The reconstructed image then becomes

$$\hat{F}(j, k) = \sum_u \sum_v \mathcal{F}(u, v) \mathcal{S}(u, v) A_C(u, j) A_R(k, v). \quad (20.3-2)$$

There are several types of zones that could logically be employed for zonal sampling. For example, a rectangular, elliptical or triangular zone. Both analytic and experimental studies (29) have indicated that the optimum zone for a mean square error criterion is the so-called maximum variance zone in which  $\mathcal{S}(u, v)$  is chosen to be unity for those transform samples having the largest variance for a given covariance model of the original image. Consequently, the mean square error  $\mathcal{E}$  for transform zonal sampling is equal to the energy of the discarded coefficients:

$$\mathcal{E} = \frac{1}{N^2} \sum_u \sum_v E\{(\mathcal{F}(u, v))^2\} [1 - \mathcal{S}(u, v)]. \quad (20.3-3)$$



Hence, the mean-square error performance of a unitary transform is determined by its degree of cumulative energy packing. In this regard, it has been shown (30,31) that the Karhunen-Loeve (K-L) transform results in the smallest mean-square error for all unitary transforms.

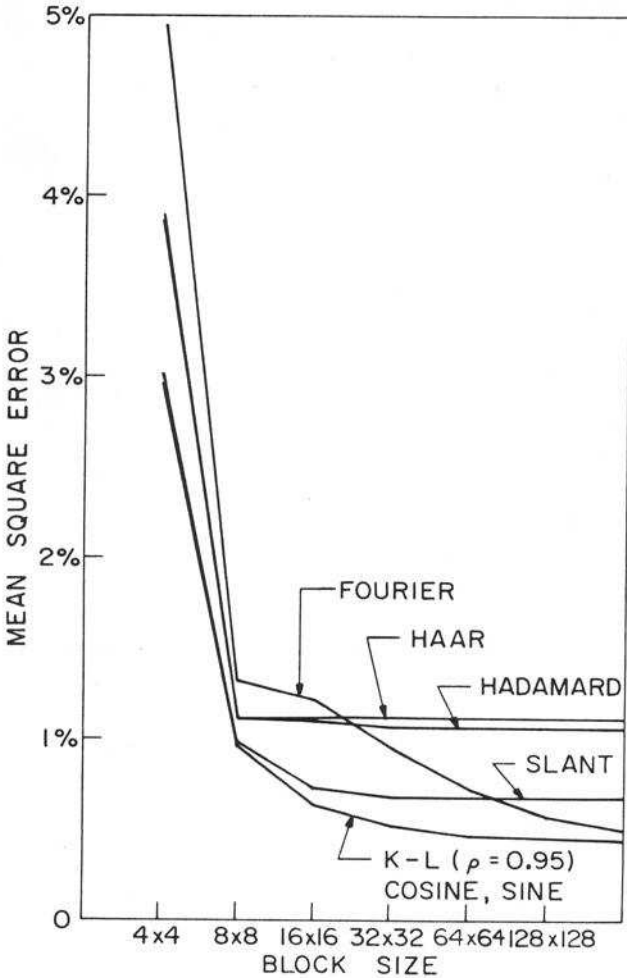


**Figure 20.3-2.** Zonal sampling mean square error performance of image transforms as a function of block size.

Figure 20.3-2 contains a plot of mean square error versus block size determined by evaluation of Eq. 20.3-3 for a transform zonal sampled image field statistically modeled as a two-dimensional Markov process with  $\rho_R = \rho_C = 0.95$ . In this plot, the 25% of the transform coefficients with the largest variances have been selected, and the remainder discarded. From the figure, it is seen that the Karhunen-Loeve transform provides the lowest mean square error. For a first-order Markov process, the mean-square error obtained by the cosine transform or by the sine transform is nearly identical to that of the optimal KL transform. Also, to be noted from the figure is that, except for the Fourier transform, the rate of decrease in mean square error for large block sizes becomes quite small after a block size of about  $16 \times 16$  is reached. The mean square error level of the Fourier transform converges relatively slowly to that of the K-L transform for large block sizes.

### 20.3.2 Zonal Coding

In the zonal transform coding system, a set of zones is established in each transform block. Transform samples in each zone are then quantized with the same number of quantization levels set proportional to the expected variance of the transform coefficients. For a constant word length code,  $N_B(u, v)$  code bits are assigned to each coefficient, resulting in

$$\mathcal{Q}(u, v) = 2^{N_B(u, v)} \quad (20.3-4)$$

quantization levels. A total of

$$T_B = \sum_u \sum_v N_B(u, v) \quad (20.3-5)$$

bits are then required to code the image. Pratt (4Ed., 673) describes an algorithm for optimal bit assignment. Figure 20.3-3 illustrates a typical bit assignment for coding in  $16 \times 16$  pixel blocks.

Figure 20.3-4 contains a plot of the mean square error for several transforms for coding of a two-dimensional Markov process array for  $\rho_R = \rho_C = 0.95$  with an average of 1.5 bits per pixel. It is possible to achieve a lower mean square error for a given channel rate by employing Huffman coding of the quantized coefficients rather than constant word length coding, but the coder will be more complex to implement.

### 20.3.3. Threshold Coding

In a threshold coding system, each sample whose magnitude is greater than a given threshold level is quantized with a fixed number of levels, and its amplitude is coded. It is necessary to code the position of each significant sample in the transform plane. A simple, but quite efficient, technique for position coding is to code the number of non-significant samples between significant samples. This run length coding scheme can be implemented as follows:

8	8	8	7	7	7	5	5	4	4	4	4	4	4	4	4	4
8	8	7	6	5	5	3	3	3	3	3	2	2	2	2	2	2
8	7	6	4	4	4	3	3	2	2	2	2	2	2	2	2	2
7	6	4	3	2	2	2	2	1	1	1	1	0	0	0	0	0
7	5	4	2	2	2	2	1	1	1	0	0	0	0	0	0	0
7	5	4	2	2	2	1	1	0	0	0	0	0	0	0	0	0
5	3	3	2	2	1	1	0	0	0	0	0	0	0	0	0	0
5	3	3	2	1	1	0	0	0	0	0	0	0	0	0	0	0
4	3	2	1	1	0	0	0	0	0	0	0	0	0	0	0	0
4	3	2	1	1	0	0	0	0	0	0	0	0	0	0	0	0
4	3	2	1	0	0	0	0	0	0	0	0	0	0	0	0	0
4	3	2	1	0	0	0	0	0	0	0	0	0	0	0	0	0
4	2	2	0	0	0	0	0	0	0	0	0	0	0	0	0	0
4	2	2	0	0	0	0	0	0	0	0	0	0	0	0	0	0
4	2	2	0	0	0	0	0	0	0	0	0	0	0	0	0	0
4	2	2	0	0	0	0	0	0	0	0	0	0	0	0	0	0

FIGURE 20.3-3. Typical bit assignments for transform zonal coding in 16 × 16 pixel blocks at a rate of 1.5 bits per pixel.

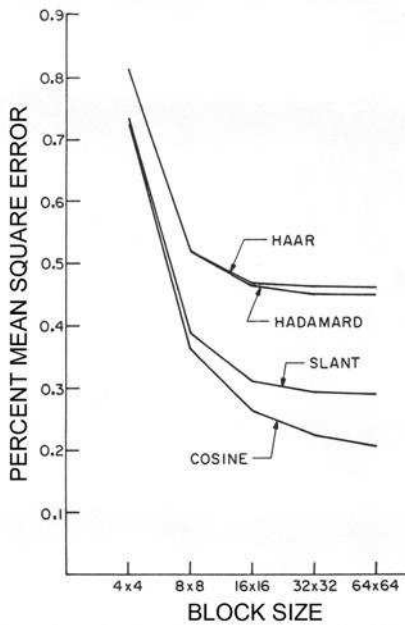


FIGURE 20.3-4. Zonal coding mean square error performance of image transforms as a function of block size for 1.5 bits/pixel and  $\rho_C = \rho_R = 0.95$ .

1. The first sample along each row in a block is coded regardless of its magnitude. A position code word of all zeros or all ones affixed to the amplitude provides a row synchronization code group;
2. The amplitude of the second run-length code word is the coded amplitude of the next significant sample. The position code is the binary count of the number of samples of the significant sample from the previous significant sample;
3. If a significant sample is not encountered after scanning the maximum run length of samples, the position and amplitude code bits are set to a unique code word to indicate a maximum run length.

The advantage of including a row synchronization code group is that it becomes unnecessary to code the row number, and the propagation of channel errors over more than one row is prevented. However, there is a coding overhead associated with this coding technique. Tescher (32) has proposed a *zigzag coding* of the transform coefficients in each block, as shown in Figure 20.3-5 for progressive raster scanning. This results in a one-dimensional ordering of transform coefficients as an approximate spatial frequency ordering. Pratt and Chen (33) have utilized Huffman coding of the zigzag coefficient amplitudes and run lengths.

As expected, because the coding process is adaptive, its performance is somewhat better than the simpler zonal coding process. With standard threshold coding, the number of coefficients, and, therefore, the number of code bits, transmitted is image dependent. A variation of threshold coding, called *N-largest coding* (34), has been developed for communication links in which the transmission bit rate and picture transmission rate is fixed. With this coding algorithm, the *N-largest* coefficients in a block are coded regardless of their values. In effect, the threshold is adaptively set for each block to achieve the desired transmission rate.

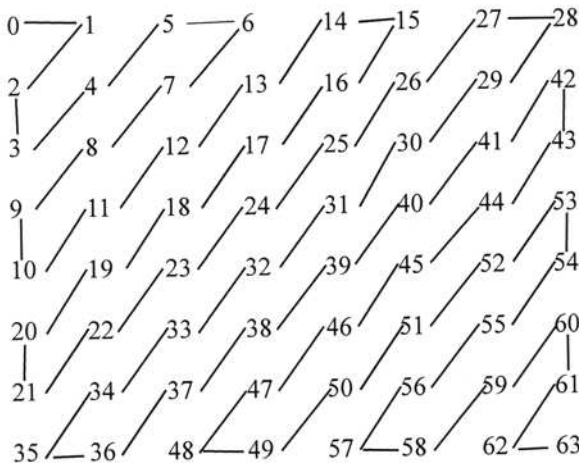
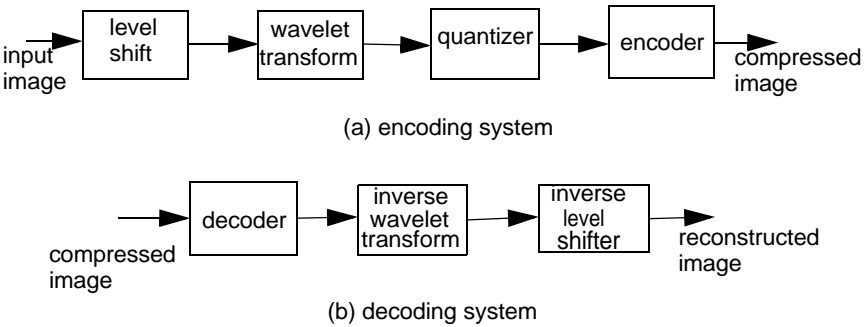


FIGURE 20.3-5. Zigzag scanning of transform coefficients.

### 20.4. WAVELET CODING OF MONOCHROME IMAGES

Figure 20.4-1 contains a simplified block diagram of a *wavelet transform* monochrome image coding system. In operation, a positive integer input image is level shifted by subtracting  $2^{Q-1}$  from each input image pixel where  $Q$  is the number of gray levels of the input image. Next, the level shifted image undergoes a two-dimensional wavelet transformation of the type described in Chapter 8. Then, the transform coefficients are quantized over a coarse-to-fine range based upon the scale level of the wavelet transform. The quantized coefficients are coded by an entropy-based symbol encoder. At the decoding system, the compressed image is decoded, and the result is subjected to an inverse wavelet transform. Finally, the image data is restored to its original range by an inverse level shifter.



**FIGURE 20.4-1.** Wavelet monochrome image coding system.

Conceptually, wavelet transform image coding, at the block diagram level, is virtually identical to unitary transform coding. Both techniques perform a linear transformation, which seeks to decorrelate and energy-compact its input image pixels in order to more efficiently quantize and code the transform coefficients on an individual basis.

The wavelet transform and inverse wavelet transform of Figure 20.4-1 are typically computed in sequential scale levels. For most image coding applications, each level is a biorthogonal transform, which produces four half-resolution subbands: a new approximation image derived from the approximation array of the previous level; a horizontal detail subimage, a vertical detail subimage; and a diagonal detail subimage. At each scale level, the wavelet transform only acts on the previous approximation image array.

Figure 20.4-2 demonstrates the nested nature of the wavelet transform for two scale levels. Typically, the quantization process is adapted to each subband array. Section 20.7 describes the functionality of the JPEG 2000 version of wavelet transform coding.

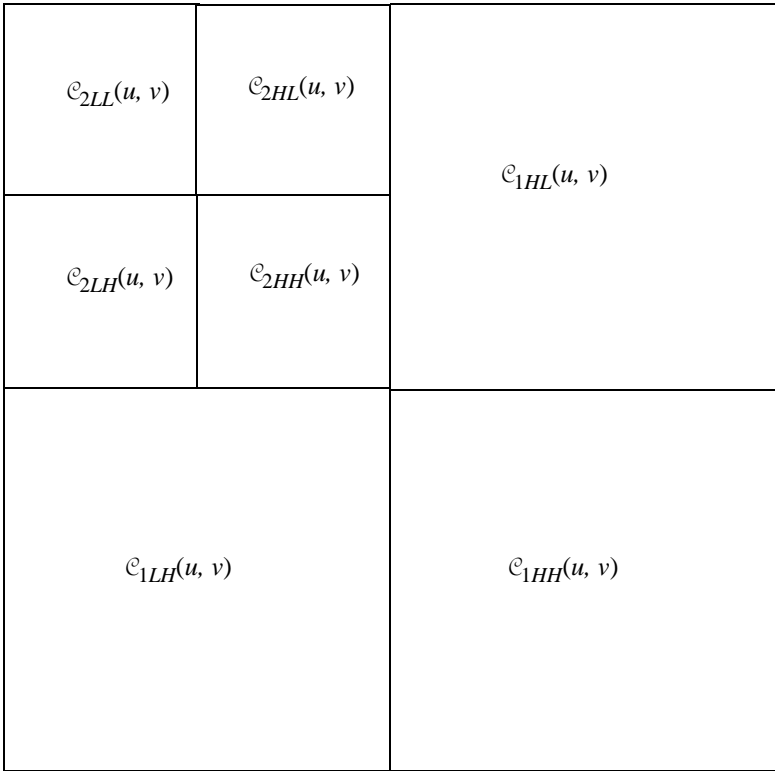


**FIGURE 20.4-2.** Wavelet transform coefficient regions for two scale levels.

**20.5. SPATIAL PROCESSING COLOR IMAGE CODING**

The spatial processing image coding techniques described in this chapter for monochrome images can be applied directly to the red, green and blue components of a color image. The resultant coding rate for a *RGB* color image will simply be three times that of a monochrome image. Improved results can be easily obtained by converting the *RGB* components to luminance (or luma) and chrominance (or chroma) components. The improvement can be realized by spatial subsampling every other row and column of the chrominance (or chroma) components with or without spatial averaging. Examples are provided for the following sections on JPEG and JPEG 2000 image coding.

### 20.6. JPEG BASELINE IMAGE CODING STANDARD

A simplified block diagram of the JPEG baseline color image coding system is shown in Figure 20.6-1. In the diagram, the input and reconstructed images are of 8-bit precision. The first step in the diagram is to level shift each input image pixel by subtracting integer 128 from it to create a two's complement image representation. The internal data paths are of 11-bit precision. Next, non-overlapping  $8 \times 8$  pixel blocks are extracted from the  $YCbCr$  components of the color image. Each block then undergoes a  $8 \times 8$  discrete cosine transform.

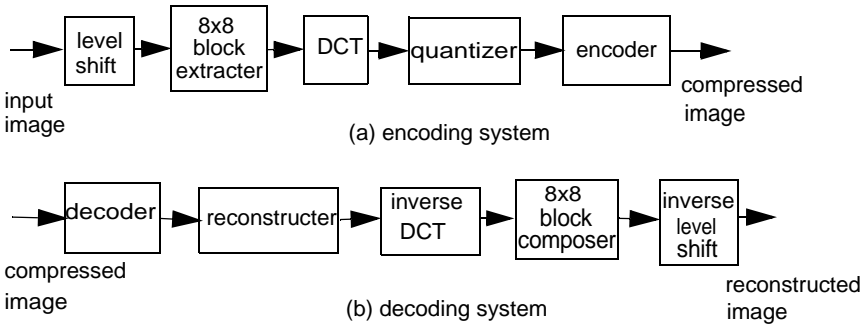


**Figure 20.6-1.** JPEG baseline color image coding system.

The transform coefficients  $\mathcal{F}(u, v)$  of Figure 20.6-1 are quantized by division by a  $8 \times 8$  quantization array  $\mathcal{Q}(u, v)$  to produce the quantized coefficients

$$\hat{\mathcal{F}}(u, v) = \left[ \frac{\mathcal{F}(u, v)}{\mathcal{Q}(u, v)} \right]_N \tag{20.6-1}$$

where  $[ \ ]_N$  indicates a nearest integer rounding operation. Figure 20.6-2 shows the baseline default luminance quantization array (35-37). Scaling of  $\mathcal{Q}(u, v)$  provides control over the degree of data compression. Figure 20.6-3 presents the JPEG baseline default chrominance array for a  $YCbCr$  color image. This array provides for a coarser quantization of DCT coefficients than for a luminance quantization array.

The next step in the encoder diagram is symbol coding of the quantized coefficients. This step is followed by Huffman entropy coding of the coefficient symbols to create the compressed image.

16	11	10	16	24	40	51	61
12	12	14	19	26	58	60	55
14	13	16	24	40	57	69	56
14	17	22	29	59	87	80	62
18	22	37	56	68	109	103	77
24	35	55	64	81	104	113	92
49	64	78	87	103	121	120	101
72	92	95	98	112	100	103	99

**FIGURE 20.6-2.** JPEG baseline default luminance quantization array, taken from Annex K1 of reference 35.

17	18	24	47	99	99	99	99
18	21	26	66	99	99	99	99
24	26	56	99	99	99	99	99
47	66	99	99	99	99	99	99
99	99	99	99	99	99	99	99
99	99	99	99	99	99	99	99
99	99	99	99	99	99	99	99
99	99	99	99	99	99	99	99

**FIGURE 20.6-3.** JPEG baseline default chrominance quantization array, taken from Annex K2 of reference 35.

At the decoding system, the Huffman encoded coefficient symbols are sequentially decoded, and the reconstructed pixels are generated by inverse scaling of the quantization process according to the relation

$$\mathcal{R}(u, v) = \hat{\mathcal{F}}(u, v) \mathcal{Q}(u, v). \tag{20.6-2}$$

An inverse DCT is followed by a composition of the reconstructed pixel blocks into a reconstructed image after an inverse level shift.

Symbol encoding is a two part process: coding of the DC and the AC coefficients of  $\mathcal{F}(u, v)$ . The following sections describe the symbol and entropy coding processes in greater detail.



**20.6.1. DC coefficient encoding**

The symbol coding process for DC coefficients begins with the generation of the difference  $\mathcal{D}(0, 0)$  of the DC coefficient of the present block from the DC coefficient of the corresponding previously processed block of the same video type. Table 20.6-1 contains a classification of the DC difference categories. There are 12 difference categories, denoted by the four bit index SSSS in the JPEG baseline standard. This table is a subset of the JPEG lossless code table of Table 19.4-2. The DC difference  $\mathcal{D}(0, 0)$  can be coded by a category index Huffman code appended by an *additional bits* code, which specifies the position within a category of a given DC difference value. As an example, the category 4 entry is listed below. If  $\mathcal{D}(0, 0)$  is equal to four, the additional bits code word is 1010.

SSSS	difference range	additional bits
4	-15, ... ,-8, 8, ..., 15	0000, ... ,0111,1000, ... ,1111

**TABLE 20.6-1.** JPEG baseline difference categories for DC coding taken from Annex F1 of reference 34.

SSSS	$\mathcal{D}(0,0)$					
0	0					
1			-1	1		
2		-3	-2	2	3	
3	-7	.....	-4	4	.....	7
4	-15	.....	-8	8	.....	15
5	-31	.....	-16	16	.....	31
6	-63	.....	-32	32	.....	63
7	-127	.....	-64	64	.....	127
8	-255	.....	-128	128	.....	255
9	-511	.....	-256	256	.....	511
10	-1023	.....	-512	512	.....	1023
11	-2047	.....	-1024	1024	.....	2047

A category Huffman code table can be created by measuring or modelling of the probability of occurrence of each category value. The JPEG baseline standard contains suggested Huffman code tables for luminance and chrominance DC differences, as shown in Table 20.6-2.

**Table 20.6-2.** Luminance and chrominance DC difference Huffman codes taken from Table K1 and K2 of reference 34.

Category	Luminance code	Chrominance code
0	00	00
1	010	01
2	011	10
3	100	110
4	101	1110
5	110	11110
6	1110	111110
7	11110	1111110
8	111110	11111110
9	1111110	111111110
10	11111110	1111111110
11	111111110	11111111110

**20.6.2. AC coefficient encoding**

The symbol coding process for AC coefficients begins with the formation of a one-dimensional array of the 63 AC coefficients by zigzag scanning of a block of DCT coefficients according to the order of Figure 20.3-2. The non-zero coefficients are run length coded to produce a code pair RRRR/SSSS where RRRR denotes the run length of zeros before the next non-zero coefficients, and SSSS is the size of the next non-zero coefficient as specified in Table 20.6-2. This table specifies the additional bits required to specify the coefficient value in a similar fashion to the additional bits for DC coefficients. Conceptually, it is convenient to consider that AC coefficient symbols to be entries of RRRR/SSSS pairs in a two-dimensional array of RRRR = 16 rows and 10 columns augmented by two special event symbols: EOB and ZRL. The symbol EOB indicates to the decoder that the last non-zero AC coefficient has been processed in a block scan. ZRL denotes a zero run length event.

Once this augmented array has been established, it is possible to assign a probability of occurrence of each of 162 entries, and subsequently, to assign a Huffman code to each entry. The JPEG standard document (35) specifies suggested Huffman code Table K5 for luminance blocks and Table K6 for chrominance blocks.

**TABLE 20.6-2.** JPEG baseline categories for AC coding

SSSS	$\mathcal{A}(u,v)$					
1			-1	1		
2			-3	-2	2	3
3	-7	.....	-4	4	.....	7
4	-15	.....	-8	8	.....	15
5	-31	.....	-16	16	.....	31
6	-63	.....	-32	32	.....	63
7	-127	.....	-64	64	.....	127
8	-255	.....	-128	128	.....	255
9	-511	.....	-256	256	.....	511
10	-1023	.....	-512	512	.....	1023

**20.7. JPEG2000 IMAGE CODING STANDARD**

For purposes of analysis, the JPEG2000 still image coding standard can be considered to be a specialization of the wavelet monochrome coding system of Figure 20.4-1 in terms of the wavelet structure, quantization strategy and encoding method

**20.7.1 JPEG2000 Discrete Wavelet Filters**

The JPEG2000 standard (38) specifies low pass and high pass analysis and synthesis finite impulse response (FIR) filters. They are the so called Daubechies (9,7) 9-tap and 7-tap FIR biorthogonal spline filters. Following the nomenclature of Chapter 8, the filters are defined below as convolution impulse response arrays.

9-tap low-pass analysis filter:  $[h_L(-4) \dots h_L(0) \dots h_L(4)]$

$$\begin{aligned} \text{where} \quad h_L(-4) &= h_L(4) = +0.026748757410810 \\ h_L(-3) &= h_L(3) = -0.016864118442875 \\ h_L(-2) &= h_L(2) = -0.078223266528988 \\ h_L(-1) &= h_L(1) = +0.266964118442872 \\ h_L(0) &= +0.602949018236358 \end{aligned}$$

7-tap high-pass analysis filter:  $[h_H(-3) \dots h_H(0) \dots h_H(3)]$

$$\begin{aligned} \text{where} \quad h_H(-3) &= h_H(3) = +0.091271763114249 \\ h_H(-2) &= h_H(2) = -0.057543526228500 \\ h_H(-1) &= h_H(1) = -0.591271763114247 \\ h_H(0) &= +1.115087052456994 \end{aligned}$$

7-tap low-pass synthesis filter:  $[g_L(-3) \dots g_L(0) \dots g_L(3)]$

$$\begin{aligned} \text{where} \quad g_L(-3) &= g_L(3) = -0.0912717631142495 \\ g_L(-2) &= g_L(2) = -0.057543526228500 \\ g_L(-1) &= g_L(1) = +0.591271763114247 \\ g_L(0) &= +1.115087052456994 \end{aligned}$$

9-tap high-pass synthesis filter:  $[g_H(-4) \dots g_H(0) \dots g_H(4)]$

$$\begin{aligned} \text{where} \quad g_H(-4) &= g_H(4) = +0.026748757410810 \\ g_H(-3) &= g_H(3) = +0.016864118442875 \\ g_H(-2) &= g_H(2) = -0.078223266528988 \\ g_H(-1) &= g_H(1) = -0.266864118442872 \\ g_H(0) &= +0.602949028236358 \end{aligned}$$

### 20.7.2. JPEG2000 Coefficient Quantization

The JPEG 2000 standard specifies uniform scalar quantization of subband coefficients  $\mathcal{C}_b(u, v)$  with a step size of  $\Delta_b$  and a zero-level step dead-zone width of  $2\Delta_b$ . The quantization operation is governed by (40)

$$\mathcal{Q}_b = \text{sgn}\{\mathcal{C}_b(u, v)\} \left[ \frac{\mathcal{C}_b(u, v)}{\Delta_b} \right]_F \quad (20.7-1)$$

where  $[\ ]_F$  denotes the floor rounding down operation on its argument. After quantization, the quantized coefficients are converted to sign-magnitude format for entropy encoding.

The standard (38) defines the step size formation in terms of an exponent  $\epsilon_b$  and a mantissa  $\mu_b$  according to the relation

$$\Delta_b = 2^{-\varepsilon_b} \left[ 1 + \frac{\mu_b}{2^{11}} \right] \quad (20.7-2)$$

where

$$0 \leq \varepsilon_b < 2^5 \quad (20.7-3a)$$

and

$$0 \leq \varepsilon_b < 2^{11}. \quad (20.7-3b)$$

### 20.7.3. JPEG2000 Entropy Encoding

The JPEG standard requires the use of bit-plane coding techniques as a form of entropy coding. The standardized specification is effective, but of complexity beyond this text. Reference 39 provides a detailed presentation of the standard entropy coding specification.

## 20.8. SPATIAL PROCESSING IMAGE COMPRESSION EXERCISES

E20.1 Develop a program that computes the discrete cosine transform of the `lena_mon` image in  $8 \times 8$  pixel blocks. Steps:

- (a) Display the source image.
- (b) Compute the  $8 \times 8$  pixel DCT.
- (c) Display the magnitude of the DCT.

The PIKS API executable `example_8x8_cosine_transform` performs this exercise.

E20.2 Develop a program that simulates the JPEG DCT monochrome image coding system of Figure 20.6-1 without symbol and entropy coding and decoding for the `lena_mon` image. Steps:

- (a) Display the source image.
- (b) Extract each  $8 \times 8$  pixel block.
- (c) Level shift each block.
- (d) Perform a DCT of each block.
- (e) Quantize each coefficient block using the luminance quantization array of Figure 20.6-2.
- (f) Perform quantization reconstruction on each quantized coefficient block.
- (g) Perform an inverse DCT on each reconstructed coefficient block.
- (h) Inverse level shift each reconstructed image block.

- (i) Compose each reconstructed image block to a reconstructed image.
- (j) Display the reconstructed image.

The PIKS API executable `example_8x8_DCT_quantization` performs this exercise.

E20.3 Develop a program that performs run length coding on the Boolean image `L_array`. Steps:

- (a) Display the source image.
- (b) Compress the source image into a work file using run length coding with a maximum run length of 16.
- (c) Decompress the work file to create the reconstructed image,
- (d) Display the reconstructed image.
- (e) Compute the compression ratio from the source image pixel count and the work file bit count.

The PIKS API executable `example_run_length` performs this exercise.

## REFERENCES

1. L. D. Davisson and R. L. Kutz, "An Operational Data Compression System Using Mini-computers," *Proc. International Telemetry Conference Record*, Houston, December 1972, 34A-1 to 34A-4.
2. C. L. May and D. J. Spencer, "Data Compression for Earth Resources Satellites," *Proc. International Telemetry Conference*, Los Angeles, **8**, October 1972, 352-362.
3. G. G. Gouriet, "Bandwidth Compression of a Television Signal," *Proc. IEE*, **104**, Part B, 15, May 1957, 265-272.
4. W. F. Schreiber and C. F. Knapp, "TV Bandwidth Reduction by Digital Coding," *IRE National Convention Record*, **6**, Part 4, 1958, 88-89.
5. A. H. Robinson and E. C. Cherry, "Results of a Prototype Television Bandwidth Compression Scheme," *Proc. IEEE*, **55**, 3, March 1967, 356-364.
6. J. Capon, "A Probabilistic Model for Run-Length Coding of Pictures," *IRE Trans. Information Theory*, **IT-5**, 4, December 1959, 157-163.
7. W. K. Pratt, "Coding Compression of a Television Bandwidth Reduction System," *Proc. IEEE (Correspondence)* **54**, 6 June 1966, 914-916.
8. S. W. Golomb, "Run Length Encodings," *IEEE Trans. Information Theory*, **IT-12**, 3, July 1966, 399-401.
9. R. B. Arps, "Binary Image Compression," W. K. Pratt, Ed., *Image Transmission Techniques*, Academic Press, New York, 1979, 219-276.
10. L. W. Gardenhire, "Redundancy Reduction, the Key to Adaptive Telemetry," *National Telemetry Conference*, Los Angeles, 1964.

11. C. M. Kortman, "Redundancy Reduction: A Practical Method of Data Compression," *Proc. IEEE*, **55**, 3, March 1967, 253-263.
12. D. Hochman, H. Katzman and D. R. Weber, "Application of Redundancy Reduction to Television Bandwidth Compression," *Proc. IEEE*, **55**, 3, March 1963, 263-267.
13. C. A. Andrews, J. M. Davies and G. R. Schwarz, "Adaptive Data Compression," *Proc. IEEE*, **55**, 3, March 1967, 267-277.
14. C. M. Kortman, "Data Reduction by Redundancy Reduction," *IEEE Spectrum*, **55**, 3, March 1967, 133-139.
15. L. Erhman, "Analysis of Some Redundancy Removal Bandwidth Compression Techniques," *Proc. IEEE*, **55**, 3, March 1967, 278-287.
16. L. D. Davisson, "Data Compression Using Straight Line Interpolation," *IEEE Trans. Information Theory*, **IT-14**, 3, May 1968, 390-394.
17. H. C. Andrews and W. K. Pratt, "Fourier Transform Coding of Images," *Hawaii International Conference on System Science*, January 1968, 677-679.
18. G. B. Anderson and T. S. Huang, "Piecewise Fourier Transformation for Picture Bandwidth Compression," *IEEE Trans. Communications*, **COM-20**, 3, June 1972, 488-491.
19. H. C. Andrews, J. Kane and W. K. Pratt, "Hadamard Transform Image Coding," *Proc. IEEE*, **57**, 1, January 1969, 58-68.
20. W. K. Pratt and H. C. Andrews, "Application of Fourier-Hadamard Transformation to Bandwidth Compression," in *Picture Bandwidth Compression*, T. S. Huang and O. J. Tretiak, Eds., Gordon and Breach, New York, 1972, 515-554.
21. J. W. Woods and T. S. Huang, "Picture Bandwidth Compression by Linear Transformation and Block Quantization," in *Picture Bandwidth Compression*, T. S. Huang and O. J. Tretiak, Eds., Gordon and Breach, New York, 1972, 555-573.
22. A. Habibi and P. A. Wintz, "Image Coding by Linear Transformation and Block Quantization," *IEEE Trans. Communications Technology*, **COM-19**, 1, February 1971, 50-63.
23. H. C. Andrews, *Computer Techniques in Image Processing*, Academic Press, New York, 1970.
24. K. R. Rao, M. A. Narasimhan and K. Revuluri, "Image Data Processing by Hadamard-Haar Transforms," *IEEE Trans. Computers*, **C-23**, 9, September 1975, 888-896.
25. H. Enomoto and K. Shibata, "Orthogonal Transform Coding System for Television Signals," *IEEE Trans. Electromagnetic Compatibility*, Special Issue on Walsh Functions, **EMC-13**, 3, August 1971, 11-17.
26. N. Ahmed, T. Natarajan and K. R. Rao, "On Image Processing and a Discrete Cosine Transform," *IEEE Trans. Computers*, **C-23**, 1, January 1974, 90-93.
27. A. K. Jain, "A Fast Karhunen-Loeve Transform for Finite Discrete Images," *National Electronics Conference*, Chicago, October 1974, 322-328.
28. H. C. Andrews and W. K. Pratt, "Transform Image Coding," in *Proc. Computer Processing in Communications*, Polytechnic Press, New York, 1969, 63-84.
29. P. A. Wintz, "Transform Picture Coding," *Proc. IEEE*, **60**, 7, July 1972, 809-823.
30. H. P. Kramer and M. V. Mathews, "A Linear Encoding for Transmitting a Set of Correlated Signals," *IRE Trans. Information Theory*, **IT-2**, September 1956, 41-46.
31. J. J. Y. Huang and P. M. Schulteiss, "Block Quantization of Correlated Gaussian Random Variables," *IEEE Trans. Communication Systems*, **CS-11**, 3, September 1963, 289-296.

32. A. G. Tescher, "Transform Image Coding," *Aerospace Corp. Research Report*, SAMSO-TR-78-127, May 1978, 1-110.
33. W. Chen and W. K. Pratt, "Scene Adaptive Coder," *IEEE Trans. Communications*, **COM-32**, 3, March 1984, 225-232.
34. W. K. Pratt, "Spatial Transform Coding of Color Images," *IEEE Trans. Communications Technology*, **COM-19**, 6, December 1971, 980-982.
35. ISO/IEC JTC1 10918-1 ITU-T Rec. T.81, *Information Technology — Digital Compression and Coding of Continuous-Tone Still Image: Requirements and Guidelines*, 1994.
36. K. R. Rao and J. J. Hwang, *Techniques and Standards for Image, Video, and Audio Coding*, Prentice Hall, Upper Saddle River, New Jersey, 1996.
37. W. B. Pennebaker and J. L. Mitchell, *JPEG Still Image Compression Standard*, Van Nostrand Reinhold, New York, 1993.
38. ISO/IEC 15444-1, *JPEG2000 Image Coding System — Part 1 Core Coding System*, 2000.
39. T. Acharya and A. K. Ray, *Image Processing Principles and Applications*, Wiley-Interscience, Hoboken, New Jersey, 20005.
40. D. S. Taubman and M. W. Marcellin, *JPEG2000 Image Compression Fundamentals, Standards and Practice*, Springer, New York, 20002.





---

# 21

---

## VIDEO COMPRESSION

This chapter provides a historical summary of the spatial and temporal coding technology employed in video compression techniques. Following these sections are descriptions of three MPEG standards: MPEG-1, MPEG-2 and MPEG-4.

### 21.1. SPATIAL VIDEO CODING TECHNIQUES

Conceptually, the simplest form of video compression is to perform two-dimensional image coding independently on each frame of a video temporal sequence. Chapter 21 has presented descriptions of several image coding methods based upon spatial processing. Among these candidates, JPEG (1) and JPEG2000 (2) appear to be the best choices for reasons of performance.

The JPEG baseline standard has been widely used as a means of video compression. In this application, the video compression technique has become to be known as *Motion JPEG*. It should be understood that Motion JPEG is not an international standard, and therefore, there is no guarantee of compatibility between various implementations.

JPEG2000, which was standardized over a decade later than JPEG baseline, has created a file format in Part 3 of the standard. When followed, it provides Motion JPEG2000 compatibility.

The choice between the two standards is a trade off between performance and implementation complexity. JPEG2000 provides about a 10% improvement in coding rate over JPEG, but JPEG2000 is considerably more complex to implement.

## 21.2. SPATIAL/TEMPORAL VIDEO CODING TECHNIQUES

This section presents a summary of the development of spatial/temporal video coding techniques leading to the MPEG-1 and MPEG-2 standards.

### 21.2.1. Frame Replenishment Coding

A large potential bandwidth reduction exists in the removal of redundancy between adjacent frames of television pictures. In most scenes, there is relatively little change in detail between adjacent frames. Thus, by only transmitting the change in detail referenced to an initially transmitted frame, a significant bandwidth reduction can be achieved.

If pixel differences are formed between adjacent frames, it is found that a majority of the pixels are virtually unchanged. This observation has led to the development of a frame-to-frame coding technique, by Mounts et al. (3-6), called frame replenishment coding, as shown in Figure 21.2-1. In operation, each source frame is digitized to 8 bits per pixel, and the first frame is stored in a reference frame memory. In subsequent frames, each pixel is compared to its counterpart in the frame memory. If a significant difference exists, the new pixel value replaces the stored value in the frame memory, and it is also placed in a buffer memory for transmission. It is also necessary to identify the position of the significant change along a scan line by its horizontal code coordinate. The first pixel along a scan line is also coded to provide a line count. An improvement in coding efficiency can be obtained by coding frame difference in clusters rather than individually.

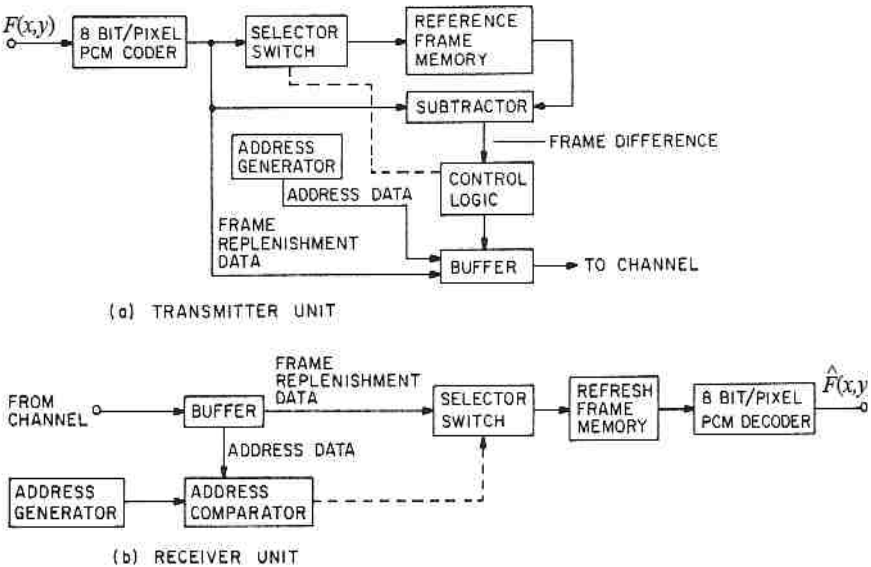


Figure 21.2-1. Frame replenishment image coding system.

Simulation studies (6) indicate that good visual quality can be obtained at a coding rate of 1.0 bits per pixel except for picture regions containing violent motion.

### 21.2.2. Differential Frame Coding

It is possible to extend the technique of predictive coding, shown in Figure 19.3-1, to utilize the redundancy between frames (6). Mounts (7) has implemented a frame-to-frame differential PCM predictive coder that derives its prediction value from a previous frame only. The performance of this coder is about the same as for a differential PCM coder using the previous pixel along a line: 3.0 bits per pixel. The frame differential coder is subject to a *temporal overload* error analogous to the *slope overload* error of DPCM.

### 21.2.3. Unitary Transform Interframe Coding

In most natural television imagery, there is a great deal of correlation in the temporal direction between frames as well as spatial correlation. Three-dimensional unitary transform coding can be utilized to provide decorrelation and energy compaction between frames as well as within each frame.

Let  $F(j, k, i)$  denote a block of  $J \times K \times I$  pixels extracted from a sequence of  $I$  image frames. The separable three-dimensional unitary transform of this block is defined as

$$\tilde{F}(u, v, w) = \sum_j \sum_k \sum_i F(j, k, i) A_C(j, u) A_R(k, v) A_T(i, w) \quad (21.2-1)$$

where  $A_C(j, u)$ ,  $A_R(k, v)$  and  $A_T(i, w)$  are the column, row and temporal transform kernels, respectively. In an interframe unitary transform coding system, each coefficient is coded following a zonal sampling, zonal coding or threshold strategy using design techniques similar to those of two-dimensional transform coding. The reconstructed transform coefficients at the decoder  $\hat{\tilde{F}}(u, v, w)$  are then inverse transformed to produce a reconstructed image block  $\hat{F}(j, k, i)$ . Figure 21.2-2 contains plots of the mean square coding error for interframe cosine transform coding of a three-dimensional Markov process image source with  $\rho_R = \rho_C = \rho_T = 0.96$  as a function of block size for zonal coding (8). Roes et al. (9) have investigated three-dimensional cosine transform coding over  $16 \times 16 \times 16$  pixel cubes. Excellent results have been obtained at coding rates down to 0.25 bits per pixel. The drawback of three-dimensional interframe transform coding is the large amount of frame storage at the coder.

### 21.2.4. Motion Compensation Interframe Coding

The coding rate of interframe coding techniques is usually limited because small movements of objects in a scene or camera movements create relatively large interframe pixel differences. This problem can be overcome by motion compensation.

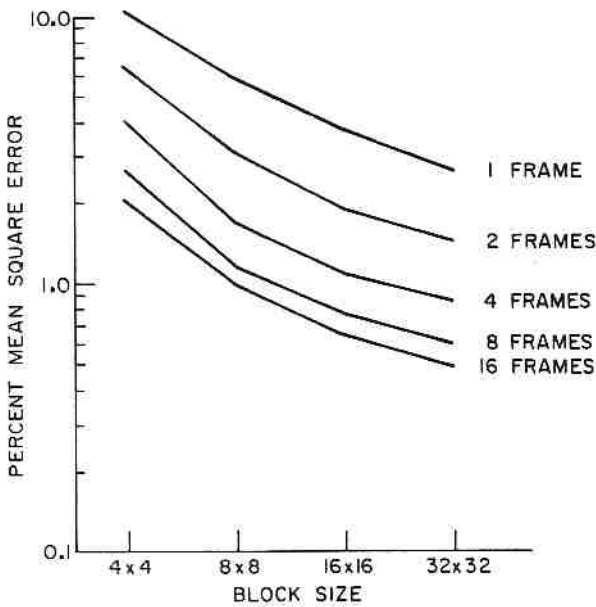


**Figure 21.2-2.** Zonal coding mean square error as a function of frame block size for interframe cosine transform coding.

In 1969, Rocca (10) introduced the concept of motion compensation for the coding of interframe differences. The concept, which is illustrated in Figure 21.2-3, following the notation of Section 18.3, consists of the search of a candidate template region  $T$  extracted from a current video frame over a search window  $S$  in a reference frame. The best match region is used to form the subsequent frame difference. Typically, the normalized cross correlation function of Eq. 18.3-6 is used as a measure of best fit.

As will be seen in the following sections, motion estimation and motion compensation play a major role in the MPEG standards.

### 21.3. MPEG-1 VIDEO CODING STANDARD

MPEG-1, an acronym for Moving Picture Experts Group, is the common name for an international standard for the digital transmission and storage of moving pictures and accompanying audio. This standard specifies the digital video and audio compression methodologies that provide storage of a video sequence on a compact disc read only device (CD-ROM) or similar bandwidth device (11). Appendix AP3.3 summarizes the standardization process of MPEG-1.

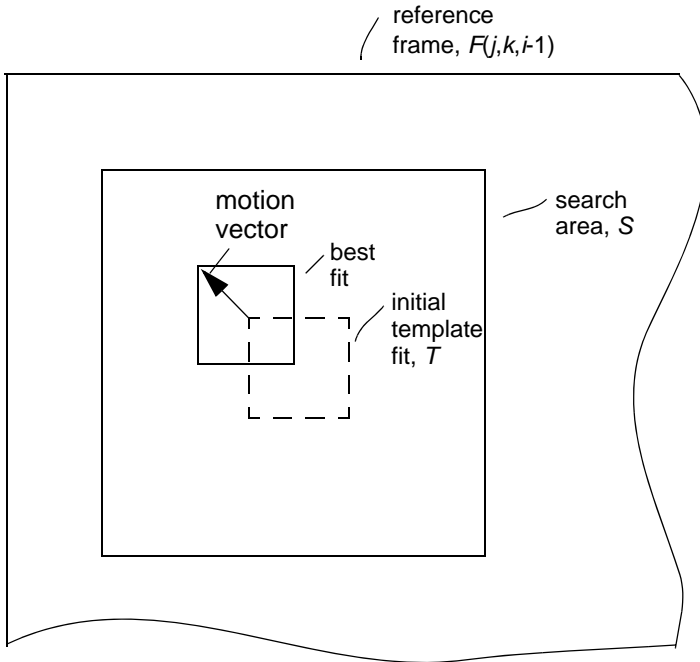


**Figure 21.2-3.** Video motion estimation.

This section of the book presents a high-level overview of the MPEG-1 video standard. References 12 and 13, as well as the standard itself (11), provide details about the implementation of MPEG-1, which is a relatively complex processor.

**21.3.1. MPEG-1 Video Data Structure**

MPEG-1 has established a hierarchical layered data structure for compression of a temporal video sequence, as shown in Figure 21.3-1. At each stage of the structure, from the video sequence to the small block level, a color picture is defined by an embedded luminance array  $Y(j, k)$  and two chrominance arrays  $C_b(j, k)$  and  $C_r(j, k)$ .

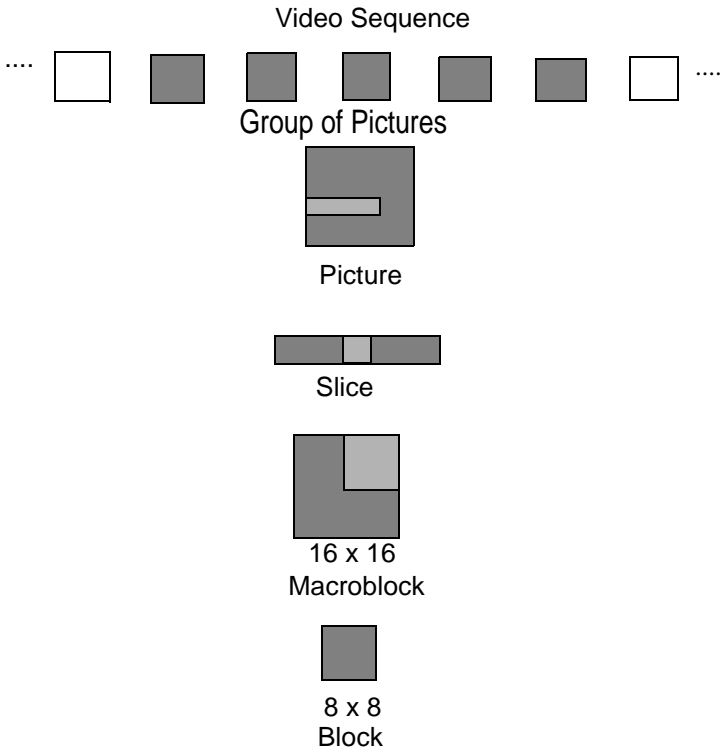


**Figure 21.3-1.** MPEG-1 hierarchial video data structure.

The following are definitions of the MPEG-1 data structures.

A **Video Sequence** is a temporal collection of one or more MPEG-1 Groups of Pictures.

A **Group of Pictures** is a temporal collection of one or more MPEG-1 Pictures (15). It begins with an *I*-picture or a *B*-picture. Figure 21.3-2 illustrates a typical Group of Pictures in display order.

There are four types of MPEG-1 pictures, which are defined as follows.

An ***I*-picture** is a MPEG-1 picture in which all  $8 \times 8$  luminance and chrominance blocks are intraframe coded using a discrete cosine transformation, linear quantization and variable length encoding process. *I*-pictures can be used to predict *P*-pictures and *B*-pictures.

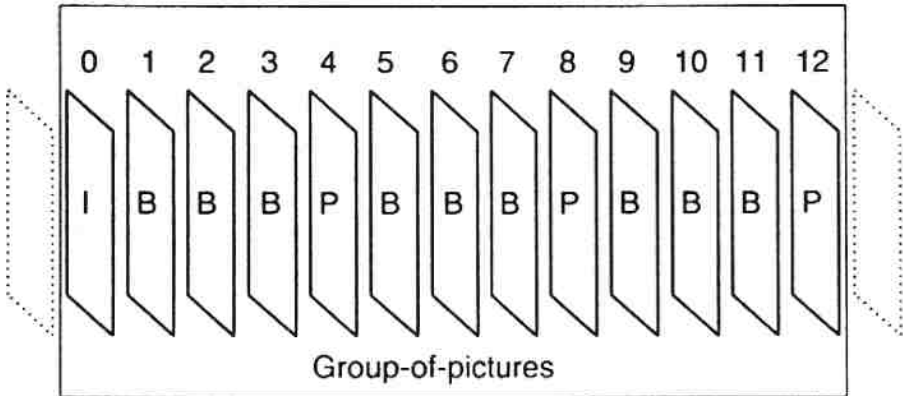


**Figure 21.3-2.** Example of a MPEG-1 Group of Pictures.

A ***P*-picture** is a MPEG-1 picture in which all  $8 \times 8$  luminance and chrominance blocks are coded using motion compensated forward prediction from a previous *I*-picture or *P*-picture. *P*-pictures pass through the feedback loop. They can be used for predicting *P*-pictures and *B*-pictures.

A ***B*-picture** is a MPEG-1 picture in which all  $8 \times 8$  luminance and chrominance blocks are coded using a past and, or, future picture as a reference by bidirectional motion compensation prediction. *B*-pictures are not allowed as a reference for any other pictures.

A ***D*-picture** is a MPEG-1 picture in which only the DC coefficients of all  $8 \times 8$  luminance and chrominance blocks are coded. This compressed video provides a simple and fast method for displaying a fast-forward version of a video sequence.

A MPEG-1 **Slice** is a contiguous sequence of Microblocks in raster scan order starting at a specified address in a picture. The slice height is 16 pixels. At the picture edge, the slice may wrap around to the next microblock row. The purpose of a slice is to permit on the fly changes in the encoder algorithm. It is also useful for error recovery.

A MPEG-1 **Macroblock** consists of an array of  $16 \times 16$  luminance pixels  $Y(j, k)$  and two  $8 \times 8$  chrominance arrays  $C_b(j, k)$  and  $C_r(j, k)$ . The luminance array is embedded into four  $8 \times 8$  arrays for encoding. The  $16 \times 16$  luminance microblock can be used for motion estimation.



A MPEG-1 **Block** is a  $8 \times 8$  array of pixels used for encoding luminance and chrominance data.

### 21.3.2. MPEG-1 Video Encoding System

The MPEG-1 standard does not mandate specific designs for the video encoder and decoder. However, the encoder must satisfy the syntax and semantics of the standard in terms of the composition of the compressed video data stream. Likewise, the decoder must be able to reconstruct a reasonable replica of the video source from the compressed video data stream.

For educational purposes, it is useful to describe a generic encoder and decoder, which could be implemented to satisfy the MPEG-1 standard. Figure 21.3-3 provides a simplified block diagram of a generic MPEG-1 encoder and decoder based upon references 12 and 14. In the figure, deletion of the shaded blocks results in an encoder whose coded data stream satisfies the MPEG standard for *I*-pictures for a macroblock input frame  $F(n)$  and its reconstructed output  $E(n) = \hat{F}(n)$ . If the shaded blocks are included, the block diagram satisfies the MPEG-1 standard for *P*-pictures and *B*-pictures.

The following subsections provide simplified descriptions of the encoding processes for MPEG-1, which are conceptually similar to those of JPEG.

***I*-picture encoding.** For intraframe encoding, the four luminance  $8 \times 8$  blocks and two  $8 \times 8$  chrominance blocks of a macroblock are sequentially extracted from frame  $F(n)$  and input to the Discrete Cosine Transform box. The DCT coefficient array is quantized by division of a quantization array and rounding of the dividend to its nearest integer value. The MPEG-1 standard provides the single quantization array shown in Figure 21.3-4<sup>1</sup>. Next, the quantized coefficients are symbol and entropy coded in two parallel paths. In the symbol encoder, the DC coefficient of the present frame is subtracted by the corresponding DC coefficient of the previous frame, and the difference is fed to an entropy encoder. The AC block coefficients are sent to a symbol coder, which performs a zigzag scanning of the 63 AC coefficients, and performs run length coding of the non-zero AC coefficients.

Tables 21.3-1 and 21.3-2 provide the default Huffman code assignments for DC and AC *I*-picture encoding (11). For brevity, the AC table is abbreviated as shown. In Table 21.3-2, the sign bit, *s*, is 0 for a positive quantity and 1 for a negative quantity. As with JPEG, it is necessary to append the Huffman codes with additional bits words. Table 21.3-2 contains two special code symbols EOB and ESC. EOB informs the decoder that there are no non-zero coefficients in the zigzag scan after the last one coded. ESC is an escape code word, which indicates that a run/level pair is not in the table, and the next 16-bit word specifies the value of the pair.

---

1. JPEG provides default quantization arrays for luminance and chrominance blocks

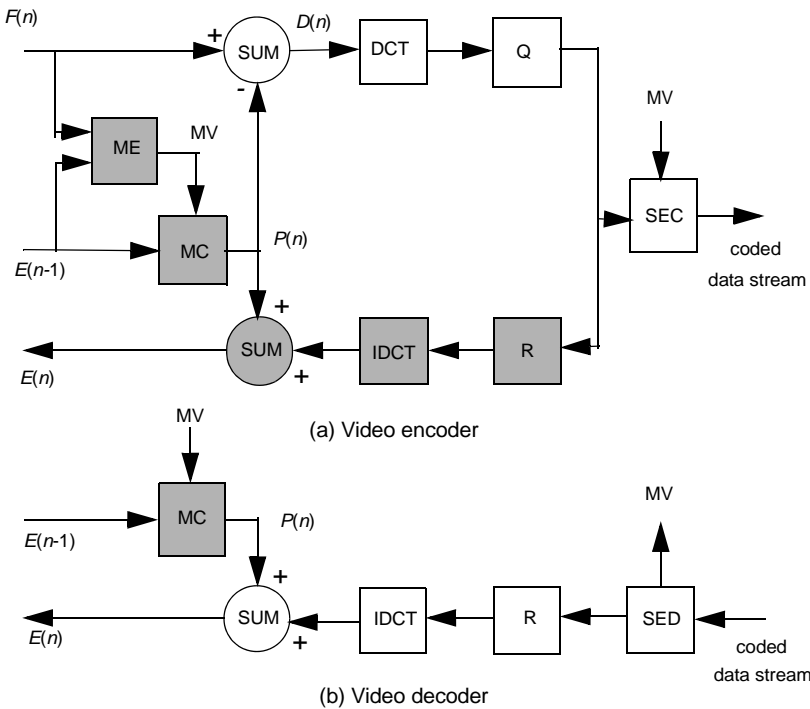


**Figure 21.3-3.** MPEG-1 video generic encoding system. Legend: DCT = Discrete Cosine Transform; Q = Quantizer; R = Reconstructor; IDCT = Inverse DCT; ME = Motion Estimate; MC = Motion Compensate; SEC = Symbol and Entropy Coder; SED = Symbol and Entropy and Decoder.

8	16	19	22	26	27	29	34
16	16	22	24	27	29	34	37
19	22	26	27	29	34	34	38
22	22	26	27	29	34	37	40
22	26	27	29	32	35	40	48
26	27	29	32	35	40	48	58
26	27	29	34	38	46	56	69
27	29	35	38	46	56	69	83

**FIGURE 21.3-4.** MPEG-1 I-picture quantization array.

At the video decoder, shown in Figure 21.3-4b, The Entropy Decoder decodes the coded bit stream to create the quantized coefficient symbols After symbol decoding, the quantized coefficients are reconstructed and subject to an inverse DCT. This produces the macroblock, which is embedded in the coded frame  $\hat{F}(n)$ , which is an estimate of  $F(n)$ .

**Table 21.3-1.** MPEG-1 DC coefficient luminance and chrominance *I*-picture codes

size	coefficient range	<i>Y</i> code	<i>C</i> code
0	0	100	00
1	-1,1	00	01
2	-3...-2,2...3	01	10
3	-7...-4,4...7	101	110
4	-15...-8,8...15	110	1110
5	-31...-16,16...31	1110	1111 0
6	-63...-32,32...63	1111 0	1111 10
7	-127...-64,64...127	1111 10	1111 110
8	-255...-128,128...255	1111 110	1111 1110

***P*-picture and *B*-picture coding.** Figure 21.3-3, with the shaded boxes included, serves as a generic model for the coding of *I*-pictures and *B*-pictures. In the diagram, the present frame  $F(n)$  is compared to the previous reference frame  $F(n-1)$  over a macroblock luminance area. Conceptually, the macroblock of the present frame is shifted horizontally and vertically until a best fit of the shifted macroblock is achieved. The shift is recorded as a *motion vector*, *MV*. Next, the *MV* is fed to a motion compensation box, which creates a prediction macroblock array  $P(n)$  that is subtracted from the  $F(n)$  macroblock to obtain a difference macroblock array  $D(n)$ .

Each  $8 \times 8$  luminance quadrant and associated  $8 \times 8$  chrominance block of the difference macroblock is transformed by the DCT box. Next, each transformed block is quantized by a quantization array, which, for *P*-pictures and *B*-pictures, is of constant value 16. The quantized coefficients are then symbol and entropy encoded to create the video part of the coded data stream. For *P*-pictures and *B*-pictures, all transform coefficients are treated as AC coefficients and coded by the Huffman code Table 23.3-2. In the table, the last bit *s* denotes the sign bit of the lrvcl. The coded video is combined with the motion vector for transmission to the decoder.

**Table 21.3-2.** MPEG-1 AC coefficient Huffman codes

run/level	code
0/1	1s (first)
0/1	11s (next)
0/2	0100 s
0/3	0010 1s
0/4	0000 110s
0/5	0010 0110 s
0/6	0010 0001 s
0/7	0000 0010 10s
0/8	0000 0001 1101 s
.	.
.	.
26/1	0000 0000 1101 1s
27/1	0000 0000 0001 1111 s
28/1	0000 0000 0001 1110 s
29/1	0000 0000 0001 1101 s
30/1	0000 0000 0001 1100 s
31/1	0000 0000 0001 1011 s
EOB	10
ESC	0000 01

Meanwhile, at the video encoder, the quantized coefficients are reconstructed, inverse transformed and added to the prediction array, which is generated from the previous reference frame using the motion vector to create a new reconstructed frame macroblock array  $\hat{F}(n)$ . The same reconstruction process occurs at the video decoder.

## 21.4. MPEG-2 VIDEO CODING STANDARD

MPEG-2 can be considered to be a superset of MPEG-1 in terms of generic design and additional features. MPEG-2 is forward compatible in the sense that a MPEG-2 compliant standard decoder can decode the compressed bit stream of a standard MPEG-1 encoder. This desirable property of MPEG-2 has been achieved by reliance upon a generic coding system, such as that of Figure 21.3-3, for both MPEG-1 and MPEG-2.

Appendix 3.4 lists some of the enhancements of MPEG-1 that MPEG-2 provides (12,13,16). In addition to these enhancements, MPEG-2 permits greater flexibility in the usage of control data and control parameters, e.g. customized DC coefficient precision rather than fixed value. References 12, 13 and 16 provide implementation details.

## 21.5. MPEG-4 VIDEO CODING STANDARDS

MPEG-4 comprises a group of standards for video and associated audio data<sup>1</sup>. Part 2 of the standard, called MPEG-4 Visual, was conceived in 1993 as a video standard for low bit rate video compression. During its standardization process, MPEG-4 Visual was substantially enlarged in its scope to encompass state of the art video compression technology. MPEG-4 Visual was standardized as an International Standards Organization document in 1999 (17). In a parallel effort, the International Telecommunications Union started the standardization efforts for H.264, a video compression standard for efficient low bit rate video compression.

The MPEG-4 Visual standard has adopted a “tool kit” approach to the application of video compression functionality for a wide variety of video data. This tool kit supports:

- conventional rectangular video frames as in MPEG-1 and MPEG-2;
- video objects of arbitrarily shaped regions within a scene;
- conventional still images as in JPEG and JPEG2000;
- still images including texture images
- hybrid images consisting of natural and computer-generated content;
- 2D and 3D mesh objects:

---

1. During the time that MPEG-2 was being standardized, there was a parallel effort to standardize MPEG-3 for the coding of high definition television (HDTV). This effort was abandoned when it was determined that MPEG-2 could support HDTV.

The MPEG-4 Visual tools can be invoked for video data, which is scalable over a range of spatial resolutions and video quality.

The H.264 standard has been drafted, intentionally, so as to minimize flexibility in favor of better coding performance. H.264 also has chosen to stress transmission issues for a range of communication channels and networks. Table 21.5-1 provides a summary comparison between MPEG-4 Visual and H.264 (14, p 95).

In 2001, the MPEG and VCEG expert groups agreed to develop a new video compression technology to be called *Advanced Video Coding*, (AVC), which is to be based upon the H.264 technology. This standard was published in 2003 by the joint documents H.264 and MPEG-4 Part 10 (18). The AVC standard has three profiles: Baseline Profile, which is sufficient for video telephony, video conferencing and mobile computing; Main Profile, which supports interlace scan, and is suitable for television broadcasting and video archiving; and Extended Profile, which is tailored for streaming video applications.

The video coding system presented in Figure 21.3.-3 is applicable for AVC encoding with one major change. The encoder needs to provide a choice between intra frame prediction or inter frame prediction. An application driven switch at the encoder directs the decision, and transmits the choice to the decoder. The decoder then chooses between intra frame and inter frame prediction.

The AVC standard requires complex processing to implement its functionality. Further description is beyond the scope of this book. Richardson (14) provides an excellent guide to the implementation of the AVC standard.

**Table 21.5-1.** Comparison of MPEG-4 Visual and H.264

Comparison	MPEG-4 Visual	H.264
data types	rectangular fields and frames, video objects, still images, synthetic-natural hybrids, 2D and 3D mesh objects	rectangular fields and frames
profiles	19	3
compression efficiency	medium	high
motion compensation block size	8 x 8	4 x 4
motion vector	half or quarter pixel	quarter pixel
transform	8 x 8 DCT	4 x 4 DCT approximation
deblocking filter	no	yes

## REFERENCES

1. ISO/IEC JTC1 10918-1 ITU-T Rec. T.81, *Information technology — Digital compression and coding of continuous-tone still image: Requirements and guidelines*, 1994.
2. ISO/IEC 15444-1, *JPEG2000 Image coding system — Part 1 Core coding system*, 2000.
3. A. J. Seyler, "The Coding of Visuals to Reduce Channel-Capacity Requirements." *Proc. IEE*, **109**, C, September 1962, 676-684.
4. F. W. Mounts, "A Video Encoding System Using Picture Element Replenishment," *Bell System Tech. Journal*, **48**, 7, September 1969, 2545-2555.
5. J. C. Candy, M. A. Franke, B. G. Haskell and F. W. Mounts, "Transmitting Television as Clusters of Frame-to-Frame Differences," *Bell System Tech. Journal*, **50**, 6, July-August 1971, 1889-1917.
6. B. G. Haskell, F. W. Mounts and J. C. Candy, "Interframe Coding of Videotelephone Pictures," *Proc. IEEE*, **60**, 7, July 1972, 792-800.
7. F. W. Mounts, "Frame-to-Frame Digital Processing of TV Pictures to Remove Redundancy," in *Picture Bandwidth Compression*, T. S. Huang and O. J. Tretiak, Eds., Gordon and Breach, New York, 1969, 653-673).
8. J. A. Roese and W. K. Pratt, "Theoretical Performance Models for Interframe and Hybrid Transform/DPCM Coders," *Proc. SPIE Conference on Advances in Image Transmission Techniques*, San Diego, August 1976.
9. J. A. Roese, W. K. Pratt and G. S. Robinson "Interframe Transform Coding and Predictive Coding Methods," *IEEE International Communications Conference*, San Francisco, June 1975.
10. F. Rocca, "Television Bandwidth Compression Utilizing Frame-to-Frame Correlation and Movement Compensation," in *Picture Bandwidth Compression*, T. S. Huang and O. J. Tretiak, Eds., Gordon and Breach, New York, 1969, 673-680).
11. ISO/IEC IS 11172, *Information technology — Coding of moving pictures and associated audio for digital storage media up to about 1,5 Mbit/sec.*, 1992.
12. K. R. Rao and J. J. Hwang, *Techniques and Standards for Image, Video, and Audio Coding*, Prentice-Hall, Upper Saddle River, New Jersey, 1996.
13. J. L. Mitchell, W. B. Pennebaker, C. E. Fogg and D. J. LeGall, *MPEG Video Compression Standard*, Kluwer, Boston, 1996.
14. I. E. G. Richardson, *H.264 and MPEG-4 Video Compression*, John Wiley and Sons, Hoboken, New Jersey, 2003
15. K. Kamikura and H. Watanabe, Video Coding for Digital Storage Media Using Hierarchical Intraframe Scheme," *SPIE/VCIP*, Lausanne, Switzerland, **1360**, October 1990, 1540-1550.
16. ISO/IEC 13818, *Information technology: Generic coding of moving pictures and associated information*, November 1994.
17. ISO/IEC 14496-2, *Coding of Audio-Visual Objects — Part 2: Visual*, 2001.
18. ISO/IEC 14496-10 and ITU-T Rec. H.264, *Advanced Video Coding*, 2003.

# APPENDIX 1

---

## VECTOR-SPACE ALGEBRA CONCEPTS

This appendix contains reference material on vector-space algebra concepts used in the book.

### AP1.1. VECTOR ALGEBRA

This section provides a summary of vector and matrix algebraic manipulation procedures utilized in the book. References 1 to 5 may be consulted for formal derivations and proofs of the statements of definition presented here.

**Vector.** An  $N \times 1$  column vector  $\mathbf{f}$  is a one-dimensional vertical arrangement,

$$\mathbf{f} = \begin{bmatrix} f(1) \\ f(2) \\ \vdots \\ f(n) \\ \vdots \\ f(N) \end{bmatrix}$$

(AP1.1-1)



of the elements  $f(n)$ , where  $n = 1, 2, \dots, N$ . An  $1 \times N$  row vector  $\mathbf{h}$  is a one-dimensional horizontal arrangement

$$\mathbf{h} = [h(1) \ h(2) \ \dots \ h(n) \ \dots \ h(N)] \tag{AP1.1-2}$$

of the elements  $h(n)$ , where  $n = 1, 2, \dots, N$ . In this book, unless otherwise indicated, all boldface lowercase letters denote column vectors. Row vectors are indicated by the transpose relation

$$\mathbf{f}^T = [f(1) \ f(2) \ \dots \ f(n) \ \dots \ f(N)] \tag{AP1.1-3}$$

**Matrix.** An  $M \times N$  matrix  $\mathbf{F}$  is a two-dimensional arrangement

$$\mathbf{F} = \begin{bmatrix} F(1, 1) & F(1, 2) & \dots & F(1, N) \\ F(2, 1) & F(2, 2) & \dots & F(2, N) \\ \vdots & \vdots & \dots & \vdots \\ F(M, 1) & F(M, 2) & \dots & F(M, N) \end{bmatrix} \tag{AP1.1-4}$$

of the elements  $F(m, n)$  into rows and columns, where  $m = 1, 2, \dots, M$  and  $n = 1, 2, \dots, N$ . The symbol  $\mathbf{0}$  indicates a null matrix whose terms are all zeros. A diagonal matrix is a square matrix,  $M = N$ , for which all off-diagonal terms are zero; that is,  $F(m, n) = 0$  if  $m \neq n$ . An identity matrix denoted by  $\mathbf{I}$  is a diagonal matrix whose diagonal terms are unity. The identity symbol is often subscripted to indicate its dimension:  $\mathbf{I}_N$  is an  $N \times N$  identity matrix. A submatrix  $\mathbf{F}_{pq}$  is a matrix partition of a larger matrix  $\mathbf{F}$  of the form

$$\mathbf{F} = \begin{bmatrix} \mathbf{F}_{11} & \mathbf{F}_{12} & \dots & \mathbf{F}_{1Q} \\ \vdots & \vdots & \dots & \vdots \\ \mathbf{F}_{P1} & \mathbf{F}_{P2} & \dots & \mathbf{F}_{PQ} \end{bmatrix} \tag{AP1.1-5}$$

**Identity Matrix.** A square matrix with ones along the diagonal and zeros elsewhere.

**Matrix Addition.** The sum  $\mathbf{C} = \mathbf{A} + \mathbf{B}$  of two matrices is defined only for matrices of the same size. The sum matrix  $\mathbf{C}$  is an  $M \times N$  matrix whose elements are  $C(m, n) = A(m, n) + B(m, n)$ .

**Matrix Multiplication.** The product  $\mathbf{C} = \mathbf{AB}$  of two matrices is defined only when the number of columns of  $\mathbf{A}$  equals the number of rows of  $\mathbf{B}$ . The  $M \times N$  product matrix  $\mathbf{C}$  of the matrix  $\mathbf{A}$  and the  $P \times N$  matrix  $\mathbf{B}$  is a matrix whose general element is given by

$$C(m, n) = \sum_{p=1}^p A(m, p)B(p, n) \tag{AP1.1-6}$$

**Matrix Inverse.** The matrix inverse, denoted by  $\mathbf{A}^{-1}$ , of a square matrix  $\mathbf{A}$  has the property that  $\mathbf{A}\mathbf{A}^{-1} = \mathbf{I}$  and  $\mathbf{A}^{-1}\mathbf{A} = \mathbf{I}$ . If such a matrix  $\mathbf{A}^{-1}$  exists, the matrix  $\mathbf{A}$  is said to be nonsingular; otherwise,  $\mathbf{A}$  is singular. If a matrix possesses an inverse, the inverse is unique. The matrix inverse of a matrix inverse is the original matrix. Thus,

$$[\mathbf{A}^{-1}]^{-1} = \mathbf{A} \tag{AP1.1-7}$$

If matrices  $\mathbf{A}$  and  $\mathbf{B}$  are nonsingular,

$$[\mathbf{AB}]^{-1} = \mathbf{B}^{-1}\mathbf{A}^{-1} \tag{AP1.1-8}$$

If matrix  $\mathbf{A}$  is nonsingular, and the scalar  $k \neq 0$ , then

$$[k\mathbf{A}] = \frac{1}{k}\mathbf{A}^{-1} \tag{AP1.1-9}$$

Inverse operators of singular square matrices and of nonsquare matrices are considered in Section AP1.3. The inverse of the partitioned square matrix

$$\mathbf{F} = \begin{bmatrix} \mathbf{F}_{11} & \mathbf{F}_{12} \\ \mathbf{F}_{21} & \mathbf{F}_{22} \end{bmatrix} \tag{AP1.1-10}$$

may be expressed as

$$\mathbf{F}^{-1} = \begin{bmatrix} [\mathbf{F}_{11} - \mathbf{F}_{12}\mathbf{F}_{22}^{-1}\mathbf{F}_{21}]^{-1} & -\mathbf{F}_{11}^{-1}\mathbf{F}_{12}[\mathbf{F}_{22} - \mathbf{F}_{21}\mathbf{F}_{11}^{-1}\mathbf{F}_{12}]^{-1} \\ -\mathbf{F}_{22}^{-1}\mathbf{F}_{21}[\mathbf{F}_{11} - \mathbf{F}_{12}\mathbf{F}_{22}^{-1}\mathbf{F}_{21}]^{-1} & [\mathbf{F}_{22} - \mathbf{F}_{21}\mathbf{F}_{11}^{-1}\mathbf{F}_{12}]^{-1} \end{bmatrix} \tag{AP1.1-11}$$

provided that  $\mathbf{F}_{11}$  and  $\mathbf{F}_{22}$  are nonsingular.

**Matrix Transpose.** The transpose of an  $M \times N$  matrix  $\mathbf{A}$  is a  $N \times M$  matrix denoted by  $\mathbf{A}^T$ , whose rows are the columns of  $\mathbf{A}$  and whose columns are the rows of  $\mathbf{A}$ . For any matrix  $\mathbf{A}$ ,

$$[\mathbf{A}^T]^T = \mathbf{A} \tag{AP1.1-12}$$

If  $\mathbf{A} = \mathbf{A}^T$ , then  $\mathbf{A}$  is said to be *symmetric*. The matrix products  $\mathbf{A}\mathbf{A}^T$  and  $\mathbf{A}^T\mathbf{A}$  are symmetric. For any matrices  $\mathbf{A}$  and  $\mathbf{B}$ ,

$$[\mathbf{AB}]^T = \mathbf{B}^T\mathbf{A}^T \tag{AP1.1-13}$$

If  $\mathbf{A}$  is nonsingular, then  $\mathbf{A}^T$  is nonsingular and

$$[\mathbf{A}^T]^{-1} = [\mathbf{A}^{-1}]^T \tag{AP1.1-14}$$

**Matrix Direct Product.** The left direct product of a  $P \times Q$  matrix  $\mathbf{A}$  and an  $M \times N$  matrix  $\mathbf{B}$  is a  $PM \times QN$  matrix defined by

$$\mathbf{C} = \mathbf{A} \otimes \mathbf{B} = \begin{bmatrix} B(1, 1)\mathbf{A} & B(1, 2)\mathbf{A} & \cdots & B(1, N)\mathbf{A} \\ B(2, 1)\mathbf{A} & B(2, 2)\mathbf{A} & \cdots & B(2, N)\mathbf{A} \\ \vdots & \vdots & & \vdots \\ B(M, 1)\mathbf{A} & \cdots & \cdots & B(M, N)\mathbf{A} \end{bmatrix} \tag{AP1.1-15}$$

A right direct product can also be defined in a complementary manner. In this book, only the left direct product will be employed. The direct products  $\mathbf{A} \otimes \mathbf{B}$  and  $\mathbf{B} \otimes \mathbf{A}$  are not necessarily equal. The product, sum, transpose, and inverse relations are:

$$[\mathbf{A} \otimes \mathbf{B}][\mathbf{C} \otimes \mathbf{D}] = [\mathbf{AC}] \otimes [\mathbf{BD}] \tag{AP1.1-16}$$

$$[\mathbf{A} + \mathbf{B}] \otimes \mathbf{C} = \mathbf{A} \otimes \mathbf{C} + \mathbf{B} \otimes \mathbf{C} \tag{AP1.1-17}$$

$$[\mathbf{A} \otimes \mathbf{B}]^T = \mathbf{A}^T \otimes \mathbf{B}^T \tag{AP1.1-18}$$

$$[\mathbf{A} \otimes \mathbf{B}]^{-1} = [\mathbf{A}^{-1} \otimes \mathbf{B}^{-1}] \tag{AP1.1-19}$$

**Matrix Trace.** The trace of an  $N \times N$  square matrix  $\mathbf{F}$  is the sum of its diagonal elements denoted as

$$\text{tr}\{\mathbf{F}\} = \sum_{n=1}^N F(n, n) \tag{AP1.1-20}$$

If  $\mathbf{A}$  and  $\mathbf{B}$  are square matrices,

$$\text{tr}\{\mathbf{AB}\} = \text{tr}\{\mathbf{BA}\} \tag{AP1.1-21}$$

The trace of the direct product of two matrices equals

$$\text{tr}\{\mathbf{A} \otimes \mathbf{B}\} = \text{tr}\{\mathbf{A}\}\text{tr}\{\mathbf{B}\} \tag{AP1.1-22}$$

**Vector Norm.** The Euclidean vector norm of the  $N \times 1$  vector  $\mathbf{f}$  is a scalar defined as

$$\|\mathbf{f}\| = \mathbf{f}^T \mathbf{f} \tag{AP1.1-23}$$

**Matrix Norm.** The Euclidean matrix norm of the  $M \times N$  matrix  $\mathbf{F}$  is a scalar defined as

$$\|\mathbf{F}\| = \text{tr}[\mathbf{F}^T \mathbf{F}] \tag{AP1.1-24}$$

**Matrix Rank.** An  $N \times N$  matrix  $\mathbf{A}$  is a rank  $R$  matrix if the largest nonsingular square submatrix of  $\mathbf{A}$  is an  $R \times R$  matrix. The rank of a matrix is utilized in the inversion of matrices. If matrices  $\mathbf{A}$  and  $\mathbf{B}$  are nonsingular, and  $\mathbf{C}$  is an arbitrary matrix, then

$$\text{rank}\{\mathbf{C}\} = \text{rank}\{\mathbf{AC}\} = \text{rank}\{\mathbf{CA}\} = \text{rank}\{\mathbf{ACB}\} \quad (\text{AP1.1-25})$$

The rank of the product of matrices  $\mathbf{A}$  and  $\mathbf{B}$  satisfies the relations

$$\text{rank}\{\mathbf{AB}\} \leq \text{rank}\{\mathbf{A}\} \quad (\text{AP1.1-26a})$$

$$\text{rank}\{\mathbf{AB}\} \leq \text{rank}\{\mathbf{B}\} \quad (\text{AP1.1-26b})$$

The rank of the sum of matrices  $\mathbf{A}$  and  $\mathbf{B}$  satisfies the relations

$$\text{rank}\{\mathbf{A} + \mathbf{B}\} \leq \text{rank}\{\mathbf{A}\} + \text{rank}\{\mathbf{B}\} \quad (\text{AP1.1-27})$$

**Vector Inner Product.** The inner product of the  $N \times 1$  vectors  $\mathbf{f}$  and  $\mathbf{g}$  is a scalar

$$k = \mathbf{g}^T \mathbf{f} \quad (\text{AP1.1-28})$$

where

$$k = \sum_{n=1}^N g(n)f(n) \quad (\text{AP1.1-29})$$

**Vector Outer Product.** The outer product of the  $M \times 1$  vector  $\mathbf{g}$  and the  $N \times 1$  vector  $\mathbf{f}$  is a matrix

$$\mathbf{A} = \mathbf{g}\mathbf{f}^T \quad (\text{AP1.1-30})$$

where  $A(m, n) = g(m)f(n)$ .

**Quadratic Form.** The quadratic form of an  $N \times 1$  vector  $\mathbf{f}$  is a scalar

$$k = \mathbf{f}^T \mathbf{A} \mathbf{f} \quad (\text{AP1.1-31})$$

where  $\mathbf{A}$  is an  $N \times N$  matrix. Often, the matrix  $\mathbf{A}$  is selected to be symmetric.

**Vector Differentiation.** For a symmetric matrix  $\mathbf{A}$ , the derivative of the quadratic form  $\mathbf{x}^T \mathbf{A} \mathbf{x}$  with respect to  $\mathbf{x}$  is

$$\frac{\partial[\mathbf{x}^T \mathbf{A} \mathbf{x}]}{\partial \mathbf{x}} = 2\mathbf{A} \mathbf{x} \quad (\text{AP1.1-32})$$

**AP1.2. SINGULAR-VALUE MATRIX DECOMPOSITION**

Any arbitrary  $M \times N$  matrix  $\mathbf{F}$  of rank  $R$  can be decomposed into the sum of a weighted set of unit rank  $M \times N$  matrices by a singular-value decomposition (SVD) (6–8).

According to the SVD matrix decomposition, there exist an  $M \times M$  unitary matrix  $\mathbf{U}$  and an  $N \times N$  unitary matrix  $\mathbf{V}$  for which

$$\mathbf{U}^T \mathbf{F} \mathbf{V} = \mathbf{\Lambda}^{1/2} \tag{AP1.2-1}$$

where

$$\mathbf{\Lambda}^{1/2} = \begin{bmatrix} \lambda^{1/2}(1) & \cdots & & 0 \\ \vdots & \ddots & & \vdots \\ 0 & \cdots & \lambda^{1/2}(1) & \vdots \\ & & & 0 \end{bmatrix} \tag{AP1.2-2}$$

is an  $M \times N$  matrix with a general diagonal entry  $\lambda^{1/2}(j)$  called a *singular value* of  $\mathbf{F}$ . Because  $\mathbf{U}$  and  $\mathbf{V}$  are unitary matrices,  $\mathbf{U}\mathbf{U}^T = \mathbf{I}_M$  and  $\mathbf{V}\mathbf{V}^T = \mathbf{I}_N$ . Consequently,

$$\mathbf{F} = \mathbf{U}\mathbf{\Lambda}^{1/2}\mathbf{V}^T \tag{AP1.2-3}$$

The columns of the unitary matrix  $\mathbf{U}$  are composed of the *eigenvectors*  $\mathbf{u}_m$  of the symmetric matrix  $\mathbf{F}\mathbf{F}^T$ . The defining relation is

$$\mathbf{U}^T [\mathbf{F}\mathbf{F}^T] \mathbf{U} = \begin{bmatrix} \lambda(1) & \cdots & & 0 \\ \vdots & \ddots & & \vdots \\ \mathbf{0} & \cdots & \lambda(R) & 0 \end{bmatrix} \tag{AP1.2-4}$$

where  $\lambda(j)$  are the nonzero *eigenvalues* of  $\mathbf{F}\mathbf{F}^T$ . Similarly, the columns of  $\mathbf{V}$  are the *eigenvectors*  $\mathbf{v}_n$  of the symmetric matrix  $\mathbf{F}^T\mathbf{F}$  as defined by

$$\mathbf{V}^T [\mathbf{F}^T\mathbf{F}] \mathbf{V} = \begin{bmatrix} \lambda(1) & \cdots & & 0 \\ \vdots & \ddots & & \vdots \\ \mathbf{0} & \cdots & \lambda(R) & 0 \end{bmatrix} \tag{AP1.2-5}$$

where the  $\lambda(j)$  are the corresponding nonzero eigenvalues of  $\mathbf{F}^T\mathbf{F}$ . Consistency is easily established between Eqs. AP1.2-3 to AP1.2-5. It is possible to express the matrix decomposition of Eq. AP1.2-3 in the series form

$$\mathbf{F} = \sum_{j=1}^R \lambda^{1/2}(j) \mathbf{u}_j \mathbf{v}_j^T \tag{AP1.2-6}$$

The outer products  $\mathbf{u}_j \mathbf{v}_j^T$  of the eigenvectors form a set of unit rank matrices each of which is scaled by a corresponding singular value of  $\mathbf{F}$ . The consistency of Eq. AP1.2-6 with the previously stated relations can be shown by its substitution into Eq. AP1.2-1, which yields

$$\mathbf{\Lambda}^{1/2} = \mathbf{U}^T \mathbf{F} \mathbf{V} = \sum_{j=1}^R \lambda^{1/2}(j) \mathbf{U}^T \mathbf{u}_j \mathbf{v}_j^T \mathbf{V} \tag{AP1.2-7}$$

It should be observed that the vector product  $\mathbf{U}^T \mathbf{u}_j$  is a column vector with unity in its  $j$ th elements and zeros elsewhere. The row vector resulting from the product  $\mathbf{v}_j^T \mathbf{V}$  is of similar form. Hence, upon final expansion, the right-hand side of Eq. AP1.2-7 reduces to a diagonal matrix containing the singular values of  $\mathbf{F}$ .

The SVD matrix decomposition of Eq. AP1.2-3 and the equivalent series representation of Eq. AP1.2-6 apply for any arbitrary matrix. Thus, the SVD expansion can be applied directly to discrete images represented as matrices. Another application is the decomposition of linear operators that perform superposition, convolution or general transformation of images in vector form.

### AP1.3. PSEUDOINVERSE OPERATORS

A common task in linear signal processing is to invert the transformation equation

$$\mathbf{p} = \mathbf{T} \mathbf{f} \tag{AP1.3-1}$$

to obtain the value of the  $Q \times 1$  input data vector  $\mathbf{f}$ , or some estimate  $\hat{\mathbf{f}}$  of the data vector, in terms of the  $P \times 1$  output vector  $\mathbf{p}$ . If  $\mathbf{T}$  is a square matrix, obviously

$$\hat{\mathbf{f}} = [\mathbf{T}]^{-1} \mathbf{p} \tag{AP1.3-2}$$

provided that the matrix inverse exists. If  $\mathbf{T}$  is not square, a  $Q \times P$  matrix pseudoinverse operator  $\mathbf{T}^+$  may be used to determine a solution by the operation

$$\hat{\mathbf{f}} = \mathbf{T}^+ \mathbf{p} \tag{AP1.3-3}$$

If a unique solution does indeed exist, the proper pseudoinverse operator will provide a perfect estimate in the sense that  $\hat{\mathbf{f}} = \mathbf{f}$ . That is, it will be possible to extract the vector  $\mathbf{f}$  from the observation  $\mathbf{p}$  without error. If multiple solutions exist, a pseudoinverse operator may be utilized to determine a minimum norm choice of solution. Finally, if there are no exact solutions, a pseudoinverse operator can provide a best approximate solution. This subject is explored further in the following sections.

References 5, 6 and 9 provide background and proofs of many of the following statements regarding pseudoinverse operators.

The first type of pseudoinverse operator to be introduced is the *generalized inverse*  $\mathbf{T}^-$ , which satisfies the following relations:

$$\mathbf{T}\mathbf{T}^- = [\mathbf{T}\mathbf{T}^-]^T \tag{AP1.3-4a}$$

$$\mathbf{T}^-\mathbf{T} = [\mathbf{T}^-\mathbf{T}]^T \tag{AP1.3-4b}$$

$$\mathbf{T}\mathbf{T}^-\mathbf{T} = \mathbf{T} \tag{AP1.3-4c}$$

$$\mathbf{T}^-\mathbf{T}\mathbf{T}^- = \mathbf{T}^- \tag{AP1.3-4d}$$

The generalized inverse is unique. It may be expressed explicitly under certain circumstances. If  $P > Q$ , the system of equations of Eq. AP1.3-1 is said to be *overdetermined*; that is, there are more observations  $\mathbf{p}$  than points  $\mathbf{f}$  to be estimated. In this case, if  $\mathbf{T}$  is of rank  $Q$ , the generalized inverse may be expressed as

$$\mathbf{T}^- = [\mathbf{T}^T\mathbf{T}]^{-1}\mathbf{T}^T \tag{APP1.3-5}$$

At the other extreme, if  $P < Q$ , Eq. AP1.3-1 is said to be *underdetermined*. In this case, if  $\mathbf{T}$  is of rank  $P$ , the generalized inverse is equal to

$$\mathbf{T}^- = \mathbf{T}^T[\mathbf{T}^T\mathbf{T}]^{-1} \tag{AP1.3-6}$$

It can easily be shown that Eqs. AP1.3-5 and AP1.3-6 satisfy the defining relations of Eq. AP1.3-4. A special case of the generalized inverse operator of computational interest occurs when  $\mathbf{T}$  is direct product separable. Under this condition

$$\mathbf{T}^- = \mathbf{T}_C^- \otimes \mathbf{T}_R^- \tag{AP1.3-7}$$

where  $\mathbf{T}_R^-$  and  $\mathbf{T}_C^-$  are the generalized inverses of the row and column linear operators.

Another type of pseudoinverse operator is the *least-squares inverse*  $\mathbf{T}^\$$ , which satisfies the defining relations

$$\mathbf{T}\mathbf{T}^\$\mathbf{T} = \mathbf{T} \tag{AP1.3-8a}$$

$$\mathbf{T}\mathbf{T}^\$ = [\mathbf{T}\mathbf{T}^\$]^T \tag{AP1.3-8b}$$

Finally, a *conditional inverse*  $\mathbf{T}^\#$  is defined by the relation

$$\mathbf{T}\mathbf{T}^\#\mathbf{T} = \mathbf{T} \tag{AP1.3-9}$$

Examination of the defining relations for the three types of pseudoinverse operators reveals that the generalized inverse is also a least-squares inverse, which in turn is also a conditional inverse. Least-squares and conditional inverses exist for a given

linear operator  $\mathbf{T}$ ; however, they may not be unique. Furthermore, it is usually not possible to explicitly express these operators in closed form.

The following is a list of useful relationships for the generalized inverse operator of a  $P \times Q$  matrix  $\mathbf{T}$ .

*Generalized inverse of matrix transpose:*

$$[\mathbf{T}^T]^- = [\mathbf{T}^-]^T \quad (\text{AP1.3-10})$$

*Generalized inverse of generalized inverse:*

$$[\mathbf{T}^-]^- = \mathbf{T} \quad (\text{AP1.3-11})$$

*Rank:*

$$\text{rank}\{\mathbf{T}^-\} = \text{rank}\{\mathbf{T}\} \quad (\text{AP1.3-12})$$

*Generalized inverse of matrix product:*

$$[\mathbf{T}^T \mathbf{T}]^- = [\mathbf{T}]^- [\mathbf{T}^T]^- \quad (\text{AP1.3-13})$$

*Generalized inverse of orthogonal matrix product:*

$$[\mathbf{A} \mathbf{T} \mathbf{B}]^- = \mathbf{B}^T \mathbf{T}^- \mathbf{A}^T \quad (\text{AP1.3-14})$$

where  $\mathbf{A}$  is a  $P \times P$  orthogonal matrix and  $\mathbf{B}$  is a  $Q \times Q$  orthogonal matrix.

## REFERENCES

1. F. Ayres, Jr., *Schaum's Outline of Theory and Problems of Matrices*, McGraw-Hill, New York, 1962.
2. R. E. Bellman, *Introduction to Matrix Analysis*, McGraw-Hill, New York, 1970.
3. H. G. Campbell, *An Introduction to Matrices, Vectors, and Linear Programming*, Appleton, New York, 1965.
4. C. G. Cullen, *Matrices and Linear Transformations*, Addison-Wesley, Reading, MA, 1966.
5. F. A. Graybill, *Introduction to Matrices with Applications in Statistics*, Wadsworth, Belmont, CA, 1969.



6. C. R. Rao and S. K. Mitra, *Generalized Inverse of Matrices and Its Applications*, Wiley, New York, 1971.
7. G. H. Golub and C. Reinsch, "Singular Value Decomposition and Least Squares Solutions," *Numerische Mathematik*, **14**, 1970, 403–420.
8. H. C. Andrews and C. L. Patterson, "Outer Product Expansions and Their Uses in Digital Image Processing," *American Mathematical Monthly*, **1**, 82, January 1975, 1–13.
9. A. Albert, *Regression and the Moore–Penrose Pseudoinverse*, Academic Press, New York, 1972.

## APPENDIX 2

---

### IMAGE ERROR MEASURES

In the development of image enhancement, restoration and coding techniques, it is useful to have some measure of the difference between a pair of similar images. The most common difference measure is the *mean-square error*. The mean-square error measure is popular because it correlates reasonably with subjective visual quality tests and it is mathematically tractable.

Consider a discrete  $F(j, k)$  for  $j = 1, 2, \dots, J$  and  $k = 1, 2, \dots, K$ , which is regarded as a reference image, and consider a second image  $\hat{F}(j, k)$  of the same spatial dimensions as  $F(j, k)$  that is to be compared to the reference image. Under the assumption that  $F(j, k)$  and  $\hat{F}(j, k)$  represent samples of a stochastic process, the mean-square error between the image pair is defined as

$$\xi_{MSE} = E\{|F(j, k) - \hat{F}(j, k)|^2\} \quad (\text{AP2-1})$$

where  $E\{\cdot\}$  is the expectation operator. The normalized mean-square error is

$$\xi_{NMSE} = \frac{E\{|F(j, k) - \hat{F}(j, k)|^2\}}{E\{|F(j, k)|^2\}} \quad (\text{AP2-2})$$

Error measures analogous to Eqs. AP2-1 and AP2-2 have been developed for deterministic image arrays. The least-squares error for a pair of deterministic arrays is defined as

$$\xi_{LSE} = \frac{1}{JK} \sum_{j=1}^J \sum_{k=1}^K |F(j, k) - \hat{F}(j, k)|^2 \quad (\text{AP2-3})$$

and the *normalized least-squares error* is

$$\xi_{NLSE} = \frac{\sum_{j=1}^J \sum_{k=1}^K |F(j, k) - \hat{F}(j, k)|^2}{\sum_{j=1}^J \sum_{k=1}^K |F(j, k)|^2} \tag{AP2-4}$$

Another common form of error normalization is to divide Eq. AP2-3 by the squared peak value of  $F(j, k)$ . This *peak least-squares error* measure is defined as

$$\xi_{PLSE} = \frac{\sum_{j=1}^J \sum_{k=1}^K |F(j, k) - \hat{F}(j, k)|^2}{[\text{MAX}\{F(j, k)\}]^2} \tag{AP2-5}$$

In the literature, the least-squares error expressions of Eqs. AP2-3 to AP2-5 are sometimes called mean-square error measures even though they are computed from deterministic arrays. Image error measures are often expressed in terms of a *signal-to-noise ratio* (SNR) in decibel units, which is defined as

$$\text{SNR} = -10 \log_{10}\{\xi\} \tag{AP2-6}$$

A common criticism of mean-square error and least-squares error measures is that they do not always correlate well with human subjective testing. In an attempt to improve this situation, a logical extension of the measurements is to substitute processed versions of the pair of images to be compared into the error expressions. The processing is chosen to map the original images into some perceptual space in which just noticeable differences are equally perceptible. One approach is to perform a transformation on each image according to a human visual system model such as that presented in Chapter 2.

## APPENDIX 3

---

# IMAGE AND VIDEO COMPRESSION STANDARDS DEVELOPMENT

This appendix summarizes the development of several widely used image and video compression standards.

### AP3.1 JPEG STILL IMAGE COMPRESSION STANDARD

In 1982, a group of digital photographic experts was formed under the auspices of the International Standards Organization ISO/TC97/SC2 WG8 with the intention of creating a standard for still image digital coding. The ISO group merged in 1986 with the CCITT SGV111 Special Rapporteurs Group. The merged group adopted the informal group name Joint Photographic Expert Group (JPEG). Definition of the JPEG baseline standard was begun in 1989. In 1993, the international standard was adopted with the publication of ISO/IEC 10918-1 ITU-T Rec. T.84, Information Technology - Digital Compression and Coding of Continuous Tone Still Images.

The JPEG standard specifies four coding modes:

*Sequential Lossless* — Single scan compression based upon predictive entropy encoding such that the reconstructed image is an exact replica of the source image.

*Sequential Lossy* — Single scan compression based upon Discrete Cosine Transform (DCT) Huffman or arithmetic entropy encoding such that the reconstructed image is a close approximation to the source image.

*Progressive* — DCT-based compression and decompression of a source image in multiple scans such that each successive scan results in a better quality reconstruction.

*Hierarchical* — DCT-based or predictive-based encoding such that a source image is compressed at multiple resolutions to accommodate different resolution displays.

The JPEG standard specifies a baseline operation in which Huffman entropy encoding is supported.

### AP3.2. JPEG2000 STILL IMAGE COMPRESSION STANDARD

JPEG2000 is a standard for still image compression<sup>1</sup>. It has been jointly developed by the International Organization for Standardization (ISO) and the International Electrotechnical Commission (IEC). The standardization effort was begun with a ISO/IEC New Work Item Proposal seeking the development of a wavelet transform based image compression system<sup>2</sup>. The standard was published in the year 2000.

The functionality of JPEG2000 has been specified by the following set of desired features<sup>3</sup>.

*Superior low bit-rate performance*

*Continuous-tone and bi-level compression*

*Progressive transmission by pixel accuracy and resolution*

*Lossless and lossy compression*

*Random code stream access and processing*

*Robustness to bit errors*

*Sequential build-up capability*

---

1. *New Work Item Proposal: JPEG2000 Image Coding System*, Technical Report N390, ISO/IEC JTC1/SC29/WG1, June 1996.

2. ISO/IEC 15444-1, *Information Technology — JPEG2000 Image Coding System — Part 1: Core Coding System*, 2000.

3.D. S. Taubman and M. W. Marcellin, *JPEG2000 Image Compression Fundamentals, Standards and Practice*, Springer, New York, 2002.

### AP3.3. MPEG-1 VIDEO COMPRESSION STANDARD

In October 1988, an ad hoc group of digital audio and video experts was formed under the auspices of the International Standards Organization (ISO) and the International Electrotechnical Commission (IEC) with the intention of developing a standard for CD-ROM storage. In November of 1992, the MPEG-1 standard was published as document IS 11172 in three parts: Part 1 Systems, Part 2 Video and Part 3 Audio. MPEG-1 Video was deliberately crafted so as to not specify the encoding process. It only specifies the syntax and semantics necessary to define the compressed video data stream and the inherent decoder signal processing. This design strategy permits the development of relatively low complexity MPEG-1 decoders without placing implementation restrictions on the design of encoders.

### AP3.4. MPEG-2 VIDEO COMPRESSION STANDARD

The following is a list of enhancements to MPEG-1 that are supported in MPEG-2.

**coding rate** MPEG-1 provides a coding bit rate of up to about 1.9 Mbps, while MPEG-2 supplies coding up to 100 Mbps.

**picture size** MPEG-1 is usually used for encoding pictures of 288 rows and 352 columns at 24 or 30 frames per second. MPEG-2 supports  $288 \times 352$ ,  $576 \times 720$ ,  $1152 \times 1440$  and  $1152 \times 1920$ .

**interlace video scanning** MPEG-2 supports interlace scanning, which is the scan mode for commercial television systems. MPEG-1 only accommodates progressive scanning.

**chrominance sampling** MPEG-1 supports 4:2:0 chrominance sampling while MPEG-2 handles 4:2:0, 4:2:2 and 4:4:4 chrominance sampling.

**profiles and levels** MPEG-2 provides five implementation profiles with up to four levels in each profile. MPEG-1 provides none.

### AP3.5. MPEG-4 VIDEO COMPRESSION STANDARDS

Richardson<sup>1</sup> provides a clear description of the development path of the MPEG-4 standards.

---

1. I. E. G. Richardson, *H.264 and MPEG-4 Video Compression*, John Wiley and Sons, Hoboken New Jersey, 2003.



# APPENDIX 4

---

## HUFFMAN CODING EXAMPLE

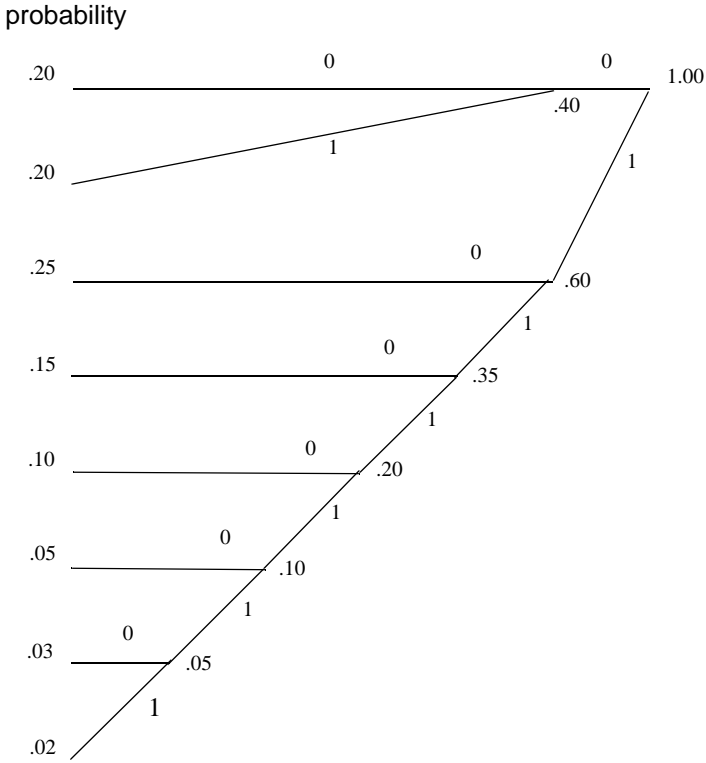
A Huffman code can be generated by the development of a code tree for a given set of symbols and their probabilities of occurrence. The following is an example of code tree development for  $Q = 8$  symbols.

- Step 1: List the  $Q$  symbols as tree nodes in descending probability order.
- Step 2: Combine the two nodes with the lowest probabilities to create a replacement node whose probability is the sum of its branch probabilities.
- Step 3: Repeat Step 2 for the remaining  $Q - 1$  nodes.
- Step 4: Continue the combination processing until there remains a single root node.
- Step 5: Label all branches of the nodes with bit 0 or 1 on the upper path and bit 1 or 0 on the lower path.
- Step 6: Concatenate all branch codes from the root node to each symbol to obtain the symbol code word.

The following figure is the code tree for the example. The table lists the Huffman code assignment for the example.



**Huffman code tree example**



symbol	probability	code	length
1	0.200	00	2
2	0.200	10	2
3	0.250	01	2
4	0.150	011	3
5	0.100	0111	4
6	0.050	01111	5
7	0.030	011111	6
8	0.020	111111	6

# ANNEX 1

---

## PIXELSOFT WEB SITE DOWN LOADABLE FILES

This annex contains a listing of down loadable files from the PixelSoft, Inc. web site pixelsoft.com. These files support software development for the CRC Press textbook *Introduction to Digital Image Processing* by William K. Pratt.

### PDF FILE FORMAT DOCUMENTATION

- PIKS Image Processing Software Tutorial
- PixelSoft PIKS Scientific API Programmer's Manual
- PIKSTool Scientific User's Manual

### IMAGE DATABASES

- PixelSoft Source Images In PIKS File Format.
- PixelSoft Source Images In TIFF File Format
- Selected TIFF Images from *Introduction to Digital Image Processing*

## **IMAGE PROCESSING SOFTWARE PACKAGES**

PixelSoft PIKS API Software

PixelSoft PIKSTool Software

## **DEMONSTRATION EXAMPLES**

PIKS API Examples

PIKSTool GUI Examples

PIKSTool Chain Examples

MATLAB Examples

## **C LANGUAGE EXECUTABLE PROGRAMMING EXERCISES**

PIKS API Exercises

## **C LANGUAGE SOURCE PROGRAMMING EXERCISES<sup>1</sup>**

PIKS API Exercises

PIKSTool Graphical User Interface Exercises

PIKSTool Chain Exercises

MATLAB Exercises

---

1. Software source files available to course instructors.

## ANNEX 2

---

### PIKS API IMAGE PROCESSING EXAMPLE

This appendix contains an example of an unsharp mask operation on a monochrome image using the PIKS application program interface software.

Equation 10.4-2 defines the unsharp mask operation on a monochrome source image  $F(j, k)$  as

$$G(j, k) = \frac{c}{2c-1}F(j, k) - \frac{1-c}{2c-1}F_L(j, k)$$

where  $c$  is a weighting constant and  $F_L(j, k)$  is low pass filtered version of the source image obtained by convolution of the source image with a low pass filter impulse response array.

The PIKS version of the unsharp mask operator is given by

$$G(j, k) = a_1F(j, k) + a_2F_L(j, k) + b$$

where  $a_1$  and  $a_2$  are weighting constants and  $b$  is a bias factor.

**AN2.1. UNSHARP MASK PIKS API C PROGRAM LISTING**

The following is a C program listing of the unsharp masking operation on a monochrome image with  $a_1 = 3.0$ ,  $a_2 = -2.0$ ,  $b = 0.0$  and the impulse response array is a 5x5 uniform array.

```

/** Program:
***
***     example_unsharp_mask.c
***
*** Function:
***
***     Apply unsharp masking to a monochrome image.
***
*** Operational steps:
***
***     Read monochrome source image file information.
***     Allocate source image
***     Read source image from file
***     Display source image
***     Perform unsharp making on source image
***     Display destination image
***
*** History:
***
***     Created 4 June 2010           W. K. Pratt
***     Revised 17 February 2011    WKP
***/

/*
** Includes
*/
#include <stdio.h>
#include <stdlib.h>
#include <piks.h>

/*
** Defines
*/
#define ND_PRECISION 8
#define RD_PRECISION 32
/*

```

```

** Main
*/
main(int argc, char **argv)
{
/*
** Local entities
*/
    char          err_name[] = "piks_errors";
    char          filename[256];
    char          hdr_name[256];
    char          datafile[256];
    void          *tnWindow1, *tnWindow2;
    FILE          *in_file;

/*
** PIKS entities
*/
    Idnimage      nSrcND, nDstND, nDstRD;
    Idnimage      nDisplay1, nDisplay2;
    Idnnbhood     nImpulse;
    Ipnerror      nErrorFile;
    Ipsobject     snObject;
    Ipsparameter_arith stAbove, stBelow, stWidth, stLevel;
    Ipfloat       rWeight1 = 3.0;
    Ipfloat       rWeight2 = -2.0;
    Ipfloat       rBias = 0.0;
    Ipfloat       rMin;
    Ipfloat       rMax;
    Ipfloat       rAbove = 255.0;
    Ipfloat       rBelow = 0.0;
    Ipfloat       rWidth, rLevel;
    Ipuint        uSrcWidth, uSrcHeight, uSrcDept,
                 uSrcTime, uSrcBands;
    Ipuint        uSrcPrecision, uSrcType,
                 uSrcOrganization;
    Ipuint        uX, uY;

/*
** Open PIKS session
*/
    if((nErrorFile = (Ipnerror)fopen(err_name, "w")) == NULL)

```

```

        exit(1);

IvOpenPIKS(nErrorFile);

/*
** Read source image header file information
*/
if (argc == 1) {
printf("Enter ND monochrome image filename (brain) \n");
scanf("%s", filename);
}
else {
    printf (filename, "%s", argv[1]);
    printf ("Image File: %s %s\n", filename, argv[1]);
}
sprintf(hdr_name,"%s.header", filename);

if ((in_file = fopen(hdr_name, "r")) == NULL) {
    fprintf(stderr, "Could not open %s\n", hdr_name);
    return 0;
}
fscanf(in_file,"%d%d%d%d%d%d", &uSrcWidth, &uSrcHeight,
    &uSrcDepth, &uSrcTime, &uSrcBands,&uSrcPrecision,
    &uSrcType, &uSrcOrganization);

fscanf(in_file, "%s", datafile);
fclose(in_file);

printf("image width = %u\n", uSrcWidth);
printf("image height = %u\n", uSrcHeight);
printf("image bands = %u\n", uSrcBands);
printf("image precision = %u\n", uSrcPrecision);

if(uSrcBands != 1) {
    printf("not a monochrome image\n");
    exit(1);
}
if(uSrcPrecision != ND_PRECISION) {
    printf("not an 8-bit unsigned integer image\n");
    exit(1);
}

```

```

uX = uSrcWidth;
uY = uSrcHeight;

/*
** Allocate images
*/
nSrcND = InPrepareMonochromeImage(uX,uY,
    IDATA_TYPE_INTERNAL_ND,ND_PRECISION);
nDstND = InPrepareMonochromeImage(uX,uY,
    IDATA_TYPE_INTERNAL_ND, ND_PRECISION);
nDstRD = InPrepareMonochromeImage(uX,uY
    IDATA_TYPE_INTERNAL_RD, RD_PRECISION);

/*
** Read source image file
*/
InInputImageFile(filename, nSrcND);

/*
** Display source image
*/
tnWindow1 = ItnOpenTitledWindow(uX, uY, uSrcBands, 1, 1,
    filename);
nDisplay1 = InAllocateDisplayImage(tnWindow1);

printf("Source image \n");
printf("Press any key in window to continue \n");

InMonochromeDisplay(nSrcND, nDisplay1);

/*
** Extract impulse response array from repository
*/
nImpulse = InReturnRepositoryId(IR_UNIFORM_5x5,
    IREPOSITORY_IMPULSE);

/*
** Perform unsharp masking
*/
InUnsharpMask(nSrcND, nDstRD, nImpulse, rWeight1, rWeight2,
    rBias);

InConvertImageDatatype(nDstRD, nDstND);
/*

```



```

** Display destination image
*/
tnWindow2 = ItnOpenTitledWindow(uX, uY, uSrcBands,
    uX+30, 1, unsharp mask");
nDisplay2 = InAllocateDisplayImage(tnWindow2);

printf("Destination image \n");
printf("Press any key in window to continue \n");

IvExtrema(nDstRD, &rMin, &rMax, IPROCESS_MODE_0, -1, NULL);
printf("W(x,y) = %5.2f to %5.2f\n", rMin, rMax);

stAbove.trArithFloat = &rAbove;
stBelow.trArithFloat = &rBelow;
stWidth.trArithFloat = &rWidth;
stLevel.trArithFloat = &rLevel;

rWidth = 255.0;
rLevel = (float)(rWidth/2.0);

InWindowLevel(nDstRD, nDstRD, stAbove, stBelow,
    stWidth, stLevel);

InConvertImageDatatype(nDstRD, nDstND);

InMonochromeDisplay(nDstND, nDisplay2);

printf("Press any key in window to continue \n");

IvEventDelay(tnWindow2);
/*
** Check for warnings
*/
fclose(nErrorFile);
if(IbErrorTest())
printf("Warning exists, check log\n");

/*
** Close PIKS session
*/
snObject.nImage = nDisplay1;

```

```
IvDeallocateDataObject (snObject) ;
IvCloseWindow (tnWindow1) ;

snObject.nImage = nDisplay2;
IvDeallocateDataObject (snObject) ;
IvCloseWindow (tnWindow2) ;

IvClosePIKS () ;
printf ("Example completed\n") ;
return 1 ;
}
```

## AN2.2. UNSHARP MASK PIKS API OPERATION

The following screen dump shows the result of window/level scaling of an unsharp masking operation on a monochrome image.



## ANNEX 3

---

# PIKSTOOL GUI IMAGE PROCESSING EXAMPLE

This appendix contains an example of an unsharp mask operation on a monochrome image using the PIKSTool graphical user interface software.

### AN3.1. UNSHARP MASK PIKSTool COMMAND SCRIPT

The following is a script for the unsharp mask operation using the PIKSTool GUI.

1. From the File option, select Open Input Image, choose the image “brain,” and click Open to view the source image in Screen 1.
2. From the Operators option, select Enhancement and unsharp\_mask to view Screen 2.
3. In the Unsharp Mask dialog box, select From Repository. Leave unchanged the default values (3, -2, 0) of the First Weight Factor, Second Weight Factor and Bias Factor, and click OK to view Screen 3.
4. In the Repository Impulse Response Kernels pull down window, select the “088 UNIFORM 5x5” object and click OK to view the unsharp mask image in Screen 4.
5. From the Operators option, select Point and window\_level to view Screen 5.

6. In the Window Level dialog box, set the Above Window and Below Window clip values to 255 and 0, respectively. Set the Width to 255, set the level to 127 and click OK to view Screen 6.
7. In the Select Source Image dialog box, leave unchanged the default of Destination, and click OK to view the output image in Screen 7.

### **AN3.2. UNSHARP MASK PIKSTool GUI OPERATION**

The following screen dumps show the results of the unsharp masking operation on a monochrome image.





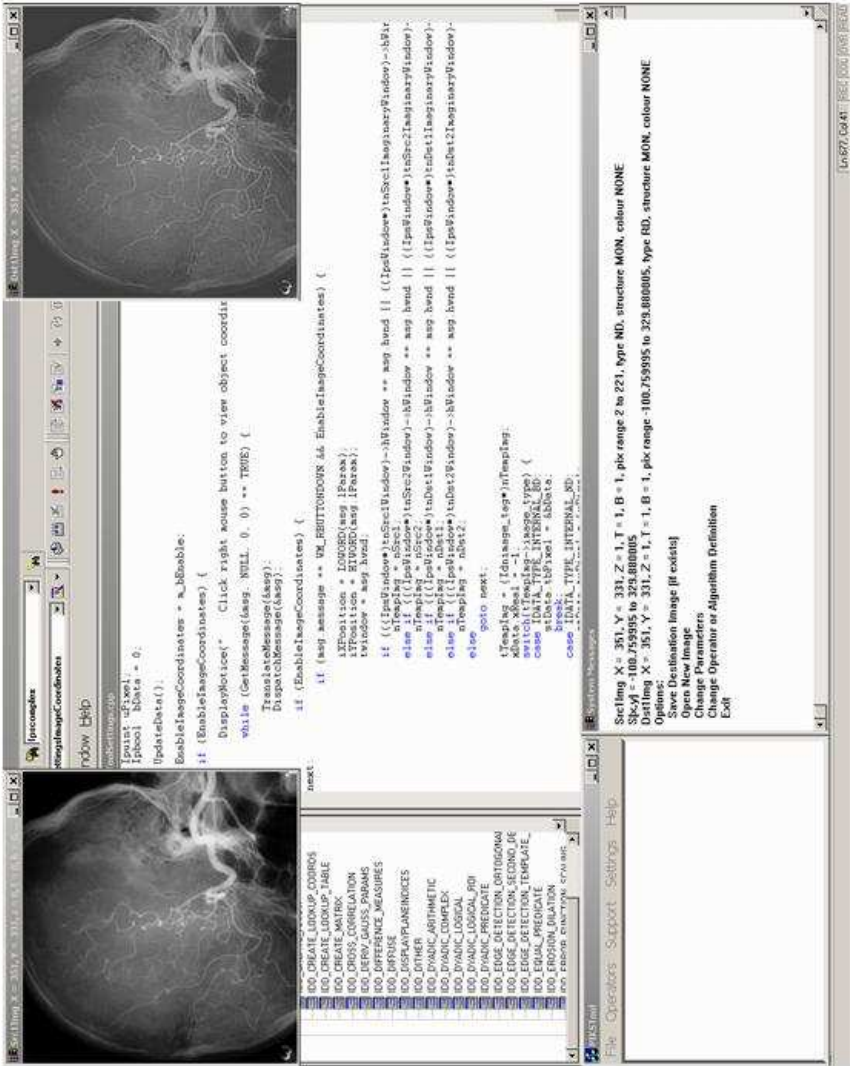
## Screen 3

The screenshot displays a software development environment with three main components:

- Code Editor:** Contains C++ code for handling mouse clicks to view object coordinates. The code includes a loop that checks for a right mouse button click and then calls `TranslateMessage` and `DispatchMessage`. A `while` loop handles the `WM_LBUTTONDOWN` message by calculating the mouse position and displaying coordinates in a message box.
- Console Window:** Lists a menu of image processing operations:
  - 100. CREATE LOOKUP COORDS
  - 100. CREATE LOOKUP TABLE
  - 100. CREATE MATRIX
  - 100. CROSS CORRELATION
  - 100. DERRIV\_GAUSS\_PARAMS
  - 100. DIFFERENCE\_MEASURES
  - 100. DIFFUSE
  - 100. DOWNSAMPLE
  - 100. EDGE\_ARITHMETIC
  - 100. DYNAMIC\_COMPLEX
  - 100. DYNAMIC\_LOGICAL
  - 100. DYNAMIC\_LOGICAL\_ROI
  - 100. DYNAMIC\_PREDICATE
  - 100. EDGE\_DETECTION\_ORIGINAL
  - 100. EDGE\_DETECTION\_SECOND\_DE
  - 100. EDGE\_DETECTION\_TEMPLATE
  - 100. EQUAL\_PREDICATE
  - 100. ERASE\_STRUCTURE
- Dialog Box:** A file selection dialog titled "Open" with the file name `081.DD.CAR_546_HORIZON.TAL`. It features "OK" and "Cancel" buttons.



Screen 4



Screen 5

The screenshot displays a software development environment with several components:

- Code Editor:** Contains C++ code for a window class. The code includes a constructor, a `displayNotice` method, and a `while` loop that checks for mouse clicks on a right mouse button to view object coordinates. It also includes a `next` method with a menu of options like `000_CREATE_LOOKUP_COORDS`, `000_CREATE_MATRIX`, `000_CROSS_CORRELATION`, etc.
- Console Window:** Shows the output of the program, including the text "Click right mouse button to view object coordinates" and "The object coordinates are: (0, 0)".
- Dialog Box:** A "Window Level" dialog box is open, allowing the user to adjust the "Window scaling of an image". It has input fields for "Above Window", "Below Window", and "Level (FPS)", along with "OK" and "Cancel" buttons.
- Image Viewers:** Two windows at the top show a grayscale image of a brain scan.







# ANNEX 4

---

## PIKSTOOL CHAIN IMAGE PROCESSING EXAMPLE

This annex contains an example of an unsharp mask operation on a monochrome image using the PIKSTool Chain command string interpretive software.

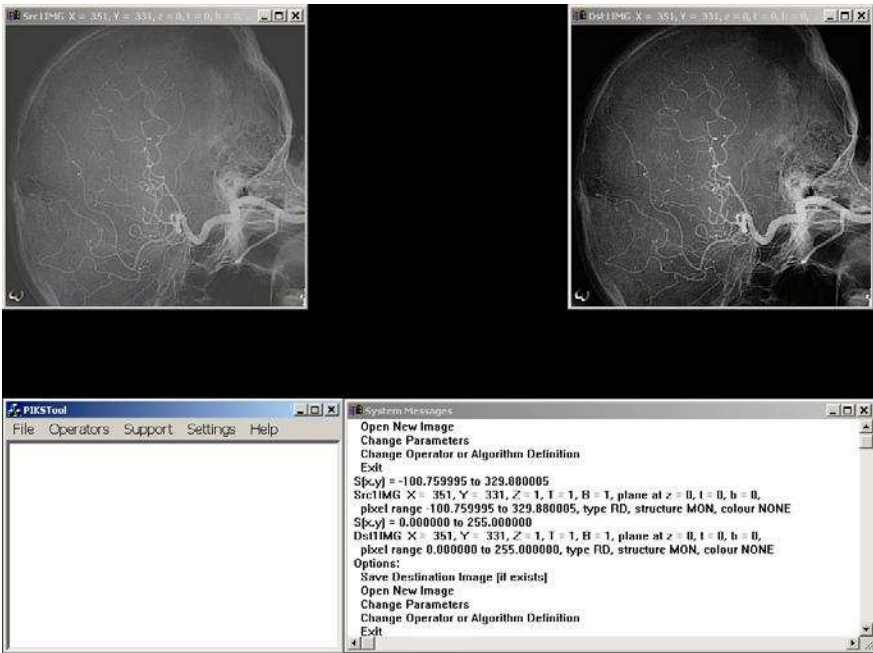
### AN4.1. UNSHARP MASK PIKSTOOL CHAIN COMMAND STRING LISTING

The following section provides a command string listing of the unsharp masking operation on a monochrome image executed with the PIKSTool Chain software.

### AN4.2. UNSHARP MASK PIKSTOOL CHAIN OPERATION

The following screen dump shows the before and after result of the unsharp masking operation on a monochrome image.

```
!PIKSTool Chain example unsharp
!Test Image Filename: brain
!Convert ND to SD
convert_image_datatype (3, Src1IMG, New)
!Multiply SD image by 3
monadic_arithmetic (3, 7, DstIMG, New)
!Save result as temporary image
save_image (Wrk1.header)
!Convolve 3xSD image with UNIFORM_5x5 array and
enclosed_array convolution option
convolve_2d (2, 88, None, DstIMG, New)
!Divide convolved image by 25
Pause
monadic_arithmetic (25, 3, DstIMG, New)
!and multiply convolved image by 2
monadic_arithmetic (2, 7, DstIMG, New)
!Subtract convolved and scaled image from 3xSD image
dyadic_arithmetic (9, Wrk1.header, DstIMG, New)
Pause
!Clip differenced image to original range
window_level (255, 0, 255, 127)
```







# ANNEX 5

---

## MATLAB IMAGE PROCESSING EXAMPLE

This annex contains an example of an unsharp mask operation on a monochrome image using the MATLAB command string interpretive software.

### AN5.1. UNSHARP MASK MATLAB COMMAND STRING LISTING

The following section provides a command string listing of the unsharp masking operation on a monochrome image executed with the MATLAB software<sup>1</sup>.

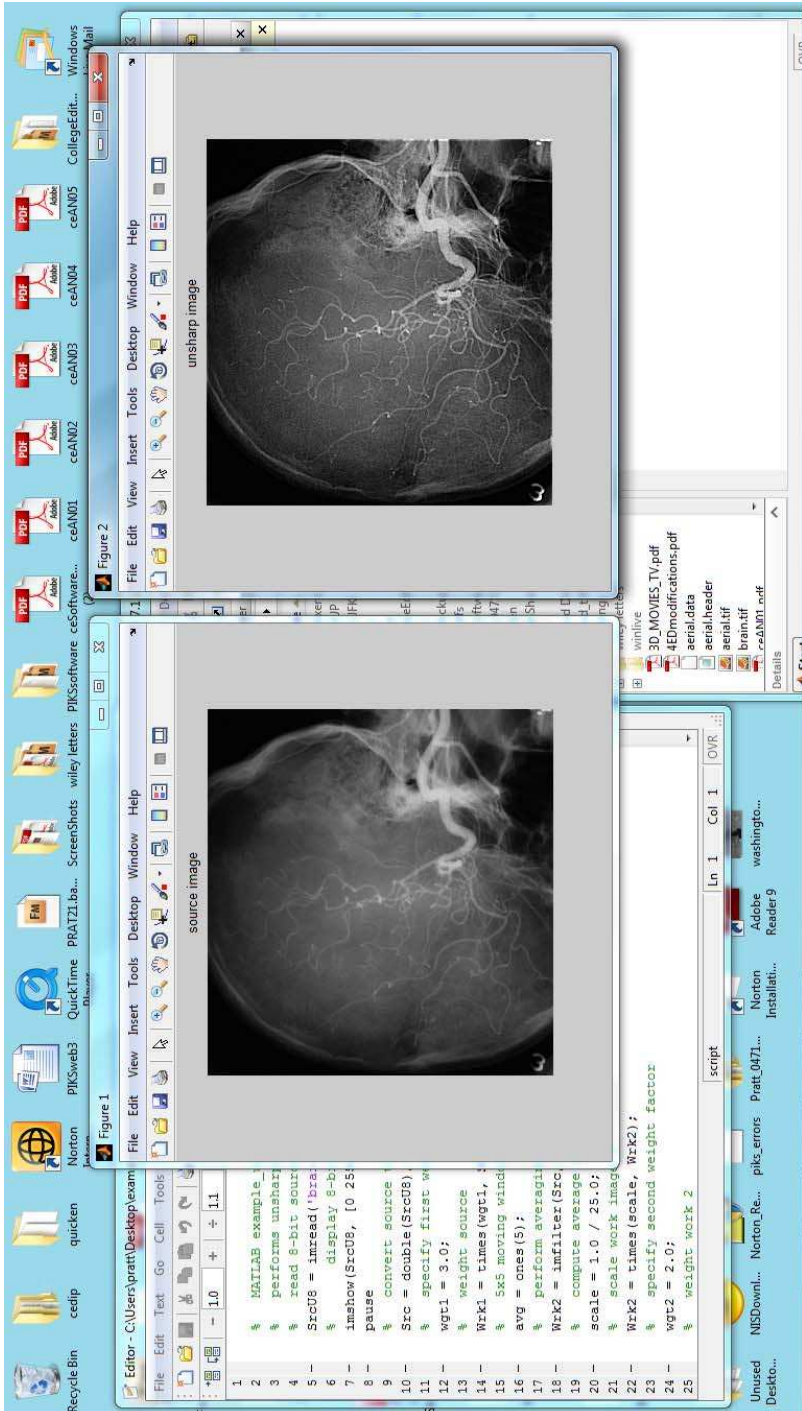
### AN5.2. UNSHARP MASK MATLAB OPERATION

The following screen dump shows the before and after result of the unsharp masking operation on a monochrome image executed with the MATLAB software.

---

1.The MATLAB command `figure` places the destination image over the source image. The two images must be separated manually to view both images simultaneously.

```
% MATLAB example_unsharp
% performs unsharp mask sharpening on a monochrome image
% read 8-bit source
SrcU8 = imread('brain.tif');
% display 8-bit source
imshow(SrcU8, [0 255]); title('source image');
pause
% convert source to double
Src = double(SrcU8);
% specify first weight factor
wgt1 = 3.0;
% weight source
Wrk1 = times(wgt1, Src);
% 5x5 moving window average array
avg = ones(5);
% perform averaging on source
Wrk2 = imfilter(Src, avg);
% compute average array scale factor
scale = 1.0 / 25.0;
% scale work image 2
Wrk2 = times(scale, Wrk2);
% specify second weight factor
wgt2 = 2.0;
% weight work 2
Wrk2 = times(wgt2, Wrk2);
% form destination
Dst = imsubtract(Wrk1, Wrk2);
% convert destination to 8-bit with 0 to 255 clipping
DstU8 = uint8(Dst);
% display 8-bit destination
imshow(SrcU8); title('source image'),
figure, imshow(DstU8); title('unsharp image');
```





# BIBLIOGRAPHY

---

- T. Acharya and A. K. Ray, *Image Processing Principles and Applications*, John Wiley and Sons, Hoboken, NJ, 2005.
- T. Acharya and P-S Tsai, *JPEG2000 Standard for Image Compression: Concepts, Algorithms and VLSI Architectures*, John Wiley and Sons, Hoboken, NJ, 2004.
- J. K. Aggarwal, R. O. Duda and A. Rosenfeld, Editors, *Computer Methods in Image Analysis*, IEEE Press, New York, 1977.
- N. Ahmed and K. R. Rao, *Orthogonal Transforms for Digital Signal Processing*, Springer-Verlag, New York, 1975.
- J. P. Allebach, *Digital Halftoning*, Vol. MS154, SPIE Press, Bellingham, WA, 1999.
- H. C. Andrews, with W. K. Pratt and K. Caspari (Contributors), *Computer Techniques in Image Processing*, Academic Press, New York, 1970.
- H. C. Andrews and B. R. Hunt, *Digital Image Restoration*, Prentice Hall, Englewood Cliffs, NJ, 1977.
- H. C. Andrews, Editor, *Digital Image Processing*, IEEE Press, New York, 1978.
- G. R. Arce, *Nonlinear Signal Processing*, Wiley-Interscience, Hoboken, NJ, 2005.
- T. Acharya and A. K. Ray, *Image Processing Principles and Applications*, John Wiley and Sons, New York, 2005.
- D. H. Ballard and C. M. Brown, *Computer Vision*, Prentice Hall, Englewood Cliffs, NJ, 1982.
- I. Bankman, Editor, *Handbook of Medical Imaging*, Academic Press, New York, 2000.
- G. A. Baxes, *Digital Image Processing: Principles and Applications*, John Wiley and Sons, New York, 1994.
- R. Bernstein, Editor, *Digital Image Processing for Remote Sensing*, IEEE Press, New York, 1978.
- J. C. Bezdek, Editor, *Fuzzy Models and Algorithms for Pattern Recognition and Image Processing*, Kluwer, Norwell, MA, 1999.
- V. Bhaskaran and K. Konstantinides, *Image and Video Compression Standards, Algorithms and Architectures*, Kluwer, 1997.
- H. Bischof and W. Kropatsch, *Digital Image Analysis*, Springer-Verlag, New York, 2000.
- A. Bovik, Editor, *Handbook of Image and Video Processing*, Academic Press, New York, 2000.
- R. N. Bracewell, *Two-Dimensional Imaging*, Prentice Hall, Englewood Cliffs, NJ, 1995.
- J. M. Brady, Editor, *Computer Vision*, North-Holland, Amsterdam, 1981.
- E. O. Brigham, *The Fast Fourier Transform and its Applications*, Prentice Hall, Upper Saddle River, NJ, 1988.

- H. E. Burdick, *Digital Imaging: Theory and Applications*, Wiley, New York, 1997.
- W. Burger and M. J. Burge, *Digital Image Processing: An Algorithmic Introduction using Java*, Springer, Berlin, 2007.
- K. R. Castleman, *Digital Image Processing*, Prentice Hall, Upper Saddle River, NJ, 1996.
- R. Chellappa and A. A. Sawchuk, *Digital Image Processing and Analysis, Vol. 1, Digital Image Processing*, IEEE Press, New York, 1985.
- E. R. Davies, *Machine Vision: Theory, Algorithms, Practicalities, Third Edition*, Morgan Kaufman, New York, 2004.
- C. Demant, B. Streicher-Abel and P. Waszlewitz, *Industrial Image Processing*, Springer-Verlag, New York, 1999.
- G. G. Dodd and L. Rossol, Editors, *Computer Vision and Sensor-Based Robots*, Plenum Press, New York, 1979.
- G. Dougherty, *Digital Image Processing for Medical Applications*, Cambridge University Press, Cambridge, 2009.
- E. R. Dougherty and C. R. Giardina, *Image Processing Continuous to Discrete, Vol. 1, Geometric, Transform and Statistical Methods*, Prentice Hall, Englewood Cliffs, NJ, 1987.
- E. R. Dougherty and C. R. Giardina, *Matrix-Structured Image Processing*, Prentice Hall, Englewood Cliffs, NJ, 1987.
- E. R. Dougherty, *Introduction to Morphological Image Processing*, Vol. TT09, SPIE Press, Bellingham, WA, 1992.
- E. R. Dougherty, *Morphological Image Processing*, Marcel Dekker, New York, 1993.
- E. R. Dougherty, *Random Processes for Image and Signal Processing*, Vol. PM44, SPIE Press, Bellingham, WA, 1998.
- E. R. Dougherty, Editor, *Electronic Imaging Technology*, Vol. PM60, SPIE Press, Bellingham, WA, 1999.
- E. R. Dougherty and J. T. Astola, Editors, *Nonlinear Filters for Image Processing*, Vol. PM59, SPIE Press, Bellingham, WA, 1999.
- R. O. Duda and P. E. Hart, *Pattern Classification and Scene Analysis*, Wiley-Interscience, New York, 1973.
- R. O. Duda, P. E. Hart and D. G. Stork, *Pattern Classification, Second Edition*, John Wiley and Sons, New York, 2001.
- M. J. B. Duff, Editor, *Computing Structures for Image Processing*, Academic Press, London, 1983.
- N. Efford, *Digital Image Processing: A Practical Introduction Using Java*, Addison Wesley, Reading MA, 2000.
- M. P. Ekstrom, Editor, *Digital Image Processing Techniques*, Academic Press, New York, 1984.
- H. Elias and E. R. Weibel, *Quantitative Methods in Morphology*, Springer-Verlag, Berlin, 1967.
- O. W. E. Gardner, Editor, *Machine-Aided Image Analysis*, Institute of Physics, Bristol and London, 1979.
- M. Ghanbari, *Video Coding: An Introduction to Standard Codecs*, IEEE Press, 1999.

- M. Ghanbari, *Standard Codecs: Image Compression to Advanced Video Coding, Third Edition*, 2011.
- R. C. Gonzalez and P. Wintz, *Digital Image Processing, Second Edition*, Addison-Wesley, Reading, MA, 1987.
- R. C. Gonzalez and R. E. Woods, *Digital Image Processing, Second Edition*, Prentice Hall, Upper Saddle River, NJ., 2002.
- R. C. Gonzalez, R. E. Woods (Contributor) and R. C. Gonzalez, *Digital Image Processing, Third Edition*, Addison-Wesley, Reading, MA, 1992.
- R. C. Gonzalez, R. E. Woods and S. L. Eddins, *Digital Image Processing Using MATLAB*, Prentice Hall, Englewood Cliffs, NJ, 2003.
- A. A. Goshtasby, *2-D and 3-D Image Registration*, Wiley-Interscience, Hoboken NJ, 2005.
- J. Goutsias and L. M. Vincent, Editors, *Mathematical Morphology and Its Applications to Image and Signal Processing*, Kluwer, Norwell, MA, 2000.
- A. Grasselli, *Automatic Interpretation and Classification of Images*, Academic Press, New York, 1969.
- E. L. Hall, *Computer Image Processing and Recognition*, Academic Press, New York, 1979.
- A. R. Hanson and E. M. Riseman, Editors, *Computer Vision Systems*, Academic Press, New York, 1978.
- R. M. Haralick and L. G. Shapiro (Contributor), *Computer and Robot Vision*, Addison-Wesley, Reading, MA, 1992.
- R. M. Haralick, *Mathematical Morphology: Theory and Hardware*, Oxford Press, Oxford, 1998.
- B. Haskell, A. Puri and A. Netravali, *Digital Video: An Introduction to MPEG-2*, Chapman and Hall, 1996.
- L. Harte, *Introduction to MPEG: MPEG-1, MPEG-2 and MPEG-4*, Althos Publishing, 2006.
- H. J. A. M. Heijmans, *Morphological Image Operators*, Academic Press, Boston, 1994.
- G. C. Holst, *Sampling, Aliasing and Data Fidelity*, Vol. PM55, SPIE Press, Bellingham, WA.
- S. Haykin, Editor, *Blind Deconvolution*, Prentice-Hall, Englewood Cliffs, NJ, 1991.
- D. T. Hoang and J. S. Vitter, *Efficient Algorithms for MPEG Video Compression*, Wiley-Interscience, Hoboken, NJ, 2002.
- B. K. P. Horn, *Robot Vision*, MIT Press, Cambridge, MA, 1986.
- T. S. Huang, Editor, *Topics in Applied Physics: Picture Processing and Digital Filtering*, Vol. 6, Springer-Verlag, New York, 1975.
- T. S. Huang, *Image Sequence Processing and Dynamic Scene Analysis*, Springer-Verlag, New York, 1983.
- B. Jahne, *Practical Handbook on Image Processing for Scientific Applications*, CRC Press, Boca Raton, FL, 1997.
- B. Jahne and B. Jahne, *Digital Image Processing: Concepts, Algorithms and Scientific Applications, Fourth Edition*, Springer-Verlag, Berlin, 1997.
- B. Jahne et al., Editors, *Handbook of Computer Vision and Applications, Package Edition*, Academic Press, London, 1999.



- B. Jahne and H. Haubecker, *Computer Vision and Applications*, Academic Press, New York, 2000.
- B. Jahne, *Digital Image Processing, Sixth Edition*, Springer, Berlin, 2012.
- P. A. Jansson, Editor, *Deconvolution of Images and Spectra*, Academic Press, New York, 1997.
- A. K. Jain, *Fundamentals of Digital Image Processing*, Prentice Hall, Englewood Cliffs, NJ, 1989.
- R. Jain, R. Kasturi and B. G. Schunck, *Machine Vision*, MIT Press and McGraw-Hill, New York, 1995.
- J. R. Jensen, *Introductory Digital Image Processing: A Remote Sensing Perspective*, Prentice Hall, Englewood Cliffs, NJ, 1985.
- I. Kabir, *High Performance Computer Imaging*, Prentice Hall, Englewood Cliffs, NJ, 1996.
- S. Kanef, Editor, *Picture Language Machines*, Academic Press, New York, 1970.
- H. R. Kang, *Color Technology for Electronic Imaging Devices*, Vol. PM28, SPIE Press, Bellingham, WA, 1997.
- H. R. Kang, *Digital Color Halftoning*, Vol. PM68, SPIE Press, Bellingham, WA, 1999.
- A. K. Katsaggelos, Editor, *Digital Image Processing*, Springer-Verlag, New York, 1991.
- F. Klette et al., *Computer Vision*, Springer-Verlag, New York, 1998.
- A. C. Kokaram, *Motion Picture Restoration*, Springer-Verlag, New York, 1998.
- P. A. Laplante and A. D. Stoyenko, *Real-Time Imaging: Theory, Techniques and Applications*, Vol. PM36, SPIE Press, Bellingham, WA, 1996.
- C. T. Leondes, Editor, *Image Processing and Pattern Recognition*, Academic Press, New York, 1997.
- M. D. Levine, *Vision in Man and Machine*, McGraw-Hill, New York, 1985.
- J. S. Lim, *Two-Dimensional Signal and Image Processing*, Prentice Hall, Englewood Cliffs, NJ, 1989.
- C. A. Lindley, *Practical Image Processing in C*, John Wiley and Sons, New York, 1991.
- B. S. Lipkin and A. Rosenfeld, Editors, *Picture Processing and Psychopictorics*, Academic Press, New York, 1970.
- R. P. Loce and E. R. Dougherty, *Enhancement and Restoration of Digital Documents: Statistical Design of Nonlinear Algorithms*, Vol. PM 29, SPIE Press, Bellingham, WA, 1997.
- D. A. Lyon, *Image Processing in Java*, Prentice Hall, Englewood Cliffs, NJ, 1999.
- A. Macovski, *Medical Imaging Systems*, Prentice Hall, Englewood Cliffs, NJ, 1983.
- Y. Mahdavih and R. C. Gonzalez, *Advances in Image Analysis*, Vol. PM08, SPIE Press, Bellingham, WA, 1992.
- V. K. Madisetti and D. B. Williams, *The Digital Signal Processing Handbook*, CRC Press, Boca Raton, FL, 1999.
- S. Mallat, *A Wavelet Tour of Signal Processing*, Academic Press, New York, 1998.
- S. Marchand-Maillet and Y. M. Sharaiha, *Binary Digital Image Processing*, Academic Press, New York, 1999.
- D. Marr, *Vision*, W. H. Freeman, San Francisco, 1982.

- A. McAndrew, *Elementary Image processing with MATLAB*, 2007.
- J. L. Mitchell, W. B. Pennebaker, C. E. Fogg and D. J. LeGall, *MPEG Video Compression Standard*, Kluwer Academic Publishers, Boston, 1996.
- S. Mitra and G. Sicuranza, Editors, *Nonlinear Image Processing*, Academic Press, New York, 2000.
- S. Montabone, *Beginning Image Processing*, Springer, New York, 2010.
- H. R. Myler, *Fundamentals of Machine Vision*, Vol. TT33, SPIE Press, Bellingham, WA, 1998.
- R. Nevatia, *Structure Descriptions of Complex Curved Objects for Recognition and Visual Memory*, Springer-Verlag, New York, 1977.
- R. Nevatia, *Machine Perception*, Prentice Hall, Englewood Cliffs, NJ, 1982.
- W. Niblack, *An Introduction to Digital Image Processing*, Prentice Hall, Englewood Cliffs, NJ, 1986.
- J. R. Parker, *Algorithms for Image Processing and Computer Vision*, John Wiley and Sons, New York, 1996.
- J. R. Parker, *Algorithms for Image Processing and Computer Vision*, Wiley Publishing, Indianapolis, 2011.
- T. Pavlidis, *Algorithms for Graphics and Image Processing*, Computer Science Press, Rockville, MD, 1982.
- W. B. Pennebaker and Joan L. Mitchell, *JPEG Still Image Data Compression Standard*, Van Nostrand Reinhold, New York, 1993.
- K. K. Parhi and T. Nishitani, Editors, *Digital Signal Processing for Multimedia Systems*, Marcel Dekker, 1999.
- W. B. Pennebaker and J. L. Mitchell, *JPEG Still Data Compression Standard*, van Nostrand Reinhold, New York, 1993.
- W. B. Pennebaker, J. L. Mitchell, C. Fogg and D. LeGall, *MPEG Digital Video Compression Standard*, Chapman and Hall, 1997.
- F. Pereira and T. Ebrahimi, Editors, *The MPEG-4 Book*, IMSC Press, 2002.
- M. Petrou, *Image Processing: The Fundamentals, Second Edition*, John Wiley and Sons, United Kingdom, 2010.
- I. Pitas, *Digital Image Processing Algorithms*, Prentice Hall, Englewood Cliffs, NJ, 1993.
- I. Pitas, *Digital Image Processing Algorithms and Applications*, John Wiley and Sons, New York, 2000.
- K. N. Plataniotis and A. N. Venetsanopoulos, *Color Image Processing and Applications*, Springer Verlag, New York, 2000.
- C. A. Poynton, *A Technical Introduction to Digital Video*, John Wiley and Sons, New York, 1996.
- W. K. Pratt, *Digital Image Processing*, Wiley-Interscience, New York, 1978.
- W. K. Pratt, Editor, *Image Transmission Techniques*, Advances in Electronics and Electron Physics, Supplement 12, Academic Press, New York, 1979.
- W. K. Pratt, *Digital Image Processing, Second Edition*, Wiley-Interscience, New York, 1991.

- W. K. Pratt, *PIKS Foundation C Programmer's Guide*, Manning Publications, Greenwich, CT, 1995.
- W. K. Pratt, *Developing Visual Applications, XIL: An Imaging Foundation Library*, Sun Microsystems Press, Mountain View, CA, 1997.
- W. K. Pratt, *Digital Image Processing, Third Edition*, Wiley-Interscience, New York, 2001.
- W. K. Pratt, *Digital Image Processing, Fourth Edition*, Wiley-Interscience, Hoboken, NJ., 2007.
- K. Preston, Jr. and L. Uhr, *Multicomputers and Image Processing, Algorithms and Programs*, Academic Press, New York, 1982.
- K. Preston, Jr. and M. J. B. Duff, *Modern Cellular Automata: Theory and Applications*, Plenum Press, New York, 1984.
- A. Puri and T. Chen, Editors, *Multimedia Systems, Standards and Networks*, Marcel Dekker, 2000.
- U. Qidwai and C. H. Chen, *Digital Image Processing: An Algorithmic Approach with MATLAB*, Chapman & Hall, 2009.
- M. Rabbani and P. W. Jones, *Digital Image Compression Techniques*, Volume TT7, SPIE - The International Society for Optical Engineering, Bellingham, WA, 1991.
- K. R. Rao and P. Yip, *Discrete Cosine Transform*, Academic Press, New York, 1990.
- K. R. Rao and J. J. Hwang, *Techniques and Standards for Image, Video, and Audio Coding*, Prentice Hall, Upper Saddle River, NJ, 1996.
- I. E. G. Richardson, *Video Codec Design*, John Wiley and Sons, New York, 2002.
- I. E. G. Richardson, *H.264 and MPEG-4 Video Compression*, John Wiley and Sons, New York, 2003.
- I. E. Richardson, *The H-264 Advanced Video Compression Standard, Second Edition*, John Wiley and Sons, Hoboken, NJ., 2010.
- M. J. Riley and I. E. G. Richardson, *Digital Video Communications*, Artech House, 1997.
- G. X. Ritter and J. N. Wilson (Contributor), *Handbook of Computer Vision Algorithms in Image Algebra*, Lewis Publications, New York, 1996.
- G. X. Ritter, *Handbook of Computer Vision Algorithms in Image Algebra, Second Edition*, Lewis Publications, New York, 2000.
- A. Rosenfeld, *Picture Processing by Computer*, Academic Press, New York, 1969.
- A. Rosenfeld; Editor, *Digital Picture Analysis*, Springer-Verlag, New York, 1976.
- A. Rosenfeld and A. C. Kak, *Digital Image Processing*, Academic Press, New York, 1976.
- A. Rosenfeld and A. C. Kak, *Digital Picture Processing, Second Edition*, Academic Press, San Diego, CA, 1986.
- J. C. Russ, *The Image Processing Handbook, Third Edition*, CRC Press, Boca Raton, FL, 1999.
- A. Sadka, *Compressed Video Communications*, John Wiley and Sons, New York, 2002.
- J. Sanchez and M. P. Canton, *Space Image Processing*, CRC Press, Boca Raton, FL, 1999.
- S. J. Sangwine and R. E. N. Horne, Editors, *The Colour Image Processing Handbook*, Kluwer, Norwell, MA, 1998.

- K. Sayood, *Introduction to Data Compression*, Morgan Kaufmann, San Francisco, 1996.
- R. J. Schalkoff, *Digital Image Processing and Computer Vision*, John Wiley and Sons, New York, 1989.
- P. Schelkens, A. Skodrrs and T. E. Branini, *The JPEG 2000 Suite*, John Wiley and Sons, Hoboken, NJ, 2009.
- R. A. Schowengerdt, *Remote Sensing: Models and Methods for Image Processing*, Academic Press, New York, 1997.
- J. Serra, *Image Analysis and Mathematical Morphology*, Academic Press, London, 1982.
- M. Seul, L. O’Gorman and M. J. Sammon, *Practical Algorithms for Image Analysis*, Cambridge University Press, New York, 2000.
- J. A. Sethian, *Level Set Methods and Fast Marching Methods, Second Edition*, Cambridge University Press, New York, 2000.
- I. Sezan and A. M. Tekalp, *Image Restoration*, Prentice Hall, Inc., Englewood Cliffs, NJ, 1992.
- M. I. Sezan, Editor, *Digital Image Restoration*, Vol. MS47, SPIE Press, Bellingham, WA, 1992.
- D. Sinha and E. R. Dougherty, *Introduction to Computer-Based Imaging Systems*, Vol. TT23, SPIE Press, Bellingham, WA, 1997.
- W. E. Snyder and H. Qi, *Machine Vision*, Cambridge University Press, New York, 2004.
- P. Soile, *Morphological Image Analysis: Principles and Applications, Second Edition*, Springer-Verlag, New York, 2003.
- C. Solomon and T. Breckon, *Fundamentals of Digital Image Processing: A Practical Approach with Examples in MATLAB*, Wiley-Blackwell, Hoboken, NJ, 2011.
- S. Sridhar, *Digital Image Processing*, Oxford University Press, United Kingdom, 2011.
- G. Stockman and L. G. Shapiro, *Computer Vision*, Prentice Hall, Englewood Cliffs, NJ, 2000.
- P. Stucki, Editor, *Advances in Digital Image Processing: Theory, Application, Implementation*, Plenum Press, New York, 1979.
- P. Symes, *Digital Video Compression (with CD-ROM)*, McGraw-Hill, New York, 2003.
- R. Szeliski, *Computer Vision: Algorithms and Applications*, Springer, London, 2011.
- T. Szoplik, Editor, *Morphological Image Processing: Principles and Optoelectronic Implementations*, Vol. MS127, SPIE Press, Bellingham, WA, 1996.
- S. Tanamoto and A. Klinger, Editors, *Structured Computer Vision: Machine Perception Through Hierarchical Computation Structures*, Academic Press, New York, 1980.
- S. L. Tanimoto and S. Olariu, *Parallel Computation in Image Processing*, Cambridge University Press, New York, 2000.
- D. Taubman and M. Marcellin, *JPEG 2000: Image Compression Fundamentals, Standards and Practice*, Kluwer Academic Publications, Boston, 2001.
- A. M. Telkap, *Digital Video Processing*, Prentice Hall, Englewood Cliffs, NJ, 1995.
- J. T. Tippett et al., Editors, *Optical and Electro-Optical Information Processing*, MIT Press, Cambridge, MA, 1965.
- M. M. Trivedi, *Digital Image Processing*, Vol. MS17, SPIE Press, Bellingham, WA, 1990.

- R. Ulichney, *Digital Halftoning*, MIT Press, Cambridge, MA, 1987.
- S. Ullman and W. Richards, Editors, *Image Understanding 1984*, Ablex Publishing, Norwood, NJ, 1984.
- S. E. Umbaugh, *Computer Vision and Image Processing*, Prentice Hall, Englewood Cliffs, NJ, 1997.
- S. E. Umbaugh, *Digital Image Processing and Analysis: Human and Computer Vision Applications with CVIptools, Second Edition*, CRC Press, Boca Raton, FL, 2010.
- A. Walsh and M. Bourges-Sevenir, Editors, *MPEG-4 Jump Start*, Prentice-Hall, Englewood Cliffs, NJ, 2002.
- A. R. Weeks, Jr., *Fundamentals of Electronic Image Processing*, Vol. PM32, SPIE Press, Bellingham, WA, 1996.
- P. F. Whelan and D. Molloy, *Machine Vision Algorithms in Java*, Springer-Verlag, New York, G. Wolberg, *Digital Image Warping*, IEEE Computer Society Press, New York, 1990.
- J. W. Woods, *Multidimensional Signal, Image, and Video Processing and Coding*, Second Edition, Academic Press, Waltham, MA, 2012.
- P. Yadav and A. Yadav, *Digital Image Processing, Kindle Edition*, University Science Press, New Delhi, 2010.
- T. Y. Young and K. S. Fu, Editors, *Handbook of Pattern Recognition and Image Processing*, Academic Press, San Diego, CA, 1986.
- N. Zuech, *Understanding and Applying Machine Vision, Second Edition*, Marcel Dekker, New York, 1999.

The subject of digital image processing has migrated from a graduate to a junior or senior level course as students become more proficient in mathematical background earlier in their college education. With that in mind, ***Introduction to Digital Image Processing*** is simpler in terms of mathematical derivations and eliminates derivations of advanced subjects. Most importantly, the textbook contains an extensive set of programming exercises for students.

The textbook examines the basic technologies needed to support image processing applications, including the characterization of continuous images, image sampling and quantization techniques, and two-dimensional signal processing techniques. It then covers the two principle areas of image processing: image enhancement and restoration techniques and extraction of information from an image. It concludes with discussions of image and video compression.

### Features:

- Covers the mathematical representation of continuous images and discrete images
- Discusses the psychophysical properties of human vision
- Analyzes and compares linear processing techniques implemented by direct convolution and Fourier domain filtering
- Details restoration models, point and spatial restoration and geometrical image modification
- Includes morphological image processing, edge detection, image feature extraction, image segmentation, object shape analysis, and object detection
- Describes coding technique applicable to still image and video coding based upon point and spatial processing
- Outlines the widely adopted JPEG and MPEG still image and video coding standards
- Text supported by a website, Pixel Soft, which provides downloading of software documentation, demonstration programs, programming exercise executables and image databases.

The author's accessible style provides historical background on the development of image processing techniques as well as a theoretical exposition. The inclusion of numerous exercises fully prepares students for further study.